NEW ADVANCES AND CHALLENGES IN SHALE OIL EXPLORATION

EDITED BY: Min Wang, Guochang Wang and Jinbu Li
PUBLISHED IN: Frontiers in Earth Science

About Frontiers

Frontiers is more than just an open-access publisher of scholarly articles: it is a pioneering approach to the world of academia, radically improving the way scholarly research is managed. The grand vision of Frontiers is a world where all people have an equal opportunity to seek, share and generate knowledge. Frontiers provides immediate and permanent online open access to all its publications, but this alone is not enough to realize our grand goals.

Frontiers Journal Series

The Frontiers Journal Series is a multi-tier and interdisciplinary set of open-access, online journals, promising a paradigm shift from the current review, selection and dissemination processes in academic publishing. All Frontiers journals are driven by researchers for researchers; therefore, they constitute a service to the scholarly community. At the same time, the Frontiers Journal Series operates on a revolutionary invention, the tiered publishing system, initially addressing specific communities of scholars, and gradually climbing up to broader public understanding, thus serving the interests of the lay society, too.

Dedication to Quality

Each Frontiers article is a landmark of the highest quality, thanks to genuinely collaborative interactions between authors and review editors, who include some of the world's best academicians. Research must be certified by peers before entering a stream of knowledge that may eventually reach the public - and shape society; therefore, Frontiers only applies the most rigorous and unbiased reviews.
Frontiers revolutionizes research publishing by freely delivering the most outstanding research, evaluated with no bias from both the academic and social point of view. By applying the most advanced information technologies, Frontiers is catapulting scholarly publishing into a new generation.

What are Frontiers Research Topics?

Frontiers Research Topics are very popular trademarks of the Frontiers Journals Series: they are collections of at least ten articles, all centered on a particular subject. With their unique mix of varied contributions from Original Research to Review Articles, Frontiers Research Topics unify the most influential researchers, the latest key findings and historical advances in a hot research area! Find out more on how to host your own Frontiers Research Topic or contribute to one as an author by contacting the Frontiers Editorial Office: frontiersin.org/about/contact

NEW ADVANCES AND CHALLENGES IN SHALE OIL EXPLORATION

Topic Editors:
Min Wang, China University of Petroleum, Huadong, China
Guochang Wang, Saint Francis University, United States
Jinbu Li, China University of Petroleum (East China), China

Table of Contents

Editorial: New Advances and Challenges in Shale Oil Exploration

Min Wang[1]*, Jinbu Li[1] and Guochang Wang[2]

[1]*Key Laboratory of Deep Oil and Gas, China University of Petroleum (East China), Qingdao, China,* [2]*Department of Engineering, Saint Francis University, Loretto, PA, United States*

Editorial on the Research Topic

New Advances and Challenges in Shale Oil Exploration

With the successful breakthrough in shale oil production, especially regarding medium to high maturity shale plays, there is now a potential resource addition to the world of energy resources. The geological theory, exploration, and development technology involved in shale oil resources have always been a hot topic. However, it remains challenging to efficiently and accurately assess shale oil reserves and identify sweet spot distribution. To improve efficiency and minimize risks in shale oil exploration and development, a special collection of high-quality original study and review articles into new advances and challenges in shale oil has been made in this Research Topic.

A total of 14 articles were received, 11 of which were accepted, that contain works on deposition, mineralogical, diagenesis, structure, geochemistry, and reservoir characterization, as well as a case study on shale oil plays such as Songliao, Ordos, Bohai Bay, and Sichuan Basin in China and the North Slope of Alaska. All articles accepted are within the scope of this Research Topic. Of the 14, 13 articles are original studies and one is a review article.

In the collected research, modeling of Tectonic-Thermal Evolution of Cretaceous Qingshankou Shale was reconstructed using the paleothermal indicator method. An improved method for 3D structural modeling using horizontal well data was developed by maximizing the utilization of horizontal well data and optimizing the quality of the structural model of shale reservoirs. In addition, shale oil enrichment was discussed from the perspective of paleosedimentary environment, lithofacies, and its heterogeneity. The influence of the diagenesis process as well as mineral composition on mudstone brittleness was proposed. The diagenetic transformation of clay minerals resulted in the increase of brittle components, thus illite and chlorite were considered to be brittle minerals for the first time. For shale oil sweet spot prediction, the role of soluble organic matter with different lithofacies, reservoir characteristics, and oil content in Hybrid Sedimentary Rocks were discussed in detail. Shale wettability and pores and surfaces are important factors that affect oil production. In this topic, the contact angle errors introduced by the pre-treatment of samples were discussed, and the wettability of the different lithofacies was characterized by an improved contact angle method. And the potential effects of the characteristics and properties of pores and surfaces on the fluid flow in shale formations were revealed. In addition to the above original studies, a review of mechanism, controls, and assessment on oil retention in shales were comprehensively investigated, and limitations and advantages of various methods were clearly noted. All of the research in this topic deepens the understanding of shale oil advances and challenges in shale oil exploration and provide a basis for further research.

AUTHOR CONTRIBUTIONS

JL wrote the manuscript, and MW revised it, and GW read the editorial abstract.

Modeling of Tectonic-Thermal Evolution of Cretaceous Qingshankou Shale in the Changling Sag, Southern Songliao Basin, NE China

Yuchen Liu[1,2], Bo Liu[2,3]*[†], LiJuan Cheng[2,3], Jilin Xing[4], Shansi Tian[2,3], Saipeng Huang[2,3] and Suying Dong[1]

[1]College of Geosciences, Northeast Petroleum University, Daqing, China, [2]Key Laboratory of Continental Shale Hydrocarbon Accumulation and Efficient Development, Ministry of Education, Northeast Petroleum University, Daqing, China, [3]Institute of Unconventional Oil and Gas, Northeast Petroleum University, Daqing, China, [4]PetroChina Jilin Oilfield Company, China National Petroleum Corporation, Songyuan, China

A series of significant shale oil discoveries have been made recently in the Upper Cretaceous Qingshankou Formation in the Songliao Basin, providing a new resource target for shale oil exploration in Northeast China. In this context, an understanding of the tectonic-thermal evolution and maturation history of the Qingshankou Formation is of great significance for shale oil exploration and evaluation. In this study, the thermal history of the Qingshankou Formation since the Late Cretaceous was reconstructed using the paleothermal indicator method. The results indicate that two stages of thermal evolution exist in the southern part of the Songliao Basin: 1) the gradual heating stage during the Late Cretaceous; the heat flow gradually increases during this period and reaches a maximum heat flow value at the end of the Cretaceous. 2) The decline stage since the Neogene; the tectonic activity is relatively stable and the geothermal heat flow is gradually reduced, and the present-day heat flow ranges from 60.1 to 100.7 mW/m^2, with an average of 78.2 mW/m^2. In addition, the maturity history of the organic-rich shale was reconstructed based on the new thermal history. The Cretaceous Qingshankou shales underwent deep burial thermal metamorphism at the end of the Cretaceous, whereas thermal has faded since the Neogene. The hydrocarbon generation and migration since the Late Cretaceous period of K_2qn_1 were modeled based on the maturity model. Two main cooling events took place in the late Nenjiang period and the late Mingshui period in the Changling sag. These two tectonic events controlled the structural style and the formation of shale oil reservoirs in the southern Songliao Basin.

Keywords: tectonic-thermal evolution, basin modeling, shale oil, Qingshankou Formation, southern Songliao Basin

INTRODUCTION

Rapid growth of the global demand for petroleum and gas resources has promoted exploration and development recently (International Energy Agency, 2011; Wang et al., 2015). Furthermore, with the successful development of shale gas in China, the exploration of shale oil has also been actively promoted (Jia et al., 2018; Sun et al., 2019; Zhang et al., 2020). The resource potential of shale oil in China has been verified and has mainly occurred in continental strata (such as the Cretaceous

formation of the Songliao Basin, the Upper Permian formation of the Junggar Basin and the Santanghu Basin, and the Upper Triassic formation of the Ordos Basin) (Liu et al., 2012; Zou et al., 2013; Gao et al., 2016). Significant exploration breakthroughs and discoveries of shale oil have been made recently in the Upper Cretaceous Qingshankou Formation in the Songliao Basin, providing a new resource target for shale oil exploration in Northeast China (Liu et al., 2017, 2019a, 2019b, 2021; Zhao et al., 2020). Previous studies mainly focused on the geochemical characteristics, lithofacies types, and the shale oil enrichment pattern of the Qingshankou Formation, indicating that the shale oil in the Qingshankou Formation (K_2qn), especially in the first member (K_2qn_1), represents a promising replacement resource for conventional oil (Liu et al., 2017, 2019a, 2019b; Zhang et al., 2020).

Thermal history is of great significance for studying the evolution of formation temperature, hydrocarbon generation, and primary migration histories (Pang et al., 2012; Kosakowski and Krzywiec, 2013; Zuo et al., 2015; Xu et al., 2018; Yu et al., 2020; Nansheng et al., 2021). The current methods for restoring the thermal history of sedimentary basins are generally divided into two categories. One is the paleothermal indicator method, mainly including vitrinite reflectance (Ro), fluid inclusions, clay mineral transformation, fission tracks (AFT and ZFT), and (U-Th)/He (Sweeney and Burnham, 1990; Crowley and Kevin, 1991; Tissot and Welte, 2013). The other uses the thermodynamic model to restore the thermal history of the basin (He et al., 2001, 2011; He, 2014). The former method has higher accuracy for sedimentary basins due to the fact that the simulation results can be verified with measured data. Previous studies mainly focused on the denudation and burial history of the Songliao Basin (Guo et al., 2009; Shi L. et al., 2019). However, little effort was put into reestablishing the thermal history and maturation histories of Qingshankou shale in the southern Songliao Basin. As the main controlling factor for source rock maturity, the pre-Cretaceous thermal history of the southern Songliao Basin should be restored to determine the hydrocarbon generation history and resource potential of the Qingshankou source rocks.

In this study, we reconstructed the tectonic-thermal evolution of the Qingshankou (K_2qn) Formation using a series of vitrinite reflectance. We modeled the thermal evolution of the source rocks in the southern Songliao Basin since the Late Cretaceous. In addition, based on the various geochemical parameters and the simulation method, the timing of hydrocarbon generation and the primary migration of the Qingshankou (K_2qn) source rocks are discussed. This study provides guidelines for shale oil exploration in the Cretaceous Qingshankou Formation of the southern Songliao Basin.

GEOLOGICAL SETTING

The Songliao Basin, located in Northeast China, has a strike extension to the northeast/north-northeast (NE–NNE). It is a composite Mesozoic–Cenozoic sedimentary basin, covering an area of approximately $2.6 km^2 \times 10^5 km^2$, extending $7.5 m \times 10^4 m$ in length and $(3.3–3.7) \times 104 m$ in width. The basin can be subdivided, based on basement morphology, major faults,

structural deformation, and sediment distribution, into six first-order tectonic units, including northern plunge, western slope, southwestern uplift, southeastern uplift, northeastern uplift, and central depression (Liu et al., 2021) (**Figure 1A**). With the Songhua River, the Nen River, and the Lalin River as the geographical boundaries, the Songliao Basin can be divided into two parts: the Daqing Oilfield exploration area in the north and the Jilin Oilfield exploration area in the south. The Jilin exploration area in the southern part of the central depression can be further divided into four secondary tectonic units: the Honggang terrace, the Changling sag, the Fuxin uplift belt, and the Huazijing terrace. For this study, the sampling wells are located in the northern part of the Changling sag (**Figure 1B**). The Changling sag is located in the southern part of the central depression. It is a large and gentle depression with a northeast trend and an area of about 6,500 km^2. It connects to the Gulong Sag to the north and is clamped by the Honggang terrace and the Huazijing terrace to the northwest and the southeast, respectively.

The Changling sag exhibits obvious characteristics of fault–depression superimposed sedimentation. During the faulting period, the main sedimentary formations are the Upper Jurassic–-Lower Cretaceous Huoshiling Formation (J_3h), Shahezi Formation (K_1sh), Yingcheng Formation (K_1yc), and Denglouku Formation (K_1d), with a maximum thickness of 5,000–7,000 m, which is dominated by terrigenous clastic rocks, volcanic rocks, and pyroclastic rocks. In the depression stage of the basin, the deposited formation includes the Lower Cretaceous Quantou Formation (K_1q) and the Upper Cretaceous Qingshankou Formation (K_2qn), Yaojia Formation (K_2y), Nenjiang Formation (K_2n), Sifangtai Formation (K_2s), and Mingshui Formation (K_2m). These strata are dominated by terrigenous clastic rocks, among which the Qingshankou Formation (K_2qn) serves as the main source rock for the shallower reservoirs in the basin (**Figure 1C**). The Qingshankou Formation can be further divided into the first member (K_2qn_1), the second member (K_2qn_2), and the third member (K_2qn_3). The K_2qn_2 and K_2qn_3 members are widely distributed in the basin with a thickness of 250–550 m. The corresponding lithology is mainly dark gray mudstone and fine sandstone, interbedded. The K_2qn_2 and K_2qn_3 members integrated contact with the K_2qn_1 member and the overlying Yaojia Formation. The lithology of the K_2qn_1 is mainly stable and thick semi-deep lake facies consisting of gray-black mudstone, which was deposited during the first large-scale lacustrine transgression in the basin (Wu et al., 2008; Feng et al., 2010; Liu et al., 2017; Zhang et al., 2020; Liu et al., 2019a, 2019b, 2021). The Songliao Basin has gone through four stages of structural evolution: the volcanic eruption and tension fracture stage (T-J3), the chasmic stage (J3-K1), the depression stage (K1-K2), and the tectonic reversal phase (K2-Q).

MODELING PROCEDURE

Burial History Model

Burial history reconstruction is the basis for thermal history modeling. In this part, the basic geological data, including the

FIGURE 1 | (A) Simplified distribution map of the tectonic units in the Songliao Basin. **(B)** Enlarged view of the southern part of the central depression of the Songliao Basin. **(C)** Composite stratigraphic columnar section of the southern part of the Songliao Basin [modified following Huang et al. (2011)].
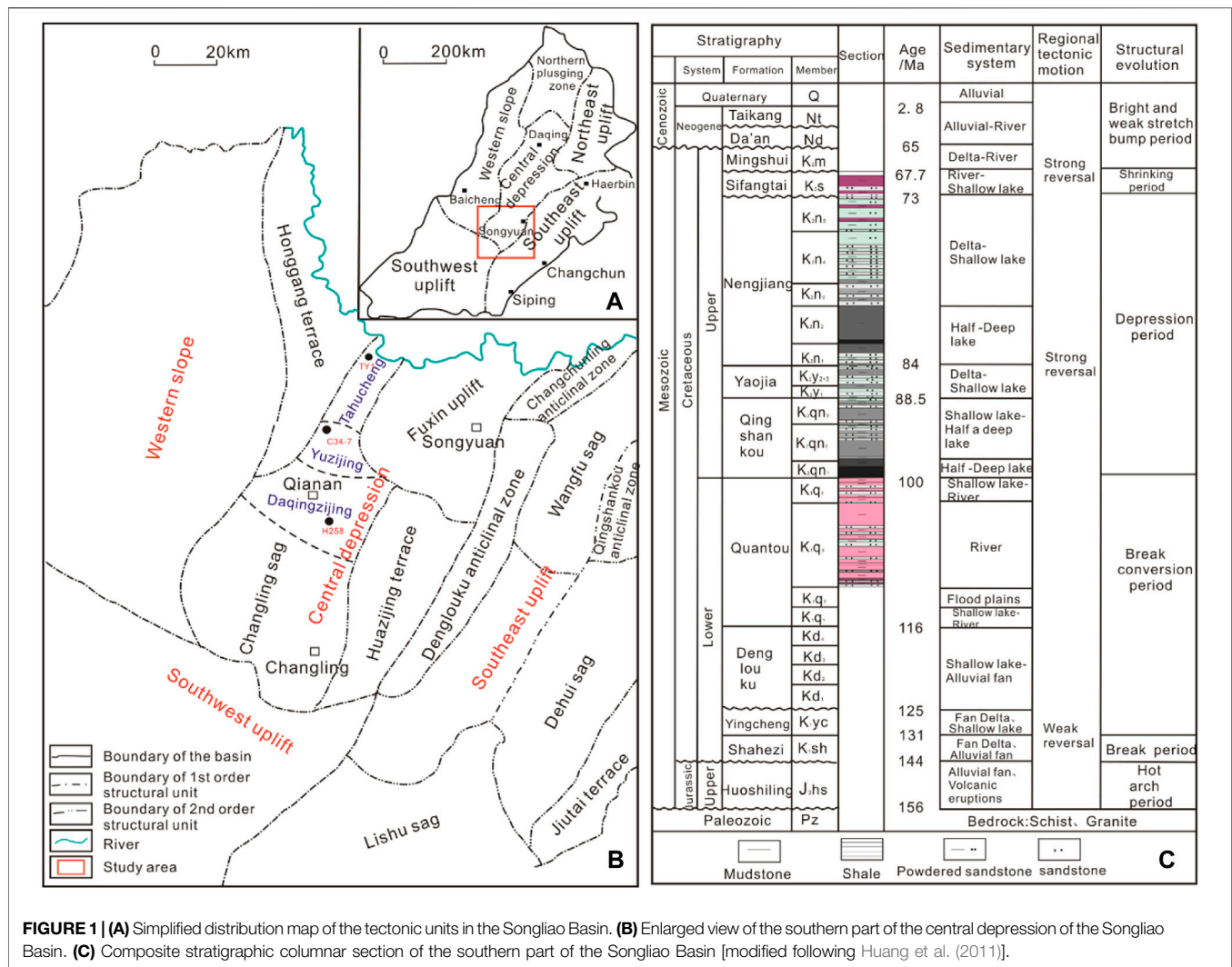
thickness, depths, lithologies, and geological ages, referred to the previous studies to construct burial histories (Shi Y. et al., 2019; Guo et al., 2009; Song et al., 2018; Fu et al., 2020). In addition, the erosion events and corresponding eroded thickness are site-specific and were thus considered separately. Since the Late Cretaceous, two main erosion events have taken place in the late Nenjiang Formation and the late Mingshui Formation of the Changling sag. As a result, two corresponding unconformities developed: the unconformity between the Sifangtai and the underlying Nenjiang strata and the unconformity between the Mingshui and the underlying Da'an strata (Guo et al., 2009; Song et al., 2018; Fu et al., 2020). The erosion amounts at the end of the Nenjiang Formation and the Mingshui Formation are 100–300 m and 200–500 m, respectively, and the extent of the erosion amounts gradually decreases from east to west (**Table 1**), which is due to the influence of the Pacific plate subducting westward in the late Paleozoic (Song et al., 2018).

Present Thermal Regime

In the thermal history recovery, the present temperature is one of the important constraints. The well-testing temperature is the ground temperature data obtained during the test oil pressure measurement in the oil-bearing interval of the development well, reflecting the temperature situation of boreholes. The present temperature and the geothermal gradient of forty-three wells in the Qingshankou Formation are shown in **Figure 2** and **Table 2**. The well-testing temperatures of boreholes demonstrated roughly linear temperature–depth relations, which means that the heat transfer in those boreholes is mainly *via* heat conduction. The present temperature in the Daqingzijing area, Yuzijing area, and Tahucheng area of the Qingshankou Formation is 95.7, 102, and 92.2°C, respectively (**Figure 2A**). The current geothermal gradient in the Daqingzijing area, Yuzijing area, and Tahucheng area of the Qingshankou Formation is 36.9, 38.9, and 40.28°C/km, respectively, showing that the present geothermal gradient gradually increases from south to north (**Figure 2B**).

TABLE 1 | Stratigraphy parameters of the Changling sag for burial history modeling.

Well #TY1

Formation or event name	Type	Begin age (Ma)	Top depth (m)	Present thickness (m)	Eroded thickness (m)
Q + N	F	0.1	0	75	–
$E_{2-3}y$	F	65	75	50	–
K_2m-erosion	E	66	–	–	–100
K_2m	F	67.7	125	300	–
K_2S	F	73	425	318.5	–
K_2n	F	84	743.5	872.68	–
K_2y	F	88.5	1,616.18	168.32	–
K_2qn2-3	F	97	1784.5	502.69	–
K_2qn_1	F	100	2,287.19	84.41	–
K_1q	F	116	2,371.6	157.4	–

Well #C34-7

Formation or event name	Type	Begin age (Ma)	Top depth (m)	Present thickness (m)	Eroded thickness (m)
Q + N	F	0.1	0	200	–
$E_{2-3}y$	F	65	200	25	–
K_2m-erosion	E	66	–	–	–217
K_2m	F	67.7	225	200	–
K_2S	F	73	425	343	–
K_2n-erosion	E	78	–	–	–100
K_2n	F	84	768	875	–
K_2y	F	88.5	1,643	140.5	–
K_2qn2-3	F	97	1783.5	517.51	–
K_2qn_1	F	100	2,301.01	87.42	–
K_1q	F	116	2,388.43	132.57	–

Well #Hei258

Formation or event name	Type	Begin age (Ma)	Top depth (m)	Present thickness (m)	Eroded thickness (m)
Q + N	F	0.1	0	100	–
$E_{2-3}y$	F	65	100	215	–
K_2m-erosion	E	66	–	–	–100
K_2m	F	67.7	315	334.5	–
K_2S	F	73	649.5	370.5	–
K_2n-erosion	E	78	–	–	–290
K_2n	F	84	1,020	653.97	–
K_2y	F	88.5	1,673.97	143.03	–
K_2qn2-3	F	97	1817	541.15	–
K_2qn_1	F	100	2,358.15	105.63	–
K_1q	F	116	2,463.78	46.22	–

Previous studies have measured the thermal conductivities from 435 core samples in the southern part of the Songliao Basin (Shi L. et al., 2019; Ma et al., 2019). These samples represent almost every lithology in different formations, including sandstone, shale, conglomerate, and volcanic. The frequency distribution histogram of the thermal conductivity of each lithological rock (**Figure 3**) shows that the average thermal conductivity value of shale is the lowest and the distribution range is 1.28–3.79 W/(mK), with a mean of 2.32 ± 0.48 W/(mK). Thus, the thermal conductivity shows a clear increasing trend with increasing depth. The thermal conductivity of sandstone is 1.85–4.48 W/(mK), with an average of 2.67 ± 0.33 W/(mK). The thermal conductivity of the conglomerate is 1.92–3.26 W/(mK), with an average of 2.72 ± 0.33 W/(mK). Finally, the volcanic thermal conductivity is relatively low, with an average of 2.54 ± 0.33W/m/K.

The present-day heat flow directly determines the thermal evolution and is a key input parameter in thermal history evolution (Qiu et al., 2012; Zhu et al., 2018). The surface heat-flow value was calculated using the temperature gradient and the harmonic mean thermal conductivity, as shown in **Eq. 1**. The harmonic mean thermal conductivity of the southern Songliao Basin is about 2.35 ± 0.33 W/(mK), using the measured thermal conductivity values and the thickness of different formations. Present-day heat flows in the southern part of the Songliao Basin range from 60.1 to 100.7 mW/m², with an average of 78.2 mW/m². Comparison with the northeast uplift, western slope, and southeast uplift of the Songliao Basin reflects a background with typically high heat flow (Ren et al., 2001; Ren et al., 2011), as shown below:

$$q_s = -K_t \cdot \frac{dT}{dZ}, \qquad (1)$$

where q_s is the surface heat flow (mW/m²), K_t is the harmonic mean thermal conductivity [W/(mK)], and $\frac{dT}{dZ}$ is the temperature gradient (°C/m²).

THERMAL HISTORY RECONSTRUCTION

Analytical Results of Equivalent Vitrinite Reflectance

We measured fifty vitrinite reflectance (%Ro) values from fourteen wells in the southern part of the Songliao Basin (**Table 3**). The vitrinite reflectance values of K_2qn_1 range from 0.99 to 1.36% Ro (average: 1.17% Ro), and the Ro of K_2qn_1 in the Tahucheng area (mean: 1.34%) is higher than that in the Yuzijing and Daqingzijing areas (mean: 1.11 and 1.10%) (**Figure 4**). In this study, the vitrinite reflectance profiles (%Ro) from three typical wells all show increasing trends with depth (**Figure 5**), indicating that all the strata reached a maximum temperature at the same time.

Burial and Thermal Results

This study used the equivalent vitrinite reflectance as the constraint condition and used the ancient heat flow method to recover the thermal history. The main steps are as follows: 1) we need to determine the amount of denudation in each period and
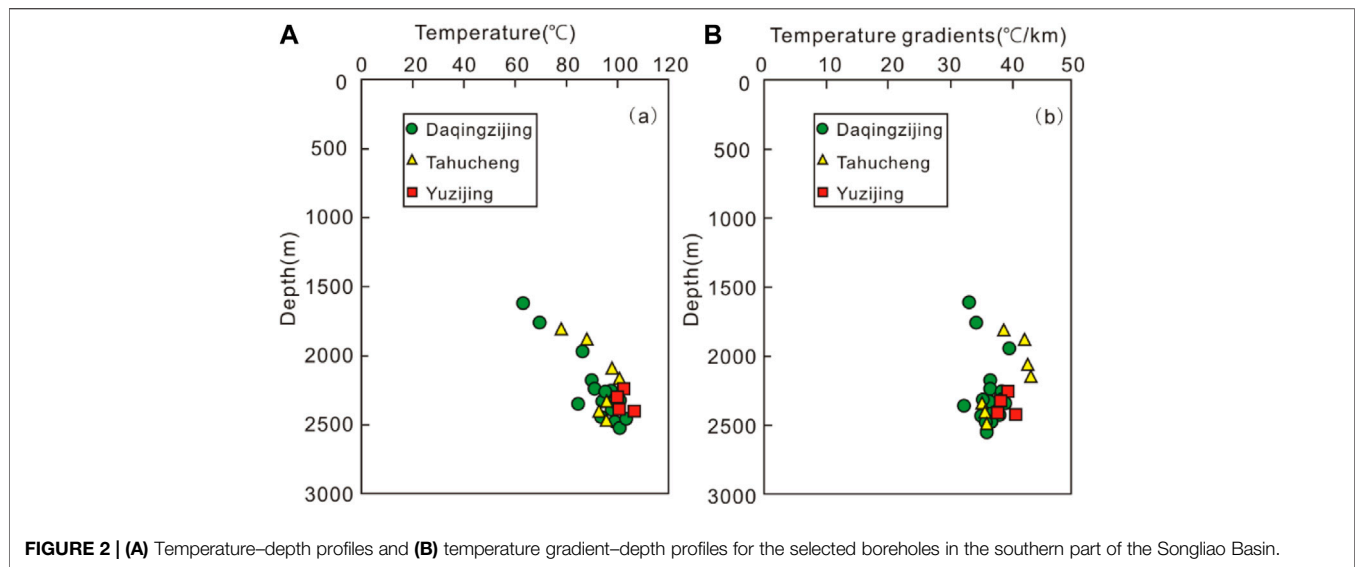
FIGURE 2 | (A) Temperature–depth profiles and **(B)** temperature gradient–depth profiles for the selected boreholes in the southern part of the Songliao Basin.

TABLE 2 | Results of temperature, geothermal gradient, and heat flow in the southern part of the Songliao Basin.

Tectonic unit	Well	Depth (m)	Temperature (°C)	Geothermal gradient (°C/km)	Heat flow (mW/m²)	Tectonic unit	Well	Depth (m)	Temperature (°C)	Geothermal gradient (°C/km)	Heat flow (mW/m²)
Daqingzijing area	H103	2,331	92.7	35.8	71.6	Daqingzijing area	H79-29-41	2,423	95.32	35.5	71.0
	H104	2,407	96.67	36.3	72.6		H80	2,521.9	101	36.4	72.7
	H111	2,458.4	102	37.7	75.5		H81	2,362.6	84.6	31.8	63.7
	H113	2,319	98.4	38.5	76.9		H87	2,254.6	96.1	38.5	77.1
	H138-1	2,394	101.15	38.4	76.8		H89-7	1946.6	87.22	40.1	80.2
	H143	2,356.6	99.61	38.4	76.7		H90-1	2,178.2	89.9	37.0	74.0
	H145	2,423.4	98.71	36.9	73.8		H91-1	2,477	101.84	37.4	74.8
	H146	2,442.6	101.7	37.9	75.7		H96-3	2,240.4	91	36.5	73.0
	H163	2,417.72	98.6	37.0	73.9		H98-3	2,306.4	98.6	38.8	77.5
	H47	2,404.6	98.9	37.3	74.6		H197	1760	69.54	34.2	68.4
	H50	2,433.4	100	37.3	74.6		H258	2,457	101.15	37.4	74.8
	H52	2,385.4	93.3	35.2	70.4		H77	2,440	94.31	34.8	69.7
	H57	2,346.2	99.9	38.6	77.3	Tahucheng area	Q160	1,624	63.38	33.3	66.6
	H59	2,512.6	98.9	35.7	71.3		Q180	2,414.9	97.3	36.5	72.9
	H59-11-3	2,508	100.6	36.4	72.8		D15	1894	87.7	41.5	82.9
	H60	2,421	97.3	36.4	72.7		D28	2,170.6	102	42.8	85.6
	H69	2,514	102	36.9	73.8		D45	2,103.6	99	42.7	85.4
	H71	2,304	97.7	38.4	76.8		D56	1812	79.26	38.6	77.3
	H72	2,438.2	101	37.6	75.3		TY1	2,356.6	93.7	35.8	71.6
	H74	2,270	95	37.8	75.6	Yuzijing area	C34-6	2,414.3	105.84	40.0	80.1
	H75	2,352.8	96.7	37.2	74.3		C93	2,383	99.32	37.8	75.6
	H76	2,372.2	98.9	37.8	75.6						

the basic geological parameters such as the thickness of the formation, the depth of the top and the bottom of the formation, lithology, and physical properties; 2) we assume a heat flow evolution history based on the tectonic geological background, and the parallel reaction model (EASY%Ro) is used to calculate the Ro value; 3) repeatedly modify the assumed thermal history so that the measured Ro value and the corresponding EASY% Ro theoretical model calculation value reach the best fit, and it is considered that the thermal history that can correctly reflect the basin's tectonic-thermal evolution process is obtained at this time. The burial and thermal

simulation results of three typical wells in different tectonic units of the Changling sag are presented in **Figures 6A,C,E**. The best matches between the measured and the modeled vitrinite reflectance were achieved (**Figures 6B,D,F**), indicating that the simulation results are reliable (Opera et al., 2013; Mohamed et al., 2016). The t-T thermal paths of three typical wells (**Figures 6A,C,E**) show that all samples underwent an overall heating stage after their deposition during the Late Cretaceous, followed by a slow cooling phase from the latest Cretaceous to recent times. In the Cretaceous, affected by the episodic westward compression from the Pacific Plate (Kusky

FIGURE 3 | Histogram of measured thermal conductivity of different lithologies in the Songliao Basin. **(A)** Shale; **(B)** sandstone; **(C)** conglomerate; **(D)** igneous rock; and **(E)** basement (modified following Shi Y. et al., 2019).
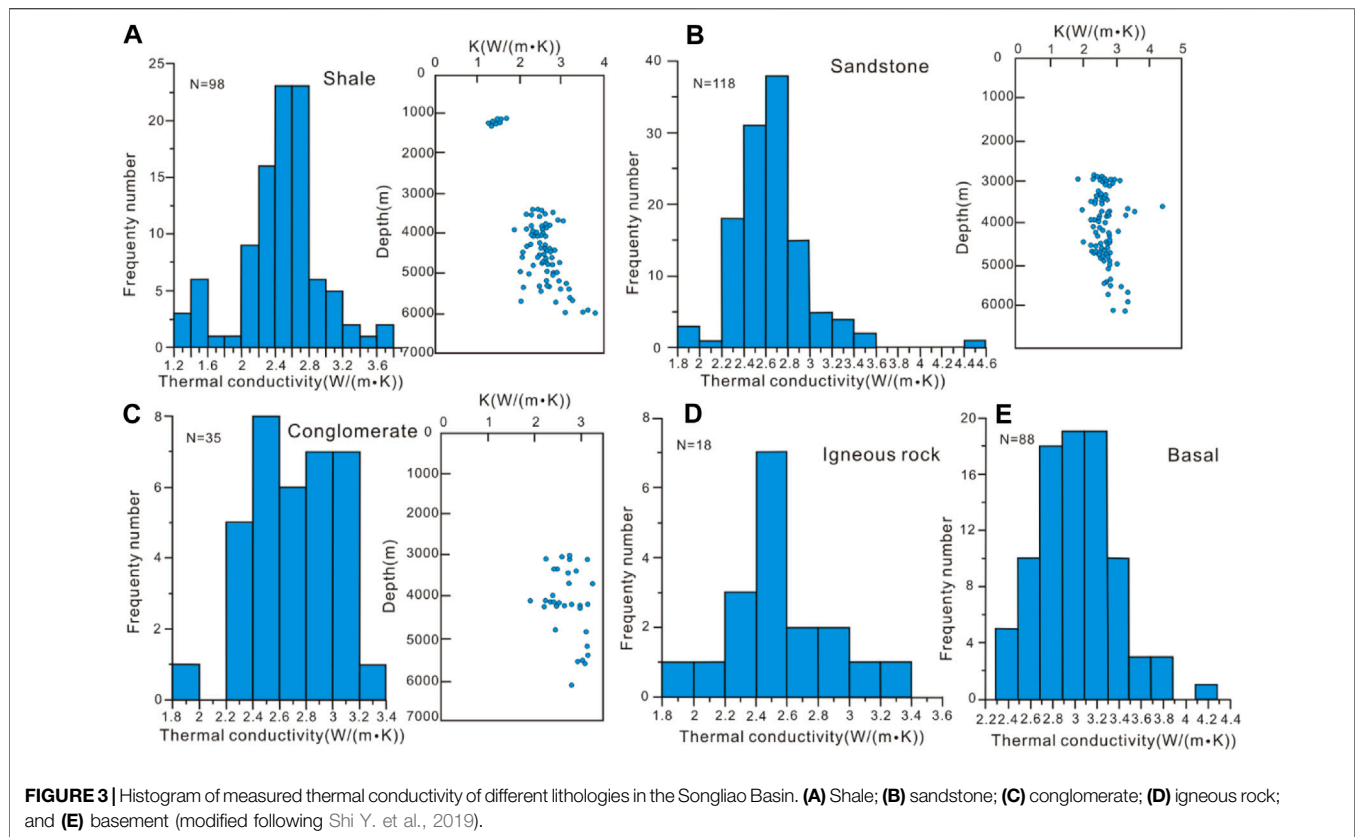
et al., 2016; Song et al., 2018; Wang et al., 2020), the sedimentary strata of the southern Songliao Basin suffered small-scale erosion. From the Early Cretaceous to the end of the Late Cretaceous, the study area subsided rapidly. The maximum subsidence rate reached nearly 120 m/Ma and reached the maximum burial depth of K_2qn_1 at a depth of ~2,400 m at the end of the Late Cretaceous. In this stage, the geothermal gradient is about ~49°C/km, and the maximum temperature of K_2qn_1 reached ~128°C. Thus, the maximum temperature and heat flow occurred at the end of the Cretaceous (**Figure 7**). This result was also proved by the apatite fission track data published by previous studies (Cheng et al., 2018; Song et al., 2018). There are two phases of heat flow evolution in the southern part of the Songliao Basin: 1) the gradual heating stage during the Late Cretaceous; the heat flow gradually increases during this period and reaches the maximum heat flow value at the end of the Cretaceous. 2) The decline stage since the Neogene; the tectonic activity is relatively stable, and the geothermal heat flow is gradually reduced during this period, while the present-day heat flows range from 60.1 to 100.7 mW/m^2, with an average of 78.2 mW/m^2.

DISCUSSION

Maturation Histories of the Qingshankou Source Rocks

The maturation histories of the source rocks control the timing of hydrocarbon generation and migration (Carminati et al., 2010;

Hudson and Hanson, 2010; Pang et al., 2012; Kosakowski and Krzywiec, 2013). The maturity histories of Qingshankou source rocks were calculated based on the constraints of newly obtained Ro data and the current temperature. The thermal model shows that the K_2qn_1 source rocks underwent an overall rapid heating stage after deposition during the Cretaceous and retained thermal maturation until the present day. In the well of C34–7 and H258, the K_2qn_1 source rocks entered the early maturation stage (0.5% < Ro<0.7%) and began to form hydrocarbons since ~85 Ma. At the end of the Late Cretaceous, with the study area subsiding rapidly, the maturity of the source rock entered the middle maturation stage (0.7% < Ro < 1.0%) and formed a large amount of oil. At present, the maturity of the source rock has mostly maintained the characteristics of the end of the Cretaceous. On the other hand, in the well of TY1 of the Tahucheng area, the thermal maturation is slightly higher than that of the Yuzijing and Daqingzijing areas (well C34–7 and H258), and it enters the late maturation stage (1.0% < Ro < 1.3%) at present. It is because the Tahucheng area is the center of deposition, and the buried depth is deeper here than it is in the other two areas. Hence, the thermal maturity of Qingshankou source rocks is slightly higher (**Figure 8**).

Based on the maturity model, the timing of hydrocarbon generation and primary migration since the Late Cretaceous period of K_2qn_1 has been modeled. The results showed that the hydrocarbon generation started from the Late Cretaceous (85 Ma). The maturity of source rocks reached the early oil stage

TABLE 3 | Results of vitrinite reflectance in the southern part of the Songliao Basin.

Well	Depth (m)	Ro (%)	Standard deviation	N	Well	Depth (m)	Ro (%)	Standard deviation	n
TY1	1,615.7	0.71	0.02	16	H258	2,368.4	1.12	0.08	23
TY1	2,370	1.36	0.1	17	H258	2,346	1.1	0.07	23
TY1	2,364.32	1.34	0.07	14	H258	2,464.1	1.18	0.07	30
TY1	2,349.2	1.32	0.07	9	H197	2,516.5	1.04	0.08	29
TY1	2,329.2	1.36	0.06	16	H197	2,529.3	1.09	0.08	30
TY1	2,317	1.21	0.01	10	H197	2,551.5	1.18	0.07	30
TY1	2,286	1.28	0.03	8	H170	1858.2	0.7	0.03	17
TY1	2,335.03	1.3	0.07	15	C34-7	2,342.05	1.1	0.07	15
TY1	2,330.2	1.35	0.06	13	C34-7	2,359.06	1.09	0.06	9
TY1	2,358.5	1.36	0.06	23	C34-7	2,369.5	1.14	0.09	17
H258	1,630	0.62	0.03	14	C19	1,590.1	0.68	0.02	6
H258	2,463.9	1.19	0.08	30	C59	2027.15	0.99	0.05	17
H258	2,451.1	1.17	0.04	30	C59	2030.7	1.07	0.06	30
H258	2,440.1	1.18	0.06	9	C59	2032.7	1.06	0.06	23
H258	2,419.5	1.13	0.08	17	C59	2034.6	1.05	0.06	25
H258	2,399.2	1.17	0.08	30	C59	2036.8	1.03	0.05	26
H258	2,358.03	1.09	0.05	9	H33-2-5	2,433.6	0.82	0.04	20
H258	2,469.7	1.2	0.08	30	H33-2-5	2,417.4	0.78	0.04	16
H258	2,451.1	1.19	0.08	30	H33-2-5	2,445	0.79	0.02	20
H258	2,441	1.16	0.06	23	H48	927.1	0.44	0.03	8
H258	2,436.1	1.18	0.06	23	H41	1,184.7	0.45	0.04	9
H258	2,421.5	1.16	0.08	23	Q193	1,460.5	0.61	0.02	16
H258	2,416.7	1.14	0.07	30	X171	809.6	0.56	0.06	19
H258	2,411.86	1.12	0.06	9	H136	726	0.46	0.04	16
H258	2,401.9	1.18	0.06	30	D51	1,142.9	0.56	0.02	10
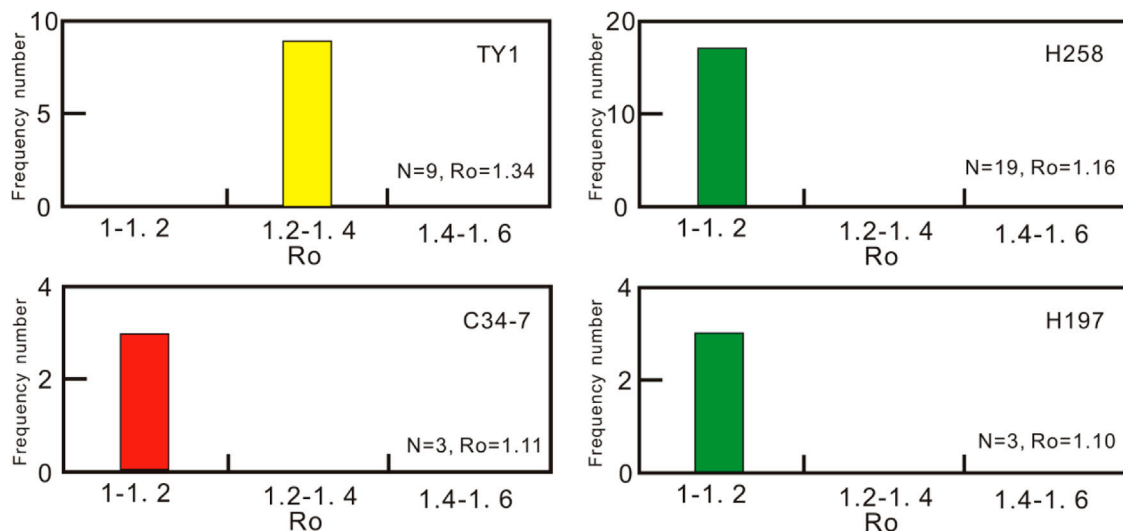
FIGURE 4 | Histograms of vitrinite reflectance of K_2qn_1 in the southern part of the Songliao Basin.

(0.5% < Ro < 0.7%) when a small amount of oil was generated, and the expulsion ratio is almost zero (**Figure 9**). At the end of the Late Cretaceous, the K_2qn_1 source rock began to generate a large amount of hydrocarbon with the rapid increase in the temperature (**Figure 9**), and the hydrocarbon migration took place at the end of the Late Cretaceous (68 Ma). Since the Neogene period, the maturity has mostly maintained characteristics of the end-Cretaceous; the hydrocarbon generation and expulsion of K_2qn_1 increase slowly, and the expulsion ratio reaches about 50%.
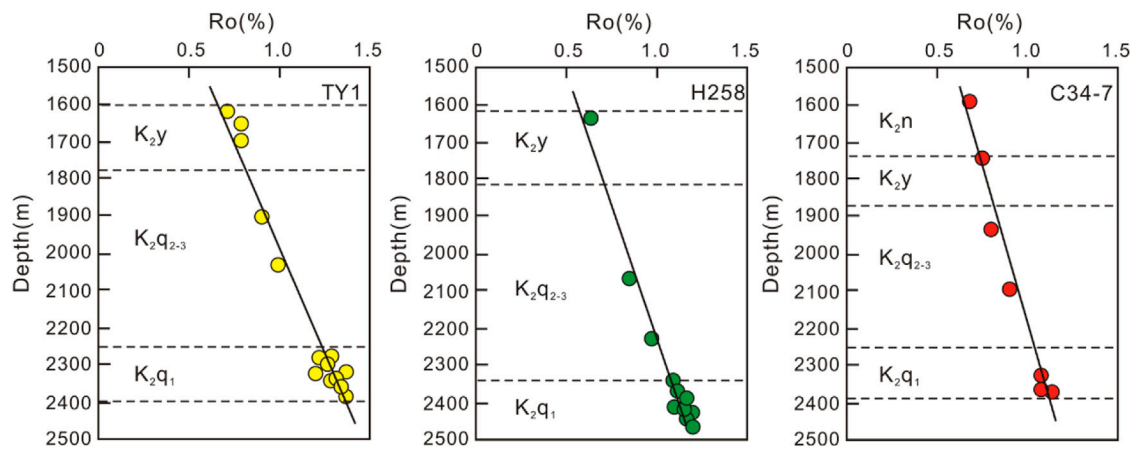
FIGURE 5 | Vitrinite reflectance (%Ro) vs. depth of three typical wells in the southern part of the Songliao Basin.

Additionally, the shale oil expulsion pattern of the K_2qn_1 was established according to the $(S1 + S2)$ and TOC data of the Songliao Basin (Fu and Pang, 2008). The inflection point of the variation of $(S1 + S2)$/TOC with burial depth is 1,900 m, indicating that the K_2qn_1 began to expel hydrocarbons from 1,900 m. According to the burial and thermal histories, hydrocarbon expulsion started at the end of the Late Cretaceous, consistent with the conclusions of modeling results. With the increase in burial depth, the rate of hydrocarbon expulsion first increases and then decreases, reaching the maximum at about 2,200 m. The corresponding hydrocarbon expulsion rate is about 20.2 mg/g.100 m. At the depth of about 2,400 m, the hydrocarbon expulsion efficiency of the source rock reaches about 50% (**Figure 10**).

In summary, the main hydrocarbon generation stage lasted from the Late Cretaceous to the Paleogene period (68–50 Ma). The rapid burial depth led to an increase in the temperature of the K_2qn_1, which greatly promoted the conversion of organic matter to hydrocarbons. This result led to significant hydrocarbon generation, forming a large amount of oil in the southern part of the Songliao Basin.

Relationship between the thermal history and tectonic evolution.

Since the Late Cretaceous, two main cooling events took place in the late Nenjiang period and the late Mingshui period of the Changling sag. In the late Nenjiang period, the Yanshan movement began to break out, and it was the squeeze fold movement covering the southern part of the Songliao Basin. During this period, the tectonic stress gradually decreases from south to north. So, the extent of cooling in the Daqingzijing area is higher than that in the Tahucheng area. The other squeeze fold movement took place in the late Mingshui period. However, the uplift amplitude is much lower than that of the uplift at the end of the Nenjiang, so the original sedimentary features are retained.

In the late Nenjiang period and the late Mingshui period, there was a period of compression tectonic movement, respectively, and the influence of these two tectonic movements on the

formation of shale oil is different. The tectonic movements of the late Nenjiang period mainly controlled the structural style of the Songliao Basin, which was the most intense structural movement affecting the entire Songliao Basin. The structural movement during this period formed the uplift belts in the eastern and southern Songliao Basin. On the other hand, the tectonic movements of the late Mingshui period mainly controlled the formation of shale oil reservoirs. During this period, the source rock matured rapidly, generating and expelling a large amount of oil. Comparing these two movements, the effect of the late Mingshui movement on the formation of shale oil reservoirs in the Changling area is significantly greater than that of the Nenjiang movement.

CONCLUSIONS

The thermal history of the southern Songliao Basin since the Late Cretaceous has been reconstructed using an integrated Ro data and Basinmod situation. The results show that two phases of thermal evolution exist in the southern part of the Songliao Basin: 1) the gradual heating stage from the Late Cretaceous to the Late Cretaceous; the heat flow gradually increases during this period, and it reaches the maximum heat flow value at the end of the Cretaceous. 2) The decline stage since the Neogene; the tectonic activity is relatively stable, and the geothermal heat flow is gradually reduced during this period, while the present-day heat flows range from 60.1 mW/m^2 to 100.7 mW/m^2, with an average of 78.2 mW/m^2.

The maturity histories of the source rocks were modeled based on the new thermal histories. The result indicates that the hydrocarbon generation started from the Late Cretaceous (85 Ma). The maturity of source rocks reached the early oil stage (0.5% < Ro < 0.7%) with a small amount of oil generation, and the expulsion ratio is almost zero. At the end of the Late Cretaceous, with the rapid increase in the temperature of the K_2qn_1 source rock, the source rock began to generate a large amount of hydrocarbon. Meanwhile, the hydrocarbon expulsion occurred at the end of the Late Cretaceous (68 Ma). Since the Neogene period, the maturity
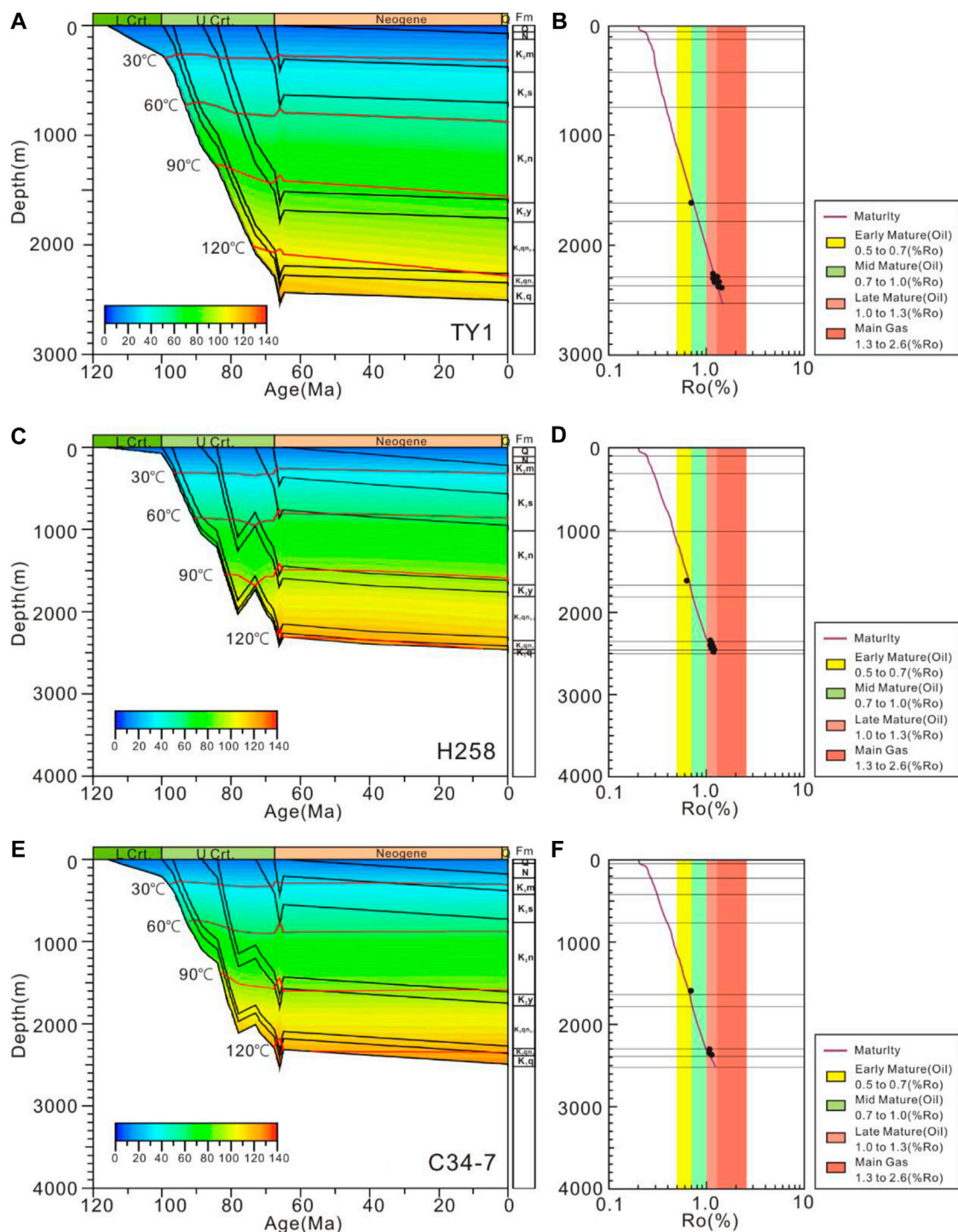
FIGURE 6 | The burial histories of the TY1 well **(A)**, the H258 well **(C)** and the C34-7 well **(E)**, and the thermal models of the TY1 well **(B)**, the H258 well **(D)** and the C34-7 well **(F)** in the southern part of the Songliao Basin.

mostly maintained the characteristics of the end of the Cretaceous; the hydrocarbon generation and expulsion of K_2qn_1 increased slowly, and the expulsion ratio is about 50%.

In summary, the Cretaceous Qingshankou source rocks underwent deep burial thermal metamorphism at the end of the Late Cretaceous and thermal fading since the Neogene. Two main cooling events took place in the late Nenjiang period and the late Mingshui period, which controlled the structural style and the formation of shale oil reservoirs in the southern Songliao Basin.
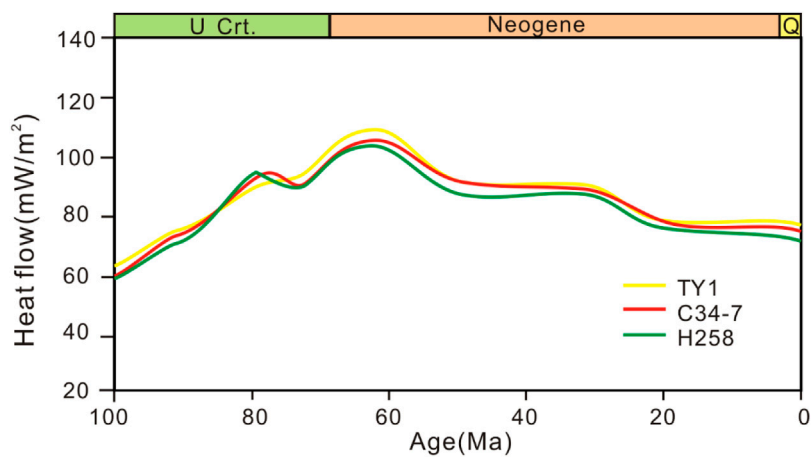
FIGURE 7 | Heat flow history of the typical wells in the southern part of the Songliao Basin.
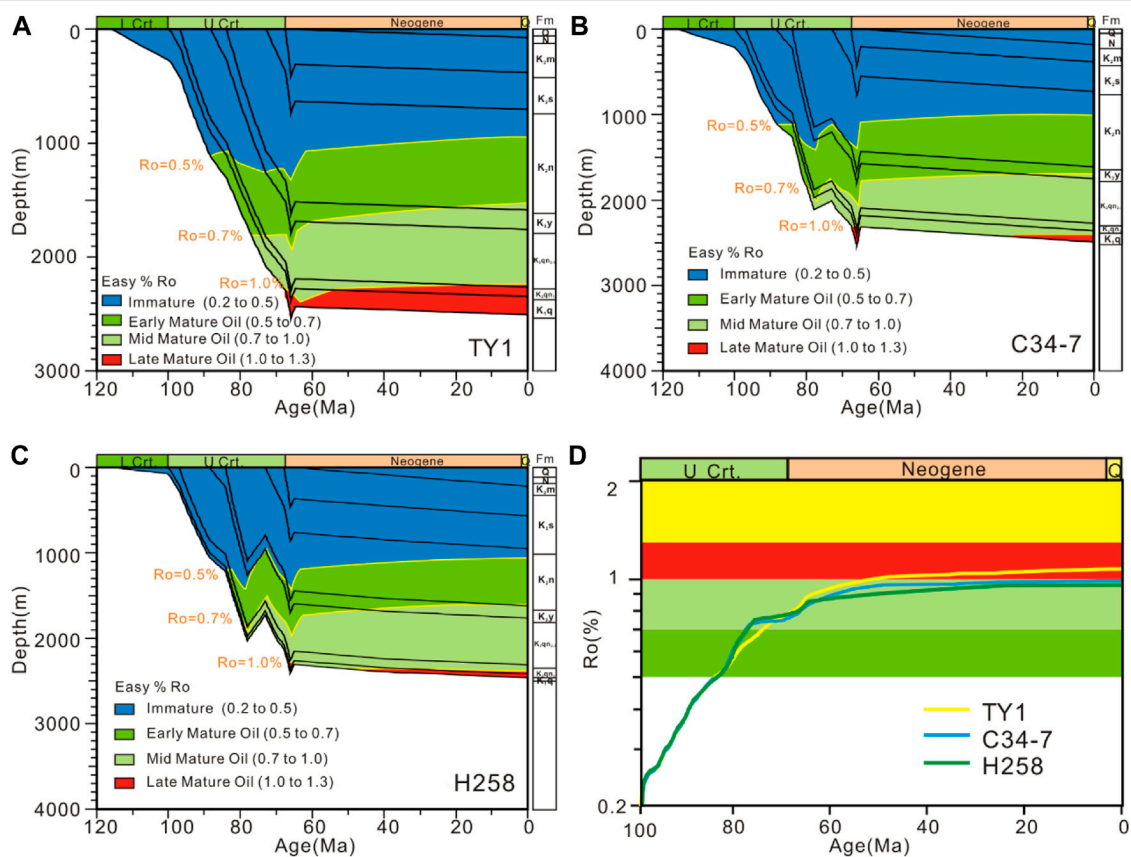
FIGURE 8 | Thermal maturity model of the TY1 well **(A)**, C34-7 well **(B)**, H258 well **(C)**, and the evolution profile of vitrinite reflectance (Ro) of three typical wells **(D)** in the southern part of the Songliao Basin. Timing of hydrocarbon generation and primary migration.
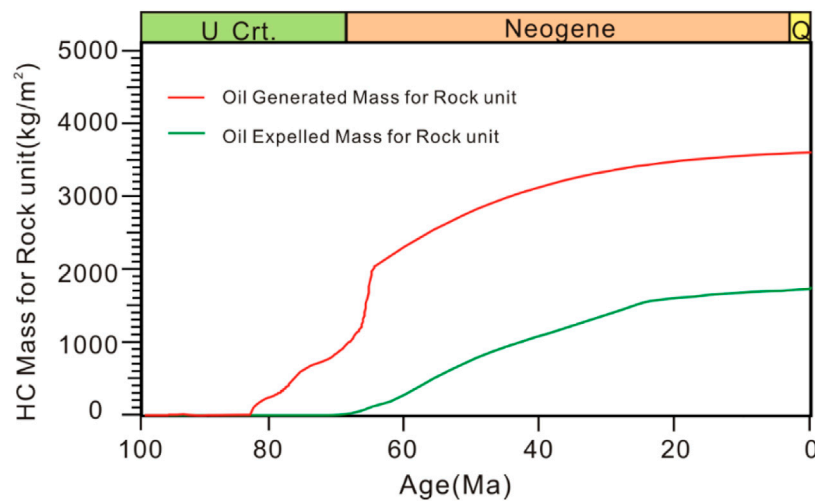
FIGURE 9 | Hydrocarbon generation and primary migration of the K_2qn_1 source rock in the southern part of the Songliao Basin.
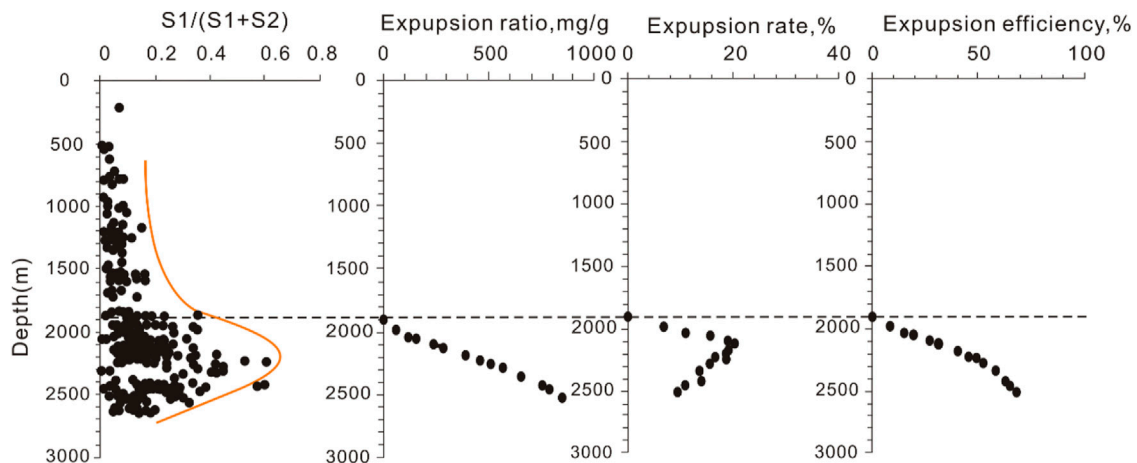
FIGURE 10 | Shale oil expulsion model of the K2qn1 in the southern part of the Songliao Basin [modified following Liu et al. (2017)].

DATA AVAILABILITY STATEMENT

The original contributions presented in the study are included in the article/Supplementary Material, further inquiries can be directed to the corresponding author.

AUTHOR CONTRIBUTIONS

BL devised the project. YL provided the main conceptual ideas and wrote the manuscript. LC, JX, SH, and ST helped with the sampling and data analysis, and SD worked on technical details and part of the thermal analysis. All authors contributed to the article and approved the submitted version.

REFERENCES

Carminati, E., Cavazza, D., Scrocca, D., Fantoni, R., Scotti, P., and Doglioni, C. (2010). Thermal and Tectonic Evolution of the Southern Alps (Northern Italy) Rifting: Coupled Organic Matter Maturity Analysis and Thermokinematic Modeling. *Bulletin* 94, 369–397. doi:10.1306/08240909069

Cheng, Y., Wang, S., Li, Y., Ao, C., Li, Y., Li, J., et al. (2018). Late Cretaceous-Cenozoic Thermochronology in the Southern Songliao Basin, NE China: New Insights from Apatite and Zircon Fission Track Analysis. *J. Asian Earth Sci.* 160, 95–106. doi:10.1016/j.jseaes.2018.04.015

Crowley, K. D., and Kevin, D. (1991). Thermal History of Michigan Basin and Southern Canadian Shield from Apatite Fission Track Analysis. *J. Geophys. Res.* 96 (B1), 697–711. doi:10.1029/90jb02174

Feng, Z., Jia, C., Xie, X., Zhang, S., Feng, Z., and Cross, T. (2010). Tectonostratigraphic Units and Stratigraphic Sequences of the Nonmarine Songliao Basin, Northeast China. *Basin Res.* 22, 79–95. doi:10.1111/j.1365-2117.2009.00445.x

Fu, X., and Pang, X. (2008). Expulsion Characteristics of Qing-1 Member Source Rock, Northern Songliao Basin. *J. Oil Gas Technol.* 30, 166–169.

Fu, X., Shi, H., Meng, Q., Liu, B., Liang, J., and He, J. (2020). Controlling Effects of the Structure and Deposition on the Shale Oil Enrichment: Taking Formation Qn1 in the Central Depression of Songliao Basin as an Instance. *Pet. Geology. Oilfield Develop. Daqing* 39, 56–71.

Gao, J., Liu, G., Yang, W., Zhao, D., Chen, W., and Liu, L. (2016). Geological and Geochemical Characterization of Lacustrine Shale, a Case Study of Lower Jurassic Badaowan Shale in the Junggar Basin, Northwest China. *J. Nat. Gas Sci. Eng.* 31, 15–27. doi:10.1016/j.jngse.2016.03.006

Guo, W., Yu, W., Liu, Z., and Ma, L. (2009). The Burial History of the Southern Songliao Basin. *J. Jilin Univ. (Earth Sci. Edition)* 39, 353–360.

He, L. (2014). Permian to Late Triassic Evolution of the Longmen Shan Foreland Basin (Western Sichuan): Model Results from Both the Lithospheric Extension and Flexure. *J. Asian Earth Sci.* 93, 49–59. doi:10.1016/j.jseaes.2014.07.007

He, L., Wang, K., Xiong, L., and Wang, J. (2001). Heat Flow and thermal History of the South China Sea. *Phys. Earth Planet. Interiors* 126, 211–220. doi:10.1016/s0031-9201(01)00256-4

He, L., Xu, H., and Wang, J. (2011). Thermal Evolution and Dynamic Mechanism of the Sichuan Basin during the Early Permian-Middle Triassic. *Sci. China Earth Sci.* 12, 1884–1891.

Huang, Q. H., Chun, W. H., and Wan, X. Q. (2011). New Progress of Integrated Chronostratigraphy of the Cretaceous in Songliao Basin. *J. Stratigr.* 35, 250–257.

Hudson, S. M., and Hanson, A. D. (2010). Thermal Maturation and Hydrocarbon Migration within La Popa Basin, Northeastern Mexico, with Implications for Other Salt Structures. *Bulletin* 94, 273–291. doi:10.1306/07130907012

International Energy Agency (2011). *World Energy Outlook*. Paris, France: Organization for Economic Cooperation and Development.

Jia, C., Zou, C., Yang, Z., Zhu, R., Chen, Z., Zhang, B., et al. (2018). Significant Progress of continental Petroleum Geological Theory in Basins of Central and Western China. *Pet. Exploration Develop.* 45, 573–588. doi:10.1016/S1876-3804(18)30064-8

Kosakowski, P., Wróbel, M., and Krzywiec, P. (2013). Modelling Hydrocarbon Generation in the Palaeozoic and Mesozoic Successions in Se Poland and West Ukraine. *J. Pet. Geology.* 36, 139–161. doi:10.1111/jpg.12548

Kusky, T. M., Polat, A., Windley, B. F., Burke, K. C., Dewey, J. F., Kidd, W. S. F., et al. (2016). Insights into the Tectonic Evolution of the North China Craton through Comparative Tectonic Analysis: A Record of Outward Growth of Precambrian Continents. *Earth-Science Rev.* 162, 387–432. doi:10.1016/j.earscirev.2016.09.002

Liu, B., Bai, L., Chi, Y., Jia, R., Fu, X., and Yang, L. (2019a). Geochemical Characterization and Quantitative Evaluation of Shale Oil Reservoir by Two-Dimensional Nuclear Magnetic Resonance and Quantitative Grain Fluorescence on Extract: A Case Study from the Qingshankou Formation in Southern Songliao Basin, Northeast China. *Mar. Pet. Geology.* 109, 561–573. doi:10.1016/j.marpetgeo.2019.06.046

Liu, B., He, S., Meng, L., Fu, X., Gong, L., and Wang, H. (2021). Sealing Mechanisms in Volcanic Faulted Reservoirs in Xujiaweizi Extension, Northern Songliao Basin, Northeastern China. *AAPG Bull.* doi:10.1306/03122119048

Liu, B., Lü, Y., Zhao, R., Tu, X., Guo, X., and Shen, Y. (2012). Formation Overpressure and Shale Oil Enrichment in the Shale System of Lucaogou Formation, Malang Sag, Santanghu Basin, NW China. *Pet. Exploration Develop.* 39, 744–750. doi:10.1016/S1876-3804(12)60099-8

Liu, B., Wang, H., Fu, X., Bai, Y., Bai, L., Jia, M., et al. (2019b). Lithofacies and Depositional Setting of a Highly Prospective Lacustrine Shale Oil Succession from the Upper Cretaceous Qingshankou Formation in the Gulong Sag, Northern Songliao Basin, Northeast China. *Bulletin* 103, 405–432. doi:10.1306/08031817416

Liu, C., Wang, Z., Guo, Z., Hong, W., Dun, C., Zhang, X., et al. (2017). Enrichment and Distribution of Shale Oil in the Cretaceous Qingshankou Formation, Songliao Basin, Northeast China. *Mar. Pet. Geology.* 86, 751–770. doi:10.1016/j.marpetgeo.2017.06.034

Ma, F., Wang, G., Sun, Z., Zhang, W., Hou, H., and Guo, X. (2019). An Analysis of Thermal Conductivity in Songliao Basin Based on Logging Parameters. *Acta Geoscientica Sinica* 40, 350–360.

Mohamed, A. Y., Whiteman, A. J., Archer, S. G., and Bowden, S. A. (2016). Thermal Modelling of the Melut basin Sudan and South Sudan: Implications for Hydrocarbon Generation and Migration. *Mar. Pet. Geology.* 77, 746–762. doi:10.1016/j.marpetgeo.2016.07.007

Nansheng, Q., Wen, L., Xiaodong, F., Wenzheng, L., Qiuchen, X., and Chuanqing, Z. (2021). Maturity Evolution of Lower Cambrian Qiongzhusi Formation Shale of the Sichuan Basin. *Mar. Pet. Geology.* 128, 105061. doi:10.1016/j.marpetgeo.2021.105061

Opera, A., Alizadeh, B., Sarafdokht, H., Janbaz, M., Fouladvand, R., and Heidarifard, M. H. (2013). Burial History Reconstruction and thermal Maturity Modeling for the Middle Cretaceous-Early Miocene Petroleum System, Southern Dezful Embayment, SW Iran. *Int. J. Coal Geology.* 120, 1–14. doi:10.1016/j.coal.2013.08.008

Pang, X., Liu, K., Ma, Z., Jiang, Z., Xiang, C., Huo, Z., et al. (2012). Dynamic Field Division of Hydrocarbon Migration, Accumulation and Hydrocarbon Enrichment Rules in Sedimentary Basins. *Acta Geologica Sinica* 86, 1559–1592. doi:10.1111/1755-6724.12023

Qiu, N., Chang, J., Zuo, Y., Wang, J., and Li, H. (2012). Thermal Evolution and Maturation of Lower Paleozoic Source Rocks in the Tarim Basin, Northwest China. *Bulletin* 96, 789–821. doi:10.1306/09071111029

Ren, Z., Xiao, D., Chi, Y., Ren, Y., and Liang, Y. (2011). Restoration of thermal History of the Permo-Carboniferous Basement in the Songliao Basin. *Oil& GAS GEOLOGY.* 32, 430–439.

Ren, Z., Xiao, D., and Chi, Y. (2001). Restoration of Paleotemperature in Songliao Basin. *Pet. Geology. Oilfield Develop. Daqing* 20, 13–16.

Shi, L., Qi, Y., Zhang, Y., Wang, Z., and Wang, B. (2019a). Numerical Simulation of Geohistory of the Qijia Area in the Songliao basin and Geological Significance. *Geology. Exploration* 55 (2), 661–672.

Shi, Y., Jiang, G., Zhang, X., Yuan, Z., Wang, Z., Qiu, Q., et al. (2019b). Present Temperature Field Characterization and Geothermal Resource Assessment in the Harbin Area, Northeast China. *Energy Exploration & Exploitation* 37, 834–848. doi:10.1177/0144598718815922

Song, Y., Ren, J., Liu, K., Shen, C., and Stepashko, A. (2018). Post-rift Anomalous thermal Flux in the Songliao Basin, NE China, as Revealed from Fission Track Thermochronology and Tectonic Analysis. *Palaeogeogr. Palaeoclimatol. Palaeoecol.* 508, 148–165. doi:10.1016/j.palaeo.2018.07.030

Sun, L., Zou, C., Jia, A., Wei, Y., Zhu, R., Wu, S., et al. (2019). Development Characteristics and Orientation of Tight Oil and Gas in China. *Pet. Exploration Develop.* 46, 1073–1087. doi:10.1016/S1876-3804(19)60264-8

Sweeney, J., and Burnham, A. (1990). Evaluation of a Simple Model of Vitrinite Reflectance Based on Chemical Kinetics. *AAPG Bull.* 10, 1559–1570. doi:10.1306/0c9b251f-1710-11d7-8645000102c1865d

Tissot, B., and Welte, D. (2013). *Petroleum Formation and Occurrence*. Springer Science & Business Media.

Wang, J., Feng, L., Steve, M., Tang, X., Gail, T. E., and Mikael, H. (2015). China's Unconventional Oil: A Review of its Resources and Outlook for Long-Term Production. *Energy* 82, 31–42. doi:10.1016/j.energy.2014.12.042

Wang, S., Cheng, Y., Zeng, L., Miao, P., Jin, R., Zhang, T., et al. (2020). Thermal Imprints of Cenozoic Tectonic Evolution in the Songliao Basin, NE China:

Evidence from Apatite Fission-Track (AFT) of CCSD-SK1 Borehole. *J. Asian Earth Sci.* 195, 104353. doi:10.1016/j.jseaes.2020.104353

Wu, H., Zhang, S., and Huang, Q. (2008). Establishment of Floating Astronomical Time Scale for the Terrestrial Late Cretaceous Qingshankou Formation in the Songliao Basin of Northeast China. *Earth Sci. Front.* 15, 159–169. doi:10.1016/s1872-5791(08)60049-4

Xu, Q., Qiu, N., Liu, W., Shen, A., and Wang, X. (2018). Thermal Evolution and Maturation of Sinian and Cambrian Source Rocks in the central Sichuan Basin, Southwest China. *J. Asian Earth Sci.* 164, 143–158. doi:10.1016/j.jseaes.2018.06.015

Yu, K., Ju, Y., and Zhang, B. (2020). Modeling of Tectono-thermal Evolution of Permo-Carboniferous Source Rocks in the Southern Qinshui Basin, China: Consequences for Hydrocarbon Generation. *J. Pet. Sci. Eng.* 193, 107343. doi:10.1016/j.petrol.2020.107343

Zhang, J., Xu, X., Bai, J., Liu, W., Chen, S., Liu, C., et al. (2020). Enrichment and Exploration of Deep Lacustrine Shale Oil in the First Member of Cretaceous Qingshankou Formation, Southern Songliao Basin, NE China. *Pet. Exploration Develop.* 47, 683–698. doi:10.1016/S1876-3804(20)60085-4

Zhao, Z., Littke, R., Zieger, L., Hou, D., and Froidl, F. (2020). Depositional Environment, thermal Maturity and Shale Oil Potential of the Cretaceous Qingshankou Formation in the Eastern Changling Sag, Songliao Basin, China: An Integrated Organic and Inorganic Geochemistry Approach. *Int. J. Coal Geology.* 232, 103621. doi:10.1016/j.coal.2020.103621

Zhu, C., Hu, S., Qiu, N., Jiang, Q., Rao, S., and Liu, S. (2018). Geothermal Constraints on Emeishan Mantle Plume Magmatism: Paleotemperature

Reconstruction of the Sichuan Basin, SW China. *Int. J. Earth Sci. (Geol Rundsch)* 107, 71–88. doi:10.1007/s00531-016-1404-2

Zou, C., Yang, Z., Cui, J., Zhu, R., Hou, L., Tao, S., et al. (2013). Formation Mechanism, Geological Characteristics and Development Strategy of Nonmarine Shale Oil in China. *Pet. Exploration Develop.* 40, 15–27. doi:10.1016/S1876-3804(13)60002-6

Zuo, Y.-h., Qiu, N.-s., Hao, Q.-q., Pang, X.-q., Gao, X., Wang, X.-j., et al. (2015). Geothermal Regime and Source Rock thermal Evolution in the Chagan Sag, Inner Mongolia, Northern China. *Mar. Pet. Geology.* 59, 245–267. doi:10.1016/j.marpetgeo.2014.09.001

The Role of Soluble Organic Matter in Shale Oil "Sweet Spots" Prediction: An Investigation of Shale With Different Lithofacies in the Dongying Sag

Jinyi He[1], Jingong Cai[1]*, Xiaojun Zhu[1]*, Mingshui Song[2], Huimin Liu[2], Xuejun Wang[2] and Xiang Zeng[1]

[1]State Key Laboratory of Marine Geology, Tongji University, Shanghai, China, [2]Research Institute of Exploration and Development, Shengli Oilfield Company, Dongying, China

Lithofacies are the fundamental geological units for shale oil and gas exploration and development, and soluble organic matter (SOM) is most similar to crude oil in composition. Both aspects attract our attention in the interpretation of SOM in different lithofacies, which can provide direct evidence to predict shale oil "sweet spots". Here, twenty-five shale samples were collected from the Eocene Shahejie Formation in the Dongying Sag and were subjected to X-ray diffraction, Rock-Eval pyrolysis, and SOM characterization. Comparison of the SOM contents in shales with different lithofacies revealed remarkable differences: 1) The contents of SOM, saturates and total hydrocarbons (THC) showed the order of detrital massive mudstone < homogenous massive mudstone < wide laminated shale < discontinuous laminated shale < fine laminated shale < gypsum-bearing mudstone, and the SOM content was controlled by lithofacies through differences in both OM and minerals. 2) The SOM in detrital and homogenous massive mudstones was mainly composed of saturates and resins. Saturates were the main component in wide and fine laminated shales. The SOM in discontinuous laminated shale was mainly composed of saturates and aromatics. The SOM in gypsum-bearing mudstone was mainly composed of saturates, and the percentage of asphaltenes was quite high. Based on the evaluation parameters of high-quality lithofacies in terms of abundance (i.e., SOM, THC or saturate contents) and quality (i.e., quality index and asphaltene percentage), the fine, wide and discontinuous laminated shales were regarded as relatively favorable lithofacies. Based on the lithofacies combination, the fine, wide and discontinuous laminated shales in Es3x and Es4ss (upper section of Es4s) in the Dongying Sag were interpreted as "sweet spots" for shale oil exploration and development. Thus, it is of great significance to study the characteristics of SOM in shale with different lithofacies for shale oil exploration and development.

Keywords: shale, soluble organic matter, lithofacies, shale oil, sweet spots

INTRODUCTION

Shale oil and gas has become a hot topic in the exploration and development of unconventional oil and gas resources around the world and has attracted wide attention from petroleum geologists (Jarvie, 2012; Wang et al., 2015; Misch et al., 2016; Kumar et al., 2017; Chen et al., 2018; Wang et al., 2020; Zou et al., 2020; Hou et al., 2021a). A lithofacies is a rock type or rock combination that forms in a certain sedimentary environment and is the main component of sedimentary facies (Yang et al., 2015). As fundamental units representing the sedimentary environment, lithofacies are mainly identified by rock color, composition, structure and other characteristics (Xie, 2009; Zhang J et al., 2016). Moreover, lithofacies are the fundamental geological units for well logging identification, stratigraphic correlation and reservoir evaluation in shale oil and gas exploration and development (Yang et al., 2015; Zhang et al., 2015; Zhang Y et al., 2016). Thus, lithofacies are of great significance to unconventional petroleum geology.

During different sedimentary stages, shale is significantly affected by its ambient physical, chemical and biological environments and can be grouped into various types of lithofacies with distinct characteristics (Seville et al., 2000; Bennett et al., 2012; Zeng et al., 2017). Many researchers have classified shale lithofacies under different rules and discussed their origin, sedimentary environment, hydrocarbon generation potential, reservoir space and diagenetic evolution (Hickey and Henk, 2007; Loucks and Ruppel, 2007; Xie, 2009; Abouelresh and Slatt, 2012; Fu et al., 2013; Wang et al., 2014; Wang et al., 2016; Zhang J et al., 2016; Zeng et al., 2017; Liang et al., 2018). Within shale, soluble organic matter (SOM) is an important product of hydrocarbon generation (Zhu et al., 2016). Normally, SOM extracted by organic solvents is mainly free in pores and physically adsorbed onto mineral surfaces (Rumpel et al., 2005; Pan and Liu, 2009; Wei et al., 2014; Zhu et al., 2016; Hou et al., 2021b), and has a composition similar to that of crude oil (Song et al., 2013; Liu et al., 2014). However, few reports have been made on the characteristics of shale oil in different lithofacies. As a consequence, understanding shale SOM in different lithofacies can help to understand the crude oil in shale and is beneficial to selecting a lithofacies that can generate high-quality shale oil. In this paper, the lithofacies that can generate high-quality shale oil is termed high-quality lithofacies.

In the present study, we selected typical shale samples from the Shahejie Formation in the Dongying Sag and employed different methods to 1) compare the differences in shale SOM in different lithofacies; 2) clarify the factors controlling the shale SOM content in different lithofacies; and 3) establish the evaluation parameters of high-quality lithofacies and predict shale oil "sweet spots". Our results are practical and significant to shale oil exploration and development.

SAMPLES AND METHODS

Samples

The Dongying Sag is a secondary structural unit in the Jiyang Depression in the Bohai Bay Basin (**Figure 1**) (Li et al., 2015; Zeng et al., 2017). A large suite of lacustrine shale was developed in the upper fourth submembers (Es4s, which can also be divided into Es4sx and Es4ss from bottom to top), lower third submembers (Es3x) and middle third submembers (Es3z) of the Eocene Shahejie Formation (**Figure 1**), which is the main source rock in the sag (Zhang et al., 2009; Zeng et al., 2017). In particular, several industrial oil-flow wells of shale oil have been developed in Es4s and Es3x in the sag (Zhang et al., 2008; Zhang L et al., 2012; Li, 2014; Bao et al., 2016). In the sag, the lithologies and sedimentary environments of the shales in different members are quite different (Zeng et al., 2017): 1) Massive mudstone and gypsum mudstone are developed in Es4sx, which comprises intermittent saltwater lake sediments; 2) gray-black oil shale and laminated shale are developed in Es4ss, which comprises perennial closed saltwater lake deposits; 3) a set of black shale and oil shale are present in Es3x, which comprises brackish and deep lake deposits; and 4) massive mudstone and siltstone are developed in Es3z, indicating that the lake was markedly shallower.

In this study, shale core samples from depths of 2,954–3,496 m are selected from Es4s, Es3x and Es3z from wells NY1 and N38 in the Dongying Sag (**Figure 1**). Sixteen samples from well NY1 were distributed in Es4s and Es3x, and nine samples from well N38 were distributed in Es3x and Es3z. These studied shales have been grouped into different lithofacies, and the lithofacies classification integrates the shale rock type, mineral composition, sedimentary structure, and OM characteristics (Zeng et al., 2017). Overall, there were six types of lithofacies: fine laminated shale (Fl), wide laminated shale (Wl), discontinuous laminated shale (Dl), homogenous massive mudstone (Hm), detrital massive mudstone (Dm) and gypsum-bearing mudstone (Gb) (**Figure 2**; **Supplementary Material**). It should be noted that there was only one sample for the discontinuous laminated shale or gypsum-bearing mudstone, resulting in that the comparisons from these two lithofacies were limited in the present study.

X-Ray Diffraction

X-ray diffraction (XRD) was used to examine the mineral composition of the original shale samples. The XRD analyses were performed under an X'PERT-PRO-MPD diffractometer (PANalytical, Amelo, Netherlands) using a CuK X-ray tube at 40 mA and 40 kV with a curved graphite monochromator. The CuK α radiation wavelength was 1.540,596 Å. The scattering slit was 1°, and the receiving slit was 0.3 mm. Each oriented slide was scanned from 3 to 30°2θ at 2°2θ/min using a step width of 0.02°2θ. The randomly oriented powder mounts were scanned from 3 to 40°2θ at 2°2θ/min using a step width of 0.02°2θ.
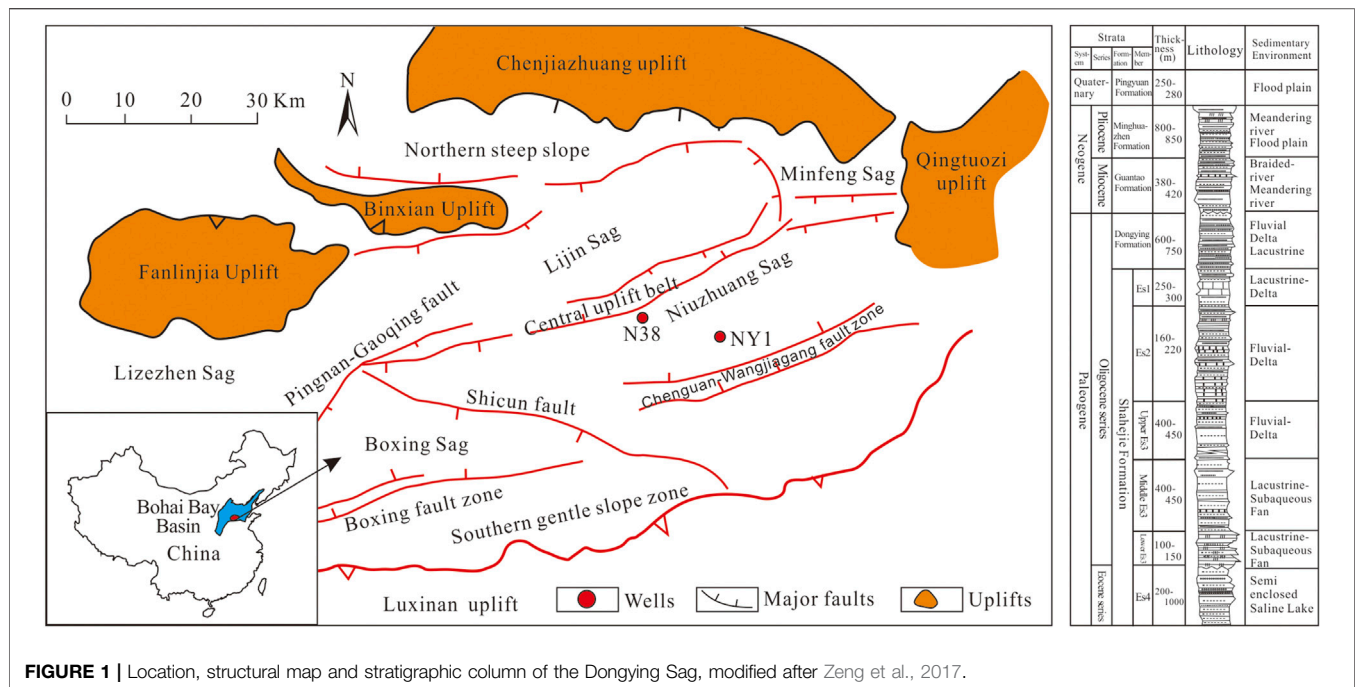
FIGURE 1 | Location, structural map and stratigraphic column of the Dongying Sag, modified after Zeng et al., 2017.

Pyrolysis

Powdered original shale samples (50 mg) were pyrolyzed by using a RockEval six pyrolysis apparatus (Vinci Technologies, France). The powdered samples were first subjected to a 3 min isotherm at 300°C, at which free hydrocarbons were volatilized (peak S_1, mg/g rock). Then, programmed pyrolysis at 50°C/min to 600°C was performed to determine the amount of potential hydrocarbons that were released by the thermal cracking of OM (peak S_2, mg/g rock). Simultaneously, the CO and CO_2 that were released during the thermal cracking of organic oxygen-bearing compounds between 300 and 390°C were measured by a thermal conductivity detector (TCD). This product was reported in mg CO_2/g rock and was referred to as the S_3 peak. A fourth peak, S_4 (mg CO_2/g rock), refers to the combustion of residual carbon under an air atmosphere at 600°C. Total organic carbon (TOC) and the hydrogen index (HI) were computed from the S_1, S_2, and S_4 peaks and were reported in weight percent. T_{max} corresponded to the temperature at the maximum S_2.

Organic Solvent Extraction

Organic solvent extraction was conducted to obtain the SOM in accordance with Zhu et al. (2016). The original shale samples were ground to a particle size of less than 0.18 mm. Shale samples (>50 g) were weighed and placed in a Soxhlet extractor. n-Pentane and dichloromethane were successively used for more than 72 h to extract and collect SOM within shale samples. The group components were separated by column chromatography (see *Column Chromatography*). Finally, the SOM and group components were accurately quantified using a balance with a precision of 1/10,000, and their contents in the shale samples were calculated.

Column Chromatography

Column chromatography has been widely used for the separation of group components of SOM and crude oil (Pan et al., 2005; Wei et al., 2012; Yang Y. et al., 2015). In this study, the SOM extracted by organic solvents was separated into saturates, aromatics, resins and asphaltenes by using conventional column chromatography. The adsorbent was a mixture of silica gel and alumina. The silica gel was extracted with chloroform until there was no fluorescence. Then, the silica gel was activated by heating in an electric oven at 150°C for 8 h. The neutral alumina was activated by heating in a muffle furnace at 450°C for 6 h. The eluents were n-pentane, dichloromethane and methanol.

RESULTS

X-Ray Diffraction

The XRD analysis showed that the bulk minerals of the studied shales were mainly composed of clay, quartz, feldspar and carbonate with minor amounts of anhydrite, siderite and pyrite (**Figure 3A**; **Supplementary Table S1**). The mineral phases of the studied shales were classified into three main constituents: detrital minerals (quartz and feldspar), clay minerals and carbonate minerals (Zeng et al., 2018; Zhu et al., 2019). Among the different shale lithofacies, the mineral compositions or constituents varied greatly (**Figure 3B**): 1) The detrital massive mudstone was characterized by high contents of clay minerals and detrital minerals and low contents of carbonate minerals. 2) The contents of the three mineral constituents in the homogenous massive mudstone were basically similar. 3) The carbonate mineral content in the wide laminated shale was very high. 4) The mineral composition of the fine laminated shale was similar to that of the wide laminated
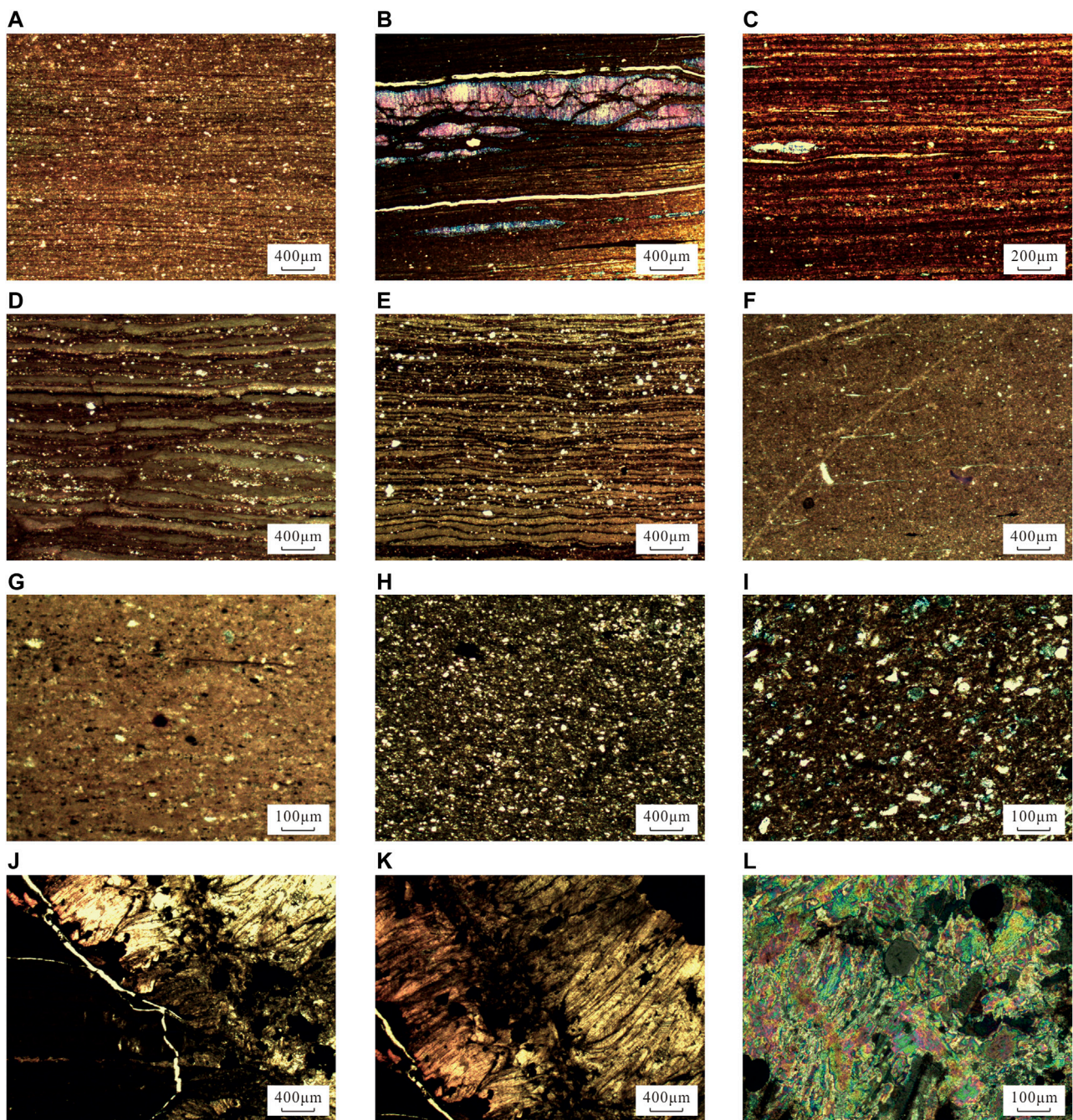
FIGURE 2 | Microscopic photographs of shale samples from the Dongying Sag. **(A)** Organic and argillaceous laminae interbedded in fine laminated shale. **(B)** Sparry calcite developed in fine laminated shale. **(C)** Fine laminated shale. **(D)** Carbonate and argillaceous laminae interbedded in wide laminated shale. The carbonate laminae were partially lenticular. **(E)** Organic laminae distributed in argillaceous matrixes in discontinuous laminated shale. **(F)** Homogenous massive mudstone mainly composed of argillaceous minerals with no obvious layers. **(G)** Detrital particles distributed in a dispersed manner in homogenous massive mudstone. **(H)** Detrital particles dispersed in argillaceous matrixes in detrital massive mudstone. **(I)** Detrital massive mudstone. **(J)** Gypsum-bearing mudstone. **(K)** Anhydrite veins developed in argillaceous matrixes. **(L)** Gypsum under orthogonal light.

shale and was characterized by a high carbonate mineral content. 5) The clay and detrital mineral contents in the discontinuous laminated shale were higher than the carbonate mineral content. 6) The gypsum-bearing mudstone was characterized by high contents of gypsum and dolomite (24 and 35%, respectively).

Rock-Eval Pyrolysis
OM Abundance and Hydrocarbon Generation Potential

The TOC of the studied shales was generally high, ranging from 1.12 to 8.30 wt% (average of 3.39 wt%) (**Figure 4A**; **Supplementary Table S2**).

FIGURE 3 | Mineral compositions **(A)** and constituents **(B)** of the shale samples.

FIGURE 4 | Average TOC **(A)** and S_1+S_2 **(B)** of shale samples with different lithofacies.
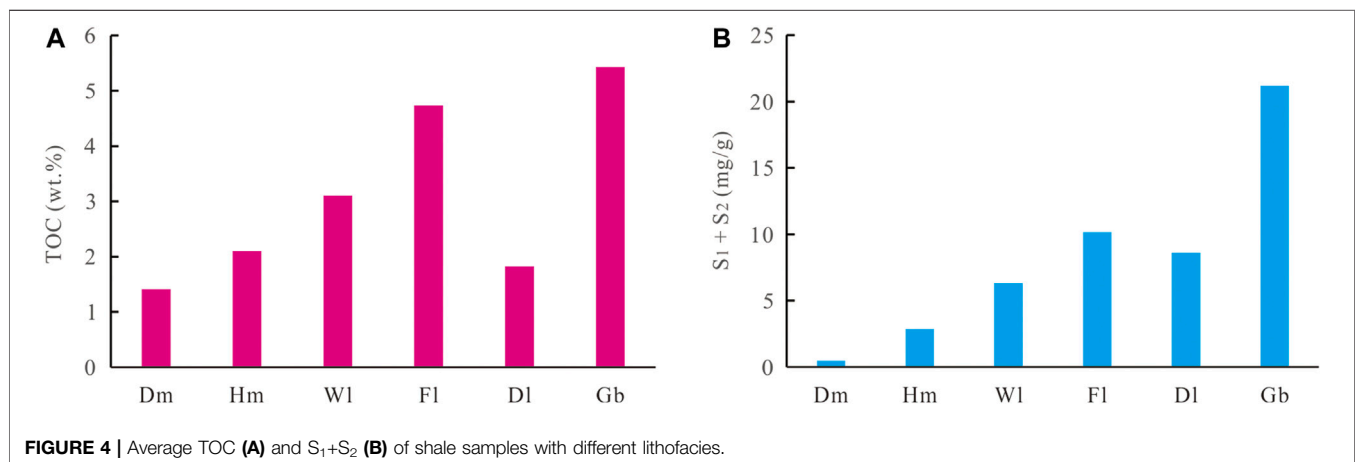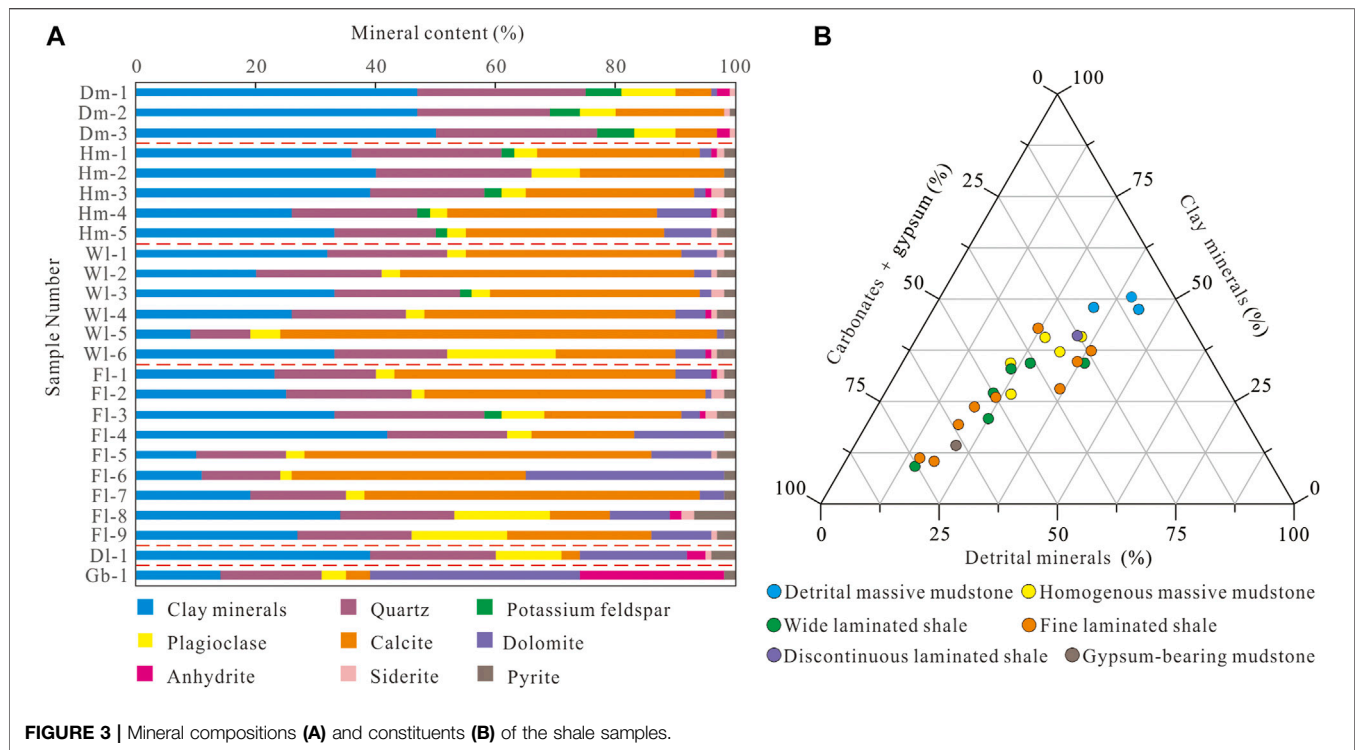
However, the TOC contents of shale with different lithofacies were significantly different (**Figure 4A**). The TOC of the fine laminated shale was the highest, ranging from 2.36 to 8.30 wt% (average of 4.73 wt%). The second highest was the gypsum-bearing mudstone (5.42 wt%). The TOC of the wide laminated shale was also relatively high, ranging from 1.74 to 4.32% (average of 3.1 wt%). The TOC of the homogenous massive mudstone ranged from 1.91 to 3.02 wt% (average of 2.41 wt%). The TOC of the discontinuously laminated shale was relatively low (1.82 wt%). The TOC of the detrital massive mudstone was the lowest, ranging from 1.12 to 1.97 wt% (average of 1.43 wt%).

In the studied shale samples, S_1+S_2 ranged from 1.60 to 60.30 mg/g (average of 19.69 mg/g) and indicated a relatively

high hydrocarbon generation potential (**Figure 4B**; **Supplementary Table S2**). The hydrocarbon generation potential of shale with different lithofacies also varied significantly (**Figure 4B**). The hydrocarbon generation potential of the fine laminated shale was the highest, with S_1+S_2 ranging from 14.23 to 60.30 mg/g (average of 31.21 mg/g). The second highest was the gypsum-bearing mudstone (23.94 mg/g). The hydrocarbon generation potential of the wide laminated shale was also high, with S_1+S_2 ranging from 11.44 to 23.73 mg/g (average of 17.88 mg/g). This was followed by homogenous massive mudstone, with S_1+S_2 ranging from 8.88 to 14.94 mg/g (average of 12.65 mg/g). The hydrocarbon generation potential of the discontinuous laminated
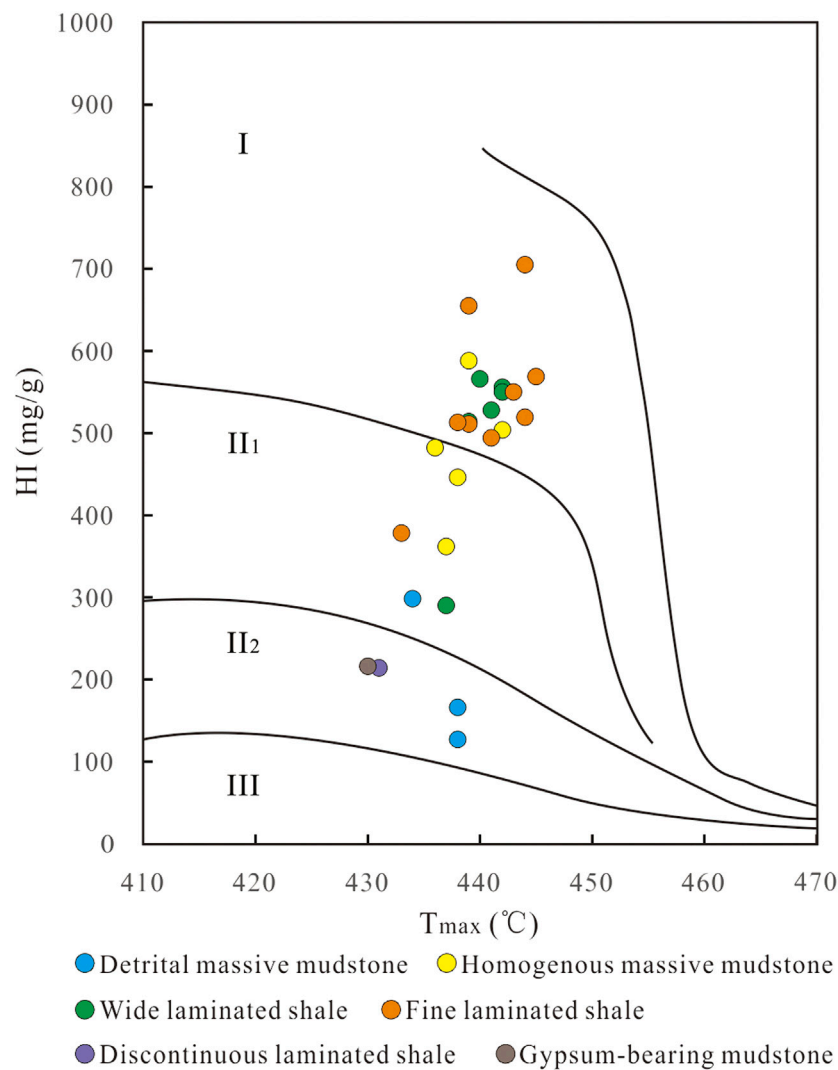
FIGURE 5 | HI versus T_{max} plot showing the OM type of shale with different lithofacies.

shale (7.05 mg/g) was low. The hydrocarbon generation potential of the detrital massive mudstone was the lowest, with S_1+S_2 ranging from 1.60 to 6.14 mg/g (average of 3.24 mg/g).

OM Type

The OM types of the studied shale samples mainly included Types I and II (**Figure 5**). In different lithofacies, the OM types varied greatly: 1) The OM in the detrital massive mudstone was mainly Type II_2. 2) The OM in the homogenous massive mudstone was Type I-II_1. 3) The OM in the fine and wide laminated shales was predominantly Type I. 4) The OM in the discontinuous laminated shale and gypsum-bearing mudstone was Type II_2.

Thermal Maturity

T_{max} and R_o are effective parameters for judging the level of thermal maturity of shales (Wang et al., 2015; Wang et al., 2021). The T_{max} values of the samples above 3,450 m ranged from 434 to 445°C with an average of 440°C (**Figure 6A**), suggesting that the

shale samples were within the early oil generation stage. However, the T_{max} values below 3,450 m rapidly inverted with increasing PI (**Figures 6A,B**). A high PI value indicates a high content of SOM in source rocks, leading to a low T_{max} value (Wang et al., 2015). Therefore, it was very uncertain to use the T_{max} values to infer the maturity of samples below 3,450 m. **Figure 6C** shows that there was a good positive trend with R_o values increasing as expected with increasing depth, in accordance with the data in Zhang S et al., 2012; Chen, 2017. According to the trend line of organic maturity (**Figure 6C**), the R_o values increased from approximately 0.50–0.65% in the depth interval of 2,900–3,500 m, suggesting that the shale samples were within the zone of early oil generation.

Soluble Organic Matter and Group Components

Significant differences in the absolute contents of SOM and group components can be found among the shale samples with different

FIGURE 6 | T_{max}, PI and R_o versus depth profiles. **(A)** T_{max}-depth. T_{max} values slightly increased with increasing depth above 3,450 m, but beneath 3,450 m, the T_{max} trend reversed, indicating suppression of T_{max}. **(B)** PI = S_1/(S_1+S_2) versus depth plot. Samples with higher PI values usually showed lower T_{max} values (Wang et al., 2015). **(C)** R_o-depth. There was a good positive trend with R_o values increasing as expected with increasing depth. The green triangle data come from Li (2011), and the blue square data come from the database of the Shengli Oil Company.

FIGURE 7 | Average absolute contents of SOM and group components in shales with different lithofacies.

lithofacies (**Figure 7**; **Supplementary Table S3**): 1) The content comparison of SOM, saturates and total hydrocarbons (THC) revealed generally similar trends, e.g., detrital massive mudstone < homogenous massive mudstone < wide laminated shale < discontinuous laminated shale < fine laminated shale <

gypsum-bearing mudstone (**Figures 7A,B,F**). 2) For aromatics, the content comparison showed the order of detrital massive mudstone < homogenous massive mudstone < wide laminated shale < fine laminated shale < discontinuous laminated shale < gypsum-bearing mudstone (**Figure 7C**). 3) The content
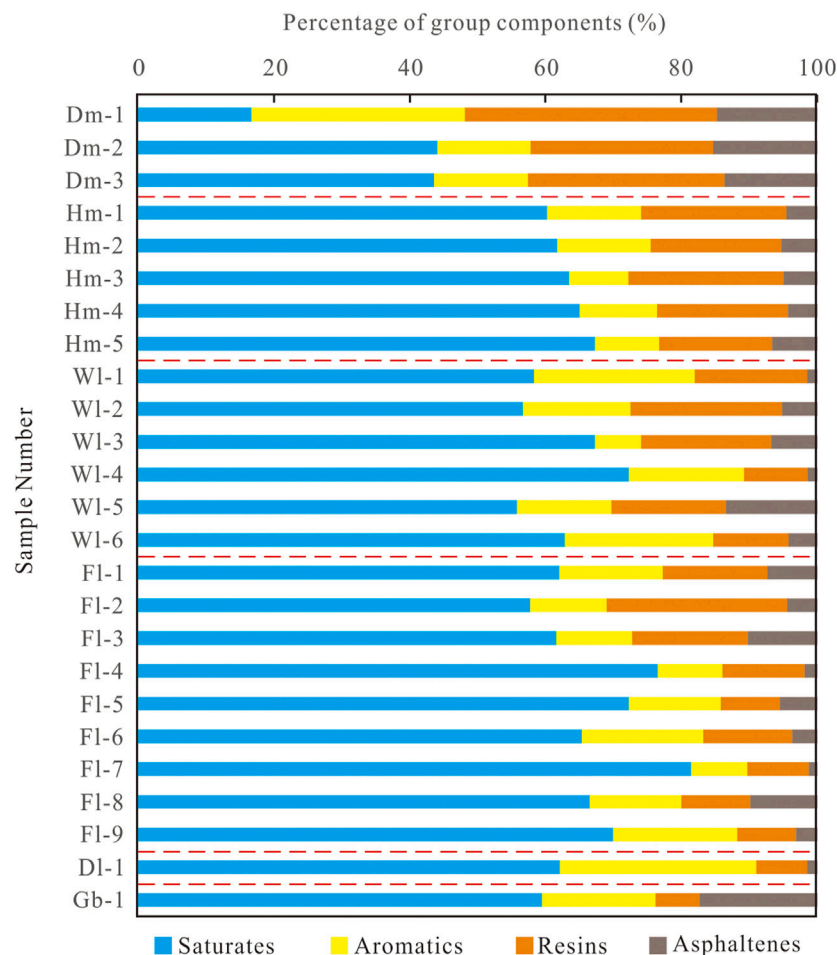
FIGURE 8 | Percentage of group components in shales with different lithofacies.

comparison of resins showed the order of detrital massive mudstone < homogenous massive mudstone ≈ discontinuous laminated shale < wide laminated shale < fine laminated shale ≈ gypsum-bearing mudstone (**Figure 7D**). 4) For asphaltenes, the content comparison showed the trend that detrital massive mudstone < discontinuous laminated shale < homogenous massive mudstone < wide laminated shale < fine laminated shale < gypsum-bearing mudstone (**Figure 7E**).

From the relative contents of SOM components in shales with different lithofacies, remarkable differences can be seen (**Figure 8**): 1) In the SOM in the detrital massive mudstone, saturates (average of 34.8%) and resins (average of 31.0%) were the main components, followed by aromatics (average of 19.7%) and asphaltenes (average of 14.5%). 2) In the SOM in the homogenous massive mudstone, saturates (average of 63.6%) were the main component. The percentage of resins (average of 19.9%) was higher than that of aromatics (average of 11.4%). The percentage of asphaltenes (average of 5.1%) was the lowest. 3) In the SOM in the wide laminated shale, saturates (average of 62.2%) were the main component. The percentage of aromatics (average of 16.5%) was roughly the same as that of resins (average

of 15.9%). The percentage of asphaltenes (average of 5.4%) was the lowest. 4) In the SOM in the fine laminated shale, saturates (average of 68.2%) were the main component, followed by aromatics (average of 13.2%), resins (average of 13.4%), and finally asphaltenes (average of 5.2%). 5) In the SOM in the discontinuous laminated shale, saturates (62.2%) were the main component, followed by aromatics (28.9%). The percentages of resins (7.5%) and asphaltenes (1.4%) were very low, especially asphaltenes. 6) In the SOM in the gypsum-bearing mudstone, saturates (average of 59.5%) were the main component. The percentage of asphaltenes (17.3%) was roughly the same as that of aromatics (16.8%). The percentage of resins (6.4%) was the lowest.

DISCUSSION

Control of Lithofacies on Soluble Organic Matter Content

The contents of SOM and group components in shale with different lithofacies were significantly different (**Figure 7**).
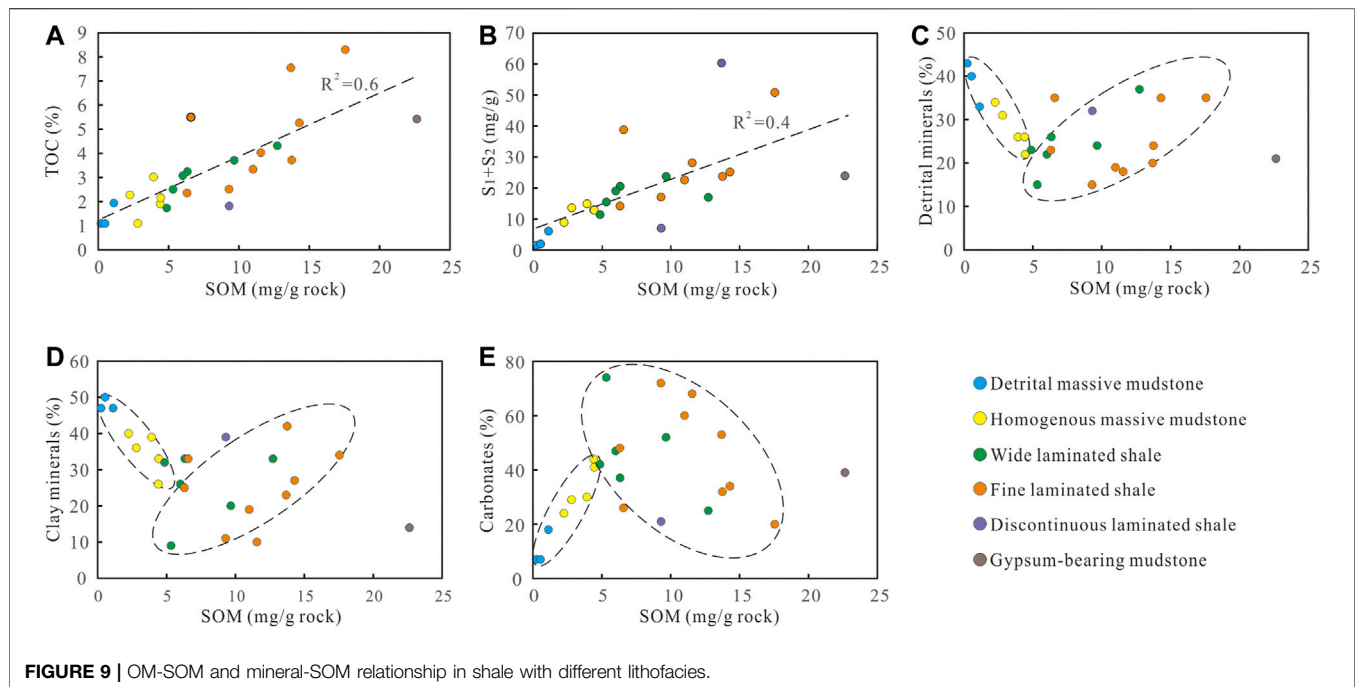
FIGURE 9 | OM-SOM and mineral-SOM relationship in shale with different lithofacies.

Because the extracted SOM is most similar to crude oil in composition (Song et al., 2013; Liu et al., 2014), it is of great significance to understand the controlling effect of lithofacies on SOM. The differences among lithofacies were mainly present in sedimentary structure, mineral composition and organic characteristics (**Figures 2–6**). The SOM content in shale had a significant positive correlation with TOC and S_1+S_2 (**Figures 9A,B**), which indicated that the OM abundance and hydrocarbon generation potential of shale were important factors affecting the content of SOM. The massive mudstone had low OM abundance, low hydrocarbon generation potential and a poor OM type (**Figures 4**, **5**), so the SOM content was low. However, the laminated shale had high OM abundance, high hydrocarbon generation potential and a better OM type (**Figures 4**, **5**), resulting in a relatively high SOM content.

Among the different lithofacies, varying relationships between the SOM and minerals in shale were observed (**Figures 9C–E**). Overall, in the massive mudstone, the SOM content is negatively correlated with the contents of detrital and clay minerals, but positively correlated with the carbonate mineral content (**Figures 9C–E**). However, in the laminated shale, the SOM content has inverse relationships with mineral content (**Figures 9C–E**). Previous studies have indicated that the SOM extracted by organic solvents in shale is mainly free in pores and physically adsorbed onto mineral surfaces (Rumpel et al., 2005; Pan and Liu, 2009; Wei et al., 2014; Zhu et al., 2016). Moreover, different minerals in shale have various contributions to shale pores and surfaces, in which SOM can exist. For example, quartz and carbonates may act as a rigid framework for pores (Loucks et al., 2012), carbonate cements may reduce the pore surface area and pore volume (Gaines et al., 2012; Loucks et al., 2012), and clay minerals contribute positively to pore development (Slatt and O'Brien, 2011; Bennett et al., 2012; Zhu et al., 2019). In

particular, carbonates in shales in the Dongying Sag clearly occur as cements (Deng and Liang, 2012; Zhang Y et al., 2016). Thus, high contents of detrital and clay minerals with a low content of carbonates in shale results in abundant shale pores and surfaces, promoting high SOM contents, and this phenomenon can be seen in the laminated shale (**Figures 9C–E**). However, the relationship between the SOM content and the mineral content in the massive mudstone is opposite that in the laminated shale (**Figures 9C–E**). This difference is attributed to the relatively poor conditions for OM preservation and enrichment, where the massive mudstone is interpreted to have been deposited close to the provenance under relatively strong water dynamics because the detrital minerals and clay minerals in the Dongying Sag are exogenous (Zeng et al., 2018). Consequently, the massive mudstone has low OM abundance and relatively low hydrocarbon generation potential (**Figure 4**). Therefore, the SOM content was controlled by lithofacies through differences in both OM and minerals.

Abundance of Shale Oil in Different Lithofacies

The oil saturation index (OSI = S_1/TOC) is widely used to evaluate mobile shale oil, and the value of this parameter varies in different regions (Jarvie et al., 2007; Jarvie, 2012; Xue et al., 2015; Xie et al., 2016; Yu, et al., 2018; Li et al., 2020). By correlating OSI with the content of SOM, saturates and THC, positive correlations are present overall (**Figure 10**). However, the correlations in specific lithofacies are not very clear, which may be attributed to limiting sample sets. From the overall positive correlations (**Figure 10**), it seems that the contents of SOM, saturates or THC might be reliable indicators to evaluate the abundance of shale oil in shale with different lithofacies.
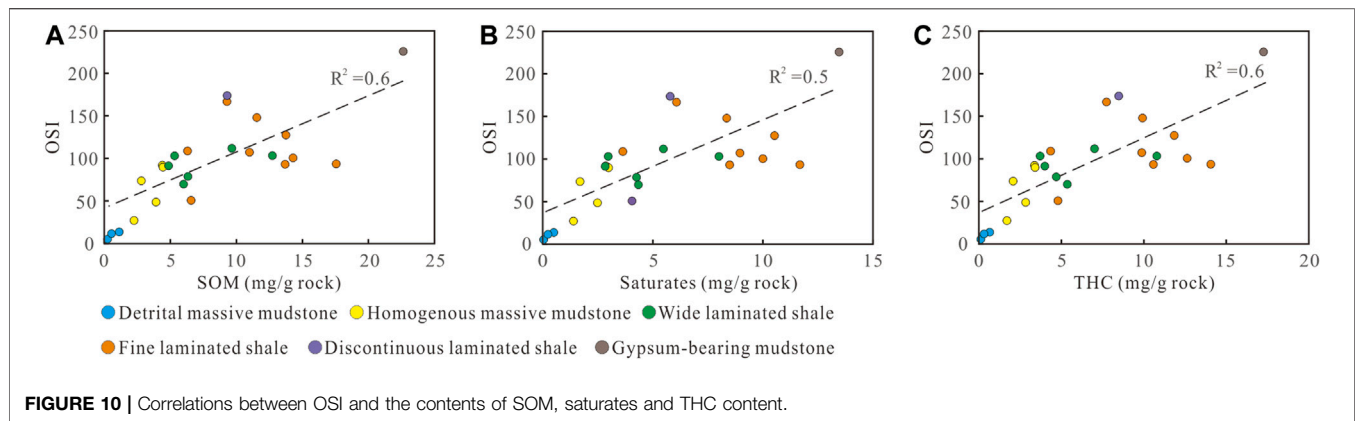
FIGURE 10 | Correlations between OSI and the contents of SOM, saturates and THC content.
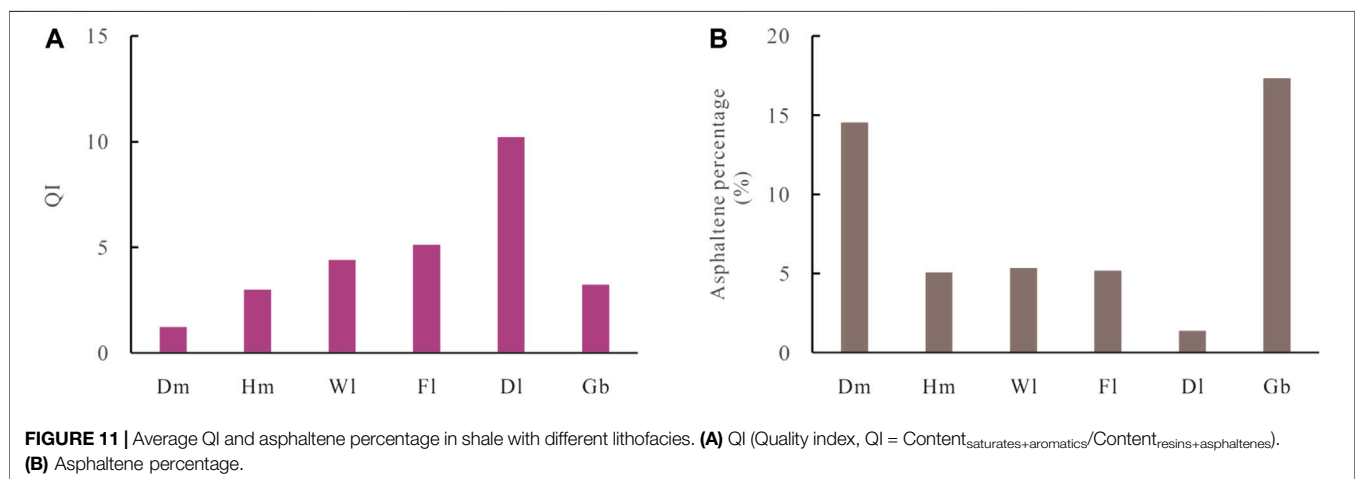
FIGURE 11 | Average QI and asphaltene percentage in shale with different lithofacies. **(A)** QI (Quality index, QI = Content$_{saturates+aromatics}$/Content$_{resins+asphaltenes}$). **(B)** Asphaltene percentage.

The composition of SOM free in the pores of shale is close to that of crude oil, and its content can effectively reflect the abundance of shale oil (Song et al., 2013; Liu et al., 2014). The contents of SOM, saturates and THC showed basically the same characteristics, that is, detrital massive mudstone < homogenous massive mudstone < wide laminated shale < discontinuous laminated shale < fine laminated shale < gypsum-bearing mudstone (**Figure 7**). Therefore, the abundance comparison of shale oil in different lithofacies showed that: 1) The contents of SOM, saturates and THC were very high in fine laminated shale, discontinuous laminated shale and gypsum-bearing mudstone, which were the relatively favorable lithofacies for shale oil exploration and development. 2) The contents of SOM, saturates and THC in the wide laminated shale were relatively high overall but low in some cases; thus, this lithofacies could also be a good target for shale oil exploration and development. 3) The detrital and homogenous massive mudstones, in which the contents of SOM, saturates and THC were relatively low, were relatively poor targets for shale oil exploration and development.

Quality of Shale Oil in Different Lithofacies

Shale oil is a mixture of hydrocarbons (mostly alkanes, cycloalkanes and aromatics) and other organic compounds containing nitrogen, oxygen, sulfur and traces of metals (Langevin and Argillier, 2016). Differences in the shale oil components affect the oil's viscosity, which directly determines the oil quality and economic value. Previous studies have suggested that the viscosity of crude oil is proportional to the contents of resins and asphaltenes and is inversely proportional to the content of saturates (Liu and Guo, 2008; Wang et al., 2010; Gai, 2011; Zhang et al., 2014). Aromatics are conducive to the dispersion of asphaltenes, so the association of resins and asphaltenes can be dispersed in the saturates (Su and Zheng, 2007), thus contributing to the reduction of viscosity. These studies imply that an increase in the hydrocarbon content is beneficial to reducing the crude oil viscosity and thus improving the quality of crude oil, while the effect of resins and asphaltenes is the opposite. Based on this, we propose a parameter, the quality index (QI, QI = Content$_{saturates+aromatics}$/Content$_{resins+asphaltenes}$), to judge the shale oil quality. Comparison of the QI values of different lithofacies revealed the following trend: detrital massive mudstone < homogenous massive mudstone < gypsum-bearing mudstone < wide laminated shale < fine laminated shale < discontinuous laminated shale (**Figure 11A**). Overall, the QI values of the discontinuous, fine and wide laminated shales were relatively high, and the quality of their shale oil was better.

Lithofacies	Microscopic features	Shale oil abundance parameters			Shale oil quality parameters		Group composition
		SOM (mg/g rock) 0 — 25	THC (mg/g rock) 0 — 20	Saturates (mg/g rock) 0 — 15	QI 0 — 15	Asphaltene percentage (%) 0 — 20	
Detrital massive mudstone							14.5% 34.8% 31.0% 19.7%
Homogenous massive mudstone							5.1% 19.9% 63.6% 11.4%
Wide laminated shale							5.4% 15.9% 62.2% 16.5%
Fine laminated shale							5.2% 13.4% 68.2% 13.2%
Discontinuous laminated shale							7.5% 1.4% 28.9% 62.2%
Gypsum-bearing mudstone							17.3% 6.4% 59.5% 16.8%

■ Saturates   ■ Aromatics   ■ Resins   ■ Asphaltenes

FIGURE 12 | Comprehensive evaluation of shale oil in shales with different lithofacies.

From the percentage of asphaltenes in shale with different lithofacies (**Figure 11B**), great variations can be seen. The percentage of asphaltenes in the gypsum-bearing mudstone and detrital massive mudstone exceeded 10%. The percentage of asphaltenes in the wide and fine laminated shales and homogenous massive mudstone was approximately 5%. The

FIGURE 13 | Lithofacies proportion of shales in different members. The data compile from Zeng et al., 2017.
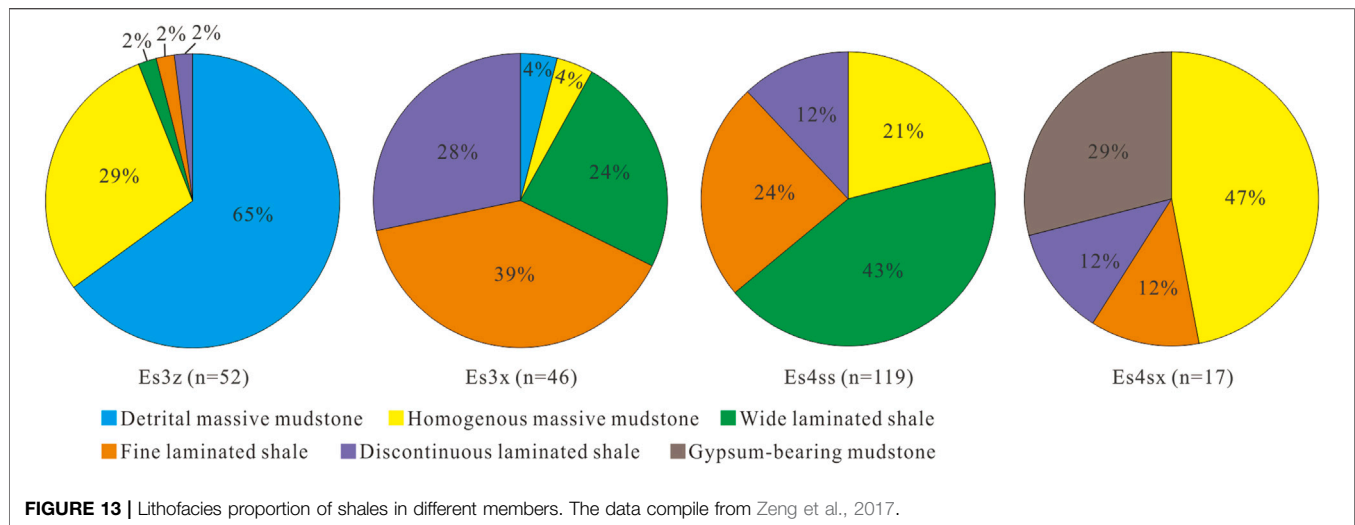
percentage of asphaltenes in the discontinuous laminated shale was very low (less than 2%). As organic macromolecules, asphaltenes easily precipitate, accumulate, block pores, and chemically adsorb onto mineral surfaces (Mikami et al., 2013; Adebiyi and Thoss, 2014; Langevin and Argillier, 2016), the increase in content of which will not only reduce the SOM or crude oil quality, but also increase the difficulty of shale oil production. Thus, the differences in the percentage of asphaltenes of different lithofacies indicated that the quality of SOM or shale oil in the wide, fine and discontinuous laminated shales and homogenous massive mudstone was relatively good.

Therefore, combining the results from the QI value and asphaltene percentage, it can be concluded that the quality of shale oil in the discontinuous, fine and wide laminated shales was obviously better than that in the detrital and homogenous massive mudstones and gypsum-bearing mudstone.

Evaluation of Shale Oil "Sweet Spots"

Based on comparisons of the characteristics of SOM in shales with different lithofacies in the Dongying Sag, the shale oil in different lithofacies was evaluated from two aspects (abundance and quality) (**Figure 12**). Combining evaluations of abundance and quality in the comparison made it clear that the fine laminated shale, wide laminated shale and discontinuous laminated shale were the high-quality lithofacies, as these lithofacies had higher contents of SOM, THC or saturates, higher QI values, and lower asphaltene percentages.

From a large sample set of shale lithofacies (*n* = 234) distributed from Es4s to Es3z in the Dongying Sag, the comparison of the proportions of different lithofacies between submembers can indicate a relatively good target for shale oil exploration and development with optimization of high-quality lithofacies. After classification of different lithofacies, the proportions of different lithofacies in the submembers in the Dongying Sag were determined (**Figure 13**): 1) The shales in Es3z were mainly composed

of detrital massive mudstone (65%) and homogenous massive mudstone (28%), and the proportion of laminated shale was less than 10%. 2) The shales in Es3x were mainly characterized by a lamellar structure. The proportions of fine laminated shale, wide laminated shale and discontinuous laminated shale were 39, 24 and 28%, respectively, and the proportion of massive mudstone was less than 10%. 3) More than 75% of the shales in Es4ss featured lamellar structures. The proportions of fine laminated shale, wide laminated shale and discontinuous laminated shale were 24, 43 and 12%, respectively, and the proportion of homogenous massive mudstone was 22%. 4) The shales in Es4sx were mainly composed of homogenous massive mudstone (65%) and gypsum-bearing mudstone (28%), and the remainder was laminated shale. From the perspective of lithofacies combinations, the shales in Es3z and Es4sx were mainly massive mudstone and gypsum-bearing mudstone, while the shales in Es3x and Es4ss were mostly laminated shale. Based on identification of high-quality lithofacies (i.e., the fine, wide and discontinuously laminated shales), the shales in Es3x and Es4ss were more favorable for shale oil development in the study area.

CONCLUSION

1) In terms of the contents of SOM, saturates and THC, the lithofacies showed the order of detrital massive mudstone < homogenous massive mudstone < wide laminated shale < discontinuous laminated shale < fine laminated shale < gypsum-bearing mudstone. The relationships of the SOM content with pyrolysis parameters (TOC, S_1+S_2) and mineral content showed that the SOM content in shales with different lithofacies was mainly influenced by differences in mineral composition and organic characteristics. The SOM in the detrital massive mudstone and homogenous massive mudstone was mainly composed of saturates and resins, especially in

the detrital massive mudstone. Saturates were the main component in the wide laminated shale and fine laminated shale. The SOM in the discontinuous laminated shale was mainly composed of saturates and aromatics. The SOM in the gypsum-bearing mudstone was mainly composed of saturates, and the percentage of asphaltenes was quite high.

2) Evaluation parameters were established to identify high-quality lithofacies and were based on abundance (i.e., the contents of SOM, THC and saturates) and quality (i.e., QI and asphaltene percentage). Comparisons of the evaluation parameters among different lithofacies showed that fine laminated shale, wide laminated shale and discontinuous laminated shale were high-quality lithofacies suitable for shale oil exploration and development, as these lithofacies had higher contents of SOM, THC or saturates, higher QI values, and lower asphaltene percentages.

3) From the perspective of lithofacies combination, the shales in Es3x and Es4ss, which were mainly laminated shales, were more favorable for shale oil development. The shales in Es3z and Es4sx, which were mainly massive mudstone and gypsum-bearing mudstone, were relatively poor targets. Therefore, it can be clearly defined that the fine laminated shale, wide laminated shale and discontinuous laminated shale in the Es3x and Es4ss in the Dongying Sag are "sweet spots" for shale oil exploration and development. It is of great significance for the exploration and development of shale oil to study the characteristics of SOM in shales with different lithofacies.

DATA AVAILABILITY STATEMENT

The original contributions presented in the study are included in the article/**Supplementary Material**, further inquiries can be directed to the corresponding authors.

AUTHOR CONTRIBUTIONS

JG and JH contributed to conception and design of the study. JH organized the database and performed the statistical analysis. JH wrote the first draft of the manuscript. JG and XZ revised and improved the manuscript. All authors contributed to manuscript revision, read, and approved the submitted version.

FUNDING

SUPPLEMENTARY MATERIAL

The Supplementary Material for this article can be found online at: https://www.frontiersin.org/articles/10.3389/feart.2021.718596/full#supplementary-material

REFERENCES

Abouelresh, M. O., and Slatt, R. M. (2012). Lithofacies and Sequence Stratigraphy of the Barnett Shale in East-central Fort Worth Basin, Texas. *AAPG Bull.* 96, 34–43. doi:10.1306/04261110116

Adebiyi, F. M., and Thoss, V. (2014). Organic and Elemental Elucidation of Asphaltene Fraction of Nigerian Crude Oils. *Fuel* 118, 426–431. doi:10.1016/j.fuel.2013.10.044

Bao, Y., Zhang, L., Zhang, J., Li, J., and Li, Z. (2016). Factors Influencing Mobility of Paleogene Shale Oil in Dongying Sag, Bohai Bay Basin. *Oil Gas Geology.* 37, 408–414. doi:10.11743/ogg20160314

Bennett, R. H., Bryant, W. R., Hulbert, M. H., Chiou, W. A., and Yamamoto, T. (2012). *Microstructure of fine-grained Sediments: From Mud to Shale* New York: Springer.

Chen, J. (2017). *Research on the Movability of Shale Oil in Dongying Sag and the Optimization Method of Favorable Zone.* East China: M.S. thesis China University of Petroleum.

Chen, Z., Jiang, W., Zhang, L., and Zha, M. (2018). Organic Matter, mineral Composition, Pore Size, and Gas Sorption Capacity of Lacustrine Mudstones: Implications for the Shale Oil and Gas Exploration in the Dongying Depression, Eastern China. *Bulletin* 102, 1565–1600. doi:10.1306/0926171423117184

Deng, M., and Liang, C. (2012). Studies on Reservoir Space of Mud Stone and Shale of the Lower Section of Es3 in Bonan Subsag: An Example from Well Luo 69. *Earth Sci. Front.* 19, 173–181.

Fu, J., Deng, X., Chu, M., Zhang, H., and Li, S. (2013). Features of deepwater Lithofacies, Yanchang Formation in Ordos Basin and its Petroleum Significance. *Acta Sedimentologica Sinica* 31, 928–938. doi:10.14027/j.cnki.cjxb.2013.05.011

Gai, P. (2011). The Relationship between the Viscosity and Fraction Characteristcs of the Heavy Oil of Shengli Oil Field. *Oilfield Chem.* 28, 54–57. doi:10.19346/j.cnki.1000-4092.2011.01.013

Gaines, R. R., Hammarlund, E. U., Hou, X., Qi, C., Gabbott, S. E., Zhao, Y., et al. (2012). Mechanism for Burgess Shale-type Preservation. *Proc. Natl. Acad. Sci.* 109, 5180–5184. doi:10.1073/pnas.1111784109

Hickey, J. J., and Henk, B. (2007). Lithofacies Summary of the Mississippian Barnett Shale, Mitchell 2 T.P. Sims Well, Wise County, Texas. *Bulletin* 91, 437–443. doi:10.1306/12040606053

Hou, L., Luo, X., Lin, S., Zhao, Z., and Li, Y. (2021b). Quantitative Measurement of Retained Oil in Organic-Rich Shale—A Case Study on the Chang 7 Member in the Ordos Basin, China. *Front. Earth Sci.* 9, 662586. doi:10.3389/feart.2021.662586

Hou, L., Ma, W., Luo, X., Liu, J., Liu, S., and Zhao, Z. (2021a). Hydrocarbon Generation-Retention-Expulsion Mechanism and Shale Oil Producibility of the Permian Lucaogou Shale in the Junggar Basin as Simulated by Semi-open Pyrolysis Experiments. *Mar. Pet. Geology.* 125, 104880. doi:10.1016/j.marpetgeo.2020.104880

Jarvie, D. M., Hill, R. J., Ruble, T. E., and Pollastro, R. M. (2007). Unconventional Shale-Gas Systems: The Mississippian Barnett Shale of north-central Texas as One Model for Thermogenic Shale-Gas Assessment. *Bulletin* 91, 475–499. doi:10.1306/12190606068

Jarvie, D. M. (2012). Shale Resource Systems for Oil and Gas: Part 2: Shale-Oil Resource Systems. *AAPG Memoir* 97, 89–119. doi:10.1306/13321446m973489

Kumar, S., Ojha, K., Bastia, R., Garg, K., Das, S., and Mohanty, D. (2017). Evaluation of Eocene Source Rock for Potential Shale Oil and Gas Generation in north Cambay Basin, India. *Mar. Pet. Geology.* 88, 141–154. doi:10.1016/j.marpetgeo.2017.08.015

Langevin, D., and Argillier, J.-F. (2016). Interfacial Behavior of Asphaltenes. *Adv. Colloid Interf. Sci.* 233, 83–93. doi:10.1016/j.cis.2015.10.005

Li, J. (2014). Oil and Gas Contents and Movable Oil Amounts of Shales in 4th Member of Shahejie Formation, Lijin Subsag, Dongying Sag. *Pet. Geology. Exp.* 36, 365–369. doi:10.11781/sysydz201403365

Li, W., Cao, J., Shi, C., Xu, T., Zhang, H., and Zhang, Y. (2020). Shale Oil in saline Lacustrine Systems: A Perspective of Complex Lithologies of fine-grained Rocks. *Mar. Pet. Geology.* 116, 104351. doi:10.1016/j.marpetgeo.2020.104351

Li, Y., Cai, J., Song, G., and Ji, J. (2015). DRIFT Spectroscopic Study of Diagenetic Organic-clay Interactions in Argillaceous Source Rocks. *Spectrochimica Acta A: Mol. Biomol. Spectrosc.* 148, 138–145. doi:10.1016/j.saa.2015.03.131

Li, Z. (2011). *Exploration Potential Analyses of the Shale Gas in Dongying Depression*. M.S. thesis Chengdu, China: Chengdu University of Technology.

Liang, C., Cao, Y., Liu, K., Jiang, Z., Wu, J., and Hao, F. (2018). Diagenetic Variation at the Lamina Scale in Lacustrine Organic-Rich Shales: Implications for Hydrocarbon Migration and Accumulation. *Geochimica et Cosmochimica Acta* 229, 112–128. doi:10.1016/j.gca.2018.03.017

Liu, B., He, J., Lv, Y., Ran, Q., Dai, C., and Li, M. (2014). Parameters and Method for Shale Oil Assessment: Taking Qinshankou Formation Shale Oil of Northern Songliao Basin. *J. Cent. South Univ. (Science Technology)* 45, 3846–3852.

Liu, H., and Guo, X. (2008). Influence of Property and Structure of Crude Oil on its Viscosity. *Xinjiang Pet. Geology.* 29, 347–349.

Loucks, R. G., Reed, R. M., Ruppel, S. C., and Hammes, U. (2012). Spectrum of Pore Types and Networks in Mudrocks and a Descriptive Classification for Matrix-Related Mudrock Pores. *AAPG Bull.* 96, 107–1098. doi:10.1306/08171111061

Loucks, R. G., and Ruppel, S. C. (2007). Mississippian Barnett Shale: Lithofacies and Depositional Setting of a Deep-Water Shale-Gas Succession in the Fort Worth Basin, Texas. *Bulletin* 91, 579–601. doi:10.1306/11020606059

Mikami, Y., Liang, Y., Matsuoka, T., and Boek, E. S. (2013). Molecular Dynamics Simulations of Asphaltenes at the Oil-Water Interface: From Nanoaggregation to Thin-Film Formation. *Energy Fuels* 27, 1838–1845. doi:10.1021/ef301610q

Misch, D., Gross, D., Mahlstedt, N., Makogon, V., and Sachsenhofer, R. F. (2016). Shale Gas/shale Oil Potential of Upper Visean Black Shales in the Dniepr-Donets Basin (Ukraine). *Mar. Pet. Geology.* 75, 203–219. doi:10.1016/j.marpetgeo.2016.04.017

Pan, C., Feng, J., Tian, Y., Yu, L., Luo, X., Sheng, G., et al. (2005). Interaction of Oil Components and clay Minerals in Reservoir Sandstones. *Org. Geochem.* 36, 633–654. doi:10.1016/j.orggeochem.2004.10.013

Pan, C., and Liu, D. (2009). Molecular Correlation of Free Oil, Adsorbed Oil and Inclusion Oil of Reservoir Rocks in the Tazhong Uplift of the Tarim Basin, China. *Org. Geochem.* 40, 387–399. doi:10.1016/j.orggeochem.2008.11.005

Rumpel, C., Seraphin, A., Dignac, M.-F., Michaelis, W., Eusterhues, K., and Kögel-Knabner, I. (2005). Effect of Base Hydrolysis on the Chemical Composition of Organic Matter of an Acid forest Soil. *Org. Geochem.* 36, 239–249. doi:10.1016/j.orggeochem.2004.08.001

Seville, J. P. K., Willett, C. D., and Knight, P. C. (2000). Interparticle Forces in Fluidisation: A Review. *Powder Tech.* 113, 261–268. doi:10.1016/s0032-5910(00)00309-0

Slatt, R. M., and O'Brien, N. R. (2011). Pore Types in the Barnett and Woodford Gas Shales: Contribution to Understanding Gas Storage and Migration Pathways in fine-grained Rocks. *Bulletin* 95, 2017–2030. doi:10.1306/03301110145

Song, G., Zhang, L., Lu, S., Xu, X., Zhu, R., Wang, M., et al. (2013). Resource Evaluation Method for Shale Oil and its Application. *Earth Sci. Front.* 20, 221–228.

Su, T., and Zheng, Y. (2007). Correlation between Heavy Oil Composition and its Viscosity. *J. Yangtze Univ. Nat. Sci. Edition* 4, 60–62. doi:10.16772/j.cnki.1673-1409.2007.01.019

Wang, E., Feng, Y., Liu, G., Chen, S., Wu, Z., and Li, C. (2021). Hydrocarbon Source Potential Evaluation Insight into Source Rocks-A Case Study of the First Member of the Paleogene Shahejie Formation, Nanpu Sag, NE China. *Energ. Rep.* 7, 32–42. doi:10.1016/j.egyr.2020.11.099

Wang, E., Liu, G., Pang, X., Li, C., Zhao, Z., Feng, Y., et al. (2020). An Improved Hydrocarbon Generation Potential Method for Quantifying Hydrocarbon Generation and Expulsion Characteristics with Application Example of Paleogene Shahejie Formation, Nanpu Sag, Bohai Bay Basin. *Mar. Pet. Geology.* 112, 104106. doi:10.1016/j.marpetgeo.2019.104106

Wang, M., Sherwood, N., Li, Z., Lu, S., Wang, W., Huang, A., et al. (2015). Shale Oil Occurring between Salt Intervals in the Dongpu Depression, Bohai Bay Basin, China. *Int. J. Coal Geology.* 152, 100–112. doi:10.1016/j.coal.2015.07.004

Wang, S., Shen, B., and Lin, R. (2010). Correlation for the Viscosity of Heavy Oil and its Chemical Composition. *Acta PetroleiSinica: Pet. Process. Section* 26, 795–799. doi:10.3969/j.issn.1001-8719.2010.05.023

Wang, Y., Wang, X., Song, G., Liu, H., Zhu, D. S., Zhu, D. Y., et al. (2016). Genetic connection between mud shale lithofacies and shale oil enrichment in Jiyang Depression, Bohai Bay Basin. *Petroleum Exploration and Dev.* 43, 696–704. doi:10.1016/s1876-3804(16)30091-x

Wang, Z., Zhang, Y., Liang, X., Cheng, F., Jin, Q., Liu, W., et al. (2014). Characteristics of shale lithofacies formed under different hydrodynamic conditions in the Wufeng-Longmaxi Formation, Sichuan Basin. *Acta Petrolei Sinica* 35, 623–632. doi:10.7623/syxb201404002

Wei, L., Mastalerz, M., Schimmelmann, A., and Chen, Y. (2014). Influence of soxhlet-Extractable Bitumen and Oil on Porosity in Thermally Maturing Organic-Rich Shales. *Int. J. Coal Geology.* 132, 38–50. doi:10.1016/j.coal.2014.08.003

Wei, Z., Zou, Y.-R., Cai, Y., Wang, L., Luo, X., and Peng, P. a. (2012). Kinetics of Oil Group-type Generation and Expulsion: An Integrated Application to Dongying Depression, Bohai Bay Basin, China. *Org. Geochem.* 52, 1–12. doi:10.1016/j.orggeochem.2012.08.006

Xie, X., Li, M., Littke, R., Huang, Z., Ma, X., Jiang, Q., et al. (2016). Petrographic and Geochemical Characterization of Microfacies in a Lacustrine Shale Oil System in the Dongying Sag, Jiyang Depression, Bohai Bay Basin, Eastern China. *Int. J. Coal Geology.* 165, 49–63. doi:10.1016/j.coal.2016.07.004

Xie, Z. (2009). Research on the Quaternary fine-fraction Lithofacies and Sedimentation Model in Tainan Area, Qaidam Basin. *Earth Sci. Front.* 16, 245–250. doi:10.1016/s1872-5791(08)60103-7

Xue, H., Tian, S., Lu, S., Zhang, W., Du, T., and Mu, G. (2015). Selection and Verification of Key Parameters in the Quantitative Evaluation of Shale Oil: A Case Study at the Qingshankou Formation, Northern Songliao Basin. *Bull. Mineralogy, Pet. Geochem.* 34, 70–78. doi:10.3969/j.issn.1007-2802.2015.01.008

Yang, W., Jiang, Y., and Wang, Y. (2015a). Study on Shale Facies Sedimentary Environment of Lower Es3-Upper Es4 in Dongying Sag. *J. China Univ. Pet.* 39, 19–26. doi:10.3969/j.issn.1673-5005.2015.04.003

Yang, Y., Lei, T., Guan, B., Tian, C., and Wu, Y. (2015b). Differences of Solvable Organic Matters with Different Occurrence States in Argillaceous Source Rocks of Coastal Shallow-lake Facie. *Lithologic Reservoirs* 27, 77–82. doi:10.3969/j.issn.1673-8926.2015.02.012

Yu, T., Lu, S., Li, J., and Zhang, P. (2018). Prediction for Favorable Area of Shale Oil Free Resources in Dongying Sag. *Fault-Block Oil and Gas Field* 25, 16–21. doi:10.6056/dkyqt201801004

Zeng, X., Cai, J., Dong, Z., Bian, L., and Li, Y. (2018). Relationship between mineral and Organic Matter in Shales: The Case of Shahejie Formation, Dongying Sag, China. *Minerals* 8, 222. doi:10.3390/min8060222

Zeng, X., Cai, J., Dong, Z., Wang, X., and Hao, Y. (2017). Sedimentary Characteristics and Hydrocarbon Generation Potential of Mudstone and Shale: a Case Study of Middle Submember of Member 3 and Upper Submember of Member 4 in Shahejie Formation in Dongying Sag. *Acta Petrolei Sinica* 38, 31–43. doi:10.7623/syxb201701004

Zhang, J., Feng, Z., Fang, W., Huo, Q., Zhang, K., Li, J., et al. (2014). Crude-oil Hydrocarbon Composition Characteristics and Oil Viscosity Prediction in the Northern Songliao Basin. *Sci. China: Earth Sci.* 44, 1324–1339. doi:10.1007/s11430-013-4656-8

Zhang, J., Jiang, Z., Jiang, X., Wang, S., Liang, C., and Wu, M. (2016). Oil Generation Induces Sparry Calcite Formation in Lacustrine Mudrock, Eocene of east China. *Mar. Pet. Geology.* 71, 344–359. doi:10.1016/j.marpetgeo.2016.01.007

Zhang, L., Li, Z., Li, J., Zhu, R., and Sun, X. (2012). Feasibility Analysis of Existing Recoverable Oil and Gas Resource in the Palaeogene Shale of Dongying Depression. *Nat. Gas Geosci.* 23, 1–13. doi:10.11764/j.issn.1672-1926.2012.01.1

Zhang, L., Li, Z., Zhu, R., Li, J., and Zhang, L. (2008). Resource Potential of Shale Gas in Paleogene in Jiyang Depression. *Nat. Gas Industry* 28, 26–29. doi:10.3787/j.issn.1000-0976.2008.12.006

Zhang, L., Liu, Q., Zhu, R., Li, Z., and Lu, X. (2009). Source Rocks in Mesozoic-Cenozoic continental Rift Basins, east China: A Case from Dongying Depression, Bohai Bay Basin. *Org. Geochem.* 40, 229–242. doi:10.1016/j.orggeochem.2008.10.013

Zhang, S., Chen, S., Yan, J., Tan, J., Zhang, Y., Gong, W., et al. (2015). Characteristics of Shale Lithofacies and Reservoir Space in the 3rd and 4th Members of Shahejie Formation, the West of Dongying Sag. *Nat. Gas Geosci.* 26, 320–332. doi:10.11764/j.issn.1672-1926.2015.02.0320

Zhang, S., Zhang, L., Li, Z., and Hao, Y. (2012). Formation Conditions of Paleogene Shale Oil and Gas in Jiyang Depression. *Pet. Geology. Recovery Efficiency* 19, 1–6. doi:10.13673/j.cnki.cn37-1359/te.2012.06.001

Zhang, Y., Chen, S., Sun, J., Ma, Y., Liu, C., Li, Z., et al. (2016). Lithofacies and Sedimentary Environment of Shale in Carboniferous Keluke Formation, Northern Qaidam Basin. *Earth Sci. Front.* 23, 86–94. doi:10.13745/j.esf.2016.05.009

Zhu, X., Cai, J., Liu, Q., Li, Z., and Zhang, X. (2019). Thresholds of Petroleum Content and Pore Diameter for Petroleum Mobility in Shale. *Bulletin* 103, 605–617. doi:10.1306/0816181617517009

Zhu, X., Cai, J., Liu, W., and Lu, X. (2016). Occurrence of Stable and mobile Organic Matter in the clay-sized Fraction of Shale: Significance for Petroleum Geology and Carbon Cycle. *Int. J. Coal Geology.* 160-161, 1–10. doi:10.1016/j.coal.2016.03.011

Zou, C., Pan, S., Jing, Z., Gao, J., Yang, Z., Wu, S., et al. (2020). Shale Oil and Gas Revolution and its Impact. *Acta Petrolei Sinica* 41, 1–12. doi:10.7623/syxb202001001

Conflict of Interest: Authors MS, HL, and XW were employed by Shengli Oilfield Company.

The remaining authors declare that the research was conducted in the absence of any commercial or financial relationships that could be construed as a potential conflict of interest.

The handling Editor declared a past co-authorship with one of the authors HL.

Shale Reservoir 3D Structural Modeling Using Horizontal Well Data: Main Issues and an Improved Method

Zhiguo Shu[1], Guochang Wang[2]*, Yang Luo[3], Chao Wang[1], Yalin Chen[1] and Xianjun Zou[1]

[1]Research Institute of Exploration and Development, SINOPEC Jianghan Oilfield Company, Wuhan, China, [2]Engineering Department, Saint Francis University, Loretto, PA, United States, [3]Key Laboratory of Tectonics and Petroleum Resource of Ministry of Education, China University of Geosciences, Wuhan, China

Shale oil and gas fields usually contain many horizontal wells. The key of 3D structural modeling for shale reservoirs is to effectively utilize all structure-associated data (e.g., formation tops) in these horizontal wells. The inclination angle of horizontal wells is usually large, especially in the lateral section. As a result, formation tops in a horizontal well are located at the distinct lateral positions, while formation tops in a vertical well are usually stacked in the same or similar lateral position. It becomes very challenging to estimate shale layer thickness and structural map of multiple formation surfaces using formation tops in horizontal wells. Meanwhile, the large inclination angle of horizontal wells indicates a complicated spatial relation with shale formation surfaces. The 3D structural modeling using horizontal well data is much more difficult than that using vertical well data. To overcome these new challenges in 3D structural modeling using horizontal well data, we developed a method for 3D structural modeling using horizontal well data. The main process included 1) adding pseudo vertical wells at formation tops to convert the uncoupled formation tops to coupled formation tops as in vertical wells, 2) estimating shale thickness by balancing the shale thickness and dip angle change of a key surface, and 3) detecting horizontal well segments landing in the wrong formations and adding pseudo vertical wells to fix them. We used our improved method to successfully construct two structural models of Longmaxi–Wufeng shale reservoirs at a well pad scale and a shale oil/gas field scale. Our research demonstrated that 3D structural modeling could be improved by maximizing the utilization of horizontal well data, thus optimizing the quality of the structural model of shale reservoirs.

Keywords: shale reservoir, horizontal well, 3D structural modeling, pseudo vertical well, landing formation

INTRODUCTION

After over 20 years of the rapid development of hydraulic fracturing in horizontal wells, many shale oil and gas fields exist, most of which are in the United States, Canada, and China (EIA, 2019; IEA, 2019). Horizontal well drilling, as one of the main techniques, opens the door for the commercial shale oil and gas production and has been extensively implemented in the shale play core areas, such as the Barnett Shale in northwestern Texas (Jarvie et al., 2007), the Marcellus Shale in southwestern Pennsylvania (Carter et al., 2011; Wang and Carr, 2013), the Utica-Point Pleasant Shale in eastern Ohio (Shahkarami and Wang, 2017), and the Wufeng–Longmaxi Shale in the Sichuan Basin (Wang, 2015). Data, including wire line logs, formation tops, well location, and well trajectory, in horizontal
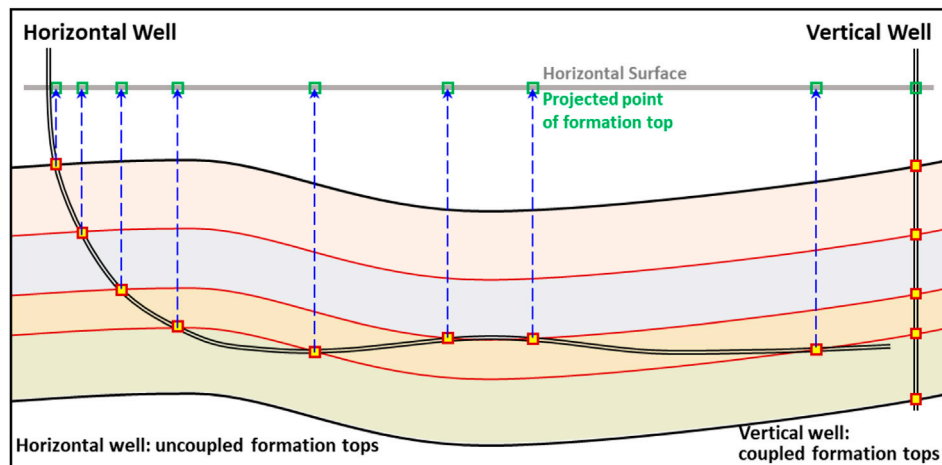
FIGURE 1 | Comparison of formation tops and wellbore trajectory characteristics in horizontal wells and vertical wells.

wells are critical for evaluating the properties of shale reservoirs. For 3D structural modeling, formation tops are the predominant data. However, the horizontal well formation top data have distinct features compared to vertical wells due to the large inclination angle of horizontal wells (**Figure 1**). The horizontal location of formation tops in one horizontal well is far from each other, while it is the same or similar in vertical wells (**Figure 1**). This raises new challenges for constructing a 3D structural model of shale reservoirs (Wang et al., 2018a; Qiao et al., 2018; Long et al., 2019; Shu et al., 2020).

Wang et al. (2018b) developed a method of adding pseudo vertical wells (PVWs) to convert formation tops in each horizontal well to more formation tops in multiple PVWs based on the shale layer thickness. This provides more control points for constructing a high-quality 3D structural model of shale reservoirs. Qiao et al. (2018) used a similar idea to build 3D structural models by transforming horizontal wells into multiple equivalent vertical wells. However, both of them did not provide details of their methods, such as how to add these PVWs and how to transform horizontal wells to multiple vertical wells. Meanwhile, shale thickness data are critical to add formation tops in PVWs, but there is rarely a published method concerning the estimation of shale formation thickness using horizontal well data. In addition, the laterals of horizontal wells are approximately parallel to the formation surfaces and could penetrate through the formation surfaces up and down multiple times, forming a complicated relationship between horizontal wells and formation surfaces. Therefore, it is not surprising that some horizontal wells are located in the wrong formations of the constructed 3D structural model. This causes it necessary to develop a method to effectively detect these errors in the 3D structural model and fix these errors.

The research aimed to present a comprehensive and effective method for 3D structural modeling using data mainly from horizontal wells. In this study, we first discussed the data features in horizontal wells for 3D structural modeling and the main issues using horizontal well data to construct 3D structural

models. Then, the developed method for 3D structural modeling using horizontal well data were illustrated in detail and its effectiveness was demonstrated by constructing two 3D structural models of the Wufeng–Longmaxi Shale in the Jiaoshiba area, eastern Sichuan Basin. Finally, an uncertainty source, a level, and a method to reduce these uncertainties were discussed for 3D structural modeling using horizontal wells.

DATA CHARACTERISTICS AND ISSUES

Uncoupled Formation Tops and Abnormal Thickness

The essential purpose of 3D structural modeling is to simultaneously implement spatial interpolation of elevation for multiple formation surfaces to generate a framework for the target formations within the study area. As a result, the spatial distribution of formations, including the formation surface structure and formation thickness, is estimated. In a specific vertical well, all formation tops are in the same or a similar horizontal position (**Figure 1**). For spatial interpolation using data in vertical wells, the control points from these coupled formation tops are distributed similarly for different formation surfaces within the study area. However, formation tops from horizontal wells are uncoupled, locating at different positions in the same horizontal well. This causes it a challenge to ensure these formation surfaces are coupled with each other because the position distribution of control points can significantly influence the spatial interpolation (Stein, 1999). This influence could be more considerable when the amount of control points is limited. Unfortunately, formation tops are usually scattered in most hydrocarbon reservoirs, and the uncoupled formation tops could cause many severe problems in the 3D structural modeling of shale reservoirs.

The generated formation surfaces using these uncoupled formation tops in horizontal wells are either too close to each other, intersected, or too far away (**Figure 2**). In the upper part of
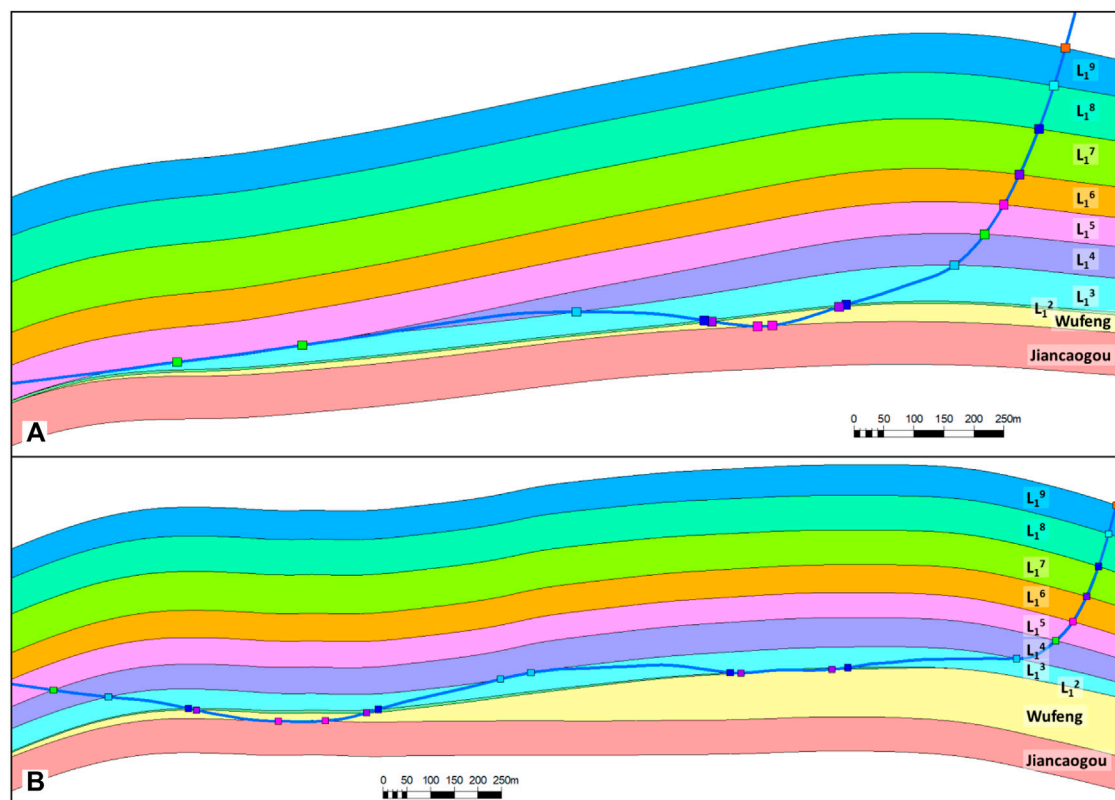
FIGURE 2 | The abnormal thickness in the lower part of the 3D structural model of the Wufeng–Longmaxi Shale reservoir in the Jiaoshiba area. **(A)** Cross section along the well JY-a; **(B)** cross section along the well JY-b.

shale reservoirs, horizontal wells usually intersect with formation surfaces with a large angle (e.g., >70°) so that formation tops in horizontal wells have a similar distribution feature as those in vertical wells (**Figure 2**). Meanwhile, a structural map of any formation surfaces, interpreted from either seismic data or other geological sources, could be used as a soft constraint of the spatial interpolation, providing the regional dip angle information. This can mitigate the problem of the abnormal thickness in the upper part of shale reservoirs. Therefore, the issue of abnormal thickness is less serious in the upper part of shale reservoirs. But this issue becomes common in the formations penetrated by horizontal laterals (usually the lower part of shale reservoirs) in which the formation tops, far away from each other laterally, are uncoupled (**Figure 2**). Although structural maps may exist, using structural maps of formation surfaces as a soft constraint fails to mitigate the abnormal thickness resulting from the uncoupled formation tops.

The Large Wellbore Inclination and Incorrect Landing Formation

The formation tops divide the well trajectory into multiple segments and each segment lands in a specific formation, which is named landing formation in this research. The landing formation data are along well trajectory, including the

location (X and Y) and formation ID (**Table 1**). In an individual vertical well, the horizontal location of landing formations is the same as or similar to their formation tops (**Figure 1**). Therefore, the formation tops in vertical wells usually ensure the vertical wells landing in the correct formations in the 3D structural model. However, landing formations and formation tops in horizontal wells are usually at different horizontal locations. It is common that some segments of horizontal wells land in the incorrect formation in the constructed 3D structural model, especially in the segments with relatively large inclination (e.g., >70°) and limited control from formation tops. In 3D structural modeling for shale reservoirs, it is critical to ensure all well segments land in the correct formation. Therefore, the landing formation data serve as a soft constraint to check errors within the 3D structural model and provide the necessary data to fix these errors.

METHODOLOGY

To construct a high-quality 3D structural model for shale reservoirs using horizontal well data, we need to deal with the uncoupled spatial interpolation and the incorrect landing formation. For the uncoupled spatial interpolation of multiple formation surfaces, our approach is to convert the uncoupled

TABLE 1 | Example of Landing Formation Data and the Inferred Elevation Range of the Landing Formation Top. The data in gray-filled cells are for the added pseudo vertical wells.

| Well segment	Well trajectory			Landing formation		Landing formation top ($\delta = 1$)		Landing formation top ($\delta = 0.95$)	
	X	Y	Z	ID	Thickness	Upper limit	Lower limit	Upper limit	Lower limit
09	50,639.08	3,210.006	−1,665.26	L_1^3	11.486	−1,653.78	−1,665.26	−1,654.35	−1,664.69
	50,636.07	3,200.926	−1,665.56	L_1^3		−1,654.07	−1,665.56	−1,654.64	−1,664.98
	50,633.08	3,191.86	−1,665.83	L_1^3		−1,654.35	−1,665.83	−1,654.92	−1,665.26
	50,630.14	3,182.914	−1,666.09	L_1^3		−1,654.61	−1,666.09	−1,655.18	−1,665.52
	50,627.1	3,173.602	−1,666.36	L_1^3		−1,654.87	−1,666.36	−1,655.45	−1,665.78
	50,624.22	3,164.678	−1,666.59	L_1^3		−1,655.10	−1,666.59	−1,655.68	−1,666.01
	50,621.3	3,155.534	−1,666.79	L_1^3		−1,655.30	−1,666.79	−1,655.88	−1,666.22
	50,618.43	3,146.511	−1,666.96	L_1^3		−1,655.48	−1,666.96	−1,656.05	−1,666.39
	50,615.62	3,137.712	−1,667.12	L_1^3		−1,655.63	−1,667.12	−1,656.20	−1,666.54
	50,612.76	3,128.893	−1,667.25	L_1^3		−1,655.77	−1,667.25	−1,656.34	−1,666.68
	50,609.82	3,119.852	−1,667.39	L_1^3		−1,655.91	−1,667.39	−1,656.48	−1,666.82
	50,606.84	3,110.715	−1,667.55	L_1^3		−1,656.06	−1,667.55	−1,656.63	−1,666.97
13	50,386.96	2,441.703	−1,699.44	W_{ufeng}	4.628	−1,694.82	−1,699.44	−1,695.05	−1,699.21
	50,384.05	2,432.744	−1,699.55	W_{ufeng}		−1,694.92	−1,699.55	−1,695.15	−1,699.32
	50,381.12	2,423.666	−1,699.66	W_{ufeng}		−1,695.03	−1,699.66	−1,695.26	−1,699.43
	50,378.22	2,414.683	−1,699.77	W_{ufeng}		−1,695.14	−1,699.77	−1,695.37	−1,699.53
	50,375.32	2,405.709	−1,699.87	W_{ufeng}		−1,695.24	−1,699.87	−1,695.48	−1,699.64
	50,372.4	2,396.597	−1,699.97	W_{ufeng}		−1,695.35	−1,699.97	−1,695.58	−1,699.74
	50,369.47	2,387.37	−1700.07	W_{ufeng}		−1,695.45	−1700.07	−1,695.68	−1,699.84
	50,366.58	2,378.323	−1700.17	W_{ufeng}		−1,695.54	−1700.17	−1,695.77	−1,699.93
	50,363.64	2,369.185	−1700.25	W_{ufeng}		−1,695.62	−1700.25	−1,695.85	−1700.02
	50,360.7	2,360.099	−1700.32	W_{ufeng}		−1,695.70	−1700.32	−1,695.93	−1700.09
	50,357.68	2,350.997	−1700.39	W_{ufeng}		−1,695.76	−1700.39	−1,695.99	−1700.16
	50,354.68	2,342.056	−1700.45	W_{ufeng}		−1,695.82	−1700.45	−1,696.05	−1700.22
	50,351.62	2,332.935	−1700.49	W_{ufeng}		−1,695.86	−1700.49	−1,696.09	−1700.26
	50,348.57	2,323.822	−1700.54	W_{ufeng}		−1,695.91	−1700.54	−1,696.14	−1700.31
	50,345.79	2,315.578	−1700.61	W_{ufeng}		−1,695.98	−1700.61	−1,696.21	−1700.38
	50,342.5	2,305.841	−1700.69	W_{ufeng}		−1,696.06	−1700.69	−1,696.29	−1700.46
	50,339.36	2,296.514	−1700.77	W_{ufeng}		−1,696.14	−1700.77	−1,696.37	−1700.54
	50,336.24	2,287.142	−1700.86	W_{ufeng}		−1,696.23	−1700.86	−1,696.47	−1700.63

formation tops to the coupled formation tops by adding pseudo vertical wells at formation top data (PVW-As) in all horizontal wells (Wang et al., 2018b; **Figure 3**). The elevation of formation tops in these PVW-As can be calculated using the elevation of the formation top at the intersection point and the thickness of shale layers (**Figure 3A**). The uncoupled formation tops in horizontal wells become coupled after adding formation tops in these PVW-As for all formations, fixing the uncoupled spatial interpolation. Now, the problem is that the thickness of shale layers is unknown. Therefore, in this method, the key is to estimate the thickness of all shale layers.

In this research, one part of our improved method is to estimate the thickness of shale layers by balancing the dip angle change and the shale thickness change. This method involves two items: the initial thickness of shale layers and the dip angle change of a key surface. The key surface should have strong responses in wire line logs and seismic data, for example, the Wufeng base in the Jiaoshiba area. First, an initial thickness of all shale layers should be estimated from the formation tops in vertical wells. Within a relatively small area (e.g., a well pad), we can assume that the shale layer thickness is constant or has little change (Wang et al., 2018a), so the formation tops in vertical wells can usually give a reasonable estimation of the initial shale thickness. In a relatively large area, the shale thickness could

change significantly, so does the dip angle of the key surface. If only limited vertical wells exist, their formation tops are usually insufficient to give a reasonable estimation of the initial shale thickness. Therefore, we developed an iterative process to repeatedly update the shale thickness and the structural map of the key surface by balancing the dip angle and shale thickness. In detail, the thickness contour map using vertical well data only is used to calculate the elevation of the key surface at all PVW-As, and then a smoothed structural map of the key surface was generated to calculate the shale thickness at all PVW-As, which were used to make their smoothed contour maps. This process could be repeated several times, and these smoothed thickness contour maps were used as the initial thickness in the study area.

The initial thickness of shale layers has two main functions: 1) to estimate the actual shale thickness by adjusting the initial thickness, and 2) to set the thickness change threshold, which is a percentage of the initial thickness. Again, the elevation of the key surface at all PVW-As was calculated using the initial thickness to generate its structural map. The dip angle change of the key surface at all PVW-As was calculated to detect any value larger than the dip angle change threshold. As shown in **Figures 3B–D**, the large dip angle change usually results from the large differences between the initial and actual thickness of shale layers. Therefore, the shale thickness should be decreased or
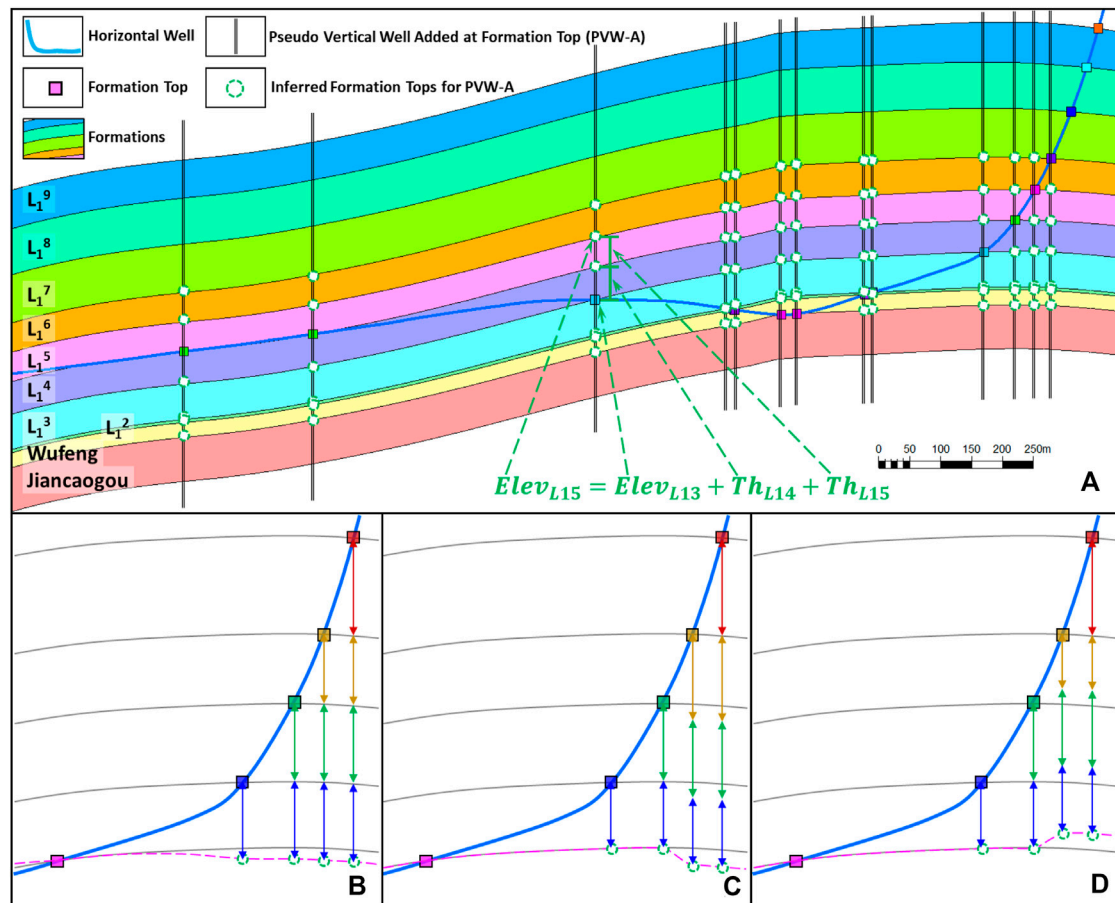
FIGURE 3 | Pseudo vertical wells added at formation tops (PVW-A) for the well JY-a in the Jiaoshiba area, Sichuan Basin **(A)** and the effects of shale layer thickness on formation top elevation calculation **(B–D)**.

increased within a range, the thickness change threshold (e.g., 10% of the original formation thickness), to reduce the dip angle change (see **Supplementary Appendix** for more details). This process continues until all dip angle changes are less than the dip angle change threshold. We developed a VBA program to achieve this process automatically. Finally, the TVTs estimated from all PVW-As and vertical wells together provide a larger dataset to analyze the distribution of formation thickness inside the area statistically. All abnormal TVTs that exist inside the study area should be double-checked.

The incorrect landing formation errors in the 3D structural model can be solved by adding a PVW for each well segment with an error (PVW-B; **Figure 4A**). The PVW-B is usually added at the middle of the well segment with an error. Different from PVW-As, a PVW-B intersects with the horizontal well within a specific formation and the relative position of the intersection point in this formation is unclear. Therefore, there is no enough data to determine the elevation of any formation tops in PVW-Bs, but we can determine the elevation range of formation tops in PVW-Bs (**Figures 4B,C**). Given that the elevation of the intersection point between a PVW-B and horizontal well is ELEV and its landing formation thickness is TH, the formation top elevation of the

intersection point's landing formation in the PVW-B must be larger than ELEV and smaller than ELEV + TH (**Table 1**; **Figures 4B,C**). The elevation range of a formation top that cannot be directly used as an input of the spatial interpolation should be converted to an exact elevation value. A straightforward method is to arbitrarily use the mid-point or a random point within the elevation range, but it is prone to cause large dip angle change at the location of PVW-Bs, especially when PVW-Bs are close to any other wells (horizontal wells, PVW-As, or other PVW-Bs). In order to minimize these dip angle changes, a better strategy is to use the point within the elevation range and closest to the formation surfaces at the location of PVW-Bs. This closest point is either the lower limit (**Figure 4B**) or the upper limit (**Figure 4C**) of the elevation range. This approach results in the slightest change of the current 3D structural model. Besides, this research introduced a confidential constant δ ($0.5 \leq \delta \leq 1$) to re-calculate the elevation range as ELEV+$(1-\delta)$TH to ELEV + δTH. This confidential constant reduces the elevation ranges, offers more options for 3D structural modeling (**Table 1**), and can fit the real geological situation better. After determining the formation top elevation of the intersection point's landing formation, all
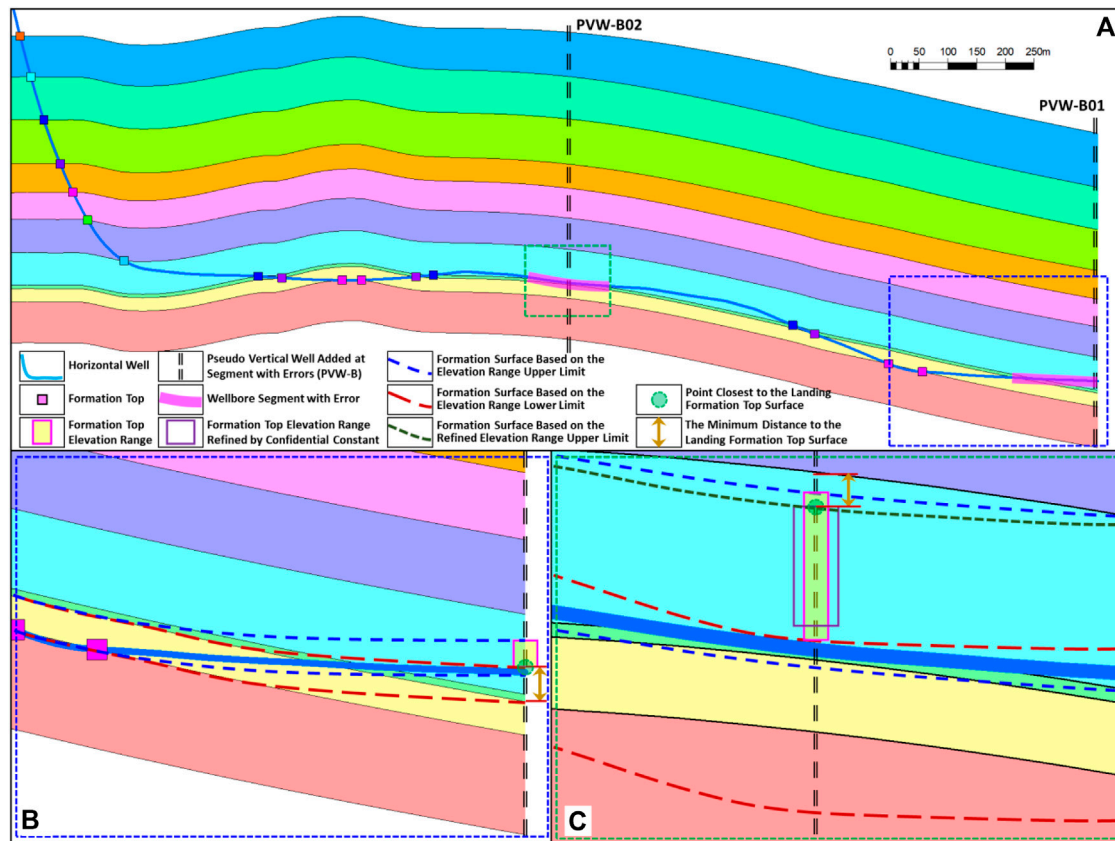
FIGURE 4 | Pseudo vertical wells added for the well segments with the incorrect landing formation (PVW-B) and the formation top of the intersection points landing formation added for PVW-Bs. **(A)** Well JY-b and the well segments with error; **(B)** elevation range and the formation top using its lower limit; and **(C)** elevation range refined by confidential constant and formation top using its upper limit. The two dash rectangles indicate the location of **Figures 4B,C**.

formation tops in PVW-Bs can be calculated using the TVT of shale layers, and the 3D structural model can be reconstructed. This process should continue until no more errors exist in the 3D structural model.

A generalized workflow of this method is shown in **Figure 5**, including adding PVW-As, iteratively updating TVTs based on dip angle changes, detecting all incorrect landing formations, and adding PVW-Bs. This workflow can be revised in terms of the data features in a specific study area.

RESULTS

Two case studies using data of the Wufeng–Longmaxi Shale in the Jiaoshiba area, eastern Sichuan Basin, have been implemented to validate the method in this research (**Table 2**). The first case is to build a 3D structural model for the JY-1 district, which was located in the northern Jiaoshiba area. This area includes eight horizontal wells and five vertical wells (one inside and four outside the JY-1 district). This case represents a typical situation to build a well pad scale 3D structural model of shale reservoirs. The second case is to construct a 3D structural model for the whole Jiaoshiba area, including 283 horizontal wells and

eight vertical wells. We assumed that the seismic data were only accessible for the second case to enlarge the differences between the two cases. Besides, we only constructed the 3D structural model of the lower six shale layers (**Figure 4A**) for the first case in which all the eight horizontal wells targeted the lower part of the Wufeng–Longmaxi Shale. In contrast, all the nine shale layers (**Figure 4A**) were analyzed in the second case.

Well Pad Scale 3D Structural Modeling: The JY-1 District

This study case represents a situation that we need to construct a 3D structural model of one or two well pads surrounded by many vertical wells. This situation is common because many shale plays are located within conventional oil and gas fields, such as the Marcellus Shale in the Appalachian Basin, the Eagle Ford Shale in the Permian Basin, and the Qingshankou Shale in the Songliao Basin. The development of conventional oil and gas has drilled a significant number of vertical wells, which can provide lots of constraint points to estimate the shale thickness. Meanwhile, when the study area is relatively small, the available vertical wells can give a reasonable estimation of shale thickness, assuming that shale formations do not or only gradually change within a small
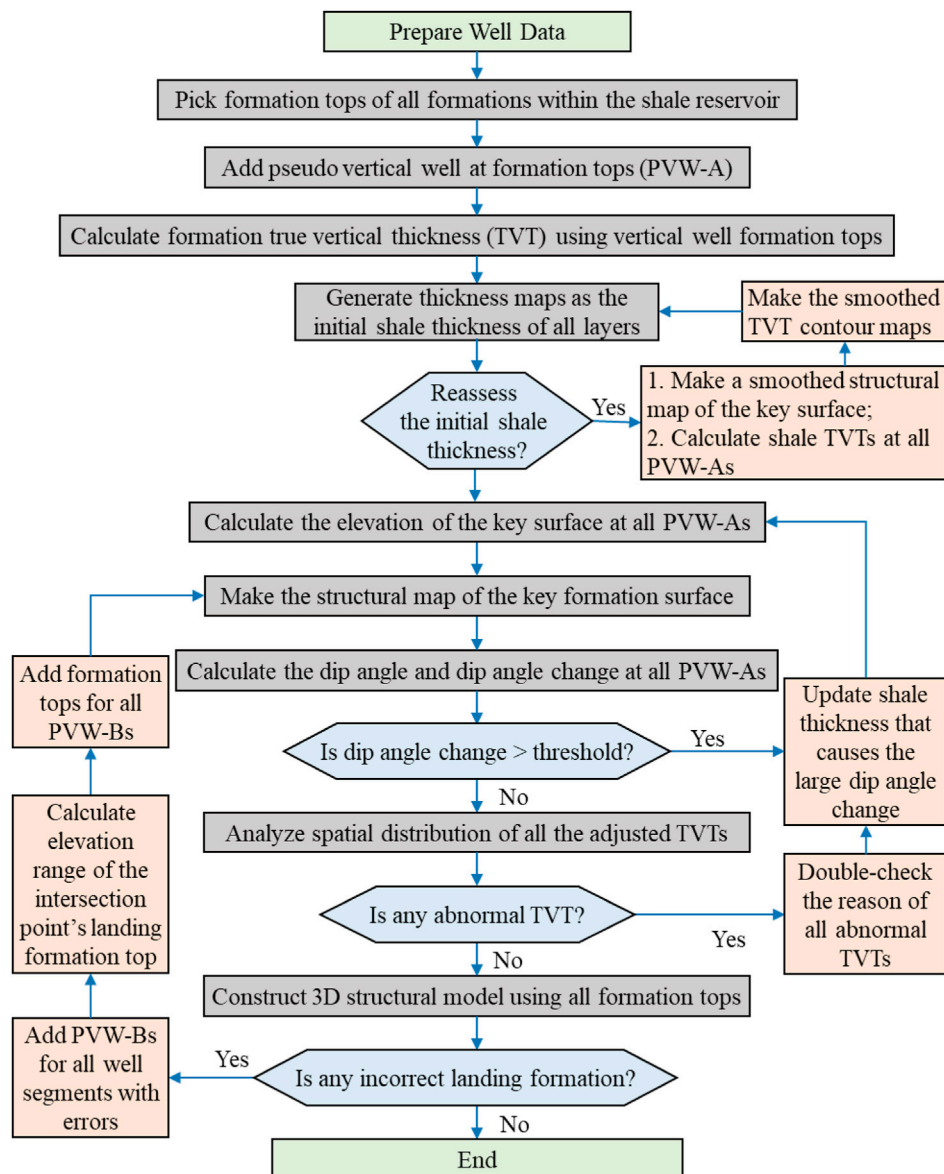
FIGURE 5 | A generalized workflow to build a 3D structural model for shale oil and shale gas fields using horizontal wells.

TABLE 2 | Data features of the two cases in the Jiaoshiba area, eastern Sichuan Basin.

Features	Case one: The JY-1 district	Case two: The entire Jiaoshiba area
WELLS	Eight horizontal wells	283 horizontal wells
	Five vertical wells (one inside and four outside)	Eight vertical wells
AREA	22.71 × 106 m²	282.32 × 106 m²
SEISMIC DATA	Not accessible	Accessible with interpreted structure map of the Wufeng base
FORMATION TOPS	78 data points in horizontal wells	4,024 data points in horizontal wells
	35 data points in vertical wells	80 data points in vertical wells

area (Wang et al., 2018b). Therefore, the data in vertical wells can make a reliable estimation of shale thickness with relatively low uncertainty, simplifying the process of 3D structural modeling.

In this case, there are a total of 94 formation top data points for the six layers within the Wufeng–Longmaxi Shale, including 87 points in the eight horizontal wells and 35 points in the vertical
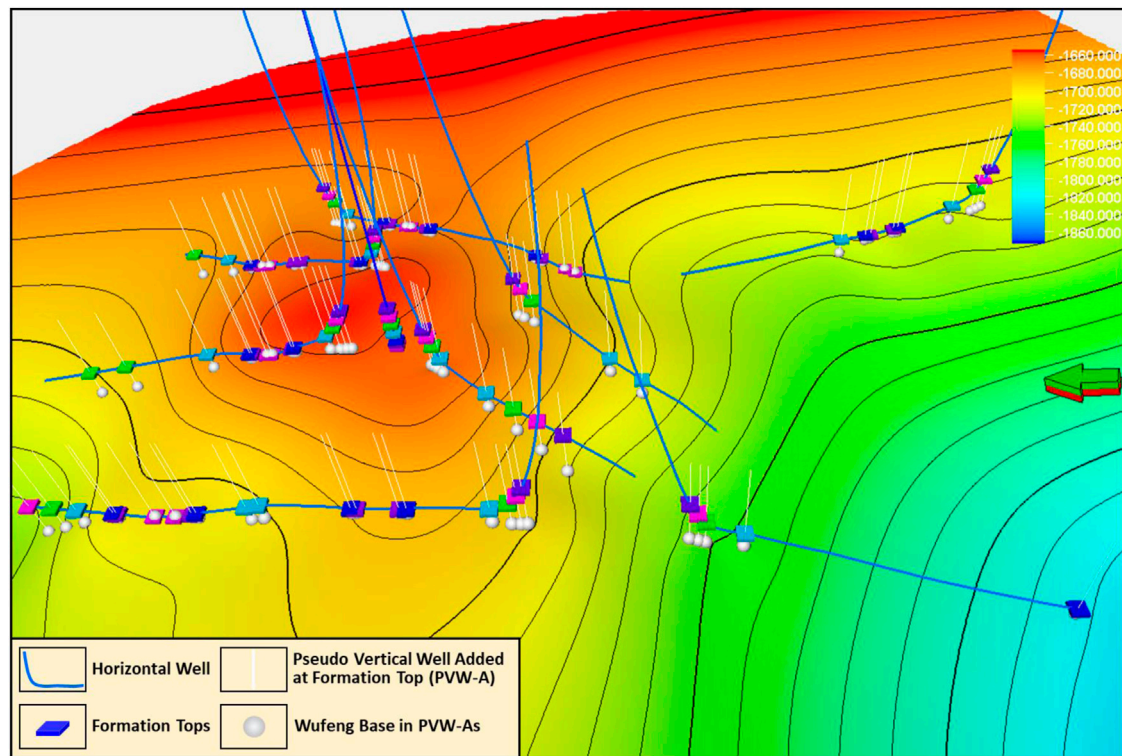
FIGURE 6 | Log-interpreted formation tops and the pseudo vertical wells added at these formation tops (PVW-As) with the inferred formation top of the Wufeng base. The structural map is the Wufeng base generated using the formation top in all wells, including the horizontal wells, the vertical wells, and PVW-As.

wells. A PVW-A was added for each formation top in the horizontal wells, adding 87 PVW-As in total (**Figure 6**). The seven formation tops in the vertical well JY-1 were used to calculate the actual vertical thickness (TVT) of the six shale layers at well JY-1, which were used as the TVTs of the six shale layers in the entire JY-1 district. Therefore, we can calculate the Wufeng base elevation at all PVW-As using the shale layer thickness and formation tops in horizontal wells (**Figure 3**). As a result, the amount of control points for Wufeng base mapping was significantly increased from 11 log-interpreted formation tops in horizontal and vertical wells to 88 points (**Figure 6**). The structural map of Wufeng base is shown in **Figures 6**, **7**. Compared to the 3D structural model along the horizontal wells JY-a and JY-b, in **Figure 2**, the 3D structural model using our improved method has a much better quality.

In the structural map of the Wufeng base, the dip angle significantly changed at the location of some PVW-As (**Figures 7**, **8**). The dip angle and curvature contour maps (**Figure 8**) helped view and summarize these dip angle changes. This mainly resulted from the significant differences between the initial thickness and actual thickness of shale layers. We mitigated the dip angle change by altering the TVTs at the location of these PVW-As automatically using our developed VBA program. For example, as shown in **Figure 7**, the dip angle change of the Wufeng base surface was reduced by increasing the thickness of L_1^4 at well JY-b and JY-c. This increased the variation of shale thickness but reduced the dip angle changes. Therefore,

we used the dip angle change threshold and thickness change threshold to limit the dip angle change and TVT change within an acceptable range. Using different values of the two thresholds, for example, the estimated thickness of the Wufeng Formation was different (**Figure 9**). The largest thickness variation occurred when setting dip angle change threshold as 1.5° and thickness change threshold as 30% (**Figure 9**). This indicated that, in order to limit the dip angle change to less than 1.5°, the thickness of the Wufeng Formation should be significantly increased or decreased. Also, the Wufeng Formation thickness was similar for all the six cases that the dip angle change threshold was set to 2.5° and 3.0° (**Figure 9**). In this research, based on the thickness change of all the six layers, we used the dip angle change threshold of 2.5° and thickness change threshold of 10% to estimate the thickness of the six shale layers (**Figure 10**). Within this small area, it is a little difficult to analyze the trend of thickness change statistically, so we directly used these TVTs to calculate the elevation of formation tops in all PVW-As (**Figure 7**).

The formation tops in all horizontal wells, the vertical well, and PVA-As were used to build the 3D structural model in the JY-1 district. However, we detected errors in six segments in four horizontal wells. **Figures 11A,B** showed an example of the errors in well JY-b. It is worth pointing out that, to check errors in all horizontal wells quickly, we extracted the landing formation information from the constructed 3D structural model and compared it with the landing formation determined from formation tops using the VBA program (**Figure 11B**). For
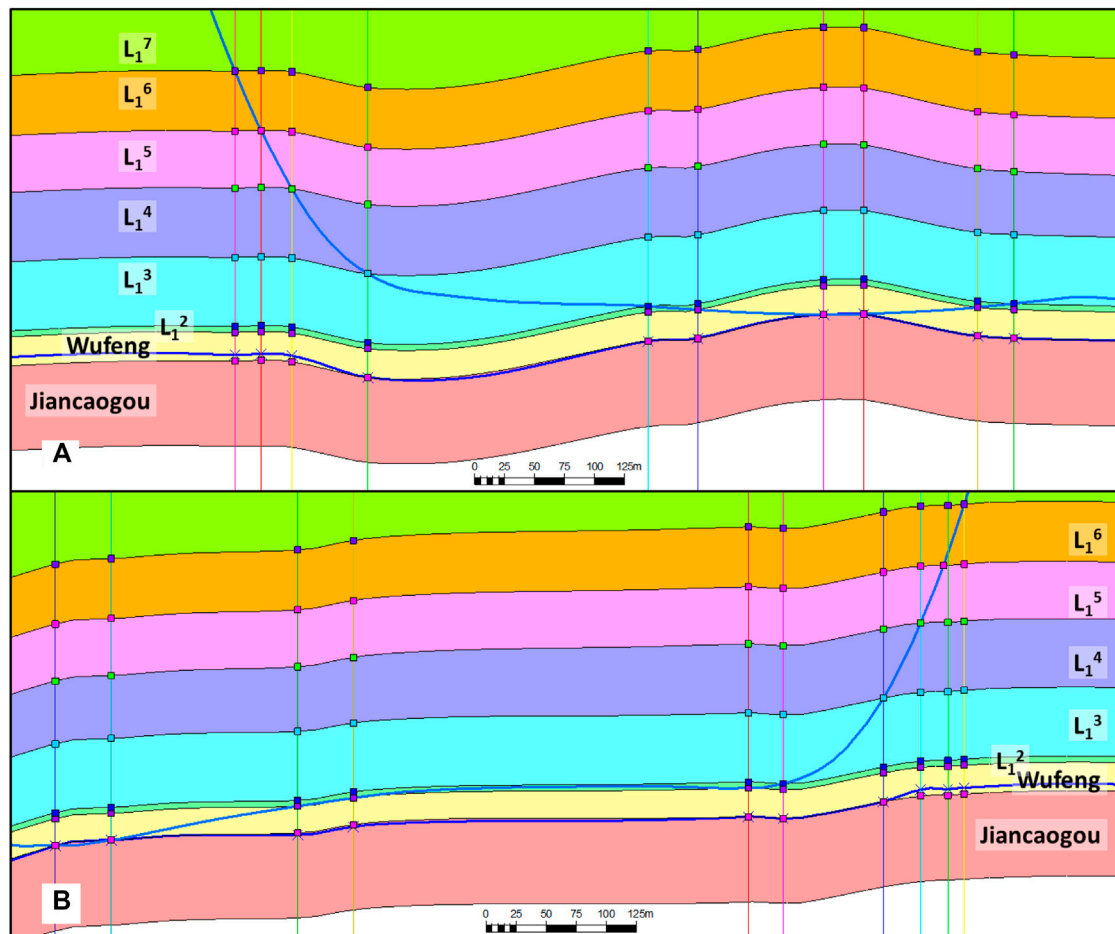
FIGURE 7 | Cross sections of wells JY-b and JY-c with the inferred formation tops in PVW-As. The blue X and the blue curve represent the formation top for the Wufeng base that was calculated using the TVTs from the well JY-1 and the Wufeng base structural map made from these inferred formation top. The color-filled squares in the PVW-As are the formation tops after adjusting the TVTs for shale layers based on the dip angle change threshold of 2.5°.

each well segment with error, we added one pseudo vertical well (PVW-B) at the middle of the well segment and calculated their formation tops with a confidential constant of 0.95 (**Figure 11C**). All errors were removed after adding these PVW-Bs and their formation tops.

Regional/Basin Scale 3D Structural Modeling: The Jiaoshiba Area

The Jiaoshiba area was much larger than the JY-1 district, with 283 horizontal wells. The data available for 3D structural modeling are summarized in **Table 1**. Similar to the first case, we added a PVW-A at each of all the 4,024 formation tops in the horizontal wells. The structural map of the Wufeng base interpreted from 3D seismic data was available (**Figure 12A**) and used as the second input for making the structural map of the key surface. Besides, within this relatively larger area, both the formation surface dip angle and thickness had a larger range. This caused two major differences from the first case in estimating the thickness of shale layers.

The first one was to deal with the differences between the true stratigraphic thickness (TST) and the true vertical thickness (TVT). When the dip angle is large, for example, ~20° in the marginal area of Jiaoshiba (**Figure 12A**), the TST is much different from TVT. Since the TVTs are affected by formation dip angle, it is better to use TST to analyze the distribution features of shale layers. In the Jiaoshiba area, the initial value of formation dip angle was estimated from the seismic-interpreted structural map of the Wufeng base (**Figure 12A**), and the formation tops in vertical wells were used to generate the TST contour maps of all shale layers (**Figure 12B**). Then, the dip angle of the Wufeng base surface, formation tops in horizontal wells, and the TST contour maps were used together to calculate the Wufeng base elevation at all PVW-As (**Figure 12A**).

The second difference was to estimate the initial thickness of shale layers using an iterative process (**Figure 5**). Within the small area of the JY-1 district, the thickness of each shale layer was considered as constant and set to the value in the vertical well JY-1. However, in the relatively larger area of the entire Jiaoshiba area, data in the limited vertical wells failed to give a high-quality
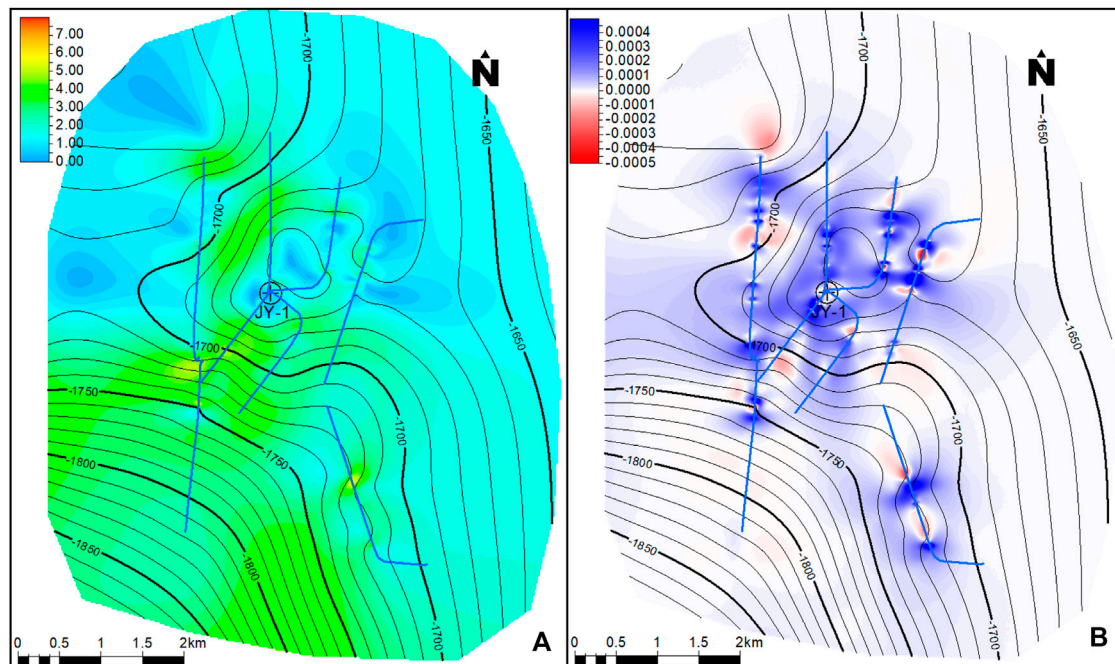
FIGURE 8 | The contour map of the dip angle **(A)** and curvature **(B)** of the Wufeng base surface that was made from the inferred formation top using shale layer TVTs from the vertical well JY-1.

estimation of shale layer thickness, especially in the areas far away from the vertical wells. Therefore, we should also take the thickness information extracted from horizontal wells into consideration by the iterative process. First, the TST data that were calculated at all PVW-As (**Figure 12C**) were used to re-evaluate the distribution features of shale layer thickness by smoothing the TST contour maps (**Figure 12D**). Then, the elevation of the Wufeng base at all PVW-As was updated again, and its dig angle was re-calculated, which was used to calculate the TSTs at all PVW-As again. Therefore, the dip angle of the Wufeng base, the TSTs at all PVW-As, and the smoothed TST contour maps were repeatedly calculated in three iterations in this research to provide a better estimation of the initial shale thickness.

The estimated initial shale thickness of shale layers was utilized to calculate the elevation of the key surface Wufeng base. Then, the dip angle change threshold and the thickness change threshold were set to 2.5° and 15%, respectively, to balance the dip angle change of the Wufeng base and thickness change of the nine shale layers. Finally, these data were combined to create a 3D structural model of the entire Jiaoshiba area, in which we found errors in 118 segments in 69 horizontal wells. Therefore, we added 118 PVW-Bs to remove all the errors in the 3D structural model. **Figure 12E** showed the final version of the 3D structural model using the formation tops in vertical wells, horizontal wells, PVW-As, and PVW-Bs.

DISCUSSION

Uncertainty is an essential component of 3D geological modeling, and it is critical to understand and estimate the uncertainties in geological models (Lelliott et al., 2009; Wellmann et al., 2014; Krajnovich et al., 2020; Liang et al., 2021). Compared to 3D structural modeling for conventional reservoirs, both data and methods were different in 3D structural modeling for shale reservoirs. Therefore, it is necessary to discuss the uncertainty in the 3D structural model of shale reservoirs. In this research, we classified the uncertainty into two groups: data-associated uncertainty and process-associated uncertainty.

Data-Associated Uncertainty

According to the features of data used for 3D structural modeling of shale reservoirs, we grouped all the data into five types and recognized their uncertainty to three levels. Well location and trajectory data are considered in the first group with the first-level uncertainty, also called hard data. They together define the spatial position of all well-related data. Uncertainty of well location and trajectory results from data measurement due to equipment and human error. In general, this uncertainty should be the least compared to all other data. Compared to well location, it is more challenging to measure the well trajectory in the underground (Zhou, 2015; Liu, 2018; Shtuka et al., 2018), and, as a result, the uncertainty of well trajectory should be higher than well location. Meanwhile, the uncertainty of well trajectory could be more significant when close to well toe since errors will accumulate along the wellbore.
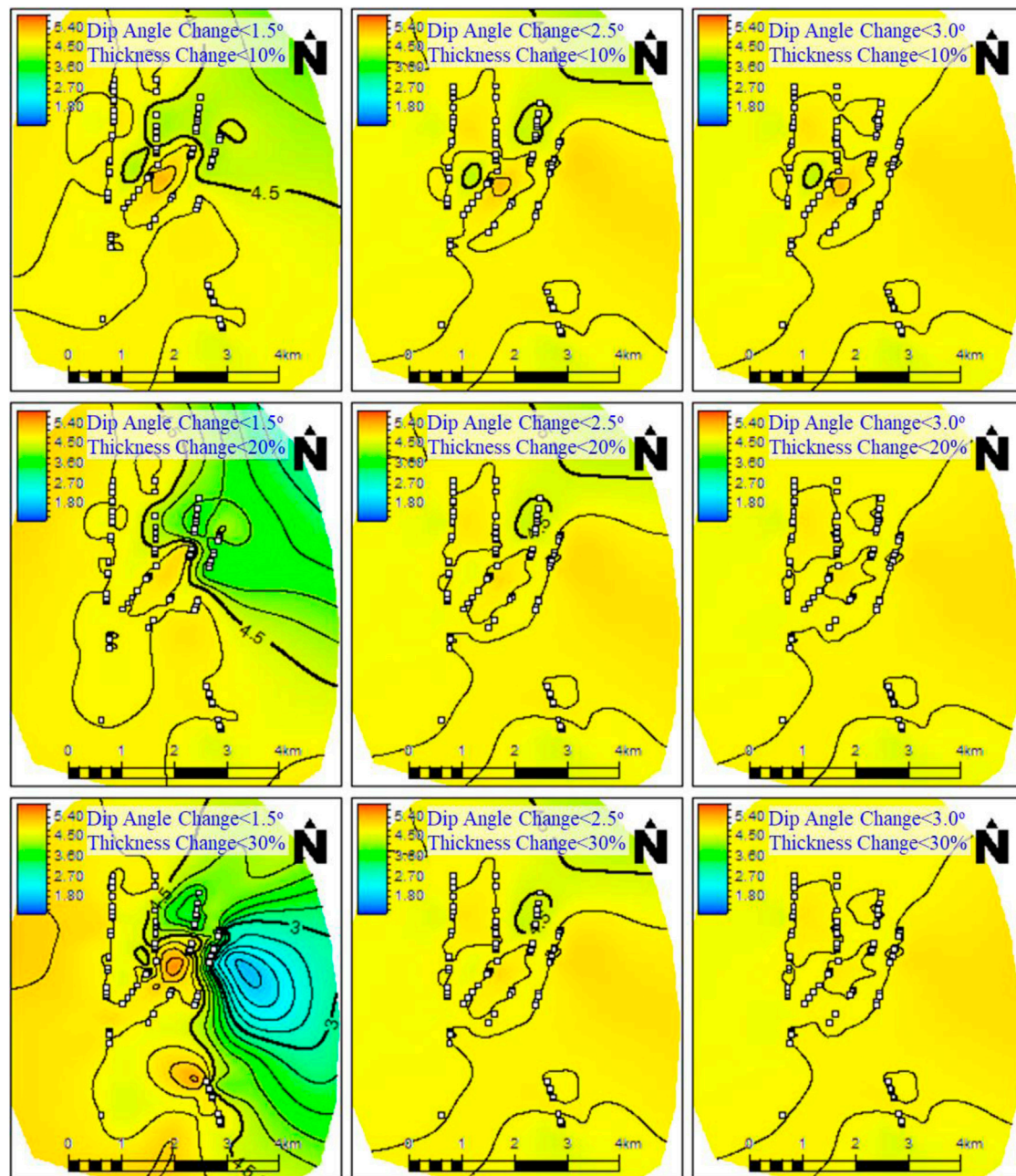
FIGURE 9 | Isopach maps of the Wufeng Formation in the JY-1 district after adjusting its TVT at the location of PVW-As using different dip angle change thresholds and thickness change thresholds. The white-filled squares represent the location of formation tops in the vertical and horizontal wells.

Formation tops are interpreted from wire line logs and their locations are determined from well location and trajectory. Therefore, the uncertainty of formation tops is affected by the uncertainty of log data (mainly gamma-ray log, resistivity log, and measured depth), well location, well trajectory, and the performance of formation top interpretation. In general, the uncertainty of formation tops is larger than well location and trajectory but smaller than the other data. This research considered the formation tops interpreted from well logs as

the second group with the first-level uncertainty. In addition, as for the performance of formation top interpretation, it is usually easier to recognize the formation tops with clear lithology changes, such as the base and top surface of the shale reservoir, and consequently, the uncertainty of formation tops with stronger log response is smaller. In addition, the uncertainty of formation tops in horizontal wells is usually more considerable than them in vertical wells because it is much more challenging to interpret formation tops in
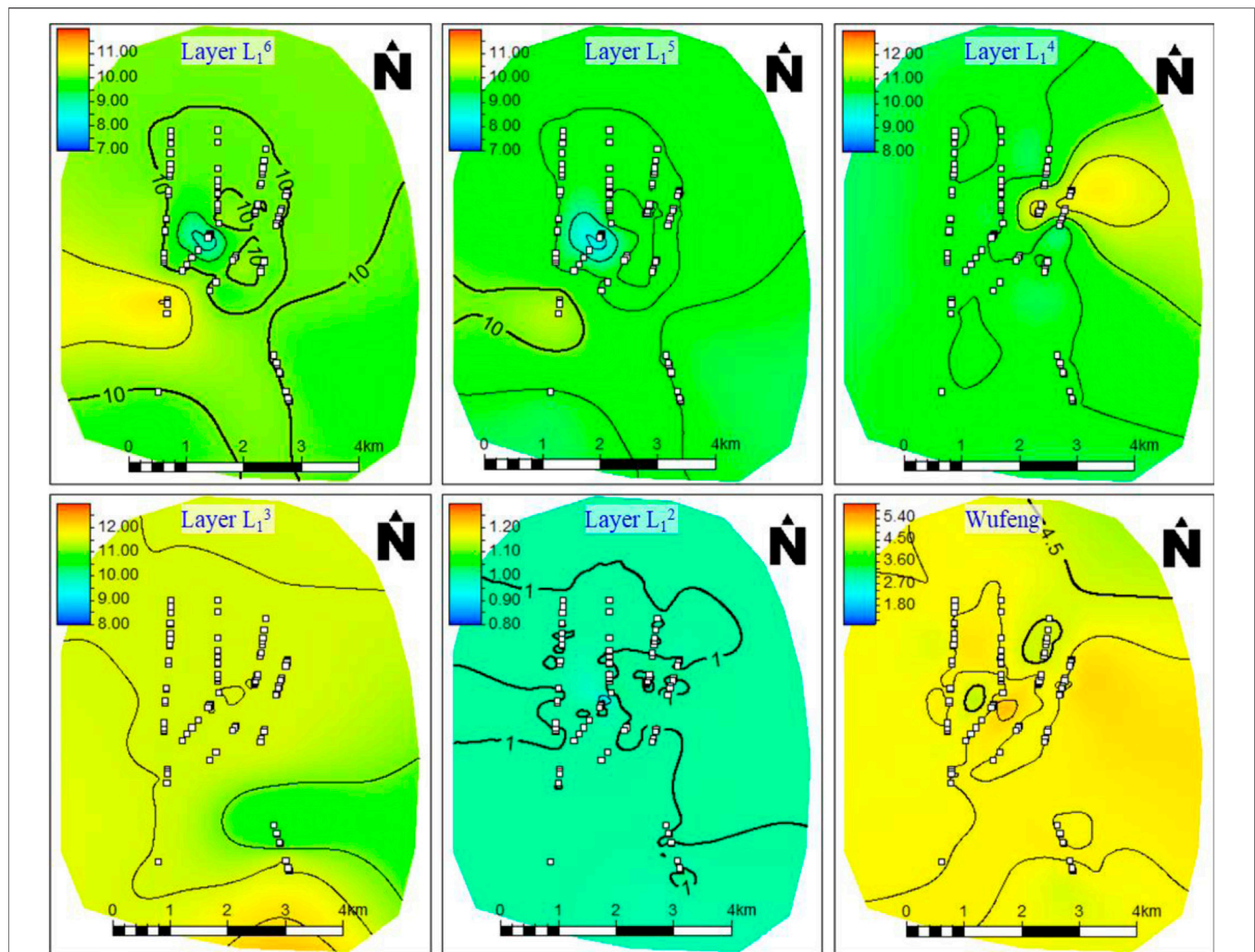
FIGURE 10 | Isopach maps of the six shale layers in the JY-1 district after adjusting their TVTs using dip angle change threshold of 2.5° and thickness change threshold of 10%. The white-filled squares represent the location of PVW-As.

horizontal wells, especially in the lateral segments due to the logging process and formation repetition (Passey et al., 2005; Griffiths et al., 2012; Maggs et al., 2014; Wang et al., 2018a).

The inferred formation tops in PVW-As are considered the third group with the second-level uncertainty, which has a relatively larger uncertainty than formation tops interpreted from wire line logs. This uncertainty is primarily affected by the estimated thickness contour maps of shale layers and the interpreted formation tops. The relatively high uncertainty of thickness contour maps is the main reason for the high uncertainty of inferred formation tops in PVW-As. In order to reduce this uncertainty, the estimation of the thickness contour maps should be improved, such as the iterative process to estimate the thickness distribution in the entire Jiaoshiba area (**Figures 12B–D**). The inferred formation tops in PVW-Bs are considered the fourth group with the third-level uncertainty, also called soft data, due to their high uncertainty. In fact, we can only determine the elevation range of formation tops in PVW-Bs. This

elevation range is strongly associated with the thickness of the landing formation of the intersection point between the horizontal well and PVW-B (**Figure 4** and **Table 1**). A feasible way to reduce this uncertainty is to recognize more shale layers within the shale reservoir to reduce the thickness of each shale layer. Besides, refining the relative vertical position of the intersection point within the landing formation can also reduce this uncertainty.

Structural map interpreted from seismic data is considered the fifth group with the third-level uncertainty (soft data). Seismic data have a relatively low vertical resolution of seismic data and the high uncertainty of velocity model to convert seismic data from time to depth domain (Fomel and Landa, 2014; Donahoe and Gao, 2016; Pinto et al., 2017). This uncertainty should be much larger than well location and trajectory, formation tops interpreted from well logs, and formation tops inferred in PVW-As. Therefore, seismic-interpreted structural maps are usually used as a soft constraint to build the 3D structural models.
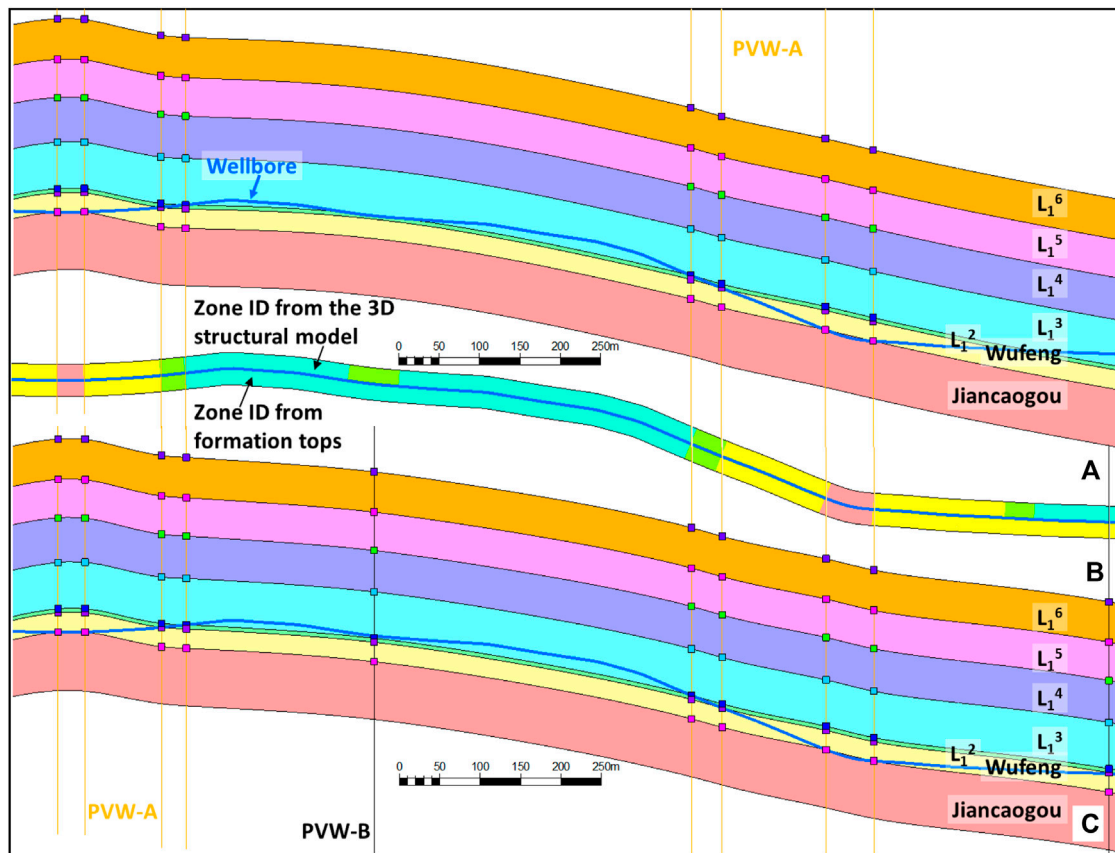
FIGURE 11 | Examples of errors in the 3D structural model **(A–B)** and the pseudo vertical wells added to fix these errors (PVW-B) **(C)**.

Process-Associated Uncertainty

In addition to the data itself, the method to process these data can also significantly affect the uncertainty within the 3D structural models. Three major processes affect the uncertainty of 3D structural modeling using horizontal well data. The first one is the initial thickness of shale layers used to calculate the elevation of the key surface (e.g., the Wufeng base) at all PVW-As since the adjustment of shale thickness is based on the initial thickness. The effect of the selected initial thickness of shale layers is small if the study area is relatively small but becomes serious within a relatively large area (e.g., the entire oil/gas field). This uncertainty can be reduced by an iterative process to update the key surface dip angle and the TSTs at all PVW-As, which helps estimate the distribution of shale thickness (**Figure 5**). The second process is to balance dip angle change and thickness change of shale layers. A larger dip angle change usually form more uniform shale thickness and vice versa. By setting different thresholds of dip angle change and thickness change, the estimated thickness of shale layers could be different (**Figure 9**). The third process is the confidential constant to calculate the formation tops in PVW-Bs. With different confidential constants, the 3D structural model should be different in the areas surrounding PVW-Bs. **Figure 13** showed an example of the

different 3D structural models using confidential constant 95, 85, and 75%, respectively. Meanwhile, the effect of the confidential constant will be larger if the landing formation of the intersection point between the horizontal well and PVW-B has a larger thickness. For example, the differences at PVW-B1 are larger than PVW-B2 since the landing thickness of the intersection point at PVW-B1 is larger. This is one of the important reasons to subdivide the shale reservoir into as many shale layers as possible.

In order to estimate these process-associated uncertainties, it is necessary to construct multiple 3D structural models using different values of the initial thickness (either a constant value or a contour map), dip angle change threshold, thickness change threshold, and confidential constant and compare their differences. Except the confidential constant, the other three parameters work together to determine the shale layer TVTs. Compared to the dip angle change threshold and thickness change threshold, the initial thickness can be estimated from formation tops in vertical wells, depositional environments, and geologic knowledge of the study area. Meanwhile, the iterative process is designed to update the initial thickness based on the dip angle and thickness change threshold. Therefore, the initial thickness usually has a relatively smaller effect on the 3D structural model. Instead of providing multiple different initial thicknesses, it is more feasible to focus on the effect of dip angle change
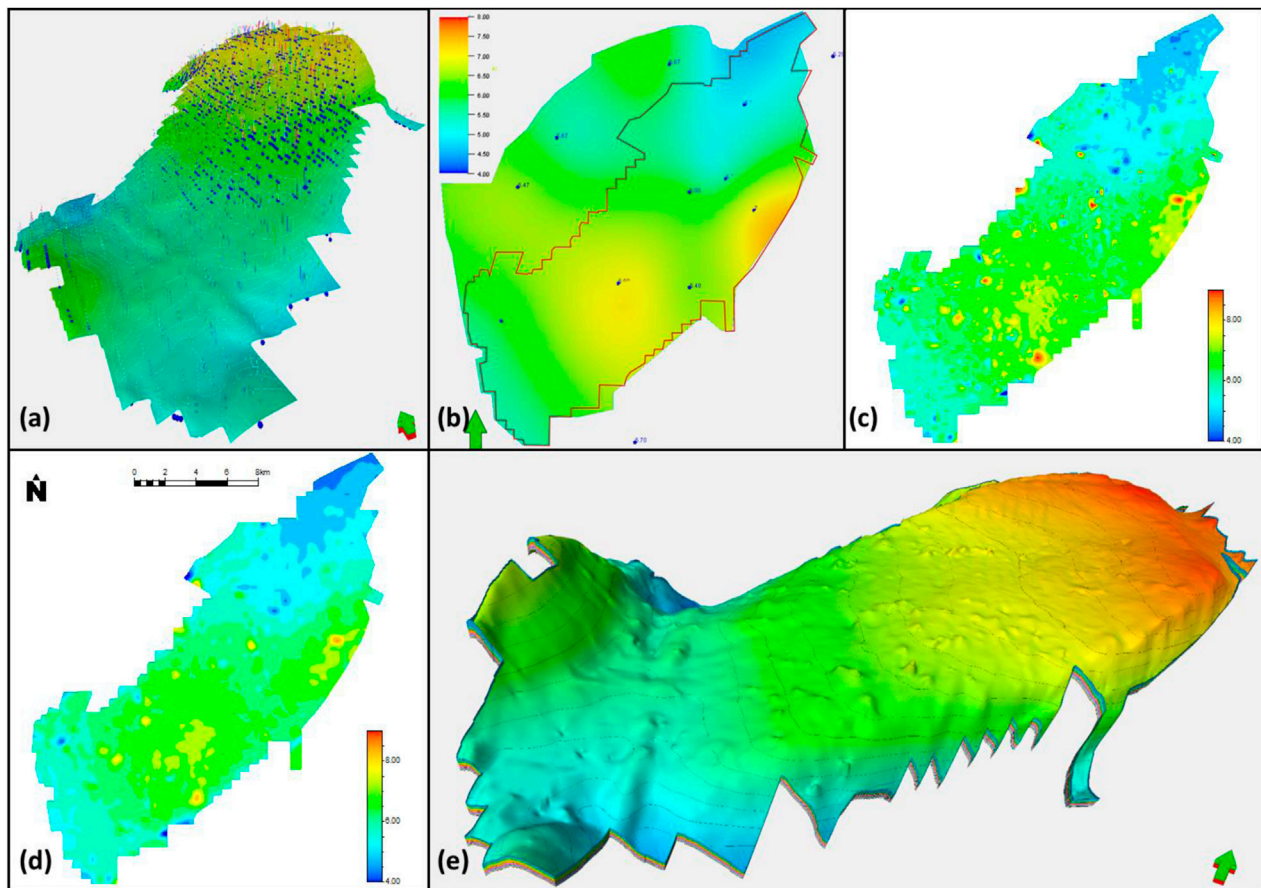
FIGURE 12 | (A) Seismic-interpreted structural map of the Wufeng base with the inferred Wufeng base elevation at PVW-As; **(B)** the Wufeng Formation TST contour map generated by formation top data in vertical wells; **(C)** the Wufeng formation TST contour map generated by formation top data in PVW-As and vertical wells; **(D)** the smoothed Wufeng formation TST contour map; and **(E)** the 3D structural model of the Jiaoshiba area in the eastern Sichuan Basin.
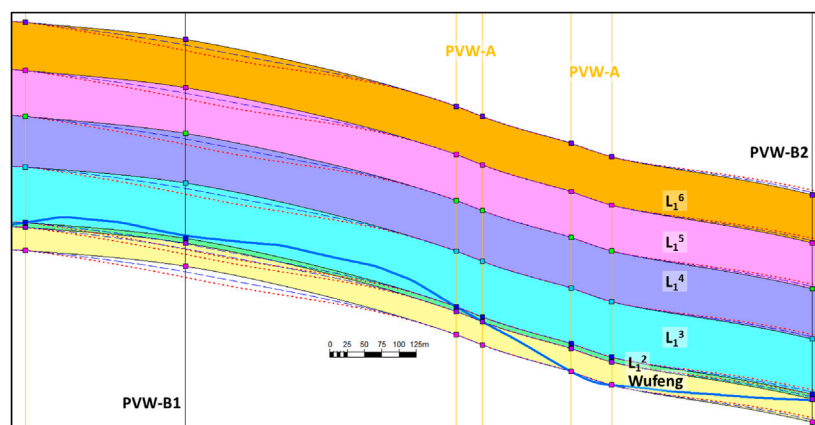
FIGURE 13 | The effect of confidential constant on the 3D structural model of shale reservoirs using the cross section along the well JY-b. The black solid lines, the blue dash lines, and the red dot lines represent the structural model using the confidential constant of 95, 85, and 75%.

and thickness change threshold. There are rare data to estimate the confidential constant, and it would be good to test three to five values.

CONCLUSION

The existence of a large number of horizontal wells in the core area of shale oil and gas plays makes its 3D structural modeling distinct from conventional reservoirs with mainly vertical wells. To construct a high-quality 3D structural model for shale oil and gas fields, it is critical to effectively use the data in horizontal wells. The uncoupled formation tops are the main reason for the abnormal thickness in the constructed 3D structural models. Our method is to add PVW-As at all formation tops in horizontal wells and infer the formation tops in all PVW-As based on the thickness of shale layers. As one key component of our method, an iterative process was developed to estimate the shale thickness using the uncoupled formation tops in horizontal wells by balancing the thickness change and dip angle change threshold. Meanwhile, we introduced a new data type, landing formation, in horizontal wells as a soft constraint for the 3D structural modeling. The landing formation data are mainly used to 1) detect whether the horizontal wells land in the correct formation in the constructed 3D structural models and 2) provide the necessary information for adding PVW-Bs if any incorrect landing formation in the 3D structural model is detected.

By adding PVW-As to convert the uncoupled formation tops to coupled formation tops, estimating shale thickness by balancing the dip angle change and the thickness change, detecting errors in the constructed 3D structural model, and adding PVW-Bs to fix these error, we are able to maximize the use of the structural-associated data in horizontal wells to optimize the quality of 3D structural modes of shale reservoirs. The data from the Jiaoshiba area in the eastern Sichuan Basin were utilized to successfully construct two 3D structural models of the Wufeng–Longmaxi Shale reservoir at the well pad scale and the field scale, respectively. Besides, we analyzed the uncertainty within the 3D structural model using horizontal well data, including the uncertainty level, the uncertainty source, and the method to reduce these uncertainties for different data types. This research, by summarizing the special features of formation tops in horizontal wells and the main issues in 3D structural modeling using horizontal well data, developed a method to maximize the data in horizontal wells to optimize the quality of 3D structural models of shale reservoirs. It should be helpful for geologists and engineers to improve their 3D structural model of shale reservoirs for property modeling, hydraulic fracturing simulation, well design, etc.

DATA AVAILABILITY STATEMENT

The raw data supporting the conclusions of this article will be made available by the authors, without undue reservation.

AUTHOR CONTRIBUTIONS

ACKNOWLEDGMENTS

SUPPLEMENTARY MATERIAL

The Supplementary Material for this article can be found online at: https://www.frontiersin.org/articles/10.3389/feart.2021.695502/full#supplementary-material

REFERENCES

Carter, K. M., Harper, J. A., Schmid, K. W., and Kostelnik, J. (2011). Unconventional Natural Gas Resources in Pennsylvania: The Backstory of the Modern Marcellus Shale Play. *Environ. Geosci.* 18 (4), 217–257. doi:10.1306/eg.09281111008

Donahoe, T., and Gao, D. (2016). Application of 3D Seismic Attribute Analysis to Structure Interpretation and Hydrocarbon Exploration Southwest Pennsylvania, Central Appalachian Basin: A Case Study. *Interpretation* 4 (3), T291–T302. doi:10.1190/INT-2015-0080.1

EIA (2019). International Energy Outlook 2019 With Projections to 2050. Available at: https://www.eia.gov/ieo. (Accessed August 10, 2020).

Fomel, S., and Landa, E. (2014). Structural Uncertainty of Time-Migrated Seismic Images. *J. Appl. Geophys.* 101, 27–30. doi:10.1016/j.jappgeo.2013.11.010

Griffiths, R., Morris, C., Ito, K., Rasmus, J., and Maggs, D. (2012). Formation Evaluation in High Angle and Horizontal wells – A New and Practical Workflow. Paper FF presented at SPWLA 53rd Annual Logging Symposium. Cartagena, Colombia. June 16-20, 2012.

IEA (2019). World Energy Outlook 2019. Available at: https://www.iea.org/reports/world-energy-outlook-2019. (Accessed August 10, 2020).

Jarvie, D. M., Hill, R. J., Ruble, T. E., and Pollastro, R. M. (2007). Unconventional Shale-Gas Systems: The Mississippian Barnett Shale of north-central Texas as One Model for Thermogenic Shale-Gas Assessment. *Bulletin* 91 (4), 475–499. doi:10.1306/12190606068

Krajnovich, A., Zhou, W., and Gutierrez, M. (2020). Uncertainty Assessment for 3D Geologic Modeling of Fault Zones Based on Geologic Inputs and Prior Knowledge. *Solid Earth* 11, 1457–1474. doi:10.5194/se-11-1457-2020

Lelliott, M. R., Cave, M. R., and Wealthall, G. P. (2009). A Structured Approach to the Measurement of Uncertainty in 3D Geological Models. *Q. J. Eng. Geology Hydrogeology* 42, 95–105. doi:10.1144/1470-9236/07-081

Liang, D., Hua, W., Liu, X., Zhao, Y., and Liu, Z. (2021). Uncertainty Assessment of a 3D Geological Model by Integrating Data Errors, Spatial Variations and

Cognition Bias. *Earth Sci. Inform.* 14, 161–178. doi:10.1007/s12145-020-00548-4

Liu, X. (2018). Borehole Trajectory Uncertainty and its Characterization. *Pet. Exploration Dev.* 46 (2), 407–412. doi:10.1016/S1876-3804(19)60021-2

Long, S., Zhang, Y., Li, J., Sun, Z., Shang, X., and Dai, C. (2019). Comprehensive Geological Modeling Technology for Shale Gas Reservoirs. *Nat. Gas Industry* 3, 47–55. doi:10.3787/j.issn.1000-0976.2019.03.006 in Chinese.

Maggs, D., Lattuada, S., Griffiths, R., Mele, M., and Valdisturlo, A. (2014). Petrophysics in High Angle and Horizontal wells. *Proc. GEO ExPro* 11 (1), 60–62.

Passey, Q. R., Yin, H., Rendero, C. M., and Fitz, D. E. (2005). Overview of High-Angle and Horizontal Well Formation Evaluation: Issues, Learning and Future Directions. Paper A, SPWLA 46th Annual Logging Symposium, New Orleans, Louisiana, June 16-20, 2012.

Pinto, V. R., Abreu, C. E. B. d. S., Monteiro, R. C., Rosseto, J., and Leahey, G. M. (2017). Seismic Uncertainty Estimation in Reservoir Structural Modelling. *First Break* 35 (10), 51–54. doi:10.3997/1365-2397.35.10.90243

Qiao, H., Jia, A., and Wei, Y. (2018). Geological Information Analysis of Horizontal wells and 3D Modeling of Shale Gas Reservoirs. *J. Southwest Pet. Univ. (Science Tech. Edition)* 40 (1), 78–88. in Chinese. doi:10.11885/j.issn.1674-5086.2017.05.10.04

Shahkarami, A., and Wang, G. (2017). Horizontal Well Spacing and Hydraulic Fracturing Design Optimization: a Case Study on Utica-Point Pleasant Shale Play. *J Sustain. Energy Engng* 5 (2), 148–162. doi:10.7569/jsee.2017.629508

Shtuka, A., Hadziavdic, V., and Sandjivy, L. (2018). Dealing with Uncertainty on Horizontal Well Trajectory when Targeting New Infill Drilling: The Brage Field Case Study. 80th EAGE Conference and Exhibition. Copenhagen, Denmark: June 11-14, 2865–2869. doi:10.3997/2214-4609.201801236

Shu, H., Wang, L., Yin, K., Li, Q., Zhang, Z., and Luo, Y. (2020). Geological Modeling of Shale Gas Reservoir during the Implementation Process of Geology-Engineering Integration. *China Pet. Exploration* 25 (2), 84–95. in Chinese. doi:10.3969/j.issn.1672-7703.2020.02.009

Stein, M. L. (1999). *Interpolation of Spatial Data: Some Theory for Kriging (Springer Series in Statistics).* Springer. doi:10.1007/978-1-4612-1494-6

Wang, G., and Carr, T. R. (2013). Organic-rich Marcellus Shale Lithofacies Modeling and Distribution Pattern Analysis in the Appalachian basin. *Bulletin* 97 (12), 2173–2205. doi:10.1306/05141312135

Wang, G., Long, S., Ju, Y., Huang, C., and Peng, Y. (2018a). Application of Horizontal wells in Three-Dimensional Shale Reservoir Modeling: A Case Study of Longmaxi-Wufeng Shale in Fuling Gas Field, Sichuan Basin. *Bulletin* 102 (11), 2333–2354. doi:10.1306/0924191908110.1306/05111817144

Wang, G., Long, S., Ju, Y., Huang, C., and Peng, Y. (2018b). Issues of Horizontal Well Log Interpretation: An Example Longmaxi-Wufeng Shale in Fuling Gas Field of Eastern Sichuan Basin. Joint Eastern Section AAPG/SPE Conference. Pittsburgh, PA: October 2018.

Wang, Z. (2015). Breakthrough of Fuling Shale Gas Exploration and Development and its Inspiration. *Oil Gas Geology* 36 (1), 1–6. doi:10.11743/ogg20150101 in Chinese.

Wellmann, J. F., Lindsay, M., Poh, J., and Jessell, M. (2014). Validating 3-D Structural Models with Geological Knowledge for Improved Uncertainty Evaluations. *Energ. Proced.* 59, 374–381. doi:10.1016/j.egypro.2014.10.391

Zhou, J. (2015). Uncertainty in Geosteering and Interpretation of Horizontal wells - the Necessity for Constraints and Geometric Models. *The Leading Edge* 34 (5), 492–499. doi:10.1190/tle34050496.1

Influence of a Paleosedimentary Environment on Shale Oil Enrichment: A Case Study on the Shahejie Formation of Raoyang Sag, Bohai Bay Basin, China

Yongbo Wei[1,2], Xiaoyan Li[3], Ruifeng Zhang[3], Xiaodong Li[3], Shuangfang Lu[1,2]*, Yan Qiu[3], Tao Jiang[3], Yuan Gao[3], Tiedong Zhao[3], Zhaojing Song[1,2] and Meihong Zhao[4]

[1]Shandong Provincial Key Laboratory of Deep Oil and Gas, Qingdao, China, [2]School of Geosciences, China University of Petroleum (East China), Qingdao, China, [3]Research Institute of Exploration and Development, PetroChina Huabei Oilfield Company, Renqiu, China, [4]Downhole Operation Branch of Bohai Drilling Engineering Co. LTD, PetroChina, Renqiu, China

The characteristics of paleosedimentary environments are of great significance for the enrichment of organic matter (OM) and hydrocarbons in lacustrine shale. This study analyzed mineralogy, well logging data, organic geochemical parameters (total organic carbon and pyrolyzed hydrocarbon), inorganic geochemical parameters (major and trace elements), and multiple geochemical proxies based on inorganic geochemical parameters. These were used to reconstruct the paleosedimentary environment of the lower 1st Member of the Shahejie Formation (Es_1^L) to reveal OM and shale oil enrichment mechanisms and establish a shale oil enrichment model. The ($Fe_2O_3+Al_2O_3$)/(CaO + MgO), Sr/Ba, Rb/Sr, Cu/Al, and Th/U parameters indicate that the Es_1^L in Raoyang Sag was deposited in a paleoenvironment dominated by arid paleoclimate, reducing conditions, and saltwater. Paleoclimate, clastic influx intensity, preservation conditions, paleoproductivity, and paleosalinity all affect OM abundance. The OM accumulation in the shale of Es_1^L was mainly controlled by the high primary productivity of surface water due to algal blooms and moderate salinities, which was achieved using stratified water columns with low oxygen conditions in bottom water. As the main valuable sites for shale oil storage, carbonate mineral depositions are of great significance for oil enrichment. As the dominant lithofacies for oil enrichment, carbonate-rich shale and calcareous shale lithofacies were deposited under a drier paleoclimate, low clastic influx intensity, strong reducing conditions, high paleoproductivity, and moderate salinity paleoenvironment. Additionally, the profile of the shale oil sweet spot was determined through the combination of lithofacies, logging, and paleosedimentary environment data.

Keywords: paleoenvironment, OM accumulation, shale oil enrichment, Shahejie formation, Raoyang sag

INTRODUCTION

Lacustrine organic-rich mudstones and shale possess conditions conducive to hydrocarbon generation, requisite storage volumes, and excellent hydrocarbon-bearing properties. These types of oil and gas reservoirs have the characteristics of continuous and stable distribution in space, high overall oil and gas content, sweet spot enrichment, and high yield (Jarvie, 2012; Zhou et al., 2020; Wei et al., 2021; Wei et al., 2021). The theory of lacustrine shale oil accumulation is a hot research topic and is directly related to the properties of source rocks (Holditch, 2013; Zou et al., 2019; Feng et al., 2020; Li et al., 2021). According to sedimentology theory, the paleosedimentary environment has a particularly significant impact on continental sedimentation at different scales (mesoscale and macroscale) (Carroll and Bohacs, 1999). At the microscale of the lacustrine sedimentary sequence, there are broad differences in mineralogy, sedimentary structure, and lithofacies (Lu et al., 2016; Li et al., 2017; Bai et al., 2020). The vertical and horizontal distribution characteristics of the different types of shale deposited in basins also have significant variations stemming from differences in paleosedimentary environments. However, total organic carbon (TOC), shale oil-bearing layers, and reservoir quality are generally considered to be the main indicators for evaluating shale oil accumulation (Bai et al., 2020). The TOC of shale denotes its oil production potential (Holditch, 2013), whereas the existence of shale oil-bearing layers (Katz, 2003) is a good indicator of shale oil sweet spots. These parameters are closely related to the mineral composition, structures, and lithofacies formed in each type of sedimentary environment and have varying degrees of influence on shale oil enrichment; a fact that has recently drawn notice (Birdwell et al., 2016; Lu et al., 2016; Zou, 2017). Thus, revealing the relationship between the paleosedimentary environment and shale oil enrichment is highly significant to in-depth investigations into the enrichment mechanism of continental shale oil, which promotes the effective exploration and efficient extraction of shale oil resources. The establishment of the shale oil accumulation model also has relevant significance to similar lacustrine basins worldwide.

The Raoyang Sag in eastern China is a representative example of an oil-bearing lacustrine basin in the Jizhong Depression. The continental organic-rich shale in the lower 1st Member of the Shahejie Formation (Es_1^L) is one of the most important source rocks in the Raoyang Sag and even in the entire Bohai Bay Basin. Recently, it has been considered as a potential shale oil reservoir (Yin et al., 2018; Chen et al., 2019a; Chen et al., 2019b; Yin et al., 2020). Previous research has focused on the characteristics of organic geochemical properties [e.g., TOC, pyrolyzed hydrocarbon (S_1)] (Chen et al., 2019a; Chen et al., 2019b; Yin et al., 2020), physical properties of shale oil reservoirs (pore characterization and storage space classification) (Chen et al., 2019a; Chen et al., 2019b), and the paleoenvironment developed through the organic and inorganic geochemistry of the Es_1^L source rocks (Yin et al., 2018; Yin et al., 2020). However, research on the inorganic and organic geochemical enrichment mechanisms of organic matter (OM) under the shale oil enrichment model of the Es_1^L in Raoyang Sag is relatively weak.

The paleosedimentary environment and shale oil enrichment model can be constructed by combining mineralogy and inorganic geochemistry. Based on the organic and inorganic geochemical parameters of four key wells in the study area, this study conducted a systematic study of the shale oil enrichment mechanism and mainly focused on the following four aspects: 1) determination of the mineralogy, organic geochemistry, and major/trace element characteristics of the Es_1^L shale; 2) reconstruction of the paleoenvironment (including clastic influx, paleoclimate, paleosalinity, redox conditions, and paleoproductivity) during the deposition of Es_1^L shale; 3) analysis of the factors influencing OM abundance and elucidating the mechanism of OM enrichment in the Es_1^L shale; and 4) confirmation of the sedimentary environment of dominant oil-bearing lithofacies and establishment of a shale oil enrichment model.

GEOLOGICAL SETTING

The Raoyang Sag is a Cenozoic fault-sag basin in the middle of the Jizhong Depression in the Bohai Bay Basin. This sag exploration area covers approximately $5.28 \times 10^3 \, km^2$, enclosed by the Xianxian Uplift to the east, the Gaoyang Low Uplift to the west, the Hengshui Fault to the south, and the Baxian Sag to the north. It is further subdivided into four oil-rich sags from north to south, namely, the Renxi, Maxi, Hejian, and Liuxi Sags, which house the largest oil and gas accumulations and the highest exploration effectiveness in the Raoyang Sag (He et al., 2017a; Yin et al., 2020) (**Figure 1A**). The strata of the Raoyang Sag are mainly composed of Paleozoic, Mesozoic, and Cenozoic rocks, from bottom to top. The Paleogene in Cenozoic rocks is generally thick and includes the Kongdian, Shahejie, and Dongying formations (He et al., 2017b; Liang et al., 2018). Amidst these, the Es_1^L in Raoyang Sag has a large area of continuous distribution of organic-rich mudstones and shale that developed in semi-deep lake facies, mainly consisting of carbonate, clay, and silica minerals (e.g., quartz and feldspar). The lithology of the middle and upper parts of the interval are complex, composed of dark gray mudstone, calcareous shale, oil shale, dolomitic mudstone, fine sandstone, and oolitic limestone. It is called "special lithology sections (SLC)". The lower part comprises "tailing sandstone (TS)," composed of fine siltstone (**Figure 1B**). This part has the appropriate geological conditions for shale oil to form an integrated source and reservoir and has good prospects for shale oil exploration.

SAMPLES AND METHODS

Samples

Core observations and 96 shale samples were collected from depths between 2,332.00 and 3,827.92 m from 14 wells in the Raoyang Sag (**Figure 1A**). Four of these wells (wells B11x, Xl25x, N202, and G103), especially wells B11x and Xl25x, have been continuously cored, and the collected samples provide a large volume of important data for analyzing the paleoenvironmental OM enrichment and shale oil accumulation in the Es_1^L.
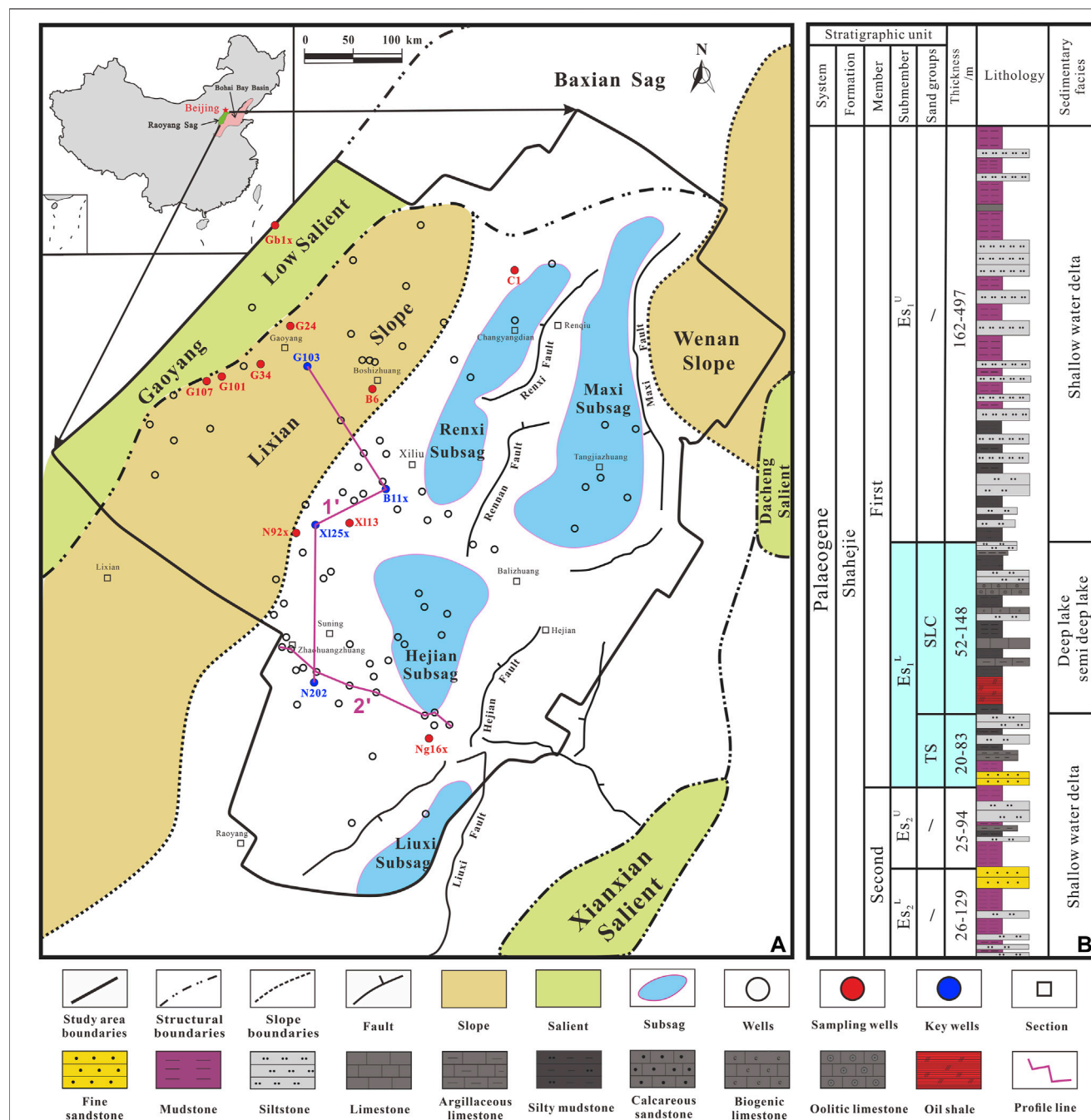
FIGURE 1 | (A) Map showing the structural characteristics within and around the Raoyang Sag and the distribution of sampling wells **(B)** Stratigraphic column of the Shahejie Formation.

Moreover, these four wells are located in different structural positions and deposition depths of the lacustrine basins and exhibit a continuous organic-rich shale interval that can reflect the continuous paleoenvironmental evolution of the Es_1^L shale.

TOC and Rock-Eval Pyrolysis Analyses

TOC and Rock-Eval pyrolysis analyses were conducted at the Key Laboratory of Deep Oil and Gas at the China University of Petroleum (East China). A total of 96 samples of from 14 wells were analyzed to obtain TOC content. Samples were crushed to an approximate mesh size of 100 and oven-dried at 80°C. The TOC content was determined using an Elab-TOC/E2000 analyzer after decarbonating with hydrochloric acid (5%). Ninety-six crushed samples (approximately 100 mg at a mesh size of 80) from the 14 wells were analyzed using a YQ-VIIA Rock-Eval instrument, by heating at a programmed rate. Then, a flame

ionization detector and thermal conductivity detector were used to quantify the hydrocarbons and carbon dioxide emitted by the OM being released from the rock. The measured parameters included the free hydrocarbon content when vaporized at a temperature of 300°C (S_1), residual hydrocarbon generation potential when the temperature was between 300 and 600°C (S_2), and temperature of the maximum pyrolysis yield (T_{max}).

X-Ray Diffraction (XRD) Measurements

XRD analysis was performed on the 96 samples to quantitatively analyze mineral composition. All the shale samples were ground into a fine powder (<40 μm) and analyzed with a Panalytical X' PertPRO MPD X-ray with Cu Kα radiation (40 kV, 40 mA) at a scanning speed of 2°/min and a testing angle range of 5°–90°. The diffraction patterns were analyzed using a computer to determine the relative abundances of various minerals, and a semi-quantitative assessment was performed.

Major and Trace Element Determination

The major element compositions of 35 samples obtained from wells B11x, Xl25x, N202, and G103 were analyzed using a Philips PW2404 X-ray fluorescence spectrometer with fused glasses consisting of a mixture of powdered samples at a temperature of 1,000°C and flux ($Li_2B_4O_7$) at a ratio of 1:8 with a weight of 5.0 g. This analysis revealed major element oxides, including SiO_2, Al_2O_3, MgO, Na_2O, K_2O, P_2O_5, TiO_2, CaO, Fe_2O_3, and MnO. The precision of the major element data was ≤5%. The 35 sample powders (40 mg) that were selected for trace element analysis were dried in an oven at 130°C for 1–2 h, cooled to room temperature (20°C), dissolved in a tightly sealed Teflon screw-cap beaker with ultrapure 0.5 ml HNO_3 + 1 ml HF + 0.5 ml $HClO_4$ with a solubility of 8 mol/L, and dried. The dried samples were digested again with 1 ml 1% HNO_3 +3 ml H_2O until a clear solution was obtained. The solution was then diluted to 1:1,000 by mass and analyzed using a Finnigan MAT inductively coupled plasma source mass spectrometer (ICP-MS) to measure trace and rare-earth elements. The testing error of these elements was generally less than 4%.

RESULTS

Organic Geochemical Characteristics

TOC content (obtained using the TOC analyzer) is one of the most important indicators for evaluating organic-rich shale. The TOC content of the shale samples from Es_1^L varied from 0.09 to 5.07% (mean 1.55%). In addition, S_1 is a direct parameter for determining the enrichment of shale oil. The mean S_1 value of the 96 samples from the Es_1^L was 0.65 mg HC/g rock (mg/g) (range: 0.01–6.27 mg/g). The ($S_1 + S_2$) values represent the OM hydrocarbon-generating potential. High ($S_1 + S_2$) values of up to 52.63 mg/g (average: 12.71 mg/g) indicate that the oil shales also have excellent potential for liquid hydrocarbon generation. According to the relationship between the hydrogen index (HI) and T_{max} (**Figure 2**), most of the measured oil shale samples belonged to Type I and Type II_1 kerogens, with a scant contribution of Type II_2 and III kerogens; This indicated that the OM of the shale samples had mainly algal and microorganism
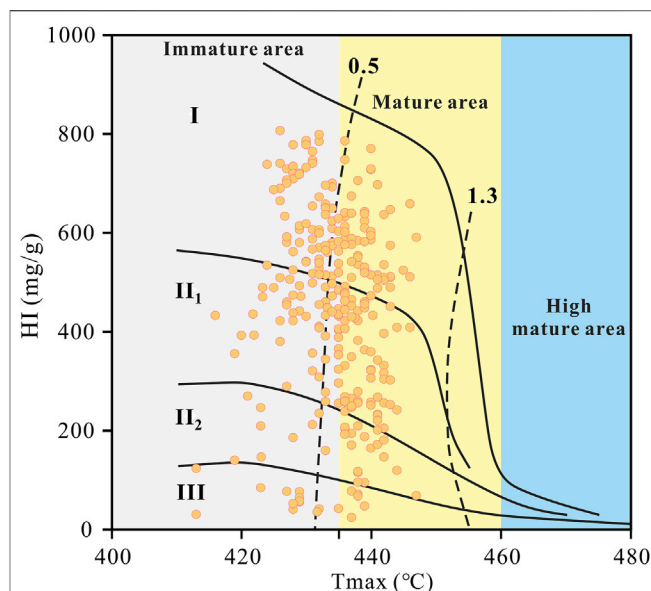
FIGURE 2 | Thermal maturity status and kerogen types (I, II_1, II_2, III) of the investigated Es1L shale samples, expressed by the relationship between HI and T_{max}.

origins (Yin et al., 2020). The T_{max} parameter from the Rock-Eval pyrolysis data was investigated to evaluate the thermal maturity level of the OM. The T_{max} value (307–449°C; average: 434°C) indicated that the OM maturity stage ranged from immature to early mature (Shekarifard et al., 2019). This is due to the shale stratum in the Es_1^L not having experienced long-term burial and higher temperatures, due to the shallow burial depth of strata, a conclusion supported by the high (S_1+S_2) value.

Mineralogy and Lithofacies of Shale

XRD analysis of the 35 shale samples from the four selected wells indicated that the Es_1^L shale was dominated by carbonate (mean 35.21%), clay (mean 32.38%), and felsic (mean 32.42%) minerals (**Table 1**). Mineralogic information indicates that these rocks are not typical of shale (defined by clay mineral contents greater than 75%) (Schieber, 1989). The American Eagle Ford shale formation is generally rich in carbonates and hydrocarbons, and the Barnett shale formation is generally considered to be rich in quartz and oil (Slatt and Rodriguez, 2012; Chermak and Schreiber, 2014; He et al., 2017a). This mineralogical information also demonstrates that the carbonate minerals associated with these shales are of particular significance. In comparison, the mineral composition of the Es_1^L shale is closer to that of the Eagle Ford shale than the American black shale. Therefore, in references to the three-terminal (carbonate, clay, quartz, and feldspar) normalized lithofacies (Zhang et al., 2016; Zhou et al., 2020), shale with a carbonate content greater than 50% was defined as carbonate-rich shale. The color of the rock samples is dark-brown, with oil display, and obvious laminar structure of carbonate minerals and clay minerals. The existence of laminar structure indicates that there may be water stratification in ancient lakes (Larsen and Macdonald, 1993) (Area A in **Figures 3A**, **4A,B**), because the water stratification can

cause serious hypoxia in the bottom water, making it difficult for benthic animals to survive, so as to avoid the damage to the texture. Shale with a clay mineral content greater than 50% was defined as clay-rich shale. The rock sample is dark-brown with massive structure, and a small amount of terrigenous clastic minerals can be seen dispersed in clay minerals (Area B in **Figures 3A, 4C,D**). Shale with a quartz and feldspar content greater than 50% was named felsic-rich shale. The rock sample is gray-yellow, compact and massive structure, and mainly composed of mixed sediments of clay minerals and fine-grained quartz or feldspar particles (Area C in **Figures 3A**, **4E,F**). Shale with three terminal elements less than 50% was defined as fine-grained hybrid shale. To further subdivide the lithofacies, the fine-grained hybrid shale was divided into calcareous shale (calcareous mineral content between 33.3 and 50%) (Area D in **Figures 3A**, **4G,H**), clay shale (clay minerals between 33.3 and 50%) (Area E in **Figures 3A**, **4I,J**), and felsic shale (felsic minerals between 33.3 and 50%) (Area F in **Figures 3A**, **4K,L**). Among them, the calcareous shale and clay shale are gray-brown, with oil display and laminar structure

(interbedding of OM, clay minerals and carbonate minerals). The felsic shale is yellow-brown, compact and massive structure, and mainly composed of mixed sediments of clay minerals and fine silty quartz or feldspar particles. The lithofacies of the Es_1^L in Raoyang Sag mainly comprise carbonate-rich shale, clay-rich shale, felsic-rich shale, calcareous shale, clay shale, and felsic shale (**Figure 3A**). In addition, B11x well and Xl25x well mainly develop carbonate-rich shale, calcareous shale, and clay shale. N202 well and G103 well mainly develop felsic-rich shale and clay shale (**Table 1**). What needs to be distinguished is that this article discusses shale oil reservoirs, which are located in shale formations with thin interlayers of various lithologies such as dolomite and siltstone. In order to facilitate the unified study of shale oil reservoirs, we had classified the fine-grained sedimentary rocks in the shale formations as shale in the work of dividing lithofacies.

The clay mineral composition of shale samples from the four key wells is plotted in a three-terminal diagram (mixed-

TABLE 1 | XRD results and the corresponding geochemical parameters of the Es_1^L shale in the Roayang Sag.

Samples	Depth (m)	Minerals content (%)			TOC (%)	S_1 (mg/g)	S_1/TOC*100 (mg/g)	S_1+S_2 (mg/g)	T_{max} (°C)	Lithofacies
		Clay	Quartz and feldspar	Carbonate						
B11x-1	3,397.85	19.88	13.91	66.22	2.91	0.57	19.61	25.93	441	A
B11x-2	3,398.15	30.57	19.87	49.55	3.94	0.59	14.98	36.32	435	D
B11x-3	3,398.95	46.88	24.46	28.65	1.60	0.37	23.13	11.70	427	E
B11x-4	3,410.41	27.95	18.42	53.63	2.87	0.79	27.57	28.10	437	A
B11x-5	3,411.30	27.02	15.53	57.45	2.62	0.57	21.77	29.29	438	A
B11x-6	3,411.65	43.98	14.28	41.74	4.76	0.35	7.35	42.19	442	E
B11x-7	3,412.33	47.08	27.30	25.62	3.77	0.68	18.05	32.95	436	E
B11x-8	3,413.02	19.42	19.84	60.74	5.02	2.01	40.07	52.44	440	A
B11x-9	3,413.93	31.21	15.97	52.82	2.55	1.47	57.56	19.83	431	A
B11x-10	3,414.56	54.51	33.92	11.57	2.11	0.65	30.86	24.85	436	B
B11x-11	3,415.01	39.77	20.12	40.11	2.87	0.39	13.59	22.25	435	D
B11x-12	3,416.17	49.30	30.78	19.92	2.66	0.84	31.63	22.05	436	E
B11x-13	3,417.15	28.68	18.64	52.68	1.79	3.05	45.20	14.54	440	A
Xl25x-2	3,324.89	33.53	19.30	47.18	1.83	0.53	29.01	22.00	439	D
Xl25x-3	3,330.06	32.57	18.88	48.55	1.96	0.51	26.06	14.13	435	D
Xl25x-4	3,331.07	39.80	16.17	44.03	1.60	0.44	27.53	10.84	434	D
Xl25x-5	3,331.99	31.81	15.77	52.42	2.44	0.72	29.45	22.49	433	A
Xl25x-6	3,339.24	21.74	8.31	69.95	1.92	0.67	34.91	14.38	434	A
Xl25x-7	3,340.17	8.97	8.45	82.58	1.30	1.57	120.91	9.82	434	A
Xl25x-8	3,340.67	31.01	13.51	55.48	1.32	0.44	33.41	10.51	443	A
Xl25x-9	3,341.27	56.32	26.51	17.18	2.12	0.78	36.82	19.54	437	B
N202-7	3,560.68	37.00	29.54	33.46	3.55	0.41	11.57	33.19	446	E
N202-8	3,562.31	44.04	32.66	23.30	2.30	0.90	39.05	18.58	439	E
N202-9	3,563.56	37.38	18.20	44.42	2.13	0.88	41.25	17.64	441	D
N202-11	3,565.25	29.91	56.53	13.56	0.32	0.04	12.54	0.67	435	C
N202-13	3,569.90	17.75	72.05	10.20	0.32	0.03	9.34	0.57	436	C
N202-14	3,572.43	21.99	55.83	22.19	0.32	0.04	12.52	0.66	432	C
N202-15	3,575.35	7.77	72.12	20.11	0.38	0.93	242.87	3.78	429	C
G103-1	2,743.60	34.27	57.05	8.68	0.63	0.10	15.79	1.86	436	C
G103-2	2,744.80	24.08	59.54	16.38	0.18	0.02	11.08	0.24	432	C
G103-4	2,748.30	49.93	42.28	7.79	0.09	0.03	32.88	0.15	429	E
G103-5	2,749.80	11.97	71.57	16.46	0.25	0.03	11.99	1.02	437	C
G103-6	2,751.80	33.56	48.88	17.57	0.60	0.04	6.69	1.31	433	F
G103-7	2,754.10	50.88	34.29	14.84	0.45	0.04	8.80	1.20	437	B
G103-8	2,765.30	10.73	84.08	5.19	2.03	6.27	308.62	24.55	431	C

FIGURE 3 | Ternary plots of mineral composition from XRD data. **(A)** Ternary diagram of main mineral components [Carbonate-rich shale **(A)**, Clay-rich shale **(B)**, Felsic-rich shale **(C)**, Calcareous shale **(D)**, Clay shale **(E)**, Felsic shale **(F)**]. **(B)** Ternary diagram of clay mineral components.

FIGURE 4 | **(A,B)**: Carbonate-rich shale, B11x-4, 3,410.41 m; **(C,D)**: Clay-rich shale, G103-7, 2,754.10 m; **(E,F)**: Felsic-rich shale, N202-11, 3,565.25 m; **(G,H)**: Calcareous shale, Xl25x-3, 3,330.06 m; **(I,J)**: Clay shale, B11x-6, 3,411.65 m; **(K,L)**: Felsic shale, G103-6, 2,751.80 m.

layer illite/smectite, kaolinite, and illite) in **Figure 3B**. The clay minerals of the Es_1^L shale samples were composed of illite (avg. 43.46%), and mixed-layer illite/smectite (avg. 41.64%), with relatively small amounts of kaolinite (avg. 8.71%) and chlorite (avg. 6.19%). The clay minerals of the Es_1^L shale are rich in mixed-layer illite/smectite and illite, while the majority of the American shales are dominated by illite with little or no kaolinite (Loucks and Ruppel, 2007;

Wilson et al., 2016). This may indicate that the evolution of the paleo-basin and paleosedimentary environment and the degree of diagenesis is different from that of American shale (Cai et al., 2015).

Geochemistry of Elements

The major element oxides SiO_2, CaO, and Al_2O_3 are the predominant constituents, with averages of 45.57 wt%,

TABLE 2 | Major elements results of the Es_1^L shale in the Raoyang Sag.

Samples	Depth (m)	SiO₂ (%)	Al₂O₃ (%)	MgO (%)	Na₂O (%)	K₂O (%)	P₂O₅ (%)	TiO₂ (%)	CaO (%)	Fe₂O₃ (%)	MnO (%)
B11x-1	3,397.85	29.24	7.59	3.56	1.19	1.58	0.16	0.35	24.72	3.00	0.06
B11x-2	3,398.15	37.71	9.08	3.43	1.20	1.86	0.13	0.40	19.31	3.48	0.08
B11x-3	3,398.95	48.72	12.12	3.21	1.44	2.66	0.20	0.57	10.46	4.71	0.07
B11x-4	3,410.41	42.20	9.59	2.64	1.27	1.86	0.10	0.39	18.94	4.26	0.10
B11x-5	3,411.30	44.62	11.86	4.26	1.43	2.48	0.11	0.52	11.58	4.75	0.06
B11x-6	3,411.65	37.82	9.87	4.49	1.34	2.06	0.16	0.43	16.08	4.83	0.08
B11x-7	3,412.33	46.72	11.87	2.39	1.43	2.49	0.13	0.56	12.57	4.34	0.06
B11x-8	3,413.02	37.96	8.35	1.74	1.10	1.51	0.23	0.34	24.67	3.92	0.10
B11x-9	3,413.93	38.14	9.17	1.77	1.31	1.78	0.09	0.37	21.61	2.82	0.03
B11x-10	3,414.56	42.93	9.83	3.73	1.43	2.03	0.11	0.41	16.26	3.30	0.07
B11x-11	3,415.01	42.23	10.71	2.08	1.23	2.38	0.10	0.44	17.84	3.55	0.07
B11x-12	3,416.17	50.58	12.37	2.61	1.41	2.76	0.09	0.52	10.40	5.41	0.08
B11x-13	3,417.15	36.22	8.66	1.62	1.26	1.80	0.10	0.36	23.39	2.83	0.06
Xl25x-2	3,324.89	43.06	10.61	2.97	1.37	2.23	0.10	0.47	15.55	4.57	0.06
Xl25x-3	3,330.06	40.72	10.65	1.95	1.48	2.20	0.09	0.47	19.46	2.20	0.03
Xl25x-4	3,331.07	37.68	9.68	1.84	1.50	1.93	0.08	0.42	22.36	2.76	0.05
Xl25x-5	3,331.99	40.06	9.59	2.03	1.26	1.94	0.15	0.39	20.96	4.05	0.08
Xl25x-6	3,339.24	28.24	7.48	2.51	0.91	1.89	0.23	0.31	29.41	2.39	0.10
Xl25x-7	3,340.17	17.08	4.40	4.22	0.56	0.82	0.26	0.15	33.09	2.41	0.13
Xl25x-8	3,340.67	30.45	7.92	3.73	1.02	1.94	0.12	0.33	23.57	3.71	0.12
Xl25x-9	3,341.27	38.12	9.83	4.37	1.26	2.46	0.13	0.48	18.35	3.53	0.10
N202-7	3,560.68	47.03	12.87	2.66	1.43	2.82	0.11	0.56	12.05	5.11	0.10
N202-8	3,562.31	46.22	11.92	2.65	1.11	3.13	0.09	0.51	14.39	3.24	0.05
N202-9	3,563.56	41.62	10.71	2.33	1.06	2.84	0.07	0.47	19.72	2.55	0.05
N202-11	3,565.25	57.67	13.58	2.39	2.09	2.90	0.13	0.60	4.48	3.88	0.05
N202-13	3,569.90	58.04	15.79	1.81	1.98	3.12	0.12	0.64	3.94	2.73	0.04
N202-14	3,572.43	55.95	13.42	2.47	1.63	3.03	0.12	0.61	7.25	4.65	0.11
N202-15	3,575.35	62.96	11.34	1.61	2.39	2.20	0.11	0.42	6.37	1.94	0.04
G103-1	2,743.60	59.69	14.83	2.53	1.45	2.80	0.10	0.67	5.03	3.74	0.06
G103-2	2,744.80	57.62	15.11	3.03	1.33	2.85	0.10	0.68	5.18	4.16	0.06
G103-4	2,748.30	55.85	16.32	3.01	1.15	3.31	0.15	0.66	3.54	4.87	0.06
G103-5	2,749.80	59.12	12.73	1.95	1.73	2.29	0.09	0.49	7.86	2.99	0.04
G103-6	2,751.80	55.18	15.54	3.26	1.20	2.99	0.11	0.74	5.99	4.14	0.06
G103-7	2,754.10	55.52	16.67	3.49	1.11	3.16	0.10	0.75	4.49	5.25	0.06
G103-8	2,765.30	71.86	11.36	0.69	2.27	1.74	0.06	0.22	3.27	1.44	/
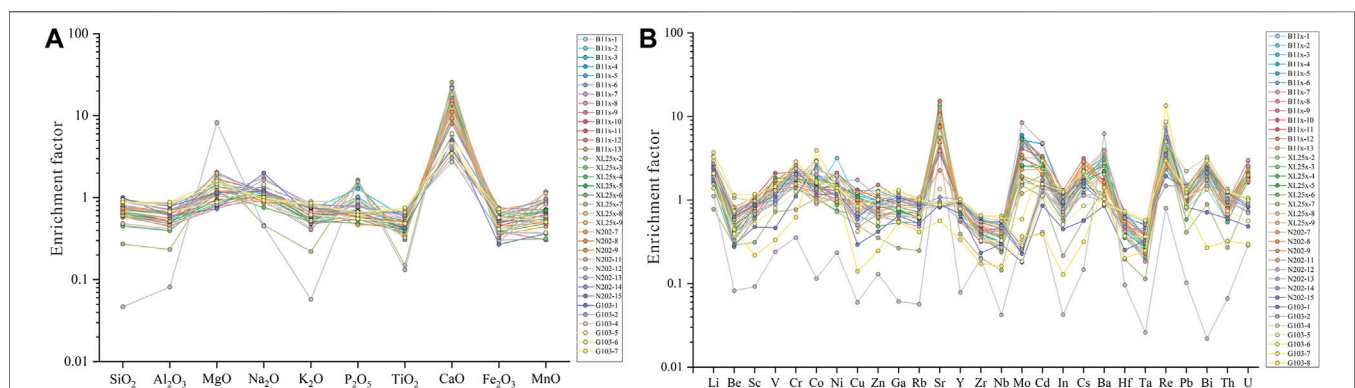
FIGURE 5 | Enrichment factor of the major elements **(A)** (relative to the PAAS, Taylor and Mclennan, 1985) and trace elements **(B)** (relative to the UCC, Taylor and Mclennan, 1985) in the Es_1^L shale.

14.69 wt%, and 11.24 wt%, respectively (**Table 2**). Compared to post-Archaean Australian shale (PAAS) (Taylor and Mclennan, 1985), the CaO, MgO, Na₂O, and P₂O₅ were relatively enriched but the SiO₂, Al₂O₃, Fe₂O₃, MnO, K₂O, and TiO₂ were depleted (**Figure 5A**). The results of the trace element analysis are presented

in **Tables 3, 4**. Compared with the Upper Continental Crust's (UCC) composition (Taylor and Mclennan, 1985), Sr has enrichment factors of 0.57–15.34 (mean 5.60), Mo had enrichment factors of 0.18–8.43 (mean 2.59), Re had enrichment factors of 1.48–13.48 (avg. 4.71), and Ba had enrichment factors of 0.85–3.98 (avg. 2.00).

TABLE 3 | Trace elements results of the Es_1^L shale in the Raoyang Sag.

Samples	Depth (m)	Li (ug/g)	Be (ug/g)	Sc (ug/g)	V (ug/g)	Cr (ug/g)	Co. (ug/g)	Ni (ug/g)	Cu (ug/g)	Zn (ug/g)	Ga (ug/g)	Rb (ug/g)	Sr (ug/g)	Y (ug/g)	Zr (ug/g)
B11x-1	3,397.85	1.66	0.40	0.62	1.03	1.41	0.93	1.08	0.77	0.62	0.57	0.52	13.47	0.58	0.34
B11x-2	3,398.15	2.18	0.45	0.77	1.26	1.77	1.27	3.17	0.96	0.93	0.70	0.65	9.11	0.65	0.43
B11x-3	3,398.95	2.71	0.69	0.96	1.42	2.11	1.42	2.10	1.31	1.28	1.05	0.90	3.52	0.95	0.60
B11x-4	3,410.41	2.02	0.33	0.83	1.80	1.90	1.35	1.53	1.14	0.97	0.77	0.63	4.05	0.77	0.44
B11x-5	3,411.30	2.58	0.77	0.95	1.32	2.09	2.04	1.40	1.22	0.98	0.97	0.82	4.28	0.86	0.58
B11x-6	3,411.65	2.37	0.67	0.84	1.54	1.95	1.97	1.32	0.97	0.92	0.82	0.72	7.41	0.71	0.43
B11x-7	3,412.33	2.52	0.58	1.00	1.78	2.25	2.02	1.67	1.75	1.08	0.97	0.85	8.38	0.88	0.53
B11x-8	3,413.02	1.61	0.34	0.62	1.59	1.56	1.06	1.40	1.05	0.66	0.55	0.48	4.25	0.59	0.42
B11x-9	3,413.93	2.00	0.41	0.67	1.30	1.45	1.25	1.02	0.99	0.71	0.67	0.59	15.34	0.55	0.32
B11x-10	3,414.56	2.23	0.49	0.76	1.42	1.69	1.50	1.10	0.90	0.65	0.75	0.68	4.83	0.72	0.46
B11x-11	3,415.01	2.41	0.62	1.08	2.09	2.17	1.36	1.30	1.33	1.05	0.89	0.83	3.75	0.88	0.49
B11x-12	3,416.17	2.80	0.74	1.01	1.70	2.53	1.51	2.13	1.13	1.51	1.05	1.03	4.43	0.88	0.54
B11x-13	3,417.15	1.72	0.33	0.74	0.91	1.56	1.32	1.12	0.70	0.71	0.67	0.60	13.21	0.79	0.34
Xl25x-2	3,324.89	2.50	0.53	0.95	1.47	2.10	1.41	1.98	1.04	0.92	0.89	0.81	7.78	0.80	0.43
Xl25x-3	3,330.06	1.99	0.50	0.85	1.32	1.85	1.47	0.89	0.89	0.80	0.82	0.71	13.82	0.74	0.42
Xl25x-4	3,331.07	1.81	0.42	0.84	1.55	1.85	1.53	0.87	1.16	0.61	0.75	0.61	10.94	0.89	0.39
Xl25x-5	3,331.99	1.96	0.44	0.80	1.84	1.74	1.79	1.53	1.09	0.84	0.73	0.64	7.40	0.73	0.39
Xl25x-6	3,339.24	1.39	0.28	0.59	1.21	1.38	1.05	0.75	0.67	0.49	0.54	0.54	7.73	0.58	0.38
Xl25x-7	3,340.17	0.78	0.29	0.31	0.72	0.77	1.05	0.73	0.50	0.35	0.27	0.25	5.58	0.39	0.20
Xl25x-8	3,340.67	1.56	0.46	0.74	0.93	1.56	0.90	1.05	0.59	0.63	0.64	0.62	10.20	0.90	0.35
Xl25x-9	3,341.27	2.01	0.66	0.81	1.20	1.83	0.95	1.31	0.77	0.83	0.81	0.80	4.95	0.87	0.51
N202-7	3,560.68	2.69	0.83	1.07	1.70	2.60	1.57	1.92	1.23	1.16	1.10	0.92	2.27	0.96	0.56
N202-8	3,562.31	2.40	0.62	0.90	1.59	2.25	1.38	1.55	1.00	0.89	0.97	1.03	7.48	0.74	0.44
N202-9	3,563.56	2.08	0.59	0.85	1.55	2.05	1.11	0.95	0.90	0.74	0.83	0.91	11.88	0.70	0.40
N202-11	3,565.25	1.88	0.72	0.72	0.92	1.83	2.98	1.25	0.47	0.68	0.98	0.81	0.82	0.86	0.42
N202-13	3,569.90	3.39	0.71	0.68	0.90	1.97	2.35	1.89	0.51	0.85	1.02	0.82	0.96	0.58	0.36
N202-14	3,572.43	1.88	0.73	0.88	1.00	2.04	1.58	1.12	0.60	1.09	0.98	0.87	1.08	1.02	0.43
N202-15	3,575.35	1.73	0.29	0.48	0.47	1.11	2.66	1.50	0.29	0.42	0.65	0.52	0.88	0.68	0.23
G103-1	2,743.60	2.46	0.63	0.86	1.12	2.39	1.16	1.20	0.64	0.93	1.09	0.89	0.83	0.93	0.56
G103-2	2,744.80	2.77	0.70	0.98	1.21	2.58	1.36	1.45	0.69	1.00	1.15	0.93	0.88	0.96	0.55
G103-4	2,748.30	2.99	1.06	0.98	1.30	2.38	2.24	1.97	0.85	0.87	1.24	1.07	0.92	0.99	0.63
G103-5	2,749.80	2.08	0.39	0.52	0.80	1.26	2.89	1.30	0.42	0.54	0.79	0.62	1.36	0.79	0.33
G103-6	2,751.80	3.26	0.74	1.14	1.48	2.88	1.68	1.48	0.85	1.01	1.27	0.98	0.91	0.98	0.65
G103-7	2,754.10	3.73	1.14	1.18	1.45	2.87	1.62	1.41	0.84	1.25	1.31	1.01	0.88	1.02	0.65
G103-8	2,765.30	1.38	0.45	0.22	0.33	0.62	3.92	1.39	0.14	0.25	0.55	0.42	0.57	0.34	0.17

However, Li, Cd, Ni, Co., and Bi showed only minor enrichments or slight depletions (**Figure 5B**). The enrichment or depletion of the above major and trace elements are closely related to changes in the paleosedimentary environment. Therefore, the distribution characteristics of these elements and their paragenetic assemblages can help us construct a connection between the paleosedimentary environment and geochemistry of shale and further reveal the mechanisms of OM input and preservation (He et al., 2017b).

DISCUSSIONS

Paleosedimentary Environment and OM
Clastic Influx Proxies

The providential input of various clastics into ancient lake basins has an impact on the concentration of OM (Ding et al., 2015). The enhanced clastic influx may directly control the enrichment of OM by diluting OM or preventing its burial and preservation (Canfield, 1994).

Areas affected by terrigenous clastics have relatively high $Fe_2O_3+Al_2O_3$ contents, and areas dominated by biochemical performance have relatively high CaO + MgO contents. The value of $(Fe_2O_3+Al_2O_3)/(CaO + MgO)$ reflects the relative strength of terrigenous clastic sedimentation and biochemical sedimentation in lake basins (Zhou et al., 2020). When the supply of terrigenous clastics increases, Fe_2O_3 and Al_2O_3 content increases, and when the capacity of terrigenous clastics is weakened and biochemical deposition is enhanced, CaO and MgO content will increase. On the plane, the migration ability of Fe_2O_3 and Al_2O_3 was weak, and the migration ability of CaO and MgO was stronger (Xu et al., 2007). Their ratios were thus high at provenance and gradually declined as the distances from the provenance increased (Zhou et al., 2020). When $(Fe_2O_3+Al_2O_3)/(CaO + MgO) > 1$, the sediment is mainly controlled by terrigenous clastics; when $(Fe_2O_3+Al_2O_3)/(CaO + MgO) < 1$, it is mainly a biochemical deposition; and when $(Fe_2O_3+Al_2O_3)/(CaO + MgO)$ is in the range of 0.5–1.0, it is in a transitional state, which is jointly controlled by terrigenous clastics and biochemical deposition in the lake basin. In the samples from the four key wells in the study area, the values of $(Fe_2O_3+Al_2O_3)/(CaO + MgO)$ were 0.50 (Xl25x), 0.76 (B11x), 1.71 (N202), and 2.54 (G103). The shale of wells G103 and N202 was obviously determined by terrigenous clastics, which is consistent with the

TABLE 4 | Trace elements results of the Es_1^L shale in the Raoyang Sag.

| Samples	Depth (m)	Nb (ug/g)	Mo (ug/g)	Cd (ug/g)	In (ug/g)	Cs (ug/g)	Ba (ug/g)	Hf (ug/g)	Ta (ug/g)	Re (ug/g)	Pb (ug/g)	Bi (ug/g)	Th (ug/g)	U (ug/g)
B11x-1	3,397.85	0.26	2.53	2.42	0.53	1.34	3.35	0.37	0.19	3.99	0.79	1.34	0.56	1.63
B11x-2	3,398.15	0.35	3.11	2.46	0.85	1.74	2.85	0.46	0.25	4.20	0.93	1.78	0.68	2.07
B11x-3	3,398.95	0.51	5.18	4.69	1.21	2.16	3.31	0.68	0.38	6.98	1.52	2.54	1.04	1.91
B11x-4	3,410.41	0.36	5.99	2.97	0.79	1.57	2.23	0.48	0.27	2.35	1.05	2.22	0.81	2.12
B11x-5	3,411.30	0.49	5.25	4.73	1.09	2.01	2.61	0.73	0.37	5.91	1.27	2.61	0.97	2.96
B11x-6	3,411.65	0.36	4.71	2.80	1.02	1.92	3.05	0.49	0.29	6.83	1.10	2.29	0.83	2.09
B11x-7	3,412.33	0.45	8.43	4.83	1.23	2.28	3.98	0.63	0.36	7.10	1.45	3.11	0.97	3.00
B11x-8	3,413.02	0.24	5.18	2.46	0.61	1.20	2.07	0.45	0.18	3.16	0.89	2.00	0.57	1.68
B11x-9	3,413.93	0.28	5.26	3.21	0.76	1.70	2.85	0.38	0.22	2.76	0.85	1.87	0.67	1.89
B11x-10	3,414.56	0.35	3.21	2.40	0.77	1.93	2.58	0.53	0.28	5.41	0.95	1.83	0.76	1.85
B11x-11	3,415.01	0.36	4.12	3.21	0.96	2.35	1.75	0.56	0.29	2.89	1.07	2.46	0.88	1.83
B11x-12	3,416.17	0.46	5.50	3.35	1.31	3.16	1.62	0.58	0.38	4.79	1.30	3.12	1.04	2.02
B11x-13	3,417.15	0.29	1.54	1.96	0.78	1.58	2.56	0.35	0.25	3.15	0.83	2.08	0.66	1.64
Xl25x-2	3,324.89	0.39	3.24	3.11	0.91	2.24	2.74	0.48	0.31	4.17	1.00	2.37	0.87	2.18
Xl25x-3	3,330.06	0.36	2.57	2.58	0.96	1.98	2.54	0.46	0.31	4.69	0.89	2.32	0.85	2.11
Xl25x-4	3,331.07	0.30	2.62	2.41	0.71	1.62	3.40	0.41	0.27	3.50	1.03	2.56	0.72	1.77
Xl25x-5	3,331.99	0.32	5.40	2.60	0.92	1.73	2.20	0.41	0.27	5.55	1.12	2.98	0.76	2.52
Xl25x-6	3,339.24	0.24	1.84	1.35	0.57	1.44	1.22	0.36	0.21	3.90	0.58	1.70	0.54	2.04
Xl25x-7	3,340.17	0.14	1.49	1.10	0.22	0.57	1.37	0.19	0.11	3.97	0.41	0.89	0.27	1.06
Xl25x-8	3,340.67	0.27	1.65	1.44	0.68	1.45	2.03	0.37	0.24	3.57	0.82	1.85	0.68	1.96
Xl25x-9	3,341.27	0.40	1.20	1.55	0.96	2.06	3.82	0.54	0.33	5.09	0.99	1.77	0.80	1.98
N202-7	3,560.68	0.50	2.30	2.36	1.18	2.49	1.56	0.60	0.40	2.49	1.30	3.04	1.03	1.76
N202-8	3,562.31	0.46	3.46	2.04	1.16	2.79	1.44	0.51	0.38	3.25	1.19	2.90	0.93	2.41
N202-9	3,563.56	0.43	1.93	1.60	0.97	2.88	1.65	0.46	0.34	2.86	0.99	2.63	0.79	2.55
N202-11	3,565.25	0.46	0.23	1.26	0.72	1.14	1.17	0.44	0.46	8.50	1.03	1.48	0.96	0.74
N202-13	3,569.90	0.48	0.26	1.31	0.79	1.13	0.97	0.42	0.47	6.17	1.53	1.74	1.00	0.70
N202-14	3,572.43	0.47	0.23	1.74	0.95	1.46	0.94	0.48	0.43	3.49	1.06	2.12	1.03	0.82
N202-15	3,575.35	0.30	0.18	0.86	0.45	0.57	0.85	0.25	0.33	7.49	0.82	0.71	0.60	0.49
G103-1	2,743.60	0.54	0.23	1.52	1.16	1.70	0.96	0.63	0.50	1.94	1.35	2.38	1.21	0.84
G103-2	2,744.80	0.56	0.27	1.41	1.08	1.91	1.03	0.62	0.51	1.48	1.46	2.70	1.24	0.90
G103-4	2,748.30	0.56	0.29	1.12	1.30	2.17	1.01	0.70	0.55	4.96	2.23	3.27	1.36	1.01
G103-5	2,749.80	0.33	0.18	1.12	0.51	0.85	1.03	0.37	0.37	8.62	1.10	1.35	0.74	0.56
G103-6	2,751.80	0.65	0.29	1.55	1.28	2.12	0.88	0.71	0.56	3.08	1.25	3.03	1.26	1.60
G103-7	2,754.10	0.61	0.59	2.98	1.25	2.20	0.90	0.73	0.57	2.97	1.35	2.94	1.26	0.99
G103-8	2,765.30	0.16	0.37	0.39	0.13	0.32	1.42	0.20	0.25	13.48	0.82	0.27	0.32	0.30

accepted source direction of Raoyang Sag (Yin et al., 2020). Well B11x was in a transitional state, and well Xl25x was mainly controlled by biochemical deposition. The input intensity of terrigenous clastics was negatively correlated with the TOC value (**Figure 6A**). When $(Fe_2O_3+Al_2O_3)/(CaO + MgO) > 1$, the TOC content is low overall. The samples from wells G103 and N202 were close to the provenance, the input intensity of terrigenous clastics was strong, and the OM was not enriched, due to dilution. Wells B11x and Xl25x were far away from the provenance, and the OM presented different degrees of enrichment. Therefore, the dilution effect of clastic influx impacts the preservation of OM; however, the correlation is not high, indicating that this factor is not the main controlling factor. Moreover, elements such as Ti, Si, and Al are considered to be parameters that can characterize the input intensity of terrigenous clastics (Murphy et al., 2000). Ti is usually associated with clay minerals and heavy minerals, whereas Si mainly exists in quartz, feldspar, and biogenic fractions (Kidder et al., 2001). The elements Ti and Si can provide key information about the variation in the imported flux of clastics from non-aluminosilicate sources after normalizing Al (Chen et al., 2016). The sample concentrations of Ti, Si, and Al from wells G103 and N202 were generally high, while the concentrations from wells B11x and Xl25x were generally low. This shows that different well positions on the plane are affected by the intensity of the clastic influx, which supports the previous discussion. The strong correlations between Ti and Al ($R^2 = 0.85$) and Si and Al ($R^2 = 0.69$) (**Figures 6B,C**) suggest a rather homogeneous detrital supply.

Paleoclimate Proxies

The paleoclimate in provenantial terrain determined the mineralogical and chemical composition of siliceous clastic sediments (Nesbitt and Young, 1982; Fedo et al., 1995). Therefore, the characteristics of mineralogical and chemical compositions in shale can potentially reflect changes in paleoclimate. Correspondingly, paleoclimatic conditions can be inferred from the discrimination charts of various elements (CIA, K_2O/Al_2O_3, Ga/Rb, and Rb/Sr) (Fedo et al., 1995; Shen et al., 2001; Roy and Roser, 2013).

The chemical index of alteration (CIA) can aid in the reconstruction of paleoclimate and weathering intensity (Fedo et al., 1995; Price and Velbel, 2003), and the CIA equation can be expressed as $[(Al_2O_3)/(Al_2O_3 + Na_2O+ CaO^* + K_2O)] \times 100$. As it is unclear whether CaO is derived from carbonate, Nesbitt and
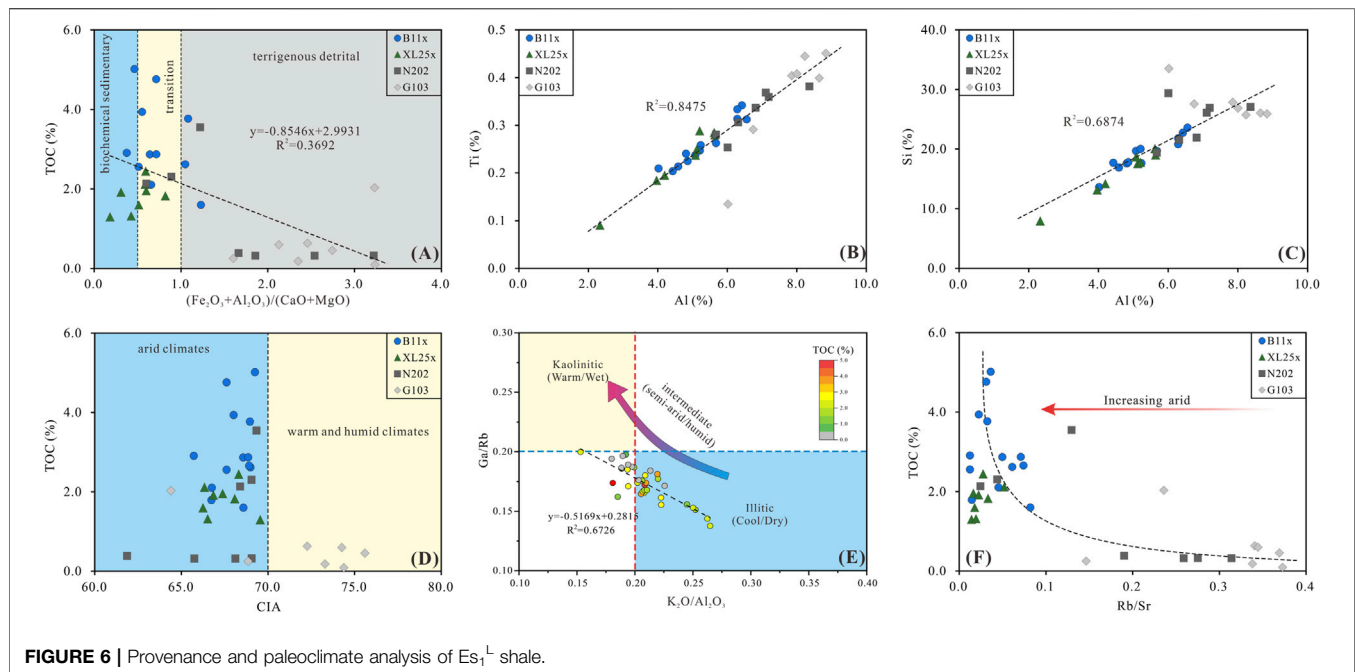
FIGURE 6 | Provenance and paleoclimate analysis of Es_1^L shale.

Young (1984) suggested excluding CaO from CIA calculations on rocks with high CaO content. As mentioned in *Mineralogy and Lithofacies of Shale*, the Es_1^L shale is rich in carbonate, and the corrected CaO content is much greater than the Na_2O content; therefore, CaO^* should be replaced by Na_2O in the CIA formula. When CIA values are high (85–100), sediments were generally deposited in hot and humid tropical paleoclimates, whereas those deposited in warm and humid paleoclimates have medium CIA values (70–85), and those deposited in cold and arid paleoclimates have minor CIA values (50–70) (Nesbitt and Young, 1982). In this study, the CIA values of shale from Es_1^L varied from 62 to 76 (mean 68), and only five samples from well G103 had values greater than 70 (**Figure 6D**), indicating that the sediments were produced in the source region, under a cold and arid paleoclimate. In addition, the Es_1^L shale seems to have been deposited in arid to semi-arid paleoclimate conditions, according to the Ga/Rb and K_2O/Al_2O_3 discriminant chart (**Figure 6E**), which is consistent with the results obtained by Ye et al. (2020). The value of Rb/Sr can also indicate the evolution of the paleoclimate. Element Rb is relatively stable, whereas Sr is easily weathered during chemical weathering. Therefore, Rb/Sr values are high in humid environments and relatively low in dry and hot environments (Shen et al., 2001; Li et al., 2019; Ye et al., 2020). The Rb/Sr values of all samples from well G103 and some of those from well N202, located at the boundary of the Raoyang Sag, were larger, while the Rb/Sr values of wells B11x and Xl25x, located in the middle of the sag, were relatively small (**Figure 6F**). In addition, it was observed that the TOC content increased with aridity (**Figure 6F**). The mineral composition of sediments can also reflect climatic change. Carbonates are deposited under dry climatic conditions because of the elevated evaporation (Kelts and Hsu, 1978; Sarnthein et al., 1994). Therefore, the degree of arid climate in Es_1^L may increase the salinity of lakes, deposition of

carbonates, and eutrophication in lake waters, resulting in algal blooms and OM enrichment. Therefore, climate has an impact on the accumulation of OM and is also a condition for the formation of basins with small areas but large resources.

Paleoredox Conditions Proxies

The paleoredox conditions of ancient lakes play a vital role in the deposition, burial, preservation, and accumulation of OM. Such conditions can usually be characterized by specific ratios of redox-sensitive elements (e.g., Th/U, V/(V + Ni), Ni/Co., and V/Cr) (Hatch and Leventhal, 1992; Jones and Manning, 1994; Wignall and Twitchett, 1996; Rimmer et al., 2004), which include Mo, U, Th, V, Ni, Co., and Cr (Zhao et al., 2016; He et al., 2017b). However, some of the specific trace elements (e.g., Cr and Co.) found in lacustrine sedimentary rocks are easily influenced by clastic influx, diagenesis, and re-oxidization after deposition (Xiong et al., 2010). Therefore, the observed ratios of some redox-sensitive elements (e.g., V/Cr and Ni/Co.) may result in misinterpretations and are no longer considered suitable for accurately reflecting paleoredox conditions.

In this study, the V/(V + Ni) values of the Es_1^L shale were between 0.42 and 0.84 (avg. 0.72). Most of the V/(V + Ni) ratios in shale samples exceeded the threshold values (i.e., V/(V + Ni) > 0.6) indicative of dysoxic/suboxic conditions (**Figure 7A**), which demonstrates that the Es_1^L shales were mainly deposited in a dysoxic/suboxic paleo-lacustrine environment. Under decreasing water conditions, organic-rich sediments are rich in U (Kochenov et al., 1977). Thus, low Th/U ratios have been widely used as indicators of anoxic paleo-sedimentary environments (Th/U < 2) (Wignall and Twitchett, 1996). The Th/U values of the shale samples were widely distributed across the range of 0.97–5.53 (mean 2.56), indicating the paleoredox conditions of ancient lake are inconsistent and there are differences in the vertical

FIGURE 7 | Analysis of paleoredox conditions, paleoproductivity, and paleosalinity.
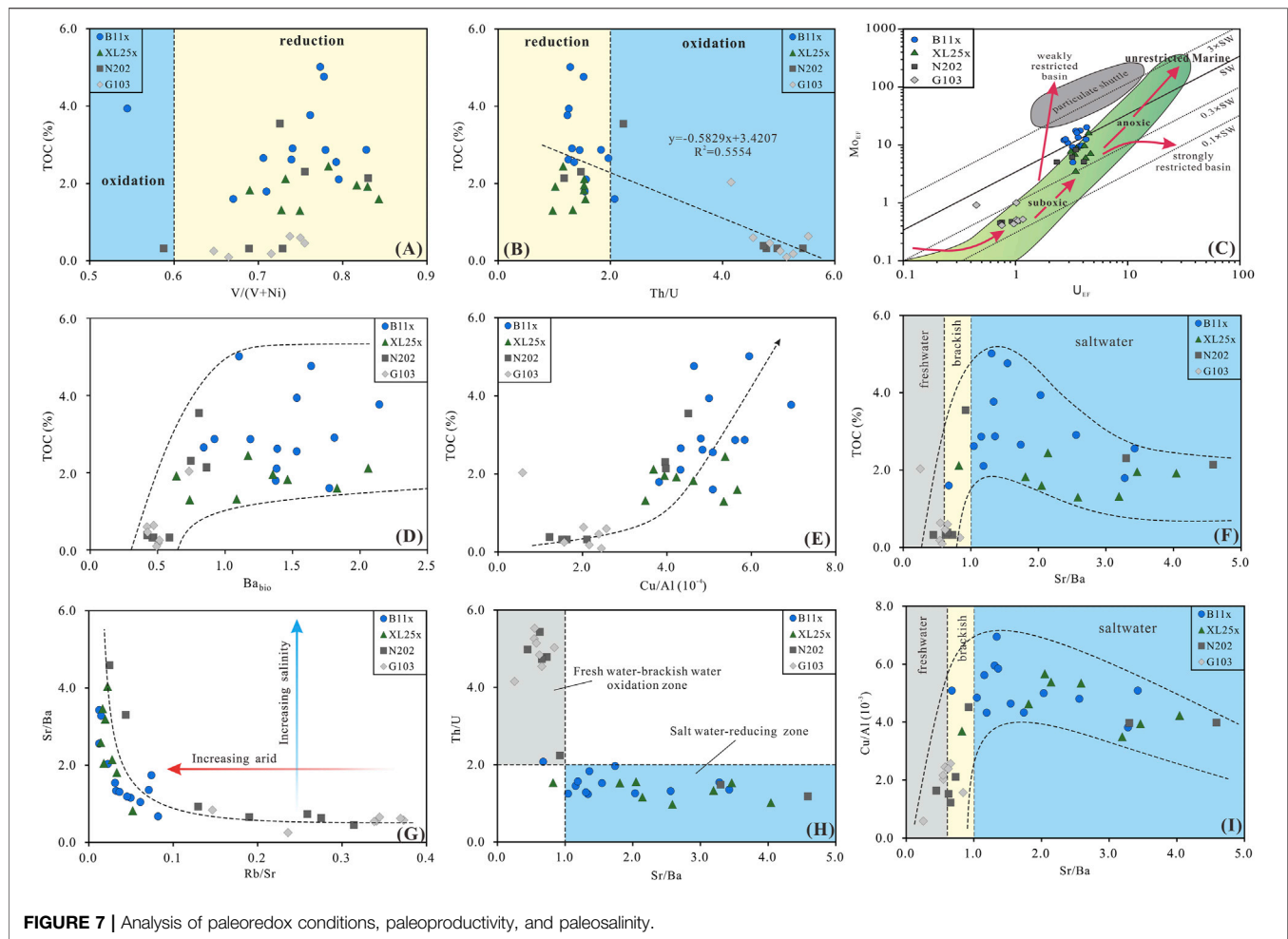
preservation conditions. The Th/U ratios of organic-rich shale (>1.7%) were usually less than 2 (mean 1.59), which indicates that these shale samples were deposited in a reducing paleoenvironment. Moreover, the TOC and Th/U ratios have a strong negative correlation ($R^2 = 0.55$) (**Figure 7B**). These observations show that paleoredox conditions, that is, preservation conditions, played a major role in controlling the enrichment of OM in the Es_1^L shale.

U and Mo are also effective paleoredox parameters that are disturbed by external factors and can accurately reflect the occurrence of paleoredox conditions during sediment deposition processes (Tribovillard et al., 2006). Previous research has shown that the patterns of U_{EF}-Mo_{EF} covariations are particularly significant for paleoredox reconstruction (Algeo and Tribovillard, 2009; Wang et al., 2017). U_{EF} and Mo_{EF} represent the element enrichment factors (MEFs) of U and Mo, respectively. The calculation formula for M_{EF} is:

$$M_{EF} = (X/Al)_{sample}/(X/Al)_{PASS} \qquad (1)$$

where X and Al are the concentrations of elements X and Al, respectively. Mo and U showed obvious enrichment in wells B11x, Xl25x and in some of the samples from N202; whereas the

elements Mo and U from the G103 well and some of the samples from the N202 well exhibited relatively moderate or less detectable enrichment (**Figure 7C**). These parameters indicate that the shale samples from wells B11x and Xl25x and some from N202 were possibly deposited in a water column with abundant H_2S, whereas the samples from well G103 and others from N202 were deposited in water with scarce H_2S (Algeo and Tribovillard, 2009; Wang et al., 2017). The semi-deep and deep lake had a reducing paleoenvironment, whereas the shallow lake sediments reflected oxic and suboxic paleoenvironments, based on the plot of the Mo_{EF}-U_{EF} covariation and sedimentary facies belt for each well location (**Figure 7C**).

Paleoproductivity Proxies
Elemental Ba and Cu can depict relative levels of paleoproductivity (Tribovillard et al., 2006). Their correlation with TOC is usually used as a proxy for the impact of primary productivity on OM enrichment (Zhao et al., 2016; Wang et al., 2017), based on the premise that OM is produced by algae (primary productivity) (Pedersen and Calvert, 1990). Indeed, previous research has determined that algae organisms are the main origin of OM in the Es_1^L source rock (Yin et al., 2020).

Therefore, paleoproductivity proxies are valuable for evaluating OM enrichment.

Barium is considered a typical index for evaluating paleoproductivity because biogenic barite is associated with phytoplankton decay (Dymond et al., 1992). Biogenic Ba (Ba_{bio}) can be used to estimate the intensity of carbon exports from the photic zone in the water column and is regarded as an effective indicator of paleoproductivity (Brumsack, 1989; Tribovillard et al., 1996). The Ba_{bio} content can be obtained using the following formula:

$$Ba_{bio} = Ba_{tot} - (Al_{tot} \times Ba / Al_{alu}) = Ba_{tot} - (Al_{tot} \times 0.0075) \quad (2)$$

where Ba_{bio} is the Ba content from the biogenic component, Ba_{tot} is the total Ba content, Ba/Al_{alu} is the Ba/Al ratio of aluminosilicate detritus in crustal rocks, and Al_{tot} is the total Al content. The Ba/Al_{alu} ratios of aluminosilicate components in crustal rocks ranged from 0.005 to 0.01 (Taylor, 1964) and the Ba/Al_{alu} ratios usually had a value of 0.0075 (Dymond et al., 1992). The Ba_{bio} contents of the samples from different regions were quite different. The samples from semi-deep lacustrine and deep lacustrine facies had higher Ba_{bio} content, whereas the Ba_{bio} content in samples from shore-shallow lake facies was relatively low. The abundance of TOC is directly related to paleoproductivity, and TOC is more abundant when Ba_{bio} content is greater than 1.0 (**Figure 7D**). Therefore, paleoproductivity is of great significance for the enrichment of OM.

OM incorporates copper (Cu) into sediments in the form of organometallic complexes, so there is a close relationship between Cu and TOC content (Tribovillard et al., 2006). Therefore, while OM may become partially or completely degraded after deposition, the Cu released from OM can be trapped by pyrite and preserved in sediment (Huerta-Diaz and Morse, 1992; Algeo and Maynard, 2004). Thus, the ratio of Cu to Al can represent the level of paleoproductivity (Tribovillard et al., 2006). The average value of Cu/Al in the shale samples was 3.86×10^{-3}, and the Cu/Al values of samples from wells B11x and Xl25x and some from N202 were much higher than those from G103 and others from N202 (**Figure 7E**). The samples from shore-shallow lake facies implied relatively low paleoproductivity, which may be due to the destruction of the phytoplankton growth environment by clastic influx. In addition, the concurrence of increased TOC content and Cu/Al (**Figure 7E**) indicates that paleoproductivity has an impact on OM enrichment.

Paleosalinity Proxies

The chemical properties of Sr and Ba are similar, and the migration ability of Ba is lower than that of Sr, so Sr can continue to migrate further towards, or away from, areas of higher salinity. Thus, Sr/Ba ratios usually indirectly indicate the salinity of the water body (Fu et al., 2018; Zhou et al., 2020). According to previous research, water can be classified as a freshwater (Sr/Ba<0.6), brackish (0.6<Sr/Ba<1.0), or saline environment (Sr/Ba>1.0) (Wang et al., 1979; Wang and Wu, 1983). The average Sr/Ba values of wells B11x, Xl25x, N202, and G103 were 1.74, 2.51, 1.61, and 0.58, respectively; indicating that the first three wells experienced saline environmental conditions,

while well G103 experienced a freshwater environment. The average depths of the sampling points of the above four wells were 3,410.04, 3,336.08, 3,567.07, and 2,751.10 m, respectively, which corresponds to their historical salinity conditions. These observations demonstrate that the semi-deep and deep lake water bodies had relatively high salinities and were vertically heterogeneous with stratified water columns.

The TOC content first increased and then decreased with increases in paleosalinity (**Figure 7F**). TOC was more enriched when the value of Sr/Ba was 1.0–3.0, indicating that both low paleosalinity and excessive paleosalinity were not conducive to the enrichment of OM, which is consistent with the results of He et al. (2018); based on their use of biomarker compounds in paleosalinity analysis.

We also found that arid climates caused evaporation to significantly reduce lake water levels, which increased the salinity of the deep lake water body (**Figure 7G**). However, the shallow lake area was more affected by the influx of terrestrial debris and experienced a high turnover of water exchange, resulting in low salinity and water column stratification. Saltwater environments in the study area also usually experienced reducing conditions, with freshwater and brackish water having oxidizing conditions [**Figures 7H**, **8** (profile 1 in **Figure 1A**)]. This indicates that water column stratification also induced different preservation conditions at different lake depths. This is also confirmed by the extensive development of laminar structures (**Figures 4B,H,J**). In addition, the productivity profile (Cu/Al) also exhibited a phenomenon in which it first increased and then decreased with increasing salinity, indicating that neither freshwater nor excessive salinity were suitable environments for ancient organisms (algae, etc.) (**Figure 7I**). Therefore, salinity is important for OM enrichment. The low input of terrestrial debris, arid climate, moderate lake salinity, reducing environment, and high productivity are conducive to OM enrichment.

OM and Shale Oil Enrichment

The first two geochemical indices that can directly reflect the oil content within shale are the amounts of chloroform bitumen S_1 and "A" (Lu et al., 2012). The former represents low-carbon hydrocarbon content, and the latter is the sum of heavier hydrocarbons, nonhydrocarbons, and asphaltenes (Li et al., 2015). The S_1 of shale samples can be used as an indicator to evaluate absolute oil content because most shale reservoirs have low permeability and produce light or condensate oil.

Figure 9A illustrates the relationship between the oil content and TOC of shale samples from Es_1^L. The oil content of the samples exhibits the characteristics of a triple-division with increases in TOC value. First, the oil content of the samples increased slowly when the TOC was low, then rose rapidly for a while, finally entering a steady state. According to the absolute oil content corresponding to the turning points of the envelope of the scattered points in **Figure 9A**, the shale samples were classified into three types, based on the TOC value of the turning points: dispersed resources (TOC < 0.6%), potential resources (0.6% <TOC<1.7%), and enriched resources (TOC > 1.7%). Enriched resources mean that the total oil generated by the OM can meet
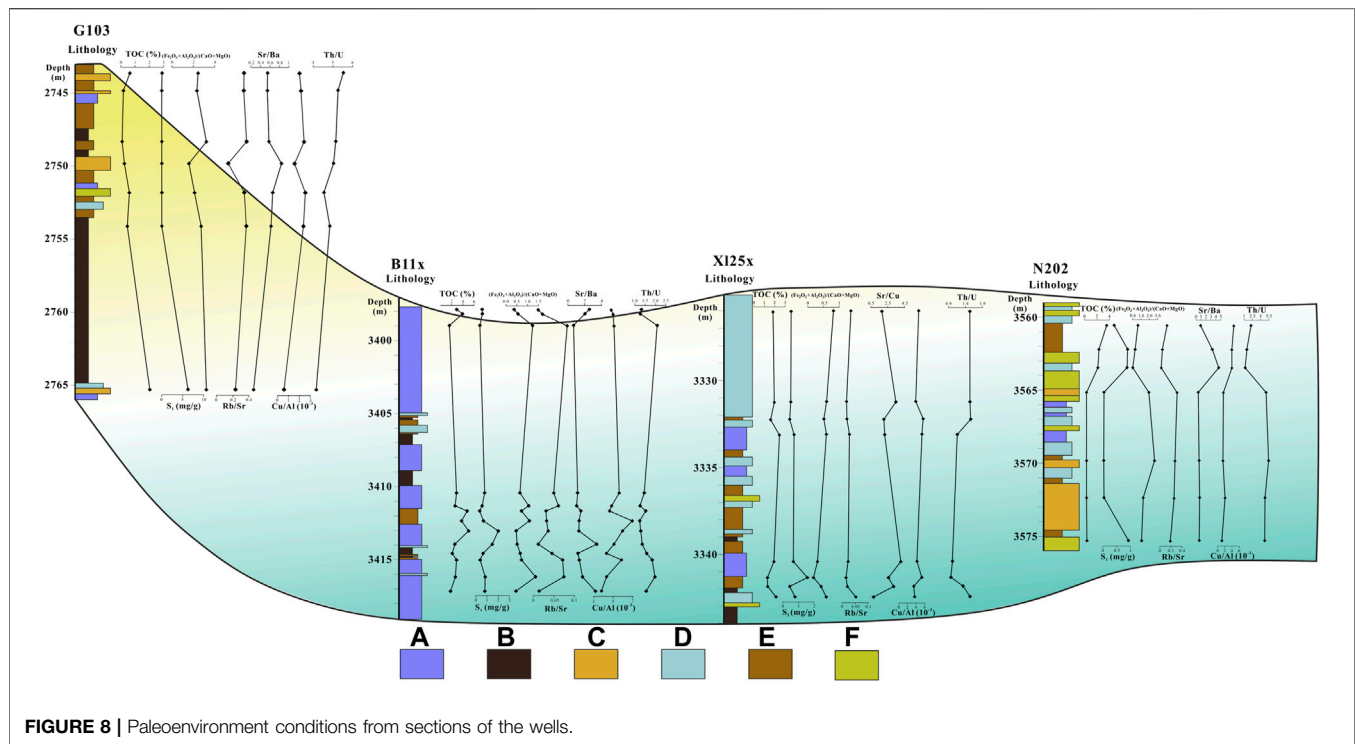
FIGURE 8 | Paleoenvironment conditions from sections of the wells.
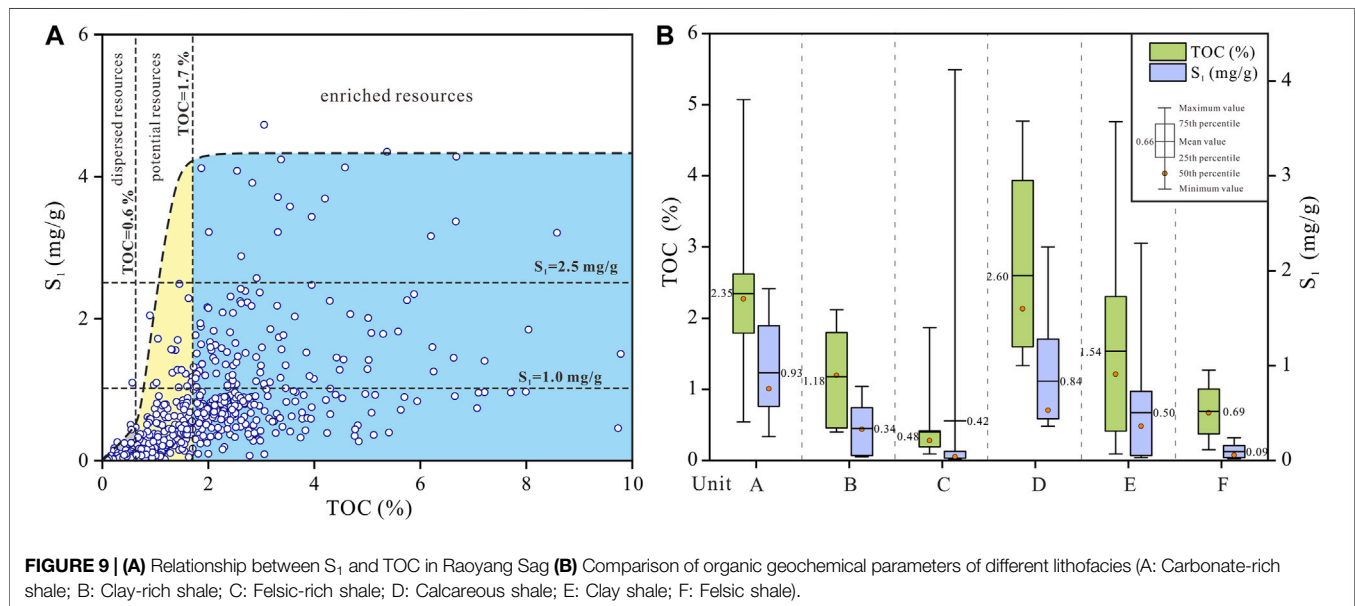
FIGURE 9 | **(A)** Relationship between S_1 and TOC in Raoyang Sag **(B)** Comparison of organic geochemical parameters of different lithofacies (A: Carbonate-rich shale; B: Clay-rich shale; C: Felsic-rich shale; D: Calcareous shale; E: Clay shale; F: Felsic shale).

the requirements of shale residual oil when the TOC reaches a critical value (1.7%). The hydrocarbons in shales are saturated, resulting in their expulsion when the TOC exceeds the critical value (Lu et al., 2012). The layer formations with enriched resource conditions are the most promising exploration targets for shale oil. In addition, the OM and hydrocarbon enrichment of different lithofacies also varied (**Figure 9B**). Types A, D, and E of OM were more enriched (mean values were 2.35, 2.60, and 1.54,

respectively) and corresponded to enriched resources. The characteristics of self-generation and self-storage of shale oil also enriched the hydrocarbons of Types A, D, and E (mean values were 0.93, 0.84, and 0.50, respectively). This shows that carbonate minerals play an important role in shale oil enrichment. Previous studies have shown that the mesopores and macropores (dissolution pores, intercrystalline pores and microfractures) existing in the lacustrine shale interval are closely

FIGURE 10 | Analysis of the sedimentary environments of different lithofacies.
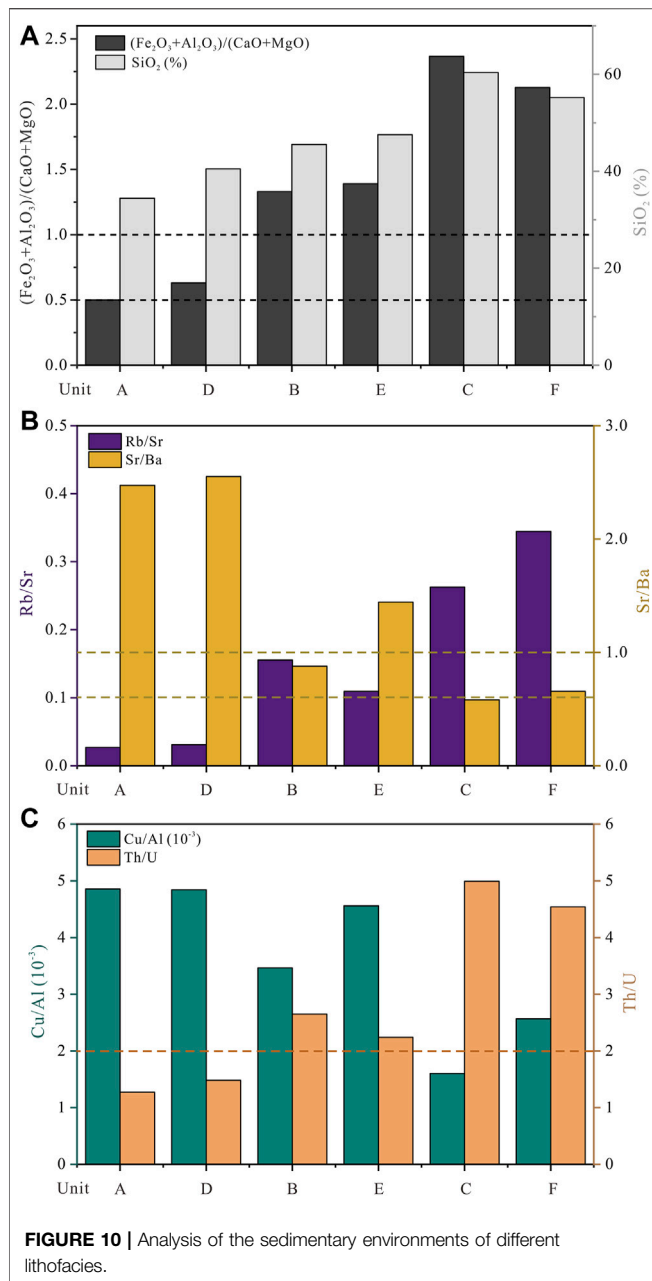
related to the carbonate composition, which is a key factor affecting the quality of the shale oil reservoir. Moreover, larger pores are most conducive to the enrichment and development of shale oil (Wang et al., 2015; Birdwell et al., 2016; Li et al., 2017; Bai et al., 2020). It is worth noting that there were abnormally high values of Type C, which may have been caused by the migration of hydrocarbons in the surrounding organic-rich shale. For shale oil reservoirs with mainly self-generation and self-storage characteristics, OM content is a cornerstone that largely determines the degree of hydrocarbon enrichment in shale. The different types of shale have varying degrees of OM enrichment because of their dissimilar sedimentary environments.

Paleosedimentary Environment and Lithofacies

The deposition period of A and D was less affected by terrigenous clastic input (($Fe_2O_3+Al_2O_3$)/(CaO + MgO) < 1.0), and TOC was rarely diluted. The paleoclimatic conditions corresponding to the two lithofacies were relatively arid, leading to increased lake concentration, moderate paleosalinity (1.0<Sr/Ba<3.0), and a massive precipitation of calcareous minerals. A favorable paleoclimatic environment and moderate paleosalinity provided a good habitat for algae and other organisms, causing them to flourish in large numbers, resulting in a significant increase in paleoproductivity. The OM formed by paleontology deposited in stratified water columns, and the strong reducing conditions (Th/U < 2.0) guaranteed the enrichment of the OM (**Figure 10**). Organic-rich shale (e.g., A and D) produced hydrocarbons in large quantities and accumulated *in situ* to form shale oil reservoirs under the changing formation temperature and pressure conditions caused by an increase in burial depth.

Types C and F are quite different from the above two lithofacies. They were greatly affected by the input of terrestrial debris—silicon content was relatively high (SiO_2 > 50%), and the OM was severely diluted. During the period of deposition, they experienced a humid paleoclimate, frequent water body exchanges, and low lake water paleosalinity (Sr/Ba < 0.6). These conditions meant that the water bodies were generally rich in oxygen and had low paleoproductivity, resulting in low OM generation, preservation, and enrichment (**Figure 10**). Although lithofacies C and F have low OM contents and lack the capacity to generate a large number of hydrocarbons because of the large amount of felsic minerals trapped by organic-rich shale, their high-quality storage capacity should be noted (**Figure 9B**).

After terrigenous detrital material was brought into the lake basin, fine-grained clay in the water body was concentrated in a suspended state. When suspension equilibrium conditions were broken, the fine-grained clay was gradually deposited in the form of single particles mixed with felsic minerals, carbonates, OM, and other components to form clay shale. The lithological compositions of B and E are mainly clay minerals and were deposited in a sedimentary environment that was not strongly affected by terrigenous clastics and was partial to reduction and brackish water-saltwater bodies (**Figure 10**).

Enrichment Model of Shale Oil

We used a BP neural network combined with logging data and measured XRD data (Li et al., 2015) to predict the rock mineral composition of 79 wells in the study area. The lithofacies profile of N201-N301 was obtained, as shown in **Figure 11**, corresponding to profile 2 in **Figure 1A**. The shale oil enrichment model of the Raoyang Sag, which takes lithofacies and sedimentary environments into account, has been established.

The overall mineral composition of the Raoyang Sag changes from felsic minerals to clay and carbonate and back to felsic minerals, from northwest to southeast, reflecting changes in the sedimentary environment. Under a background of arid paleoclimate, rainfall decreased, weathering and denudation of source rock areas weakened, and the detrital material transported by the river decreased. Because lake water evaporation was greater

FIGURE 11 | Accumulation model of shale oil in the Es_1^L of the Raoyang Sag.
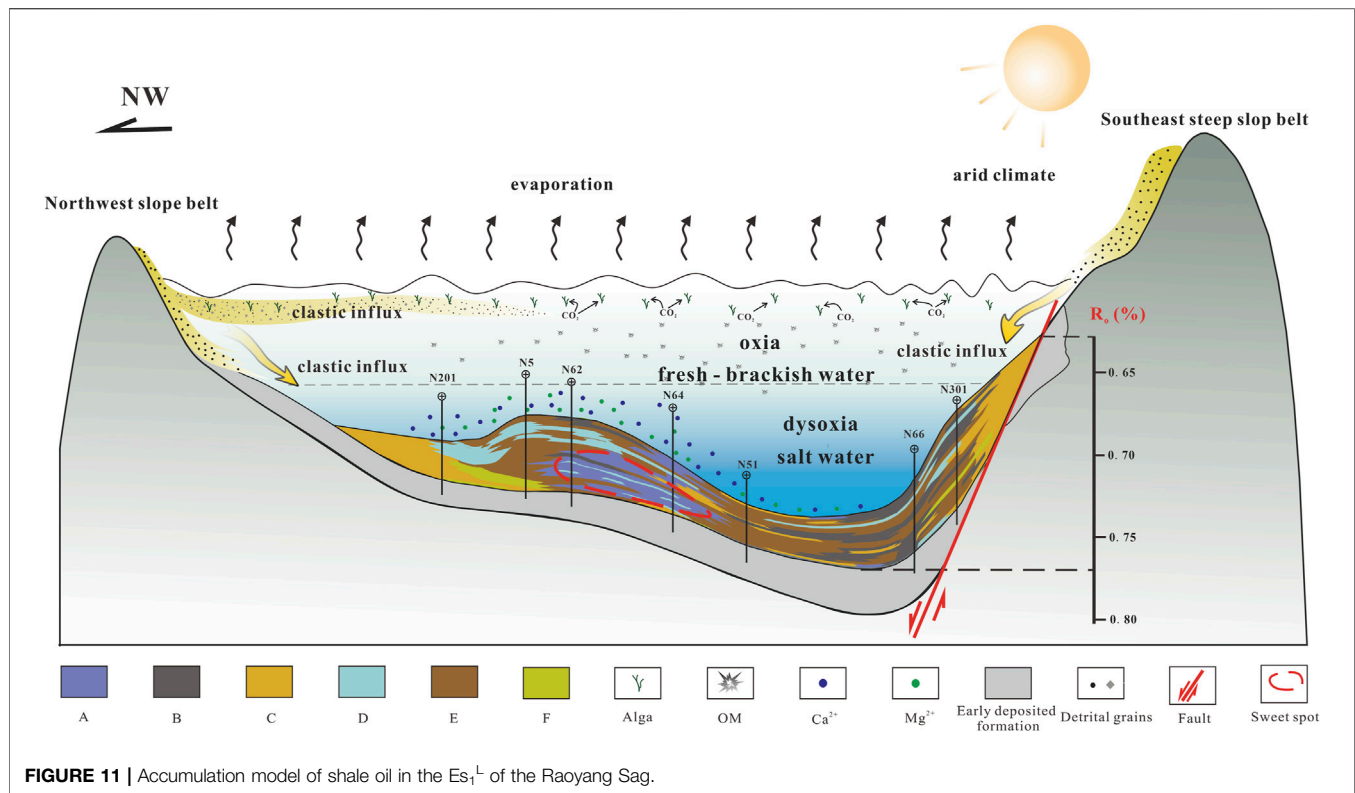
than the inflow, the lake level entered a downward cycle, the concentration of Ca^{2+} and Mg^{2+} in the lake water gradually increased, and the lake basin entered a salty period. Under appropriate lake water salinity, algae bloomed and consumed the CO_2 in the water body, and a large amount of OM was deposited in the stratified water column. Good storage conditions (strongly reducing) and an environment far from the material source provided conditions for OM enrichment. OM and the seasonal deposition of carbonate rocks deposited under biological and chemical sedimentation formed organic-rich calcareous shale, which is a favorable source reservoir for shale oil. A large volume of terrigenous debris was imported, and the water body was relatively turbulent, which can be attributed to the shallow water high-energy oxidation environment in the slope belt and steep slope belt of the Raoyang Sag. Most of the provenantial felsic minerals entered the lake directly to form C and F near their provenance. Externally sourced fine-grained clay minerals were dispersed and suspended in the lake water, and they were mixed with felsic minerals, carbonates and adsorbed OM deposited in semi-deep and deep lake regions.

Because the lithofacies of A and D were mostly formed in a depositional environment with low debris influx, an arid paleoclimate, moderate paleosalinity, high paleoproductivity, and good preservation conditions, the OM was abundantly enriched. With the increase in stratum burial depth, the OM generated hydrocarbons to form self-generated and self-stored *in situ* shale oil reservoirs (sweet spots) (**Figure 11**). Although clay minerals usually carry OM and are deposited on the bottom of lakes, this type of shale oil reservoir has low movable oil content and generally poor

development characteristics due to the strong adsorption and poor fracturing properties of clay minerals (Ju et al., 2018; Li et al., 2018). In addition, the C and F types of lithofacies sandwiched by mature organic-rich shale might also have been enriched oil due to the short-distance migration of hydrocarbons from the organic-rich shale.

CONCLUSION

In this study, the reconstruction of the paleoenvironment of the Es_1^L shale in the Raoyang Sag was based on geochemical, mineralogical, and well logging data, and was used to establish an enrichment model of OM and shale oil that corresponds to the paleosedimentary environment.

The shale oil enrichment model of the Es_1^L in Raoyang Sag was established through a combination of lithofacies and paleosedimentary environments. The kerogen type of the Es_1^L shale is mainly Type I. The shales are also rich in carbonate minerals, with an obvious enrichment of major elements (e.g., CaO, MgO, and Na_2O) and trace elements (e.g., Sr, Mo, and Re). These elements reflect the relationship between the specific paleosedimentary environment and OM. The parameters $(Fe_2O_3+Al_2O_3)/(CaO + MgO)$, Sr/Ba, Rb/Sr, Cu/Al, and Th/U indicate that the Es_1^L shale in the Raoyang Sag was deposited under an arid paleoclimate, reducing conditions, and a paleoenvironment dominated by saline water. OM accumulation in the shale was mainly controlled by the high paleoproductivity of surface water from algal blooming and moderate salinity, with the help of a stratified water column under strong reducing water

conditions. The influx of clastics had a significant effect on the OM. Carbonate plays an important role in shale oil enrichment, and class A and D shales are the dominant lithofacies for shale oil and OM enrichment. Owing to deposition occurring in an arid paleoclimate, conducive salinity water bodies, high paleoproductivity, lower clastic influx, and anoxic preservation conditions were beneficial for OM and shale oil enrichment.

DATA AVAILABILITY STATEMENT

The raw data supporting the conclusion of this article will be made available by the authors, without undue reservation.

REFERENCES

Algeo, T. J., and Maynard, J. B. (2004). Trace-element Behavior and Redox Facies in Core Shales of Upper Pennsylvanian Kansas-type Cyclothems. *Chem. Geology.* 206, 289–318. doi:10.1016/j.chemgeo.2003.12.009

Algeo, T. J., and Tribovillard, N. (2009). Environmental Analysis of Paleoceanographic Systems Based on Molybdenum-Uranium Covariation. *Chem. Geology.* 268, 211–225. doi:10.1016/j.chemgeo.2009.09.001

Bai, C., Yu, B., Han, S., and Shen, Z. (2020). Characterization of Lithofacies in Shale Oil Reservoirs of a Lacustrine basin in Eastern China: Implications for Oil Accumulation. *J. Pet. Sci. Eng.* 195, 107907. doi:10.1016/j.petrol.2020.107907

Birdwell, J. E., Berg, M., Johnson, R. C., Mercier, T. J., Boehlke, A. R., and Brownfield, M. D. (2016). *Geological, Geochemical and Reservoir Characterization of the Uteland Butte Member of the Green River Formation.* Utah: Uinta Basin.

Brumsack, H.-J. (1989). Geochemistry of Recent TOC-Rich Sediments from the Gulf of California and the Black Sea. *GEOL. RUNDSCH* 78, 851–882. doi:10.1007/bf01829327

Cai, Y., Liu, D., Pan, Z., Yao, Y., and Li, C. (2015). Mineral Occurrence and its Impact on Fracture Generation in Selected Qinshui Basin Coals: An Experimental Perspective. *Int. J. Coal Geology.* 150-151, 35–50. doi:10.1016/j.coal.2015.08.006

Canfield, D. E. (1994). Factors Influencing Organic Carbon Preservation in marine Sediments. *Chem. Geology.* 114, 315–329. doi:10.1016/0009-2541(94)90061-2

Carroll, A. R., and Bohacs, K. M. (1999). Stratigraphic Classification of Ancient Lakes: Balancing Tectonic and Climatic Controls. *Geol* 27, 99–102. doi:10.1130/0091-7613(1999)027<0099:scoalb>2.3.co;2

Chen, C., Mu, C.-L., Zhou, K.-K., Liang, W., Ge, X.-Y., Wang, X.-P., et al. (2016). The Geochemical Characteristics and Factors Controlling the Organic Matter Accumulation of the Late Ordovician-Early Silurian Black Shale in the Upper Yangtze Basin, South China. *Mar. Pet. Geology.* 76, 159–175. doi:10.1016/j.marpetgeo.2016.04.022

Chen, F., Zhao, H., Lu, S., Ding, X., and Ju, Y. (2019a). The Effects of Composition, Laminar Structure and Burial Depth on Connected Pore Characteristics in a Shale Oil Reservoir, the Raoyang Sag of the Bohai Bay Basin, China. *Mar. Pet. Geology.* 101, 290–302. doi:10.1016/j.marpetgeo.2018.12.012

Chen, F., Zheng, Q., Lu, S., Ding, X., Ju, Y., and Zhao, H. (2019b). Classification of the Tight Oil Reservoir Storage Space in the Raoyang Sag of the Jizhong Depression in the Bohai Bay Basin, China. *Energy Sci. Eng.* 8, 74–88. doi:10.1002/ese3.510

Chermak, J. A., and Schreiber, M. E. (2014). Mineralogy and Trace Element Geochemistry of Gas Shales in the United States: Environmental Implications. *Int. J. Coal Geology.* 126, 32–44. doi:10.1016/j.coal.2013.12.005

Ding, X., Liu, G., Zha, M., Huang, Z., Gao, C., Lu, X., et al. (2015). Relationship between Total Organic Carbon Content and Sedimentation Rate in Ancient Lacustrine Sediments, a Case Study of Erlian basin, Northern China. *J. Geochemical Exploration* 149, 22–29. doi:10.1016/j.gexplo.2014.11.004

Dymond, J., Suess, E., and Lyle, M. (1992). Barium in Deep-Sea Sediment: A Geochemical Proxy for Paleoproductivity. *Paleoceanography* 7, 163–181. doi:10.1029/92pa00181

AUTHOR CONTRIBUTIONS

YW and ZS collected the samples. YQ, TJ, and YG prepared the samples. YW and ZS completed part of the experimental test. XyL, RZ, XdL, TJ, TZ, and MZ provided some data. YW and SL conceived the project, analyzed the samples, and wrote the manuscript. All authors reviewed the manuscript.

FUNDING

Fedo, C. M., Wayne Nesbitt, H., and Young, G. M. (1995). Unraveling the Effects of Potassium Metasomatism in Sedimentary Rocks and Paleosols, with Implications for Paleoweathering Conditions and Provenance. *Geol* 23, 921–924. doi:10.1130/0091-7613(1995)023<0921:uteopm>2.3.co;2

Feng, Q., Xu, S., Xing, X., Zhang, W., and Wang, S. (2020). Advances and Challenges in Shale Oil Development: A Critical Review. *Adv. Geo-energy Res.* 4, 406–418. doi:10.46690/ager.2020.04.06

Fu, J., Li, S., Xu, L., and Niu, X. (2018). Paleo-sedimentary Environmental Restoration and its Significance of Chang 7 Member of Triassic Yanchang Formation in Ordos Basin, NW China. *Pet. Exploration Dev.* 45, 998–1008. doi:10.1016/s1876-3804(18)30104-6

Hatch, J. R., and Leventhal, J. S. (1992). Relationship between Inferred Redox Potential of the Depositional Environment and Geochemistry of the Upper Pennsylvanian (Missourian) Stark Shale Member of the Dennis Limestone, Wabaunsee County, Kansas, U.S.A. *Chem. Geology.* 99, 65–82. doi:10.1016/0009-2541(92)90031-y

He, F., Gao, X., Zhao, X., Yang, D., Wang, Q., Fan, B., et al. (2017a). The Lower Part of the First Member of the Shahejie Formation (Es1x) as a Source Rock for Oil Found in Lixian Slope, Raoyang Sag, Bohai Bay Basin, Northern China. *ARAB J. GEOSCI.* 10, 101. doi:10.1007/s12517-017-2890-7

He, J., Ding, W., Jiang, Z., Jiu, K., Li, A., and Sun, Y. (2017b). Mineralogical and Chemical Distribution of the Es3L Oil Shale in the Jiyang Depression, Bohai Bay Basin (E China): Implications for Paleoenvironmental Reconstruction and Organic Matter Accumulation. *Mar. Pet. Geology.* 81, 196–219. doi:10.1016/j.marpetgeo.2017.01.007

He, T., Lu, S., Li, W., Tan, Z., and Zhang, X. (2018). Effect of Salinity on Source Rock Formation and its Control on the Oil Content in Shales in the Hetaoyuan Formation from the Biyang Depression, Nanxiang Basin, Central China. *Energy Fuels* 32, 6698–6707. doi:10.1021/acs.energyfuels.8b01075

Holditch, S. A. (2013). Unconventional Oil and Gas Resource Development - Let's Do it Right. *J. Unconventional Oil Gas Resour.* 1-2, 2–8. doi:10.1016/j.juogr.2013.05.001

Huerta-Diaz, M. A., and Morse, J. W. (1992). Pyritization of Trace Metals in Anoxic marine Sediments. *Geochimica et Cosmochimica Acta* 56, 2681–2702. doi:10.1016/0016-7037(92)90353-k

Jarvie, D. M. (2012). Shale Resource Systems for Oil and Gas: Part 2—Shale-Oil Resource Systems. *AAPG Mem.* 97, 89–119.

Jones, B., and Manning, D. A. C. (1994). Comparison of Geochemical Indices Used for the Interpretation of Palaeoredox Conditions in Ancient Mudstones. *Chem. Geology.* 111, 111–129. doi:10.1016/0009-2541(94)90085-x

Ju, Y., Sun, Y., Tan, J., Bu, H., Han, K., Li, X., et al. (2018). The Composition, Pore Structure Characterization and Deformation Mechanism of Coal-Bearing Shales from Tectonically Altered Coalfields in Eastern china. *Fuel* 234, 626–642. doi:10.1016/j.fuel.2018.06.116

Katz, B. J. (2003). Hydrocarbon Shows and Source Rocks in Scientific Ocean Drilling. *Int. J. Coal Geology.* 54, 139–154. doi:10.1016/s0166-5162(03)00028-4

Kelts, K., and Hsü, K. J. (1978). "Freshwater Carbonate Sedimentation," in *Lakes: Chemistry, Geology, Physics.* Editor A. Lerman (Berlin: Springer-Verlag), 295–323. doi:10.1007/978-1-4757-1152-3_9

Kidder, D. L., Erwin, D. H., Erwin, D., and Xa, H. (2001). Secular Distribution of Biogenic Silica through the Phanerozoic: Comparison of Silica-Replaced Fossils

and Bedded Cherts at the Series Level. *J. Geology.* 109, 509–522. doi:10.1086/320794

Kochenov, A. V., Korolev, K. G., Dubinchuk, V. T., and Medvedev, Y. L. (1977). Experimental Data on the Conditions of Precipitation of Uranium from Aqueous Solutions. *Geochem. Int.* 14, 82–87.

Larsen, C. P. S., and Macdonald, G. M. (1993). Lake Morphometry, Sediment Mixing and the Selection of Sites for fine Resolution Palaeoecological Studies. *Quat. Sci. Rev.* 12, 781–792. doi:10.1016/0277-3791(93)90017-g

Li, J., Lu, S., Cai, J., Zhang, P., Xue, H., and Zhao, X. (2018). Adsorbed and Free Oil in Lacustrine Nanoporous Shale: A Theoretical Model and a Case Study. *Energy Fuels* 32, 12247–12258. doi:10.1021/acs.energyfuels.8b02953

Li, J., Lu, S., Xie, L., Zhang, J., Xue, H., Zhang, P., et al. (2017a). Modeling of Hydrocarbon Adsorption on continental Oil Shale: A Case Study on N-Alkane. *Fuel* 206, 603–613. doi:10.1016/j.fuel.2017.06.017

Li, J., Lu, S., Xue, H., Xie, L., and Zhang, P. (2015b). Quantitative Evaluation on the Elastic Property of Oil-Bearing Mudstone/shale from a Chinese continental basin. *Energy Exploration & Exploitation* 33, 851–868. doi:10.1260/0144-5987.33.6.851

Li, J., Wang, W., Cao, Q., Shi, Y., Yan, X., and Tian, S. (2015a). Impact of Hydrocarbon Expulsion Efficiency of continental Shale upon Shale Oil Accumulations in Eastern China. *Mar. Pet. Geol.* 59, 467–479.

Li, J., Yang, Z., Wu, S., and Pan, S. (2021). Key Issues and Development Direction of Petroleum Geology Research of Source Rock Strata in China. *Adv. Geo-energy Res.* 5, 121–126. doi:10.46690/ager.2021.02.02

Li, T., Jiang, Z., Li, Z., Wang, P., Xu, C., Liu, G., et al. (2017b). Continental Shale Pore Structure Characteristics and Their Controlling Factors: A Case Study from the Lower Third Member of the Shahejie Formation, Zhanhua Sag, Eastern China. *J. Nat. Gas Sci. Eng.* 45, 670–692. doi:10.1016/j.jngse.2017.06.005

Li, Y., Wang, Z., Gan, Q., Niu, X., and Xu, W. (2019). Paleoenvironmental Conditions and Organic Matter Accumulation in Upper Paleozoic Organic-Rich Rocks in the East Margin of the Ordos basin, china. *Fuel* 252, 172–187. doi:10.1016/j.fuel.2019.04.095

Liang, C., Wu, J., Jiang, Z., Cao, Y., and Song, G. (2018). Sedimentary Environmental Controls on Petrology and Organic Matter Accumulation in the Upper Fourth Member of the Shahejie Formation (Paleogene, Dongying Depression, Bohai Bay Basin, China). *Int. J. Coal Geology.* 186, 1–13. doi:10.1016/j.coal.2017.11.016

Loucks, R. G., and Ruppel, S. C. (2007). Mississippian Barnett Shale: Lithofacies and Depositional Setting of a Deep-Water Shale-Gas Succession in the Fort Worth Basin, Texas. *Bulletin* 91, 579–601. doi:10.1306/11020606059

Lu, S., Huang, W., Chen, F., Li, J., Wang, M., Xue, H., et al. (2012). Classification and Evaluation Criteria of Shale Oil and Gas Resources: Discussion and Application. *Pet. Exploration Dev.* 39, 268–276. doi:10.1016/s1876-3804(12)60042-1

Lu, S., Xue, H., Wang, M., Xiao, D., Huang, W., Li, J., et al. (2016). Several Key Issues and Research Trends in Evaluation of Shale Oil. *ACTA PETROL. SIN* 37, 1309–1322.

Murphy, A. E., Sageman, B. B., Hollander, D. J., Lyons, T. W., and Brett, C. E. (2000). Black Shale Deposition and Faunal Overturn in the Devonian Appalachian Basin: Clastic Starvation, Seasonal Water-Column Mixing, and Efficient Biolimiting Nutrient Recycling. *Paleoceanography* 15, 280–291. doi:10.1029/1999pa000445

Nesbitt, H. W., and Young, G. M. (1982). Early Proterozoic Climates and Plate Motions Inferred from Major Element Chemistry of Lutites. *Nature* 299, 715–717. doi:10.1038/299715a0

Nesbitt, H. W., and Young, G. M. (1984). Prediction of Some Weathering Trends of Plutonic and Volcanic Rocks Based on Thermodynamic and Kinetic Considerations. *Geochimica et Cosmochimica Acta* 48, 1523–1534. doi:10.1016/0016-7037(84)90408-3

Pedersen, T. F., and Calvert, S. E. (1990). Anoxia vs. Productivity: what Controls the Formation of Organic-Carbon-Rich Sediments and Sedimentary Rocks? *AAPG Bull.* 74, 454–466. doi:10.1306/0C9B232B-1710-11D7-8645000102C1865D

Price, J. R., and Velbel, M. A. (2003). Chemical Weathering Indices Applied to Weathering Profiles Developed on Heterogeneous Felsic Metamorphic Parent Rocks. *Chem. Geology.* 202, 397–416. doi:10.1016/j.chemgeo.2002.11.001

Rimmer, S., Thompson, J., Goodnight, S., and Robl, T. (2004). Multiple Controls on the Preservation of Organic Matter in Devonian-Mississippian marine Black

Shales: Geochemical and Petrographic Evidence. *Palaeogeogr. Palaeoclimatol. Palaeoecol.* 215, 125–154. doi:10.1016/s0031-0182(04)00466-3

Roy, D. K., and Roser, B. P. (2013). Climatic Control on the Composition of Carboniferous-Permian Gondwana Sediments, Khalaspir basin, Bangladesh. *Gondwana Res.* 23, 1163–1171. doi:10.1016/j.gr.2012.07.006

Sarnthein, M., Pflaumann, U., and Wang, P. (1994). Preliminary Report on Sonne-95 Cruise "Monitor Monsoon" to the south China Sea. *Rep. Geol.—Palaeontol. Insitut Univ. Kiel* 68, 1–125.

Schieber, J. (1989). Facies and Origin of Shales from the Mid-proterozoic Newland Formation, Belt Basin, Montana, USA. *Sedimentology* 36, 203–219. doi:10.1111/j.1365-3091.1989.tb00603.x

Shekarifard, A., Daryabandeh, M., Rashidi, M., Hajian, M., and Röth, J. (2019). Petroleum Geochemical Properties of the Oil Shales from the Early Cretaceous Garau Formation, Qalikuh Locality, Zagros Mountains, Iran. *Int. J. Coal Geology.* 206, 1–18. doi:10.1016/j.coal.2019.03.005

Shen, J., Zhang, E., and Xia, W. (2001). Records from lake Sediments of the Qinghai lake to Mirror Climatic and Environmental Changes of the Past. *J. QUATERNARY SCI.* 21, 508–513.

Slatt, R. M., and Rodriguez, N. D. (2012). Comparative Sequence Stratigraphy and Organic Geochemistry of Gas Shales: Commonality or Coincidence? *J. Nat. Gas Sci. Eng.* 8, 68–84. doi:10.1016/j.jngse.2012.01.008

Taylor, S. R., and Mclennan, S. M. (1985). The Continental Crust: Its Composition and Evolution *J. Geol.* 94, 57–72.

Taylor, S. R. (1964). Abundance of Chemical Elements in the continental Crust: a New Table. *Geochimica et Cosmochimica Acta* 28, 1273–1285. doi:10.1016/0016-7037(64)90129-2

Tribovillard, N., Algeo, T. J., Lyons, T., and Riboulleau, A. (2006). Trace Metals as Paleoredox and Paleoproductivity Proxies: An Update. *Chem. Geology.* 232, 12–32. doi:10.1016/j.chemgeo.2006.02.012

Tribovillard, N. P., Caulet, J. P., Vergnaud-Grazzini, C., Moureau, N., and Tremblay, P. (1996). Geochemical Study of a Glacial–Interglacial Transition in the Upwelling Influenced Somalia Margin, N-W Indian Ocean: An Unexpected Lack of Organic Matter Accumulation. *Mar. Geol.* 133, 157–182

Wang, C., Wang, Q., Chen, G., He, L., Xu, Y., Chen, L., et al. (2017). Petrographic and Geochemical Characteristics of the Lacustrine Black Shales from the Upper Triassic Yanchang Formation of the Ordos Basin, China: Implications for the Organic Matter Accumulation. *Mar. Pet. Geology.* 86, 52–65. doi:10.1016/j.marpetgeo.2017.05.016

Wang, M., Wilkins, R. W. T., Song, G., Zhang, L., Xu, X., Li, Z., et al. (2015). Geochemical and Geological Characteristics of the Es3L Lacustrine Shale in the Bonan Sag, Bohai Bay Basin, China. *Int. J. Coal Geology.* 138, 16–29. doi:10.1016/j.coal.2014.12.007

Wang, Y., Guo, W., and Zhang, G. (1979). Application of Some Geolochemical Indicators in Determining of Sedimentary Environment of the Funing Group (Paleogene), Jinhu Depression, Jiangsu Province. *J. Tongji Univ:nat Sci. Ed.* 2, 51–60.

Wang, Y., and Wu, P. (1983). Geochemical Markers of Coastal Sediments in Jiangsu and Zhejiang Provinces. 11. *J. Tongji Univ:nat Sci. Ed.* 4, 79–87.

Wei, Y., Li, J., Du, Y., Lu, S., Li, W., Yang, J., et al. (2021b). Classification Evaluation of Gas Shales Based on High-Pressure Mercury Injection: A Case Study on Wufeng and Longmaxi Formations in Southeast Sichuan, China. *Energy Fuels* 35, 9382–9395. doi:10.1021/acs.energyfuels.1c00973

Wei, Y., Li, J., Lu, S., Song, Z., Zhao, R., Zhang, Y., et al. (2021a). Comprehensive Evaluation Method of Sweet Spot Zone in Lacustrine Shale Oil Reservoir and its Application: A Case Study of Shale Oil in Lower 1st Member of the Shahejie Formation in the Raoyang Sag. *J. CHINA U MIN TECHNO* 4, 1–12.

Wignall, P. B., and Twitchett, R. J. (1996). Oceanic Anoxia and the End Permian Mass Extinction. *Science* 272, 1155–1158. doi:10.1126/science.272.5265.1155

Wilson, M. J., Shaldybin, M. V., and Wilson, L. (2016). Clay Mineralogy and Unconventional Hydrocarbon Shale Reservoirs in the USA. I. Occurrence and Interpretation of Mixed-Layer R3 Ordered Illite/smectite. *Earth-Science Rev.* 158, 31–50. doi:10.1016/j.earscirev.2016.04.004

Xiong, G., Jiang, X., Cai, X., and Wu, H. (2010). The Characteristics of Trace Element and REE Geochemistry of the Cretaceous Mudrocks and Shales from Southern Tibet and its Analysis of Redox Condition. *Adv. Earth Sci.* 25, 730–745.

Xu, S., Zhai, S., Zhang, A., Zhang, X., and Zhang, H. (2007). Distribution and Environment Significance of Redox Sensitive Trace Elements of the Changjiang Estuary Hypoxia Zone and its Contiguous Sea Area. *Acta Sedimentologica Sinica* 2007, 759–766.

Ye, L., Zhu, X., Zhang, R., Xie, S., Gao, Y., Tang, H., et al. (2020). Sedimentary Environment of Shallow-Water delta and beach-bar of the Member 1 of Shahejie Formation in Lixian Slope of Raoyang Sag, Jizhong Depression. *J. Palaeogeog-chinese* 22, 587–600.

Yin, J., Wang, Q., Hao, F., Guo, L., and Zou, H. (2018). Palaeoenvironmental Reconstruction of Lacustrine Source Rocks in the Lower 1st Member of the Shahejie Formation in the Raoyang Sag and the Baxian Sag, Bohai Bay Basin, eastern China. *Palaeogeogr. Palaeoclimatol. Palaeoecol.* 495, 87–104.

Yin, J., Hao, F., Wang, Z., Chen, X., and Zou, H. (2020). Lacustrine Conditions Control on the Distribution of Organic-Rich Source Rocks: An Instance Analysis of the Lower 1st Member of the Shahejie Formation in the Raoyang Sag, Bohai Bay Basin. *J. Nat. Gas Sci. Eng.* 78, 103320. doi:10.1016/j.jngse.2020.103320

Zhang, S., Chen, S., Pu, X., Wang, Y., and Tan, M. (2016). Lithofacies Types and Reservoir Characteristics of fine-grained Sedimentary Rocks in Paleogene, Southern Bohai Fault-Depressed Lacustrine basin. *J. CHINA U MIN TECHNO* 45, 568–581.

Zhao, J., Jin, Z., Jin, Z., Geng, Y., Wen, X., and Yan, C. (2016). Applying Sedimentary Geochemical Proxies for Paleoenvironment Interpretation of Organic-Rich Shale Deposition in the Sichuan Basin, China. *Int. J. Coal Geology.* 163, 52–71. doi:10.1016/j.coal.2016.06.015

Zhou, L., Han, G., Ma, J., Chen, C., Yang, F., Zhang, L., et al. (2020). Geological Characteristics and Exploration Breakthrough of Shale Oil in Member 3 of Shahejie Formation of Qibei Subsag, Qikou Sag. *ACTA PETROL. SIN* 41, 903–917.

Zou, C. (2017). *Unconventional Petroleum Geology.* second ed. Elsevier, 275–321. doi:10.1016/b978-0-12-812234-1.00010-8Shale Oil and Gas

Zou, C., Yang, Z., Zhu, R., Wu, S., Fu, J., Lei, D., et al. (2019). Geologic Significance and Optimization Technique of Sweet Spots in Unconventional Shale Systems. *J. Asian Earth Sci.* 178, 3–19. doi:10.1016/j.jseaes.2018.07.005

Oil Retention in Shales: A Review of the Mechanism, Controls and Assessment

Yue Feng[1], Xianming Xiao[1]*, Enze Wang[2], Jian Sun[1] and Ping Gao[1]

[1]School of Energy Resources, China University of Geosciences (Beijing), Beijing, China, [2]School of Earth and Space Sciences, Peking University, Beijing, China

Shale oil is a vital alternative energy source for oil and gas and has recently received an extensive attention. Characterization of the shale oil content provides an important guiding significance for resource potential evaluation, sweet spot prediction, and development of shale oil. In this paper, the mechanism, evaluation and influencing factors of oil retention in shales are reviewed. Oil is retained in shales through adsorption and swelling of kerogen, adsorption onto minerals and storage in shale pores. Quite a few methods are developed for oil content evaluation, such as three-dimensional fluorescence quantitation, two-dimensional nuclear magnetic resonance (2D NMR), solvent extraction, pyrolysis, multiple extraction-multiple pyrolysis-multiple chromatography, logging calculation, statistical regression, pyrolysis simulation experiment, and mass balance calculation. However, the limitations of these methods represent a challenge in practical applications. On this basis, the influencing factors of the oil retention are summarized from the microscale to the macroscale. The oil retention capacity is comprehensively controlled by organic matter abundance, type and maturity, mineral composition and diagenesis, oil storage space, shale thickness, and preservation conditions. Finally, oil mobility evaluation methods are introduced, mainly including the multitemperature pyrolysis, 2D NMR, and adsorption-swelling experiment, and the influencing factors of movable shale oil are briefly discussed. The aim of this paper is to deepen the understanding of shale oil evaluation and provide a basis for further research.

Keywords: shale oil, retention mechanism, evaluation method, influencing factors, movable oil

INTRODUCTION

Compared to conventional petroleum systems, shale strata exhibit the characteristics of low porosity and ultralow permeability, and shale oil and gas have received insufficient attention for a long time due to the great difficulty of exploitation (Jarvie, 2012; Chen L. et al., 2019b; Soeder and Borglum, 2019). However, in recent years, with the progress of horizontal drilling, multistage hydraulic fracturing and other engineering techniques, shale oil and gas have become resources with an appreciable development potential (Wang et al., 2015a; Kumar et al., 2017; Zou et al., 2017; Zhao et al., 2018; Chen L. et al., 2019b; Ghanizadeh et al., 2020; Chen et al., 2021). The large-scale development of shale oil in the Permian Basin, Gulf Basin and Williston Basin has provided a new perspective for oil exploration and development (Bai et al., 2020). In 2019, the proven reserves in key shale oil exploration areas in the United States reached 232.40×10^8 bbl, shale oil production yielded 22.78×10^8 bbl (US Energy Information Administration, 2021), and shale oil exploitation is
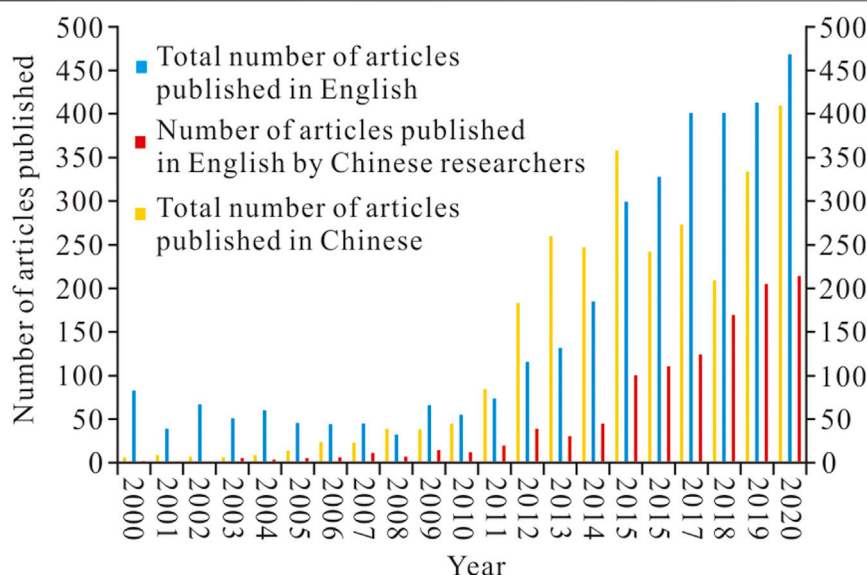
FIGURE 1 | Statistical histogram of literature on shale oil research. The data of English articles come from ScienceDirect, the blue column represents total data, the red column represents researchers from Chinese research institutions, and the data of Chinese articles (orange column) comes from CNKI. The search methods are all through title, abstract and keywords.

conducive to energy security and economic growth (Soeder and Borglum, 2020; Solarin, 2020). Russia, Argentina, Canada and other countries also possess a colossal shale oil resource potential, with recoverable shale oil resources of 746×10^8 bbl, 270×10^8 bbl, and 88×10^8 bbl, respectively (US Energy Information Administration, 2015). Inspired by the success of shale oil exploitation in the United States, these countries have launched shale oil exploration and development projects. The daily output of shale oil in Canada and Argentina is approximately 40×10^4 bbl/d and 5×10^4 bbl/d, respectively (Yang and Jin, 2019), the shale oil contained in the Mesozoic Bazhenov-Abalak Formations has been experimentally exploited in Russia, and the average horizontal well production reached 55.13 bbl/d in 2016 (Liang et al., 2019).

China contains abundant shale oil resources, the geological resources are estimated to be 27195×10^8 bbl (Yang et al., 2019), and the recoverable reserves of shale oil are 367.5×10^8 bbl (Zou et al., 2019b). With the deepening of petroleum exploration, shale oil has been found in the Ordos, Sichuan, Bohai Bay, Songliao, Junggar, Santanghu and other petroliferous basins, and notable exploration production has been documented from the Permian Lucaogou Formation in the Junggar Basin and Santanghu Basin, the Triassic Yanchang Formation in the Ordos Basin, the Cretaceous Qingshankou Formation in the Songliao Basin and the Paleogene Kongdian Formation in the Bohai Bay Basin (Wang et al., 2019a; Yang et al., 2019; Zhao W. Z. et al., 2020; Hu et al., 2020).

In recent years, an increasing number of studies on shales has been performed on their evolution of hydrocarbon generation, retention and expulsion (Shao et al., 2020; Song et al., 2021a; Sun J. et al., 2021; Hou et al., 2021b; Song et al., 2021b; Stockhausen et al., 2021), oil retention mechanism (Ritter, 2003; Tian et al., 2014; Li et al., 2016; Qiu et al., 2016; Han et al., 2017; Tian et al., 2017; Hou et al., 2020), influencing factors of shale oil enrichment

(Han et al., 2015; Zou et al., 2019a; Sun et al., 2019; Chen et al., 2020; Zhao X. Z. et al., 2020; Milliken et al., 2021) and geological evaluation (Lu et al., 2012; Kumar et al., 2017; Hu et al., 2018; Qian et al., 2018; Wang et al., 2019b; Yang and Zou, 2019; Li J. B. et al., 2020b; Wang B. Y. et al., 2021). Literatures on shale oil are increasing year by year, shale oil has become a hot topic, and Chinese scholars have carried out much shale oil research work and achieved outstanding contributions (**Figure 1**).

In contrast to conventional petroleum systems (oil migrates from source rocks to high-porosity reservoirs), shale oil is directly produced from shale strata and its associated fine-grained or organic-lean interlayers (Wang et al., 2019a). The more hydrocarbons are generated and retained, the higher the shale oil exploration potential (Wang E. Z. et al., 2021). Therefore, it is urgent to understand the oil and movable oil retained in shales. Although there have been many studies on shale oil, there is a lack of systematic investigation and summary on the mechanism of oil retention in shales and the influencing factors of oil-bearing properties.

Starting from the mechanism of shale oil retention, this paper compares various methods to quantify the total oil content in shales, summarizes its influencing factors from microcosmic to macroscopic perspectives, and then examines some available methods to estimate the movable oil in shales and discuss its influencing factors. It is anticipant that this paper could deepen the understanding of shale oil geology and provide a theoretical basis for shale oil resource evaluation and favorable exploration area prediction.

RETENTION MECHANISM OF SHALE OIL

Organic-rich shales were generally considered as source rocks in conventional petroleum systems. The relative research has

focused on the mechanism (Tissot and Welte, 1984; Huang, 1996; Kelemen et al., 2006; Zhang et al., 2006; Zhang et al., 2011; Wang et al., 2012; Liu et al., 2015; Spigolon et al., 2015; Nie et al., 2016; Burnham, 2017), characteristics, evaluation (Chen et al., 2004; Pang et al., 2005; Han et al., 2015; Hadad et al., 2017; Li J. et al., 2018; Wang et al., 2020), and influencing factors of petroleum generation and expulsion (Lewan and Stephanie, 2011; Eseme et al., 2012; Chen et al., 2014; Ma et al., 2016; Su et al., 2020; Stockhausen et al., 2021). With increasing attention given to shale oil exploration and development, research on the mechanism and influencing factors of oil retention in shales has gradually become another focus (Zou et al., 2019a; Zhao X. Z. et al., 2020; Shao et al., 2020; Hou et al., 2021b; Sun J. et al., 2021).
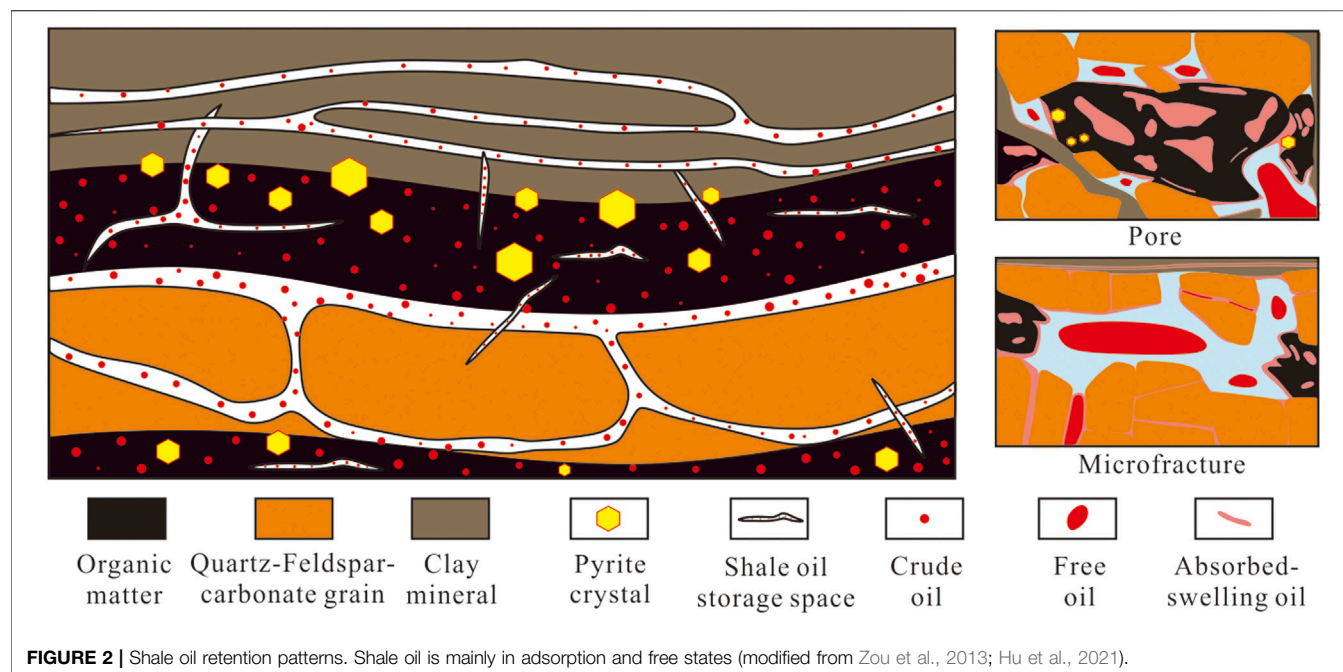
There may be a sizable capillary pressure causing oil to be drawn into and become stored in kerogen (Alfi et al., 2014). The dissolution of oil in kerogen causes kerogen volume expansion, which is similar to the swelling of organic polymers (Sandvik et al., 1992). The kerogen contained in an organic-rich shale exhibits a high cross-link density, and hydrogen bonds do not play a significant role in the intermolecular bonds of the network (Larsen and Shang, 1994; Larsen and Shang, 1997; Larsen et al., 2002; Ertas et al., 2006). The kerogen swelling behavior is controlled by the available free volume of kerogen and the size and shape of the adsorbed molecules (Stainforth, 2009). When hydrocarbon molecules are dissolved in kerogen, the interaction between the molecules and kerogen decreases, and the kerogen volume increases. Previous studies indicated that various solvents impose different swelling effects on kerogen (Larsen and Shang, 1997; Ritter, 2003). Therefore, as a multicomponent mixture, the swelling capacity of liquid petroleum depends on the contribution of each component (Pathak et al., 2017). Moreover, kerogen absorbs different components according to its preference, and oil components with similar values of Hildebrand parameter (δ) are more easily absorbed by kerogen (Ritter, 2003; Wei et al., 2012). The influence of kerogen swelling on the oil retention capacity of shales cannot be ignored. The swelling capacity of different types of kerogen varies. Tian et al. (2014) calculated that the swelling capacities of type I, II$_1$ and II$_2$ kerogens (Ro = 0.5%) are 141.7, 119.2, and 94.9 mg hydrocarbons/g TOC, respectively. Adsorption of kerogen is an important retention mode of oil (pepper, 1991), in which active kerogen provides the most active adsorption sites (Han et al., 2015). Kerogen in shale can absorb oil on the basis of satisfying the swelling effect of oil (Tian et al., 2014), with the increase of maturity, the specific surface area of kerogen gradually change and are capable of adsorbing hydrocarbons on their surface (Zhang S. J. et al., 2020). Tian et al. (2020) calculated that the adsorbed oil and the specific surface area of kerogen increased first and then decreased, the adsorbed oil content reaches its peak at Ro = 1.0%.

The shale is dominated by nanosized pore system, therefore, the interaction of fluids and pores is prominent, in other words, the influence of the adsorption of mineral particles on shale oil retention is of importance (Liu and Zhang, 2019; Wu et al., 2021). Generally, the adsorption between oil and mineral surfaces is attributed to physical interactions (such as van der Waals forces, and hydrogen bonds) or chemical interactions (Yusupova et al., 2002; Dudášová et al., 2008; Cui and Cheng, 2017; Cao et al.,

2020). According to hydrocarbon-solution adsorption tests, it is believed that the asphaltene adsorption capacity of feldspar (7.0 mg/g) is higher than that of quartz (4.5 mg/g), which is related to differences in the crystal structure and chemical composition between quartz and feldspar (Ribeiro et al., 2009). The maximum adsorption capacity of calcite for extracted shale oil-asphaltene reaches only 2.16 mg/g (Mohammadi and Sedighi, 2013), and the adsorption capacity is relatively low, which may be related to the fact that calcite (a neutral mineral) generally exhibits no electric charge (Zhang et al., 2015). Among inorganic mineral components, clay minerals provide the main adsorption surfaces for shale oil (Li et al., 2016; Ning et al., 2020).Due to the difference in cation substitution mechanism, charge and layer charge among clay minerals, the adsorption capacity of various clay minerals or even different surfaces within the same clay minerals for oil is different: 1) Al^{3+} in the montmorillonite crystal layer is replaced by divalent cations to generate a negative charge, which can attract Ca^{2+} or Na$^+$, while Si^{4+} ions in the illite crystal layer are located on the lattice surface, and the negative charge due to Al^{3+} substitution generates a greater attraction force to K$^+$ so that illite can adsorb more negative organic macromolecules (Zhang et al., 2015); 2) kaolinite with an octahedral-tetrahedral structure, which is different from that of other clay minerals, contains oil-wet silicate surfaces and water-wet alumina surfaces, and the adsorption capacity of oil components per unit area is 2.47 and 1.44 mg/m^2, respectively (Tian et al., 2018). Moreover, different types of clay minerals have various specific surface areas, which may also affect adsorbed oil content (Zhu et al., 2012). However, Li et al. (2016) obtained the oil adsorption capacity of clay minerals (18 mg/g), quartz (3 mg/g) and carbonate minerals (1.8 mg/g) based on oil adsorption experiments of shale minerals. Compared to the adsorption capacity of kerogen, the oil adsorption capacity of these minerals may not be dominant in organic-rich shales. Zhao et al. (2019) reported that only 5–10% of hydrocarbons are adsorbed onto the surface of mineral particles. Considering the water-bearing capacity of shale reservoirs, the oil adsorption capacity in the water-bearing state is mainly controlled by kerogen (the remaining oil per unit of TOC is approximately 179 mg/g), which may be related to the hydrophilicity of mineral particles in shales (Wang et al., 2019b).

Nano- and micron-sized pores and microfractures are widely developed in shale oil reservoirs, constituting the reservoir space of shale oil (Zou et al., 2013; Su et al., 2018; Jin et al., 2021). The occurrence states of shale oil in pores of different scales are distinct. Free oil occurs in microfractures (Cui and Cheng, 2017; Song et al., 2020) and large pores (for example, the threshold of free oil enrichment is 30 nm, based on Liu H. M. et al. (2019), such as intergranular, intergranular and dissolution pores. The oil contained in smaller nanoscale pores coexists in the free and adsorption states (Wang et al., 2015a). With decreasing pore size, the oil in pores increasingly exhibits the adsorption state (for example, the threshold is 5 nm, based on Wang et al. (2019b)).

For a sum up from above discussion, the swelling of kerogen, adsorption of kerogen and mineral particles, and pore and fracture storage are the critical reasons for shale oil retention (**Figure 2**).

FIGURE 2 | Shale oil retention patterns. Shale oil is mainly in adsorption and free states (modified from Zou et al., 2013; Hu et al., 2021).

EVALUATION OF RETAINED OIL IN SHALES

Oil content in shales is one of the key indexes to evaluate shale oil enrichment. The characterization and evaluation of the shale oil content involve various methods, including the three-dimensional quantitative fluorescence method, two-dimensional nuclear magnetic resonance (2D NMR) method, extraction method, pyrolysis method, multiple extraction-multiple pyrolysis-multiple chromatography method, logging calculation method, statistical regression method, pyrolysis simulation experiment method and material balance method. These methods exhibit distinct characteristics (**Table 1**). The three methods of the pyrolysis, thermal simulation experiment and material balance will be futher presented, which are commonly adopted to evaluate the shale oil conten based on geochemical data.

Pyrolysis Method

The free hydrocarbon content (S_1) based on Rock-Eval pyrolysis is considered to determine the oil content in shales quickly. However, light hydrocarbon losses inevitably occur in the sampling and experimental processes (Jarvie, 2012; Jarvie, 2014). The heavy components present in kerogen, micropores and disconnected pore systems in the adsorption state can only be released at higher temperatures or when the pyrolysis temperature of organic matter is reached (Jarvie, 2012; Li M. W. et al., 2020). Zink et al. (2016) proposed that the amount of extractable S_2 component is 2.2–3.6 times the measured S_1 amount, and if this part of high-carbon number alkanes and aromatic hydrocarbons is ignored, the shale retained oil content is much underestimated. Jarvie (2012) pointed out that the oil content can be obtained according to S_1 and S_2 before and after extraction as presented in **Eq. 1**. It formed tha basis to calculate the shale oil content.

Han et al. (2015) found that the extracted S_1 (S_{1x}) component mainly comprised the extraction solvent, which suggested that the amount of shale oil should be the sum of the S_1 before and the S_2 difference before and after extraction. However, Li M. W. et al. (2018) reported that S_{1x} might be isolated hydrocarbons in nanopores, which could be regarded as part of the adsorbed hydrocarbons. In order to describe the oil content of shales more accurately, some improved pyrolysis methods have been applied (Jiang Q. G. et al., 2016; Abrams et al., 2017; Romero-Sarmiento, 2019; Gentzis et al., 2021). These oil content evaluation methods do not consider the light hydrocarbon loss attributed to sample collection and preservation and experimental operation. Cooles et al. (1986) considered that light hydrocarbons (C_{14-}) accounted for 35% of the total oil, but most of these light hydrocarbons were lost. Jiang C. Q. et al. (2016) analyzed the light hydrocarbon loss of samples *via* Rock-Eval analysis and thermal desorption-gas chromatography-mass spectrometry (TD-GC-MS)/flame ionization detection (FID) and reported that the S_1 loss for organic-rich shales could reach 15% after 360 h of open storage. Chen J. Q. et al. (2018) found that the loss rate of hydrocarbon evaporation ranged from 11 to 89% when analyzing the shale of the Middle Permian Lucaogou Formation in the Jimusar Sag. Therefore, it is necessary to correct the light hydrocarbon loss for the accurate evaluation of the shale oil content (Beti et al., 2020). Based on light hydrocarbon loss correction, Abrams et al. (2017) added a S_1 loss term (**Eq. 2**) to the original oil content equation.

With increasing maturity, the light components in shales that are easily lost in the process of core preservation and experimental analysis, and the light hydrocarbon loss exhibits an increasing dynamic trend (Zhu et al., 2015; Li J. B. et al., 2020b). Based on the above reasons, according to the difference in pyrolytic hydrocarbons between sealed freezing treatment and conventional preservation treatment (Zhu et al., 2015), newly proposed oil formation volume factor (FVF) (Chen Z. H.
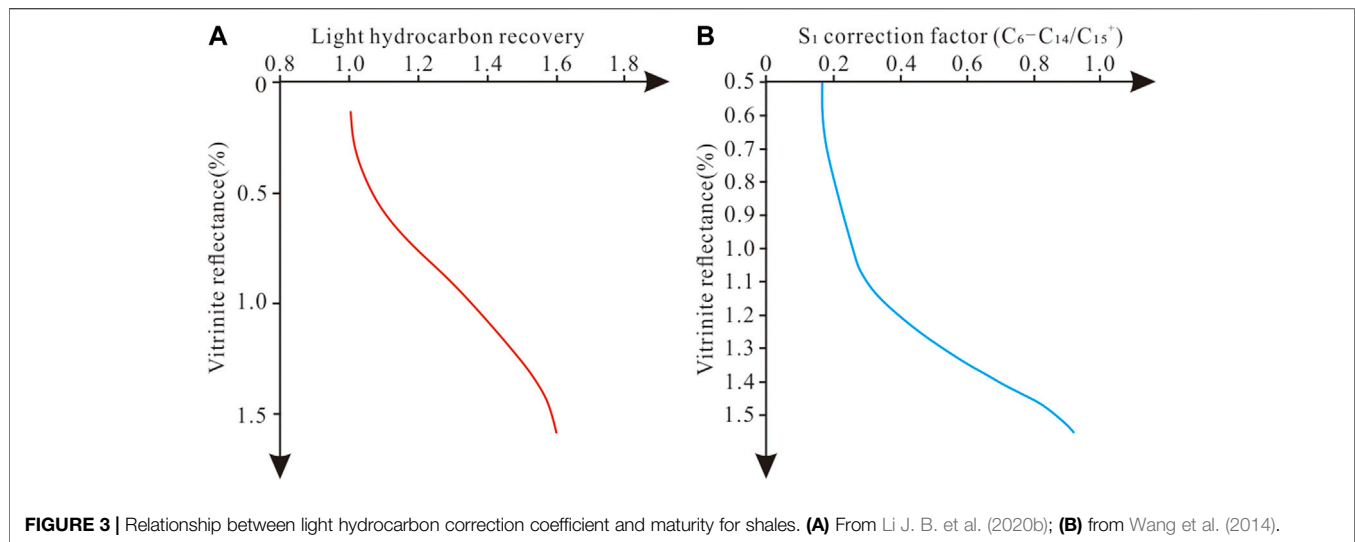
TABLE 1 | An overview of determination of retained oil content in shales.

Method	Operation step		Parameter	Characteristics	Reference
Three-dimensional quantitative fluorescence method	Shale particles with a mass of M (g) are placed in a solvent with a volume of V (L). The immersion solution is collected and detected *via* quantitative three-dimensional fluorescence. The fluorescence oil concentration C (mg/L) can be converted into the fluorescence oil content C_o (mg/g)		$C_o = C \times V_{solvent}/M$	The method is fast and efficient, but the experimental results are affected by the particle size, extraction time, ultrasound assistance and calibration curve	Liu B. et al. (2019); Qian et al. (2020)
Two-dimensional nuclear magnetic resonance (2D NMR) method	2D NMR experiments are carried out on shale samples		The total amount of ^1H compounds multiplied by the percentage of the adsorbed oil and free oil signals in the total signal	The oil and free oil contents can be determined, but the boundaries of the different fluid distribution intervals are difficult to define	Bai et al. (2019); Li J. B. et al. (2020a)
Extraction method	Chloroform extraction method	An amount M (g) of shale is heated and extracted with chloroform, and the extract is concentrated. The content of chloroform bitumen A is calculated according to the weight M_1 (g) of the weighing bottle and the weight M_2 (g) of chloroform asphalt. Correction coefficient K_a is calculated according to the light hydrocarbon (C_6-C_{14}) content in chloroform bitumen A (K_1, %), the light hydrocarbon content in alkanes of crude oil (K_2, %), and the alkane content in chloroform bitumen A (sat, %)	Total oil = chloroform bitumen A $\times K_a$ = chloroform bitumen A $\times (1 + K_1)$ = chloroform bitumen A $\times [1 + (sat \times K_2)]$	The experimental results are easy to obtain, but there is a severe loss of light hydrocarbons (C_6-C_{14}) in the process of sample preparation and solvent evaporation. The correct result of C_{14-} light hydrocarbons depends on the matching between the components of crude oil and chloroform bitumen A and the thermal maturity of the samples	Zhu et al. (2015)
	Sequential extraction method	Shale samples are extracted with different polar solvent systems, including weak polar solvents, strong polar solvents or highly polar solvents	Total oil = cumulative amount of solvent extraction (mg/g rock)	The content of shale oil in different occurrence states can be determined. Sequential extraction does not completely separate soluble organic matter with different occurrence states, and the change in solvent and extraction mode may cause a change in experimental data	Qian et al. (2017); Zhang H. et al. (2020)
Pyrolysis method	Rock-Eval pyrolysis method	The amount of thermovaporized free hydrocarbons (S_1, mg hydrocarbons/g rock) can be obtained by heating shale samples in an open pyrolysis system	Total oil = S_1	The experimental results are easy to obtain, but there are light and heavy hydrocarbon losses	Behar et al. (2001); Lu et al. (2012)
	Single routine Rock-Eval experiment	The temperature threshold (T_{OK}) is determined by the cumulative amplitude of shale and solvent-extracted shale, and cracking hydrocarbons (S_{2K}) and heavy hydrocarbons (S_{2oil}) are then rapidly separated	Total oil = $S_1 + S_{2oil}$	Conventional pyrolysis data sets can be employed to directly calculate the total oil production based on the temperature threshold, but the light hydrocarbon loss should be considered	Li J. B. et al. (2019)
	Multistep on-column thermal extraction method	Shale samples can be analyzed in a multi-step thermal extraction system to obtain a high-resolution thermal extraction curve, and the thermal peak areas can be analyzed to evaluate the oil content	Total oil = total multistep thermal extraction system (MiSTE) $\sum$(P200°C + P250°C + P300°C + P350°C)	The experimental method is inexpensive, fast and efficient, and it can measure the oil in place. However, the evaluation results should be corrected for light hydrocarbons	Abrams et al. (2017)

TABLE 1 | (Continued) An overview of determination of retained oil content in shales.

Method	Operation step		Parameter	Characteristics	Reference
	Multistep pyrolysis method	The component contents in the different temperature ranges are obtained via programmed step-by-step pyrolysis experiment	Total oil = pyrolytic hydrocarbon peaks of nonkerogen cracking	The method is easy to operate, but it is difficult to determine the heat release temperature limit of hydrocarbons in different occurrence states in shale, and it is necessary to recover the loss of light hydrocarbons	Jiang Q. G. et al. (2016); Romero-Sarmiento (2019); Ghanizadeh et al. (2020); Gentzis et al. (2021)
Multiple extraction-multiple pyrolysis-multiple chromatographic analysis method	The total oil in shale is calculated through low-temperature immersion of cores, multiple extractions (dichloromethane and chloroform solutions), multiple pyrolysis steps, and multiple chromatographic analyses		Total oil = WO1 (amount of C_5–C_7) + WO2 (amount of C_{6+} and weight of the residual evaporation solution) + WO3 (amount of dichloromethane extraction) + WO4 (amount of chloroform extraction) + WO5 (hydrocarbons retained in shale after chloroform extraction)	The operation steps and process of this method are complex, but the loss of hydrocarbons is fully considered in this experimental method, and the analysis result is reliable	Hou et al. (2021a)
Logging calculation method	Based on logging data of the resistivity and porosity, a variable-coefficient ΔlogR model is applied to calculate the oil content		$S_1 = a \times \Delta log R_{S1} + b$ Chloroform bitumen A = c × $\Delta log R_A + d$ (a, b, c and d are fitting coefficients of the equation)	The data for this method are easy to obtain, and the model is easy to apply and can obtain continuous oil content analysis data. However, the influence of the data quality on logging model predictions cannot be ignored. The calculation results must be corrected for light hydrocarbons and/or heavy hydrocarbons	Liu et al. (2014); Li J. B. et al. (2020b)
	With the use of NMR logging and the factor analysis method, oil saturation index (OSI) and S1 are estimated by using the bin porosity (33 ≤ $T_{2cutoff} < 80$) corresponding to hydrocarbon production		$S_{1NMR} = (120 \times bp6 + 100) \times$ TOC/100	Continuous oil content analysis data can be obtained, but the signals of the different fluids overlap, and the prediction results may contain errors	Piedrahita and Roberto (2017)
Statistical regression method	A regression statistical model can be established according to the relationship between oil retention and TOC, mineral composition and other control factors		$S_1^{cal} = 0.320 \times$ TOC + 0.062 × quartz −0.007 (for the second interval)	There may exist collinearity among the control factors, which leads to distortion of the regression model	Han et al. (2015)
Thermal simulation experiment method	Shale samples are tested via thermal simulations		The oil content in shale samples is determined corresponding to different temperature points	The experimental results are intuitive, but the experimental conditions (whether water occurs, open vs. closed vs. semiopen systems, and sample conditions) exert an impact on the results	Peng et al. (2018); Shao et al. (2020)
Material balance method	The principle of carbon mass (component) conservation is applied to determine the retained oil content		Total oil = hydrocarbon generation quantity-hydrocarbon expulsion quantity	The method is easy to calculate, but its accuracy depends on the satisfaction of certain assumptions and the quality of data	Pang et al. (2005); Wang E. Z. et al. (2021)

FIGURE 3 | Relationship between light hydrocarbon correction coefficient and maturity for shales. **(A)** From Li J. B. et al. (2020b); **(B)** from Wang et al. (2014).

et al., 2019; Li M. W. et al., 2020), and hydrocarbon generation kinetics calculations (Wang et al., 2014) consider the recovery method of S_{1loss} at different maturities, the recovery coefficient of light hydrocarbon loss becomes larger as the maturity increases (**Figure 3**), which means the light hydrocarbon calibration is necessary in the mature and high-mature stage of shale.

$$\text{Total oil} = (S_{1\,\text{whole rock}} - S_{1\,\text{extracted rock}}) \\ + (S_{2\,\text{whole rock}} - S_{2\,\text{extracted rock}}) \tag{1}$$

$$\text{Total oil} = (S_{1\,\text{whole rock}} - S_{1\,\text{extracted rock}}) \\ + (S_{2\,\text{whole rock}} - S_{2\,\text{extracted rock}}) + S_{1\,\text{loss}} \tag{2}$$

Material Balance Method

The mass of organic matter in shales that can be converted into petroleum should be constant during thermal evolution if there is not material exchange with the external environment. According to this idea, Pang et al. (2005) proposed the hydrocarbon generation potential method of rock pyrolysis, which is a statistical method based on the principle of mass balance, to calculate the hydrocarbon generation, retention and expulsion of shales. For a specific shale sample, its hydrocarbon generation potential index ($Q_g = 100 \times (S_1+S_2)/TOC$) should remain unchanged. The only reason for its change is hydrocarbon expulsion. Hence, the difference between hydrocarbon generation and expulsion is the amount of retained hydrocarbons in the shale (**Figure 4A**). However, this method does not consider the data error caused by light hydrocarbon evaporation (Chen J. Q. et al., 2018), and does not provide a clear limit on the recovery coefficient of the hydrocarbon generation potential.

Chen and Jiang (2016) statistically fitted an empirical model of the hydrocarbon index (HI) and T_{max} based on the measured data of shale samples (**Eq. 3**), converted this empirical relationship into the hydrocarbon conversion rate (Tr) (**Eq. 4**) and further clarified the hydrocarbon expulsion efficiency (**Eq. 5**). On this basis, Wang et al. (2020) thought that S_1 could be regarded as being wholly derived from S_2 *via* transformation, so the original hydrogen index (H_I^0) was selected to define the maximum value of the hydrocarbon generation capacity

of the different types of kerogen, and the hydrocarbon generation, retention and expulsion processes of shales were characterized, then the shale oil resource potential can be evaluated by the hydrocarbon retention potential (Q_r) (mg HC/g TOC) (**Figure 4B**).

In the above previous methods, the determination of the hydrocarbon expulsion threshold depends on the inflection point of the hydrocarbon generation potential index, and the determination of the hydrocarbon expulsion threshold may not be accurate. Li C. R. et al. (2020) adopted a hydrocarbon generation statistical model to simulate the changes in the hydrogen index and Q_g during the evolution of shales and proposed a quantifiable hydrocarbon expulsion efficiency (Er) (**Eq. 6**), and shale oil resources can be calculated by the difference between Tr and Er, which was applied to the Qingshankou Formation in the Songliao Basin and achieved a reasonable result (**Figure 4C**).

$$H_I = H_I^0 \left[1 - exp\left\{ -\left(\frac{T_{max}}{\beta}\right)^{\theta} \right\} \right] + c \tag{3}$$

$$T_r = \frac{(1000/\alpha) \times (H_I^0 - H_I)}{H_I^0 \left((1000/\alpha) - H_I \right)} \tag{4}$$

$$E_r = 1 - \frac{s_1 \times (1 - T_r)}{s_2 T_r} \tag{5}$$

$$E_r = \frac{(1000/\alpha) \times (Q_{go} - Q_g)}{Q_{go} \times \left((1000/\alpha) - Q_g \right)} \tag{6}$$

where β and θ are variables related to the type of kerogen, c is the error correction factor, α is the weight fraction of carbon relative to the generated hydrocarbons, its average value is considered to be 83.3%, Q_{go}(GPI$_o$) represents the original hydrocarbon generation potential index.

Thermal Simulation Method

Because it is challenging to collect shale sample from immature to overmature stages, the hydrocarbon generation, retention and expulsion evolution profiles of shales can be established through thermal simulation experiments (Ma et al., 2018). Thermal

FIGURE 4 | Hydrocarbon generation potential model of rock pyrolysis. **(A)** Modified from Pang et al., 2005; **(B)** modified from Wang et al., 2020; **(C)** modified from Li C. R. et al., 2020.
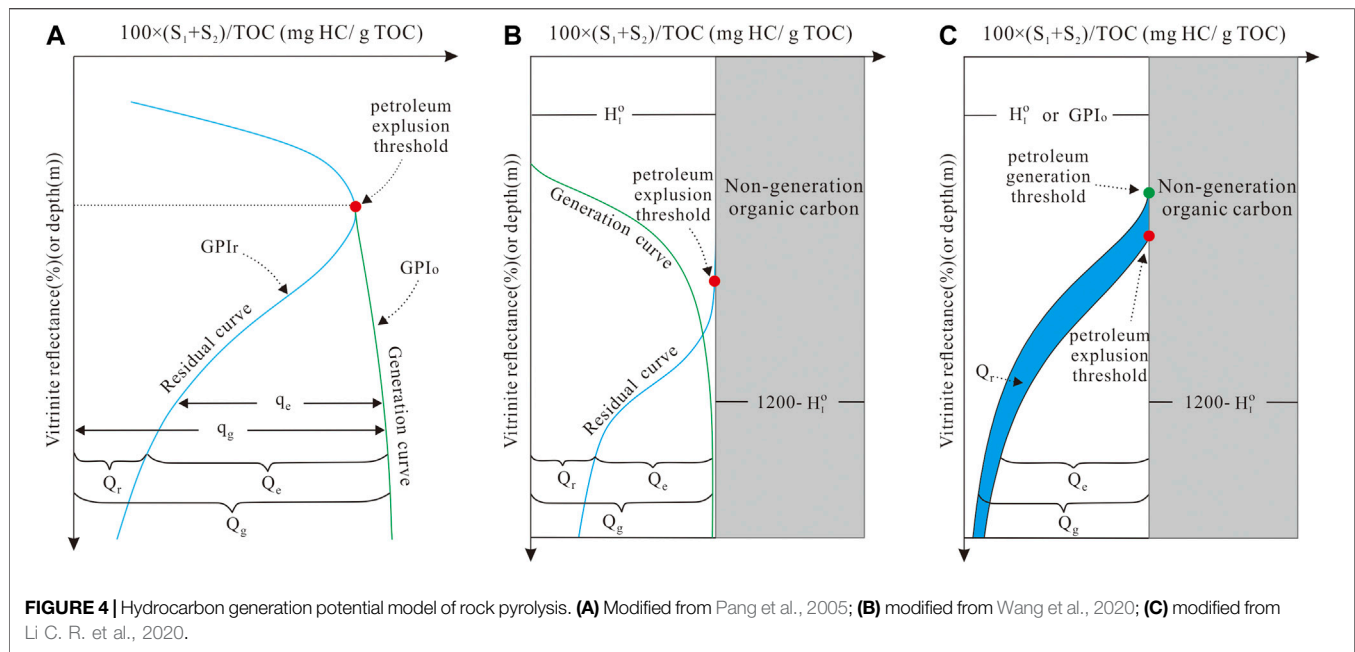
simulation systems can be divided into open, closed and semiclosed systems, and they produce different results (Ghanizadeh et al., 2020). Under geological conditions, petroleum generation, retention and expulsion follow a kinetic evolution process. In a semiclosed system, thermal simulation products are allowed to be discharged during generation, which may be more suitable for uses of geological evaluation (Li J. et al., 2018; Ma et al., 2018; Zhang D. W. et al., 2020).

Thermal simulation results cannot be directly applied to the geological evaluation and prediction. According to simulation experimental data on hydrocarbon generation in low-maturity shales, kinetic parameters such as activation energy (Ea) and frequency factor (A) can be obtained, and the hydrocarbon generation, retention and expulsion characteristics of shales under geological conditions can be obtained *via* extrapolation of these parameters. A series of kinetic models of hydrocarbon generation, such as the overall reaction model, series reaction model and parallel reaction model, have been proposed. Wang et al. (2011) compared different kinetic models and considered that the discretely distributed parallel first-order kinetic model might be the most suitable model to describe the hydrocarbon generation process. At present, it is widely accepted that the thermal decomposition process of kerogen is similar to a series of independent parallel first-order chemical reactions (Wang et al., 2011; Chen et al., 2017). Although Stainforth (2009) suggested that the assumption of independent first-order reactions may be too simplistic, the prediction of a hydrocarbon generation kinetics model controlled by first-order chemical kinetics seems to be supported by actual maturity measurements (Peters et al., 2018). The vitrinite reflectance corresponding to different temperatures can be calculated with Easy%Ro (Sweeney and Burnham, 1990), PresRo™ (Carr, 1999), Pa%Ro (Xiao et al., 2005), Basin%Ro (Nielsen et al., 2017) and Easy%RoDL (Peters et al., 2018) at various heating temperature and duration, combined with thermal simulation results, to determine the oil generation, retention and expulsion characteristics of shales at different maturation stages.

INFLUENCING FACTORS OF OIL RETENTION IN SHALES

Shale oil is the oil remaining in shales during oil generation and expulsion, which is influenced by various factors. To explore the influencing factors more clearly, we examines the influencing factors of oil retention from the microscale to the macroscale. Microscopically, the oil retention in TOC per unit weight is chosen as the subject, and the influence of the organic matter type and thermal maturity on the shale oil content is investigated. Semimicroscopically, the research object is the oil retention in unit rock weight and micron-to-centimeter-scale deposition structure, and the effects of organic matter abundance, pore development and rock mineral composition on oil retention are compared. Macroscopically, the shale section is selected as the research object, and the influence of the shale thickness and preservation conditions on shale oil retention and resource evaluation is clarified.

Restriction of Organic Matter Properties on Oil Retention

Shales with oil potential mainly contains sapropelic organic matter, with a kerogen type of I or II, which exhibit a high effective organic carbon ratio and good oil generation potential (Chen and Jiang, 2015; Ma et al., 2018; Li M. W. et al., 2019b; Zou et al., 2019b; Zhao W. Z. et al., 2021). The kerogen type in shales exerts apparent control over their oil-bearing properties. Generally, type I kerogen retained more oil than type II kerogen (Bai et al., 2017; He et al., 2019). Sun J. et al. (2021), also vertified that the retained content of shales exhibits growing trend with the increase of their original HI within the "oil window" stage through thermal simulation experiments. However, some
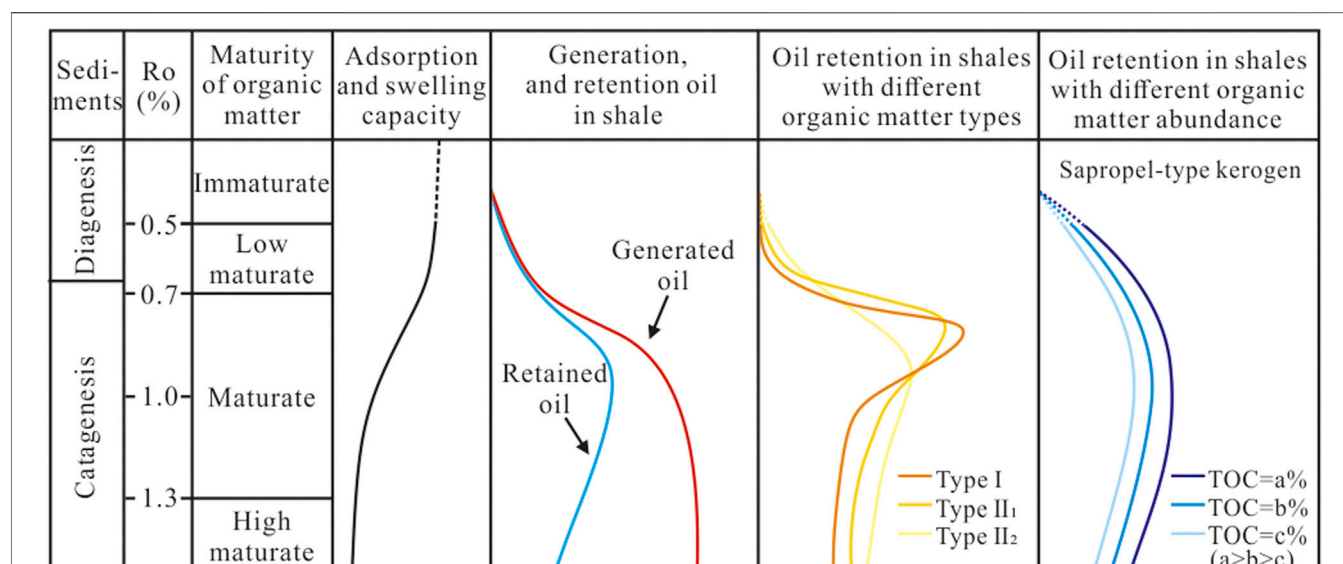
FIGURE 5 | Retention pattern of shale oil under different influence factors (modified from Tian et al., 2014; Li J. et al., 2015; Li J. et al., 2018; Yang and Zou, 2019; Zhao X. Z. et al., 2020).
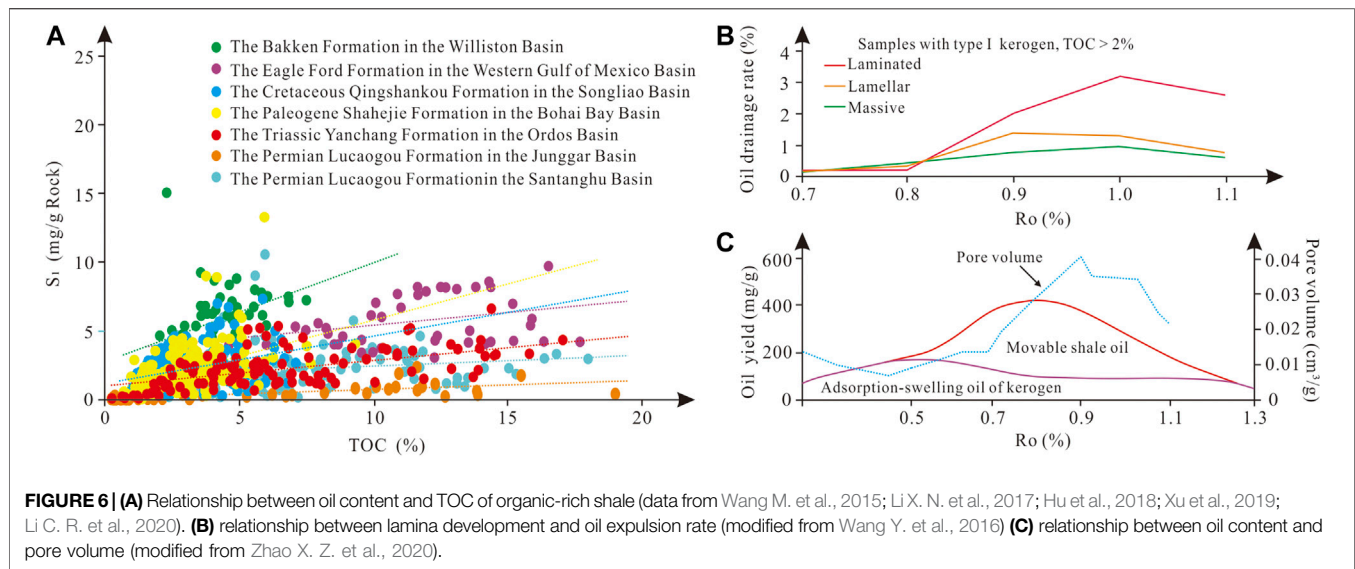
geological observations indicate that shales containing type II kerogen may contain more considerable shale oil resources compared to shales with type I kerogen (Li J. J. et al., 2015; Hu et al., 2018). This may occur because the better the type of organic matter is, the greater the hydrocarbon expulsion amount per unit of organic carbon (Chen et al., 2014; Huang et al., 2017; Ma et al., 2018; Sun J. et al., 2021), resulting in a lower retainded oil content. Tian et al. (2014) analyzed shales in the Qingshankou Formation in the northern Songliao Basin and reported that for Ro > 0.9%, the oil content per unit mass of TOC of type II kerogen is higher than that of type I kerogen, which seems to be related to the faster reduction in volume of type I kerogen per unit mass of TOC (**Figure 5**). In addition, a shale containing type II kerogen exhibits a high oxygen content, which facilitates the formation of organic acids, and the hydrocarbon expulsion efficiency is lower than that of a shale containing type I kerogen, thereby its shale oil content is higher (Li J. J. et al., 2015).

The oil content in shales is relatively low at the immature stage. Nevertheless, if the thermal maturity is too high, this leads to the so-called secondary cracking of oil into gas in shales, and oil is not effectively retained (Zhang P. Y. et al., 2021). Exploration practices of shale oil revealed that the Ro value in the shale oil palys broadly ranges from 0.5 to 1.6% (Cardott, 2012; Zhao W. Z. et al., 2020). Maturity affects the shale oil content based on the amount of oil generated and affects the hydrocarbon expulsion ability according to the composition of evolution products. With increasing thermal maturation, the density and viscosity of oil generally decrease, which encourages the flow and expulsion of oil (Wang et al., 2019b; Zhao W. Z. et al, 2021). The adsorption-swelling oil amount per unit of organic carbon is negatively correlated with increasing thermal maturity (Zhao X. Z. et al., 2021). When the oil storage space remains fixed, this inevitably

leads to the expulsion of oil. Moreover, Panahi et al. (2019) proposed that the formation, opening of hydrocarbon expulsion microfractures and fluid expulsion rate are related to thermal maturity levels based on experiments. Therefore, a moderate degree of thermal evolution is conducive to shale oil enrichment. Yang and Zou (2019) pointed out that the amount of retained oil in shales with Ro values between 0.9 and 1.3% reaches a maximum (**Figure 5**).

Control of TOC Content, Oil Storage Space and Mineral Composition on Oil Retention

Organic matter enrichment constitutes the basis of shale oil accumulation, and shales with a certain shale oil potential often exhibit a higher TOC content (Zou et al., 2013). When the type and maturity of organic matter are fixed, the TOC content determines the oil generation capacity of shales (Ma et al., 2018). Although a high TOC content suggests an increase in hydrocarbon expulsion efficiency (Sun J. et al., 2021), analysis data from shale oil plays and thermal simulation revealed that the TOC content is usually positively correlated with the shale oil content (**Figure 5**) (Li J. et al., 2015; Han et al., 2015). Hou et al. (2020) noted that shales with a high TOC content still yield a notable advantage in oil retention due to their high oil generation efficiency. An increase in TOC content also increases the content of adsorbed oil (Cao et al., 2017; Wang et al., 2019b). In addition, studies have demonstrated that a higher TOC content indicates that more organic acids are produced during the hydrocarbon generation process, which facilitates the development of dissolution pores and recrystallized intergranular pores (Liang et al., 2017; Hu et al., 2019) and provides essential oil storage spaces (Zhang et al., 2016). Therefore, an increase in organic matter abundance is conducive to shale oil enrichment. As shown

FIGURE 6 | (A) Relationship between oil content and TOC of organic-rich shale (data from Wang M. et al., 2015; Li X. N. et al., 2017; Hu et al., 2018; Xu et al., 2019; Li C. R. et al., 2020). **(B)** relationship between lamina development and oil expulsion rate (modified from Wang Y. et al., 2016) **(C)** relationship between oil content and pore volume (modified from Zhao X. Z. et al., 2020).

in **Figure 6A**, the oil content per unit mass of rock becomes larger as the organic matter abundance increases.

Shales comprise terrigenous detritus, clay minerals, carbonate, pyrite and other inorganic minerals and organic matter (Chen L. et al., 2019a). Inorganic components (clay minerals, pyrite, etc.) affect the shale oil content through oil generation and retention capacity. Clay minerals can influence the hydrocarbon generation process and mechanism through a carbon ion mechanism and/or participate in the desorption and hydrogenation/decarboxylation of solid acids (Du et al., 2021; Song et al., 2021a). Transition group elements such as Fe, Co and V in shales impose a catalytic effect on organic matter hydrocarbon generation, which can generate more oil and gas in organic-rich shales at the early burial stage (Xi et al., 2020). Studies have shown that local cementation can reduce the discharge of shale oil *via* compaction inhibition, and carbonate minerals can react with organic acids to increase oil storage spaces (Hu et al., 2019; Milliken et al., 2021). Although the wettability of shale surfaces exhibits mixed characteristics (Gao et al., 2019), clay minerals still provide considerable oil adsorption surfaces, and the increase in the clay mineral content is beneficial to the increase in oil content to a certain extent (Li Z., 2020). Furthermore, laminae are widely developed sedimentary structures in shales, representing the directional arrangement of organic matter or inorganic minerals. Shales containing laminae exhibit a high hydrocarbon generation ability, and shales containing fine laminae formed *via* biochemical deposition exhibit a more pronounced hydrocarbon generation ability (Zeng et al., 2017; Su et al., 2019). The interbedding of micron-to centimeter-scale laminae composed of different components reflects the microscale source-reservoir configuration of shales (Han et al., 2021; Liu B. et al., 2021). Shales with well-developed laminae often attain a higher oil expulsion efficiency (Wang Y. et al., 2016; Du et al., 2019) (**Figure 6B**). A considerable amount of oil migrates into feldspar-quartz laminae or carbonate laminae at the semi-to microscale after meeting the oil retention

requirements of organic-rich laminae, resulting in relatively high oil-bearing properties (Xi et al., 2020; Han et al., 2021).

Oil is adsorbed onto kerogen and mineral particles and occurs in pores and fractures in shales. The development of shale pores exerts an important control on the oil content (Li J. J. et al., 2018; Zhao X. Z. et al., 2020) (**Figure 6C**). Chen G. H. et al. (2018) reported that 80% of shale oil is distributed in macropores. In fact, with increasing pore size, pore volume and porosity, the oil content in shales usually increases (Wang et al., 2019b; Song et al., 2020; Wang B. Y. et al., 2021). Because the density of the generated oil and gas is lighter than that of kerogen, the volume expansion and the overpressure phenomenon occurs in shales, resulting in the generation of oil expulsion fractures (Sun L. D. et al., 2021). Although shale microfractures form effective oil migration channels and oil storage spaces, when the scale of microfractures reaches a certain extent, this may reduce the shale oil content. Liu B. et al. (2021) pointed out that a higher fracture density resulted in a vertical migration of shale oil, which does not promote shale oil enrichment. Zhao X. Z. et al. (2020) indicated that natural fracture development limited to the shale interior is relatively favorable to the seepage and preservation of retained oil in shales.

Influences of Shale Thickness and Preservation Conditions on Oil Retention

The thickness of organic-rich shales macroscopically controls the shale oil content. A thick shale, especially at its center part, does not facilitate oil expulsion (Leythaeuser et al., 1984). It seems that there is an effective petroleum expulsion thickness in geological conditions, and the shale beyond the thickness would have a weak oil expulsion (Jiang et al., 1986; Wang et al., 2005; Hou et al., 2017). Based on the pyrolysis experiment and geological model, Hou et al. (2017) found that the increase of the shale thickness during the oil generation stage would significantly reduce the oil expulsion efficiency. The thinner a single shale seam in a shale-

sandstone interbedding stratum, the more frequent the shale-sandstone configuration and the lower the retention of oil in the shale (Fan and Shi, 2019), while the oil-bearing properties of the interlayers (i.e., the sandstone seams) within the shale seams are improved (Raji et al., 2015). Exploration practices have verified that fault systems impart complementary control effects on both conventional and shale reservoirs, the retained oil in the shale may migrate to the shallow layers along the faults remaining active, which is unfavorable for shale oil enrichment (Fu et al., 2020; Liu B. et al., 2021). However, thick shales are not easily broken through (Fu et al., 2018). Microfractures extending only in the interior of a shale increase the shale oil storage space and fluidity, which is more benefit to shale oil enrichment (Zhao X. Z. et al., 2020). Therefore, the shale thickness plays a positive role in the oil-bearing capacity (Fan and Shi, 2019; Zhao W. Z. et al., 2021).

Preservation conditions are also important for shale oil enrichment. Lin et al. (2020) calculated that the decisive tectonic action in the Miquan area of the Junggar Basin caused a loss of 78.9% of the original shale oil resources. A relatively stable tectonic environment and high-quality top and bottom seal layers of a shale seam play positive roles in the preservation of shale oil (Liu et al., 2018; Li M. W. et al., 2019b; Liu B. et al., 2021).

EVALUATION AND INFLUCEING FACTORS OF MOVABLE OIL IN SHALES

The movable oil content in shales is the key to a high yield of shale oil (Jarvie, 2012; Li J. Q. et al., 2018; Li M. W. et al., 2019a; Li H. et al., 2020; Hu et al., 2021). It is highly important to determine the amount of movable oil and its influencing factors for shale oil prediction. This section mainly introduces three feasible and realistic methods to evaluate the shale movable oil content, including the pyrolysis, 2D NMR and adsorption-swelling calculation methods. In addition, the influencing factors of movable oil in shales are also discussed.

Evaluation of Movable Oil
Pyrolysis Method
According to available empirical data of shale oil production, Jarvie (2012) proposed the oil crossover effect, i.e., OSI > 100 mg hydrocarbons/g TOC as the indicator of movable oil in shales (**Figure 7A**). Quite a few authors have applied this standard to evaluate movable shale oil because it eliminates the influence of organic matter adsorption (Wang M. et al., 2015; Cao et al., 2017; Hu et al., 2018; Zhao X. Z. et al., 2020). Zhao X. Z. et al. (2020) indicated that the movable oil content is equal to the difference between the amount of retained oil and the oil crossover effect value (**Figure 7B**). However, the OSI method may not be fully applicable in lacustrine shales (Xue et al., 2015; Huang et al., 2020), and the OSI value and oil crossover effect dynamically change with the maturity. With increasing maturity, the OSI values gradually increase until a maximum retention capacity is reached, and then a subsequent decrease is show (**Figure 7C**) (Han et al., 2017).
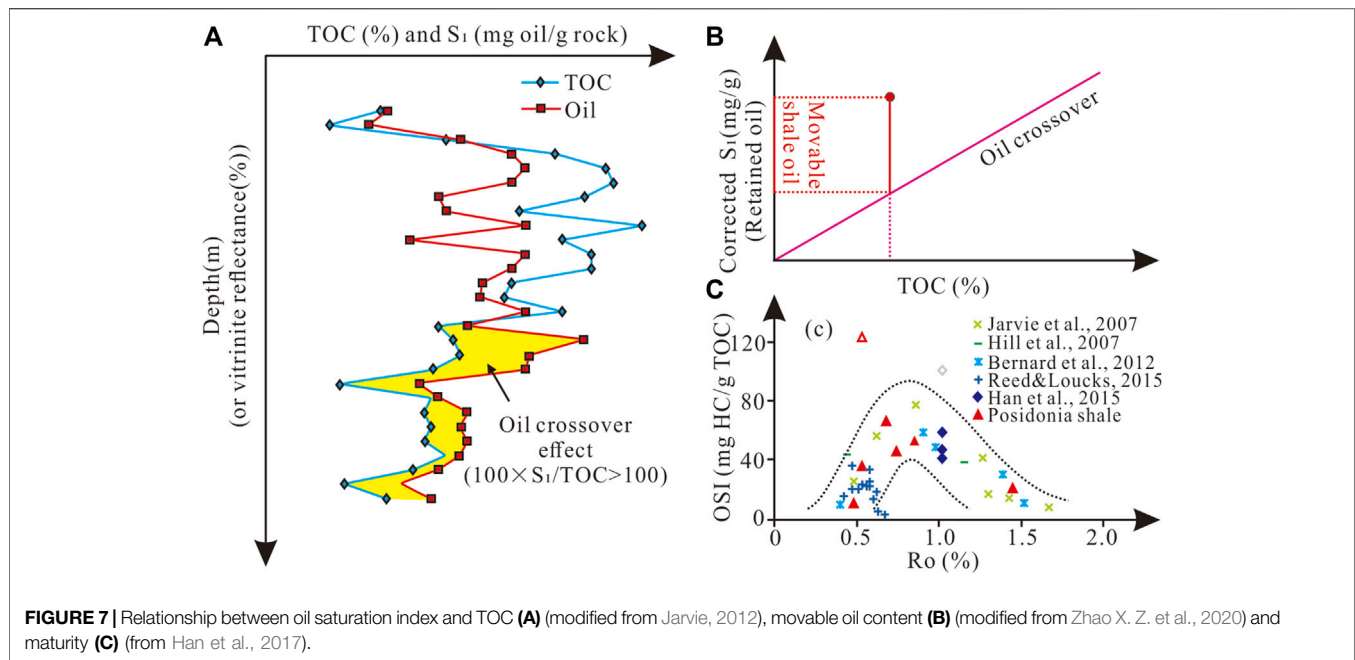
The light components contained in macropores and connected pore systems in the free state can be released at lower temperatures. In contrast, the heavy components in kerogen, and micropores and disconnected pore systems in the adsorption state can only be released at higher temperatures or when the temperature of organic matter cracking is reached (Jiang Q. G. et al., 2016). Therefore, the amount of movable shale oil can be evaluated by the thermally released hydrocarbon peak obtained under the constant-heating rate mode. Maende (2016) noted in the HAWK Petroleum Assessment Method that the movable oil content is the sum of Oil-1, Oil-2, Oil-3 and Oil-4 (**Figure 8A**). Jiang Q. G. et al. (2016) and Li J. B. et al. (2020a) considered that the thermally released hydrocarbon peak (S_{1-1}) at 200°C could represent the actual movable oil content, and the maximum movable oil content is the sum of S_{1-1} and S_{1-2} (at 350°C) (**Figure 8B**). Romero-Sarmiento (2019) proposed that sorbed liquid hydrocarbons is adsorbed on the residual solid OM, and thus the movable oil content of shales can be determined according to the area difference of thermal peaks (Sh0 (at 100–200°C) and Sh1 (at 200–350°C)) of whole rock sample and the corresponding isolated OM (**Figures 8C,D**). Chen Z. H. et al. (2019) and Li M. W. et al. (2020) applied the thermally released hydrocarbon peak (S_{1a}) at or below 300°C to represent the residual free hydrocarbons (**Figure 8E**) and believed that the shale oil discounted by the critical saturation is not limited by adsorption forces and nanopore bonds but exhibits fluidity (**Eq. 7**). Gentzis et al. (2021) thought that L1, L2 and a part of L3 represented movable oil, whereas the remaining L3 and L4 containing heavy n-alkanes, resins, asphaltenes and NSO compounds represented immovable oil (**Figure 8F**). Multistep pyrolysis method has low cost and easy operation, but it should be pointed out that the recovery of light hydrocarbon loss is necessary.

$$\emptyset_{mob} = \begin{cases} 0, & S_{1c} \leq \widetilde{TOC} \\ S_{1c} - \widetilde{TOC}, & S_1 > \widetilde{TOC} \end{cases} \tag{7}$$

where S_{1c} is total free hydrocarbons after light hydrocarbon correction, $\widetilde{TOC}$ represents the amount of adsorption discount (mg HC/g TOC), which is equivalent to the percentage content of TOC in the sample.

NMR Method
A shale is characterized by complex porous media and multiple fluid occurrences (oil, gas, water and kerogen). The standard T_2 relaxation time distribution obtained by 1D NMR provides limited information, and signal overlap between the different fluids is severe (Birdwell and Washburn, 2015). Although T_2-D can be used to distinguish the fluid phase (oil, gas and water) in shales, the solid-like organic matter signal and kerogen signal in micro/nanopores cannot be effectively distinguished (Li J. B. et al., 2018; Bai et al., 2019; Song and Kausik, 2019). In contrast, 2D NMR, especially high-frequency 2D NMR, can improve the detection ability of trace signals and can more efficiently distinguish light oil, heavy components, kerogen, bound water and other fluids in shales. Specifically, kerogen (with high T_1) and structural water have shorter T_2 and wider

FIGURE 7 | Relationship between oil saturation index and TOC **(A)** (modified from Jarvie, 2012), movable oil content **(B)** (modified from Zhao X. Z. et al., 2020) and maturity **(C)** (from Han et al., 2017).

T_1, oil generally has a higher T_1/T_2 ratio than water (with low T_1), and the T_2 value of adsorbed oil is lower than that of movable oil (Li J. B. et al., 2018; Khatibi et al., 2019; Song and Kausik, 2019; Zhang P. F. et al., 2020) (**Figure 9A**). Based on the principle that 2D NMR can effectively distinguish hydrogen nuclei of fluids in different occurrence states, researchers have combined 2D NMR with geochemical experiments, such as rock pyrolysis, solvent extraction, and quantitative grain fluorescence on extract, to comprehensively analyze the content of movable shale oil (Bai et al., 2019; Liu B. et al., 2019; Li J. B. et al., 2020a; Gentzis et al., 2021). For example, Li J. B. et al. (2020a) extracted organic hydrogen T_2 spectra of kerogen, adsorbed oil and free oil at T_1 intervals corresponding to the original samples, samples pyrolyzed at 350°C and extracted samples. Their accumulative amplitude determined the T_2 cutoff values of free oil and adsorbed oil, and a nondestructive method for the direct evaluation of the free oil content was then provided (**Figures 9B,C**). However, it should be noted that the threshold value of the T_1-T_2 spectrum is related to the echo interval and frequency of the instrument itself (Nicot et al., 2016; Song and Kausik, 2019). The temperature and state of the samples and the magnetic minerals in shales would change the distribution of signal response interval (Bai et al., 2019). Furthermore, it is difficult to define the boundary of the T_1/T_2 ratio of movable and nonmovable fluids, which may lead to uncertainty in movable oil evaluation. Overall, for different testing method, they both have advantages and limitations, for accurate desriping movable oil content, various methods should be using synthetically.

Adsorption-swelling Calculation Method

The shale oil adsorbed onto minerals and kerogen is usually immovable, and the movable oil content can be regarded as the difference betwee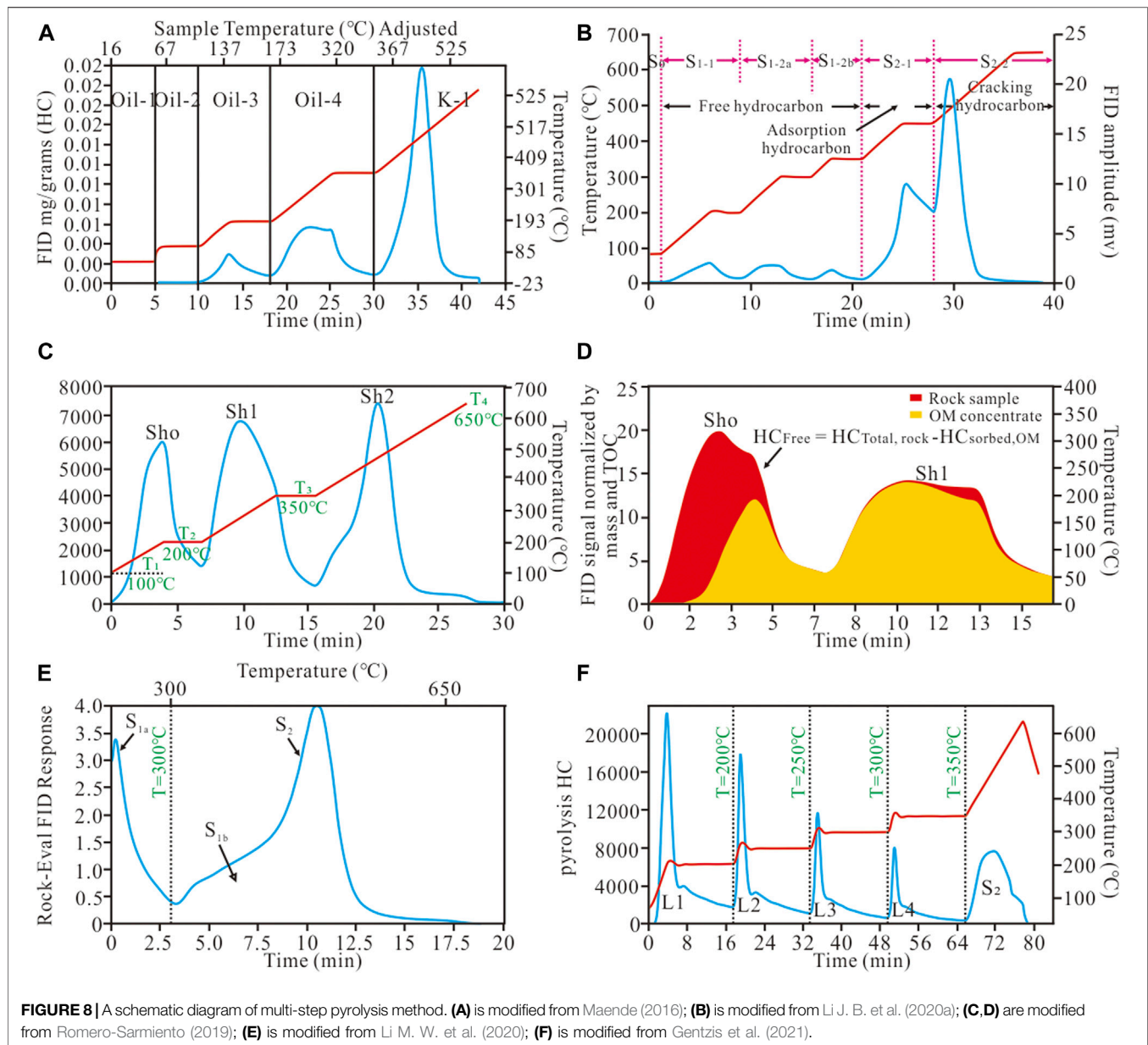n the total oil content and the adsorption-swelling oil content. Because the adsorption capacity of kerogen is much higher than that of minerals for shale oil, previous studies have mainly focused on the calculation of the adsorption and swelling capacities of kerogen (Wei et al., 2012; Tian et al., 2014), but this has caused an overestimation of the movable oil content. Therefore, Li et al. (2016) proposed the adsorption potential S_p model (**Eq. 8**) to calculate the oil adsorption amount in shale, and the difference between S_p and S_1 is suitable within a broader range of TOC and maturity levels (Zou et al., 2018). The adsorption-swelling oil quantity ($Q_{a\text{-}s}$) can also be calculated *via* molecular dynamics simulations (**Eq. 9**) (Tian et al., 2017; Tian et al., 2020). The swelling capacity of kerogen (Q_S) is calculated according to the shale oil density curve for kerogen. According to the density curve and specific surface area of shale oil in kerogen and mineral pores, the adsorbed oil quantity (Q_a) can be deduced. However, the adsorption-swelling calculation method is primarily a simplified model of shale under geological conditions. There may be differences between the premise and assumed parameters and the geological conditions, which results in insufficiently accurate calculations of adsorption-swelling oil content. Optimization of this model is a future research direction.

$$S_p = p_o x_o + \left[\frac{\varphi}{\varphi_0}\right]^{2/3} \sum_{i=1}^{n} p_i x_i \tag{8}$$

$$Q_{a-s} = Q_s + Q_a = \int_{L_{o1}}^{L_{o2}} S_{ko}\rho_{ko}dL + \int_{L_{k2}}^{L_{k1}} S_{ko}\rho_{ko}dL + \int_{L_{m2}}^{L_{m1}} S_{mo}\rho_{mo}dL \tag{9}$$

where p_O and x_O are the proportion and adsorption capacity of OM respectively; p_i and x_i are the proportion of the ith mineral and its adsorbed oil amount respectively; $p_o + \sum_{i=1}^{n} p_i = 1$; φ and φ_o is porosity and shale initial porosity respectively; L_{o1} and L_{o2}

FIGURE 8 | A schematic diagram of multi-step pyrolysis method. **(A)** is modified from Maende (2016); **(B)** is modified from Li J. B. et al. (2020a); **(C,D)** are modified from Romero-Sarmiento (2019); **(E)** is modified from Li M. W. et al. (2020); **(F)** is modified from Gentzis et al. (2021).
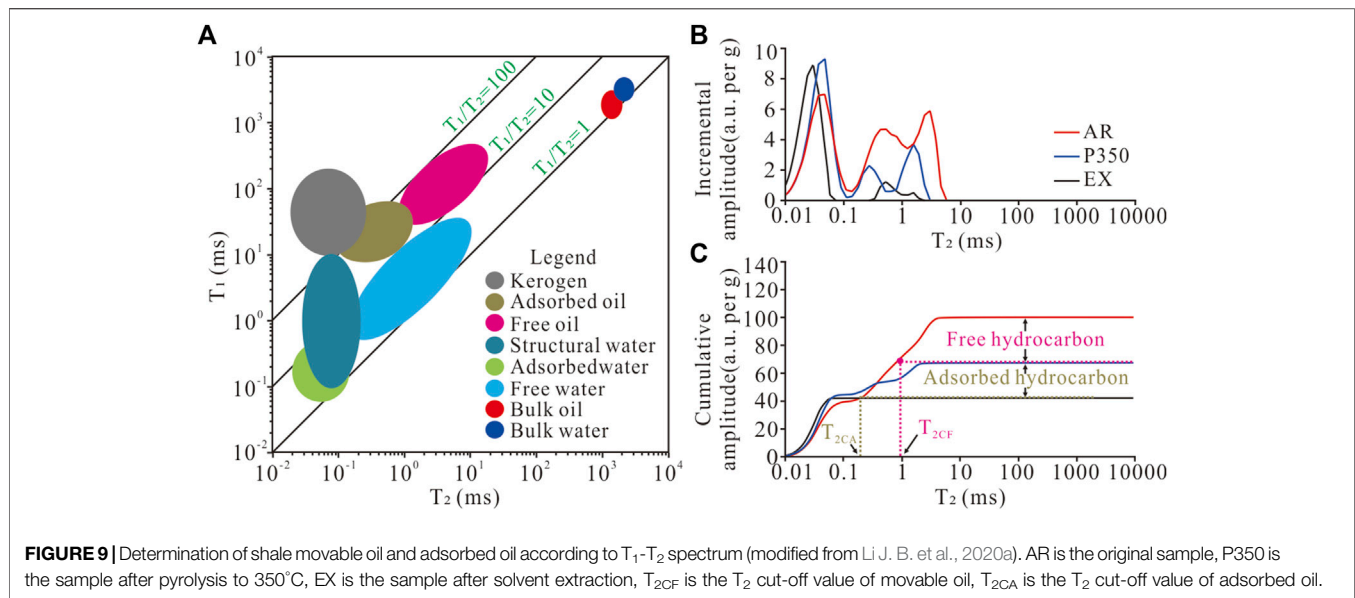
are the starting and ending positions of the intersection of kerogen density curve and shale oil density curve respectively; L_{k1} and L_{k2} are the starting point and end of kerogen adsorption layer respectively; L_{m1} and L_{m2} are the starting point and end of mineral component adsorption layer respectively; S_{ko} is the cross-sectional area of swelling and adsorption model of shale oil in kerogen, ρ_{ko} is the density curve of shale oil, S_{mo} is the adsorption model area of shale oil in mineral pores, and ρ_{mo} is the density curve of shale oil in mineral pores.

Influencing Factors of Movable Oil

Great effort has been made to explore the influencing factors of the shale oil mobility through various means of production and experimental analysis methods. It is recognized that occurrences of retained oil in shales have a great influence on its fluidity. Adsorption-swelling oil occurs in the form of high-density solid-like or embedded kerogen on the surface of organic and inorganic pores (Wang et al., 2015b), and it is immovable without additional forces (Zhao X. Y. et al., 2021). The shale organic matter abundance exerts two impacts on the shale oil mobility. Even considering shale hydrocarbon expulsion, a high TOC is still beneficial to an increase in the shale oil and movable oil contents (Lu et al., 2012; Hu et al., 2021; Zhao W. Z. et al., 2021). However, in shales with the same oil content, an increase in the TOC content suggests a decrease in the movable oil content (Wang et al., 2019b). The relationship between the organic matter type and movable oil indicates that a higher oil generating capacity per

FIGURE 9 | Determination of shale movable oil and adsorbed oil according to T_1-T_2 spectrum (modified from Li J. B. et al., 2020a). AR is the original sample, P350 is the sample after pyrolysis to 350°C, EX is the sample after solvent extraction, T_{2CF} is the T_2 cut-off value of movable oil, T_{2CA} is the T_2 cut-off value of adsorbed oil.

unit of organic carbon means a higher movable oil content (He et al., 2019). It has been reported that the proportion of movable oil will increases with increasing burial depth. This phenomenon is related to the decrease in oil viscosity and density due to increasing temperature and light components (Wang et al., 2019b; Scheeder et al., 2020; Zhao W. Z. et al., 2021), which is conducive to a reduction in the oil film thickness and a relative increase in free oil in pores with the same pore size (Liu Y. S. et al., 2021). The increase in thermal maturity also leads to a decrease in the adsorption and swelling capacities of kerogen (Song et al., 2015; Wang et al., 2015b; Wang et al., 2019b). Li J. Q. et al. (2017) reported that the decrease in adsorption capacity could be attributed to the reduction in TOC content with increasing maturity. Wang et al. (2015b), based on molecular dynamics simulation analysis, proposed that with increasing maturity, the number of carbonyl in kerogen gradually decreases, which leads to the weakening of the adsorption capacity of kerogen for alkanes. Zhao X. Z. et al. (2020) conducted thermal simulation and kerogen swelling experiments on Paleogene shales obtained from the Huanghua depression of the Bohai Bay Basin and observed that an middle thermal maturity is the superior evolution stage for movable oil enrichment in lacustrine shale, which was attributed to the optimum matching of hydrocarbon generation and organic matter adsorption-swelling.

Mineral particles and composition play specific roles in controlling movable shale oil. Overall, although intergranular pores can be formed among clay minerals, tiny intergranular pores and the high surface adsorption capacity of clay minerals hinder the storage of movable liquid hydrocarbons (Su et al., 2018; Ning et al., 2020). The adsorption affinity of quartz and carbonate minerals for oil is low (Raji et al., 2015; Li et al., 2016), and the increase in their contents promotes the development of microcracks (Ougier-Simonin et al., 2016) and the preservation of macropores (Zhang P. L. et al., 2021), which facilitate the occurrence of mobile liquid hydrocarbons. However, Hu et al. (2021) analyzed the lacustrine shale of the Paleogene Shahejie

Formation in the Dongpu Sag of the Bohai Bay Basin. Their results revealed that the movable oil content first increases and then decreases with the content of clay minerals (25% as the inflection point) and quartz minerals (15% as the inflection point), which depends on the coupling effect of the mineral content on the porosity, adsorption capacity and TOC content. In addition, due to the petroleum fractionation effect, feldspar-quartz or carbonate laminae interbedded with organic-rich laminae at the microscale and interbedded shale, sandstone, carbonate, and mixed rock layers in shale strata at the macroscale contain more light oil components that easily flow (Jarvie, 2014; Li J. Q. et al., 2018; Fan and Shi, 2019; Pan et al., 2019; Liu B. et al., 2021).

Shale reservoir conditions are fundamental to the flow ability of shale oil. Bao (2018) speculated that shales within the oil generation window and a porosity higher than 6.5% promoted the storage of movable oil through the relationship between the OSI and porosity for the Paleogene shale in the Dongying Sag. The shale pore structure is a crucial factor controlling the shale oil mobility (Davudov et al., 2020; Jiang et al., 2020; Liu et al., 2020; Ning et al., 2020). Zou et al., 2015 found that oil cannot flow through pores below the lower limit of the flow threshold (20 nm) through simulations of a nanoporous template with a controllable pore diameter. Wang et al. (2015a), through adsorption simulations of alkanes onto a graphene surface (oil-wet), proposed that alkanes only flowed after exceeding the critical pore size. Conversely, they all occurred in the adsorption state. The pore size of shale reservoirs should exceed the flow threshold, which is a necessary condition for movable shale oil. The proportion of movable oil gradually increases with increasing pore size (Zhang P. F. et al., 2020) because the pore connectivity of macropores is higher and provides a considerable pore volume for movable oil (Li T. W. et al., 2017; Jiang et al., 2020; Ning et al., 2020), and the diffusion coefficient of oil increases with increasing pore diameter (Wang H. et al., 2016; Zhang et al., 2019). When the pore throat radius is large, the diffusion motion of

hydrocarbon molecules of different sizes in throats is not restricted by the diffusion energy barrier (Jiang et al., 2018). Cui and Cheng (2017) suggested that movable shale oil was also related to the porosity and pore size of organic pores, and the movable oil content decreased with increasing organic porosity ratio. The porosity and permeability of shales are low, and fractures can effectively improve the seepage capacity of shale reservoirs (Soeder and Borglum, 2019). Microfractures in shales are conducive to increasing the shale movable oil proportion and effective production (Song et al., 2020). Moreover, flow experiments have demonstrated that the shale oil fluidity is related to the fracture strength and direction, and bedding microfractures play an essential role in shale oil migration (Xie et al., 2019).

CONCLUSION

(1) The oil generated from organic-rich shales can be partly retained in themselves *via* through adsorption and swelling of kerogen, adsorption onto minerals and storage in pores. These mechanisms have been applied to explain to oil retention in shales under geological conditions, while the relative thermal dynamics is looked forward to further development.

(2) Quite a few methods have been developed to characterize and evaluate the oil in shales. The pyrolysis, thermal simulation experiment and material balance methods are most common use to quantify the oil content in shales.

(3) The shale oil retention capacity is bascially controlled by the organic matter abundance and properties (type and maturity), mineral composition, oil storage space, shale thickness and preservation conditions, but inconsistent

recoginitions exist, and are mainly from different scale research. It is necessary to strengthen a comprehensive study from the microscale to the macroscale.

(4) The study on the movable oil in shales still remains at the exploratory stage.

Although a few method are believed to be effective to estimate the movable oil content in shales, their limitations indicate needs for the supplement and verification of geological data. Especially, the influencing factors of shale movable oil are complex and variable. More accurate evaluation parameters and correction methods on this topic will become a research focus.

AUTHOR CONTRIBUTIONS

YF: Investigation, Writing - Original Draft. XX: Conceptualization, Methodology, Review and Editing. EW: Review and Editing. JS: Review and Editing. PG: Review. All authors contributed to the article and approved the submitted version.

FUNDING

ACKNOWLEDGMENTS

REFERENCES

Abrams, M. A., Gong, C., Garnier, C., and Sephton, M. A. (2017). A New Thermal Extraction Protocol to Evaluate Liquid Rich Unconventional Oil in Place and Iin-Ssitu Fluid Chemistry. *Mar. Pet. Geology.* 88, 659–675. doi:10.1016/j.marpetgeo.2017.09.014

Alfi, M., Yan, B., Cao, Y., An, C., Wang, Y., He, J., and Killough, J. E. (2014). "How to Improve Our Understanding of Gas and Oil Production Mechanisms in Liquid-Rich Shale," in SPE Annual Technical Conferences and Exhibition, Amsterdam, Netherlands, October 27–29, 2014. doi:10.2118/170959-MS

Bai, G. P., Qiu, H. H., Deng, Z. Z., Wang, W. Y., and Chen, J. (2020). Distribution and Main Controls for Shale Oil Resources in USA. *Pet. Geology. Exp.* 42 (04), 524–532. doi:10.11781/sysydz202004524 (in Chinese with English Abstract).

Bai, J., Xu, X. Y., and Chen, S. (2017). Analysis of Controlling Factors of Shale Oil Renrichment and Recoverable Capacity in continental Shale, A Case Study from Qingshankou Formation. *Geol. Rev.* 63 (S1), 117–118. doi:10.16509/j.georeview.2017.s1.056 (in Chinese with English Abstract).

Bai, L. H., Liu, B., Chi, Y. A., Jin, L., Yang, L., and Gao, S. (2019). Application of 2-D NMR Technique to Characterize Organic Matter in Shale deposit -A Case Study from the Qingshankou Formation in Southern Songliao Basin. *Oil Gas Geology.* 1–12. (in Chinese with English Abstract).

Bao, Y. S. (2018). Effective Reservoir Spaces of Paleogene Shale Oil in the Dongying Depression, Bohai Bay Basin. *Pet. Geology. Exp.* 40 (04), 479–484. doi:10.11781/sysydz201804479 (in Chinese with English Abstract).

Behar, F., Beaumont, V., and De B. Penteado, H. L. (2001). Rock-Eval 6 Technology: Performances and Developments. *Oil Gas Sci. Technol. - Rev. IFP* 56 (2), 111–134. doi:10.2516/ogst:2001013

Beti, D. R., Panja, P., Jiang, C., Milovic, M., Robinson, R., Ring, T. A., et al. (2020). Change in Hydrocarbon Composition in Rock Samples as a Function of Time: A Thermodynamic Evaporation Model. *J. Nat. Gas Sci. Eng.* 77, 103238. doi:10.1016/j.jngse.2020.103238

Birdwell, J. E., and Washburn, K. E. (2015). Multivariate Analysis Relating Oil Shale Geochemical Properties to NMR Relaxometry. *Energy Fuels* 29, 2234–2243. doi:10.1021/ef502828k

Burnham, A. K. (2017). *Global Chemical Kinetics of Fossil Fuels: How to Model Maturation and Pyrolysis.* Switzerland: Springer, 75–105. doi:10.1007/978-3-319-49634-4

Cao, H., Zou, Y.-R., Lei, Y., Xi, D., Wan, X., and Peng, P. A. (2017). Shale Oil Assessment for the Songliao Basin, Northeastern China, Using Oil Generation-Sorption Method. *Energy Fuels* 31 (5), 4826–4842. doi:10.1021/acs.energyfuels.7b00098

Cao, Z., Jiang, H., Zeng, J. H., Saibi, H., Lu, T. Z., Xie, X. M., et al. (2021). Nanoscale Liquid Hydrocarbon Adsorption on Clay Minerals: A Molecular Dynamics Simulation of Shale Oils. *Chem. Eng. J.* 420, 127578. doi:10.1016/j.cej.2020.127578

Cardott, B. J. (2012). Thermal Maturity of Woodford Shale Gas and Oil Plays, Oklahoma, USA. *Int. J. Coal Geology.* 103, 109–119. doi:10.1016/j.coal.2012.06.004

Carr, A. D. (1999). A Vitrinite Reflectance Kinetic Model Incorporating Overpressure Retardation. *Mar. Pet. Geol.* 16 (4), 355–377. doi:10.1016/S0264-8172(98)00075-0

Chen, G. H., Lu, S. F., Zhang, J. F., Pervukhina, M., Liu, K. Y., Wang, M., et al. (2018). A method for determining oil-bearing pore size distribution in shales: A case study from the Damintun Sag, China. *J. Pet. Sci. Eng.* 166, 673–678. doi:10.1016/j.petrol.2018.03.082

Chen, J. Q., Pang, X. Q., Pang, H., Chen, Z. H., and Jiang, C. Q. (2018). Hydrocarbon Evaporative Loss Evaluation of Lacustrine Shale Oil Based on Mass Balance Method: Permian Lucaogou Formation in Jimusaer Depression, Junggar Basin. *Mar. Pet. Geology.* 91, 422–431. doi:10.1016/j.marpetgeo.2018.01.021

Chen, J. P., Sun, Y. G., Zhong, N. N., Huang, Z. K., Deng, C. P., Xie, L. J., et al. (2014). The Efficiency and Model of Petroleum Expulsion from the Lacustrine Source Rocks Within Geological Frame. *Acta Geologica Sinica* 88 (11), 2005–2032. doi:10.1111/1755-6724.12373_3 (in Chinese with English Abstract).

Chen, L., Jiang, Z. X., Liu, Q. X., Jiang, S., Liu, K. Y., Tan, J. Q., et al. (2019a). Mechanism of Shale Gas Occurrence: Insights from Comparative Study on Pore Structures of Marine and Lacustrine Shales. *Mar. Pet. Geology.* 104, 200–216. doi:10.1016/j.marpetgeo.2019.03.027

Chen, L., Liu, K. Y., Jiang, S., Huang, H. X., Tan, J. Q., and Zuo, L. (2021). Effect of Adsorbed Phase Density on the Correction of Methane Excess Adsorption to Absolute Adsorption in Shale. *Chem. Eng. J.* 420, 127678. doi:10.1016/j.cej.2020.127678

Chen, L., Zuo, L., Jiang, Z. X., Jiang, S., Liu, K. Y., Tan, J. Q., et al. (2019b). Mechanisms of Shale Gas Adsorption: Evidence from Thermodynamics and Kinetics Study of Methane Adsorption on Shale. *Chem. Eng. J.* 361, 559–570. doi:10.1016/j.cej.2018.11.185

Chen, Y. Y., Lin, S. H., Bai, B., Zhang, T. S., Pang, Z. L., Tao, S. Z., et al. (2020). Effects of Petroleum Retention and Migration Within the Triassic Chang 7 Member of the Ordos Basin, China. *Int. J. Coal Geology.* 225, 103502. doi:10.1016/j.coal.2020.103502

Chen, Z. H., Li, M. W., and Jiang, C. Q. (2019). Shale Oil Resource Potential and Mobility Assessment: A Case Study of Upper Devonian Duvernay Shale in the Western Canada Sedimentary Basin. *Oil Gas Geology.* 40 (6), 459–468. doi:10.11743/ogg20190302 (in Chinese with English Abstract).

Chen, Z. H., Zha, M., and Jin, Q. (2004). An Investigation on Generation and Expulsion of Hydrocarbon from Source Rocks of the Shahejie Formation in the Well Niu-38, Dongying Depression. *Scientia Geologica Sinica* 39 (3), 356–366. (in Chinese with English Abstract).

Chen, Z. H., and Jiang, C. Q. (2015). A Data Driven Model for Studying Kerogen Kinetics with Application Examples from Canadian Sedimentary Basins. *Mar. Pet. Geol.* 67, 795–807. doi:10.1016/j.marpetgeo.2015.07.004

Chen, Z. H., and Jiang, C. Q. (2016). A Revised Method for Organic Porosity Estimation in Shale Reservoirs using Rock-Eval data: Example from Duvernay Formation in the Western Canada Sedimentary Basin. *AAPG Bull.* 100, 405–422. doi:10.1306/08261514173

Chen, Z. H., Liu, X. J., and Jiang, C. Q. (2017). Quick Evaluation of Source Rock Kerogen Kinetics Using Hydrocarbon Pyrograms from Regular Rock-Eval Analysis. *Energy Fuels* 31 (2), 1832–1841. doi:10.1021/acs.energyfuels.6b01569

Cooles, G. P., Mackenzie, A. S., and Quigley, T. M. (1986). Calculation of Petroleum Masses Generated and Expelled from Source Rocks. *Org. Geochem.* 10 (1-3), 235–245. doi:10.1016/0146-6380(86)90026-4

Cui, J., and Cheng, L. (2017). A Theoretical Study of the Occurrence State of Shale Oil Based on the Pore Sizes of Mixed Gaussian Distribution. *Fuel* 206, 564–571. doi:10.1016/j.fuel.2017.06.047

Davudov, D., Moghanloo, R. G., and Zhang, Y. (2020). Interplay Between Pore Connectivity and Permeability in Shale Sample. *Int. J. Coal Geology.* 220, 103427. doi:10.1016/j.coal.2020.103427

Du, J. Z., Cai, J. G., Lei, T. Z., and Li, Y. L. (2021). Diversified Roles of mineral Transformation in Controlling Hydrocarbon Generation Process, Mechanism, and Pattern. *Geosci. Front.* 12 (2), 725–736. doi:10.1016/j.gsf.2020.08.009

Du, J. H., Hu, S. Y., Pang, Z. L., Lin, S. H., and Zhu, R. K. (2019). The Types, Potentials and Prospects of Continental Shale Oil in China. *China Pet. Exploration* 24 (05), 560–568. doi:10.3969/j.issn.1672-7703.2019.05.003 (in Chinese with English Abstract).

Dudášová, D., Sébastien, S., Hemmingsen, P. V., and Sjöblom, J. (2008). Study of Asphaltenes Adsorption onto Different Minerals and Clays: Part 1. Experimental Adsorption with UV Depletion Detection. *Colloids Surf. A: Physicochemical Eng. Aspects* 317 (1-3), 1–9. doi:10.1016/j.colsurfa.2007.09.023

Ertas, D., Kelemen, S. R., and Halsey, T. C. (2006). Petroleum Expulsion Part 1. Theory of Kerogen Swelling in Multicomponent Solvents. *Energy Fuels* 20 (1), 295–300. doi:10.1021/ef058024k

Eseme, E., Krooss, B. M., and Littke, R. (2012). Evolution of Petrophysical Properties of Oil Shales During High-Temperature Compaction Tests: Implications for Petroleum Expulsion. *Mar. Pet. Geology.* 31 (1), 110–124. doi:10.1016/j.marpetgeo.2011.11.005

Fan, B., and Shi, L. (2019). Deep-Lacustrine Shale Heterogeneity and its Impact on Hydrocarbon Generation, Expulsion, and Retention: A Case Study from the Upper Triassic Yanchang Formation, Ordos Basin, China. *Nat. Resour. Res.* 28, 241–257. doi:10.1007/s11053-018-9387-2

Fu, X. F., Shi, H. D., Meng, Q. A., Liu, B., Liang, J. P., He, J. L., et al. (2020). Controlling Effects of the Structure and Deposition on the Shale Oil Enrichment: Taking Formation Qn1in the Central Depression of Songliao Basin as an Instance. *Pet. Geology. Oilfield Develop. Daqing* 39 (03), 56–71. doi:10.19597/J.ISSN.1000-3754.202005011 (in Chinese with English Abstract).

Fu, X. F., Wu, T., Lv, Y. F., Liu, S. B., Tian, H., and Lu, M. X. (2018). Research Status and Development Trend of the Reservoir Caprock Sealing Properties. *Oil Gas Geology.* 39 (03), 454–471. doi:10.11743/ogg20180304 (in Chinese with English Abstract).

Gao, Z. Y., Fan, Y. P., Hu, Q. H., Jiang, Z. X., Cheng, Y., and Xuan, Q. X. (2019). A Review of Shale Wettability Characterization Using Spontaneous Imbibition Experiments. *Mar. Pet. Geology.* 109, 330–338. doi:10.1016/j.marpetgeo.2019.06.035

Gentzis, T., Carvajal-Ortiz, H., Harry Xie, Z., Hackley, P. C., and Fowler, H. (2021). An Integrated Geochemical, Spectroscopic, and Petrographic Approach to Examining the Producibility of Hydrocarbons from Liquids-Rich Unconventional Formations. *Fuel* 298, 120357. doi:10.1016/j.fuel.2021.120357

Ghanizadeh, A., Clarkson, C. R., Clarke, K. M., Yang, Z., Rashidi, B., Vahedian, A., et al. (2020). Effects of Entrained Hydrocarbon and Organic-Matter Components on Reservoir Quality of Organic-Rich Shales: Implications for "Sweet Spot" Identification and Enhanced-Oil-Recovery Applications in the Duvernay Formation (Canada). *SPE J.* 25, 1351–1376. doi:10.2118/189787-pa

Hadad, Y. T., Hakimi, M. H., Abdullah, W. H., and Makeen, Y. M. (2017). Basin Modeling of the Late Miocene Zeit Source Rock in the Sudanese Portion of Red Sea Basin: Implication for Hydrocarbon Generation and Expulsion History. *Mar. Pet. Geology.* 84, 311–322. doi:10.1016/j.marpetgeo.2017.04.002

Han, W. Z., Zhao, W. Z., Jin, F. M., Pu, X. G., Chen, S. Y., Mou, L. G., et al. (2021). Sweet Spots Evaluation and Exploration of Lacustrine Shale Oil of the 2nd Member of Paleogene Kongdian Formation in Cangdong Sag, Dagang Oilfield, China. *Petrol. Explor. Dev.* 48 (4), 777–786. doi:10.11698/PED.2021.04.10

Han, Y. J., Horsfield, B., Wirth, R., Mahlstedt, N., and Bernard, S. (2017). Oil Retention and Porosity Evolution in Organic-Rich Shales. *AAPG Bull.* 101 (6), 807–827. doi:10.1306/09222116069

Han, Y. J., Mahlstedt, N., and Horsfield, B. (2015). The Barnett Shale: Compositional Fractionation Associated with Intraformational Petroleum Migration, Retention, and Expulsion. *AAPG Bull.* 99 (12), 2173–2202. doi:10.1306/06231514113

He, T. H., Li, W. H., Tan, Z. Z., Wang, Y., Zhang, W. B., and Zhang, X. W. (2019). Mechanism of Shale Oil Accumulation in the Hetaoyuan Formation from the Biyang Depression, Nanxiang Basin. *Oil Gas Geology.* 40 (6), 1259–1269. doi:10.11743/ogg20190610 (in Chinese with English Abstract).

Hou, L. H., Luo, X., Lin, S. H., Zhao, Z. Y., and Li, Y. (2021a). Quantitative Measurement of Retained Oil in Organic-Rich Shale-A Case Study on the Chang 7 Member in the Ordos Basin, China. *Front. Earth Sci.* 9, 662586. doi:10.3389/feart.2021.662586

Hou, L. H., Ma, W. Z., Luo, X., and Liu, J. Z. (2020). Characteristics and Quantitative Models for Hydrocarbon Generation-Retention-Production of Shale Under ICP Conditions: Example from the Chang 7 Member in the Ordos Basin. *Fuel* 279, 118497. doi:10.1016/j.fuel.2020.118497

Hou, L. H., Ma, W. J., Luo, X., Liu, J. Z., Liu, S. H., and Zhao, Z. Y. (2021b). Hydrocarbon Generation-Retention-Expulsion Mechanism and Shale Oil Producibility of the Permian Lucaogou Shale in the Junggar Basin as Simulated by Semi-open Pyrolysis Experiments. *Mar. Pet. Geology.* 125, 104880. doi:10.1016/j.marpetgeo.2020.104880

Hou, Q. J., Jin, Q., Li, P. P., Jiang, W. M., Zhang, F. J., and Tian, F. (2017). A Computational Method for Determining Oil Expulsion Efficiency Based on the

Ideal Effective Oil Expulsion Mode. *J. Petrol. Explor Prod. Technol.* 7, 925–931. doi:10.1007/s13202-017-0337-z

Hu, S. Y., Zhao, W. Z., Hou, L. H., Yang, Z., Zhu, R. K., Wu, S. T., et al. (2020). Development Potential and Technical Strategy of continental Shale Oil in China. *Pet. Exploration Develop.* 47 (4), 877–887. doi:10.1016/S1876-3804(20)60103-3

Hu, T., Pang, X. Q., Jiang, F. J., Wang, Q. F., Liu, X. H., Wang, Z., et al. (2021). Movable Oil Content Evaluation of Lacustrine Organic-Rich Shales: Methods and a Novel Quantitative Evaluation Model. *Earth-Science Rev.* 214, 103545. doi:10.1016/j.earscirev.2021.103545

Hu, T., Pang, X. Q., Jiang, S., Wang, Q. F., Zheng, X. W., Ding, X. G., et al. (2018). Oil Content Evaluation of Lacustrine Organic-Rich Shale with strong Heterogeneity: A Case Study of the Middle Permian Lucaogou Formation in Jimusaer Sag, Junggar Basin, NW China. *Fuel* 221, 196–205. doi:10.1016/j.fuel.2018.02.082

Hu, W. X., Yao, S. P., Lu, X. C., Wu, H. G., Sun, F. N., and Jin, J. (2019). Effects of Organic Matter Evolution on Oil Reservoir Property During Diagenesis of Typical Continental Shale Sequences. *Oil Gas Geology.* 40 (05), 947–956. doi:10.11743/ogg20190501 (in Chinese with English Abstract).

Huang, D. F. (1996). Advances in Hydrocarbon Generation Theory –(I) Immature Oils and Generating Hydrocarbon and Evolutionary Model. *Adv. Earth Sci.* (4), 2–10. (in Chinese with English Abstract).

Huang, W. B., Salad Hersi, O., Lu, S. F., and Deng, S. W. (2017). Quantitative Modelling of Hydrocarbon Expulsion and Quality Grading of Tight Oil Lacustrine Source Rocks: Case Study of Qingshankou 1 Member, central Depression, Southern Songliao Basin, China. *Mar. Pet. Geology.* 84, 34–48. doi:10.1016/j.marpetgeo.2017.03.021

Huang, Z. K., Hao, Y. Q., Li, S. J., Wo, Y. J., Sun, D. S., Li, M. W., et al. (2020). Oil-bearing Potential, Mobility Evaluation and Significance of Shale Oil in Chang 7 Shale System in the Ordos Basin: A Case Study of Well H317. *Geology. China* 47 (01), 210–219. doi:10.12029/gc20200117 (in Chinese with English Abstract).

Jarvie, D. M. (2014). Components and Processes Affecting Producibility and Commerciality of Shale Resource Systems. *Geologica Acta* 12 (4), 307–325. doi:10.1344/GeologicaActa2014.12.4.3

Jarvie, D. M. (2012). "Shale Resource Systems for Oil and GasPart 2 Shale-Oil Resource Systems," in *Shale Reservoirs-Giant Resources for the 21st century.* Editor J. A. Breyer (Tulsa: American Association of Petroleum Geologists), 97, 89–119. doi:10.1306/13321447M973489

Jiang, C. Q., Chen, Z. H., Mort, A., Milovic, M., Robinson, R., Stewart, R., et al. (2016). Hydrocarbon Evaporative Loss from Shale Core Samples as Revealed by Rock-Eval and Thermal Desorption-Gas Chromatography Analysis: Its Geochemical and Geological Implications. *Mar. Pet. Geology.* 70, 294–303. doi:10.1016/j.marpetgeo.2015.11.021

Jiang, N. H., Jia, F. Y., and Shen, J. M. (1986). The Primary Oil Migration and Effective Hydrocarbon Expelling Thickness of Source Rocks in Biyang Depression. *Pet. Explor. Dev.* (2), 19–24. (in Chinese with English Abstract).

Jiang, Q. G., Li, M. W., Ma, Y. Y., Cao, T. T., Liu, P., Qian, M. H., et al. (2018). Molecular Geochemical Evaluation of Shale Oil Mobility: A Case Study of Shale Oil in Jiyang Depression. *Pet. Geology. Exp.* 40 (06), 849–854. doi:10.11781/sysydz201806849 (in Chinese with English Abstract).

Jiang, Q. G., Li, M. W., Qian, M. H., Li, Z. M., Li, Z., Huang, Z. K., et al. (2016). Quantitative Characterization of Shale Oil in Different Occurrence States and its Application. *Pet. Geology. Exp.* 38 (06), 842–849. doi:10.11781/sysydz201606842 (in Chinese with English Abstract).

Jiang, Z. X., Li, T. W., Gong, H. J., Jiang, T., Chang, J. Q., Ning, C. X., et al. (2020). Characteristics of Low-Mature Shale Reservoirs in Zhanhua Sag and Their Influence on the Mobility of Shale Oil. *Acta Petrolei Sinica* 41 (12), 1587–1600. doi:10.7623/syxb202012011 (in Chinese with English Abstract).

Jin, J., Yang, Z., Chen, X. K., Li, L. L., Yang, H. X., Ju, Y. W., et al. (2021). Characteristics of Micro/nano Pores and Hydrocarbon Accumulation in a continental Shale Oil Reservoir-A Case Study of the Lucaogou Formation in the Jimsar Sag, Junggar Basin, Northwest China. *j nanosci nanotechnol* 21 (1), 262–273. doi:10.1166/jnn.2021.18749

Kelemen, S. R., Walters, C. C., Ertas, D., Freund, H., and Curry, D. J. (2006). Petroleum Expulsion Part 3. A Model of Chemically Driven Fractionation during Expulsion of Petroleum from Kerogen. *Energy Fuels* 20 (1), 309–319. doi:10.1021/ef058023s

Khatibi, S., Ostadhassan, M., Xie, Z. H., Gentzis, T., Bubach, B., Gan, Z., et al. (2019). NMR Relaxometry A New Approach to Detect Geochemical Properties of Organic Matter in Tight Shales. *Fuel* 235, 167–177. doi:10.1016/j.fuel.2018.07.100

Kumar, S., Ojha, K., Bastia, R., Garg, K., Das, S., and Mohanty, D. (2017). Evaluation of Eocene Source Rock for Potential Shale Oil and Gas Generation in north Cambay Basin, India. *Mar. Pet. Geology.* 88, 141–154. doi:10.1016/j.marpetgeo.2017.08.015

Larsen, J. W., and Li, S. (1997). An Initial Comparison of the Interactions of Type I and III Kerogens with Organic Liquids. *Org. Geochem.* 26 (5–6), 305–309. doi:10.1016/S0146-6380(97)00016-8

Larsen, J. W., and Li, S. (1994). Solvent Swelling Studies of Green River Kerogen. *Energy Fuels* 8 (4), 932–936. doi:10.1021/ef00046a017

Larsen, J. W., Parikh, H., and Michels, R. (2002). Changes in the Cross-Link Density of Paris Basin Toarcian Kerogen During Maturation. *Org. Geochem.* 33 (10), 1143–1152. doi:10.1016/S0146-6380(02)00102-X

Lewan, M. D., and Roy, S. (2011). Role of Water in Hydrocarbon Generation from Type-I Kerogen in Mahogany Oil Shale of the Green River Formation. *Org. Geochem.* 42 (1), 31–41. doi:10.1016/j.orggeochem.2010.10.004

Leythaeuser, D., Mackenzie, A., Schaefer, R. G., and BjorØy, M. (1984). A Novel Approach for Recognition and Quantification of Hydrocarbon Migration Effects in Shale-sandstone Sequences. *AAPG Bull.* 68 (2), 196–219. doi:10.1306/AD4609FE-16F7-11D7-8645000102C1865D

Li, C. R., Pang, X. Q., Huo, Z. P., Wang, E. Z., and Xue, N. (2020). A Revised Method for Reconstructing the Hydrocarbon Generation and Expulsion History and Evaluating the Hydrocarbon Resource Potential: Example from the First Member of the Qingshankou Formation in the Northern Songliao Basin, Northeast China. *Mar. Pet. Geology.* 121, 104577. doi:10.1016/j.marpetgeo.2020.104577

Li, H., Lu, J. L., Wang, B. H., Lu, K., Zhou, Y., Wang, M., et al. (2020). Critical Controlling Factors of Enrichment and High-Yield of Land Shale Oil. *Geoscience* 34 (04), 837–848. doi:10.19657/j.geoscience.1000-8527.2020.04.19 (in Chinese with English Abstract).

Li, J. B., Huang, W. B., Lu, S. F., Wang, M., Chen, G. H., Tian, W. C., et al. (2018). Nuclear Magnetic Resonance T1-T2 Map Division Method for Hydrogen-Bearing Components in Continental Shale. *Energy Fuels* 32 (9), 9043–9054. doi:10.1021/acs.energyfuels.8b01541

Li, J. B., Jiang, C. Q., Wang, M., Lu, S. F., Chen, Z. H., Chen, G. H., et al. (2020a). Adsorbed and Free Hydrocarbons in Unconventional Shale Reservoir: A New Insight from NMR T1-T2 Maps. *Mar. Pet. Geology.* 116, 104311. doi:10.1016/j.marpetgeo.2020.104311

Li, J. J., Wang, W. M., Cao, Q., Shi, Y. L., Yan, X. T., and Tian, S. S. (2015). Impact of Hydrocarbon Expulsion Efficiency of Continental Shale Upon Shale Oil Accumulations in Eastern China. *Mar. Pet. Geol.* 59, 467–479. doi:10.1016/j.marpetgeo.2014.10.002

Li, J. J., Liu, Z., Li, J. Q., Lu, S. F., Zhang, T. Q., Zhang, X. W., et al. (2018). Fractal Characteristics of Continental Shale Pores and its Significance to the Occurrence of Shale Oil in China: A Case Study of Biyang Depression. *Fractals* 26 (2), 1840008. doi:10.1142/S0218348X1840008X

Li, J. Q., Lu, S. F., Cai, J. C., Zhang, P. F., Xue, H. T., and Zhao, X. B. (2018). Adsorbed and Free Oil in Lacustrine Nanoporous Shale: A Theoretical Model and A Case Study. *Energy Fuels* 32 (12), 12247–12258. doi:10.1021/acs.energyfuels.8b02953

Li, J. Q., Lu, S. F., Xie, L. J., Zhang, J., Xue, H. T., Zhang, P. F., et al. (2017). Modeling of Hydrocarbon Adsorption on continental Oil Shale: A Case Study on N-Alkane. *Fuel* 206, 603–613. doi:10.1016/j.fuel.2017.06.017

Li, J., Ma, W., Wang, Y. F., Wang, D. L., Xie, Z. Y., Li, Z. S., et al. (2018). Modeling of the Whole Hydrocarbon-Generating Process of Sapropelic Source Rock. *Pet. Exploration Develop.* 45 (03), 461–471. doi:10.1016/S1876-3804(18)30051-X

Li, J. B., Wang, M., Chen, Z. H., Lu, S. F., Jiang, C. Q., Chen, G. H., et al. (2019). Evaluating the Total Oil Yield Using a Single Routine Rock-Eval experiment on As-Received Shales. *J. Anal. Appl. Pyrolysis* 144, 104707. doi:10.1016/j.jaap.2019.104707

Li, J. B., Wang, M., Lu, S. F., Chen, G. H., Tian, W. C., Jiang, C. Q., et al. (2020b). A New Method for Predicting Sweet Spots of Shale Oil Using Conventional Well Logs. *Mar. Pet. Geology.* 113, 104097. doi:10.1016/j.marpetgeo.2019.104097

Li, J., Wang, Y. F., Ma, W., Wang, D. L., Ma, C. H., and Li, Z. S. (2015). Evaluation on Occluded Hydrocarbon in Deep-Ultra Deep Ancient Source Rocks and its

Cracked Gas Resources. *Nat. Gas Industry B* 2 (6), 499–505. doi:10.1016/j.ngib.2015.12.003

Li, M. W., Chen, Z. H., Ma, X. X., Cao, T. T., Li, Z. M., and Jiang, Q. G. (2018). A Numerical Method for Calculating Total Oil Yield Using a Single Routine Rock-Eval Program: A Case Study of the Eocene Shahejie Formation in Dongying Depression, Bohai Bay Basin, China. *Int. J. Coal Geology.* 191, 49–65. doi:10.1016/j.coal.2018.03.004

Li, M. W., Chen, Z. H., Ma, X. X., Cao, T. T., Qian, M. H., Jiang, Q. G., et al. (2019a). Shale Oil Resource Potential and Oil Mobility Characteristics of the Eocene-Oligocene Shahejie Formation, Jiyang Super-depression, Bohai Bay Basin of China. *Int. J. Coal Geology.* 204, 130–143. doi:10.1016/j.coal.2019.01.013

Li, M. W., Chen, Z. H., Qian, M. H., Ma, X. X., Jiang, Q. G., Li, Z. M., et al. (2020). What Are in Pyrolysis S1 Peak and what Are Missed? Petroleum Compositional Characteristics Revealed from Programed Pyrolysis and Implications for Shale Oil Mobility and Resource Potential. *Int. J. Coal Geology.* 217, 103321. doi:10.1016/j.coal.2019.103321

Li, M. W., Ma, X. X., Jiang, Q. G., Li, Z. M., Pang, X. Q., and Zhang, C. T. (2019b). Enlightenment from Formation Conditions and Enrichment Characteristics of Marine Shale Oil in North America. *Pet. Geology. Recovery Efficiency* 26 (1), 13–28. doi:10.13673/j.cnki.cn37-1359/te.2019.01.002 (in Chinese with English Abstract).

Li, T. W., Jiang, Z. X., Xu, C. L., Liu, B., Liu, G. H., Wang, P. F., et al. (2017). Effect of Pore Structure on Shale Oil Accumulation in the Lower Third Member of the Shahejie Formation, Zhanhua Sag, Eastern China: Evidence from Gas Adsorption and Nuclear Magnetic Resonance. *Mar. Pet. Geology.* 88, 932–949. doi:10.1016/j.marpetgeo.2017.09.030

Li, X. N., Ren, J. H., Xin, M., Liang, H., Zhang, P., Ma, Q., et al. (2017). Discussions on Movable Hydrocarbons in Source-Rock Oil in the Second Member of Permian Lucaogou Formation, Santanghu Basin. *Xinjiang Pet. Geology.* 38 (03), 296–301. doi:10.7657/XJPG20170307 (in Chinese with English Abstract).

Li, Z. (2020). Comparison of oil-bearing properties and oil mobility of shale with different lithologies in continental basins: a case study of the upper fourth member of Paleogene Shahejie Formation in Dongying Sag, Bohai Bay Basin. *Petrol. Geol. Exp.* 42, 545–595. doi:10.11781/sysydz202004545 (in Chinese with English Abstract)

Li, Z., Zou, Y.-R., Xu, X.-Y., Sun, J.-N., Li, M., and Peng, P. A. (2016). Adsorption of Mudstone Source Rock for Shale Oil - Experiments, Model and a Case Study. *Org. Geochem.* 92, 55–62. doi:10.1016/j.orggeochem.2015.12.009

Liang, C., Cao, Y., Jiang, Z. X., Wu, J., Song, G. Q., and Wang, Y. S. (2017). Shale Oil Potential of Lacustrine Black Shale in the Eocene Dongying Depression: Implications for Geochemistry and Reservoir Characteristics. *AAPG Bull.* 101 (11), 1835–1858. doi:10.1306/01251715249

Liang, X. P., Jin, Z. J., Shpilman, A., Yin, J. Y., Liu, Q. Y., and Uspensky, B. (2019). Geological Characteristics and Latest Progress in Exploration and Development of Russian Shale Oil. *Oil Gas Geology.* 40 (03), 478–490. doi:10.11743/ogg20190304 (in Chinese with English Abstract).

Lin, H. X., Song, M. S., Wang, S. Z., and Zhang, K. H. (2020). Shale Oil Resource Evaluation in Complex Structural Belt of Superimposed Basin: A Case Study of Middle Permian Lucaogou Formation in Bogda Area,southeast Margin of Junggar Basin. *Pet. Geology. Recovery Efficiency* 27 (02), 7–17. doi:10.13673/j.cnki.cn37-1359/te.2020.02.002 (in Chinese with English Abstract).

Liu, B., Bai, L. H., Chi, Y. A., Jia, R., Fu, X. F., and Yang, L. (2019). Geochemical Characterization and Quantitative Evaluation of Shale Oil Reservoir by Two-Dimensional Nuclear Magnetic Resonance and Quantitative Grain Fluorescence on Extract: A Case Study from the Qingshankou Formation in Southern Songliao Basin, Northeast China. *Mar. Pet. Geology.* 109, 561–573. doi:10.1016/j.marpetgeo.2019.06.046

Liu, B., Shi, J. X., Fu, X. F., Lv, Y. F., Sun, X. D, Gong, L., et al. (2018). Petrological Characteristics and Shale Oil Enrichment of Lacustrine fine-grained Sedimentary System: A Case Study of Organic-Rich Shale in First Member of Cretaceous Qingshankou Formation in Gulong Sag, Songliao Basin, NE China. *Pet. Exploration Develop.* 45 (05), 884–894. doi:10.1016/s1876-3804(18)30091-0

Liu, B., Sun, J. H., Zhang, Y. Q., He, J. L., Fu, X. F., Yang, L., et al. (2021). Reservoir Space and Enrichment Model of Shale Oilin the First Member of Cretaceous Qingshankou Formationin the Changling Sag, Southern Songliao Basin, NE China. *Pet. Explor. Dev.* 48 (03), 521–535. doi:10.1016/s1876-3804(21)60049-6

Liu, C., Lu, S. F., and Xue, H. T. (2014). Variable-coefficient ΔlogR Model and its Application in Shale Organic Evaluation. *Prog. Geophys.* 29 (01), 312–317. doi:10.6038/pg20140144

Liu, H. M., Zhang, S., Bao, S. Y., Fang, Z. W., Yao, S. P., and Wang, Y. (2019). Geological Characteristics and Effectiveness of the Shale Oil Reservoir in Dongying Sag. *Oil Gas Geology.* 40 (3), 512–523. doi:10.11743/ogg20190307 (in Chinese with English Abstract).

Liu, X. P., Lai, J., Fan, X. C., Shu, H. L., Wang, G. C., Ma, X. Q., et al. (2020). Insights in the Pore Structure, Fluid Mobility and Oiliness in Oil Shales of Paleogene Funing Formation in Subei Basin, China. *Mar. Pet. Geol.* 114, 104228. doi:10.1016/j.marpetgeo.2020.104228

Liu, X. P., Zhan, J.-H., Lai, D. G., Liu, X. X., Zhang, Z. J., and Xu, G. W. (2015). Initial Pyrolysis Mechanism of Oil Shale Kerogen with Reactive Molecular Dynamics Simulation. *Energy Fuels* 29 (5), 2987–2997. doi:10.1021/acs.energyfuels.5b00084

Liu, X. Y., and Zhang, D. X. (2019). A Review of Phase Behavior Simulation of Hydrocarbons in Confined Space: Implications for Shale Oil and Shale Gas. *J. Nat. Gas Sci. Eng.* 68, 102901. doi:10.1016/j.jngse.2019.102901

Liu, Y. S., Dong, X. H., Chen, Z. X., Hou, Y. N., Luo, Q. L., and Chen, Y. H. (2021). A Novel Experimental Investigation on the Occurrence State of Fluids in Microscale Pores of Tight Reservoirs. *J. Pet. Sci. Eng.* 196, 107656. doi:10.1016/j.petrol.2020.107656

Lu, S. F., Huang, W. B., Chen, F. W., Li, J. J., Wang, M., Xue, H. T., et al. (2012). Classification and Evaluation Criteria of Shale Oil and Gas Resources: Discussion and Application. *Pet. Exploration Develop.* 39 (2), 268–276. doi:10.1016/S1876-3804(12)60042-1

Ma, W., Li, J., Wang, D. L., Wang, Y. F., Ma, C. H., Wang, Z. H., et al. (2016). Hydrocarbon Expulsion Efficiency of Source Rocks and its Influencing Factors. *Nat. Gas Geosci.* 27 (09), 1742–1751. doi:10.11764/j.issn.1672-1926.2016.09.1742 (in Chinese with English Abstract).

Ma, Z. L., Zheng, L. J., Yu, X. L., Zhao, Z. J., and Li, Z. M. (2018). Effective Oil Expulsion Threshold of Argillaceous Source Rocks and Geological Significance of Shale Oil. *J. China Univ. Pet. (Edition Nat. Science)* 42 (1), 32–39. doi:10.3969/j.issn.1673-5005.2018.01.004 (in Chinese with English Abstract).

Maende, A. (2016). Wildcat Compositional Analysis for Conventional and Unconventional Reservoir Assessments, HAWK Petroleum Assessment Method (HAWK-PAM). Appl. Note 052016-1, 11p, Texas, Wildcat Technologies. Available at: https://www.wildcattechnologies.com/hawk-pam-petroleum-assessment.

Milliken, K. L., Zhang, T. W., Chen, J. P., and Ni, Y. Y. (2021). Mineral Diagenetic Control of Expulsion Efficiency in Organic-Rich Mudrocks, Bakken Formation (Devonian-Mississippian), Williston Basin, North Dakota, U.S.A. *Mar. Pet. Geology.* 127, 104869. doi:10.1016/j.marpetgeo.2020.104869

Mohammadi, M., and Sedighi, M. (2013). Modification of Langmuir Isotherm for the Adsorption of Asphaltene or Resin onto Calcite Mineral Surface: Comparison of Linear and Non-linear Methods. *Prot. Met. Phys. Chem. Surf.* 49 (4), 460–470. doi:10.1134/S2070205113040205

Nicot, B., Vorapalawut, N., Rousseau, B., Madariaga, L. F., Hamon, G., and Korb, J. P. (2016). Estimating Saturations in Organic Shales Using 2D NMR. *Petrophysics* 57 (1), 19–29.

Nie, H. K., Zhang, P. X., Bian, D. K., Wu, X. L., and Zhai, C. B. (2016). Oil Accumulation Characteristics of China continental Shale. *Earth Sci. Front.* 23 (02), 55–62. doi:10.13745/j.esf.2016.02.007 (in Chinese with English Abstract).

Nielsen, S. B., Clausen, O. R., and McGregor, E. (2017). basin%Ro: A Vitrinite Reflectance Model Derived from Basin and Laboratory Data. *Basin Res.* 29, 515–536. doi:10.1111/bre.12160

Ning, C. X., Ma, Z. L., Jiang, Z. X., Su, S. Y., Li, T. W., Zheng, L. J., et al. (2020). Effect of Shale Reservoir Characteristics on Shale Oil Movability in the Lower Third Member of the Shahejie Formation, Zhanhua Sag. *Acta Geologica Sinica - English Edition* 94 (02), 352–363. doi:10.1111/1755-6724.14284

Ougier-Simonin, A., Renard, F., Boehm, C., and Vidal-Gilbert, S. (2016). Microfracturing and Microporosity in Shales. *Earth-Science Rev.* 162, 198–226. doi:10.1016/j.earscirev.2016.09.006

Pan, S. Q., Zou, C. N., Li, J., Yang, Z., Liu, E., and Han, Y. (2019). Unconventional Shale Systems: A Comparative Study of the "In-Source Sweet Spot" Developed in the Lacustrine Chang 7 Shale and the marine Barnett Shale. *Mar. Pet. Geology.* 100, 540–550. doi:10.1016/j.marpetgeo.2018.12.015

Panahi, H., Kobchenko, M., Meakin, P., Dysthe, D. K., and Renard, F. (2019). Fluid Expulsion and Microfracturing During the Pyrolysis of an Organic Rich Shale. *Fuel* 235, 1–16. doi:10.1016/j.fuel.2018.07.069

Pang, X. Q., Li, M. W., Li, S. M., and Jin, Z. J. (2005). Geochemistry of Petroleum Systems in the Niuzhuang South Slope of Bohai Bay Basin: Part 3. Estimating Hydrocarbon Expulsion from the Shahejie Formation. *Org. Geochem.* 36, 497–510. doi:10.1016/j.orggeochem.2004.12.001

Pathak, M., Kweon, H., Deo, M., and Huang, H. (2017). Kerogen Swelling and Confinement: Its Implication on Fluid Thermodynamic Properties in Shales. *Sci. Rep.* 7, 12530. doi:10.1038/s41598-017-12982-4

Peng, W. L., Hu, G. Y., Liu, Q. Y., Jia, N., Fang, C. C., Gong, D. Y., et al. (2018). Research Status on Thermal Simulation Experiment and Several Issues of Concern. *J. Nat. Gas Geosci.* 3 (5), 283–293. doi:10.1016/j.jnggs.2018.11.006

Pepper, A. S. (1991). Estimating the Petroleum Expulsion Behaviour of Source Rocks: A Novel Quantitative Approach. *Geol. Soc. Lond. Spec. Publications* 59, 9–31. doi:10.1144/GSL.SP.1991.059.01.02

Peters, K. E., Burnham, A. K., Walters, C. C., and Schenk, O. (2018). Guidelines for Kinetic Input to Petroleum System Models from Open-System Pyrolysis. *Mar. Pet. Geology.* 92, 979–986. doi:10.1016/j.marpetgeo.2017.11.024

Piedrahita, J., and Aguilera, R. (2017). "Estimating Oil Saturation Index OSI from NMR Logging and Comparison with Rock-Eval Pyrolysis Measurements in a Shale Oil Reservoir," in The SPE Unconventional Resources Conference, Calgary, AB, Canada, February 15–16, 2017. doi:10.2118/185073-MS

Qian, K.-R., He, Z.-L., Liu, X.-W., and Chen, Y.-Q. (2018). Intelligent Prediction and Integral Analysis of Shale Oil and Gas Sweet Spots. *Pet. Sci.* 15, 744–755. doi:10.1007/s12182-018-0261-y

Qian, M. H., Jiang, Q. G., Li, M. W., Li, Z. M., Liu, P., Ma, Y. Y., et al. (2017). Quantitative Characterization of Extractable Organic Matter in Lacustrine Shale with Different Occurrences. *Pet. Geology. Exp.* 39 (02), 278–286. doi:10.11781/sysydz201702278 (in Chinese with English Abstract).

Qian, M. H., Jiang, Q. G., Li, M. W., Li, Z. M., and Liu, P. (2020). Three-dimensional Quantitative Fluorescence Analysis and Application in Shale. *Pet. Geology. Exp.* 42 (02), 311–318. doi:10.11781/sysydz202002311 (in Chinese with English Abstract).

Qiu, Z., Lu, B., Qiu, Z. S., Dong, D. Z., Wang, H. Y., Zhou, J., et al. (2016). Residual Accumulation and Resource Assessment of Shale Oil from the Permian Lucaogou Formation in Jimusar Sag. *Nat. Gas Geosci.* 27 (10), 1817–1827. doi:10.11764/j.issn.1672-1926.2016.10.1817 (in Chinese with English Abstract).

Raji, M., Gröcke, D. R., Greenwell, H. C., Gluyas, J. G., and Cornford, C. (2015). The Effect of Interbedding on Shale Reservoir Properties. *Mar. Pet. Geology.* 67, 154–169. doi:10.1016/j.marpetgeo.2015.04.015

Ribeiro, R. C., Correia, J. C. G., and Seidl, P. R. (2009). The Influence of Different Minerals on the Mechanical Resistance of Asphalt Mixtures. *J. Pet. Sci. Eng.* 65 (3-4), 171–174. doi:10.1016/j.petrol.2008.12.025

Ritter, U. (2003). Solubility of Petroleum Compounds in Kerogen. *Org. Geochem.* 34 (3), 319–326. doi:10.1016/S0146-6380(02)00245-0

Romero-Sarmiento, M.-F. (2019). A Quick Analytical Approach to Estimate Both Free Versus Sorbed Hydrocarbon Contents in Liquid-Rich Source Rocks. *AAPG Bull.* 103, 2031–2043. doi:10.1306/02151918152

Sandvik, E. I., Young, W. A., and Curry, D. J. (1992). Expulsion from Hydrocarbon Sources: The Role of Organic Absorption. *Org. Geochem.* 19 (1-3), 77–87. doi:10.1016/0146-6380(92)90028-V

Scheeder, G., Weniger, P., and Blumenberg, M. (2020). Geochemical Implications from Direct Rock-Eval Pyrolysis of Petroleum. *Org. Geochem.* 146, 104051. doi:10.1016/j.orggeochem.2020.104051

Shao, D. Y., Zhang, T. W., Ko, L. T., Li, Y. F., Yan, J. P., Zhang, L. L., et al. (2020). Experimental Investigation of Oil Generation, Retention, and Expulsion Within Type II Kerogen-Dominated Marine Shales: Insights from Gold-Tube Nonhydrous Pyrolysis of Barnett and Woodford Shales Using Miniature Core Plugs. *Int. J. Coal Geology.* 217, 103337. doi:10.1016/j.coal.2019.103337

Soeder, D. J., and Borglum, S. J. (2020). "Part II the Future of Fossil Fuels," in *The Fossil Fuel Revolution: Shale Gas and Tight Oil*. Editors D. J. Soeder and S. J. Borglum (New York, NY: Elsevier), 173–174. doi:10.1016/B978-0-12-815397-0.02002-4

Soeder, D. J., and Borglum, S. J. (2019). "Unconventional Tight Oil and Shale Gas Resources," in *The Fossil Fuel Revolution: Shale Gas and Tight Oil*. Editors

D. J. Soeder and S. J. Borglum (New York, NY: Elsevier), 31–61. doi:10.1016/B978-0-12-815397-0.00003-3

Solarin, S. A. (2020). The Effects of Shale Oil Production, Capital and Labour on Economic Growth in the United States: A Maximum Likelihood Analysis of the Resource Curse Hypothesis. *Resour. Pol.* 68, 101799. doi:10.1016/j.resourpol.2020.101799

Song, D. J., Wang, X. Q., Tuo, J. C., Wu, C. J., Zhang, M. F., Su, L., et al. (2021a). A Comprehensive Study on the Impacts of Rock Fabric on Hydrocarbon Generation and Pore Structure Evolution of Shale Under Semi-confined Condition. *Mar. Pet. Geology.* 124, 104830. doi:10.1016/j.marpetgeo.2020.104830

Song, D. J., Wang, X. Q., Wu, C. J., Meng, S. W., Zhang, M. F., Li, H. D., et al. (2021b). Petroleum Generation, Retention, and Expulsion in Lacustrine Shales Using an Artificial thermal Maturation Approach: Implications for the Iin-Ssitu Conversion of Shale Oil. *Energy Fuels* 35 (1), 358–373. doi:10.1021/acs.energyfuels.0c03045

Song, L. P., Xue, H. T., Lu, S. F., and Tian, S. S. (2015). The Research Progress on the Occurrence Mechanism of Detained Hydrocarbon. *Acta Geologica Sinica - English Edition* 89 (S1), 164–165. doi:10.1111/1755-6724.12303_6

Song, M. S., Liu, H. M., Wang, Y., and Liu, Y. L. (2020). Enrichment Rules and Exploration Practices of Paleogene Shale Oil in Jiyang Depression, Bohai Bay Basin, China. *Pet. Exploration Develop.* 47 (02), 242–253. doi:10.1016/S1876-3804(20)60043-X

Song, Y.-Q., and Kausik, R. (2019). NMR Application in Unconventional Shale Reservoirs - A New Porous Media Research Frontier. *Prog. Nucl. Magn. Reson. Spectrosc.* 112-113, 17–33. doi:10.1016/j.pnmrs.2019.03.002

Spigolon, A. L. D., Lewan, M. D., de Barros Penteado, H. L., Coutinho, L. F. C., and Mendonça Filho, J. G. (2015). Evaluation of the Petroleum Composition and Quality with Increasing thermal Maturity as Simulated by Hydrous Pyrolysis: A Case Study Using a Brazilian Source Rock with Type I Kerogen. *Org. Geochem.* 83-84, 27–53. doi:10.1016/j.orggeochem.2015.03.001

Stainforth, J. G. (2009). Practical Kinetic Modeling of Petroleum Generation and Expulsion. *Mar. Pet. Geology.* 26 (4), 552–572. doi:10.1016/j.marpetgeo.2009.01.006

Stockhausen, M., Galimberti, R., Elias, R., Di Paolo, L., and Schwark, L. (2021). Expulsinator Assessment of Oil/Gas Generation and Expulsion Characteristics of Different Source Rocks. *Mar. Pet. Geology.* 129, 105057. doi:10.1016/j.marpetgeo.2021.105057

Su, K. M., Lu, J. G., Zhang, H. X., Chen, S. J., Li, Y., Xiao, Z. L., et al. (2020). Quantitative Study on Hydrocarbon Expulsion Mechanism Based on Micro-fracture. *Geosci. Front.* 11 (6), 1901–1913. doi:10.1016/j.gsf.2020.05.013

Su, S. Y., Jiang, Z. X., Shan, X. L., Ning, C. X., Zhu, Y. F., Wang, X. Y., et al. (2019). Effect of Lithofacies on Shale Reservoir and Hydrocarbon Bearing Capacity in the Shahejie Formation, Zhanhua Sag, Eastern China. *J. Pet. Sci. Eng.* 174, 1303–1308. doi:10.1016/j.petrol.2018.11.048

Su, S. Y., Jiang, Z. X., Shan, X. L., Zhang, C. W., Zou, Q. T., Li, Z., et al. (2018). The Effects of Shale Pore Structure and Mineral Components on Shale Oil Accumulation in the Zhanhua Sag, Jiyang Depression, Bohai Bay Basin, China. *J. Pet. Sci. Eng.* 165, 365–374. doi:10.1016/j.petrol.2018.02.030

Sun, J., Xiao, X. M., Cheng, P., and Tian, H. (2019). Formation and Evolution of Nanopores in Shales and its Impact on Retained Oil During Oil Generation and Expulsion Based on Pyrolysis Experiments. *J. Pet. Sci. Eng.* 176, 509–520. doi:10.1016/j.petrol.2019.01.071

Sun, J., Xiao, X. M., Cheng, P., Wang, M., and Tian, H. (2021). The Relationship Between Oil Generation, Expulsion and Retention of Lacustrine Shales: Based on Pyrolysis Simulation Experiments. *J. Pet. Sci. Eng.* 196, 107625. doi:10.1016/j.petrol.2020.107625

Sun, L. D., Liu, H., He, W. Y., Li, G. X., Zhang, S. C., Zhu, R. K., et al. (2021). An Analysis of Major Scientific Problems and Research Paths of Gulong Shale Oil in Daqing Oilfield, NE China. *Pet. Exploration Develop.* 48 (3), 527–540. doi:10.1016/S1876-3804(21)60043-5

Sweeney, J. J., and Burnham, A. K. (1990). Evaluation of a Simple Model of Vitrinite Reflectance Based on Chemical Kinetics. *AAPG Bull.* 74 (10), 1559–1570. doi:10.1306/0C9B251F-1710-11D7-8645000102C1865D

Tian, S. S., Erastova, V., Lu, S. F., Greenwell, H. C., Underwood, T. R., Xue, H. T., et al. (2018). Understanding Model Crude Oil Component Interactions on Kaolinite Silicate and Aluminol Surfaces: Toward Improved Understanding of Shale Oil Recovery. *Energy Fuels* 32 (2), 1155–1165. doi:10.1021/acs.energyfuels.7b02763

Tian, S. S., Liu, B., Fu, X. F., Zeng, F., Chi, Y. A., Wu, T., et al. (2020). *A Shale Oil Detection Method and System Based on Occurrence States*. Heilongjiang, China (in Chinese).

Tian, S. S., Xue, H. T., Lu, S. F., and Chen, G. H. (2014). "Discussion on the Mechanism of Different Types of Kerogen Remaining Oil and Gas," in *2014 Annual Meeting of Chinese Geoscience Union* (Beijing: Annual Meeting of Chinese Geoscience Union), 2509–2512. (in Chinese)

Tian, S. S., Xue, H. T., Lu, S. F., Zeng, F., Xue, Q. Z., Chen, G. H., et al. (2017). Molecular Simulation of Oil Mixture Adsorption Character in Shale System. *j nanosci nanotechnol* 17 (9), 6198–6209. doi:10.1166/jnn.2017.14487

Tissot, B. P., and Welte, D. H. (1984). "From Kerogen to Petroleum," in *Petroleum Formation and Occurrence* (Berlin: Springer-Verlag), 160–198. doi:10.1007/978-3-642-87813-8_10

US Energy Information Administration (2021). *US Crude Oil and Natural Gas Proved Reserves, Year-End 2019*. Washington, DC: U.S. Department of Energy.

US Energy Information Administration (2015). *World Shale Resource Assessments*. Washington, DC: U.S. Department of Energy.

Wang, B. Y., Liu, B., Sun, G. X., Bai, L. H., Chi, Y. A., Liu, Q., et al. (2021). Evaluation of the Shale Oil Reservoir and the Oil Enrichment Model for the First Member of the Lucaogou Formation, Western Jimusaer Depression, Junggar Basin, NW China. *ACS Omega* 6 (18), 12081–12098. doi:10.1021/acsomega.1c00756

Wang, E. Z., Feng, Y., Liu, G. Y., Chen, S. R., Wu, Z. Y., and Li, C. R. (2021). Hydrocarbon Source Potential Evaluation Insight into Source Rocks-A Case Study of the First Member of the Paleogene Shahejie Formation, Nanpu Sag, NE China. *Energ. Rep.* 7, 32–42. doi:10.1016/j.egyr.2020.11.099

Wang, E. Z., Liu, G. Y., Pang, X. Q., Li, C. Q., Zhao, Z. F., Feng, Y., et al. (2020). An Improved Hydrocarbon Generation Potential Method for Quantifying Hydrocarbon Generation and Expulsion Characteristics with Application Example of Paleogene Shahejie Formation, Nanpu Sag, Bohai Bay Basin. *Mar. Pet. Geology.* 112, 104106. doi:10.1016/j.marpetgeo.2019.104106

Wang, H., Wang, X. Q., Jin, X., and Cao, D. P. (2016). Molecular Dynamics Simulation of Diffusion of Shale Oils in Montmorillonite. *J. Phys. Chem. C* 120 (16), 8986–8991. doi:10.1021/acs.jpcc.6b01660

Wang, K., Zha, M., and Qu, J. X. (2005). Quantitative Calculation of Hydrocarbon-Generation and Hydrocarbon-Expulsion Amounts in Consideration of Source Rock Heterogeneity. *Acta Petrolei Sinica* (03), 44–47. (in Chinese with English Abstract).

Wang, M., Guo, Z. Q., Jiao, C. X., Lu, S. F., Li, J. B., Xue, H. T., et al. (2019a). Exploration Progress and Geochemical Features of Lacustrine Shale Oils in China. *J. Pet. Sci. Eng.* 178, 975–986. doi:10.1016/j.petrol.2019.04.029

Wang, M., Lu, S. F., Dong, Q., Xue, H. T., and Huang, L. M. (2011). Comparison on Hydrocarbon Generation Kinetic Models. *J. China Univ. Pet. (Edition Nat. Science)* 35 (03), 12–18. (in Chinese with English Abstract).

Wang, M., Lu, S. F., Xue, H. T., Guo, X. B., Chen, G. H., Tian, S. S., et al. (2012). Bulk Pyrolysis and Chemical Kinetic Characteristics of Om Related to the Occurrence of Immature-Low Mature Oils. *Energy Exploration & Exploitation* 30 (1), 71–88. doi:10.1260/0144-5987.30.1.71

Wang, M., Ma, R., Li, J. B., Lu, S. F., Li, C. M., Guo, Z. Q., et al. (2019b). Occurrence Mechanism of Lacustrine Shale Oil in the Paleogene Shahejie Formation of Jiyang Depression, Bohai Bay Basin, China. *Pet. Exploration Develop.* 46 (4), 833–846. doi:10.1016/S1876-3804(19)60242-9

Wang, M., Tian, S. S., Chen, G. H., Xue, H. T., Huang, A. H., and Wang, W. G. (2014). Correction Method of Light Hydrocarbons Losing and Heavy Hydrocarbon Handling for Residual Hydrocarbon (S1) from Shale. *Acta Geologica Sinica - English Edition* 88 (06), 1792–1797. doi:10.1111/1755-6724.12345

Wang, M., Wilkins, R. W. T., Song, G., Zhang, L., Xu, X., Li, Z., et al. (2015). Geochemical and Geological Characteristics of the Es3L Lacustrine Shale in the Bonan Sag, Bohai Bay Basin, China. *Int. J. Coal Geology.* 138, 16–29. doi:10.1016/j.coal.2014.12.007

Wang, S., Feng, Q. H., Javadpour, F., Xia, T., and Li, Z. (2015a). Oil Adsorption in Shale Nanopores and its Effect on Recoverable Oil-In-Place. *Int. J. Coal Geology.* 147-148, 9–24. doi:10.1016/j.coal.2015.06.002

Wang, S., Feng, Q. H., Zha, M., Lu, S. F., Qin, Y., Xia, T., et al. (2015b). Molecular Dynamics Simulation of Liquid Alkane Occurrence State in Pores and Slits of Shale Organic Matter. *Pet. Exploration Develop.* 42 (6), 844–851. doi:10.1016/S1876-3804(15)30081-1

Wang, Y., Wang, X. J., Song, G. Q., Liu, H. M., Zhu, D. S., Zhu, D. Y., et al. (2016). Genetic Connection Between Mud Shale Lithofacies and Shale Oil Enrichment in Jiyang Depression, Bohai Bay Basin. *Pet. Exploration Develop.* 43 (5), 759–768. doi:10.1016/S1876-3804(16)30091-X

Wei, Z., Zou, Y.-R., Cai, Y., Wang, L., Luo, X., and Peng, P. A. (2012). Kinetics of Oil Group-type Generation and Expulsion: An Integrated Application to Dongying Depression, Bohai Bay Basin, China. *Org. Geochem.* 52, 1–12. doi:10.1016/j.orggeochem.2012.08.006

Wu, T., Pan, Z. J., Liu, B., Connell, L. D., Sander, R., and Fu, X. F. (2021). Laboratory Characterization of Shale Oil Storage Behavior: A Comprehensive Review. *Energy Fuels* 35 (9), 7305–7318. doi:10.1021/acs.energyfuels.0c04082

Xi, K. L., Li, K., Cao, Y. C., Lin, M. R., Niu, X. B., Zhu, R. K., et al. (2020). Laminae Combination and Shale Oil Enrichment Patterns of Chang 73 Sub-member Organic-Rich Shales in the Triassic Yanchang Formation, Ordos Basin, NW China. *Pet. Exploration Develop.* 47 (06), 1342–1353. doi:10.1016/S1876-3804(20)60142-8

Xiao, L. H., Meng, Y. L., Zhang, L. X., Wei, A. J., Li, J., Zhang, W. C., et al. (2005). Vitrinite Reflectance Modeling in the Over-pressured Formations. *Pet. Explor. Dev.* (01), 14–17. (in Chinese with English Abstract).

Xie, X. M., Krooss, B. M., Littke, R., Amann-Hildenbrand, A., Li, M. W., Li, Z. M., et al. (2019). Accessibility and Mobility of Hydrocarbons in Lacustrine Shale: Solvent Flow-Through Extraction Experiments on Eocene Oil Shales from Bohai Bay Basin, Eastern China. *Org. Geochem.* 127, 23–36. doi:10.1016/j.orggeochem.2018.11.006

Xu, Z. J., Liu, L. F., Liu, B. J. M., Wang, T. G., Zhang, Z. H., Wu, K. J., et al. (2019). Geochemical Characteristics of the Triassic Chang 7 Lacustrine Source Rocks, Ordos Basin, China: Implications for Paleoenvironment, Petroleum Potential and Tight Oil Occurrence. *J. Asian Earth Sci.* 178, 112–138. doi:10.1016/j.jseaes.2018.03.005

Xue, H. T., Tian, S. S., Lu, S. F., Zhang, W. H., Du, T. T., and Mu, G. D. (2015). Selection and Verification of Key Parameters in the Quantitative Evaluation of Shale Oil: A Case Study at the Qingshankou Formation, Northern Songliao Basin. *Bull. Mineralogy. Petrol. Geochem.* 34 (01), 70–78. doi:10.3969/j.issn.1007-2802.2015.01.008 (in Chinese with English Abstract).

Yang, L., and Jin, Z. J. (2019). Global Shale Oil Development and Prospects. *China Pet. Exploration* 24 (05), 553–559. doi:10.3969/j.issn.1672-7703.2019.05.002 (in Chinese with English Abstract).

Yang, Z., and Zou, C. N. (2019). "Exploring Petroleum inside Source Kitchen": Connotation and Prospects of Source Rock Oil and Gas. *Pet. Exploration Develop.* 46 (01), 181–193. doi:10.1016/S1876-3804(19)30018-7

Yang, Z., Zou, C. N., Wu, S. T., Lin, S. H., Pan, S. Q., Niu, X. B., et al. (2019). Formation, Distribution and Resource Potential of the "Sweet Areas (Sections)" of Continental Shale Oil in China. *Mar. Pet. Geol.* 102, 48–60. doi:10.1016/j.marpetgeo.2018.11.049

Yusupova, T. N., Romanova, U. G., Gorbachuk, V. V., Muslimov, R. K., and Romanov, G. V. (2002). Estimation of the Adsorption Capacity of Oil-Bearing Rocks: A Method and its Prospects. *J. Pet. Sci. Eng.* 33 (1–3), 173–183. doi:10.1016/S0920-4105(01)00184-X

Zeng, X., Cai, J. G., Dong, Z., Wang, X. J., and Hao, Y. Q. (2017). Sedimentary Characteristics and Hydrocarbon Generation Potential of Mudstone and Shale: A Case Study of Middle Submember of Member 3 and Upper Submember of Member 4 in Shahejie Formation in Dongying Sag. *Acta Petrolei Sinica* 38 (01), 31–43. doi:10.7623/syxb201701004 (in Chinese with English Abstract).

Zhang, D. W., Wang, L. H., Su, L., Wu, Y. D., Sun, R., Wu, C. J., et al. (2020). The Chemical Kinetics of the Semi-open Hydrous Pyrolysis System: Time Series Analysis of Lithostatic Pressure and Fluid Pressure. *Int. J. Coal Geology.* 220, 103418. doi:10.1016/j.coal.2020.103418

Zhang, H., Huang, H. P., Li, Z., and Liu, M. (2020). Comparative Study Between Sequential Solvent-Extraction and Multiple Isothermal Stages Pyrolysis: A Case Study on Eocene Shahejie Formation Shales, Dongying Depression, East China. *Fuel* 263, 116591. doi:10.1016/j.fuel.2019.116591

Zhang, L. Y., Xu, X. Y., Liu, Q., Kong, X. X., and Zhang, S. C. (2011). Hydrocarbon Formation and Accumulation of the Deep Paleogene of the Jiyang Depression, Shengli Oilfield. *Pet. Exploration Develop.* 38 (5), 530–537. doi:10.1016/S1876-3804(11)60053-0

Zhang, L. Y., Bao, S. Y., Li, J. Y., Li, Z., Zhu, R. F., Zhang, L., et al. (2015). Hydrocarbon and Crude Oil Adsorption Abilities of Minerals and Kerogens in Lacustrine Shales. *Pet. Geology. Exp.* 37 (6), 776–780. doi:10.11781/sysydz201506776 (in Chinese with English Abstract).

Zhang, P. F., Lu, S. F., Li, J. Q., and Chang, X. C. (2020). 1D and 2D Nuclear Magnetic Resonance (NMR) Relaxation Behaviors of Protons in clay, Kerogen and Oil-Bearing Shale Rocks. *Mar. Pet. Geology.* 114, 104210. doi:10.1016/j.marpetgeo.2019.104210

Zhang, P. L., Misch, D., Hu, F., Kostoglou, N., Sachsenhofer, R. F., Liu, Z. J., et al. (2021). Porosity Evolution in Organic Matter-Rich Shales (Qingshankou Fm.; Songliao Basin, NE China): Implications for Shale Oil Retention. *Mar. Pet. Geology.* 130, 105139. doi:10.1016/j.marpetgeo.2021.105139

Zhang, P. Y., Jiang, F. J., Zhu, C. X., Huang, R. D., Hu, T., Xu, T. W., et al. (2021). Gas Generation Potential and Characteristics of Oil-Prone Shale in the Saline Lacustrine Rifting Basins: A Case Study of the Dongpu Depression, Bohai Bay Basin. *Energy Fuels* 35, 2192–2208. doi:10.1021/acs.energyfuels.0c03965

Zhang, S. J., Li, Y. H., and Pu, H. (2020). Studies of the Storage and Transport of Water and Oil in Organic-Rich Shale Using Vacuum Imbibition Method. *Fuel* 266, 117096. doi:10.1016/j.fuel.2020.117096

Zhang, S., Liu, H. M., Song, G. Q., Wang, Y. S., Chen, S. Y., and Zhang, S. P. (2016). Genesis and Control Factors of Shale Oil Reserving Space in Dongying Sag. *Acta Petrolei Sinica* 37 (12), 1495–1507. doi:10.7623/syxb201612005 (in Chinese with English Abstract).

Zhang, W., Feng, Q. H., Wang, S., and Xing, X. D. (2019). Oil Diffusion in Shale Nanopores: Insight of Molecular Dynamics Simulation. *J. Mol. Liquids* 290, 111183. doi:10.1016/j.molliq.2019.111183

Zhang, W. Z., Yang, H., Li, J. F., and Ma, J. (2006). Leading Effect of High-Class Source Rock of Chang 7 in Ordos basin on Enrichment of Low Permeability Oil-Gas Accumulation-Hydrocarbon Generation and Expulsion Mechanism. *Pet. Explor. Dev.* 33 (3), 289–293. (in Chinese with English Abstract).

Zhao, W. Z., Hu, S. Y., and Hou, L. H. (2018). Connotation and Strategic Role of In-Situ Conversion Processing of Shale Oil Underground in the Onshore China. *Pet. Exploration Develop.* 45 (4), 563–572. doi:10.1016/S1876-3804(18)30063-6

Zhao, W. Z., Hu, S. Y., Hou, L. H., Yang, T., Li, X., Guo, B. C., et al. (2020). Types and Resource Potential of Continental Shale Oil in China and its Boundary with Tight Oil. *Pet. Exploration Develop.* 47 (1), 1–11. doi:10.1016/S1876-3804(20)60001-5

Zhao, W. Z., Zhang, B., Wang, X. M., Wu, S. T., Zhang, S. C., Liu, W., et al. (2021). Differences in Source Kitchens for Lacustrine In-Source and Out-Source Hydrocarbon Accumulations Onshore China. *Pet. Exploration Develop.* 48 (03), 464–475. doi:10.1016/s1876-3804(21)60044-7

Zhao, X. Y., Sang, Q., Li, Y. J., Shi, L. Y., Liu, H. M., and Dong, M. Z. (2021). Mobilization of Oil in Organic Matter and its Contribution to Oil Production During Primary Production in Shale. *Fuel* 287, 119449. doi:10.1016/j.fuel.2020.119449

Zhao, X. Z., Zhou, L. H., Pu, X. G., Jin, F. M., Shi, Z. N., Han, W. Z., et al. (2020). Formation Conditions and Enrichment Model of Retained Petroleum in Lacustrine Shale: A Case Study of the Paleogene in Huanghua Depression, Bohai Bay Basin, China. *Pet. Exploration Develop.* 47 (05), 916–930. doi:10.1016/S1876-3804(20)60106-9

Zhao, X. Z., Pu, X. G., Zhou, L. H., Jin, F. M., Han, H. M., Shi, Z. N., et al. (2021). Enrichment Theory, Exploration Technology and Prospects of Shale Oil in Lacustrine Facies Zone of Deep Basin: A Case Study of the Paleogene in Huanghua depression, Bohai Bay Basin. *Acta Petrolei Sinica* 42 (02), 143–162. doi:10.7623/syxb202102001 (in Chinese with English Abstract).

Zhao, X. Z., Zhou, L. H., Pu, X. G., Jin, F. M., Shi, Z. N., Xiao, D. Q., et al. (2019). Favorable Formation Conditions and Enrichment Characteristics of Lacustrine Facies Shale Oil in Faulted Lake basin: A Case Study of Member 2 of Kongdian Formation in Cangdong Sag,Bohai Bay Basin. *Acta Petrolei Sinica* 40 (09), 1013–1029. doi:10.7623/syxb201909001 (in Chinese with English Abstract).

Zhu, R. F., Zhang, L. Y., Li, J. Y., Liu, Q., Li, Z., Wang, R., et al. (2015). Quantitative Evaluation of Residual Liquid Hydrocarbons in Shale. *Acta Petrolei Sinica* 36 (01), 13–18. doi:10.7623/syxb201501002 (in Chinese with English Abstract).

Zhu, X. J., and Cai, J. G. (2012). Progress and Significance of Research on Relation Between Specific Surface Area and Organic Matter in Argillaceous Source Rocks. *Oil Gas Geology.* 33 (03), 375–384. (in Chinese with English Abstract).

Zink, K.-G., Scheeder, G., Stueck, H. L., Biermann, S., and Blumenberg, M. (2016). Total Shale Oil Inventory from an Extended Rock-Eval Approach on Non-extracted and Extracted Source Rocks from Germany. *Int. J. Coal Geology.* 163, 186–194. doi:10.1016/j.coal.2016.06.023

Zou, C. N., Jin, X., Zhu, R. K., Gong, G. M., Sun, L., Dai, J. X., et al. (2015). Do Shale Pore Throats Have a Threshold Diameter for Oil Storage? *Sci. Rep.* 5, 13619. doi:10.1038/srep13619

Zou, C. N., Ding, Y. H., Lu, Y. J., Liu, G. X., Chen, J. J., Wang, X., et al. (2017). Theory, Technology and Practice of "Man-made Reservoirs". *Pet. Explor. Dev.* 44 (1), 144–154. doi:10.1016/s1876-3804(17)30019-8

Zou, C. N., Pan, S. Q., Horsfield, B., Yang, Z., Hao, S. Y., Liu, E. T., et al. (2019a). Oil Retention and Intrasource Migration in the Organic-Rich Lacustrine Chang 7 Shale of the Upper Triassic Yanchang Formation, Ordos Basin, central China. *AAPG Bull.* 103 (11), 2627–2663. doi:10.1306/01301917052

Zou, C. N., Yang, Z., Cui, J. W., Zhu, R. K., Hou, L. H., Tao, S. Z., et al. (2013). Formation Mechanism, Geological Characteristics and Development Strategy of Nonmarine Shale Oil in China. *Pet. Exploration Develop.* 40 (1), 15–27. doi:10.1016/S1876-3804(13)60002-6

Zou, C. N., Zhu, R. K., Chen, Z.-Q., Ogg, J. G., Wu, S. T., Dong, D. Z., et al. (2019b). Organic-matter-rich Shales of China. *Earth-Science Rev.* 189, 51–78. doi:10.1016/j.earscirev.2018.12.002

Zou, Y.-R., Sun, J.-N., Li, Z., Xu, X., Li, M., and Peng, P. A. (2018). Evaluating Shale Oil in the Dongying Depression, Bohai Bay Basin, China, Using the Oversaturation Zone Method. *J. Pet. Sci. Eng.* 161, 291–301. doi:10.1016/j.petrol.2017.11.059

Heterogeneity Characteristics of Lacustrine Shale Oil Reservoir Under the Control of Lithofacies: A Case Study of the Dongyuemiao Member of Jurassic Ziliujing Formation, Sichuan Basin

Peng Li[1,2], Zhongbao Liu[2], Haikuan Nie[1,2]*, Xinping Liang[1,2,3]*, Qianwen Li[2] and Pengwei Wang[2]

[1]State Key Laboratory of Shale Oil and Gas Enrichment Mechanisms and Effective Development, Beijing, China, [2]Petroleum Exploration and Production Research Institute, SINOPEC, Beijing, China, [3]Institute of Energy, Peking University, Beijing, China

The lacustrine shale in the Dongyuemiao Member of the Fuling area, Sichuan Basin, is widely distributed and has huge shale oil resource potential. It is one of the important replacement areas for shale oil exploration in China. To investigate the key shale oil evaluation well, Well FY10, in the Fuling area, X-ray diffraction (XRD) mineral analysis, Rock-Eval, argon ion polishing-scanning electron microscope (SEM), Mercury injection capillary pressure (MICP), and low pressure nitrogen adsorption were launched to determine the heterogeneity of the pore system in the lacustrine shale of the Dongyuemiao Member. The mineral composition exhibits a high degree of heterogeneity, and the shale can be divided into two main lithofacies: argillaceous shale and mixed shale. The porosity ranges from 2.95 to 8.43%, and the permeability ranges from 0.05 to $1.07 \times 10^{-3} \, \mu m^2$. The physical properties of mixed shale are obviously better than those of argillaceous shale. Inorganic mineral pores, such as linear pores between clay minerals and calcite dissolution pores, are mainly developed, while a small amount of organic pores can be observed. The average total pore volume (V_p) is 0.038 ml/g with an average specific surface area of 5.38 m^2/g. Mesopores provide the main V_p (average 61.72%), and micropores provide mostly specific surface area. TOC imposes a strong controlling effect on the development of micropores. Clay minerals are the main contributors to mesopores and macropores. The organic-inorganic interaction during the process of diagenesis and hydrocarbon generation controls the formation of shale pore systems.

Keywords: heterogeneity, lacustrine shale, lithofacies, dongyuemiao member, sichuan basin

INTRODUCTION

With the commercial exploitation of shale oil in the Bakken Formation in the Williston Basin, the Eagle Ford Formation in Southern Texas, and the Barnett Formation in the Fort Worth Basin, shale oil has altered the American energy structure and imposes a profound impact on the world energy pattern (Hill et al., 2007; Zhang et al., 2017; Saputra et al., 2019). In recent years, with the rapid
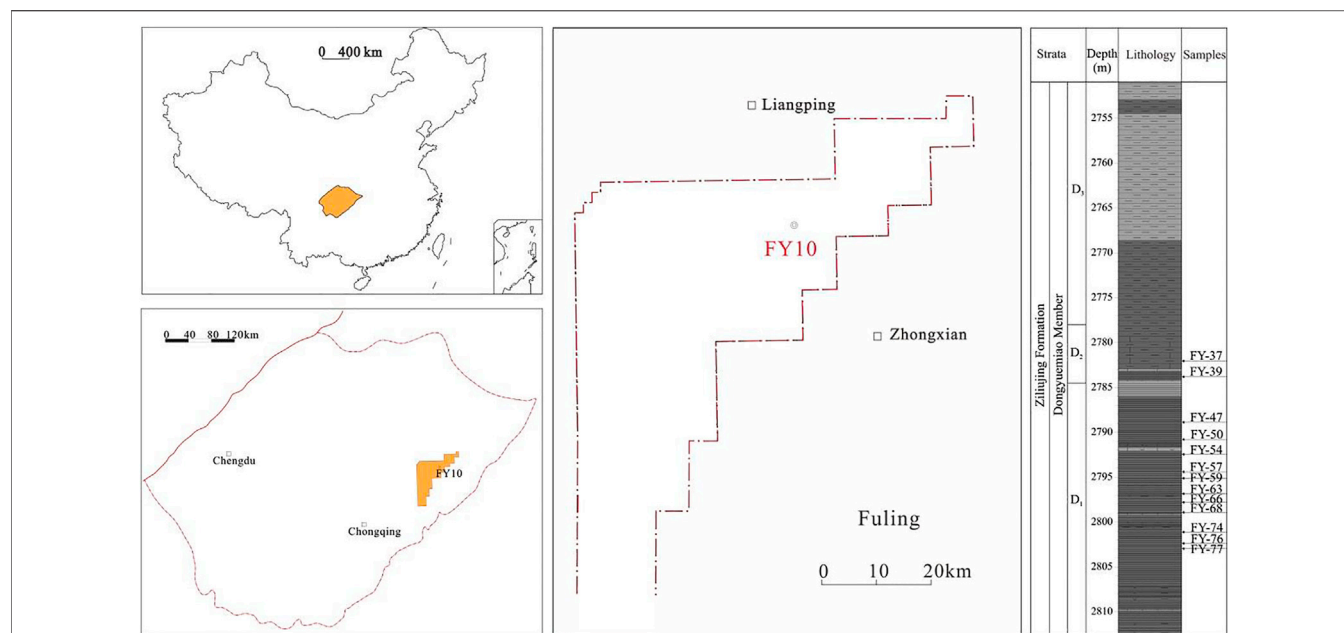
FIGURE 1 | Geologic map and stratigraphic column of the Dongyuemiao shale and the sampling sites in the Fuling area in the eastern Sichuan Basin, China.

development of China's economy, the demand for oil and gas has increased substantially, and the degree of dependence on foreign oil and natural gas has continued to increase. There is an urgent requirement to find new types of oil and gas resources, achieve theoretical and technological breakthroughs, and form a contribution to domestic oil and gas production (Jia et al., 2012; Zou et al., 2020). Among the known new resource types, shale oil is one of the most realistic exploration and development targets (Zou et al., 2013; Jin et al., 2019). Shale oil refers to the oil contained in the organic-rich shale strata (including the thin interbedded tight carbonate and clastic rock layers in the shale). There is no production capacity under natural conditions, and unconventional technology is required to realize economies of scale exploitation (Jin et al., 2019).

Organic rich shale is widely distributed in China, which not only provides abundant conventional oil and gas resources, but also contains plentiful shale oil and gas resources (Jin et al., 2019; Zou et al., 2019). Many breakthroughs have been achieved in the Permian Lucaogou Formation in the Junggar Basin, Triassic Yanchang Formation in the Ordos Basin, Cretaceous Qingshankou Formation in the Songliao Basin, middle-lower Jurassic formations in the Sichuan Basin, and Paleogene Shahejie Formation in the Bohai Bay Basin, and industrial production has been realized in some regions (Zhang et al., 2018; Liu et al., 2019; Song et al., 2020; Fu et al., 2021; Liu et al., 2021; Zhang et al., 2021).

Lacustrine shale is characterized by very developed strata, wide distribution, and massive exploration potential (Jia et al., 2012; Jin et al., 2019; Zou et al., 2019; Liu et al., 2021). However, there are still some unresolved problems such as strong heterogeneity, an unclear occurrence mechanism, and the main controlling factors of enrichment (Guo et al., 2016; Li et al., 2020; Song et al., 2020).

Based on the comprehensive study of the geological conditions of Dongyuemiao shale of Jurassic Ziliujing Formation in Sichuan Basin, the heterogeneity of lacustrine shale under lithofacies constraints in Fuling area is studied, in order to provide support for promoting the exploration and development process of lacustrine shale oil and gas in the Sichuan Basin and enrich the geological theory of lacustrine shale oil and gas.

GEOLOGICAL SETTING

The Jurassic formation in the Sichuan Basin is a set of important petroleum-bearing strata containing both oil and gas (Liu et al., 2019). During the early and middle Jurassic, most of the Sichuan Basin was composed of shore shallow lacustrine and semi-deep lacustrine sediments (Li and He, 2014). Vertically, three sets of organic rich shales are developed in the Dongyuemiao Member, Da'anzhai Member of Ziliujing formation, and Lianggaoshan Formation (Zheng et al., 2013). During the deposition period of Dongyuemiao Member, the sedimentary center of Sichuan Basin is mainly located around Liangping-Guang'an-Fuling area in the east of Sichuan Province. The black shale exhibits a relatively high abundance of organic matter and a wide distribution area (Shu et al., 2021).

The Fuling area is located in the eastern of the Sichuan Basin (**Figure 1**). During the Dongyuemiao sedimentary period, the Fuling area experienced a large-scale lake transgression, depositing a set of shore shallow lacustrine to semi-deep lacustrine black shale interbedded with thin shell limestone, with regional thickness of 60–70 m. The Dongyuemiao Member in the area can be further divided into three sub members: the first sub member is black shale

interbedded with thin layers of shell limestone, with a thickness of 28 m. The second sub member is composed of black argillaceous limestone with a thickness of 6.5 m. The third sub member is dark mudstone with a thickness of 27 m. In general, the lacustrine water body of the Dongyuemiao Member in the study area has experienced a change process from shallow to deep to shallow.

In March 2020, the FY10 well deployed by Sinopec Jianghan Oilfield Company was successfully fractured and became the first production well of shale oil and gas in the area (**Figure 1**). It obtained a daily gas production of $5.58 \times 10^4 \, \mathrm{m^3}$ and oil production of $17.6 \, \mathrm{m^3}$. The total organic carbon (TOC) content of the favorable interval of Well FY10 is 2.11%, the porosity is 6.11%, and the permeability is $0.127 \times 10^{-3} \, \mathrm{\mu m^2}$, showing good reservoir performance in general. The Ro of the shale in Dongyuemiao Member is between 1.23 and 2.09%. The organic matter has evolved to a high mature stage, that is, the condensate to wet gas stage (Shu et al., 2021).

SAMPLES AND METHODS

A total of 13 shale samples were carefully selected from the shale strata in the Dongyuemiao Member of Well FY10. Each sample is divided into several parts for different analyses.

Experimental Method

The analyses in this study were all launched at the Wuxi Research Institute of Sinopec Petroleum Exploration and Development Research Institute. First, 13 samples were analyzed for TOC content, rock pyrolysis, and XRD mineral composition. The analyses process comply with the operating steps outlined in the National Standard (SY/T) 14506.28-2010 and Chinese Oil and Gas Industry Standard (GB/T) 19145-2003. Nine of the samples were selected for thin slice identification analysis. Meanwhile, eight shale samples were launched for argon ion polishing-scanning electron microscopy analysis to observe the development characteristics of pores.

To quantitatively characterize the full-scale pore size distribution characteristics of shale, eight samples were selected for Mercury injection capillary pressure (MICP) and low pressure nitrogen adsorption, under the experimental procedure proposed in the National Standard (GB/T) 21650.1-2008 and (GB/T) 19587-2017 (Li et al., 2016, 2017). Theoretically speaking, the measurement range of the nitrogen adsorption method is from 0.35 to 500 nm. Due to the limitations of various formulas and models, the nitrogen adsorption method only has high measurement accuracy for pores below 50 nm, while the precision of the test results for large pores is reduced. The measurement range of the MICP method is from 6.5 nm to 63 μm. Because high pressure can damage the shale structure and then affect the results, the MICP has high measurement accuracy for pores above 50 nm (Li et al., 2017). In general, only by combining the two methods can it get the continuous pore distribution of shale. The method used in this paper is to combine the nitrogen adsorption data below 50 nm with the MICP data above 50 nm. In the meantime, the Brunauer Emmett

Teller (BET) method was applied to calculate the specific surface area.

Lithofacy Classification Method

According to the quantitative analysis of the total mineral composition of lacustrine shale, the two-level lithofacies' division is carried out on the basis of the graphic method of clay minerals, QMF (quartz, mica, and feldspar), and carbonate minerals as three terminal elements. In the first-level division process, the traditional petrological classification method is respected, and the name of vary rock is determined with 50% as the boundary. At the three ends of the triangle diagram, the shale area (I), sandstone area (III), and limestone area (IV) are determined, respectively. In the meantime, the middle area where the content of the three components does not exceed 50% is named the mixed rock area (II) (**Figure 2A**). On this basis for the I, III, and IV areas, taking the mineral content of 25% as the boundary, the secondary division is carried out. For example, the shale area (I) is further divided into three secondary areas: argillaceous shale, silty shale, and carbonate shale. For the mixed rock area, it is named mixed shale (**Figure 2B**).

On the basis of the above-mentioned three-terminal division, it is also necessary to identify the structure (including grain structure and morphology), genesis, and related sedimentary characteristics of the two non-clay minerals, quartz and calcite in shale, to improve the division of lithofacies.
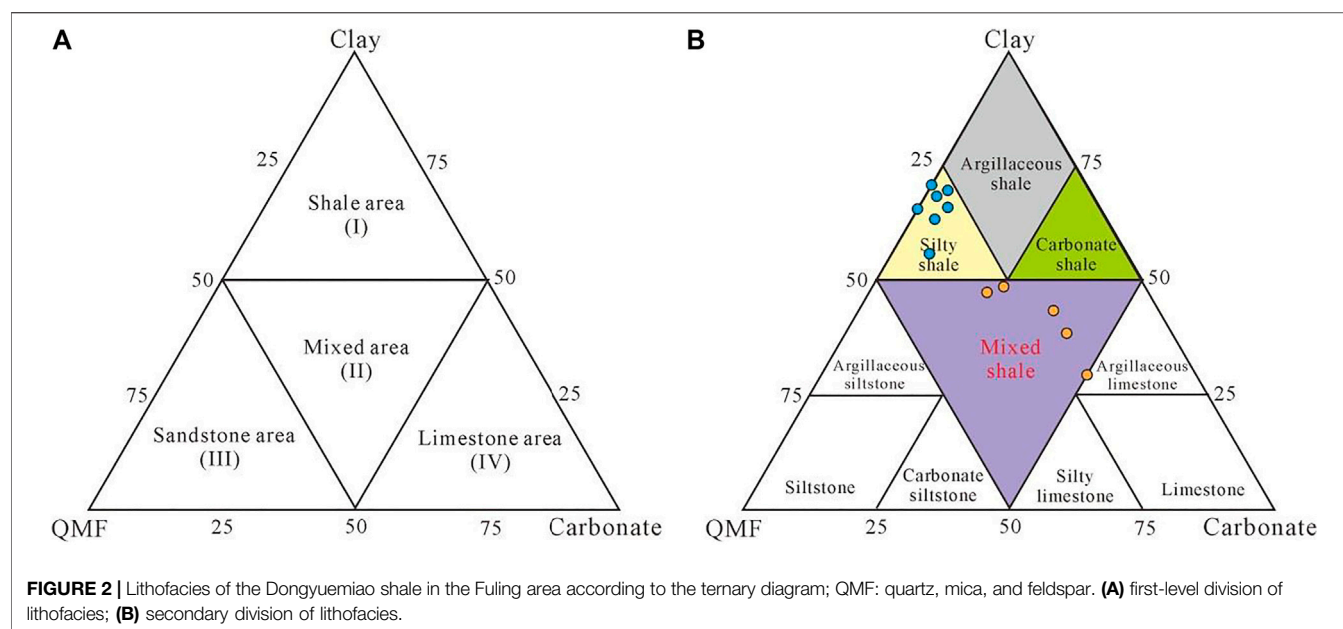
RESULTS

Mineral Contents

The detailed results of XRD mineral analysis are shown in **Table 1**. The mineral composition of the shale in the Dongyuemiao Member is highly heterogeneous, mainly including clay minerals, quartz, calcite, and a small amount of feldspar, dolomite, and pyrite. The content of clay minerals ranges from 25.9 to 69.0%, with an average value of 55.0%. The quartz content ranges from 17.8 to 29.4%, with an average value of 23.5%. The calcite content is between 0 and 51.2%, with an average value of 14.0% (**Table 1**). The three primary minerals accounted for 92.4% of the contents of the total minerals. Except for the relatively stable quartz content, the contents of clay minerals and calcite are both highly heterogeneous and fluctuate with each other.

Types of Lithofacies

On account of the ternary diagram of the lithofacies classification, two lithofacies of the Dongyuemiao shale can be identified, namely, mixed shale and silty shale (**Figure 2**). But for quartz, thin-section observation shows that the grain size structure of quartz in the shale is different from that of normal sandstone. Taking the two samples of the same silty shale (FY-74 and FY-77) as an example, the clay mineral contents are greater than 50%, and the quartz contents are 21 and 25.5%, respectively, which are all argillaceous structures, and it is difficult to identify obvious quartz particles (particle size <0.039 mm) (**Figures 3A,B**).

FIGURE 2 | Lithofacies of the Dongyuemiao shale in the Fuling area according to the ternary diagram; QMF: quartz, mica, and feldspar. (A) first-level division of lithofacies; (B) secondary division of lithofacies.

TABLE 1 | Mineral contents of the Dongyuemiao shale in the Fuling area, eastern Sichuan Basin.

Sample	Depth (m)	Content (%)							
		Clay	Quartz	Potash feldspar	Plagioclase	Calcite	Dolomite	Siderite	Pyrite
FY-37	2,782.04	25.9	18.2		1.3	51.2	1.5		1.9
FY-39	2,783.81	37.3	17.8		1.9	34.0	5.7		3.3
FY-47	2,788.87	67.0	24.1		3.3	2.9		2.1	
FY-50	2,790.79	46.5	25.2	1.6	3.1	21.0			2.6
FY-54	2,792.46	48.2	22.7	1.5	2.1	23.8		1.0	
FY-57	2,794.41	69.0	25.0		3.0			1.9	
FY-59	2,795.11	64.2	29.4		4.2			1.2	
FY-63	2,796.84	43.9	20.2			26.1	9.8		
FY-66	2,797.81	61.0	25.7	1.7	3.6	4.4		2.3	
FY-68	2,798.91	63.6	21.1	2.0	4.1	5.6		2.3	
FY-74	2,801.11	68.4	21.0	1.6	3.3	3.6		2.1	
FY-76	2,802.37	52.4	29.4	1.6	3.7	6.5		2.5	3.9
FY-77	2,802.97	67.0	25.5		3.2	2.4		1.9	
Average		55.0	23.5	0.8	2.8	14.0	1.3	1.3	0.9

Obviously, it is inappropriate to define it as silty shale, and it is more suitable to identify it as argillaceous shale. For the calcite mineral in mixed shale, core observation and thin-section identification analysis exhibit that it is mainly the product of calcification and cementation of the original biological shell, which is caused by bio-chemical sedimentation. Under the microscope, two-stage calcite cementation can be seen in individual shells (**Figure 3C**), and there exist different degrees of recrystallization (**Figure 3D**), but in most cases the original biological structure is still better.

By determining the structure and genesis of minerals, the definition of certain rocks can be effectively corrected, and the lithofacies of the same interval in the triangle diagram of mineral quantitative analysis can be distinguished. According to the results of XRD mineral analysis and thin slice observation, the Dongyuemiao shale of Well FY10 mainly develops argillaceous shale and mixed shale. The vertical lithofacies change and the water depth fluctuation have a certain synergism.

Organic Geochemical and Physical Characteristics

Total organic carbon (TOC) is usually the main indicator for evaluating the abundance of source rocks (Li et al., 2016; Liu et al., 2019; Feng et al., 2020). The TOC content of the shale in the Dongyuemiao shale of Well FY10 ranges from 0.77 to 3.13%, with an average value of 1.67% (**Table 2**). Rock pyrolysis hydrocarbons are composed of adsorbed hydrocarbons (S_1) and pyrolysis hydrocarbons (S_2). Their contents vary with the abundance and type of organic matter, and are direct indicators for
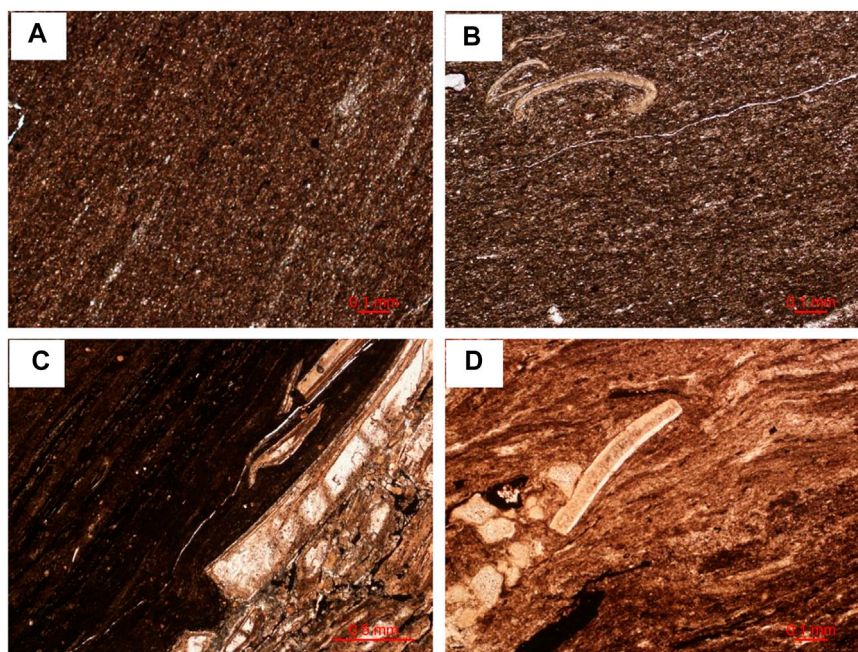
FIGURE 3 | Microscopic Features of Main Lithofacies in Dongyuemiao shale of Well FY10 **(A)** argillaceous shale, 2,801.11 m; **(B)** argillaceous shale, 2,802.97 m; **(C)** mixed shale, 2,790.79 m; **(D)** mixed shale, 2,792.46 m.

TABLE 2 | Petrologic properties of the Dongyuemiao shale in the Fuling area.

Sample	Depth (m)	Lithofacies	TOC (%)	S_1 (mg/g)	OSI (mg/ g TOC)	$\delta^{13}C$ of kerogen (‰)	Type of kerogen	Porpsity (%)	Permeablity ($10^{-3}\mu m^2$)
FY-37	2,782.04	Mixed shale	0.77	0.48	62.34	−30.7	I	6.22	0.16
FY-39	2,783.81	Mixed shale	1.46	0.85	58.22	−29.5	I	8.43	0.56
FY-47	2,788.87	Argillaceous shale	1.84	0.82	44.57	−25.8	II2	6.70	0.10
FY-50	2,790.79	Mixed shale	1.62	0.59	36.42	−25.5	II2	5.27	1.07
FY-54	2,792.46	Mixed shale	3.13	1.10	35.14	−26.7	II1	4.08	0.62
FY-57	2,794.41	Argillaceous shale	1.56	0.70	44.87	−26.8	II1	2.97	0.07
FY-59	2,795.11	Argillaceous shale	1.44	0.59	40.97	−26.3	II1	4.35	0.12
FY-63	2,796.84	Mixed shale	1.28	0.67	52.34	−28.6	I	3.79	0.14
FY-66	2,797.81	Argillaceous shale	1.36	0.58	42.65	−26.8	II1	5.93	0.21
FY-68	2,798.91	Argillaceous shale	1.39	0.68	48.92	−26.2	II1	5.88	0.17
FY-74	2,801.11	Argillaceous shale	1.75	0.66	37.71	−25.3	II2	3.97	0.06
FY-76	2,802.37	Argillaceous shale	2.14	0.77	35.98	−25.1	II2	2.95	0.05
FY-77	2,802.97	Argillaceous shale	2.01	0.62	30.85	−25.0	II2	3.30	0.06
Average			1.67	0.70	43.92	−26.79		4.91	0.26

evaluating the quality of source rocks (Huang et al., 2020). S_1 ranges from 0.48 to 1.10 mg/g, with an average value of 0.70 mg/g. Hydrocarbon generation potential (PG = S_1+S_2) is an important indicator to characterize the abundance of organic matter (Huang et al., 2020). With the increase of maturity, the PG will obviously

decrease. The PG of the Dongyuemiao shale of Well FY10 ranges from 1.16 to 3.08 mg/g, with an average value of 1.91 mg/g, which makes it a generally medium source rock. PG and TOC exhibit an obviously positive relationship, but there exist certain differences between argillaceous shale and mixed shale (**Figure 4**). The range

FIGURE 4 | Intersection diagram of TOC and hydrocarbon generation potential.
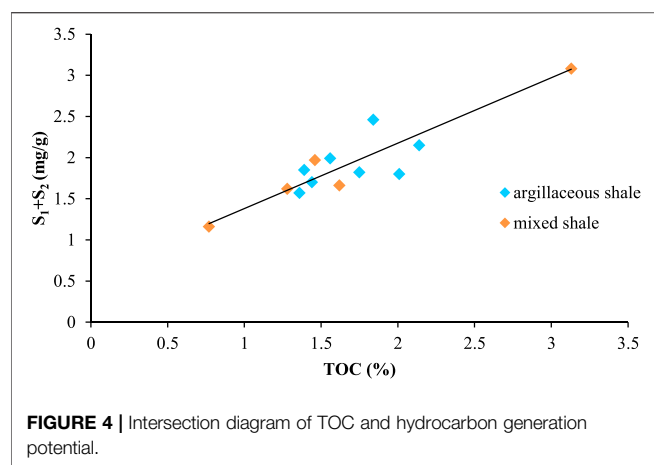
of PG and TOC of the argillaceous shale is small, showing a certain degree of homogeneity. In contrast, the distribution of PG and TOC of the mixed shale is large and exhibits strong heterogeneity.

To express the oiliness of shale, Jarvie (2012); Jarvie (2014) proposed the Oil Saturation Index (OSI), that is, the ratio of the TOC of the shale to its pyrolysis S_1 (S_1/TOC). The OSI of shale in Dongyuemiao Member of Well FY10 ranges from 30.85 to 62.34 mg/gTOC, with an average value of 43.92 mg/gTOC, and there exist no significant differences between different types of shale. The analysis suggests that S_1 reflects the remaining oil in the source rock, but is affected by sampling conditions, evolution stages, and oil and gas migration. The shale in the study area has evolved to a high maturity stage of the condensate to wet gas stage, so the light hydrocarbon components are easily lost, which has a certain impact on the results. The $\delta^{13}C$ of kerogen ranges from -25.0‰ to -30.7‰, which indicates that type II kerogen is dominant in organic matter.

Through physical experiments, the porosity and permeability of the Dongyuemiao shale can be obtained. The porosity ranges from 2.95 to 8.43%, with an average value of 6.84%; the permeability ranges from 0.05 to 1.07×10^{-3} μm^2, with an average value of 0.26×10^{-3} μm^2 (**Table 2**). The physical properties of mixed shale are obviously better than those of argillaceous shale, but the relation between porosity and permeability of mixed shale is unclear, and the porosity and permeability of argillaceous shale exhibit an obvious positive correlation (**Figure 5**).

Pore Types and Full-Scale Pore Distribution

A combination of argon ion polishing-SEM, low-temperature nitrogen adsorption, and MICP was launched to carry out qualitative observation and quantitative analysis of shale micro-pores. To fully consider the contact and genetic relationship between inorganic mineral particles, organic matter, and pores, the pores of the Dongyuemiao shale in the study area are finally divided into organic pores and inorganic pores. Inorganic pores can be further divided into clay mineral pores and calcite-related pores.

Pore Morphology From Scanning Electron Microscope

Inorganic Pores

The development of inorganic pores, in essence, is similar to conventional reservoirs. There are two main formation mechanisms for the development of inorganic pores. One is the residual pores developed after the early intergranular pores undergo diagenetic compaction and cementation, and the other is the dissolution pores formed by the later dissolution modification (which can occur between and within grains); in addition, some pores also develop during mineral diagenetic alteration. The inorganic mineral pores in the shale of Dongyuemiao Member are mainly calcite dissolved pores and linear pores between clay minerals.

Compared with the marine Wufeng-Longmaxi shale (Dai et al., 2014; Feng et al., 2016; Nie et al., 2018), the Jurassic lacustrine shale has a higher content of clay minerals (>50%), and the average content of clay minerals in the Dongyuemiao shale of Well FY 10 can reach 55.0%. SEM observation reveals that the shale of Dongyuemiao Member widely develop linear micropores related to clay minerals (**Figures 6A,B**), that mainly exist between illite flakes or illite and mineral particles. Linear pores vary in length and width, and some of the pores are filled with solid asphalt. Therefore, the organic matter content in different samples has a significant effect on the development of linear pores. This type of pore is mainly composed of primary pores between early clay minerals. With the continuous increase of burial depth, due to the weak anti-compaction ability between clay minerals, the pores rapidly shrink to form residual linear pores. This type of pore basically develops along the cleavage direction of clay minerals, forming slit-shaped or linear pores, which can extend several microns.

Calcite dissolved pores are developed in the Dongyuemiao shale of Well FY10. Calcite is mainly composed of a crystalline granular structure, and the development of dissolution pores is various, mainly in three forms (**Figures 6C–E**). The first is the dissolution pores at the edge of calcite grains with irregular shapes. The second is the dissolution of macropores in the calcite grains, with various shapes, having clay minerals or dissolution residual calcite in the pores. The third is the dissolution needle-like pores in the calcite grains, and the individual is significantly smaller than the formers. The

FIGURE 5 | Intersection diagram of porosity and permeability.
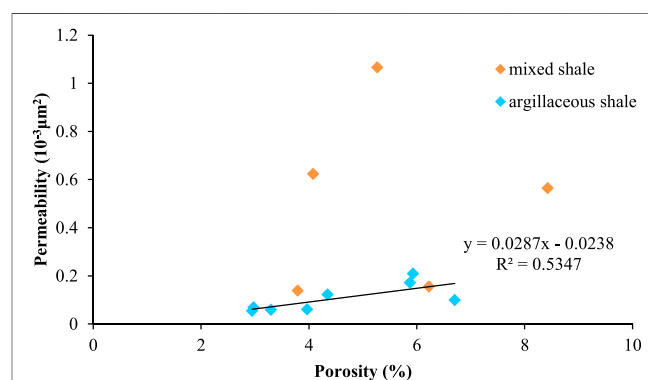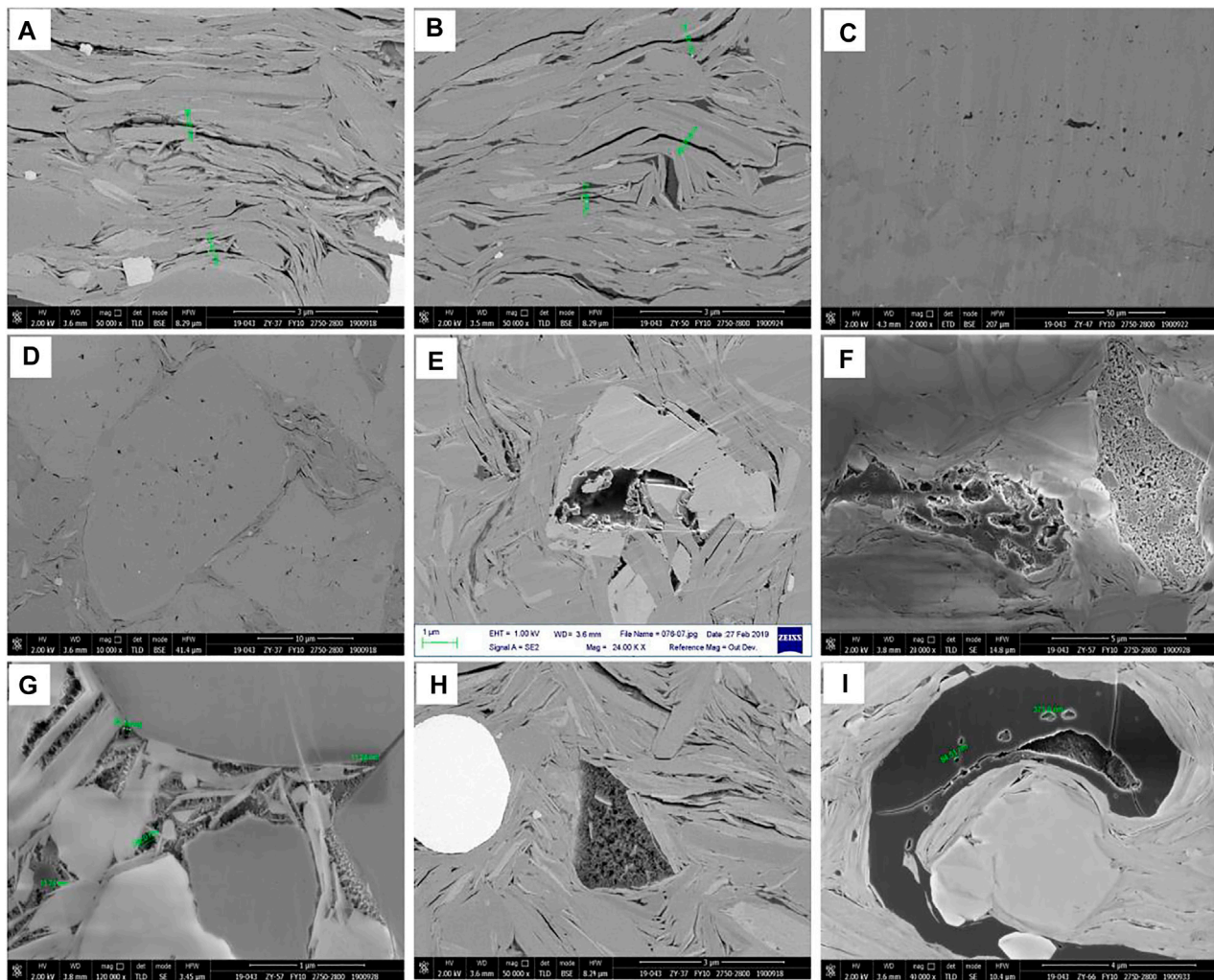
FIGURE 6 | Pore morphology from SEM of Dongyuemiao shale **(A)** linear pores between clay minerals, 2,782.04 m; **(B)** linear pores between clay minerals, 2,790.79 m; **(C)** calcite dissolved pores, 2,788.87 m; **(D)** calcite dissolved pores, 2,782.04 m; **(E)** calcite dissolved pores, 2,802.37 m; **(F)** organic pores, 2,794.41 m; **(G)** Organic pores, 2,794.41 m; **(H)** organic pores, 2,782.04 m; **(I)** organic pores, 2,797.81 m.

formation of calcite-related dissolved pores may be mainly related to the dissolution of organic acids during hydrocarbon generation.

Organic Pores

Observations of most shale samples from the Dongyuemiao Member reveal that the organic pores are well developed in the solid asphalt filled within inorganic minerals. The pore shapes vary, and include oval, irregular, slit, and honeycomb shapes (**Figures 6F–H**). The pore diameter is mainly in nanometers, but the size is not uniform, from tens of nanometers to hundreds of nanometers (the long axis of the pore size) are developed, and some samples show the development of micron-scale organic pores. The development of organic pores is mainly controlled by organic matter components. The organic pores in the solid asphalt are generally developed. For vitrinite, most of them did not

develop organic pores except for a few which were modified by bacteria (**Figure 6I**).

Pore-Throat Structure Parameters and Pore Size Distribution

The entry pressure of the lacustrine shale is 0.46 MPa on average. The corresponding maximum pore-throat radius is 580.61 nm. The average median pressure reaches 20.88 MPa. The corresponding median radius is 8.09 nm. There exists no obvious difference in pore-throat structure parameters of different lithofacies shale.

The total pore volume (V_p) distribution range of Dongyuemiao shale is 0.0097–0.0163 cm^3/g, the average value is 0.038 cm^3/g, and the specific surface area ranges from 2.93 to 9.65 m^2/g, with the average value of 5.38 m^2/g (**Table 3**). According to the IUPAC pore classification standard, pores are classified into micropores (<2.0 nm), mesopores

TABLE 3 | Pore volume and surface area statistics of the Dongyuemiao shale in the Fuling area.

Sample	Depth(m)	Lithofacies	Entry pressure (MPa)	Maximum pore-throat radius (nm)	Median pressure (MPa)	Median radius (nm)	V_p (cm³/g)				V_p proportion (%)			Specific surface area (m²/g)
							Micro-	Meso-	Macro-	Total	Micro-	Meso-	Macro-	
FY-37	2,782.04	Mixed shale	0.93	156.80	15.90	9.20	0.0012	0.0068	0.0017	0.0097	11.85	70.17	17.98	2.93
FY-47	2,788.87	Argillaceous shale	0.27	533.50	13.90	10.50	0.0017	0.0090	0.0038	0.0146	11.95	61.93	26.13	4.41
FY-50	2,790.79	Mixed shale	0.31	467.00	17.70	8.20	0.0024	0.0101	0.0038	0.0163	14.89	61.83	23.29	6.20
FY-54	2,792.46	Mixed shale	1.25	116.80	42.10	3.50	0.0041	0.0081	0.0024	0.0145	28.10	55.65	16.25	9.65
FY-57	2,794.41	Argillaceous shale	0.08	1797.20	12.00	12.20	0.0014	0.0071	0.0043	0.0129	11.17	55.22	33.62	3.60
FY-66	2,797.81	Argillaceous shale	0.22	647.10	16.80	8.70	0.0023	0.0088	0.0035	0.0147	15.97	60.13	23.90	5.66
FY-74	2,801.11	Argillaceous shale	0.34	423.20	28.50	5.10	0.0020	0.0102	0.0030	0.0152	13.05	67.07	19.88	5.69
FY-77	2,802.97	Argillaceous shale	0.29	503.30	20.10	7.30	0.0020	0.0078	0.0028	0.0126	15.86	61.78	22.36	4.92
Average			0.46	580.61	20.88	8.09	0.0021	0.0085	0.0032	0.0138	15.35	61.72	22.93	5.38

(2–50 nm), and macropores (>50 nm) according to their size (Loucks et al., 2012; Thommes et al., 2015). In general, the average proportions of micropores (<2 nm), mesopores (2–50 nm), and macropores (>50 nm) are 15.35, 61.72, and 22.93%, respectively. It can be seen that the proportion of mesopores is dominant and the proportion of macropores is also relatively high. The shale of the marine Wufeng-Longmaxi Formation is dominated by micropores and mesopores, the contents of which are similar, and together they can account for more than 95% of the total V_p (Li et al., 2016; Feng et al., 2018, 2019). In general, compared with the marine shale, the proportion of meso-macropores in the Dongyuemiao Member of the lacustrine shale is higher, which is very beneficial for improving the reservoir performance of shale.

From the full pore size distribution of shale, it can be detected that the distribution of different samples still has certain differences. The pore size distribution of the argillaceous shale is similar to that of the mixed shale. An obvious main peak of the pore size distribution exits and the main body is in the range of mesopores (2–20 nm) (**Figures 7A,B**). The pores of the two types of shale are mainly mesopores, which accounts for more than 60% on average. The proportion of micropores in mixed shale is slightly lower than that of macropores, with average values of 18.28 and 19.17%, respectively (**Figure 7C**; **Table 3**). The proportion of macropores in argillaceous shale is significantly higher than that of micropores, with average values of 25.18 and 13.60%, respectively (**Figure 7D**; **Table 3**). This difference in pore size distribution may be due to the different organic and inorganic mineral compositions of the two types of shale.

It can be detected from the intersection of pore volume and specific surface area that the total V_p and specific surface area have a certain positive correlation, but the correlation is not strong (**Figure 8A**). The relationship between the corresponding V_p of pores in different scales and specific surface areas is very different. The V_p of micropores and specific surface areas show a significant positive correlation, R^2 can reach 0.9787 (**Figure 8B**), while V_p of mesopores and macropores have no obvious correlation with specific surface area (**Figures 8C,D**), indicating that micropores are the main contributor to the specific surface area, which is consistent with marine shale. Different types of shale also exhibit obvious differences. The V_p of micropores of mixed shale is only positively correlated with the specific surface area, while the V_p of micropores and mesopores of argillaceous shale exhibit an obvious positive correlation with specific surface area, indicating that the development of pores in argillaceous shale imposes a stronger controlling effect on surface area than mixed shale, which achieves more obvious regularity characteristics.

DISCUSSION

To probe the differences between shale porosity and pore size distribution of different lithofacies, based on the material composition of shale, the reason for these differences is analyzed comprehensively from the composition of organic matter and inorganic mineral.

FIGURE 7 | Pore size distribution characteristics of different lithofacies shale. **(A)** pore size distribution of mixed shale; **(B)** pore size distribution of argillaceous shale; **(C)** proportion characteristics of pores in different scales of mixed shale; **(D)** proportion characteristics of pores in different scales of argillaceous shale.
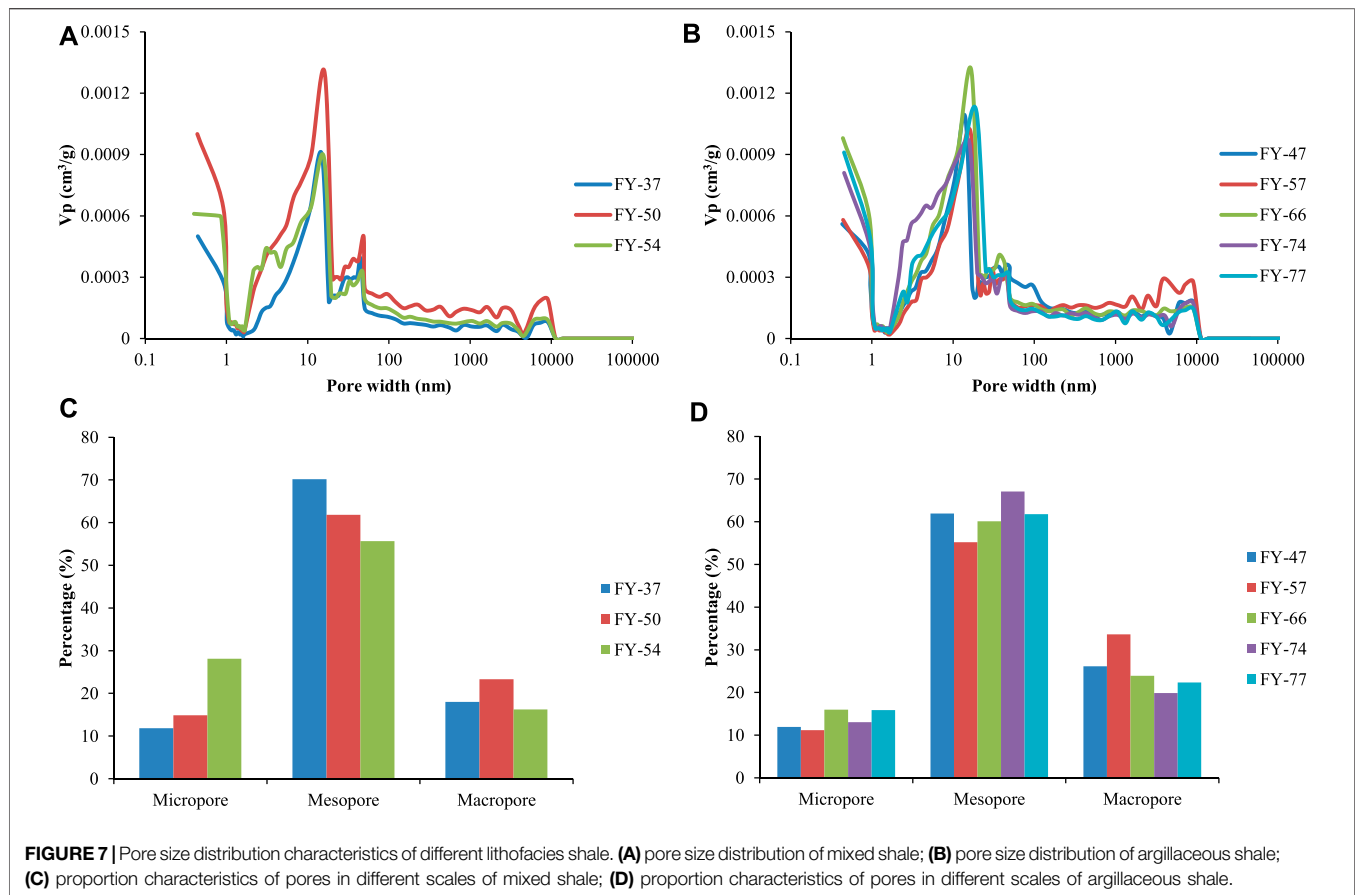
The Relationship Between Total Organic Carbon and Pore Structure Parameters

As an important part of the shale pore system, organic pores are formed during the process of hydrocarbon generation. The development of organic pores is of great significance to evaluate the gas storage capacity of shale intervals. Therefore, the formation mechanism of organic pores has always been a hot issue in the field of shale reservoirs. The development of organic pores in the Dongyuemiao shale is unique, which exhibits that some organic matter in the same sample is compact and uniform and develops no internal pores, while some organic matter has relatively developed internal pores. The organic matter with undeveloped pores is mostly in the shape of a strip or block. It is a microscopic component formed by the humification and gelation of the lignocellulosic tissue of higher plants (mainly vitrinite). The organic matter with organic pores is mostly unfixed, controlled by the original pore carrier (surrounding inorganic minerals), and is solid asphalt.

As shown in **Figure 9**, the V_P of micropores and specific surface areas are positively correlated with TOC content, indicating that micropores are mainly developed in organic matter. TOC content seems to be the main parameter controlling micropores' development. However, there exists no obvious correlation between the V_P of mesopores and macropores and the TOC content, which indicates that the

pores in organic matter are not the main contributors of mesopores and macropores.

In general, TOC content was positively correlated with micropore volume, indicating that organic matter could be used as the main index of micropore development. The higher the TOC content is, the more micropores and the larger the specific surface area in shale, which is consistent with the previous research results of marine shale (Loucks et al., 2012; Feng et al., 2019).

The Relationship Between Mineral Composition and Pore Structure Parameters

There are mainly two types of inorganic mineral pores in the Dongyuemiao shale of Well FY10, namely linear pores between clay minerals and calcite dissolved pores (**Figure 6**), which are closely related to the mineral composition of the shale. The average content of clay minerals in the Dongyuemiao shale is about 55%. The high clay content leads to weak compaction resistance, and the clay minerals are mostly oriented and distributed in layers, with residual clay minerals interlayers. The interlayer linear micropores of residual clay minerals are the main pores of lacustrine shale. Although the intergranular pores between clay minerals and mineral particles are developed,

FIGURE 8 | Intersection diagrams of pore volume and specific surface area. **(A)** total V_p and specific surface area; **(B)** micro-V_p and specific surface area; **(C)** meso-V_p and specific surface area; **(D)** macro-V_p and specific surface area

FIGURE 9 | Intersection diagrams of TOC and pore structure parameters. **(A)** TOC and micro-V_p; **(B)** TOC and meso-V_p; **(C)** TOC and macro-V_p; **(D)** TOC and specific surface area.

FIGURE 10 | Intersection diagrams of clay minerals and pore structure parameters. **(A)** clay minerals and micro-V_p; **(B)** clay minerals and meso-V_p; **(C)** clay minerals and macro-V_p.

the number of pores is relatively small, and most of the large pores have been filled by solid asphalt. According to the statistics of the relationship between clay minerals and pore volume, it can be detected that with the increase of clay minerals, the V_p of mesopores and macropores tends to become larger, and the correlation coefficient with macropores is higher, showing a better relevance (**Figure 10**). It is shown that its contribution to micropores and mesopores is relatively apparent, and the linear pores between clay minerals provide the main reservoir space for the shale in the study area.

The calcite of Dongyuemiao Member is dominated by a crystalline granular structure with various dissolved pores, but there is no obvious regularity in its development. It is speculated that the formation of calcite-related dissolved pores mainly related to the organic acid dissolution during the hydrocarbon generation process. According to the statistics of the relationship

between calcite and pore volume, it can be detected that, with the increase of calcite content, the V_p of mesopores and macropores tends to decrease, but there is no obvious correlation with the V_p of micropores. Although calcite may develop various types of pores, its contribution to pores in different sizes is relatively limited, so calcite dissolved pore is not the main contributor of reservoir space of lacustrine shale (**Figure 11**).

Diagenesis-Hydrocarbon Generation Controls the Formation and Evolution of Pores

The pore development and evolution of shale is complex, and is closely related to the compaction during the diagenesis process, the hydrocarbon generation and expulsion of organic matter, and the precipitation and dissolution of carbonate minerals. In addition to various inorganic minerals (clay minerals, quartz,

FIGURE 11 | Intersection diagrams of calcite and pore structure parameters. **(A)** calcite and micro-V_p; **(B)** calcite and meso-V_p; **(C)** calcite and macro-V_p.
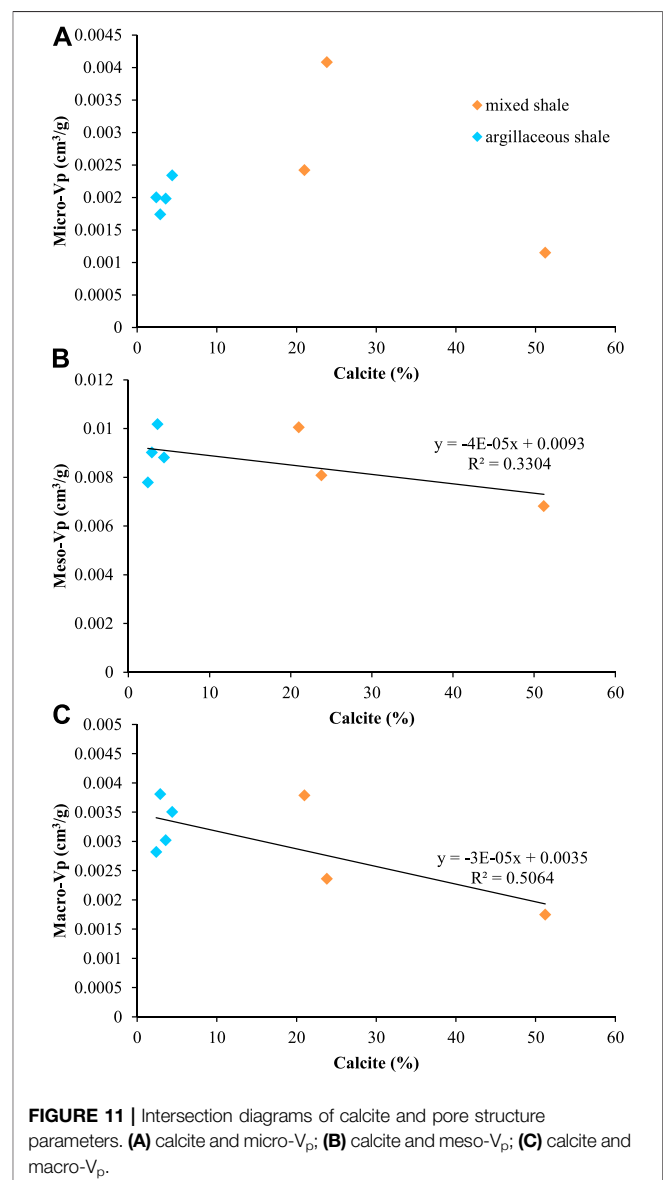
feldspar, calcite, etc.), shale is also rich in organic matter, and organic pores that contribute to the accumulation of oil and gas are found inside. With the increase of the buried depth of the shale, the organic matter also evolves with the increase of the temperature in the process of the inorganic mineral diagenesis. Inorganic pores formed by the diagenetic evolution of inorganic minerals coexist with the pores formed by the hydrocarbon generation of organic matter, which reveals the formation and evolution of diagenesis, hydrocarbon generation, and pores as an integrated whole.

The shale in the Dongyuemiao Member of the Fuling area has entered the middle diagenetic stage B, with strong compaction; a large amount of montmorillonite was transformed into lamellar illite, the intergranular pores and intragranular pores have become smaller and the number decreased, but a large number of mesopores and macropores still formed, which are the main contributors to the shale reservoir space. The maturity (Ro) of shale is 1.5%, and it has entered a high evolutionary stage. Organic pores begin to form during the secondary pyrolysis of petroleum. Observation under the SEM exhibits that organic pores, mainly micropores, are widely developed in the asphalt. To some extent, it increases the porosity and contributes to the total porosity. Therefore, the difference in the reservoir space of different lithofacies is only a characteristic phenomenon. The organic-inorganic interaction controls the formation of shale pore systems in different lithofacies during diagenesis-hydrocarbon generation.

CONCLUSION

According to the mineral contents and thin slice analysis, the Dongyuemiao shale is divided into two main shale lithofacies: argillaceous shale and mixed shale. The porosity ranges from 2.95 to 8.43%, and the permeability ranges from 0.05 to $1.07 \times 10^{-3} \mu m^2$. The physical properties of the mixed shale are obviously better than those of the argillaceous shale.

The shale in the Dongyuemiao Member is mainly composed of inorganic mineral pores, such as linear pores, between clay minerals and calcite dissolved pores, while a few organic pores are also developed. It is characterized by a high proportion of macropores and a predominance of mesopores. The mesopores provide the main pore volume (61.72% on average), while the micropores provide the main specific surface area.

The TOC content of the shale in the Dongyuemiao Member imposes the main parameter controlling the development of micropores. Clay minerals influence the development of mesopores and macropores, and the combined interaction of diagenesis and hydrocarbon generation controls the formation of pore systems in shale of different lithofacies.

DATA AVAILABILITY STATEMENT

The original contributions presented in the study are included in the article/Supplementary Material, further inquiries can be directed to the corresponding authors.

AUTHOR CONTRIBUTIONS

PL: Conceptualization, Methodology, Data curation, Writing-Reviewing and Editing. ZL: Supervision. HN: Reviewing and Editing. XL: Reviewing and Editing. QL: Validation. PW: Validation.

FUNDING

ACKNOWLEDGMENTS

REFERENCES

Dai, J., Zou, C., Liao, S., Dong, D., Ni, Y., Huang, J., et al. (2014). Geochemistry of the Extremely High thermal Maturity Longmaxi Shale Gas, Southern Sichuan Basin. *Org. Geochem* 74, 3–12. doi:10.1016/j.orggeochem.2014.01.018

Feng, Z., Dong, D., Tian, J., Qiu, Z., Wu, W., and Zhang, C. (2018). Geochemical Characteristics of Longmaxi Formation Shale Gas in the Weiyuan Area, Sichuan Basin, China. *J. Pet. Sci. Eng* 167, 538–548. doi:10.1016/j.petrol.2018.04.030

Feng, Z., Dong, D., Tian, J., Wu, W., Cai, Y., Shi, Z., et al. (2019). Geochemical Characteristics of Lower Silurian Shale Gas in the Changning-Zhaotong Exploration Blocks, Southern Periphery of the Sichuan Basin. *J. Pet. Sci. Eng* 174, 281–290. doi:10.1016/j.petrol.2018.11.022

Feng, Z., Hao, F., Dong, D., Zhou, S., Wu, W., Xie, C., et al. (2020). Geochemical Anomalies in the Lower Silurian Shale Gas from the Sichuan Basin, China: Insights from a Rayleigh-type Fractionation Model. *Org. Geochem* 142, 103981. doi:10.1016/j.orggeochem.2020.103981

Feng, Z., Liu, D., Huang, S., Wu, W., Dong, D., Peng, W., et al. (2016). Carbon Isotopic Composition of Shale Gas in the Silurian Longmaxi Formation of the Changning Area, Sichuan Basin. *Pet. Exploration Develop* 43 (5), 769–777. doi:10.1016/s1876-3804(16)30092-1

Fu, S. T., Jin, Z. J., Fu, J. H., Li, S. X., and Yang, W. W. (2021). Transformation of Understanding from Tight Oil to Shale Oil in the Member 7 of Yanchang Formation in Ordos Basin and its Significance of Exploration and Development. *Acta Petrolei Sinica* 42 (05), 561–569.

Guo, X. S., Hu, D. F., Li, Y. P., Wei, X. F., Liu, R. B., Liu, Z. J., et al. (2016). Analyses and Thoughts on Accumulation Mechanisms of marine and Lacustrine Shale Gas: A Case Study of Longmaxi Formation and Da'anzhai Section of Ziliujing Formation in Sichuan Basin. *Earth Sci. Front* 23 (2), 18–28.

Hill, R. J., Zhang, E., Katz, B. J., and Tang, Y. (2007). Modeling of Gas Generation from the Barnett Shale, Fort worth basin, texas. *Bulletin* 91 (4), 501–521. doi:10.1306/12060606063

Huang, Z. K., Hao, Y. Q., Li, S. J., Wo, Y. J., Sun, D. S., Li, M. W., et al. (2020). Oil – Bearing Potential, Mobility Evaluation and Significance of Shale Oil in Chang 7

Shale System in the Ordos Basin:A Case Study of Well H317. *Geology. China* 47 (1), 210–219. doi:10.12029/gc20200117

Jarvie, D. M. (2014). Components and Processes Affecting Producibility and Commerciality of Shale Resource Systems. *Geologica Acta* 12, 307–325. doi:10.1344/GeologicaActa2014.12.4.3

Jarvie, D. M. (2012). Shale Resource Systems for Oil and Gas: Part 2: Shale-Oil Resource Systems. *AAPG Memoir* 97, 89–119. doi:10.1306/13321447M973489

Jia, C. Z., Zheng, M., and Zhang, Y. F. (2012). Unconventional Hydrocarbon Resources in china and the prospect of Exploration and Development. *Pet. Exploration Develop* 49 (8), 43–44. doi:10.1016/s1876-3804(12)60026-3

Jin, Z. J., Bai, Z. R., Gao, B., and Li, M. W. (2019). Has China Ushered in the Shale Oil and Gas Revolution? *Oil Gas Geology* 40 (3), 5–12.

Li, M. W., Jin, Z. J., Dong, M. Z., Ma, X. X., Li, Z. M., Jiang, Q. G., et al. (2020). Advances in the Basic Study of Lacustrine Shale Evolution and Shale Oil Accumulation. *Pet. Geology. Exp* 42 (04), 489–505. doi:10.11781/sysydz202004489

Li, P., Jiang, Z., Zheng, M., Bi, H., and Chen, L. (2016). Estimation of Shale Gas Adsorption Capacity of the Longmaxi Formation in the Upper Yangtze Platform, China. *J. Nat. Gas Sci. Eng* 34, 1034–1043. doi:10.1016/j.jngse.2016.07.052

Li, P., Zheng, M., Bi, H., Wu, S., and Wang, X. (2017). Pore Throat Structure and Fractal Characteristics of Tight Oil sandstone: A Case Study in the Ordos Basin, China. *J. Pet. Sci. Eng* 149, 665–674. doi:10.1016/j.petrol.2016.11.015

Li, Y. Q., and He, D. F. (2014). Evolution of Tectonic-Depositional Environment and Prototype Basins of the Early Jurassic in Sichuan Basin and Adjacent Areas. *Acta Petrolei Sinica* 35 (2), 219–232. doi:10.7623/syxb201402002

Liu, B., Sun, J. H., Zhang, Y. Q., He, J. L., Fu, X. F., Yang, L., et al. (2021). Reservoir Space and Enrichment Model of Shale Oil in the First Member of Cretaceous Qingshankou Formation in the Changling Sag, Southern Songliao Basin, NE China. *Pet. Exploration Develop* 48 (03), 521–535. doi:10.1016/s1876-3804(21)60049-6

Liu, Q., Li, P., Jin, Z., Liang, X., Zhu, D., Wu, X., et al. (2021). Preservation of Organic Matter in Shale Linked to Bacterial Sulfate Reduction (BSR) and Volcanic Activity under marine and Lacustrine Depositional Environments. *Mar. Pet. Geology* 127, 104950. doi:10.1016/j.marpetgeo.2021.104950

Liu, Z. B., Liu, G. X., Hu, Z. Q., Feng, D. J., Zhu, T., Bian, R. K., et al. (2019). Lithofacies Types and Assemblage Features of continental Shale Strata and Their Significance for Shale Gas Exploration: A Case Study of the Middle and Lower Jurassic Strata in the Sichuan Basin. *Natur. Gas Ind* 39 (12), 10–21. doi:10.3787/j.issn.1000-0976.2019.12.002

Loucks, R. G., Reed, R. M., Ruppel, S. C., and Hammes, U. (2012). Spectrum of Pore Types and Networks in Mudrocks and a Descriptive Classification for Matrix-Related Mudrock Pores. *Bulletin* 96, 1071–1098. doi:10.1306/08171111061

Nie, H., Jin, Z., and Zhang, J. (20182018). Characteristics of Three Organic Matter Pore Types in the Wufeng-Longmaxi Shale of the Sichuan Basin, Southwest China. *Sci. Rep* 8 (1), 7014–1098. doi:10.1038/s41598-018-25104-5

Saputra, W., Kirati, W., and Patzek, T. (2019). Generalized Extreme Value Statistics, Physical Scaling and Forecasts of Oil Production in the Bakken Shale. *Energies* 12 (19), 3641. doi:10.3390/en12193641

Shu, Z. G., Zhou, L., Li, X., Liu, H. T., Zeng, Y., Xie, H. G., et al. (2021). Geological Characteristics of Gas Condensate Reservoirs and Their Exploration and Development prospect in the Jurassic continental Shale of the Dongyuemiao Member of Ziliujing Formation, Fuxing Area, Eastern Sichuan Basin. *Oil Gas Geology* 42 (01), 212–223. doi:10.11743/ogg20210118

Song, M., Liu, H., Wang, Y., and Liu, Y. (2020). Enrichment Rules and Exploration Practices of Paleogene Shale Oil in Jiyang Depression, Bohai Bay Basin, China. *Pet. Exploration Develop* 47 (2), 242–253. doi:10.1016/s1876-3804(20)60043-x

Song, Y., Gao, F. L., Tang, X. L., Chen, L., and Wang, X. M. (2020). Influencing Factors of Pore Structure Differences between marine and Terrestrial Shale Reservoirs. *Acta Petrolei Sinica* 41 (12), 1501–1512. doi:10.7623/syxb202012005

Thommes, M., Kaneko, K., Neimark, A. V., Olivier, J. P., Rodriguez-Reinoso, F., Rouquerol, J., et al. (2015). Physisorption of Gases, with Special Reference to the Evaluation of Surface Area and Pore Size Distribution (IUPAC Technical Report). *Pure Appl. Chem* 87, 1051–1069. doi:10.1515/pac-2014-1117

Zhang, P., Misch, D., Hu, F., Kostoglou, N., Sachsenhofer, R. F., Liu, Z., et al. (2021). Porosity Evolution in Organic Matter-Rich Shales (Qingshankou Fm.; Songliao Basin, NE China): Implications for Shale Oil Retention. *Mar. Pet. Geology* 130 (1), 105139. doi:10.1016/j.marpetgeo.2021.105139

Zhang, S., Liu, C., Liang, H., Wang, J., Bai, J., Yang, M., et al. (2018). Paleoenvironmental Conditions, Organic Matter Accumulation, and Unconventional Hydrocarbon Potential for the Permian Lucaogou Formation Organic-Rich Rocks in Santanghu Basin, NW China. *Int. J. Coal Geology* 185, 44–60. doi:10.1016/j.coal.2017.11.012

Zhang, T. W., Sun, X., Milliken, L. K., Ruppel, C. S., and Enriquez, D. (2017). Empirical Relationship between Gas Composition and thermal Maturity in eagle ford Shale, South texas. *AAPG Bull* 101 (8), 1277–1307. doi:10.1306/09221615209

Zheng, R. C., He, L., Liang, X. W., and Xu, W. L. (2013). Forming Conditions of Shale Gas (Oil) Plays in the Lower Jurassic Da'anzhai Member in the Eastern Sichuan Basin. *Natur. Gas Ind* 33 (12), 30–40. doi:10.3787/j.issn.1000-0976.2013.12.004

Zou, C. N., Yang, Z., Sun, S. S., Zhao, Q., Bai, W. H., Liu, H. L., et al. (2020). Exploring Petroleum inside Source Kitchen": Shale Oil and Gas in Sichuan basin. *Sci. China Earth Sci* 63 (7). doi:10.1007/s11430-019-9591-5

Zou, C., Yang, Z., Cui, J., Zhu, R., Hou, L., Tao, S., et al. (2013). Formation Mechanism, Geological Characteristics and Development Strategy of Nonmarine Shale Oil in china. *Pet. Exploration Develop* 40 (1), 15–27. doi:10.1016/s1876-3804(13)60002-6

Zou, C., Zhu, R., Chen, Z.-Q., Ogg, J. G., Wu, S., Dong, D., et al. (2019). Organic-matter-rich Shales of China. *Earth-Science Rev* 189, 51–78. doi:10.1016/j.earscirev.2018.12.002

frontiers
in Earth Science

Characteristics of Shale Wettability by Contact Angle and Its Influencing Factors: A Case Study in Songliao

Haitao Xue[1], Zhentao Dong[1]*, Shansi Tian[2], Shuangfang Lu[1], Ce An[1], Yuan Zhou[1], Boheng Li[1] and Xiaoyi Xin[3]

[1]School of Geosciences, China University of Petroleum (East China), Qingdao, China, [2]Key Laboratory of Continental Shale Hydrocarbon Accumulation and Efficient Development (Northeast Petroleum University), Ministry of Education, Northeast Petroleum University, Daqing, China, [3]School of Art and Media, Xian Technological University, Xian, China

Wettability is a significant factor in the exploration and development of shale oil. Currently, shale wettability has yet to reach a unified understanding. The contact angle is widely used in the study of shale wettability. However, the pre-treatment of the shale profoundly affects the contact angle. In this paper, the contact angle errors introduced by the pre-treatment of samples are discussed. Shale wettability is influenced by many factors, and there is not yet a systematic study of its influencing factors. Based on the above issues, the shale of the northern Songliao Basin was taken as the subject. The wettability of the different lithofacies is characterized by an improved contact angle method. The compositional characteristics of the shales and oil in the study area were analyzed. Fresh minerals, a single component of oil, and different temperature/pressure conditions were set up to investigate the influencing factors of shale wettability. The studies show that Organic matter abundance and thermal maturity have a positive correlation with oil-wet. Siliceous minerals are positively correlated with water-wet. Carbonate and clay minerals are negatively correlated with water-wet. The mineralogical composition of the shale, the composition of the oil, the characteristics of the aqueous media, the asphaltene deposits on the surface, temperature, and pressure all impact wettability. The affinity of minerals for hydrocarbons is iron minerals > carbonate minerals > clay minerals > siliceous minerals. Minerals are more hydrophilic at low salinity conditions. The deposition of non-hydrocarbons and asphaltenes renders the surface oleophilic. Increasing temperatures will reduce the hydrophilicity of the "oil-water-rock".

Keywords: wettability, shale oil, contact angle, Northern Songliao basin, liquid-liquid extraction

INTRODUCTION

Shale wettability is the tendency for oil to expand or adhere to the pore surface (Roshan et al., 2016). It is one of the most significant properties of the surface characteristics of shale reservoirs (Alvarez et al., 2016a). Wettability controls the process of shale oil enrichment (Yong et al., 2016; Liu et al., 2018; Song et al., 2020; Liu et al., 2021). The process of enrichment of shale oil can be divided into two processes. Firstly, the oil is enriched within the internal pore network of the organic matter (OM) (Athy et al., 1930). Once the shale oil has met the retention capacity of the OM, it flows out of the OM pores and into the inorganic mineral pores, where it is enriched (Loucks et al., 2014; Liu et al., 2021). Before the oil enters the inorganic pores from the OM pore network, it is hydrophilic due to the film of water on the surface of the inorganic minerals (Li et al., 2017). The capillary forces are the resistance as the shale oil

moves from the OM pores into the inorganic minerals pores. After the oil enters the inorganic mineral pores, the polar compounds in the crude oil will break the water film on the mineral surface, replacing the water molecules adsorbed on the mineral surface (Buckley et al., 2001). Then, the surface absorption by oil will change from hydrophilic to lipophilic (Drummond et al., 2004). This reduces the capillary resistance of oil entering the inorganic minerals pores, making it easier to enrich. Wettability determines the lower limit and type of pore throat for oil filling. In the field of shale oil development, regulating reservoir wettability is key to improving shale oil recovery (Marsden et al., 1965; Ehrlich et al., 1974; Alvarez et al., 2016b; Jia et al., 2021). Wettability is important for selecting the appropriate fracturing fluid to minimize fracturing fluid losses. It is generally accepted that the highest crude oil recovery is achieved under low oil-water interfacial tension and weak water-wetting conditions during water displacement (He et al., 2018; Li et al., 2021; He et al., 2022).

The surface of shale pore throats is composed of very complex minerals and organic matter, and this composition makes the surface both oil-wet and water-wet (Yang et al., 2019). Generally, shale pores can be divided into relatively large micropores and smaller nanopores (Barnett et al., 2012; Chalmers et al., 2012). Micropores are predominantly found in inorganic minerals, while nanopores are mainly found in organic matter and clay minerals. Inorganic pores are widely considered to be hydrophilic. In contrast, organic pores are considered lipophilic and become more lipophilic as the maturity of the organic matter increases (Begum et al., 2019). The simultaneous presence of inorganic water-wet macropores and organic oil-wet micropores makes the shale double-wetting, distinguishing the shale wettability from conventional reservoirs (Tao Zhang et al., 2018).

Nowadays, shale wettability is characterized by five main methods viz. contact angle method (Siddiqui et al., 2018) (CA), spontaneous imbibition (Li et al., 2019) (SI), zeta potential method (Hoxha et al., 2016), nuclear magnetic resonance (NMR) (Chen et al., 2006), atomic force microscopy (AFM) (Kumar et al., 2005), and molecular dynamics simulation (MD) (Xue et al., 2021). The CA method is convenient, with a test range from strong water-wet to strong oil-wet, and has clear mechanical and thermodynamic significance, satisfying qualitative and quantitative studies and suitable for mechanistic studies. Therefore, CA is widely used in the study of shale wettability (Siddiqui et al., 2018). CA is mainly divided into the sessile drop method, which is used to express the wettability of the "gas-flow-rock system," and the captive bubble drop method, which represents the wettability of the "liquid-liquid-solid" system (Pan et al., 2020). However, numerous factors influence the contact angle. The pre-treatment process of shale samples (organic contamination of the surface and roughness) can severely impact the results. Therefore, the errors introduced by the pre-treatment of shale samples need to be analyzed.

The factors influencing the wettability of shale oil reservoirs can be summarized in the following five aspects: *1) Mineral and shale oil composition* (Borysenko et al., 2009; Lu et al., 2019). *2) Water medium characteristics* (Agbalaka et al., 2009; Berg et al., 2010). Brine concentration and pH control the wettability by influencing mineral surface chemistry and oil-water interfacial tension; DLVO theory can describe the interaction between the rock surface/brine and oil/brine interfaces, where "oil-water-rock" wettability depends on the balance between the two forces of electrostatic repulsion and van der Waals forces. *3) pore throat scale* (Yu et al., 1986). The smaller the droplet scale, the greater the effect of the upper line tension on the three-phase circumference and the more significant the change in contact angle. *4) Pore throat surface physicochemical properties* (Nakae et al., 1998). Cassie (1944) found that the greater the roughness of a solid surface, the more hydrophilic the surface would be. Whereas the surface of reservoir rocks is not smooth and flat, its surface roughness affects wettability. Asphaltenes in shale oil can break the water film on the surface of inorganic minerals in shale and adsorb to its surface, causing changes in wettability *5) Temperature and pressure conditions* (Zhang et al., 2018). Changes in temperature and pressure conditions can affect water-rock, oil-rock, oil-water, and oil-water interfacial tensions, thus affecting the wettability of the "oil-water-rock" system. Current research on the factors influencing wettability is scattered, and no systematic studies have been carried out.

Based on the above issues, Qingshankou (K_2qn) and Nenjiang (K_2n) in the northern Songliao Basin were taken as the subjects. The wettability of the different lithofacies is characterized by an improved contact angle method. The compositional characteristics of the shales and oil in the study area were analyzed. Fresh minerals, single components of oil, and different temperature/pressure conditions were set up to investigate the factors influencing the wettability of the shale oil reservoirs.

GEOLOGICAL BACKGROUND AND SAMPLES
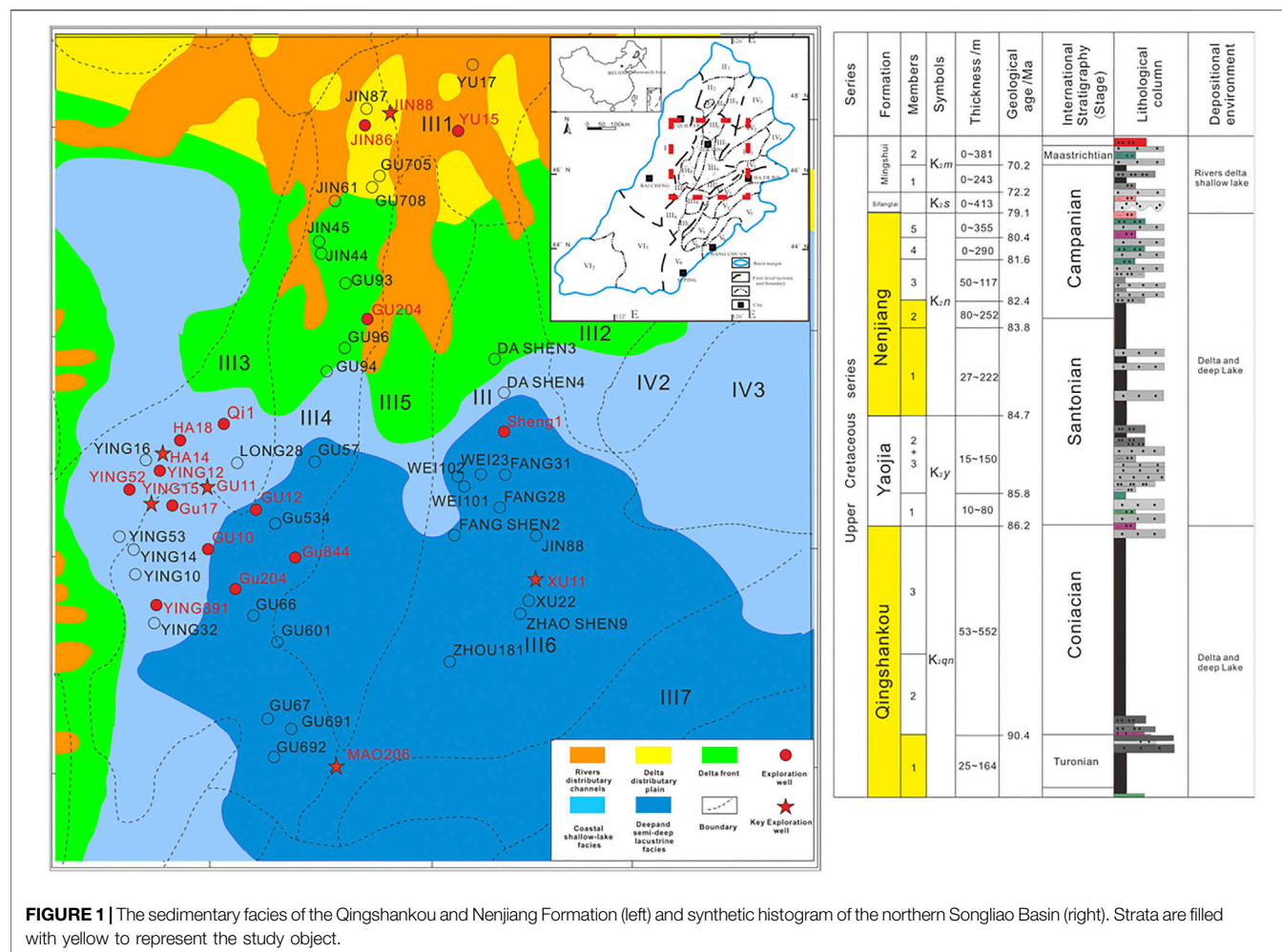
Geological Background of the Study Area

The target area of this study is the northern Songliao Basin (**Figure 1**). The Late Cretaceous is a deep and semi-deep lacustrine facies formation developed in the depressional stage of the basin, which is the main source rock and an important shale oil layer in the northern Songliao Basin. The target formations studied are the Qingshankou (K_2qn) and the Nengjiang (K_2n). The thickness of the K_2qn is usually in the range of 200–500 m, and the primary lithology is black-brown mud shale interbedded with a small amount of oil shale, and its lithology and petrography are highly variable. The stratigraphy of the K_2n is generally in the range of 100–450 m in thickness, with the lower part of it being sandstone transformed into mudstone and oil shale deposits and the upper part being interbedded with purple-red and green mudstone deposits (Hou et al., 2000; Bechtel et al., 2012; Jia et al., 2013).

Samples Information

Shales were taken from vital exploratory wells in the Qijia-Gulong Depression, the southern Daqing Changyuan area, and the Sanzhao Depression. Forty-six samples were selected for rock pyrolysis and whole-rock X-ray diffraction analysis (**Supplementary Table S1**). Then 33 of the samples were chosen for contact angle and liquid-liquid extraction experiments.

Samples from K_2qn are all shale with high maturity and high organic matter abundance. In contrast, samples from the K_2n had

FIGURE 1 | The sedimentary facies of the Qingshankou and Nenjiang Formation (left) and synthetic histogram of the northern Songliao Basin (right). Strata are filled with yellow to represent the study object.

lower maturity and organic matter abundance (**Supplementary Table S1**).

Figure 2 illustrates the mineralogical composition of the samples. The main minerals that make up the samples are quartz, plagioclase, calcite, dolomite, pyrite, siderite, illite, and kaolinite. The minerals were classified according to their elemental composition and similarity in the crystal structure (**Figure 2C**) as *siliceous minerals* (quartz and feldspar), *clay minerals* (kaolinite and illite), *carbonate minerals* (calcite and iron dolomite), and *iron minerals* (pyrite and siderite).

The K_2n (**Figure 2B**) has a higher siliceous mineral content than the K_2qn (**Figure 2A**), with an average value of 63.7%. The content of clay minerals is lower than that of the K_2qn, with the percentage of content distributed between 13.5 and 44.3% and the mean value of 27.82%. The carbonate and iron mineral content is similarly distributed at a lower level.

Referring to the delineation scheme of Liu (Liu et al., 2019) for the shales of the Qingshankou Formation in the southern Songliao Basin, the lithofacies were delineated in terms of the *macrostructure* (**Figure 3**), *TOC,* and *mineral composition* of the samples. Lu (Shuangfang et al., 2012) proposed a "trichotomous method" for shale oil resource evaluation, in which a TOC of 1 wt

% and 2 wt% is the threshold for classifying high and low organic matter. In this paper, the samples are divided into **high organic matter** (TOC ≥ 2 wt%), **medium organic matter** (1 wt% ≤ TOC < 2 wt%), and **low organic matter** (TOC < 1 wt%).

EXPERIMENTAL METHODS

Experimental Materials

Fresh minerals were selected concerning the mineral composition of the shale: quartz, plagioclase, calcite, iron dolomite, pyrite, rhodochrosite, illite, and kaolinite. Wettability characterization of single and pure minerals is fundamental to explore the effect of different mineral compositions on the overall wettability of shale. Whole-rock X-ray diffraction analysis of the fresh minerals showed that the purity of the minerals was essentially greater than 97%.

Regarding the shale oil composition, several common compounds were selected for this study, respectively: n-hexane, n-dodecane, and n-octadecane for the *saturated hydrocarbon component*; benzene for the *aromatic component*; and 3-dodecylthiophene and N,N-dimethyldodecylamine for the *non-hydrocarbon*
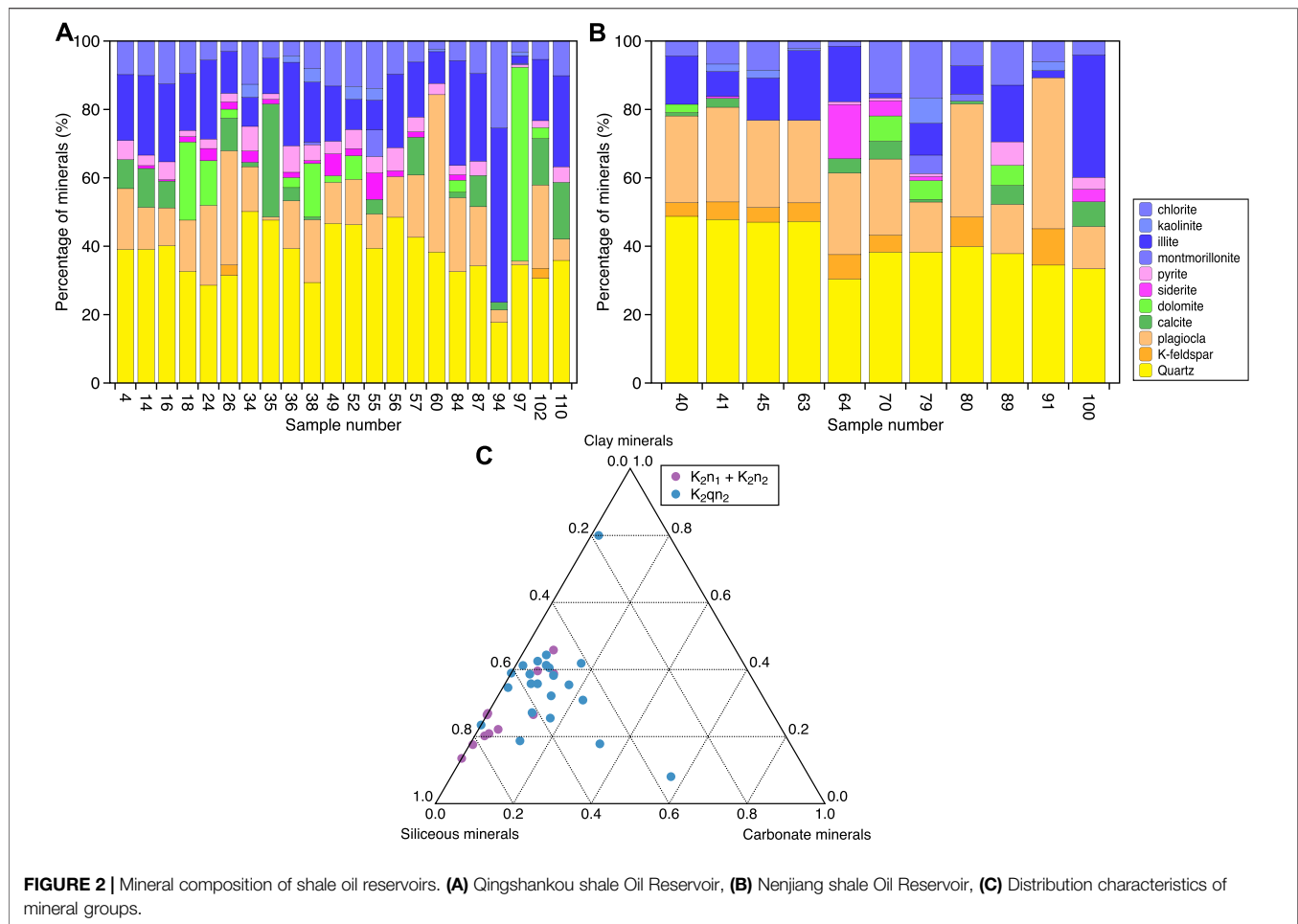
FIGURE 2 | Mineral composition of shale oil reservoirs. **(A)** Qingshankou shale Oil Reservoir, **(B)** Nenjiang shale Oil Reservoir, **(C)** Distribution characteristics of mineral groups.

component. The compounds purchased were Dr. Germany brand products, whose chemical parameters and specifications are shown in **Supplementary Table S2**. Crude oil samples and kerosene were also used in the experiments. Kerosene was used to represent the low carbon number mixture of hydrocarbons in crude oil, whose main components are alkanes of n-C_{12} ~ n-C_{14} and contain small amounts of aromatic hydrocarbons, unsaturated hydrocarbons, cyclic hydrocarbons, and other impurities such as sulfides and gums.

Liquid-Liquid Extraction

Liquid-Liquid Extraction (LLE) qualitatively evaluates the affinity of shale particles for two liquid phases (**Supplementary Figure S1**). Samples were crushed to 160 mesh to reduce the effect of buoyancy on results. 0.6 g of rock powder, water, and kerosene is mixed together, stirred thoroughly and shaken for 5 min, and then left for a while. Different particles have different hydrophilic or oleophilic properties on the surface, which determines whether they sink in water or are suspended in the oil phase. The distribution of the particles is used to qualitatively determine the affinity of the rock particles for water or oil.

Pre-treatment of Samples for Contact Angle

It was not known what the ideal level of polishing required for the sample was. To solve this problem, uartz and calcite chips were polished separately using different grit sizes (80, 160, 400, 1,200, 2,000, 6,000, 8,000, 10,000 grit and mirror polish). The "oil-water-rock" contact angle of calcite with different roughness was compared to determine the grinding method required for this study surface.

The roughness of a surface can be expressed in terms of R_a, which is the arithmetic mean of the absolute values of the distances from the points on the measured profile to the reference line within the sampling length L. The roughness R_a of different surfaces was measured using the stylus method with a Hommel-Etamic T8000 roughness profiler from Suzhou Winters Measurement Technology Co.

As shown in **Figure 4A**, as the grit of the sandpaper is increased, the Ra value decreases, which means a smoother surface. The mirror-polished surface has a meager Ra value of only 20 nm, so the surface can be considered smooth. The contact angle results for different roughness are shown in **Figure 4B**. As predicted by the Cassie-Baxter model, the contact angle decreases to a specific value and then remains constant as the surface roughness decreases. For highly rough surfaces (Ra > 0.8 μm), the contact angle is
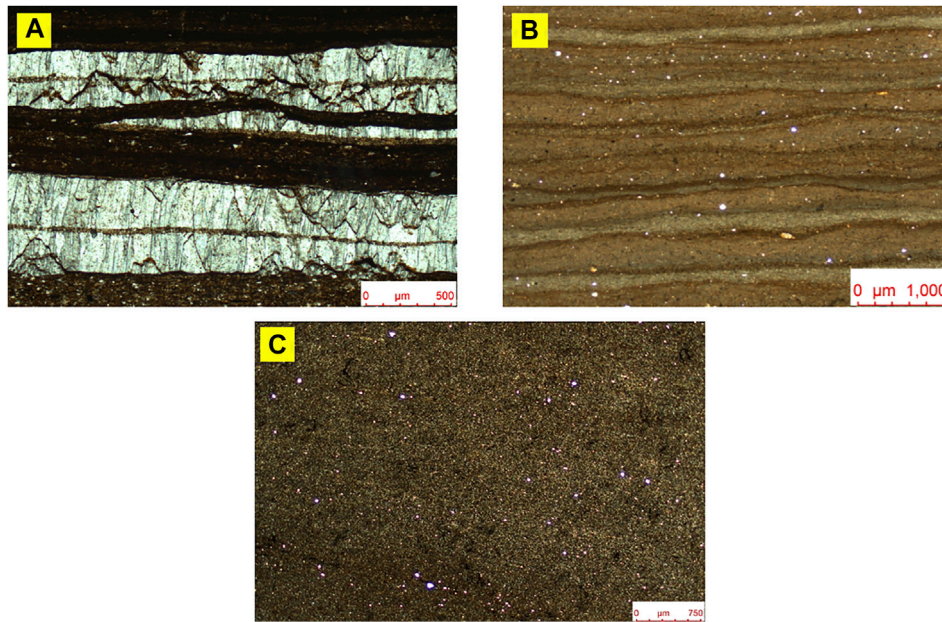
FIGURE 3 | Structural characteristics of shale oil reservoir samples. **(A)** Bedded structure, sample #97; **(B)** Laminar structure, sample #110; **(C)** Massive structure, sample #60.
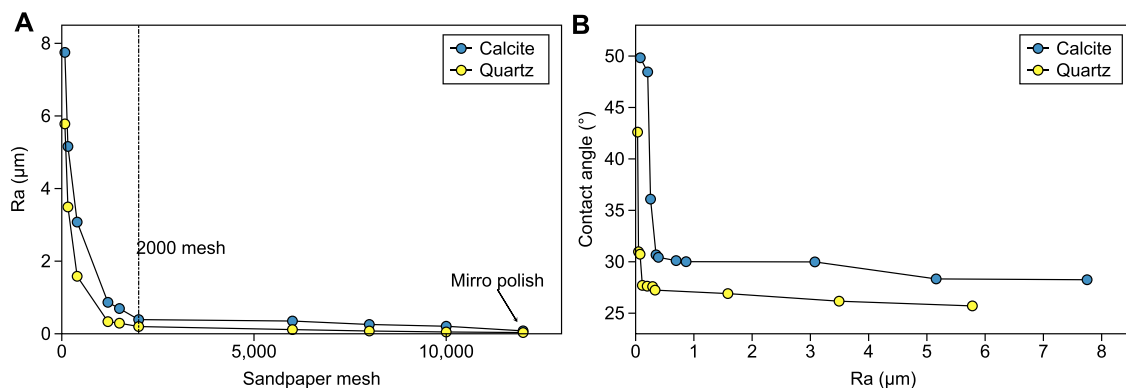
FIGURE 4 | Roughness and contact angle after polishing with different meshes of sandpaper. **(A)** Sandpaper mesh vs. R_a, **(B)** R_a vs. contact angle.

almost constant but considerably different from Young's contact angle. However, for relatively smooth surfaces (R_a < 0.8 μm), the contact angle varies significantly. Therefore, there is a solid need to mirror polish the surfaces.

Contact Angle Experiments
"Oil-Water Rock" Contact Angle Prediction Model for Shale

The "oil-water-rock" contact angle (**Figure 5B**) from the captive bubble method appears to be more consistent with geological conditions than the sessile drop method (**Figure 5A**). However, when the "oil-water-rock" contact angle of shale is measured using the captive bubble drop method, some samples are found to break up

due to the high clay content when immersed in water. Some samples have a very stable water film on the surface, making it difficult for oil droplets to reach the shale surface (**Figures 5C,D**). Such samples cannot be subjected to the captive bubble method.

Comparison of the "gas-water-rock" and "gas-oil-rock" contact angles for the sessile drop method does not allow for a determination of whether the test sample is more hydrophilic or more lipophilic. To illustrate this point, separate "gas-water-rock" (**Figure 6B**), "gas-oil-rock" (**Figure 6A**), and "oil-water-rock" (**Figures 6C,D**) contact angle experiments were carried out to compare the oil-wetness and water-wetness of quartz surfaces (**Figure 6**). The results of the "gas-oil-rock" experiment showed that the contact angle of hexane on the quartz surface was 0° and
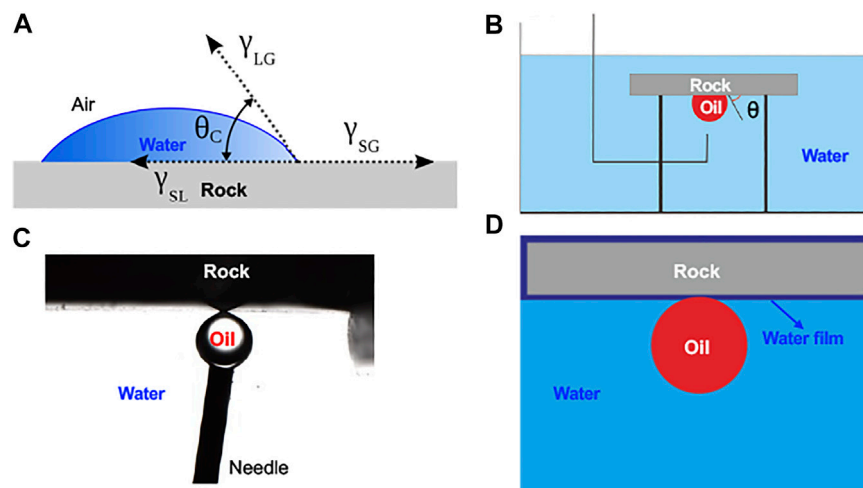
FIGURE 5 | (A) Schematic of sessile drop methods for contact angle measurements; (B) captive bubble methods; (C,D) illustrating the failure of oil droplets to contact the shale surface due to the water film.
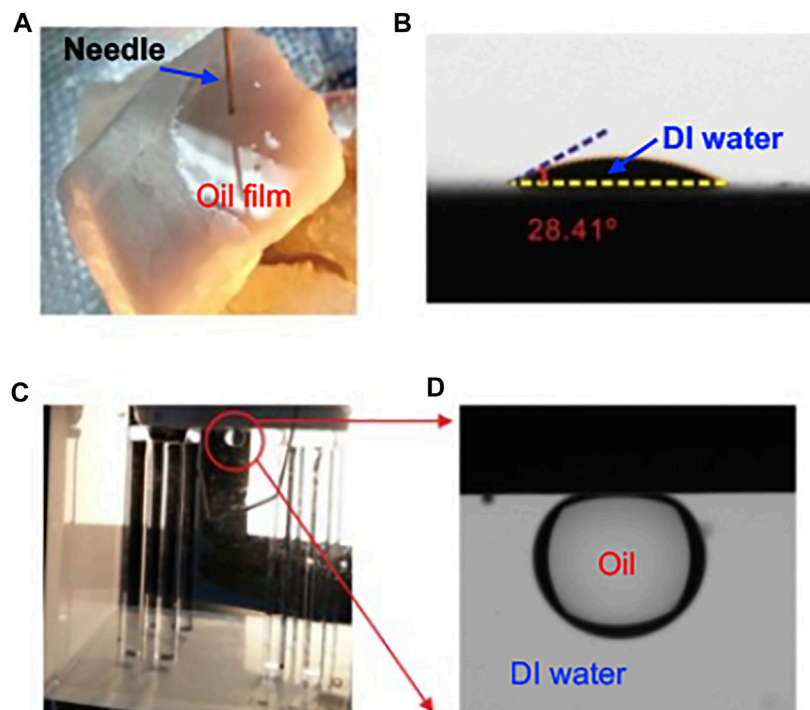
FIGURE 6 | (A) Spreading phenomenon of oil on the quartz surface, (B) Contact angle of DI water on the quartz surface, (C,D) illustrating the hydrophilic nature of quartz.

the quartz was completely oil-wet; the contact angle of DI water on the quartz surface was 28.41°, and the quartz was not completely water-wet. From the experimental assessment of the relative lipophilicity and hydrophilicity of the quartz surface by the sessile drop method, it can be concluded that the surface of quartz is lipophilic. However, the results of the "oil-water-rock" experiments by the captive bubble method show an oil contact angle of 157° compared to a water contact angle of 23°. Quartz is hydrophilic. This contradicts the conclusions obtained by the sessile drop method. It is clear that the results of the suspended-drop method are accurate for an oil-water environment and that the seated-drop method is not sufficient to determine whether the surface is more lipophilic or hydrophilic.

FIGURE 7 | (A) Wettability characteristics of the all shale oil reservoir samples, **(B)** Wettability characteristics of samples from the Qingshankou and Nengjiang Formations.
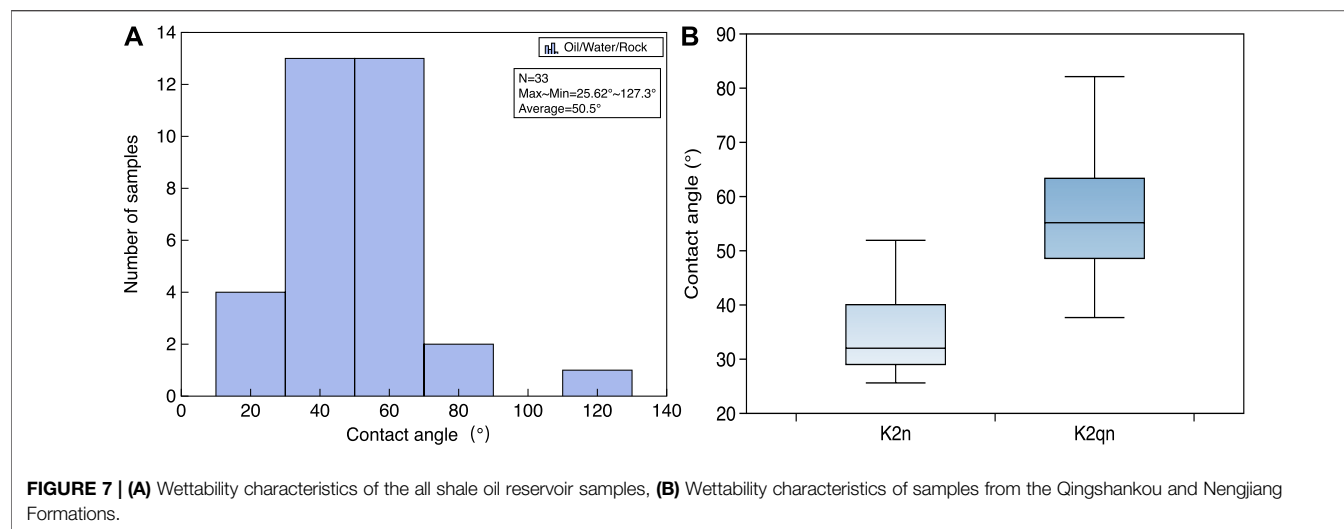
TABLE 1 | Samples of different lithofacies for contact angle and liquid-liquid extraction experiments.

Lithofacies	Number of samples	TOC (%)	Siliceous minerals (%)	Carbonatite minerals (%)	Clay minerals (%)
Low organic matter silica-rich massive shale	41	0.64	76.9	2.5	20.1
Low organic matter laminated silica-rich shale	91	0.64	86.5	0.0	13.5
Low organic matter bedded silica-rich shale	80	0.97	81.6	0.8	17.6
High organic matter laminated siliceous shale	49	2.15	51.8	1.7	37.5
High organic matter massive siliceous shale	14	2.88	48.7	10.8	36.8
High organic matter massive clay shale	94	4.33	18.1	1.9	80.0

FIGURE 8 | Wettability of different lithofacies. Samples 41, 91, and 80 have high organic matter content and low siliceous mineral content; 14, 94, and 49 are the contrary.

FIGURE 9 | Correlation between wettability and material composition of shale. **(A)** TOC, **(B)** S_1, **(C)** R_o, **(D)** Siliceous minerals, **(E)** Carbonate minerals, **(F)** Clay minerals.
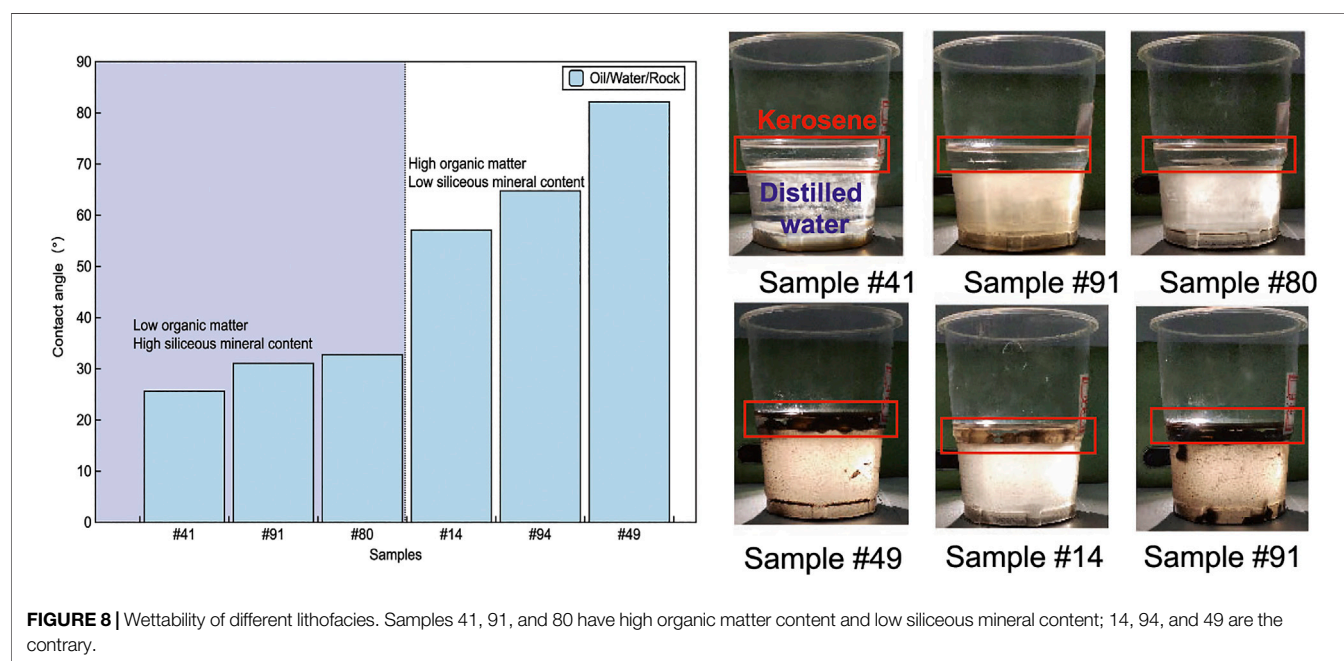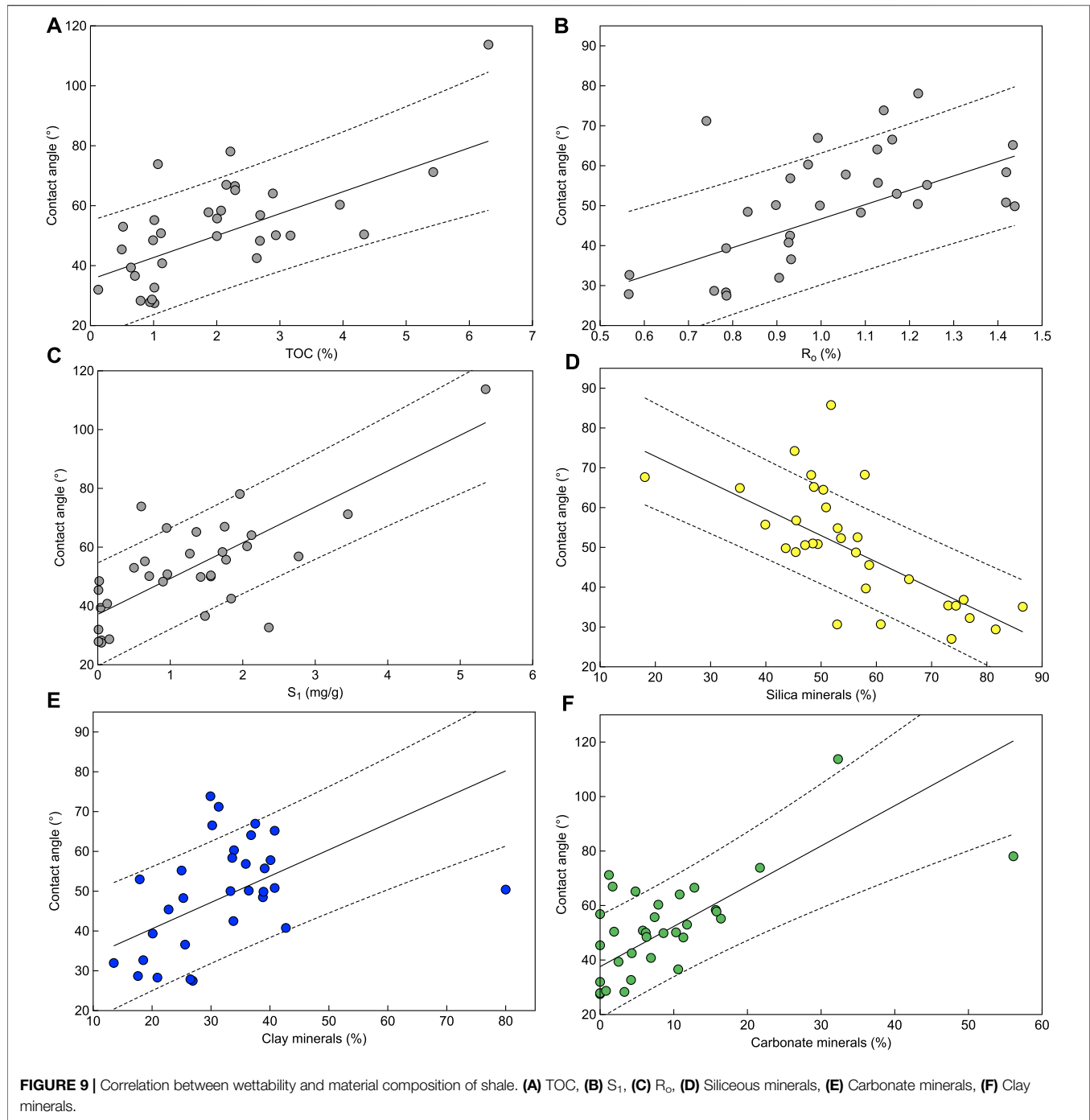
Siddiqui (2018) proposed **Eq. 1** to achieve the conversion of "gas-water-rock" contact angles on shale surfaces to "oil-water-rock" contact angles.

$$\theta_{o-w} = \cos^{-1}\left(\frac{\gamma_{o-g}\cos_{o-g} - \gamma_{w-g}\cos\theta_{w-g}}{\gamma_{o-w}}\right) \qquad (1)$$

Where oil surface tension γ_{o-g}, mN/m; water surface tension γ_{w-g}, mN/m; oil-water interfacial tension γ_{o-w}, mN/m;

"gas-oil-rock" contact angle θ_{o-g}; "gas-water-rock" contact angle θ_{w-g}; "oil-water-rock" contact angle θ_{o-w}.

To verify the accuracy of **Eq. 1**, 10 samples were selected to carry out "gas-oil-rock", "gas-water-rock" and "oil-water-rock" contact angle experiments. The water samples were ionized water, and the oil samples were kerosene. The parameters and the calculated "oil-water-rock" contact angles are shown in **Supplementary Table S3**.
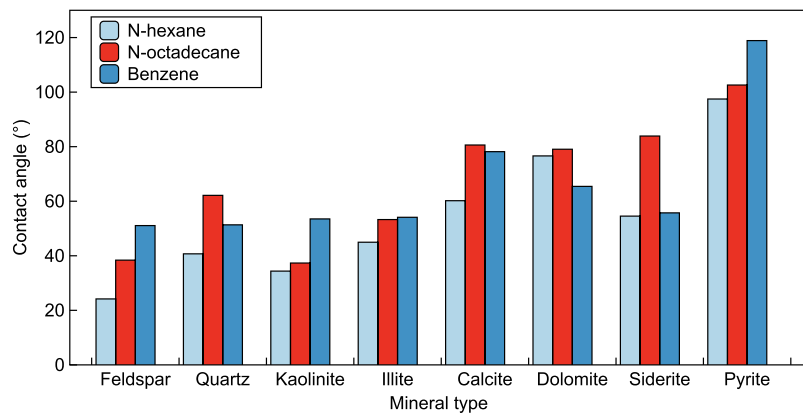
FIGURE 10 | Wettability of fresh minerals. Fresh minerals are the main components of shale.
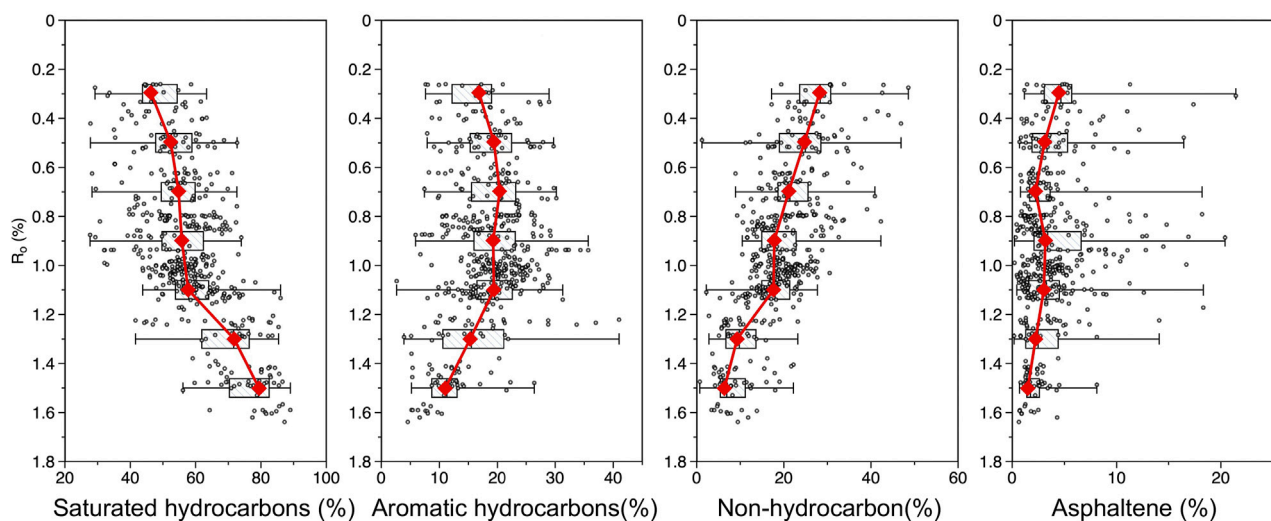
FIGURE 11 | Characteristics of shale oil components in the target area with maturity.

The excellent correlation between measured and calculated contact angles (**Supplementary Figure S2**) demonstrates that this formula can be applied to calculate the "oil-water-rock" contact angle for shales. However, the measured values are always less than the theoretical oil-water contact angle, which means that the measured results are more hydrophilic than the theoretical ones, probably because the rock sheet is preferentially wholly immersed in water and a film is formed on the surface, which increases the hydrophilicity of the rock sheet.

High Temperature and Pressure Contact Angle Experiments

A high temperature and pressure contact angle experiment was carried out to study temperature and pressure on the wettability of "oil-water-rock" (**Supplementary Figure S3**). The instrument includes a high temperature and pressure chamber, water

injection pump, oil injection pump (or gas injection pump), high precision camera, and computer processing.

RESULT AND DISCUSSION

Wettability Characteristics of Shales
Comparison of Different Formations

The "oil-water-rock" contact angle (θ) results for the samples are shown in **Figure 10**. The samples are almost all hydrophilic, with θ overwhelmingly in the range of 25–80°. The samples can be further classified according to the differences in water-wetting properties: **strong water-wetting** ($\theta < 30°$), **medium water-wetting** ($30° < \theta < 60°$) and **weak water-wetting** ($60° < \theta < 90°$). The majority of samples were medium water-wet, with fewer samples being strong or weak water-wet. However, sample 35 is
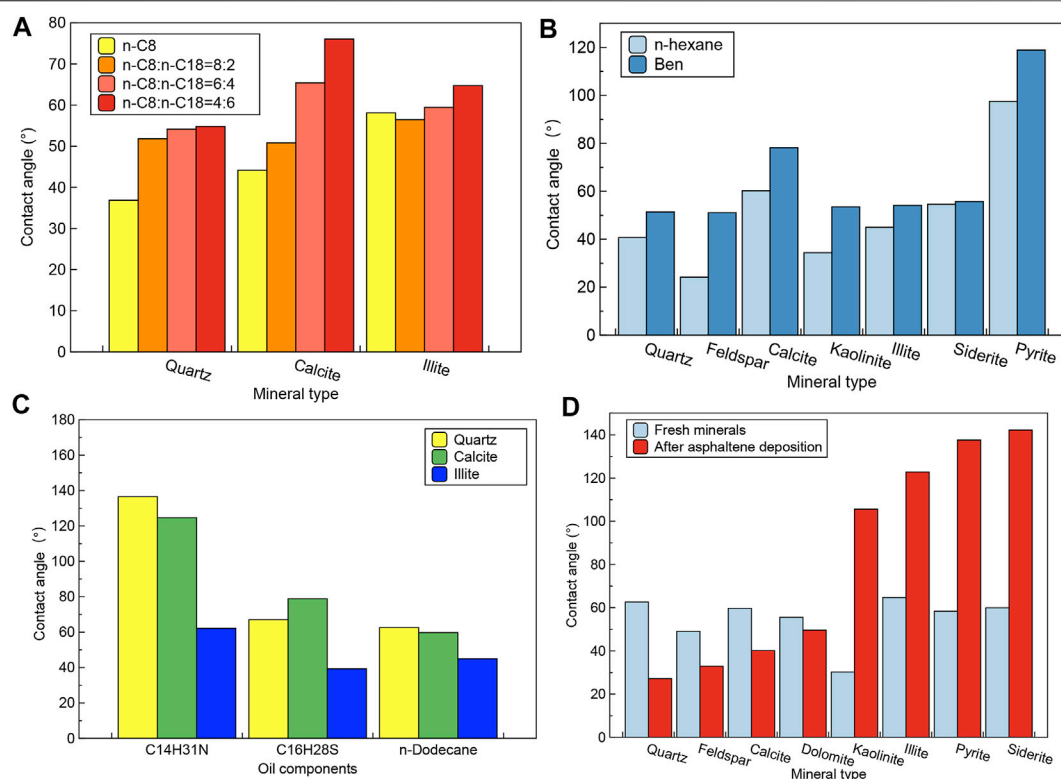
FIGURE 12 | (A) Effect of heavy hydrocarbon content on wettability, (B) Effect of aromatic content on wettability, (C) Effect of non-hydrocarbon content on wettability, (D) Effect of asphaltene deposition on wettability.

oil-wet (θ = 90.15°) owing to the high TOC (6.3 wt%) and carbonate minerals content (32.3%).

Figure 7 shows that the water-wetness of the Nengjiang is significantly better than that of the Qingshankou. The two have a similar mineral composition, so minerals are not the cause of the difference in wettability. The TOC of the Qingshankou is slightly higher than that of the Nengjiang, but the maturity of organic matter is significantly higher than that of the Nengjiang. The Qingshankou Formation has completed a large amount of hydrocarbon expulsion (S_1 and S_2 are high), and the adsorption of polar oil components renders wettability towards oil wetting. The low maturity Nengjiang has not yet undergone significant hydrocarbon expulsion (S_1 and S_2 are low), and the reservoir is in primitive water-wetting. Maturity is the reason for the difference in wettability between the Qingshankou and Nengjiang.

Comparison of Different Lithofacies

Table 1 illustrates the major lithofacies in the target area. The samples can be divided into two groups according to their TOC and mineral content. The first group, 41, 91, and 80, are characterized by low TOC (<1 wt%), low clay mineral content (≤20.1%), and high siliceous mineral content (≥76.9%). The second group is 49, 14, and 94, which are characterized by high TOC (>2%) and higher clay mineral (≥36.8%) content.

The results of the "oil -water-rock" contact angle measurements for the rocks are shown in Figure 8. The first group of rock samples (41, 91, and 80) have contact angles in the range of 26°–31°, which are strongly hydrophilic. The second group of rock samples (14, 94, and 49) have contact angles in the range of 58°–80°, respectively, and are weak water-wetness, presumably related to their high TOC and clay mineral content.

The results of the LLE are consistent with the CA (Figure 8). The first group of rock particles is mainly distributed in the water layer, while only a few particles are distributed in the oil-water interface and kerogen. This indicates that all rock particles in the first group are hydrophilic. The second group is partly suspended at the kerosene, partly suspended in DI water. This shows that they are both hydrophilic and oleophilic. The number of oleophilic particles is related to the TOC.

Factors Influencing Shale Wettability
Organic Matter and Mineral Composition Characteristics

The relationship between contact angle and organic characteristics is analyzed in Figures 9A–C. TOC, S_1, and R_o have a positive correlation with oil-wet. Recently, various studies have shown the lipophilic of organic matter (Siddiqui et al., 2018). This means that the higher the organic matter abundance the more oil-wet the sample is, which is consistent with the conclusions obtained from Figure 8. S_1 is related to the oil content. As the oil content increases, the surface gradually shifts from water-wet to oil-wet. Previous

FIGURE 13 | Variation of wettability with $CaCl_2$ concentration. **(A)** quartz, **(B)** calcite, **(C)** siderite, **(D)** illite.
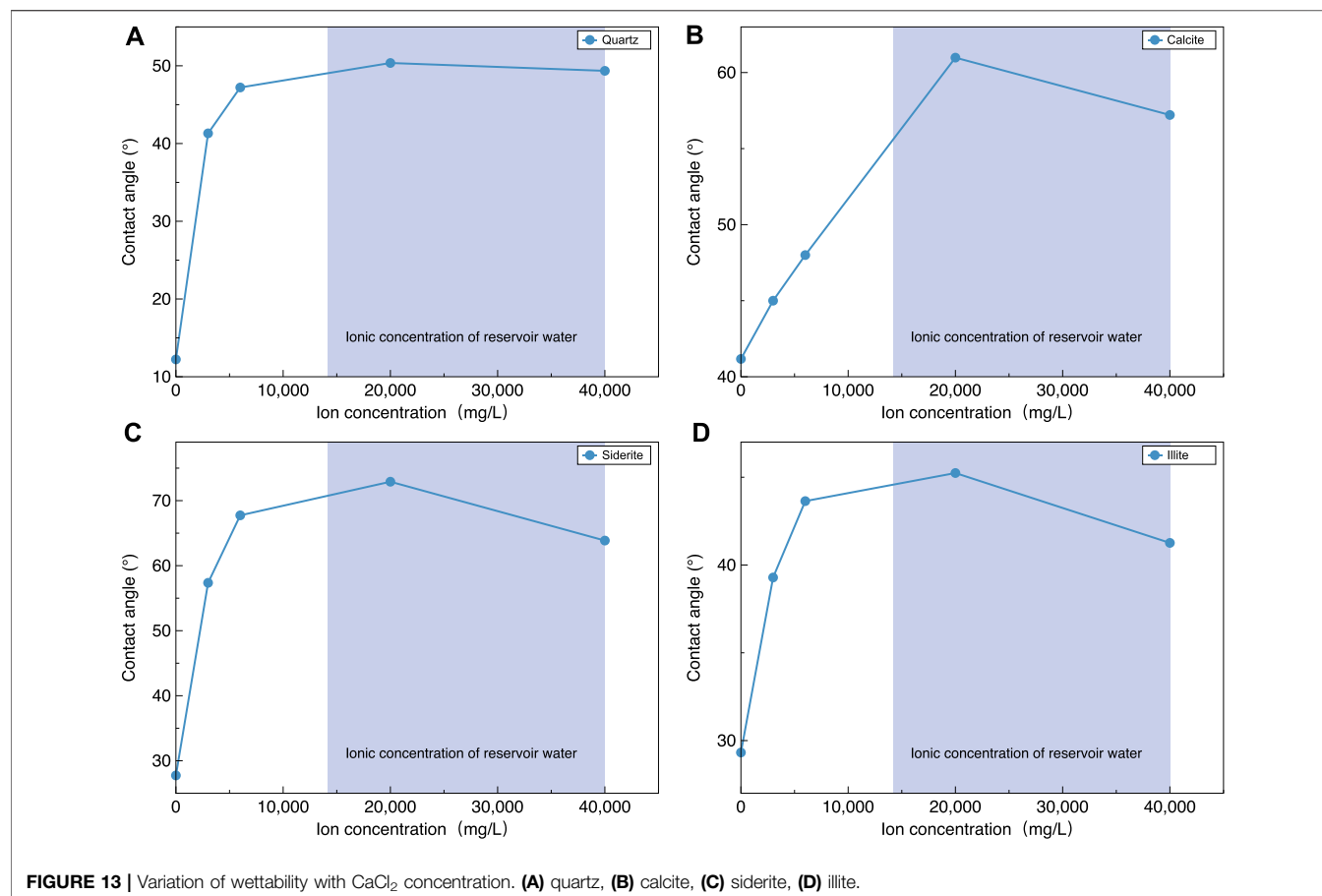
molecular dynamics results (Jagadisan et al., 2019) have shown that low maturity organic matter is more hydrophilic. In addition, the low maturity means that the oil has not yet been generated in large quantities and it is difficult to shift the surface to oil-wetness.

The relationship between contact angle and mineral composition characteristics is analyzed in **Figures 9D–F**. Siliceous minerals are positively correlated with water-wet. However, carbonate and clay minerals are negatively correlated with water-wet. The strong water-wet of siliceous minerals and the weak water-wet of carbonate minerals have been confirmed, but there is no agreed understanding of the wettability of clay minerals. Therefore, it was necessary to carry out wettability experiments with a single pure mineral to verify the conclusions of **Figures 9D–F**.

Figure 10 compares the affinity of different fresh minerals for hydrocarbons (saturated and aromatic hydrocarbons). Eight minerals exhibit hydrophilic properties ($\theta < 90°$). The order of affinity of minerals to hydrocarbons is carbonate minerals > clay minerals > siliceous minerals. Siliceous minerals exhibit strong water-wetting, and calcareous minerals exhibit weak water-wetting. The shale is essentially medium water-wetting. Then, an increase in siliceous/calcareous minerals will shift the shale towards strong/weak water-wetting. This is consistent with the conclusions obtained in **Figure 9**. However, the wettability of the clay minerals obtained from **Figures 9F, 10** is inconsistent. Considering that no experiments were carried out to remove oil from the cores after the samples were extracted

in situ, a certain amount of colloidal asphaltene is deposited on the surface of the clay minerals. It is the deposition of colloidal asphaltene that reverses the wettability, giving a seemingly unreasonable negative correlation between clay mineral content and water-wetting.

Oil Components

The physicochemical properties of shale oil are related to its composition (saturated hydrocarbons, aromatic hydrocarbons, non-hydrocarbons, asphaltenes), which varies with the maturity of the organic matter. **Figure 11** shows the composition of shale oil for different maturity of organic matter. The results show that as the depth of burial increases, i.e., the maturity of the organic matter (Ro) increases, the saturated hydrocarbon fraction tends to grow, the aromatic and non-hydrocarbon fractions tend to decrease, the asphaltene does not change much, and the ratio of saturated to aromatic hydrocarbons tends to increase.

High carbon number alkanes show more affinity to mineral surfaces than low carbon number alkanes (**Figure 12A**). Since n-octadecane is a solid at room temperature, solutions of different ratios of n-octadecane and n-octadecane have been configured to represent high carbon number alkanes. **Figure 12A** shows that as the $n-C_{18}/n-C_8$ increases, the contact angle increases and the affinity of the mineral to the oil is stronger.

For the same carbon number, aromatic hydrocarbons have a stronger affinity for minerals than alkanes (**Figure 12B**). The proportion of aromatics decreases as the depth of formation

FIGURE 14 | Effect of temperature and pressure on wettability. The system is "quartz - kerosene- distilled water".
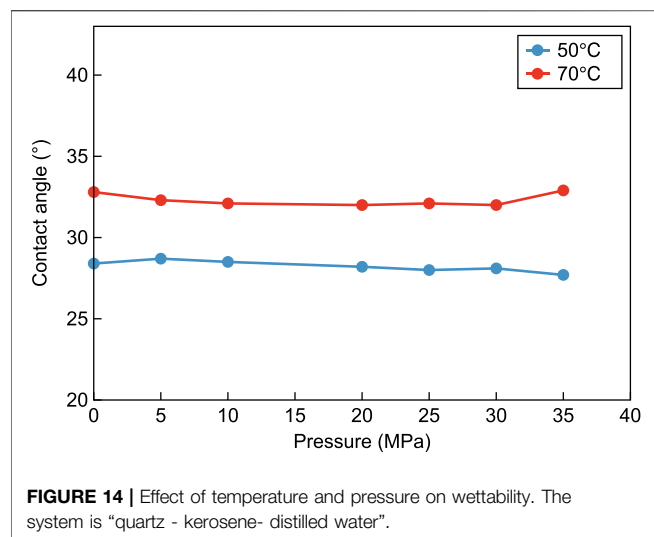
increases, this reduces the affinity of the oil to the reservoir surface.

Polar oil components have a greater affinity for minerals than non-polar oil components (**Figure 12C**). The affinity of oil components for minerals is nitrogenous compounds > sulfurous compounds > alkanes. Most of the mineral surfaces that exist in nature are polar, so it is not difficult to understand this. It is the extremely strong affinity of polar compounds that renders the surface to oil-wetness. The proportion of non-hydrocarbons decreases as the depth of formation increases, this reduces the affinity of the oil to the reservoir surface.

Asphaltene deposition converts the surface to lipophilic, especially for clay minerals (**Figure 12D**). The wettability of fresh minerals is compared with that of minerals immersed in crude oil for 48 h. The wettability of the clay minerals undergoes a dramatic shift from strongly water-wet to oil-wet. The water-wetness of the siliceous and carbonate minerals increased instead, probably due to the short immersion time.

Brine Salinity
Considering that $CaCl_2$ is the main additive in fracturing fluids, this study investigates the change in wettability of different salinities of $CaCl_2$ (**Figure 13**). As the brine salinity increases, the contact angle tends to rise and then fall for all four mineral types. Low salinity flooding may be the way to enhance shale oil recovery.

Temperature and Pressure Conditions
The experimental results are shown in **Figure 14**. When the temperature is 50°C or 70°C, the contact angle does not change significantly as the pressure increases. At the same ambient pressure, as the temperature increases (by 20°C), the contact angle value becomes larger (by approximately 5°) and the oil wettability increases. It is worth noting that an increase in pressure can lead to a rupture of the water film on the reservoir surface and thus a decrease in water wettability.

CONCLUSION

This manuscript characterizes the wettability of the Qingshankou and Nengjiang formations in the northern Songliao Basin by using contact angle and liquid-liquid extraction experiments. Fresh minerals, a component of oil, and different temperature/pressure conditions were set up to investigate the factors influencing the wettability of the shale oil reservoirs.

1) Low organic matter maturity is the main factor for the Nenjiang Formation being more hydrophilic than the Qingshankou Formation.
2) TOC, S_1, and R_o of shale have a positive correlation with oil-wet. Siliceous minerals are positively correlated with water-wet. Carbonate and clay minerals are negatively correlated with water-wet.
3) The mineralogical composition of the shale, the composition of the oil, the characteristics of the aqueous media, the asphaltene deposits on the surface, temperature, and pressure all have an impact on wettability. The affinity of minerals for hydrocarbons is iron minerals > carbonate minerals > clay minerals > siliceous minerals. Minerals are more hydrophilic at low salinity conditions. The deposition of non-hydrocarbons and asphaltenes renders the surface oleophilic. Increasing temperatures will reduce the hydrophilicity of the "oil-water-rock".(Lu et al., 2012; Wang et al., 2016; Zhang et al., 2018).

DATA AVAILABILITY STATEMENT

The original contributions presented in the study are included in the article/**Supplementary Material**, further inquiries can be directed to the corresponding author.

AUTHOR CONTRIBUTIONS

HX designed the project and wrote the main manuscript. ZD and ST help to draw the figures and to draft the manuscript. SL defined the statement of the problem. CA helped to discuss the problems and revise the manuscript. YZ helped to discuss the main idea and helped to draft the manuscript. BL help to calculate the data and draw the figures. XX helped to revise the figures. All authors reviewed the manuscript.

FUNDING

SUPPLEMENTARY MATERIAL

The Supplementary Material for this article can be found online at: https://www.frontiersin.org/articles/10.3389/feart.2021.736938/full#supplementary-material

REFERENCES

Agbalaka, C. C., Dandekar, A. Y., Patil, S. L., Khataniar, S., and Hemsath, J. R. (2009). Coreflooding Studies to Evaluate the Impact of Salinity and Wettability on Oil Recovery Efficiency. *Transp Porous Med.* 76 (1), 77–94. doi:10.1007/s11242-008-9235-7

Alvarez, J. O., and Schechter, D. S. (2016a). Application of Wettability Alteration in the Exploitation of Unconventional Liquid Resources. *Pet. Exploration Dev.* 43 (5), 832–840. doi:10.1016/S1876-3804(16)30099-4

Alvarez, J. O., and Schechter, D. S. (2016b). Application of Wettability Alteration in the Exploitation of Unconventional Liquid Resources. *Pet. Exploration Dev.* 43 (5), 832–840. doi:10.1016/S1876-3804(16)30099-4

Athy, L. F. (1930). Compaction and Oil Migration. *AAPG Bull.* 14, 25–35. doi:10.1306/3d93289f-16b1-11d7-8645000102c1865d

Bechtel, A., Jia, J., Strobl, S. A. I., Sachsenhofer, R. F., Liu, Z., Gratzer, R., et al. (2012). Palaeoenvironmental Conditions during Deposition of the Upper Cretaceous Oil Shale Sequences in the Songliao Basin (NE China): Implications from Geochemical Analysis. *Org. Geochem.* 46, 76–95. doi:10.1016/j.orggeochem.2012.02.003

Begum, M., Yassin, M. R., Dehghanpour, H., and Of Alberta, U. (2019). Effect of Kerogen Maturity on Organic Shale Wettability: A Duvernay Case Study. *Mar. Pet. Geology.* 110, 483–496. doi:10.1016/j.marpetgeo.2019.07.012

Berg, S., Cense, A. W., Jansen, E., and Bakker, K. (2010). Direct Experimental Evidence of Wettability Modification by Low Salinity. *Petrophysics-The SPWLA J. Formation Eval. Reservoir Description* 51 (5), 314–322. doi:10.1016/j.petrol.2010.08.016

Borysenko, A., Clennell, B., Sedev, R., Burgar, I., Ralston, J., Raven, M., et al. (2009). Experimental Investigations of the Wettability of Clays and Shales. *J. Geophys. Res.* 114. doi:10.1029/2008JB005924

Buckley, J. S. (2001). Effective Wettability of Minerals Exposed to Crude Oil. *Curr. Opin. Colloid Interf. Sci.* 6, 191–196. doi:10.1016/s1359-0294(01)00083-8

Chalmers, G. R., Bustin, R. M., Power, I. M., Bustin, R. M., and Power, I. M. (2012). Characterization of Gas Shale Pore Systems by Porosimetry, Pycnometry, Surface Area, and Field Emission Scanning Electron Microscopy/transmission Electron Microscopy Image Analyses: Examples from the Barnett, Woodford, Haynesville, Marcellus, and Doig Units. *Bulletin* 96 (6), 1099–1119. doi:10.1306/10171111052

Chalmers, G. R., Bustin, R. M., and Power, I. M. (2012). Characterization of Gas Shale Pore Systems by Porosimetry, Pycnometry, Surface Area, and Field Emission Scanning Electron Microscopy/transmission Electron Microscopy Image Analyses: Examples from the Barnett, Woodford, Haynesville, Marcellus, and Doig Units. *Bulletin* 96, 1099–1119. doi:10.1306/10171111052

Chen, J., Hirasaki, G. J., and Flaum, M. (2006). NMR Wettability Indices: Effect of OBM on Wettability and NMR Responses. *J. Pet. Sci. Eng.* 52, 161–171. doi:10.1016/j.petrol.2006.03.007

Drummond, C., and Israelachvili, J. (2004). Fundamental Studies of Crude Oil–Surface Water Interactions and its Relationship to Reservoir Wettability. *J. Petrol. Sci. Eng.* 45 (5), 61–81. doi:10.1016/j.petrol.2004.04.007

Ehrlich, R., Hasiba, H. H., and Raimondi, P. (1974). Alkaline Waterflooding for Wettability Alteration-Evaluating a Potential Field Application. *J. Pet. Tech.* 26 (3), 1335–1343. doi:10.2118/4905-pa

He, T., Li, W., Lu, S., Pan, W., Ying, J., Zhu, P., et al. (2022). Mechanism and Geological Significance of Anomalous Negative δ13Ckerogen in the Lower Cambrian, NW Tarim Basin, China. *J. Pet. Sci. Eng.* 208, 109384. doi:10.1016/j.petrol.2021.109384

He, T., Lu, S., Li, W., Tan, Z., and Zhang, X. (2018). Effect of Salinity on Source Rock Formation and its Control on the Oil Content in Shales in the Hetaoyuan Formation from the Biyang Depression, Nanxiang Basin, Central China. *Energy Fuels* 32 (6), 6698–6707. doi:10.1021/acs.energyfuels.8b01075

Hideo Nakae, H., Ryuichi Inui, R., Yosuke Hirata, Y., and Hiroyuki Saito, H. (1998). Effects of Surface Roughness on Wettability. *Acta Materialia* 46 (7), 2313–2318. doi:10.1016/s1359-6454(98)80012-8

Hou, D., Li, M., and Huang, Q. (2000). Marine Transgressional Events in the Gigantic Freshwater lake Songliao: Paleontological and Geochemical Evidence. *Org. Geochem.* 31 (7-8), 763–768. doi:10.1016/S0146-6380(00)00065-6

Hoxha, B. B., Sullivan, G., Van Oort, E., Daigle, H., and Schindler, C. (2016). "Determining the Zeta Potential of Intact Shales via Electrophoresis," in SPE

Europec featured at 78th EAGE Conference and Exhibition.. June 2016, Vinna,Austria, doi:10.2118/180097-ms

Jagadisan, A., and Heidari, Z. (2019). "Demystifying Wettability Alteration in Kerogen as a Function of its Geochemistry and Reservoir Temperature and Pressure Using Molecular Dynamics Simulations," in SPE Annual Technical Conference and Exhibition.. Sep 30 2019, Calgary, AB Canada, doi:10.2118/195863-ms

Jia, J., Liu, Z., Bechtel, A., Strobl, S. A. I., and Sun, P. (2013). Tectonic and Climate Control of Oil Shale Deposition in the Upper Cretaceous Qingshankou Formation (Songliao Basin, NE China). *Int. J. Earth Sci. (Geol Rundsch)* 102 (6), 1717–1734. doi:10.1007/s00531-013-0903-7

Jia, L., Li, K., Shi, X., Zhao, L., and Linghu, J. (2021). Application of Gas Wettability Alteration to Improve Methane Drainage Performance: A Case Study. *Int. J. Mining Sci. Tech..* 31 (4):621–629 doi:10.1016/j.ijmst.2021.04.002

Kumar, K., Dao, E., and Mohanty, K. K. (2005). AFM Study of mineral Wettability with Reservoir Oils. *J. Colloid Interf. Sci.* 289, 206–217. doi:10.1016/j.jcis.2005.03.030

Li, C., Singh, H., and Cai, J. (2019). Spontaneous Imbibition in Shale: A Review of Recent Advances. *Capillarity* 2, 17–32. doi:10.26804/capi.2019.02.01

Li, J., Li, X., Wu, K., Feng, D., Zhang, T., and Zhang, Y. (2017). Thickness and Stability of Water Film Confined inside Nanoslits and Nanocapillaries of Shale and clay. *Int. J. Coal Geology.* 179, 253–268. doi:10.1016/j.coal.2017.06.008

Li, W., Lu, S., Li, J., Wei, Y., Feng, W., Zhang, P., et al. (2021). Geochemical Modeling of Carbon Isotope Fractionation during Methane Transport in Tight Sedimentary Rocks. *Chem. Geology.* 566, 120033. doi:10.1016/j.chemgeo.2020.120033

Liu, B., Bai, L., Chi, Y., Jia, R., Fu, X., and Yang, L. (2019). Geochemical Characterization and Quantitative Evaluation of Shale Oil Reservoir by Two-Dimensional Nuclear Magnetic Resonance and Quantitative Grain Fluorescence on Extract: A Case Study from the Qingshankou Formation in Southern Songliao Basin, Northeast China. *Mar. Pet. Geology.* 109, 561–573. doi:10.1016/j.marpetgeo.2019.06.046

Liu, B., Shi, J., Fu, X., Lyu, Y., Sun, X., Gong, L., et al. (2018). Petrological Characteristics and Shale Oil Enrichment of Lacustrine fine-grained Sedimentary System: A Case Study of Organic-Rich Shale in First Member of Cretaceous Qingshankou Formation in Gulong Sag, Songliao Basin, NE China. *Pet. Exploration Dev.* 45 (5), 884–894. doi:10.1016/S1876-3804(18)30091-0

Liu, B., Sun, J., Zhang, Y., He, J., Fu, X., Yang, L., et al. (2021). Reservoir Space and Enrichment Model of Shale Oil in the First Member of Cretaceous Qingshankou Formation in the Changling Sag, Southern Songliao Basin, NE China. *Pet. Exploration Dev.* 48 (3), 608–624. doi:10.1016/S1876-3804(21)60049-6

Loucks, R. G., and Reed, R. M. (2014). *Scanning-electron-microscope Petrographic Evidence for Distinguishing Organic-Matter Pores Associated with Depositional Organic Matter versus Migrated Organic Matter in Mudrock [J]*.

Lu, S., Huang, W., Chen, F., Li, J., Wang, M., Xue, H., et al. (2012). Classification and Evaluation Criteria of Shale Oil and Gas Resources: Discussion and Application. *Pet. exploration Dev.* 39 (2), 268–276. doi:10.1016/S1876-3804(12)60042-1

Lu, Y., Zeng, L., Sari, A., Chen, Y., Jin, Y., and Xie, Q. (2019). Wetting Behavior of Shale Rocks and its Relationship to Oil Composition. *Energy Fuels* 33, 12270–12277. doi:10.1021/acs.energyfuels.9b02935

Marsden, S. S. (1965). Wettability-Its Measurement and Application to Waterflooding. *J. Jpn. Assoc. Petrol. Technol.* 30 (1), 1–10. doi:10.3720/japt.30.1

Pan, B., Yin, X., and Iglauer, S. (2020). A Review on clay Wettability: From Experimental Investigations to Molecular Dynamics Simulations. *Adv. Colloid Interf. Sci.* 285 (1), 102266. doi:10.1016/j.cis.2020.102266

Roshan, H., Al-Yaseri, A. Z., Sarmadivaleh, M., and Iglauer, S. (2016). On Wettability of Shale Rocks. *J. Colloid Interf. Sci.* 475, 104–111. doi:10.1016/j.jcis.2016.04.041

Siddiqui, M. A. Q., Ali, S., Fei, H., and Roshan, H. (2018). Current Understanding of Shale Wettability: A Review on Contact Angle Measurements. *Earth-Science Rev.* 181, 1–11. doi:10.1016/j.earscirev.2018.04.002

Song, M., Liu, H., Wang, Y., and Liu, Y. (2020). Enrichment Rules and Exploration Practices of Paleogene Shale Oil in Jiyang Depression, Bohai Bay Basin, China. *Pet. Exploration Dev.* 47 (2), 242–253. doi:10.1016/S1876-3804(20)60043-X

Wang, Y., Wang, X., Song, G., Liu, H., Zhu, D., Zhu, D., et al. (2016). Genetic Connection between Mud Shale Lithofacies and Shale Oil Enrichment in Jiyang Depression, Bohai Bay Basin. *Pet. Exploration Dev.* 43 (5), 759–768. doi:10.1016/s1876-3804(16)30091-x

Xue, H., Dong, Z., Chen, X., Tian, S., Lu, S., and Lu, S. (2021). Simulation of Oil-Water Rock Wettability of Different Constituent Alkanes on Kaolinite Surfaces at the Nanometer Scale. *j nanosci nanotechnol* 21, 225–233. doi:10.1166/jnn.2021.18727

Yang, R., Hu, Q., He, S., Hao, F., Guo, X., Yi, J., et al. (2019). Wettability and Connectivity of Overmature Shales in the Fuling Gas Field, Sichuan Basin (China). *Bulletin* 103 (3), 653–689. doi:10.1016/S1876-3804(16)30091-X

Yu, L., and Wardlaw, N. C. (1986). The Influence of Wettability and Critical Pore-Throat Size Ratio on Snap-Off. *J. Colloid Interf. Sci.* 109 (2), 461–472. doi:10.1016/0021-9797(86)90324-3

Zhang, T., Li, X., Shi, J., Sun, Z., Yin, Y., Wu, K., et al. (2018). An Apparent Liquid Permeability Model of Dual-Wettability Nanoporous media: A Case Study of Shale. *Chem. Eng. Sci.* 187, 280–291. doi:10.1016/j.ces.2018.05.016

Zhang, Y., Zeng, J., Qiao, J., Feng, X., and Dong, Y. (2018). Investigating the Effect of the Temperature and Pressure on Wettability in Crude Oil-Brine-Rock Systems. *Energy Fuels* 32 (9), 9010–9019. doi:10.1021/acs.energyfuels.8b01404

A Comparative Study on Microscopic Characteristics of Volcanic Reservoirs in the Carboniferous Kalagang and Haerjiawu Formations in the Santanghu Basin, China

Weiming Wang[1], Weihao La[1]*, Tanguang Fan[2], Xiongfei Xu[2], Yingnan Liu[1] and Qixia Lv[1]

[1]School of Earth Science and Technology, China University of Petroleum (East China), Qingdao, China, [2]Research Institute of Exploration and Development, PetroChina Tuha Oilfield Company, Hami, China

Self-jetting high-yield oil flow was obtained from Ma 67 and Ma 36 wells drilled in the volcanic reservoirs of the Haerjiawu Formation in the Santanghu Basin, China. This has shifted the prospectors' attention to the Haerjiawu Formation from the Kalagang Formation, which is generally considered to have favorable physical properties. To further explain the geological reasons why oil flow can jet itself from the volcanic rocks in the Haerjiawu Formation with poor physical properties, this study carries out a systematic comparison on the microscopic pore structures of volcanic rocks through unconventional tests such as low-temperature nitrogen adsorption, high-pressure mercury injection, and constant-rate mercury injection based on the analyses of physical properties and minerals. The results obtained are as follows. The volcanic rocks of the Kalagang Formation have relatively high pore permeability. However, their micropores have a wide distribution range of pore size and feature highly meandering structures and strong heterogeneity. Meanwhile, small pore throats connect large pores in the volcanic rocks, resulting in a relatively high pore/throat ratio. All these are conducive to the occurrence of tight oil and gas but unfavorable for the flow of oil and gas. The volcanic rocks in the Haerjiawu Formation have relatively low volcanic permeability. However, small pores connect large pore throats in the volcanic rocks; thus, leading to a relatively low pore/throat ratio. Meanwhile, the volcanic rocks feature low meandering structures, strong homogeneity, and high connectivity. All these are favorable for the formation of tight oil and gas reservoirs. These assessment results also indicate that the assessment indices of tight volcanic reservoirs should not only include porosity and permeability. Instead, more attention should be paid to the microscopic pore structures, and it is necessary to analyze the charging and flow of tight oil from the configuration of pores and pore throats. This study not only explains the geological factors of the wells with self-jetting high-yield oil flow in the Haerjiawu Formation from the perspective of microscopic pore structures but also provides a new idea and comparison method for the assessment of tight reservoirs in other areas.

Keywords: Santanghu basin, Kalagang formation, Haerjiawu formation, micropore structure, pore/throat configuration, volcanic rock

INTRODUCTION

The Santanghu Basin is located in the northeast of Xinjiang Uygur autonomous region, China, and lies in the part where the Siberia and Kazakhstan plates converge. Carboniferous strata are widely developed in the basin, with hugely thick source rocks of marine–continental transitional facies deposited and hugely thick volcanic rocks built, thus forming independent petroliferous associations (Li et al., 2010; Wang et al., 2010; Liu et al., 2013; Tian et al., 2019). With an increase in the attention to oil and gas exploration of volcanic rocks, many oil and gas reservoirs have been discovered in the Malang Sag of the Santanghu Basin (Ma et al., 2017; Su et al., 2020; Yang et al., 2019; Liu, Bechtel, Sachsenhofer). In particular, oil and gas manifestations were discovered in 23 layers (height: about 294 m) in the Kalagang Formation during the drilling of Well Niudong 110 that was deployed in the southern wing of the Niudong structure in the Malang Sag in 2015, with the highest daily oil production of 21.08 m^3. This opened the exploration of the tight oil in Carboniferous volcanic rocks in the Santanghu Basin. Owing to the intense exploration of volcanic oil and gas reservoirs, the corresponding exploration technologies and theoretical understanding have also been rapidly improved. (Hou et al., 2011; Huang et al., 2012). However, the exploration of the volcanic rocks in the Santanghu Basin suffers a late start and a low level. As a result, much geological understanding of the volcanic rocks is still at the exploratory stage overall, and most especially the pore structures in the volcanic reservoirs are yet to be ascertained. Previous researchers compared and assessed the Carboniferous volcanic reservoirs using conventional test analysis methods such as casting thin section, core observation, conventional mercury injection, and porosity and permeability analysis. Accordingly, they generally believed that the volcanic rocks in the Kalagang Formation should be the focus of Carboniferous exploration due to their relatively high porosity and permeability. However, self-jetting high-yield oil flow with the highest daily oil production of 65.60 m^3 was discovered in the Haerjiawu Formation in Ma 67 well in the Malang Sag later. This confirms that the Haerjiawu Formation with poor physical properties also has great development potential. Then some geological questions have been raised, such as why high-yield spontaneous oil flow was obtained from the volcanic rocks in the Haerjiawu Formation with low physical properties and whether the phenomenon of self-jetting oil flow indicates that the tight oil in the Haerjiawu Formation has better mobility. To answer these questions, it is necessary to start with the research on the refined microscopic pore structure of the reservoirs. Therefore, based on various high-precision methods such as HPMI, CRMI, and LTNA tests, this study compares and analyzes the differences in the microscopic pore structures in the target layers of the Kalagang and Haerjiawu formations and reasonably explains the difference in enrichment conditions of tight oil between the two formations, thus providing a basis for further exploration.

SAMPLES AND EXPERIMENTS

Geological Background

The Santanghu Basin is adjacent to the Junggar and Tuha basins in the southwest across Dahei and Barkol mountains and borders Mongolia in the northeast. It lies between the Altai and Tianshan mountains and is distributed in the form of a long strip in the NW-SE trending, with a length of about 500 km, a width of 40–70 km, and an area of 2.3×10^4 km^2. Therefore, it is a long and narrow intermountain superimposed basin. The first-order tectonic units in the basin are present in an NW-trending macroscopic pattern of two uplifts sandwiching one depression (i.e., the northeastern thrust uplift zone, the southwestern thrust nappe uplift belt, and the central depression zone). Among them, the central depression zone can be divided into four convex and five concave tectonic units (**Figure 1**), each of which is long and narrow in the south–north direction and is convex in the south and gentle in the north in terms of strata (Hou et al., 2011; Liu, Bechtel, Sachsenhofer). The central depression zone serves as the major oil and gas accumulation area, and most of the oil and gas discovered so far are concentrated in the Malang Sag in the central depression zone. The main Carboniferous target layers in the Malang Sag include the Kalagang and Haerjiawu formations. Among them, the Kalagang Formation is dominated by onshore eruption-overflow facies, with amygdaloidal lava developing and multiple-stage eruptive discontinuities visible inside. Therefore, weathered and leached volcanic reservoirs have developed inside. In terms of lithology, these reservoirs mainly include amygdaloidal basalts and autoclastic brecciated basalts, followed by autoclastic brecciated andesite and amygdaloidal andesite. Among them, the amygdala is mostly unfilled and semi-filled or shows corrosion characteristics (Liang et al., 2011; Liu et al., 2015). The Kalagang Formation is mainly distributed on the southwestern edge of the Malang Sag. It grows thinner from west to east and pinches out on the Fangliang Salient, with a regional thickness of 540–1,600 m. The Haerjiawu Formation is dominated by dotted central volcanic eruptions. In terms of lithology, it mainly includes the interbeds consisting of volcaniclastic sedimentary rocks, pyroclastic rocks, and volcanic lava, interbedded with carbonaceous mudstones, tuffaceous mudstones, and marls as a whole. The Haerjiawu Formation is widely distributed. It is thick in the southwestern, southeastern, and north-central parts of the Santanghu Basin, with a general residual thickness of 400–1,451 m.

Tests and Analyses

To accurately characterize the microscopic pores in the Carboniferous volcanic reservoirs in the Malang Sag of the Basinhu Basin, targeted LTNA (JiaChengzao and Li, 2012; Yu, 2013; Yang et al., 2013a; Hadlari, 2015; Chen et al., 2015; Liu, Gao, Liu; Liu, Sun, Zhang), CRMI, and HPMI tests were carried out on samples based on the analyses of porosity, permeability, X-ray diffraction, and scanning electron microscopy in this study. All the samples were regular column samples (about 2.5 cm in diameter). They were washed to remove oil and dried before tests. LTNA tests were conducted using a BSD-PS-series automatic specific surface area and porosity analyzer, and the steps are as follows. First, the samples were degassed at a high temperature of 150°C for 3 h. Then the isotherm adsorption–desorption curves of the samples were obtained by the static volume method at an absolute temperature of 77 K. The

FIGURE 1 | Location of the study area in the Santanghu Basin.
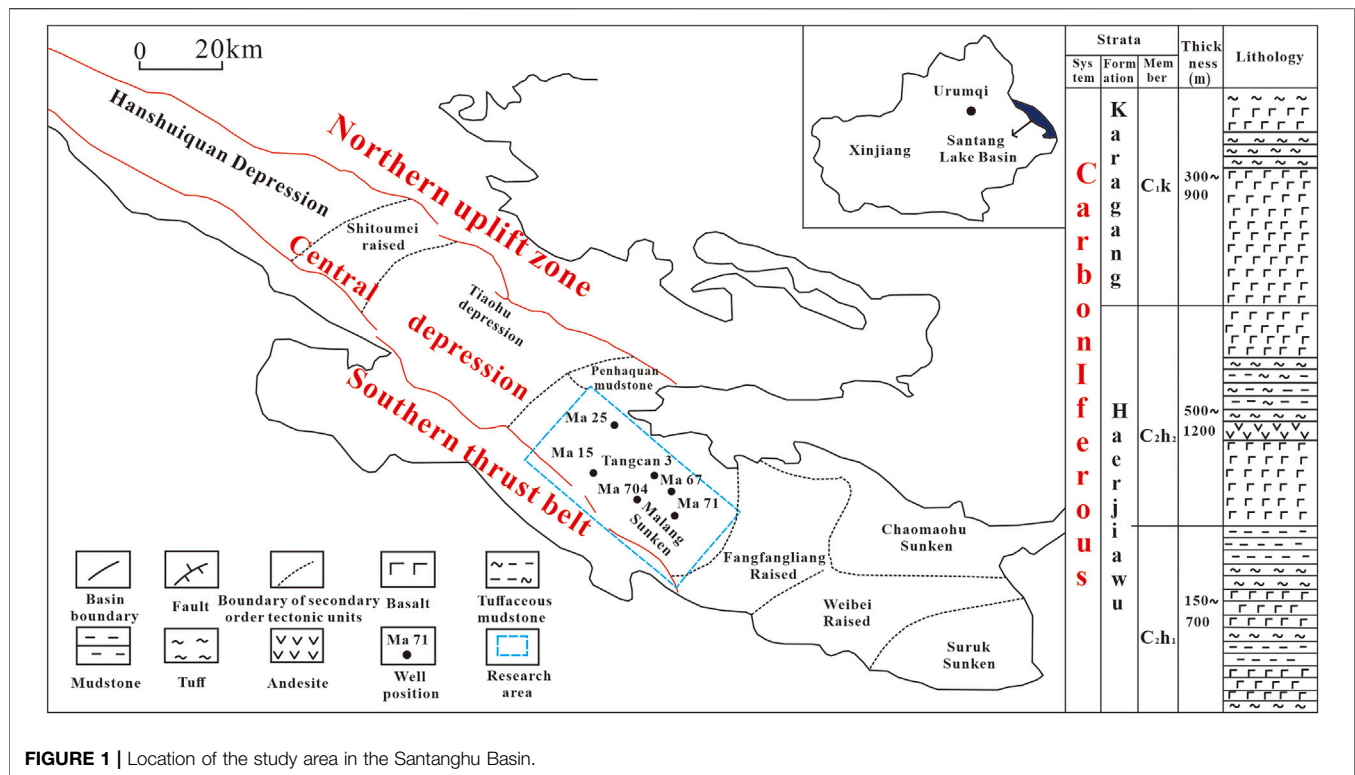
detection range of pore size was 0.4–200 nm in the tests. CRMI tests were performed using an ASPE-730 constant-rate porosimeter. In detail, liquid mercury was injected into the samples at a low constant velocity, and the information on pore structure can be reflected by the mercury injection pressure. The temperature and relative humidity of the measurement environment were 25°C and 34–48%, respectively, in the tests. HPMI tests were conducted using an AutoPore IV 9505 mercury porosimeter. During the test, the samples were first processed, liquid mercury was then injected into the samples, and afterward, pores were detected under a high-pressure condition. The temperature and relative humidity of the measurement environment were 21.3–21.5°C and 40–44%, respectively. Meanwhile, the maximum mercury injection pressure was 200 MPa, which corresponded to the minimum pore throat size of 3.68 nm.

RESULT ANALYSIS

Comparison of Basic Characteristics of Volcanic Reservoirs

1) Lithology and lithofacies

The volcanic rocks in the Malang Sag have complex and diverse lithology, with volcanic lava, pyroclastic rocks, and transition rocks developing. The lithology of the volcanic rocks in the target layers was determined based on multiple means such as core observation, thin section identification, and logging identification (Dong et al., 2012; Chen et al., 2013a; Chen

et al., 2013b; Chen et al., 2018). The Kalagang Formation is a set of extrusive rocks erupting from volcanoes interbedded with the transitional facies sedimentary tuff and volcanic breccia formed during the intermission between volcanic eruptions. Meanwhile, lacustrine volcanic depression deposits have developed in local areas of the formation. The Kalagang Formation is gray and dark gray overall and is in light colors such as brown and dark brown in the eruption discontinuities or regions with weathering crust developing. The lithology of the formation is dominated by basic basalts, followed by andesite, tuff, and volcanic breccia. The volcanic rocks of the Haerjiawu Formation are dominated by dotted central volcanic eruptions, with thick laminated basalt facies, basalt facies interbedded with source rocks, and tuff facies mainly developing, and tuff and mudstones widely distributed in the vertical direction. The formation is mostly grayish-brown and brownish-green. The lithology of the Haerjiawu Formation is also dominated by basic basalts. However, unlike the Kalagang Formation, the basalts in the Haerjiawu Formation are distributed among carbonaceous or tuffaceous mudstones. According to the analyses of geochemical indicators, previous researchers unanimously agreed that the carbonaceous mudstones in the Haerjiawu Formation feature high abundance and favorable types and reach the standard of source rocks. Therefore, the basalts in the Haerjiawu Formation are called "basalts interbedded with source rocks," which denote the interbeds consisting of basalts and source rocks (**Figure 2**).

In terms of lithofacies distribution, the Kalagang Formation is dominated by thick laminated basalt facies and the facies of tuff interbedded with source rocks, with source rock development
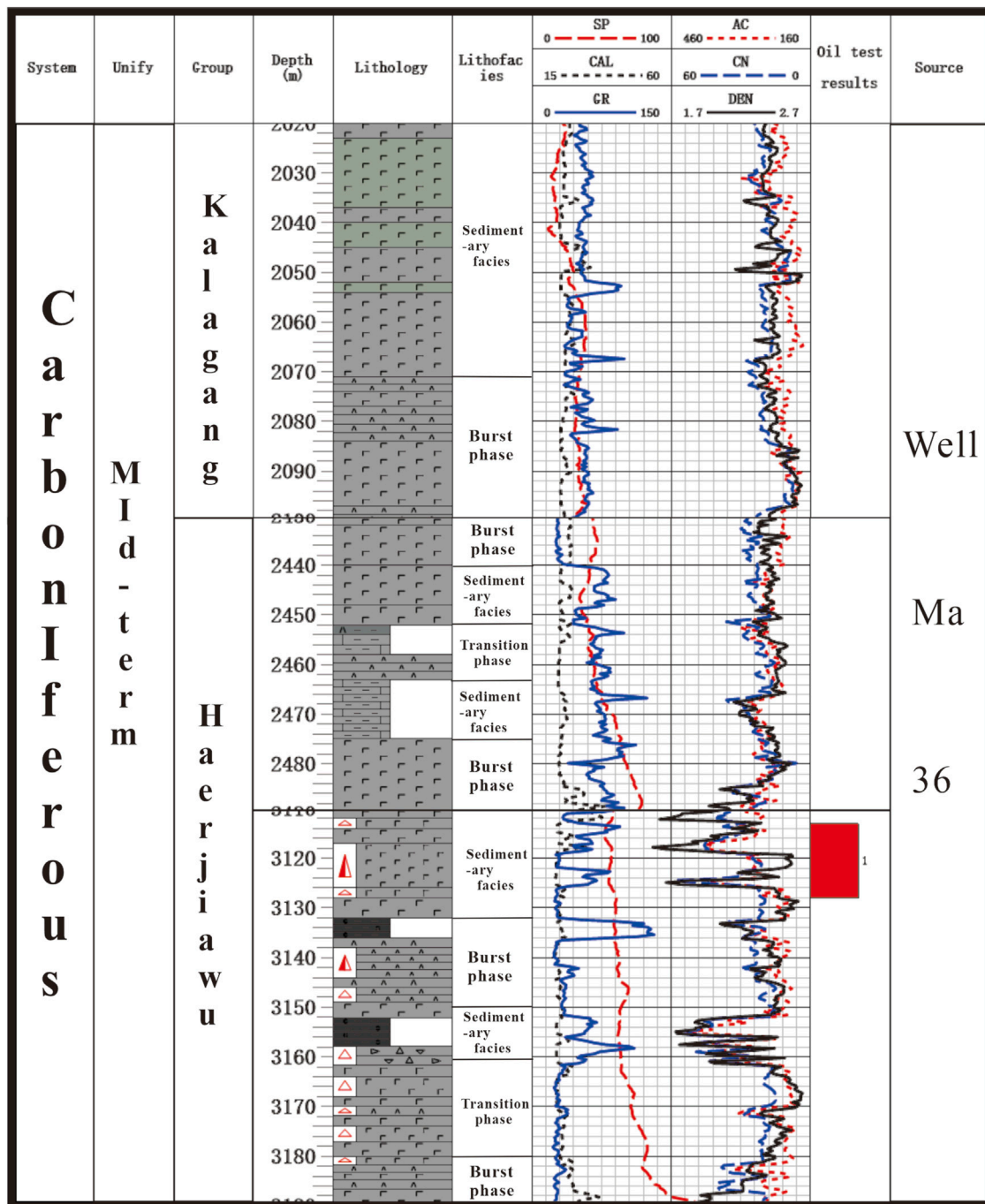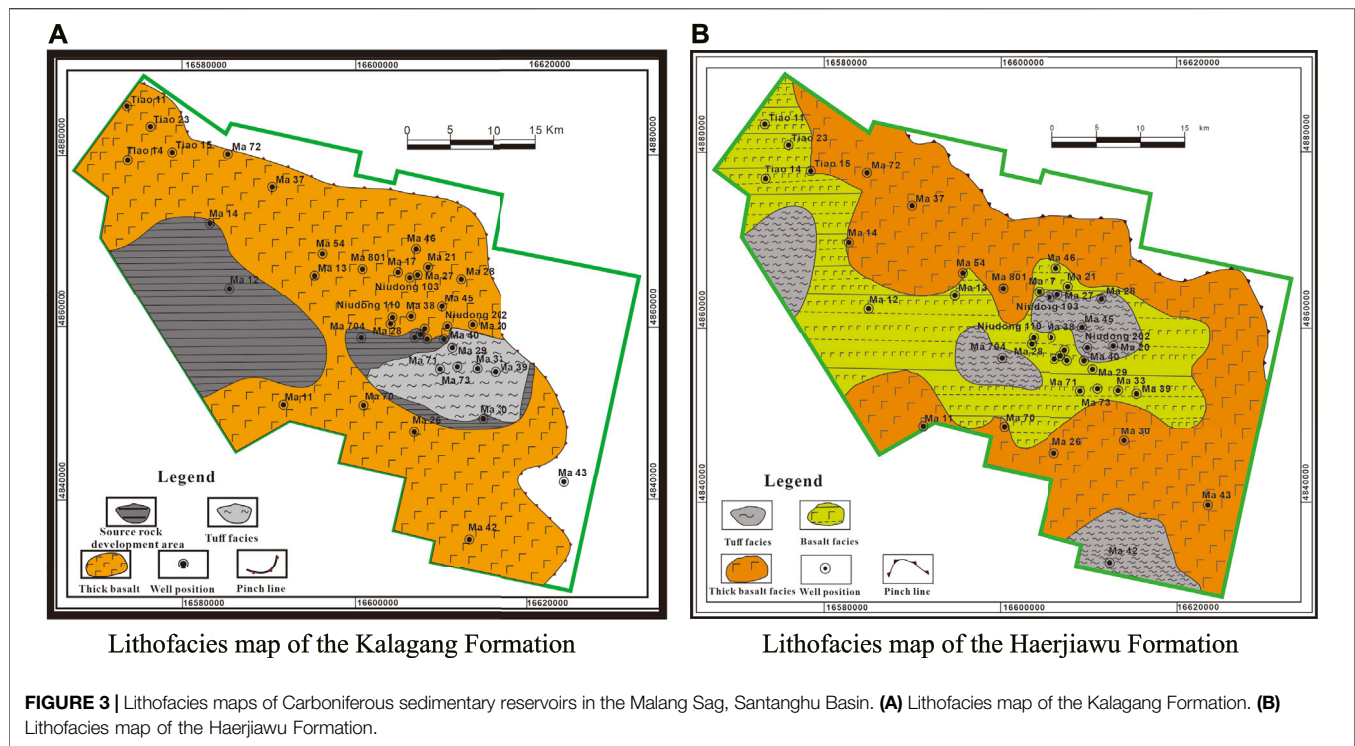
FIGURE 2 | Comprehensive histogram of Carboniferous sedimentary reservoirs in the Malang Sag, Santanghu Basin.

areas locally distributed (**Figure 3**). Among them, the facies of tuff interbedded with source rocks has mainly developed in blocks of Ma71, Ma73, Ma33, and Ma39 wells, in which the source rocks are more than 80 m thick, indicating a shallow lake zone. The thick laminated basalt facies in the Kalagang Formation feature abundantly developed basalts. Furthermore, dense pore or amygdala belts are common at the top of volcanic rocks owing to gas volatilization, with amygdaloidal pores visible and the amygdala mostly filled with chlorites and zeolites. The way of volcanic eruptions is obviously different between the Haerjiawu and Kalagang formations. The Haerjiawu Formation is dominated by dotted central volcanic eruptions, with thick laminated basalt facies, the facies of basalts interbedded with source rocks, and tuff facies primarily developing. The obvious difference between the two formations is that the tuff and mudstones in the Haerjiawu Formation have widely developed

FIGURE 3 | Lithofacies maps of Carboniferous sedimentary reservoirs in the Malang Sag, Santanghu Basin. **(A)** Lithofacies map of the Kalagang Formation. **(B)** Lithofacies map of the Haerjiawu Formation.

in various vertical depths, indicating that the basalts in the Haerjiawu Formation are deposited underwater. Pores are not fully developed in the Haerjiawu Formation since the water pressure hinders the escape of gas in magma, which affects the physical properties of the formation to a certain extent.

2) Physical characteristics of reservoirs

The physical properties of reservoirs serve as the direct indicators of pore development and storage capacity of volcanic reservoirs (Pang et al., 2007; Qin, 2011). The analytical results of the porosity and permeability of the samples from the Kalagang and Haerjiawu formations are as follows (**Figure 4**). For the Kalagang Formation, the maximum and average porosity were 12.78 and 8.31%, respectively, and the maximum and average permeability were $11.15 \times 10^{-3}\mu m^2$ and $2.67 \times 10^{-3}\mu m^2$, respectively. For the Haerjiawu Formation, the maximum and average porosity were 14.07 and 4.46%, respectively, and the maximum and average permeability were $8.04 \times 10^{-3}\mu m^2$ and $1.12 \times 10^{-3}\mu m^2$, respectively. Therefore, the porosity of the Kalagang Formation is notably higher than that of the Haerjiawu Formation (**Figures 4C,D**), while the permeability of the two formations is slightly different. The microscopic pore structure of reservoirs is composed of pores and pore throats. The pore size affects the porosity, while the pore throat size affects the permeability. Therefore, the results of above analysis indirectly prove that the pores greatly differ, but the pore throats slightly differ between the two formations and that the pore/throat ratio of the Kalagang Formation must be higher than that of the Haerjiawu Formation.

3) Comparison of reservoir space characteristics

Volcanic reservoirs have various types of storage space and complex pore structures and are strongly affected by secondary diagenism. Pores, joints, and cavities are intertwined in volcanic reservoirs, showing strong heterogeneity both microscopically and macroscopically.

Weathered and leached volcanic reservoirs have developed in the Kalagang Formation, with various types of storage space developing inside the reservoirs, such as corroded pores, pores inside amygdala, residual pores, intercrystalline micropores, contraction joints of amygdala, and tectonic fractures. Among them, the corroded pores, residual pores, and pores inside the amygdala are the most developed, followed by tectonic fractures. Furthermore, the corroded pores are large in scale, with a pore size of up to several hundred microns and above (**Figure 5**). The basalt reservoirs interbedded with source rocks have developed in the Haerjiawu Formation. The reservoir space inside the reservoirs is dominated by tectonic fractures and corroded micropores, followed by the pores inside amygdala and the contraction joints of amygdala. Moreover, dual media consisting of corroded micropores and tectonic fractures are visible, and a large number of corroded nanopores can be observed under a scanning electron microscope (**Figure 6**).

Carboniferous basalts have the lowest porosity since they have been filled with magmatic-hydrothermal fluids. Therefore, burial-induced compaction has minor effects on their porosity. The overflow facies, vesicular andesites, and basalts at the top of the Kalagang Formation bear large numbers of contraction pores as a

FIGURE 4 | Physical property statistics of Carboniferous reservoirs in the Malang Sag, Santanghu Basin.
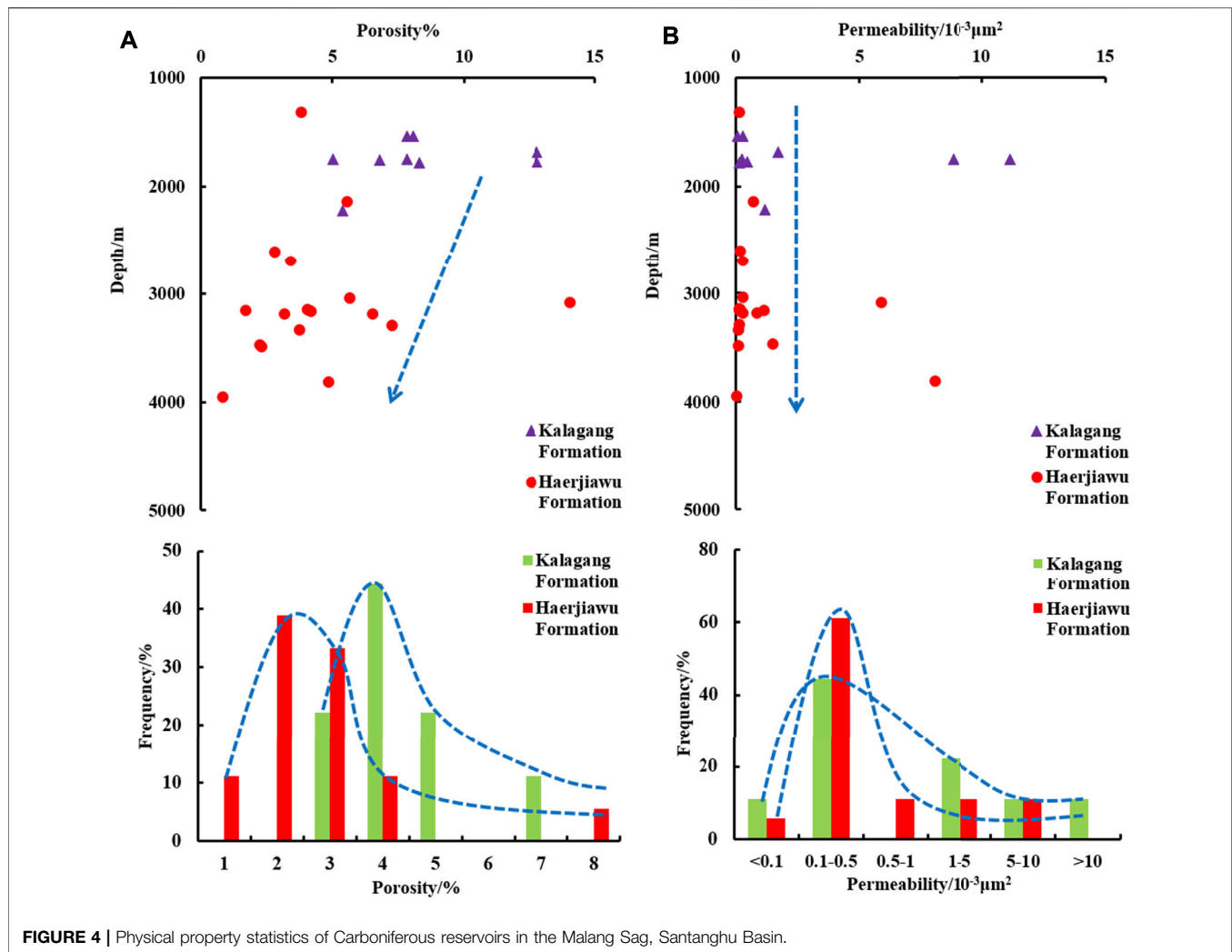
result of condensation and shrinkage. Owing to later weathering and leaching, the contraction pores feature large porosity but small pore throats. In contrast, the reservoirs in the Haerjiawu Formation feature improved physical properties since soluble silicates have been corroded by rich organic acids formed from the coal-bearing carbonaceous mudstones in the early stage and the organic acids generated from the maturation of organic matter. Therefore, the combination of small pores and small pore throats in the Haerjiawu Formation is superior to the combination of large pores and small pore throats of the Kalagang Formation.

4) Mineral composition characteristics

Table 1 shows the whole-rock X-ray diffraction analysis results of the Kalagang and Haerjiawu formations in the Malang Sag. According to the analysis results, the minerals in the two formations are dominated by feldspars, quartz, and zeolites, followed by pyroxenes and carbonate minerals, as well as low content of clay minerals. The two formations notably

differ in quartz and heulandite content. In detail, the quartz content of the Kalagang Formation is relatively low, which is generally less than 10%, while the quartz content of the Haerjiawu Formation is relatively high, which is greater than 10%. Meanwhile, the zeolite content of the Kalagang Formation is relatively high, which is higher than 50% mostly, while the zeolite content of the Haerjiawu Formation is relatively low, which is less than 50% mostly. Given that quartz has strong weathering resistance and heulandite is liable to dissolve, it can be inferred that the volcanic reservoirs in the Kalagang Formation are more liable to suffer weathering and leaching. As a result, corrosion-induced large pores have been formed. Furthermore, the minerals newly formed after corrosion are liable to block the pore throats, which makes the microscopic pore structures more complicated, increases the tortuosity of the pore–throat system, and contributes to the formation of high-porosity and low-permeability reservoirs. This conclusion is not in contradiction to the comparison results of the physical properties of the two formations. Instead, it is consistent with
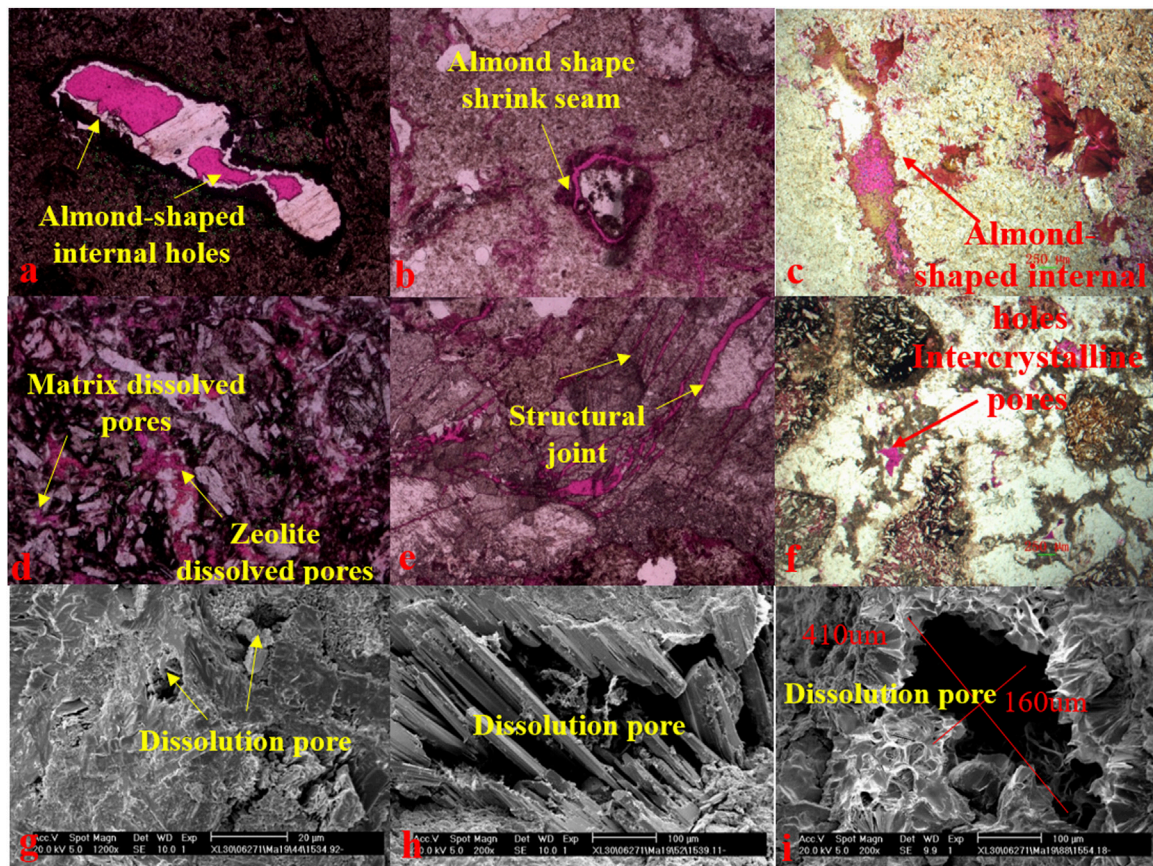
FIGURE 5 | Reservoir space types of weathered and leached volcanic reservoirs in the Kalagang Formation. Note: **(A)** Well Ma 38, 1,523.7 m deep, altered amygdaloidal andesite and basalts, with pores inside amygdala visible; **(B)** Well Ma 38, 1,684.61 m deep, clastic altered amygdaloidal basalts, with contraction joints of amygdala visible; **(C)** Well Niudong110, 1769.77–1769.9 m deep, altered amygdaloidal andesitic basalts, with pores inside amygdala visible; **(D)** Well Ma 19, 1,559 m deep, andesite, with zeolite dissolved pores and matrix dissolved pores filled with amygdala visible; **(E)** Well Ma 38, 1,684.61 m deep, clastic altered amygdaloidal basalts, with tectonic fractures visible; **(F)** Well Niudong110, 1776.32–1776.5 m deep, altered and brecciated clastic amygdaloidal basalts, with intercrystalline pores visible; **(G)** Well Ma 19, 1,535.015 m deep, grayish-green fluorescent andesite, with dissolved pores visible; **(H)** Well Ma 19, 1,539.24 m deep, grayish-green andesite bearing oil spots, with intragranular dissolved pores visible; **(I)** Well Ma 19, 1,554.23 m deep, grayish-green andesite bearing oil traces, with intragranular dissolved pores visible.

the discovery of weathered and leached reservoirs in the Kalagang Formation during practical exploration.

Comparison of Microscopic Pore Structures of Volcanic Rocks

1) Characteristics of capillary pressure curves

The morphology of capillary pressure curves can reflect the development of microscopic pores in reservoirs. However, owing to extremely strong heterogeneity, the capillary pressure curves have greatly different characteristics at different structural positions of even the same horizon in the volcanic reservoirs. Nearly 20 samples from the Kalagang and Haerjiawu formations were selected for the HPMI test and analysis in this study. Given the heterogeneity of the volcanic reservoir plane and to make a representative comparison of longitudinal microscopic pore structures, this article only exhibits three samples of the same

lithology (basalts) at different depths (A, B, and C) of the same well (Well Niudong 110). Among them, samples A and B were collected from the Kalagang Formation and sample C was taken from the Haerjiawu Formation. In terms of curve morphology (**Figure 7**), the mercury injection curves become increasingly gentle with an increase in depth, indicating that the pores are better sorted as depth increases. In terms of mercury injection and mercury ejection efficiency, the maximum mercury saturation and mercury ejection efficiency increased as depth increased, although the porosity decreased with an increase in depth. In detail, the maximum mercury saturation increased from 87.795 to 96.228%, and the mercury ejection efficiency increased from 24.256 to 37.789%. In terms of the structure coefficient (**Figure 8**), the structure coefficient gradually decreased with an increase in depth, indicating that the pore–throat system of the Haerjiawu Formation has small tortuosity and favorable pore throat structures. As indicated by the comparison of the three microscopic parameters, the volcanic rocks in the Haerjiawu
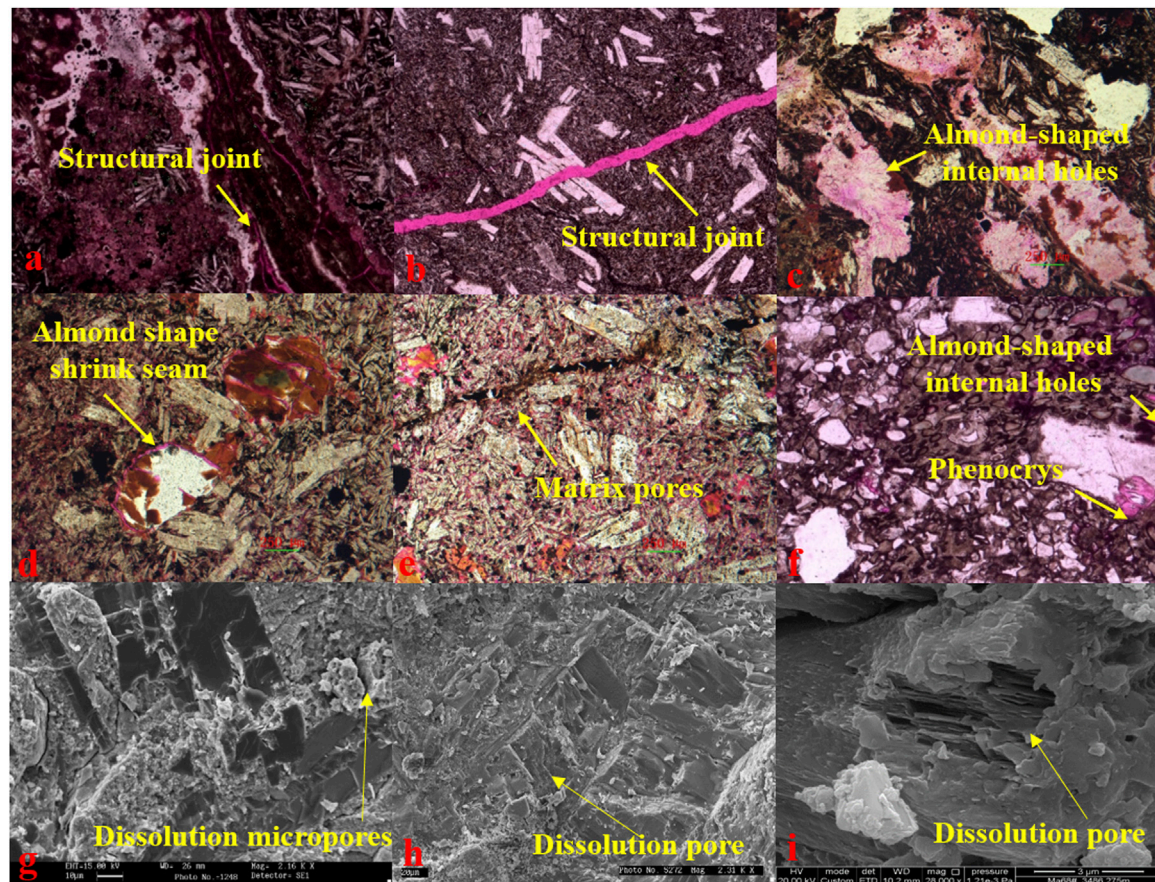
FIGURE 6 | Reservoir space types of basalt reservoirs in the Haerjiawu Formation. Note: **(A)** Well Niudong 201, 3,172.255 m deep, brecciated clastic basalts, with tectonic fractures visible; **(B)** Well Niudong 201, 3,141.835 m deep, slightly clastic basalts, with tectonic fractures visible; **(C)**- Well Ma67H, 2,969.53–2,696.71 m, slag-like basalts, with pores inside amygdala visible; **(D)** Well Ma67H, 2,562.78–2,562.97 m deep, (altered) amygdaloidal basalts, with contraction joints of amygdala visible; **(E)** Well Ma67H, 2,562.78–2,562.97 m deep, (altered) amygdaloidal basalts, with matrix micropores visible; **(F)** Well Ma361, 3,161.665 m deep, basaltic crystal lithic fine-grained tuff, with pores inside the amygdala in basaltic breccias, phenocryst dissolved pores inside breccias, and intragranular fractures visible; **(G)** Well Niudong 201, 3,172.255 m deep, basaltic crystal basalts, with mixed layers consisting of illite and montmorillonite and dissolved micropores visible; **(H)** Well Ma68, 3,483.945 m deep, grayish-green fluorescent basalts, with feldspar dissolved pores visible; **(I)**- Well Ma68, 3,486.275 m deep, grayish-green fluorescent basalts, with dissolved pores visible.

Formation pores are well sorted, despite their poor physical properties, which is more conducive to fluid flow.

2) Characteristics of LTNA curves

Nitrogen isothermal adsorption at a low temperature and low pressure can be used to effectively reflect the pore size distribution of micropores and mesopores in rock samples. Furthermore, the specific surface area can be calculated using the BET equation, the pore volume distribution can be calculated using the BJH equation, and the pore shapes can be predicted according to the isothermal adsorption curves (Yang et al., 2013b; Yang et al., 2013c).

The distribution curves of pore volume increments—pore sizes of the 17 samples—were plotted using the parameters of microscopic pore structures obtained from the LTNA tests (**Figure 9**). According to **Figure 9**, the volcanic reservoirs of

the Kalagang and Haerjiawu formations show roughly similar pore size distribution curves, with peaks basically occurring in the range of 30–100 nm. However, the pore volume increments corresponding to pore sizes are different. The weathered and leached volcanic reservoirs of the Kalagang Formation are relatively dispersed and show relatively high pore volume increments, indicating a wide distribution range of pore sizes. In contrast, the basalt volcanic reservoirs in the Haerjiawu Formation show relatively low pore volume increments and small but more concentrated pore size distribution. Once again as indicated by the above analytical results, the Kalagang Formation features complicated microscopic configuration of pores and pore throats and a wide pore size distribution range, while the reservoirs in the Haerjiawu Formation feature relatively small pore sizes and high homogeneity.
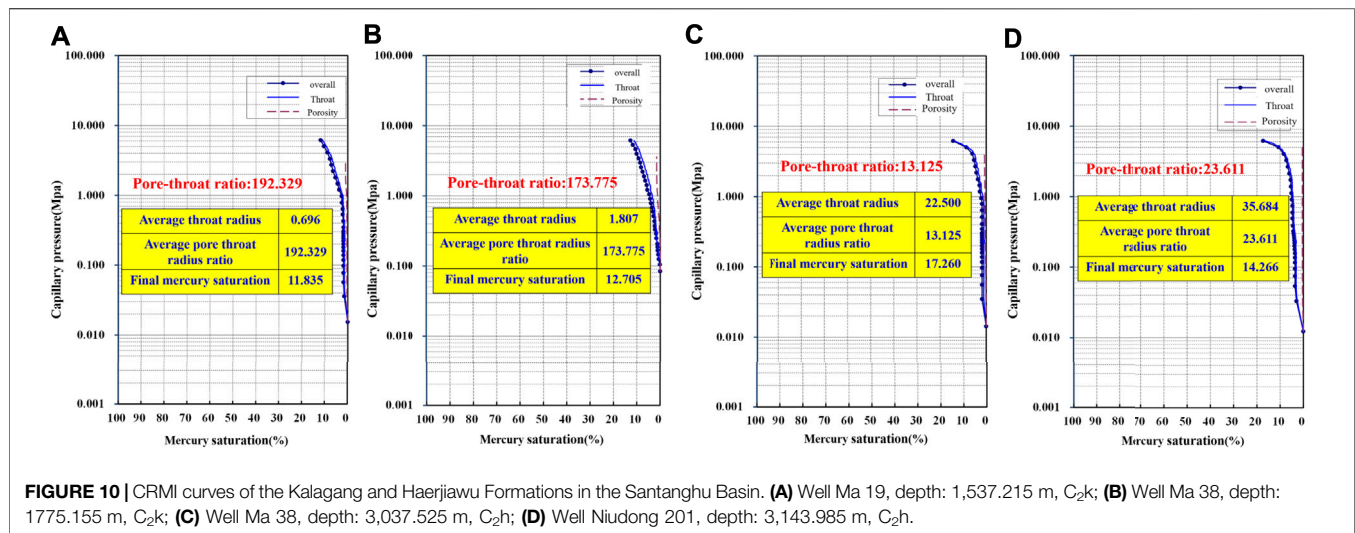
3) Characteristic of CRMI curves

TABLE 1 | X-ray diffraction analysis results of the Kalagang and Haerjiawu formations in the Malang Sag.

Well	Depth (m)	Formation	Lithology description	Quartz (%)	Feldspar (%)	Calcite (%)	Dolomite (%)	Siderite (%)	Pyrite (%)	Laumontite (%)	Heulandite (%)	Pyroxene (%)	Clay minerals (%)
Well Niudong 110	1748.925	C$_2$k	Grayish-green fluorescent basalt	3.7	83.3	2.7	—	—	—	—	—	3.7	6.5
Well Niudong 110	1781.58	C$_2$k	Gray oil trace-bearing basalts	1.2	53.6	18.2	1.4	—	—	—	6.1	15.8	3.6
Well Ma 38	1,684.77	C$_2$k	Gray oil spotted basalts	7.1	12.2	—	1.2	1.1	1.6	—	49.3	9.2	18.3
Well Ma 38	1775.155	C$_2$k	Gray oil trace-bearing andesite	1.1	18.4	—	—	—	—	—	70.2	5.5	4.8
Well Ma 25	2,217.915	C$_2$k	Gray oil trace-bearing basalts	9.8	64.2	—	2.4	—	—	—	—	15.5	8.1
Well Ma 19	1,537.215	C$_2$k	Grayish-green fluorescent andesite	0.8	27.8	—	—	0.5	0.7	—	54.1	7.2	7.1
Well Ma 19	1,540.53	C$_2$k	Grayish-green oil trace-bearing basalts	—	15.3	—	—	1.2	1.9	—	55.2	8	18.4
Well Ma 67H	3,083.06	C$_2$h	Gray fluorescent basalt	2.3	13.2	1.9	1.7	0.6	1	54.9	10.2	4.8	5.7
Well Niudong 201	3,143.985	C$_2$h	Gray oil trace-bearing basalts	5.3	26.3	2.2	2.5	1.2	1.9	—	2	16.4	4
Well Niudong 201	3,151.345	C$_2$h	Dark gray fluorescent basalts	5.9	53.3	7	2	1.7	2.6	—	5.1	18.4	4.1
Well Niudong 201	3,155.82	C$_2$h	Gray oil trace-bearing basalts	19	32	5.8	—	1	1.5	15.5	10.6	6.4	8.3
Well Niudong 201	3,162.875	C$_2$h	Dark gray basalts	27.7	50.7	7.3	—	—	—	—	—	7.6	6.7
Well Niudong 201	3,184.74	C$_2$h	Dark gray fluorescent andesite	10.4	69.8	—	0.6	1.1	1.7	—	—	11.6	4.7
Well Ma 704	3,470.865	C$_2$h	Gray fluorescent basalt	14.8	50.8	2.2	—	—	—	20.6	—	—	11.6
Well Niudong 110	2,599.525	C$_2$h	Dark gray fluorescent basalts	2.9	62.9	—	5.8	—	—	—	—	24.9	3.4
Well Ma 68	3,486.275	C$_2$h	Grayish-green fluorescent basalts	10.4	63.5	2.3	—	1.4	2.1	—	—	7.1	13.3
Well Ma 43	1,319.95	C$_2$h	Brown basalts	—	51.2	—	5.6	—	—	—	5.2	25.7	12.2
Well Ma 26	3,811.945	C$_2$h	Grayish-green fluorescent andesite	—	50.7	0.3	—	—	—	34.7	3.1	4.7	6.6
Well Ma 25	3,336.12	C$_2$h	Taupe fluorescent basalts	6.8	42.9	—	5.4	—	—	14.3	2.8	15.1	12.7
Well Ma 20	2,141.875	C$_2$h	Gray basalts	27.9	43.9	6.3	—	—	—	—	3.5	4.4	14.1

FIGURE 7 | Distribution of capillary pressure curves of the Kalagang and Haerjiawu formations. **(A)** Well Niudong 110, depth: 1748.925 m, C_2k; **(B)** Well Niudong 110, depth: 1781.58 m, C_2k; **(C)**- Well Niudong 110, depth: 2,599.925 m, C_2h.

FIGURE 8 | Comparison of micro-parameters of the Kalagang and Haerjiawu formations. **(A)** Well Niudong 110, depth: 1748.925 m, C_2k; **(B)** Well Niudong 110, depth: 1781.58 m, C_2k; **(C)** Well Niudong 110, depth: 2,599.925 m, C_2h.

FIGURE 9 | Distribution of pore volume increments—pore size of nanopores—in the volcanic reservoir of the Santanghu Basin. **(A)** Weathered crust basalts in the Kalagang Formation; **(B)** Basalts interbedded with source rocks in the Haerjiawu Formation.

FIGURE 10 | CRMI curves of the Kalagang and Haerjiawu Formations in the Santanghu Basin. **(A)** Well Ma 19, depth: 1,537.215 m, C$_2$k; **(B)** Well Ma 38, depth: 1775.155 m, C$_2$k; **(C)** Well Ma 38, depth: 3,037.525 m, C$_2$h; **(D)** Well Niudong 201, depth: 3,143.985 m, C$_2$h.

CRMI is a high-precision technique used to characterize pore–throat structures. Different from conventional HPMI tests, CRMI is to inject mercury into the throat and pores in rocks at a very low quasi-static constant rate (5×10^{-5} ml/min) and then to determine the microscopic pore structure according to the natural pressure fluctuation occurring when the meniscus of mercury front passes through different microscopic pore shapes (Igathinathane et al., 2008; Shan et al., 2019). It possesses the technical advantage that it can distinguish the pore throats from the pores and thus can determine pore sizes and pore throat size separately.

Four samples from the Kalagang and Haerjiawu formations were selected for the CRMI tests. According to **Figure 10**, the morphology of the total mercury saturation curves roughly approximates to that of the throat mercury saturation curves. The volume of mercury injected into pores was low, with the maximum pore mercury saturation of lower than 20% generally, indicating that the pores in the samples from the study area are undeveloped overall. Different samples showed slightly different pore size distribution but significantly different pore throat sizes and pore/throat ratios. In detail, the pore throat sizes of the Kalagang Formation were 0.696 and 1.807, while those of the Haerjiawu Formation were 22.5 and 35.684. Meanwhile, the pore/throat ratios of the Kalagang Formation were 192.329 and 173.775, while those of the Haerjiawu Formation were 13.125 and 23.611. This intuitively indicates that the Haerjiawu Formation has larger throat sizes, lower pore/throat ratios, and high uniformity of pores and pore throats than the Kalagang Formation.

DISCUSSION

According to the systematic comparison of the lithology, lithofacies, physical properties, reservoir space, mineral constituents, and microscopic pore structures between the Kalagang and Haerjiawu formations (**Table 2**), the reservoirs in the two formations notably differ in porosity, permeability, the configuration of pores and pore

throats, mineral constituents, and reservoir space. The differences in lithology and lithofacies are that the basalts in the Haerjiawu Formation are interbedded with carbonaceous mudstones—a type of source rocks. In terms of physical properties, the two formations show similar permeability, even though the Haerjiawu Formation has low porosity. In terms of reservoir space, the Kalagang Formation is dominated by large-scale weathered and leached pores, while the Haerjiawu Formation is dominated by small-scale corroded micropores. In terms of mineral constituents, heulandites conducive to the formation of weathered corroded pores have developed in the Kalagang Formation, while quartz conducive to the formation of fractures have developed in the Haerjiawu Formation. According to the comparison of HPMI tests, the Kalagang Formation has low maximum mercury saturation, low mercury ejection efficiency, and high pore structure tortuosity, while the Haerjiawu Formation has high maximum mercury saturation, high mercury ejection efficiency, and low pore structure tortuosity despite low porosity. The LTNA tests show that the Kalagang Formation features a wide distribution range of nanopore sizes, while the Haerjiawu Formation has a relatively concentrated distribution range of pore sizes. Meanwhile, CRMI tests indicate that the pore/throat ratio of the Kalagang Formation is significantly higher than that of the Haerjiawu Formation. According to the comparison of the above various geological characteristics (whether the comparison of lithologic associations and pore morphology or the quantitative comparison of microscopic pores), the volcanic rocks of the Kalagang Formation have the microscopic pore structure of large pores and small pore throats compared with those of the Haerjiawu Formation. The geological reason is that the volcanic rocks in the two formations were formed in different geological environments. The Kalagang Formation is of thick laminated basalt facies, with large numbers of basalts developing. Furthermore, dense pore or amygdala belts are common at the top of the formation owing to gas volatilization, with amygdaloidal pores visible and amygdala mostly filled with chlorites and zeolites, indicating notable weathering and leaching. In contrast, the basalts in the Haerjiawu Formation are in a multistage eruption pattern. The volcanic activities weakened in the later stage. As a result,

TABLE 2 | Comparison of microscopic characteristics of Carboniferous volcanic reservoirs in the Malang Sag, Santanghu Basin.

Serial number	Parameter	Kalagang Formation	Haerjiawu Formation	Supporting data
1	Lithology	Basalt	Basalt	Lithology section (**Figure 2**)
2	Lithofacies	Thick laminated basalt facies formed from the volcanic rock eruptions above water	Basalts interbedded with source rocks formed from underwater eruptions of the volcanic rocks	Lithography (**Figure 3**)
3	Mineral constituents	Low content of quartz and high content of zeolite	High content of quartz and low content of zeolite	X-ray diffraction analysis (**Table 1**)
4	Reservoir space	Corroded pores, gas pores, and pores inside amygdala	Corroded pores (joints), tectonic fractures, contraction joints of amygdala, pores inside amygdala, intercrystalline pores of zeolites, and matrix micropores	Observation of cast thin sections (**Figure 9** and **Figure 10**)
5	Porosity	High	Low	Physical property analysis (**Figure 4**)
6	Permeability	Similar	Similar	Physical property analysis (**Figure 4**)
7	Configuration of pores and pore throats	Pores connecting small pore throats	Pores connecting large pore throats	HPMI and CRMI analysis (**Figure 5**-**Figure 8**)
8	Pore/throat ratio	> 150	< 30	CRMI analysis (**Figure 8**)
9	Schematic diagram	Large difference between a pore and a pore throat	Small differences between a pore and a pore throat	Comprehensive test analysis
10	Favorable conditions for tight oil accumulation	Far from provenance, low mobility	Near to provenance and high mobility	Exploration facts of self-jetting oil flow in the volcanic rocks of the Haerjiawu Formation in wells Ma 67 and Ma 36

volcanic explosions failed to occur due to insufficient eruption power, and the energy of the volcanic activities was released in the form of relatively gentle overflow (i.e., underwater eruptions of volcanic rocks). Furthermore, the Haerjiawu Formation features a special lithologic association—interbeds consisting of basalts and source rocks, and the organic acids generated during the evolution of the source rocks promoted the corrosion of the reservoirs. All these not only open the channels for oil and gas charging but also provide the oil and gas occurrence space.

CONCLUSION

1) The volcanic rocks of the Kalagang and Haerjiawu formations are similar in lithology and are both dominated by basalts. However, their formation environments are notably different. The Kalagang Formation is of thick laminated basalt facies formed from volcanic rock eruptions above water, while the Haerjiawu Formation is of basalt interbed facies formed from underwater volcanic eruptions. Furthermore, the Kalagang Formation has relatively high porosity and high zeolite content, with large-scale corroded pores and pores inside amygdala developing. In contrast, the Haerjiawu Formation has relatively low porosity and permeability and low zeolite content, with corroded pores and tectonic fractures developing.
2) The volcanic reservoirs in the Kalagang and Haerjiawu formations have notably different microscopic characteristics. Although nanopores and micropores have developed in the reservoirs of both the formations, the volcanic rocks in the Kalagang Formation have more complex microscopic pore structures and a larger distribution range of pore sizes, while the volcanic rocks of the Haerjiawu Formation have more homogeneous microscopic pores and concentrated pore size distribution. Moreover, in terms of the

configuration of pores and pore throats, large pores connect small pore throats in the Kalagang Formation, while small pores connect large pore throats in the Haerjiawu Formation.
3) Tight reservoirs should not be assessed only using physical properties (porosity and permeability) as direct indicators. A systematic assessment of microscopic pore structures should be performed based on microscopic experiments. In particular, it should be noted that it is the pore–throat configuration that serves as the key parameter determining reservoir quality.

DATA AVAILABILITY STATEMENT

The original contributions presented in the study are included in the article/supplementary material; further inquiries can be directed to the corresponding author.

AUTHOR CONTRIBUTIONS

All authors listed have made a substantial, direct, and intellectual contribution to the work and approved it for publication.

ACKNOWLEDGMENTS

REFERENCES

Chen, C., Huang, Z., and Chen, X. (2018). The Formation Conditions of the Upper Carboniferous Near-Source Tuff Tight Oil Reservoir Santanghu Basin, Xinjiang Province. *Geol. Bull. China* 37 (1), 83–92. doi:10.3969/j.issn.1671-2552.2018.01.009

Chen, H., Jiang, P., and Zhang, D. (2013). Classification and Distribution Evaluation of Pore Structure of Volcanic Reservoirs: Taking the Volcanic Reservoirs of the First Member of Yingcheng Formation in Xudong Area of Songliao Basin as an Example [J]. *J. Cent. South Univ. (Natural Sci. Edition)* 44 (04), 1453–1463.

Chen, L., Lu, Y., Jiang, S., Li, J., Guo, T., and Luo, C. (2015). Heterogeneity of the Lower Silurian Longmaxi marine Shale in the Southeast Sichuan Basin of China. *Mar. Pet. Geology.* 65, 232–246. doi:10.1016/j.marpetgeo.2015.04.003

Chen, W., Xueqiang, S., and Zhi, F. (2013). Diagenesis of Volcanic Reservoir of Karagang Formation in Santang Lake Basin [J]. *J. Southwest Pet. Univ. (Natural Sci. Edition)* 35 (04), 35–42. doi:10.3863/j.issn.1674-5086.2013.04.005

Dong, G., Zhang, Q., and Zhu, X. (2012). Current Status and Problems of Volcanic Reservoir Study: an Example from the Lower Per-Mian Volcanic Rocks in Ke-Xia Area of Junggar Basin[J]. *Oil & Gas Geology.* 33 (4), 511519. doi:10.11743/ogg20120403

Hadlari, T. (2015). Oil Migration Driven by Exhumation of the Canol Formation Oil Shale: A New Conceptual Model for the Norman Wells Oil Field, Northwestern Canada. *Mar. Pet. Geology.* 65, 172–177. doi:10.1016/j.marpetgeo.2015.03.027

Hou, L., Wang, J., and Zou, C. (2011). Controlling Factors of Volcanic Weathering Reservoirs: Taking the Carboniferous Karagang Formation as an Example [J]. *Acta Geologica Sinica* 85 (04), 557–568.

Huang, Z., Liu, B., and Luo, Q. (2012). Main Controlling Factors and Models of Hydrocarbon Accumulation in Carboniferous Volcanic Rock Series in Malang Sag, Santang Lake Basin [J]. *Acta Geologica Sinica* 86 (08), 1210–1216. doi:10.3969/j.issn.0001-5717.2012.08.004

Igathinathane, C., Pordesimo, L. O., and Columbus, E. P. (2008). Shape Identification and Particles Size Distribution from Basic Shape Parameters Using Image. *Comput. Electron. Agric.* 63 (2), 168–182. doi:10.1016/j.compag.2008.02.007

JiaChengzao, Z., and Li, J. (2012). Assessment Criteria, Main Types, Basic Features and Resouece Prospects of the Tight Oil in China [J]. *Acta Petrolei Sinica* 33 (3), 343–350. doi:10.7623/syxb201203001

Li, G., Mao, S., and Chen, F. (2010). Key Controlling Fac-Tors and Exploration Direction of Volcanic Reservoir in Kalagang Formation of Malang Sag in Santanghu Basin[J]. *China Pet. Exploration* 15 (1), 11–15. doi:10.3969/j.issn.1672-7703.2010.01.003

Liang, H., Gou, H., and Wang, Z.. (2011), Volcanic Lithology and Lithofacies Characteristics of the Karagang Formation in Malang Sag. *Santanghu Basin* 29 (06), 1156–1163.

Liu, B., Gao, Y., and Liu, K. (2021), Pore Structure and Adsorption Hysteresis of the Middle Jurassic Xishanyao Shale Formation in the Southern Junggar Basin, Northwest China. *Energy Exploration & Exploitation* 39, 761–778. doi:10.1177/0144598720985136

Liu, B., Sun, J., and Zhang, Y. (2021), Reservoir Space and Enrichment Model of Shale Oil in the First Member of Cretaceous Qingshankou Formation in the Changling Sag, Southern Songliao Basin, NE China. *Pet. Exploration Develop.* 48 (3), 608–624. doi:10.1016/j.coal.2017.03.011

Liu, B., Bechtel, A., and Sachsenhofer, R. F. (2017c), Depositional Environment of Oil Shale within the Second Member of Permian Lucaogou Formation in the Santanghu Basin, Northwest China. *Int. J. Coal Geology.* 175, 10–25. doi:10.11743/ogg20130602

Liu, B., Chi, Y., and Huang, Z. (2013). Permian Hydrocarbon Migration Mechanism and Shale Oil Enrichment Law in Malang Sag, Santang Lake Basin [J]. *Oil & gas Geology.* 34 (06), 725–730. doi:10.11743/ogg20130602

Liu, B., Jia, M., and Huang, Z. (2015). Identification and Prediction of Carboniferous Volcanic Rock Source Rocks in Malang Sag, Santang Lake Basin [J]. *Pet. Geology. Exp.* 37 (04), 452–459. doi:10.11781/sysydz201504452

Ma, S., Luo, J., and Chen, C. (2017). Classification and Evaluation of Micro Pore Structure of Volcanic Reservoirs: A Case Study of the Carboniferous Volcanic Rocks in the Xiquan Area in the Eastern Junggar Basin [J]. *Pet. Geology. Exp.* 39 (05), 647–654. doi:10.11781/sysydz201705647

Pang, Y., Zhang, F., and Qiu, H. (2007). Microscopic Pore Structure and Physical Parameter Characteristics of Acid Volcanic Reservoirs [J]. *Acta Petrolei Sinica* 28 (06), 72–77. doi:10.3321/j.issn:0253-2697.2007.06.014

Qin, Hao. (2011). Research on Volcanic Reservoir Classification Method Based on Micro Pore Structure [J]. *J. Oil Gas Technol.* 33 (01), 98–102. + 168. doi:10.3969/j.issn.1000-9752.2011.01.022

Shan, P., Mei, Q., and Zhang, H. (2019). Characteristics of Reservoir Pore Size Distribution Based on Thin Section and Rate-Controlled Mercury Injection and its Differential Mechanisms: An Example of Chang-2 Reservoir of Yanchang Formation in a Block of Ordos Basin [J]. *Acta Scientiarum Naturalium Universitatis Pekinensis* 55 (5), 907–914. doi:10.13209/j.0479-8023.2019.055

Su, D., Wang, Z., and Yuan, Y. (2020). Weathered Volcanic Reservoir Characteristics and Their Controlling Factorson Permian Fengcheng Formation in Southern Mahu Depression, Junggar Basin[J], *Nat. Gas Geosci.*, 31, 2, 209–219. doi:10.11764/j.issn.1672-1926.2019.10.003

Sun, Z., Jiang, Y., and Ming, Z. (2013). Lithology-lithofacies Model of Carboniferous Volcanic Reservoirs in the Junggar Basin, NW China [J]. *J. China Univ. Mining &Technology* 425, 782–789.

Tian, W., Lu, S., Wang, W., Jinbu, L., Zhuang, L., and Jie, L. (2019). Evolution Mechanism of Micronano-Scale Pores in Volcanic Weathering Crust Reservoir in the Kalagang Formation in Santanghu Basin and Their Relationship with Oil-Bearing Property[J]. *Oil & gas Geology.* 40 (06), 1281–1294. doi:10.11743/ogg20190612

Wang, L., Li, W., and Tong, L. (2010). Comparative Analysis of Volcanic Reservoir Development Characteristics and Reservoir Formation Controlling Factors of Onshore and Underwater Eruption: a Case Study of the Carboniferous Volcanic Reservoirs in the Santang Lake Basin [J]. *Scientific Geology.* 45 (04), 1088–1097. doi:10.3969/j.issn.0563-5020.2010.04.013

Yang, F., Ning, F., and Kong, D. (2013). Pore Structure of Shales from High Pressure Mercury Injection and Nitrogen Adsorption Method[J]. *Nat. Gas Geosci.* 24 (3), 450–455. doi:10.3969/j.issn.0563-5020.2010.04.013

Yang, F., Ning, Z., and Zhang, S. (2013). Characterization of Pore Structures in Shales through Nitrogen Adsorption Experiment[J]. *Nat. Gas Industry* 33 (4), 135–140. doi:10.3787/j.issn.1000-0976.2013.04.025

Yang, H., Wang, D., and Gao, Y. (2019). Neogene Gas Origin and Oil and Gas Differential Enrichment Mechanism in the basin Margin of the Bohai Bay Basin: A Case Study of Eastern Slope in the Yellow River Mouth Depression [J]. *Acta Petrolei Sinica* 40 (05), 509–518.

Yu, B. S. (2013). Classification and Characterization of Gas Shale Pore System. *Earth Sci. Front.* 20 (4), 211–220. (in Chinese with English abstract).

Characteristics of Shale Pores and Surfaces and Their Potential Effects on the Fluid Flow From Shale Formation to Fractures

Xu Li[1,2], Jingong Cai[2]*, Bo Gao[1], Shengxiang Long[1], Dongjun Feng[1], Zeyang Peng[1] and Benqiang Guo[2]

[1]State Key Laboratory of Shale Oil and Gas Enrichment Mechanisms and Effective Development, SINOPEC, Beijing, China, [2]State Key Laboratory of Marine Geology, Tongji University, Shanghai, China

Fluid flow is critical for the efficient exploitation of shale resources and can be split into two stages: the flow in the artificial fractures and, more importantly, the flow from shale formations to the artificial fractures. In this study, X-ray diffraction, N_2 adsorption, mercury intrusion, and ethylene glycol monoethyl ether adsorption were conducted on the shales collected from Es_3^{middle}, Es_3^{lower}, and Es_4^{upper} sub-members in the Dongying Sag to reveal the potential effects of the characteristics and properties of pores and surfaces on the fluid flow in shale formations. The results are indicated as follows: 1) The shales from Es_3^{middle} and Es_3^{lower} contain more I/S and detrital minerals but less illite and carbonate minerals than those of Es_4^{upper}. 2) The shales from Es_3^{middle} and Es_3^{lower} are mainly composed of smaller pores present in larger surface areas and lead to the steeper slope between the BrunauerEmmettTeller specific surface area (BET-SSA) and pore volumes. 3) Clay minerals mainly contribute to pore development, and carbonate minerals inhibit pore development. All kinds of surface areas (especially the inner surface area) are sourced by clay minerals, while I/S and illite present opposite effects. 4) Pore size and surface properties affect significantly the fluid flow in shale formations. The shales from Es_4^{upper} are the favorable interval for shale oil accumulation and flow, especially for the shales with depth ranges of 3360~3410 m, which possess high carbonates, illite and total organic carbon content, low clay mineral content, large pore volume, high large pore content, and small surface areas. Additionally, fluid composition needs to be paid more concern in the future.

Keywords: pore characteristics, surface characteristics, mineral composition, interfacial interaction, fluid flow

INTRODUCTION

Hydraulic fracturing is one of the most important technologies for the successful exploitation of unconventional oil and gas resources with ultra-low porosity and permeability, especially for shale resources (Osiptsov, 2017; Wang and Sheng, 2017; Lu et al., 2018; Aadnøy and Looyeh, 2019; Yang and Guo, 2019; Lu et al., 2020; Shi et al., 2020; Xie et al., 2020; Wang et al., 2022). One of the key concerns of the exploitation of shale resources is the evaluation of the production performance after fracturing (Jarvie et al., 2007; Wang and Gale, 2009; Jin et al., 2014; Tang et al., 2019; Wei et al., 2020). Previous studies have observed that the fracturing fluids interact significantly with minerals and

change their properties such as wettability, morphology, composition, water-bearing properties, and cation exchange capacity (CEC) (Chen et al., 2016; Chen et al., 2018a; Chen et al., 2018b; Lu et al., 2018; Sari et al., 2019; Zeng et al., 2019), leading to problems such as low flowback recovery of fracturing fluids, environment hazard, hydration, expansion, and rheology of clay minerals (O'Brien and Chenevert, 1973; Makhanov et al., 2014; Al-Ameri et al., 2018; Sui et al., 2018; Aadnøy and Looyeh, 2019; Zeng et al., 2019) and will impact seriously on the production progress. Therefore, to better understand the mechanisms of these problems and their potential effect on production performance, a detailed analysis of the characteristics of shale pores and surface structures and their potential interactions with the fracturing fluids and the confined fluids in shale formations is of great significance.

The fluid flow after hydraulic fracturing in the shales can be divided into two stages: the flow from shale formations to the fractures and the flow in the fractures. Because the ultimate and the most important purpose of hydraulic fracturing is to release oil and gas occluded in pores or adsorbed on surfaces as much as possible, the former stage is more important and is affected more significantly by pore and surface attributes. The international union of pure and applied chemistry (IUPAC) classified the pores into micropore (<2 nm), mesopore (2~50 nm), and macropore (>50 nm) according to the pore size, adsorption properties, and capillary condensation (Sing, 1985). Shale presents pores with a wide diameter range, and the capillary pressure that relates closely to fluid flow differs according to the pore size if the properties of pore walls are the same. More importantly, the fluid flow in nanopores and the space close to surfaces do not follow Darcy's law because of the strong interactions between fluids and pore walls (Zeng et al., 2011; Wang et al., 2015; Wang Z. et al., 2016; Wang and Sheng, 2017; Yu et al., 2017; Song et al., 2018; Cheng et al., 2019). Pore walls are constructed by minerals or organic matter (OM) that presents significant divergences in their physical and chemical properties. Differences in the origin of the pores result in the differences in the morphology, size, and attributes of pore walls (surfaces). For example, the pores formed by plate-like clay minerals tend to be slit-like (Curtis et al., 2012; Kuila and Prasad, 2013; Mathia et al., 2016); micropores and small mesopores are mainly related to clay minerals and organic matter (Chalmers and Bustin, 2008; Klaver et al., 2012; Zhang et al., 2012; Kuila and Prasad, 2013; Kuila et al., 2014). Therefore, the distribution of confined fluids differs greatly according to the shale pore structure and surface properties, which are closely related to the shale mineral composition and burial evolution. For example, nanopores with higher elastic buckling pressure increase with increasing depth (Curtis et al., 2012; Kuila and Prasad, 2013); mineral composition changes significantly due to diagenesis including illitization, dolomitization, recrystallization (Li W. et al., 2016; Wilson et al., 2016a; Mathia et al., 2016; Bai et al., 2018; Cai et al., 2018; Liang et al., 2018; Du et al., 2019; Wang and Guo, 2019), leading to the changes of pore and surface properties (Klaver et al., 2012; Li W. et al., 2016; Wilson et al., 2016b; Wang and Guo, 2019). In summary, shale pores and surfaces are complex, and their characteristics and properties change significantly according to the mineral composition and burial evolution. These complexities control the interactions between pore walls and confined fluids, and they must affect the shale oil mobility and production performance.

To further illustrate the potential impacts of the complexity of the characteristics and properties of pores and surfaces on the fluid flow from shale formation to fractures, the interactions between fluids and pores or surfaces in different fracturing stages were summarized. During the pumping stage, fracturing fluids are pumped into shale formation and forming fractures. Then, fracturing fluids gradually intrude into shale rocks under high fluid pressure. After pumping, the well will be shut. Shut-in is commonly used and is important for the formation of stable fractures and provides time for the water blockage removal (Al-Ameri et al., 2018; Wijaya and Sheng, 2019). During this stage, fracturing fluids imbibe into the formation spontaneously. It is important to note that spontaneous imbibition also happens during the fluid pumping, the flowback, and the long-term production stage (Al-Ameri et al., 2018; Zeng et al., 2019). The strength of the imbibition is greatly affected by the wettability, the pore structure, and the pore connectivity of the rock (Dehghanpour et al., 2012; Xu and Dehghanpour, 2014; Wilson et al., 2016b; Zolfaghari et al., 2016; Sun et al., 2017; Yu et al., 2017; Yang et al., 2018). In addition, the wettability of some surfaces can be changed from oil wetting to water wetting due to imbibition (Chen et al., 2016; Roshan et al., 2016; Chen et al., 2018a; Chen et al., 2018b; Zeng et al., 2019), and the pore structure can also be changed by fracturing fluids and surfactant (Xu and Dehghanpour, 2014; Lu et al., 2019), which will further change the flow characteristics conversely. During the flowback stage, part of the fracturing fluids is adsorbed by the minerals (especially the clay minerals) or trapped into the pores with narrow throat, leading to low flowback recovery of the fracturing fluids (Xu and Dehghanpour, 2014; Al-Ameri et al., 2018; Wijaya and Sheng, 2019). Meanwhile, the chemical properties of the flowback fluids change obviously due to the mass exchange between the fracturing fluids and the pore fluids or the mineral components (Haluszczak et al., 2013; Engle and Rowan, 2014; Zolfaghari et al., 2016). Additionally, the strength of the impacts differs according to mineral types because of the divergences in their physical and chemical properties (Zolfaghari et al., 2016). For example, smectite and I/S impact more on the flowback water chemical properties than illite (Zolfaghari et al., 2016). In summary, characteristics and properties of pores and surfaces will impact the absolute permeability of shale and, more importantly, the relative permeability of oil. Thus, the analysis of the characteristics and properties of shale pores and surfaces is important for the evaluation of shale oil potential, but they are seldomly considered previously.

In this study, shale samples with different mineral compositions and degrees of evolution were collected from different shale formations in the Dongying Sag, Jiyang Depression. The complete shale pore's size distribution and surfaces with different properties were analyzed by N_2 adsorption, mercury intrusion porosimetry, and EGME adsorption methods. Then, the mineral composition, pore, and surface characteristics and properties were compared among the shales at different intervals. Based on all these detections and
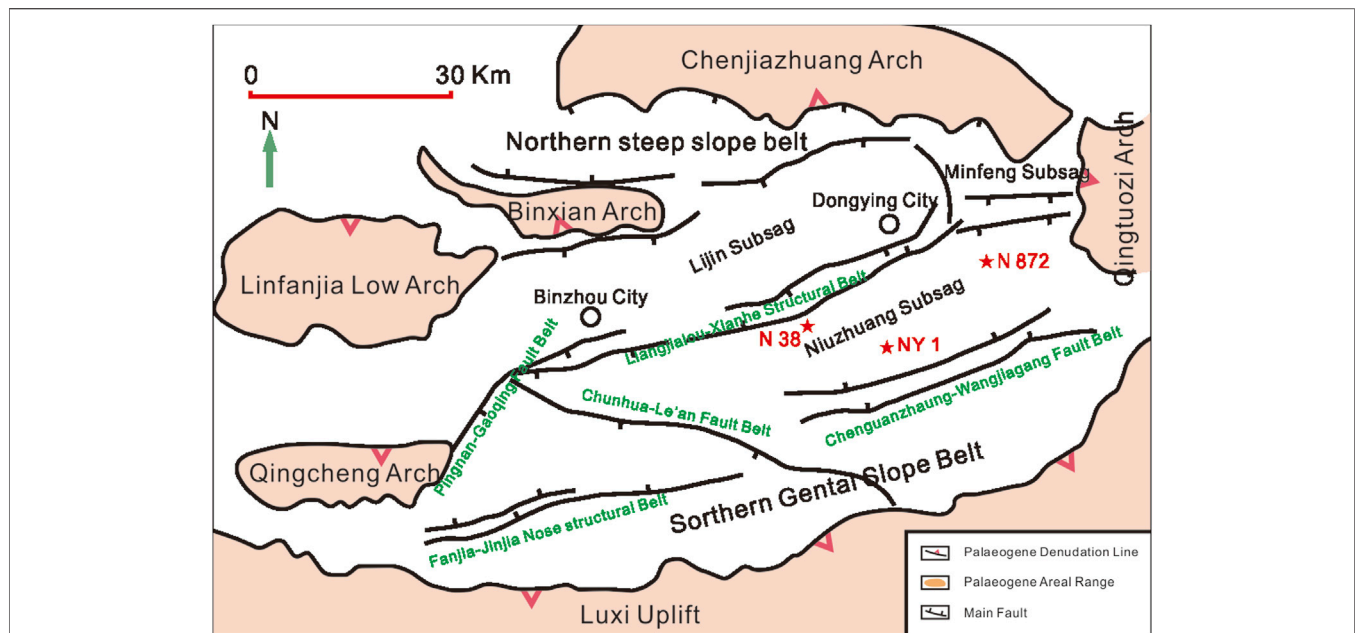
FIGURE 1 | Structural map and sampling well locations of the Dongying Sag (modified from Li et al., 2020).

comparisons, the fluids flow from shale formation to the hydraulic fractures was evaluated, and the favorable interval for shale oil storage and flow was obtained on the profile from the perspective of potential fluid flow properties. This study can benefit the selection of fracturing fluids, the implementation of fracturing, and the accurate evaluation of shale oil production performance.

MATERIALS AND METHODS

Materials

The Dongying Sag locates in the southeastern of Bohai Bay Basin, northern China. Previous exploration has confirmed the great shale oil potential in the third and fourth members of Shahejie Formation (Li Z. et al., 2016; Li et al., 2020). In order to characterize the influence of pore structure on the fracturing of the shales with different compositions, thirty-four argillaceous source rocks were selected for detection, which were taken from well NY1, N38, and N872 at depths of 3000~3500 m in the middle and lower section of the third member (Es_3^{middle} and Es_3^{lower}) and upper section of the fourth member (Es_4^{upper}) of Shahejie Formation (**Figure 1**; **Table 1**) in the Dongying Sag. All the bulk samples were detected by X-ray diffraction (XRD), Rock-Eval VI pyrolysis, N_2 adsorption, mercury injection porosimetry (MIP), and ethylene glycol monoethyl ether (EGME) adsorption methods. The clay fraction of each sample was detected by XRD to obtain the clay mineral composition. For the separation of the clay-sized fractions, the bulk rocks were ground to less than 1 mm and were then soaked in deionized water within a 2000-ml beaker at room temperature via natural sedimentation.

Methods

X-Ray Diffraction (XRD)

An X'pert-MPD diffraction instrument (Philips Corp) was employed for XRD measurements. The samples were crushed to a particle size of 320 mesh. The test conditions include a copper butt, pipe pressure of 30 kV, conduit flow of 40 mA, and scanning speed of 2° (2θ)/min. The bulk mineral composition was detected by a natural thin section of bulk rock. The clay mineral composition detection was conducted on natural ethylene glycol saturated and 550 C heated orientation sheet of clay fractions. The ethylene glycol-saturated orientation sheet was made by exposing the naturally oriented sheet in ethylene glycol vapor at 60°C for 8 h, and 550°C heated orientation sheet was made by heating at 550°C for 2 h.

Pore Characteristics Determination

N_2 Adsorption

Pore size distribution (PSD) of pores with diameters ranging from approximately 1–50 nm was conducted with the low-temperature (77 K) N_2 adsorption methods on the JW-BK adsorption instrument (Beijing JWGB SCI & Tech Corp). Approximately 2~4 g of sample was crushed to a particle size smaller than 3 mm and degassed by heating at 80°C for more than 6 h under vacuum (10 μm Hg) to remove adsorbed moisture and volatile matter prior to the analysis. Measurements in adsorption mode were performed over the relative pressure (P/P0) range of 0.1 ~ 0.95 to obtain the adsorption isotherm. The PSD was obtained by inverting the adsorption branch of the isotherm using BarrettJoynerHalenda (BJH) method (Barrett et al., 1951).

TABLE 1 | Sample information and mineral composition.

| Sample no. | Well | Depth | Member | Bulk mineral composition/% | | | Clay mineral composition/% | | | |
		M		Clay	Detrital	Carbonate	I/S	Illite	Kaolinite	Chlorite
1	NY1	3334.36	Es_4^{upper}	37	21	39	61	36	2	1
2	NY1	3355.61	Es_4^{upper}	22	26	49	67	33	0	0
3	NY1	3372.01	Es_4^{upper}	8	24	66	0	100	0	0
4	NY1	3378.36	Es_4^{upper}	9	25	64	30	70	0	0
5	NY1	3380.21	Es_4^{upper}	15	21	62	28	72	0	0
6	NY1	3382.16	Es_4^{upper}	48	33	16	35	65	0	0
7	NY1	3385.76	Es_4^{upper}	22	19	56	12	88	0	0
8	NY1	3390.45	Es_4^{upper}	13	24	62	0	100	0	0
9	NY1	3398.90	Es_4^{upper}	6	19	74	0	100	0	0
10	NY1	3408.00	Es_4^{upper}	24	21	53	0	100	0	0
11	NY1	3468.63	Es_4^{upper}	44	39	14	50	50	0	0
12	NY1	3479.73	Es_4^{upper}	5	12	83	0	100	0	0
13	NY1	3494.45	Es_4^{upper}	9	10	38	0	100	0	0
14	NY1	3497.90	Es_4^{upper}	15	15	31	3	97	0	0
15	N38	3022.00	Es_3^{middle}	42	50	4	74	14	7	5
16	N38	3025.00	Es_3^{middle}	31	46	20	76	13	6	5
17	N38	3034.81	Es_3^{middle}	27	38	32	69	15	9	7
18	N38	3089.52	Es_3^{middle}	47	42	11	68	22	6	4
19	N38	3137.61	Es_3^{middle}	42	35	21	81	15	2	2
20	N38	3140.91	Es_3^{middle}	45	39	14	74	19	4	3
21	N38	3143.41	Es_3^{middle}	45	50	5	68	20	7	5
22	N38	3147.41	Es_3^{middle}	51	41	6	73	20	4	3
23	N38	3336.60	Es_3^{lower}	43	44	13	65	30	3	2
24	N38	3342.60	Es_3^{lower}	41	34	22	59	41	0	0
25	N872	3050.80	Es_3^{middle}	30	33	31	72	20	4	4
26	N872	3049.70	Es_3^{middle}	34	28	32	71	17	7	5
27	N872	3053.50	Es_3^{middle}	37	40	21	71	25	2	2
28	N872	3072.30	Es_3^{middle}	32	50	16	73	22	3	2
29	N872	3074.30	Es_3^{middle}	26	53	20	73	22	3	2
30	N872	3201.00	Es_3^{lower}	25	35	35	52	40	4	4
31	N872	3203.00	Es_3^{lower}	29	27	39	69	27	2	2
32	N872	3208.70	Es_3^{lower}	18	29	49	57	36	4	3
33	N872	3327.30	Es_4^{upper}	19	36	43	5	95	0	0
34	N872	3329.40	Es_4^{upper}	38	35	24	49	51	0	0

Mercury Intrusion Porosimetry

The PSD of pores with diameters ranging from approximately 3.2 nm–40 μm was determined using the mercury intrusion method on a Micromeritics Autopore IV 9500 series apparatus. Samples (2~4 g) were crushed to a particle size smaller than 3 mm and were oven-dried (80°C) and evacuated under vacuum (30 μm Hg) for 30 min prior to mercury intrusion. The measured pressure ranged from 0.5 to 60,000 psia, and the PSD was calculated by the Washburn equation (Schmitt et al., 2013). In our calculations, the interfacial tension of Hg was 485 mN/m, the wetting angle was 140°, and the density of Hg was 13.5335 g/ml.

Combination of N₂ Adsorption and MIP and Calculation of Pore Characteristics Parameters

Previous researchers have established several methods to combine N_2 adsorption method and MIP for obtaining the complete PSD of shales (Spitzer et al., 1976; Echeverria et al., 1999; Schmitt et al., 2013; Kenvin et al., 2015). In this study, we obtained the complete PSD referring to the method proposed by Schmitt et al. (2013) and Li et al. (2020). The junction point of

each sample is listed in **Table 2**. After achieving the complete PSD, the total pore volume (Vt) was calculated.

Surface Areas Measurement

N₂ Adsorption

The determination procedure is the same as the *Surface Areas Measurement section*. After obtaining the adsorption isotherms, the outer surface area (BET-SSA) for each sample was determined by inversion of the adsorption branch of the isotherm using the BrunauerEmmettTeller (BET) analysis procedure (Brunauer et al., 1938), with a relative pressure range of 0.05 ~ 0.3. The molecular sectional area of N_2 was 0.162 nm^2.

EGME Adsorption

For the EGME procedure, a vacuum pump (with a vacuum pressure of 609 mmHg) and an electronic analytical balance (with an accuracy of 0.0001 g) were employed. Approximately 1 g of sample was weighed and put in the oven at 80°C for more than 6 h. Then, the sample was taken out and put in the aluminum tare (with a diameter of 5 cm and a height of 8 mm), and 3 ml EGME solution (analytical grade) was quickly

TABLE 2 | Junction points, pore volumes and contents, surface areas.

Sample no	Junction point	Vt	V1	V2	V3	V1%	V2%	V3%	TSA	ISA	BET-SSA
	nm	cm^3/g	cm^3/g	cm^3/g	cm^3/g	%	%	%	m^2/g	m^2/g	m^2/g
1	10.72	0.007799	0.003210	0.001605	0.002984	41.16	20.58	38.26	122.69	120.87	1.82
2	18.32	0.003750	0.000341	0.001806	0.001604	9.08	48.16	42.76	78.91	78.76	0.15
3	14.08	0.011062	0.000187	0.001401	0.009474	1.69	12.67	85.64	34.14	33.85	0.29
4	13.52	0.007807	0.000553	0.003219	0.004035	7.09	41.23	51.69	34.92	34.07	0.85
5	6.75	0.003593	0.003106	0.000163	0.000324	86.44	4.53	9.03	70.74	67.70	3.05
6	36.79	0.088121	0.000608	0.007541	0.079972	0.69	8.56	90.75	129.65	128.31	1.34
7	17.66	0.027352	0.009051	0.006746	0.011555	33.09	24.66	42.24	65.80	60.06	5.74
8	26.33	0.005770	0.000029	0.001438	0.004303	0.50	24.92	74.58	32.00	30.07	1.93
9	18.73	0.004906	0.000048	0.000763	0.004095	0.98	15.56	83.46	22.16	21.51	0.65
10	25.52	0.021793	0.003493	0.007661	0.010639	16.03	35.15	48.82	51.58	49.04	2.54
11	13.74	0.087995	0.036221	0.036579	0.015195	41.16	41.57	17.27	128.88	98.35	30.53
12	25.33	0.005556	0.000308	0.002110	0.003138	5.55	37.97	56.48	20.91	19.74	1.17
13	31.85	0.006996	0.001080	0.005282	0.000634	15.43	75.50	9.06	23.20	22.37	0.83
14	15.92	0.014206	0.002730	0.010687	0.000789	19.22	75.23	5.56	40.15	38.43	1.72
15	12.67	0.009972	0.005662	0.003765	0.000545	56.78	37.75	5.47	107.98	102.15	5.83
16	15.42	0.013532	0.005506	0.006636	0.001391	40.69	49.03	10.28	117.03	109.31	7.72
17	13.31	0.005320	0.002438	0.002114	0.000768	45.83	39.73	14.44	109.86	107.72	2.14
18	17.47	0.027000	0.016127	0.010290	0.000583	59.73	38.11	2.16	160.87	131.25	29.62
19	14.26	0.027401	0.012389	0.012697	0.002316	45.21	46.34	8.45	151.98	131.77	20.21
20	14.75	0.020501	0.011490	0.007354	0.001657	56.05	35.87	8.08	155.70	140.25	15.45
21	23.39	0.028910	0.013045	0.012291	0.003575	45.12	42.51	12.37	115.33	91.45	23.88
22	19.71	0.030813	0.016797	0.012868	0.001148	54.51	41.76	3.73	162.53	132.96	29.57
23	17.56	0.026642	0.014331	0.011117	0.001195	53.79	41.73	4.48	122.70	104.95	17.74
24	21.06	0.018754	0.004835	0.005779	0.008139	25.78	30.82	43.40	147.47	144.01	3.46
25	24.95	0.006979	0.000583	0.003136	0.003260	8.35	44.94	46.71	125.03	123.97	1.05
26	13.47	0.006426	0.002081	0.003374	0.000971	32.39	52.51	15.11	134.92	132.97	1.95
27	12.13	0.015185	0.009051	0.004849	0.001286	59.60	31.93	8.47	151.86	141.16	10.70
28	14.69	0.020578	0.012020	0.006391	0.002167	58.41	31.06	10.53	138.95	124.26	14.69
29	18.94	0.018109	0.008317	0.009056	0.000736	45.93	50.01	4.06	116.64	106.58	10.06
30	14.26	0.007901	0.000140	0.004101	0.003660	1.77	51.90	46.33	113.77	113.16	0.61
31	27.63	0.004121	0.000020	0.002119	0.001982	0.49	51.42	48.09	153.49	151.88	1.61
32	27.63	0.005280	0.000067	0.002008	0.003205	1.27	38.03	60.71	93.85	91.93	1.92
33	15.70	0.009027	0.001751	0.003340	0.003936	19.40	37.00	43.61	62.81	60.96	1.85
34	24.59	0.088952	0.006882	0.024590	0.057480	7.74	27.64	64.62	124.09	119.36	4.73

added to the sample with a pipette and swirled gently until the sample was soaked. Afterward, the aluminum tares with mixture were placed in a sealed desiccator with EGME solution, calcium chloride (CaCl$_2$), and phosphorus pentoxide (P$_2$O$_5$). The desiccator was evacuated for approximately 1 hour to remove water vapor. More than 8 h later, the tares were weighed after the desiccator was evacuated again. The process of evacuation was repeated, and they were weighed until a constant weight was attained (the mass difference between the two measurements was less than 0.001 g). Finally, the total surface area (TSA) of the sample was calculated based on the absorbed quantity of EGME molecules (the conversion factor is 2.86×10^{-4} g/m^2), and the inner surface area (ISA) was the differences between TSA and BET-SSA.

RESULTS

Mineral Composition
Bulk Mineral Composition
It is found from the XRD curves of typical bulk rocks (**Figure 2A**) that although clay, quartz, calcite are the main mineral types of all the shales, the relative contents of different types of minerals vary greatly among the shales from different sections. For example, the shales from Es$_4$^{upper} contain more dolomite, especially for the deeper burial samples. Comparison of bulk mineral composition of the shales from different sections (**Figure 2B**) shows that the shales from Es$_3$^{middle} contain the most amount of clay (37.62%) and detrital (41.92%) minerals and the least amount of carbonate (17.92%) minerals; the shales from Es$_4$^{upper} are composed of much more calcite (31.94%) and dolomite (15.31%) than those of Es$_3$^{middle} and Es$_3$^{lower}; the shales from Es$_3$^{lower} contain moderate content of almost all types of minerals.

Clay Mineral Composition
From the analysis of the composition of clay minerals (**Table 1**; **Figure 2C**), the average contents of mixed-layer illite/smectite (I/S) (46.62%) and illite (49.26%) of all the shales were found to be high, while there are also great differences among the shales from different sections. The shales from Es$_3$^{middle} contain the most amount of I/S (72.54%) and the least amount of illite (18.77%); the shales from Es$_4$^{upper} are composed of much more illite (78.56%) than those of Es$_3$^{middle} and Es$_3$^{lower}; the shales from
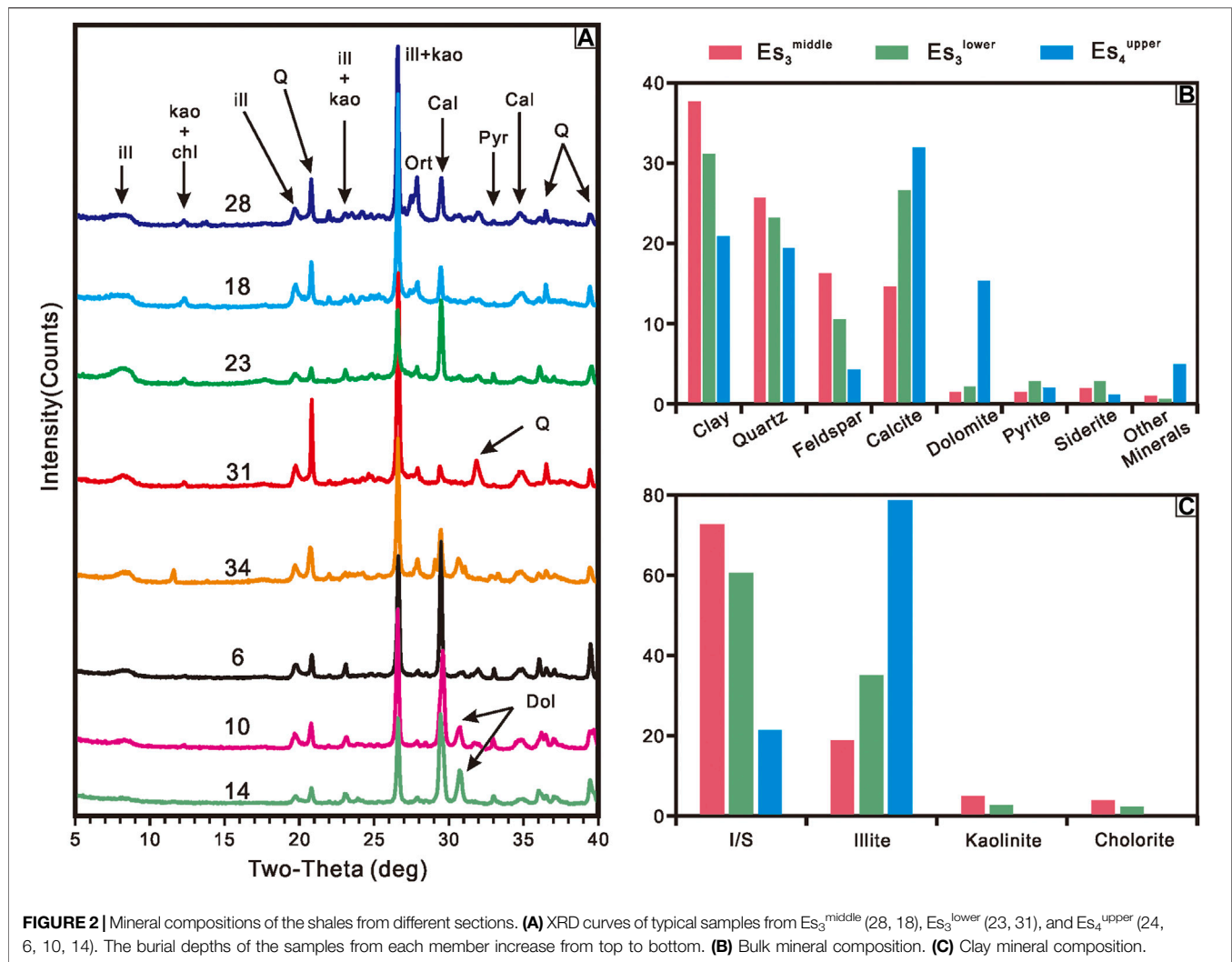
FIGURE 2 | Mineral compositions of the shales from different sections. **(A)** XRD curves of typical samples from Es_3^{middle} (28, 18), Es_3^{lower} (23, 31), and Es_4^{upper} (24, 6, 10, 14). The burial depths of the samples from each member increase from top to bottom. **(B)** Bulk mineral composition. **(C)** Clay mineral composition.

Es_3^{lower} contain moderate content of I/S (60.40%) and illite (34.80%).

Pore and Surface Characteristics
Surface Characteristics
From the results of the N_2 adsorption measurement (**Tables 2**; **Figure 3A**), the shales from Es_3^{middle} have the largest average BET-SSA (13.30 m^2/g), which ranges from 1.05 to 29.62 m^2/g; the BET-SSA of the shales from Es_3^{lower} ranges from 0.61 to 17.74 m^2/g with an average of 5.07 m^2/g; the shales from Es_4^{upper} possess BET-SSA ranges from 0.15 to 30.53 m^2/g, with 3.70 m^2/g on average. According to the EGME measurement (**Table 2**; **Figure 3C**), the shales from Es_3^{middle} possess the largest average TSA (134.51 m^2/g), which ranges from 107.98 to 162.53 m^2/g; the TSA of the shales from Es_3^{lower} ranges from 93.85 to 153.49 m^2/g with an average of 126.26 m^2/g; the shales from Es_4^{upper} present minimal TSA ranges from 20.91 to 129.65 m^2/g, with 65.17 m^2/g on average. Based on N_2 adsorption and EGME measurements (**Table 2**; **Figure 3B**), the ISA can be calculated. The results show that the shales

from Es_3^{middle} and Es_3^{lower} also present larger ISA (with 121.21 m^2/g and 121.19 m^2/g on average, respectively), while the shales from Es_4^{upper} have much smaller ISA (61.47 m^2/g).

Pore Characteristics
According to the complete pore size distribution (PSD) curves of the shales from different sections (**Figure 4**), most of the shales are mainly composed of the large mesopore (10~50 nm) and small macropore (50~100 nm), while most of the shales from Es_4^{upper} contain a significant amount of pores with diameter >100 nm (**Figures 4A–D**). In addition, the PSD of the shales from different sections shows great differences. Qualitatively, the shales from Es_4^{upper} contain more pores with larger diameter than the shales from Es_3^{middle} and Es_3^{lower}, while the shales from Es_3^{middle} present a very low amount of larger pores. Considering the characteristics of the PSD curves, the volumes of the pores with diameter <10 nm (V1), 10~100 nm (V2), and >100 nm (V3) were further calculated by interpolation (**Table 2**).

Based on these findings, Vt, V1, V2, and V3 and their relative contents of the shales from different sections were further
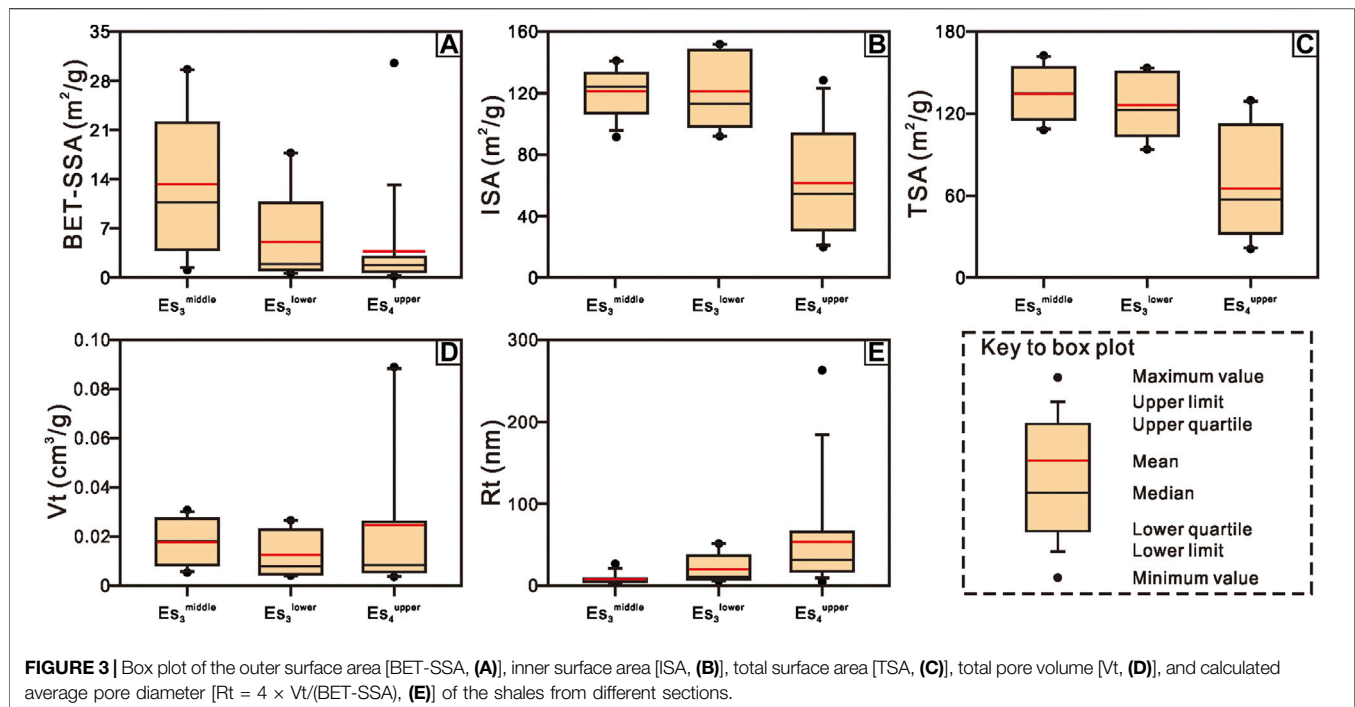
FIGURE 3 | Box plot of the outer surface area [BET-SSA, **(A)**], inner surface area [ISA, **(B)**], total surface area [TSA, **(C)**], total pore volume [Vt, **(D)**], and calculated average pore diameter [Rt = 4 × Vt/(BET-SSA), **(E)**] of the shales from different sections.

calculated and compared (**Table 2**; **Figures 3D,E, 5**). The Vt of the shales from Es_3^{middle} ranges from 0.005320 to 0.030813 cm^3/g, with 0.017748 cm^3/g on average; the Vt of the shales from Es_3^{lower} ranges from 0.004121 to 0.026642 cm^3/g, with 0.012539 cm^3/g on average; the Vt of the shales from Es_4^{upper} ranges from 0.003593 to 0.088952 cm^3/g, with an average of 0.024668 cm^3/g (**Table 2**; **Figure 3D**). Further comparing the pore volumes of the pores with different diameter ranges (**Figures 5A–C**), it can be found that the shales from Es_3^{middle} have the largest V1 (0.008885 cm^3/g) and V2 (0.007294 cm^3/g) and minimal V3 (0.001569 cm^3/g); the shales from Es_3^{lower} possess minimal V1 (0.003879 cm^3/g) and V2 (0.005025 cm^3/g) and moderate V3 (0.003636 cm^3/g), while the shales from Es_4^{upper} have maximal V3 (0.013135 cm^3/g) and moderate V1 (0.004350 cm^3/g) and V2 (0.007183 cm^3/g). Viewing from the contents of V1, V2, and V3 (**Figures 5D–F**), the shales from Es_3^{middle} contain the most amount of V1 (46.81%) and the least amount of V3 (11.53%), the shales from Es_3^{lower} possess minimal V1 (16.62%) and maximal V2 (42.78%), the shales from Es_4^{upper} present maximal V3 (47.74%) and minimal V2 (33.18%).

DISCUSSIONS

Relationships Between Pores and Surfaces

Pores and outer surfaces are the places where shale oil occurs. Their relationships depend on the relative contribution of free oil and adsorbed oil. Therefore, the relationships between pore volumes and the BET-SSA were analyzed firstly. It can be found that Vt of the shales from Es_3^{middle} and Es_3^{lower} presents a better relationship with BET-SSA (especially for Es_3^{middle}) than that of Es_4^{upper} (**Figure 6A**). Viewing from the pores with

different diameter ranges (**Figures 6B,C**), the correlation coefficients of the relationships between V1 of the shales from each section with BET-SSA are high (>0.95), while the correlation coefficients of the relationships between V2 of the shales from each section are smaller, especially for the shales from Es_4^{upper}; there are no relationships between V3 and BET-SSA (the data were not shown in **Figure 6**). These observations coincide well with previous researches; that is, the pores with small size contribute primarily to the outer surface area, while the pores with larger size mainly contribute to the pore volume (Beliveau, 1993; Chalmers et al., 2012; Curtis et al., 2012; Wang and Guo, 2019). Further comparison of the shales from different sections suggests that (**Figure 6**) the slopes of the shales from Es_3^{middle} and Es_3^{lower} are steeper than those of Es_4^{upper}, especially for V2 and Vt, indicating the differences in their pore size and in the ratio between pore volume and outer surface area. It has been confirmed previously that pores with different sizes have different ratios between pore volume and outer surface area, leading to the difference in the proportion of oil with different occurrence states (Chalmers et al., 2012; Curtis et al., 2012; Wang and Guo, 2019). MDSs and spontaneous imbibition experiments also showed that the intensity of the interfacial interaction of the pores with different pore volume/surface area ratios (or pore diameter) differs significantly (Xu and Dehghanpour, 2014; Yu et al., 2017). The pores with smaller pore volume and larger surface area possess stronger interfacial interaction intensity and larger capillary force, leading to larger adsorption potential to wetting phase fluids and stronger inhibition to non-wetting phase fluids (Wang et al., 2015; Wang S. et al., 2016; Yu et al., 2017; Zeng et al., 2019). Therefore, the shales from Es_4^{upper} which present larger pore volume and smaller surface area are more conducive to fluid flow without considering the properties of the pore walls.
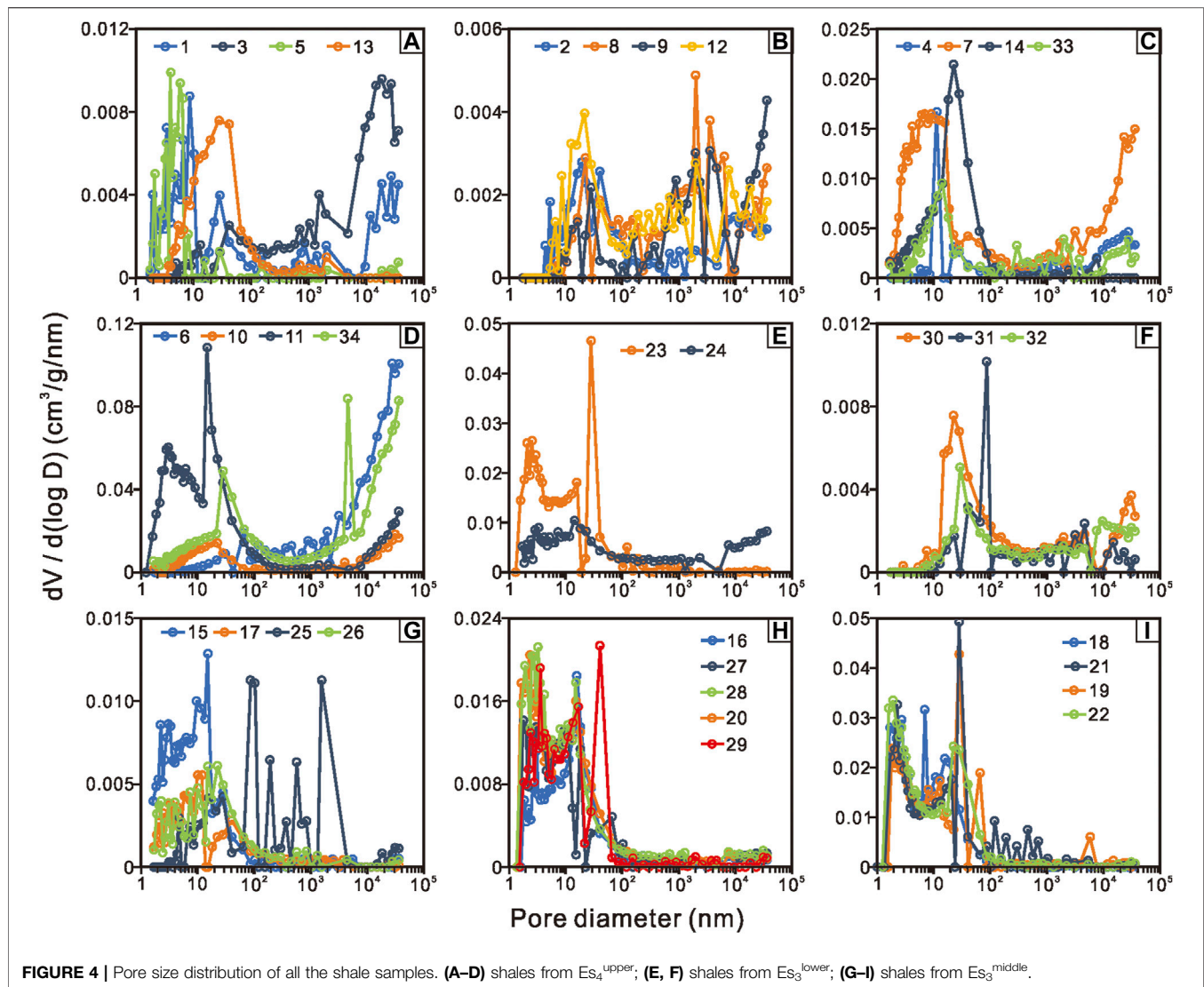
FIGURE 4 | Pore size distribution of all the shale samples. **(A–D)** shales from Es_4^{upper}; **(E, F)** shales from Es_3^{lower}; **(G–I)** shales from Es_3^{middle}.

However, shales are composed of varieties of minerals which present divergence attributes. Thus, to analyze the properties of pore walls and their influence on fluid mobility of the shales from different sections, the relationships between minerals and pores/surfaces were further analyzed.

Contributions of Mineral Components to Pores and Surfaces
Pores

Clay minerals (I/S, illite), detrital minerals (quartz, feldspar), and carbonate minerals (calcite, dolomite) are the main bulk mineral components in shale rocks (**Table 1**; **Figure 2**). According to the relationships between bulk mineral compositions with Vt (**Figure 7**), it is found that Vt positively correlates with clay and detrital mineral content but negatively correlates with carbonate mineral content for the shales from all sections and generally presents a high correlation coefficient. These correlations indicate that inorganic pores are the main pore

type of the studied area, while clay and detrital minerals contribute to the shale pores and carbonate minerals generally inhibit the development of pores. These findings are similar to previous studies on the shales from similar locations (Zhang et al., 2016; Zhu et al., 2019; Zhang et al., 2019; Liu et al., 2019). Previous studies have confirmed the chemical instability of carbonate minerals, and they probably destroy or block the pores by digenesis such as dissolution, precipitation, and recrystallization (Chalmers et al., 2012; Gaines et al., 2012; Loucks et al., 2012; Liu et al., 2019). In addition, the correlations between Vt and clay and carbonate mineral are usually better than those of detrital minerals, indicating the stronger control of clay and carbonate minerals in shale pores.

Comparison of the correlations of the shales from different sections shows that the slopes of the shales from Es_4^{upper} are much larger than those of the other two sections (**Figure 7**), suggesting the greater role of mineral components in the development of pores, especially for the relatively larger pores. The conclusion can be certificated by the previous studies
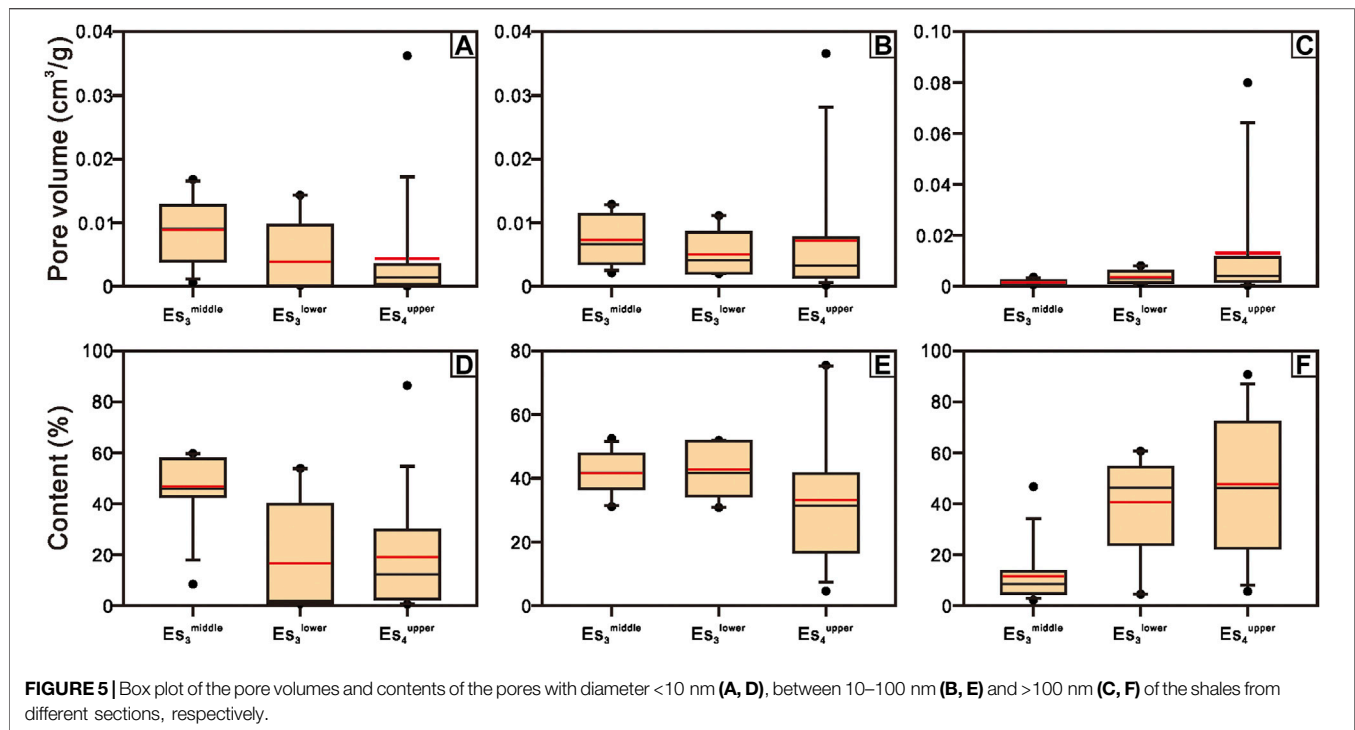
FIGURE 5 | Box plot of the pore volumes and contents of the pores with diameter <10 nm **(A, D)**, between 10–100 nm **(B, E)** and >100 nm **(C, F)** of the shales from different sections, respectively.
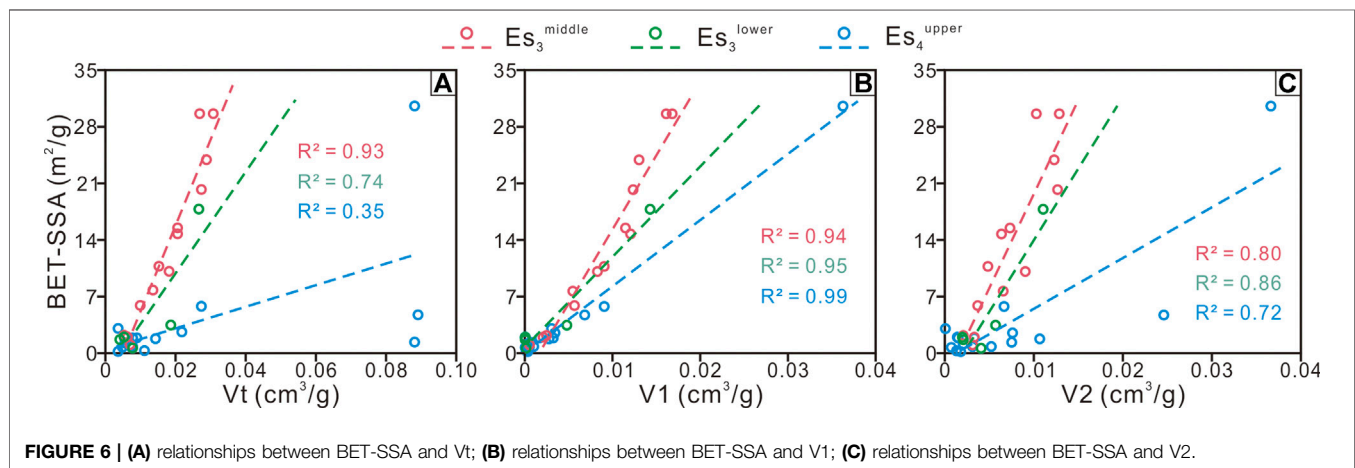
FIGURE 6 | **(A)** relationships between BET-SSA and Vt; **(B)** relationships between BET-SSA and V1; **(C)** relationships between BET-SSA and V2.

indicating that clay minerals mainly relate to micropores and small mesopores while carbonate minerals generally correlate well with pores with larger diameter (Chalmers et al., 2012; Klaver et al., 2012; Kuila and Prasad, 2013; Mathia et al., 2016; Liu et al., 2019; Zhang et al., 2020) and the relatively high carbonate mineral content of the shales from Es_4^{upper}. Moreover, based on the relationships between clay mineral content and pore volumes of pores with different diameter range (**Figure 8**), it can be found that V3 of the shales from Es_4^{upper} correlates well with clay mineral content while present no obvious relationships for the shales from Es_3^{middle} and Es_3^{lower}. On the contrary, the correlation coefficients between V1 and clay mineral contents for the shales from Es_3^{middle} and Es_3^{lower} are much higher than that of Es_4^{upper} (**Figure 8**). The results indicate that although clay

minerals mainly benefit the development of pores, the relative contributions of clay minerals to pores with different diameters for the shales from different sections differ significantly. Previous studies indicated that illitization, dolomitization, and dissolution benefit the shale reservoir properties and create more macropores for oil accumulation and flow (Chalmers et al., 2012; Li W. et al., 2016; Mathia et al., 2016; Bai et al., 2018; Liang et al., 2018; Wang and Guo, 2019). Thus, considering differences in mineral composition of different sections (**Figure 2**), we attribute these divergences to the clay mineral composition of the shales from different sections. In summary, the shales from Es_4^{upper} contain more carbonate minerals and undergone a higher degree of illitization and dolomitization than those of Es_3^{middle} and Es_3^{lower}, thus leading to more pores with larger diameter

FIGURE 7 | (A) relationships between Vt and clay mineral content; **(B)** relationships between Vt and detrital mineral content; **(C)** relationships between Vt and carbonate mineral content.

FIGURE 8 | (A) relationships between V1 and clay mineral content; **(B)** relationships between V2 and detrital mineral content; **(C)** relationships between V3 and carbonate mineral content.
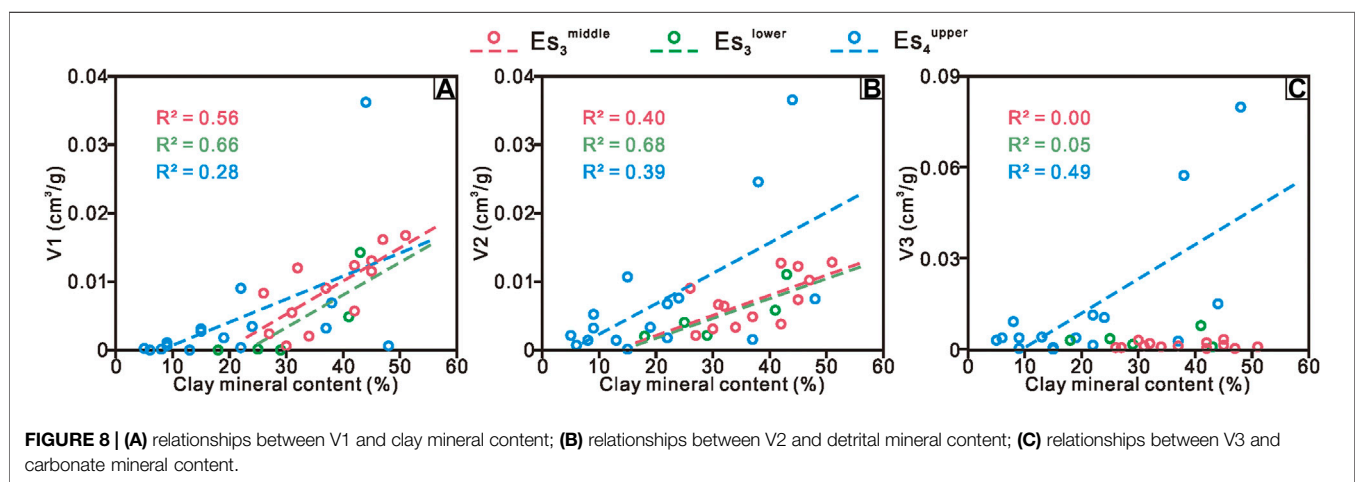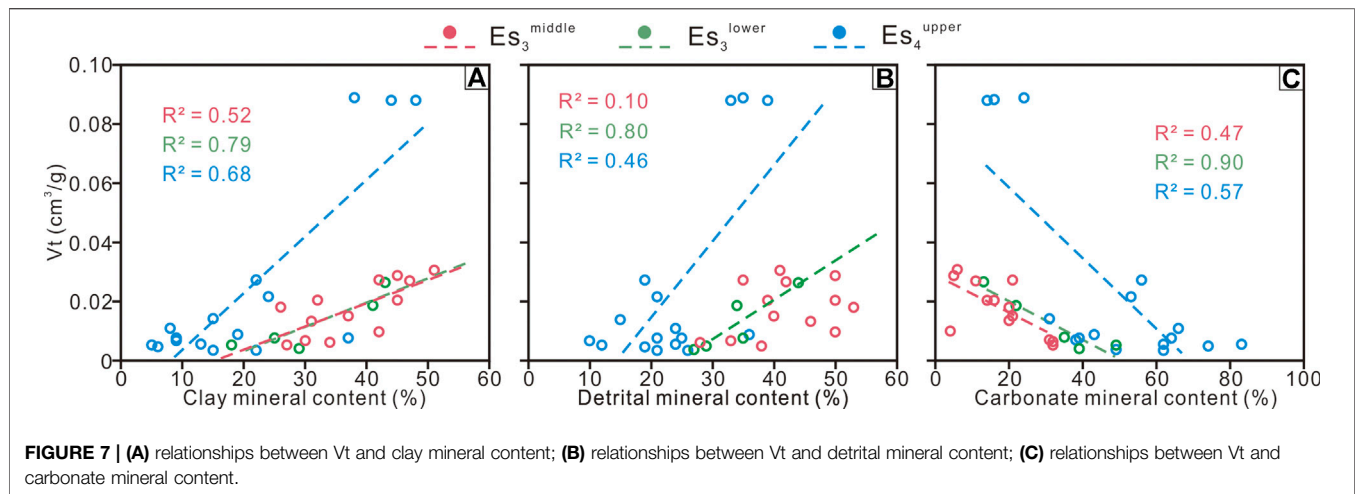
(**Table 2**; **Figures 3–5**). Therefore, the shales from Es_4^{upper} present a higher potential for oil accumulation and flow from shale formations to fractures.

Surfaces

Clay minerals correlate with smaller pores with large correlation coefficients (**Figure 8**) (Kuila and Prasad, 2013) and possess larger outer surface area than detrital and carbonate minerals (Beliveau, 1993; Chalmers and Bustin, 2008; Chalmers et al., 2012; Kuila and Prasad, 2013; Zhu et al., 2015; Saidian et al., 2016). Additionally, clay minerals such as smectite and I/S have inner surface areas between clay sheets, and ISA is usually one or two orders of magnitude larger than the outer surface area (Macht et al., 2011; Zhu et al., 2015). Thus, we only analyze the contributions of clay minerals to surface areas. Comparison of the clay mineral composition of the shales from different sections (**Table 1**) indicates that I/S and illite contents of the shales from Es_3^{middle} and Es_3^{lower} only distribute in a narrow range ($\approx$20~30%), which is much smaller than that of Es_4^{upper}. Therefore, it is more appropriate to put all the shales from different sections together when analyzing the relationships between clay

mineral composition and surface areas. The results show that all kinds of surface areas correlate with clay mineral content, in which BET-SSA mainly trend correlates with clay mineral contents, while ISA and TSA present excellent correlations with clay mineral contents (**Figures 9A–C**). Further comparison of the relationships between surfaces areas and specific clay mineral types indicates that all types of surface areas positively correlate with I/S content while negatively correlate with illite content (**Figures 9D–I**). Also, BET-SSA only shows trend relations with I/S and illite contents, while ISA and TSA present an excellent correlation with I/S and illite contents. These findings indicate that surfaces are mainly constructed by clay minerals, especially for ISA, while I/S and illite present the opposite effect. Therefore, the lower clay mineral content and higher illite content of the shales from Es_4^{upper} lead to its smaller surface areas (**Figures 2, 3**).

According to **Figure 9**, the correlation coefficients for BET-SSA are much worse than those of ISA. To understand these differences, it must be noted that the measured surface areas are the surface areas after the release of hydrocarbon or other confined fluid during coring and subsequent sample preservation (Jiang et al.,
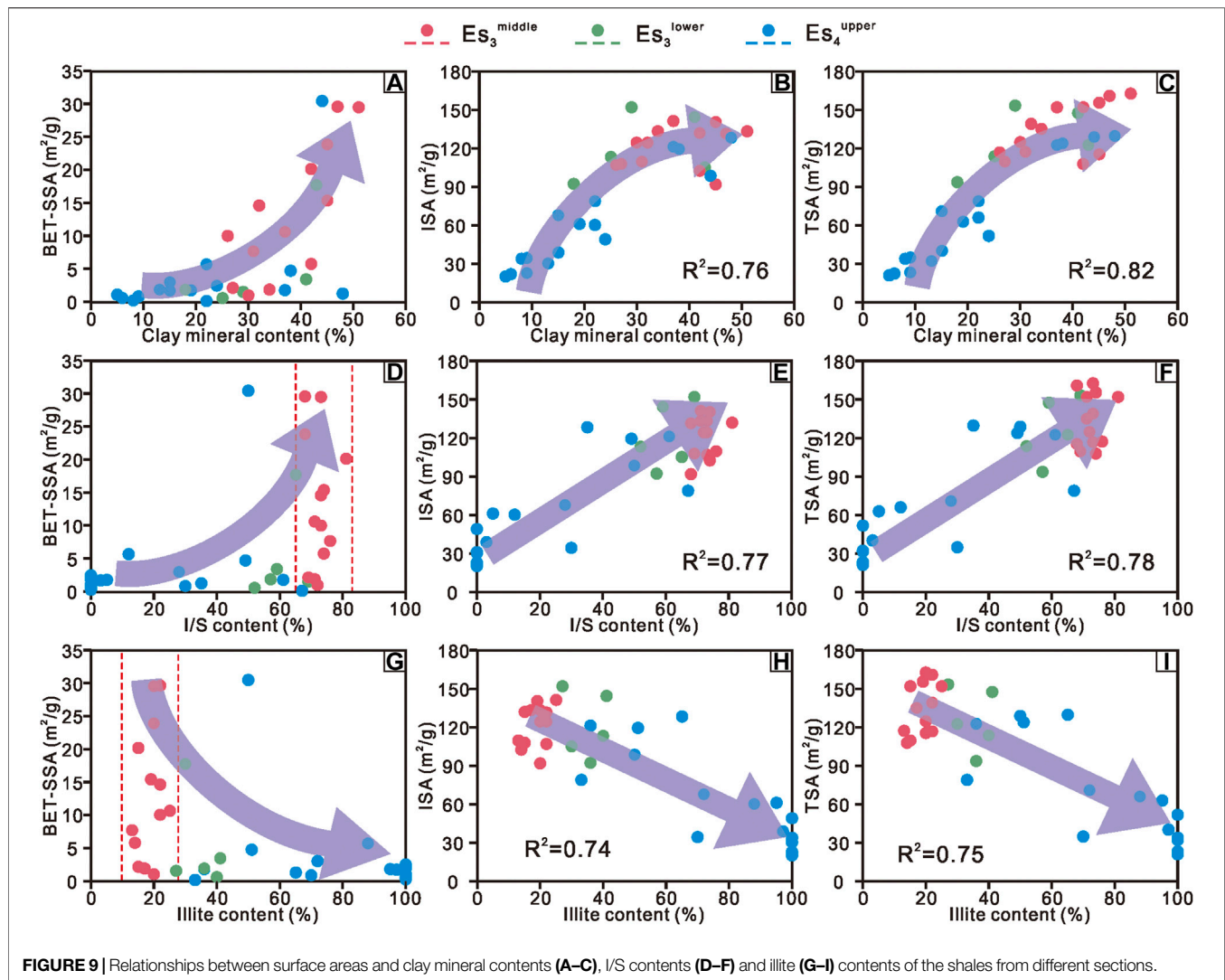
FIGURE 9 | Relationships between surface areas and clay mineral contents **(A–C)**, I/S contents **(D–F)** and illite **(G–I)** contents of the shales from different sections.

2016; Li et al., 2020; Wang et al., 2022). It has been demonstrated that free and physically adsorbed hydrocarbons or OM is mainly occurred on the outer surface, and they vaporize much easier and faster than chemically adsorbed hydrocarbons or OM which mainly occur on the inner surface (Jiang et al., 2016; Zhu et al., 2016). Therefore, the outer surface area is affected by hydrocarbons or OM that is confined in the shale pores more remarkably, and leading to relatively poor relationships between BET-SSA and mineral compositions.

To summarize, pores and surfaces are all greatly affected by mineral components, especially clay minerals. Previous studies have indicated that the physical and chemical properties differ significantly according to mineral types and clay minerals are more active. For example, clay minerals mainly correlate with smaller pores; smectite and I/S are easier to hydrate and swell than illite and kaolinite (Zolfaghari et al., 2016; Al-Ameri et al., 2018; Sui et al., 2018), and their higher CEC will lead to stronger impacts on the chemical properties of flowback water (Greenland, 1971; Han et al., 2016; Saidian et al., 2016; Zolfaghari et al., 2016); along with burial evolution, smectite with large ISA will transfer

to illite with no ISA by illitization, leading to the decreasing of ISA (Zhu et al., 2015; Wilson et al., 2016b; Singh et al., 2016) and the change of pore structure and BET-SSA (Wu et al., 2015; Wang and Guo, 2019). These differences will result in divergences in the interactions between pore walls and fluids and then affect the fluid flow significantly.

Effects of Pore and Surface Characteristics and Properties on Fluid Flow

Based on the discussions above, a hypothesis model was established to illustrate the effects of the characteristics and properties of pores and surfaces on the fluid flow from shale formation to hydraulic fractures (**Figure 10**). It has been confirmed that the affinity to fluids of different minerals follows the order: I/S > illite > carbonate minerals ≈ detrital minerals (Zhang et al., 2012; Singh et al., 2016; Zolfaghari et al., 2016; Al-Ameri et al., 2018; Saikia et al., 2018). Therefore, if the pore size and fluid condition are assumed to be the same: for the pores constructed by I/S, more fluids will be adsorbed onto the
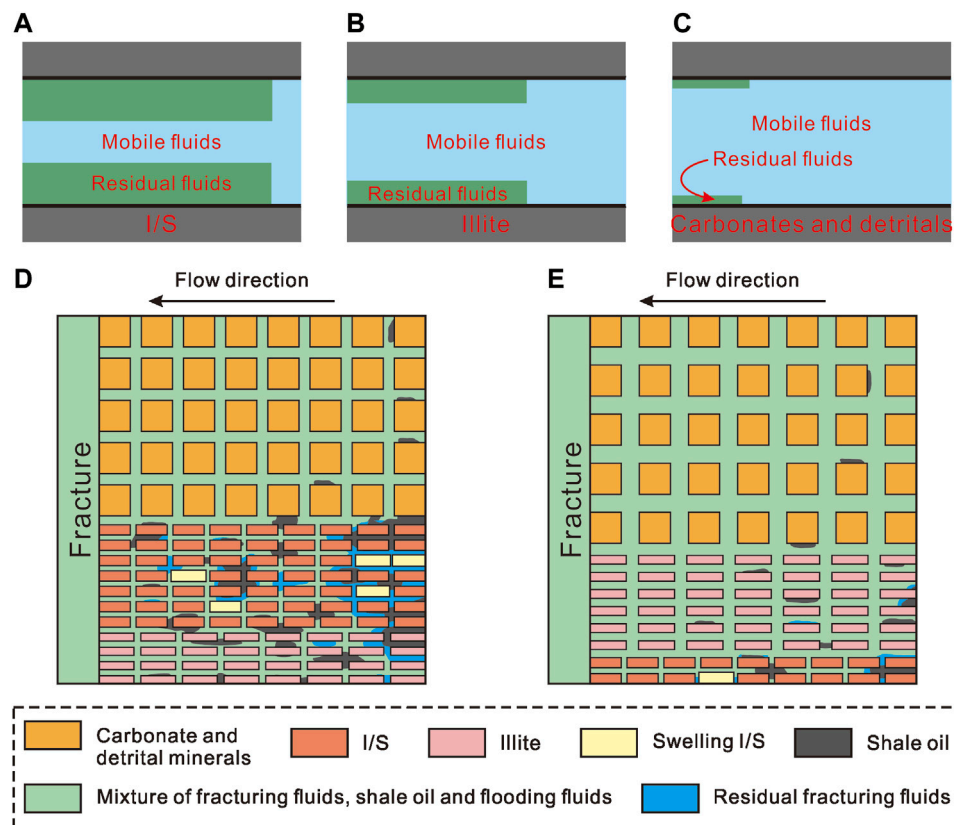
FIGURE 10 | Hypothetical model to explain the effects of characteristics and properties of pores and surfaces on the fluid flow from shale formation to fractures.
(A–C) Distribution of mobile and residual fluids in the pores with different surface properties. **(D)** Distribution of fluids after flow from shale formation to fractures for the shales from Es_3^{middle} and Es_3^{lower}. **(E)** Distribution of fluids after flow from shale formation to fractures for the shales from Es_4^{upper}.

pore walls, and the mobility pore diameter is much smaller than the real pore diameter (**Figure 10A**); for the pores related to illite, the thickness and distribution range of residual fluids are smaller than those of the I/S (**Figure 10B**); for pores related to carbonate and detrital minerals, the thickness of the residual fluids reduces further and the distribution is localized (**Figure 10C**).

Combined with the features and the differences in the mineral composition and pore and surface characteristics of the shales from different sections (**Figures 2–9**), the fluid distribution and flow pattern were established to illustrate the differences in the production potential of the shales from different sections (**Figures 10D,E**). Comparison of the fluid flow characteristics between the same mineral types of the shales from different sections indicates that because the interfacial interaction strength of pores with a smaller diameter is much larger than that of larger pores (Wang S. et al., 2016; Yu et al., 2017), more oil is retained in shale formation (**Figures 10D,E**) for the shales from Es_3^{middle} and Es_3^{lower} than that of Es_4^{upper} (**Figures 4, 5**). In addition, fracturing fluids that intruded into the shales may also be trapped more seriously in the shales with smaller pores and leading to more oil blocked in shale formation if the trapped fracturing fluids block the pores or pore throat (**Figures 10D,E**). Further comparison of the fluid flow characteristics between different mineral types

shows that (**Figures 10D,E**) more oil and intruded fracturing fluids are trapped in shale formations due to the generally smaller pore size of the pores correlate to clay minerals than those of carbonate and detrital minerals (Klaver et al., 2012; Kuila and Prasad, 2013; Malik and Lu, 2015; Li W. et al., 2016; Mathia et al., 2016) and the larger affinity to fluids of clay minerals, especially for I/S (Zhang et al., 2012; Singh et al., 2016; Zolfaghari et al., 2016; Al-Ameri et al., 2018; Saikia et al., 2018). In summary, the fluid flow in shale formation is controlled both by the pore size and by the properties of pore walls (surfaces). Due to the larger Vt, V2, V3, and smaller surface areas, as well as the high carbonate and illite content, the shales from Es_4^{upper} possess better production potential (**Figures 10D,E**).

Significances and Prospects

The breakability of shale is one of the key characteristics that depend on the fracturing and extraction of oil and gas occluded within shale play (Aadnøy and Looyeh, 2019). Brittle mineral content is the main concern when evaluating breakability. Jarvie et al. (2007) viewed quartz as the main brittle mineral in the Barnett Shale and used its relative content for stimulation evaluation (Jarvie et al., 2007). In addition to quartz, Wang and Gale (2009) also regarded dolomite as a brittle mineral (Wang and Gale, 2009). Based on the study of the mechanical
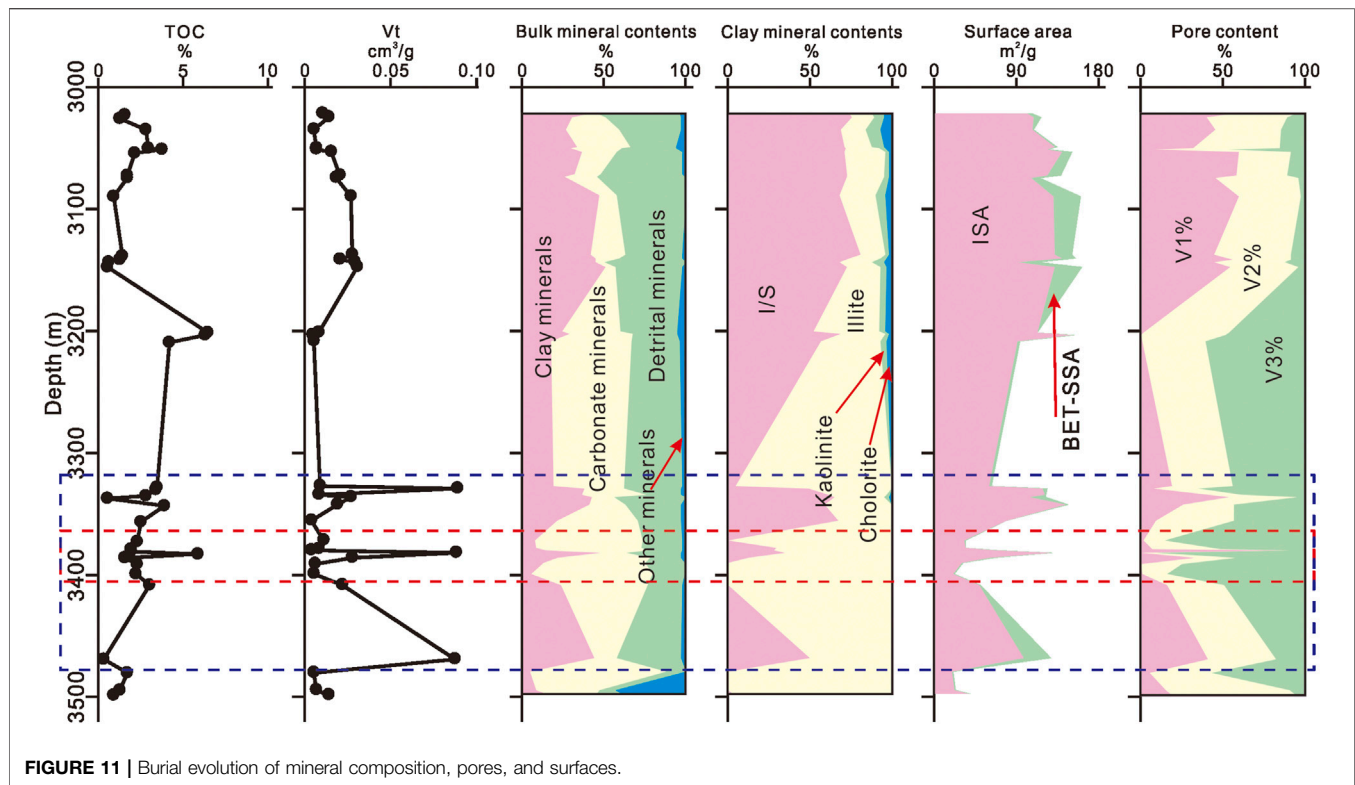
FIGURE 11 | Burial evolution of mineral composition, pores, and surfaces.

properties of minerals, Jin et al. (2014) further classified feldspar, calcite, and mica as brittle minerals (Jin et al., 2014). In summary, it is widely accepted that breakability relates closely to mineral composition. The rocks with relatively high detrital minerals and carbonate minerals and low amount of clay mineral content present better breakability (Aadnøy and Looyeh, 2019). However, to efficiently exploit shale resources, brittle mineral content is not the only concerning factor, characteristics and properties of pores and surfaces should also be paid attention to because of their significant effects on fluid flow in shale formation (**Figure 10**). On the one hand, pores with different diameters present divergence capillary force and specific surface area, leading to differences in the adsorption potential and flow profile. On the other hand, the physical and chemical properties of minerals and their relationships with pores and surfaces differ significantly according to mineral types, leading to divergences in the interfacial interactions between the pore walls and the confined fluids. These divergences will change the distribution, occlusion, and flow of fracturing fluid and oil. Furthermore, water is the main component in fracturing fluids, and it will interact with clay minerals (especially I/S) significantly during the pumping, flowback, and production stages (O'Brien and Chenevert, 1973; Makhanov et al., 2014; Xu and Dehghanpour, 2014; Sui et al., 2018; Shi et al., 2020) and might lead to the low flowback recovery, the changes of pore and surface properties, and the reduction of oil relative permeability. Therefore, characteristics and properties of pores and surfaces are the indispensable factors that need to be taken into the evaluation of shale oil potential. Take the research area as an instance, based

on the burial evolution profile of TOC, pore volume, surface areas, mineral composition, and composition of pores, the deep burial shales from Es_4^{upper} are the favorable interval for shale oil accumulation and flow, especially for the shales with depth ranges of 3360~3410 m (**Figure 11**), which present high carbonate minerals, illite and TOC content, low clay mineral content, large total pore volume, more pores with a larger diameter and small surface areas.

Remarkable changes of mineral composition and pore structure along with burial evolution are some of the most important characteristics of shale resources. For example, diagenesis such as compaction, recrystallization, and cementation increases the brittleness of rocks and result in the increase of breakability of rocks; diagenesis such as illitization, dissolution, and dolomitization improves reservoir properties by forming more large pores and reducing surface areas (Chalmers et al., 2012; Li W. et al., 2016; Mathia et al., 2016; Zhang et al., 2016; Bai et al., 2018; Liang et al., 2018; Wang and Guo, 2019); I/S that contains interlayer space decreases by illitization and forms illite that without interlayer space (Wilson et al., 2016a; Wilson et al., 2016b; Saidian et al., 2016), thus leading to the decreases in the clay mineral swelling, the retention of fracturing fluids, and the effects on flowback water chemical properties (Zolfaghari et al., 2016; Al-Ameri et al., 2018). Furthermore, the flow properties are greatly affected by the fluid composition due to the divergences in the physical and chemical properties of different components and the interfacial interactions of different components with pore walls (Xu and Dehghanpour, 2014; Wang S. et al., 2016; Chen et al., 2016). Additionally, the

fluid composition also changes along with the maturation of OM and the generation of lighter hydrocarbons, leading to the increase of the mobility of shale oil (Wang et al., 2022). Ion is the other chemical additive that is important for the efficient production of shale resources. Previous studies have confirmed that the wettability of mineral surfaces or bulk rocks is significantly affected by brine (Chen et al., 2018a; Chen et al., 2018b; Zeng et al., 2019). In summary, evaluation of the hydraulic fracturing and production performance of shale resources need to consider not only the brittleness of minerals but also the characteristics and properties of pores and surfaces. In addition, diagenesis, shale oil composition, and chemical composition of fracturing and flooding fluids are also important factors that need to be paid more attention in the future.

CONCLUSION

In this study, shales samples were collected from different sections and were detected by XRD, N_2 adsorption, EGME adsorption, and mercury intrusion methods to analyze the characteristics of pores and surfaces and their potential effects on fluid flow from shale formation to hydraulic fractures. The main conclusions were listed as below:

1) The shales from Es_3^{middle} and Es_3^{lower} contain more clay minerals (especially I/S) and less carbonate minerals than those of Es_4^{upper}. Clay minerals mainly contribute to pore development, and carbonate minerals inhibit pore development. More importantly, the contributions of clay minerals to pores with different diameter ranges differ according to sections, and we attribute these divergences to clay mineral composition. All kinds of surface areas are mainly sourced by clay minerals, while I/S correlates positively to surface areas and illite correlates negatively to surfaces areas, especially for ISA.
2) Pores with smaller diameters present larger outer surface area while large pores contribute minor to surface area. The shales

from Es_3^{middle} and Es_3^{lower} are mainly composed of smaller pores, leading to the larger surface areas and steeper slope between pore volume and surface area.
3) Mineral composition, fluid composition, pore structure, and surface properties are the factors that need to be considered for the evaluation of fluid flow in shale formation. The shales with high carbonate and illite content, larger total pore volume, larger pores, and smaller surface areas present better shale oil accumulation and fluid flow conditions. To better evaluate shale oil flow and production potential, fluid compositions of both the fracturing fluids and shale oil need more concern in the future.

DATA AVAILABILITY STATEMENT

The original contributions presented in the study are included in the article/Supplementary Material, and further inquiries can be directed to the corresponding author.

AUTHOR CONTRIBUTIONS

XL: conceptualization, methodology, investigation, data curation, formal analysis, writing—original draft preparation, writing—review and editing. JC: conceptualization, resources, supervision, project administration, methodology. BG: methodology, data curation, writing—review and editing. SL: resources, funding acquisition. DF: funding acquisition, project administration. ZP: resources. BG: data curation. All authors contributed to the article and approved the submitted version.

REFERENCES

Aadnøy, B. S., and Looyeh, R. (2019). "Shale Oil, Shale Gas, and Hydraulic Fracturing," in *Petroleum Rock Mechanics*. Editors B. S. Aadnøy and R. Looyeh. 2nd Edn (Cambridge, United States: Gulf Professional Publishing), 357–389.

Al-Ameri, A., Gamadi, T., and Ispas, I. (2018). Evaluation of the Near Fracture Face Formation Damage Caused by the Spontaneously Imbibed Fracturing Fluid in Unconventional Gas Reservoirs. *J. Pet. Sci. Eng.* 171, 23–36. doi:10.1016/j.petrol.2018.07.021

Bai, C., Yu, B., Liu, H., Xie, Z., Han, S., Zhang, L., et al. (2018). The Genesis and Evolution of Carbonate Minerals in Shale Oil Formations from Dongying Depression, Bohai Bay Basin, China. *Int. J. Coal Geology.* 189, 8–26. doi:10.1016/j.coal.2018.02.008

Barrett, E. P., Joyner, L. G., and Halenda, P. P. (1951). The Determination of Pore Volume and Area Distributions in Porous Substances. I. Computations from Nitrogen Isotherms. *J. Am. Chem. Soc.* 73 (1), 373–380. doi:10.1021/ja01145a126

Beliveau, D. (1993). Honey, I Shrunk the Pores!. *J. Can. Petrol. Technol.* 32 (8), 309–319. doi:10.2118/93-08-01

Brunauer, S., Emmett, P. H., and Teller, E. (1938). Adsorption of Gases in Multimolecular Layers. *J. Am. Chem. Soc.* 60 (2), 309–319. doi:10.1021/ja01269a023

Cai, J., Du, J., Chen, Z., Lei, T., and Zhu, X. (2018). Hydrothermal Experiments Reveal the Influence of Organic Matter on Smectite Illitization. *Clays Clay Miner.* 66 (1), 28–42. doi:10.1346/ccmn.2017.064084

Chalmers, G. R. L., and Bustin, R. M. (2008). Lower Cretaceous Gas Shales in Northeastern British Columbia, Part I: Geological Controls on Methane Sorption Capacity. *Bull. Can. Pet. Geology.* 56 (1), 1–21. doi:10.2113/gscpgbull.56.1.1

Chalmers, G. R., Bustin, R. M., and Power, I. M. (2012). Characterization of Gas Shale Pore Systems by Porosimetry, Pycnometry, Surface Area, and Field Emission Scanning Electron Microscopy/transmission Electron Microscopy Image Analyses: Examples from the Barnett, Woodford, Haynesville, Marcellus, and Doig Units. *Bulletin* 96 (6), 1099–1119. doi:10.1306/10171111052

Chen, T., Liu, F., Huang, S., Zhang, W., Wang, H., Hou, Q., et al. (2016). "Peeling off" Mechanism of Asphaltenes from Solid/Liquid Interface in the Presence of a Highly Charged Amphiphilic Macromolecule. *Energy Fuels* 30, 9250–9259. doi:10.1021/acs.energyfuels.6b01971

Chen, Y., Xie, Q., Pu, W., and Saeedi, A. (2018a). Drivers of pH Increase and Implications for Low Salinity Effect in sandstone. *Fuel* 218, 112–117. doi:10.1016/j.fuel.2018.01.037

Chen, Y., Xie, Q., Sari, A., Brady, P. V., and Saeedi, A. (2018b). Oil/Water/Rock Wettability: Influencing Factors and Implications for Low Salinity Water Flooding in Carbonate Reservoirs. *Fuel* 215, 171–177. doi:10.1016/j.fuel.2017.10.031

Cheng, Z., Ning, Z., Wang, Q., Zeng, Y., Qi, R., Huang, L., et al. (2019). The Effect of Pore Structure on Non-Darcy Flow in Porous media Using the Lattice Boltzmann Method. *J. Pet. Sci. Eng.* 172, 391–400. doi:10.1016/j.petrol.2018.09.066

Curtis, M. E., Sondergeld, C. H., Ambrose, R. J., and Rai, C. S. (2012). Microstructural Investigation of Gas Shales in Two and Three Dimensions Using Nanometer-Scale Resolution Imaging. *Bulletin* 96 (4), 665–677. doi:10.1306/08151110188

Dehghanpour, H., Zubair, H. A., Chhabra, A., and Ullah, A. (2012). Liquid Intake of Organic Shales. *Energy Fuels* 26, 5750–5758. doi:10.1021/ef3009794

Du, J., Cai, J., Chen, Z., Lei, T., Zhang, S., and Xie, Z. (2019). A Contrastive Study of Effects of Different Organic Matter on the Smectite Illitization in Hydrothermal Experiments. *Appl. Clay Sci.* 168, 249–259. doi:10.1016/j.clay.2018.11.016

Echeverría, J. C., Morera, M. T., Mazkiarán, C., and Garrido, J. J. (1999). Characterization of the Porous Structure of Soils: Adsorption of Nitrogen (77 K) and Carbon Dioxide (273 K), and Mercury Porosimetry. *Eur. J. Soil Sci.* 50 (3), 497–503. doi:10.1046/j.1365-2389.1999.00261.x

Engle, M. A., and Rowan, E. L. (2014). Geochemical Evolution of Produced Waters from Hydraulic Fracturing of the Marcellus Shale, Northern Appalachian Basin: A Multivariate Compositional Data Analysis Approach. *Int. J. Coal Geology.* 126, 45–56. doi:10.1016/j.coal.2013.11.010

Gaines, R. R., Hammarlund, E. U., Hou, X., Qi, C., Gabbott, S. E., Zhao, Y., et al. (2012). Mechanism for Burgess Shale-Type Preservation. *Proc. Natl. Acad. Sci.* 109 (14), 5180–5184. doi:10.1073/pnas.1111784109

Greenland, D. J. (1971). Interactions between Humic and Fulvic Acids and Clays. *Soil Sci.* 111 (1), 34–41. doi:10.1097/00010694-197101000-00004

Haluszczak, L. O., Rose, A. W., and Kump, L. R. (2013). Geochemical Evaluation of Flowback Brine from Marcellus Gas wells in Pennsylvania, USA. *Appl. Geochem.* 28, 55–61. doi:10.1016/j.apgeochem.2012.10.002

Han, L., Sun, K., Jin, J., and Xing, B. (2016). Some Concepts of Soil Organic Carbon Characteristics and Mineral Interaction from a Review of Literature. *Soil Biol. Biochem.* 94, 107–121. doi:10.1016/j.soilbio.2015.11.023

Jarvie, D. M., Hill, R. J., Ruble, T. E., and Pollastro, R. M. (2007). Unconventional Shale-Gas Systems: The Mississippian Barnett Shale of North-Central Texas as One Model for Thermogenic Shale-Gas Assessment. *Bulletin* 91 (4), 475–499. doi:10.1306/12190606068

Jiang, C., Chen, Z., Mort, A., Milovic, M., Robinson, R., Stewart, R., et al. (2016). Hydrocarbon Evaporative Loss from Shale Core Samples as Revealed by Rock-Eval and Thermal Desorption-Gas Chromatography Analysis: Its Geochemical and Geological Implications. *Mar. Pet. Geology.* 70, 294–303. doi:10.1016/j.marpetgeo.2015.11.021

Jin, X. C., Shah, S. N., Roegiers, J. C., and Zhang, B. (2014). Fracability Evaluation in Shale Reservoirs - An Integrated Petrophysics and Geomechanics Approach. *Spe J.* 20 (3), 518–526. doi:10.2118/168589-ms

Kenvin, J., Jagiello, J., Mitchell, S., and Pérez-Ramírez, J. (2015). Unified Method for the Total Pore Volume and Pore Size Distribution of Hierarchical Zeolites from Argon Adsorption and Mercury Intrusion. *Langmuir* 31 (4), 1242–1247. doi:10.1021/la504575s

Klaver, J., Desbois, G., Urai, J. L., and Littke, R. (2012). BIB-SEM Study of the Pore Space Morphology in Early Mature Posidonia Shale from the Hils Area, Germany. *Int. J. Coal Geology.* 103, 12–25. doi:10.1016/j.coal.2012.06.012

Kuila, U., and Prasad, M. (2013). Specific Surface Area and Pore-Size Distribution in Clays and Shales. *Geophys. Prospect.* 61 (2), 341–362. doi:10.1111/1365-2478.12028

Kuila, U., McCarty, D. K., Derkowski, A., Fischer, T. B., Topór, T., and Prasad, M. (2014). Nano-scale Texture and Porosity of Organic Matter and clay Minerals in Organic-Rich Mudrocks. *Fuel* 135, 359–373. doi:10.1016/j.fuel.2014.06.036

Li, W., Lu, S., Xue, H., Zhang, P., and Hu, Y. (2016a). Microscopic Pore Structure in Shale Reservoir in the Argillaceous Dolomite from the Jianghan Basin. *Fuel* 181, 1041–1049. doi:10.1016/j.fuel.2016.04.140

Li, Z., Zou, Y.-R., Xu, X.-Y., Sun, J.-N., Li, M., and Peng, P. A. (2016b). Adsorption of Mudstone Source Rock for Shale Oil - Experiments, Model and a Case Study. *Org. Geochem.* 92, 55–62. doi:10.1016/j.orggeochem.2015.12.009

Li, X., Cai, J. G., Liu, H. M., Zhu, X. J., Li, Z., and Liu, J. (2020). Characterization of Shale Pore Structure by Successive Pretreatments and its Significance. *Fuel* 269, 117412. doi:10.1016/j.fuel.2020.117412

Liang, C., Cao, Y., Liu, K., Jiang, Z., Wu, J., and Hao, F. (2018). Diagenetic Variation at the Lamina Scale in Lacustrine Organic-Rich Shales: Implications for Hydrocarbon Migration and Accumulation. *Geochimica et Cosmochimica Acta* 229, 112–128. doi:10.1016/j.gca.2018.03.017

Liu, H., Zhang, S., Song, G., Xuejun, W., Teng, J., Wang, M., et al. (2019). Effect of Shale Diagenesis on Pores and Storage Capacity in the Paleogene Shahejie Formation, Dongying Depression, Bohai Bay Basin, east China. *Mar. Pet. Geology.* 103, 738–752. doi:10.1016/j.marpetgeo.2019.01.002

Loucks, R. G., Reed, R. M., Ruppel, S. C., and Hammes, U. (2012). Spectrum of Pore Types and Networks in Mudrocks and a Descriptive Classification for Matrix-Related Mudrock Pores. *Bulletin* 96 (6), 1071–1098. doi:10.1306/08171111061

Lu, Y., Wang, H., Guan, B., Liu, P., Guo, L., Wu, J., et al. (2018). Reasons for the Low Flowback Rates of Fracturing Fluids in marine Shale. *Nat. Gas Industry B* 5 (1), 35–40. doi:10.1016/j.ngib.2017.11.006

Lu, Y., Yang, M., Ge, Z., Zhou, Z., Chai, C., and Zhao, H. (2019). Influence of Viscoelastic Surfactant Fracturing Fluid on Coal Pore Structure under Different Geothermal Gradients. *J. Taiwan Inst. Chem. Eng.* 97, 207–215. doi:10.1016/j.jtice.2019.01.024

Lu, Y., Wang, L., Ge, Z., Zhou, Z., Deng, K., and Zuo, S. (2020). Fracture and Pore Structure Dynamic Evolution of Coals during Hydraulic Fracturing. *Fuel* 259, 116272. doi:10.1016/j.fuel.2019.116272

Macht, F., Eusterhues, K., Pronk, G. J., and Totsche, K. U. (2011). Specific Surface Area of clay Minerals: Comparison between Atomic Force Microscopy Measurements and Bulk-Gas (N2) and -liquid (EGME) Adsorption Methods. *Appl. Clay Sci.* 53 (1), 20–26. doi:10.1016/j.clay.2011.04.006

Makhanov, K., Habibi, A., Dehghanpour, H., and Kuru, E. (2014). Liquid Uptake of Gas Shales: A Workflow to Estimate Water Loss during Shut-In Periods after Fracturing Operations. *J. Unconventional Oil Gas Resour.* 7, 22–32. doi:10.1016/j.juogr.2014.04.001

Malik, Z., and Lu, S. G. (2015). Pore Size Distribution of Clayey Soils and its Correlation with Soil Organic Matter. *Pedosphere* 25 (2), 240–249. doi:10.1016/S1002-0160(15)60009-1

Mathia, E. J., Bowen, L., Thomas, K. M., and Aplin, A. C. (2016). Evolution of Porosity and Pore Types in Organic-Rich, Calcareous, Lower Toarcian Posidonia Shale. *Mar. Pet. Geology.* 75, 117–139. doi:10.1016/j.marpetgeo.2016.04.009

O'Brien, D. E., and Chenevert, M. E. (1973). Stabilizing Sensitive Shales with Inhibited, Potassium-Based Drilling Fluids. *J. Petrol. Technol.* 25 (09), 1089–1100.

Osiptsov, A. A. (2017). Fluid Mechanics of Hydraulic Fracturing: A Review. *J. Pet. Sci. Eng.* 156, 513–535. doi:10.1016/j.petrol.2017.05.019

Roshan, H., Al-Yaseri, A. Z., Sarmadivaleh, M., and Iglauer, S. (2016). On Wettability of Shale Rocks. *J. Colloid Interf. Sci.* 475, 104–111. doi:10.1016/j.jcis.2016.04.041

Saidian, M., Godinez, L. J., and Prasad, M. (2016). Effect of clay and Organic Matter on Nitrogen Adsorption Specific Surface Area and Cation Exchange Capacity in Shales (Mudrocks). *J. Nat. Gas Sci. Eng.* 33, 1095–1106. doi:10.1016/j.jngse.2016.05.064

Saikia, B. D., Mahadevan, J., and Rao, D. N. (2018). Exploring Mechanisms for Wettability Alteration in Low-Salinity Waterfloods in Carbonate Rocks. *J. Pet. Sci. Eng.* 164, 595–602. doi:10.1016/j.petrol.2017.12.056

Sari, A., Chen, Y., Xie, Q., and Saeedi, A. (2019). Low Salinity Water Flooding in High Acidic Oil Reservoirs: Impact of pH on Wettability of Carbonate Reservoirs. *J. Mol. Liquids* 281, 444–450. doi:10.1016/j.molliq.2019.02.081

Schmitt, M., Fernandes, C. P., da Cunha Neto, J. A. B., Wolf, F. G., and dos Santos, V. S. S. (2013). Characterization of Pore Systems in Seal Rocks Using Nitrogen Gas Adsorption Combined with Mercury Injection Capillary Pressure Techniques. *Mar. Pet. Geology.* 39 (1), 138–149. doi:10.1016/j.marpetgeo.2012.09.001

Shi, W., Wang, X., Guo, M., Shi, Y., Feng, A., Liang, R., et al. (2020). Water Use for Shale Gas Development in China's Fuling Shale Gas Field. *J. Clean. Prod.* 256, 120680. doi:10.1016/j.jclepro.2020.120680

Sing, K. S. W. (1985). Reporting Physisorption Data for Gas/solid Systems with Special Reference to the Determination of Surface Area and Porosity (Recommendations 1984). *Pure Appl. Chem.* 57 (4), 603–619. doi:10.1351/pac198557040603

Singh, M., Sarkar, B., Biswas, B., Churchman, J., and Bolan, N. S. (2016). Adsorption-Desorption Behavior of Dissolved Organic Carbon by Soil clay Fractions of Varying Mineralogy. *Geoderma* 280, 47–56. doi:10.1016/j.geoderma.2016.06.005

Song, W., Yao, J., Li, Y., Sun, H., and Yang, Y. (2018). Fractal Models for Gas Slippage Factor in Porous media Considering Second-Order Slip and Surface Adsorption. *Int. J. Heat Mass Transfer* 118, 948–960. doi:10.1016/j.ijheatmasstransfer.2017.11.072

Spitzer, Z., Bíba, V., and Kadlec, O. (1976). The Complete Pore Structure Analysis of Fine Porous Solids. *Carbon* 14 (3), 151–156. doi:10.1016/0008-6223(76)90095-6

Sui, W., Tian, Y., and Yao, C. (2018). Investigation of Microscopic Pore Structure Variations of Shale Due to Hydration Effects through SEM Fixed-Point Observation Experiments. *Pet. Exploration Develop.* 45 (5), 955–962. doi:10.1016/s1876-3804(18)30099-5

Sun, M., Yu, B., Hu, Q., Yang, R., Zhang, Y., and Li, B. (2017). Pore Connectivity and Tracer Migration of Typical Shales in south China. *Fuel* 203, 32–46. doi:10.1016/j.fuel.2017.04.086

Tang, J., Li, J., Tang, M., Du, X., Yin, J., Guo, X., et al. (2019). Investigation of Multiple Hydraulic Fractures Evolution and Well Performance in Lacustrine Shale Oil Reservoirs Considering Stress Heterogeneity. *Eng. Fracture Mech.* 218, 106569. doi:10.1016/j.engfracmech.2019.106569

Wang, F. P., and Gale, J. F. W. (2009). Screening Criteria for Shale-Gas Systems. *Gulf Coast Assoc. Geol. Societies Trans.* 59, 779–793.

Wang, F., and Guo, S. (2019). Influential Factors and Model of Shale Pore Evolution: A Case Study of a Continental Shale from the Ordos Basin. *Mar. Pet. Geology.* 102, 271–282. doi:10.1016/j.marpetgeo.2018.12.045

Wang, X., and Sheng, J. J. (2017). Effect of Low-Velocity Non-Darcy Flow on Well Production Performance in Shale and Tight Oil Reservoirs. *Fuel* 190, 41–46. doi:10.1016/j.fuel.2016.11.040

Wang, S., Feng, Q., Javadpour, F., Xia, T., and Li, Z. (2015). Oil Adsorption in Shale Nanopores and its Effect on Recoverable Oil-In-Place. *Int. J. Coal Geology.* 147-148, 9–24. doi:10.1016/j.coal.2015.06.002

Wang, S., Javadpour, F., and Feng, Q. (2016a). Molecular Dynamics Simulations of Oil Transport through Inorganic Nanopores in Shale. *Fuel* 171, 74–86. doi:10.1016/j.fuel.2015.12.071

Wang, Z., Jin, X., Wang, X., Sun, L., and Wang, M. (2016b). Pore-Scale Geometry Effects on Gas Permeability in Shale. *J. Nat. Gas Sci. Eng.* 34, 948–957. doi:10.1016/j.jngse.2016.07.057

Wang, E., Li, C., Feng, Y., Song, Y., Guo, T., Li, M., et al. (2022). Novel Method for Determining the Oil Moveable Threshold and an Innovative Model for Evaluating the Oil Content in Shales. *Energy* 239 (A), 121848. doi:10.1016/j.energy.2021.121848

Wei, S., Jin, Y., Xia, Y., and Lin, B. (2020). The Flowback and Production Analysis in Sub-saturated Fractured Shale Reservoirs. *J. Pet. Sci. Eng.* 186, 106694. doi:10.1016/j.petrol.2019.106694

Wijaya, N., and Sheng, J. J. (2019). Effect of Desiccation on Shut-In Benefits in Removing Water Blockage in Tight Water-Wet Cores. *Fuel* 244, 314–323. doi:10.1016/j.fuel.2019.01.180

Wilson, M. J., Shaldybin, M. V., and Wilson, L. (2016a). Clay Mineralogy and Unconventional Hydrocarbon Shale Reservoirs in the USA. I. Occurrence and Interpretation of Mixed-Layer R3 Ordered Illite/smectite. *Earth-Science Rev.* 158, 31–50. doi:10.1016/j.earscirev.2016.04.004

Wilson, M. J., Wilson, L., and Shaldybin, M. V. (2016b). Clay Mineralogy and Unconventional Hydrocarbon Shale Reservoirs in the USA. II. Implications of Predominantly Illitic Clays on the Physico-Chemical Properties of Shales. *Earth-Science Rev.* 158, 1–8. doi:10.1016/j.earscirev.2016.04.005

Wu, S., Zhu, R., Cui, J., Cui, J., Bai, B., Zhang, X., et al. (2015). Characteristics of Lacustrine Shale Porosity Evolution, Triassic Chang 7 Member, Ordos Basin, NW China. *Pet. Exploration Develop.* 42 (2), 185–195. doi:10.1016/s1876-3804(15)30005-7

Xie, J. N., Xie, J., Ni, G. H., Sheìk, R., Sun, Q., and Wang, H. (2020). Effects of Pulse Wave on the Variation of Coal Pore Structure in Pulsating Hydraulic Fracturing Process of Coal Seam. *Fuel* 264, 116906. doi:10.1016/j.fuel.2019.116906

Xu, M., and Dehghanpour, H. (2014). Advances in Understanding Wettability of Gas Shales. *Energy Fuels* 28 (7), 4362–4375. doi:10.1021/ef500428y

Yang, X., and Guo, B. (2019). Productivity Analysis of Multi-Fractured Shale Oil wells Accounting for the Low-Velocity Non-Darcy Effect. *J. Pet. Sci. Eng.* 183, 106427. doi:10.1016/j.petrol.2019.106427

Yang, R., Hu, Q., He, S., Hao, F., Guo, X., Yi, J., et al. (2018). Pore Structure, Wettability and Tracer Migration in Four Leading Shale Formations in the Middle Yangtze Platform, China. *Mar. Pet. Geology.* 89, 415–427. doi:10.1016/j.marpetgeo.2017.10.010

Yu, H., Chen, J., Zhu, Y., Wang, F., and Wu, H. (2017). Multiscale Transport Mechanism of Shale Gas in Micro/nano-Pores. *Int. J. Heat Mass Transfer* 111, 1172–1180. doi:10.1016/j.ijheatmasstransfer.2017.04.050

Zeng, B., Cheng, L., and Li, C. (2011). Low Velocity Non-linear Flow in Ultra-low Permeability Reservoir. *J. Pet. Sci. Eng.* 80 (1), 1–6. doi:10.1016/j.petrol.2011.10.006

Zeng, L., Chen, Y., Hossain, M. M., Saeedi, A., and Xie, Q. (2019). Wettability Alteration Induced Water Uptake in Shale Oil Reservoirs: A Geochemical Interpretation for Oil-Brine-OM Interaction during Hydraulic Fracturing. *Int. J. Coal Geology.* 213, 103277. doi:10.1016/j.coal.2019.103277

Zhang, T., Ellis, G. S., Ruppel, S. C., Milliken, K., and Yang, R. (2012). Effect of Organic-Matter Type and thermal Maturity on Methane Adsorption in Shale-Gas Systems. *Org. Geochem.* 47, 120–131. doi:10.1016/j.orggeochem.2012.03.012

Zhang, J., Jiang, Z., Jiang, X., Wang, S., Liang, C., and Wu, M. (2016). Oil Generation Induces Sparry Calcite Formation in Lacustrine Mudrock, Eocene of east China. *Mar. Pet. Geology.* 71, 344–359. doi:10.1016/j.marpetgeo.2016.01.007

Zhang, P., Lu, S., and Li, J. (2019). Characterization of Pore Size Distributions of Shale Oil Reservoirs: A Case Study from Dongying Sag, Bohai Bay basin, China. *Mar. Pet. Geology.* 100, 297–308. doi:10.1016/j.marpetgeo.2018.11.034

Zhang, S., Liu, H., Liu, Y., Wang, Y., Wang, M., Bao, Y., et al. (2020). Main Controls and Geological Sweet Spot Types in Paleogene Shale Oil Rich Areas of the Jiyang Depression, Bohai Bay basin, China. *Mar. Pet. Geology.* 111, 576–587. doi:10.1016/j.marpetgeo.2019.08.054

Zhu, X., Cai, J., Song, G., and Ji, J. (2015). Factors Influencing the Specific Surface Areas of Argillaceous Source Rocks. *Appl. Clay Sci.* 109-110, 83–94. doi:10.1016/j.clay.2015.02.016

Zhu, X., Cai, J., Liu, W., and Lu, X. (2016). Occurrence of Stable and Mobile Organic Matter in the Clay-Sized Fraction of Shale: Significance for Petroleum Geology and Carbon Cycle. *Int. J. Coal Geology.* 160-161, 1–10. doi:10.1016/j.coal.2016.03.011

Zhu, X., Cai, J., Liu, Q., Li, Z., and Zhang, X. (2019). Thresholds of Petroleum Content and Pore Diameter for Petroleum Mobility in Shale. *Bulletin* 103 (3), 605–617. doi:10.1306/0816181617517009

Zolfaghari, A., Dehghanpour, H., Noel, M., and Bearinger, D. (2016). Laboratory and Field Analysis of Flowback Water from Gas Shales. *J. Unconventional Oil Gas Resour.* 14, 113–127. doi:10.1016/j.juogr.2016.03.004

Publisher's Note: All claims expressed in this article are solely those of the authors and do not necessarily represent those of their affiliated organizations, or those of the publisher, the editors, and the reviewers. Any product that may be evaluated in this article, or claim that may be made by its manufacturer, is not guaranteed or endorsed by the publisher.

Reservoir Characteristics and Controlling Factors of Oil Content in Hybrid Sedimentary Rocks of the Lucaogou Formation, Western Jimusar Sag, Junggar Basin

Haitao Xue, Ce An, Zhentao Dong*, Dianshi Xiao, Jinliang Yan, Guozhi Ding, Penglei Yan and Jinxu Zhang

Shandong Provincial Key Laboratory of Deep Oil and Gas, China University of Petroleum (East China), Qingdao, China

Hybrid sedimentary rocks (HSR) are a major reservoir type in unconventional oil exploration. The reservoir characteristics and controlling factors of the oil content of HSR are not clear, restricting the understanding of the storage mechanism and sweet spots within HSR. The Lucaogou Formation in the western Jimusar Sag is taken as a case study. Starting with the classification of the lithofacies system, differences in the microscopic pore structure, oil content and controlling factors of HSR reservoirs are revealed. The results show that seven lithofacies are recognized based on mineral composition, sedimentary structure, and organic matter characteristics, exhibiting rapid vertical and horizontal changes affected by the sedimentary environment. Layered mudstone lithofacies of the shallow lake mud and massive dolomitic mudstone lithofacies of dolomitic mud flats have the worst physical properties and oil content properties. However, they do have high organic matter contents and are the main source rocks of the Lucaogou Formation. The massive argillaceous siltstone and massive argillaceous dolomite lithofacies interbed frequently. Although their physical properties are moderate, "source-reservoir integrated" unconventional oil reservoirs can be formed, due to the adjacent to the source rock. Massive dolomitic siltstone, massive siltstone, and massive silty dolomite lithofacies are developed in the middle of the Lucaogou Formation, with the highest proportion of mesopores and macropores, which is indicative of good storage properties. When these lithofacies are filled with crude oil generated from source rocks at the top and bottom of the formation, "source storage adjacent" unconventional oil reservoirs be formed. The oil content is also controlled by the pore structure and specific surface area. The proportion of macropores and mesopores is positively correlated with oil content. The oil content of the samples is very low, when the specific surface area exceeds 2 m²/g. This manuscript provides a geological basis for evaluating and establishing reasonable interpretation models of HSR sweet spots.

Keywords: hybrid sedimentary rocks, lithofacies type, reservoir properties, factors affecting oil content, lucaogou formation

1 INTRODUCTION

In recent years, excellent examples of resource potential from the Lucaogou Formation have researchers to focus on the reservoir characteristics of this lacustrine deep-water sedimentary (Hu et al., 2018; Pang et al., 2018; Yang et al., 2018). Hybrid sedimentary rocks (HSR) are the result of multi-source mixed accumulation Mount (1984), such as clastic sediments, chemical sediments and volcanism. It has the characteristics of fine-grained sedimentation, diverse lithofacies, and frequent interbeds (Li et al., 2015). Although breakthroughs have been made in exploring marine shale, scholars are continuing to make progress in the deposition, structure, and distribution characteristics (Schieber, 1990; Plint et al., 2012). HSR exploration and development still have uncertainties, such as their lithofacies type, pore structure description, and oil evaluation.

The key factor affecting the resource potential of the HSR is considered to be the heterogeneity of lithofacies (Cao et al., 2017a). Lithofacies is a synthesis of various petrological information. Lithofacies represents the sedimentary environment (Liu et al., 2019). Previous studies have resulted in a large number of lithofacies classification of marine shale (Zhao et al., 2016; Zhang et al., 2018). Most studies used mineral composition, structure, and organic matter content as the standard for classification of lithofacies. At present, there is a lack of systematic research on lithofacies changes, because the Lucaogou Formation has been considered as a high-quality source rock before.

The pore size of porous medium classification proposed by International Union of Pure and Applied Chemistry (IUPAC) was generally accepted for chemical products and coal in 1972. Specifically, the pores were divided based on diameter into micropores (<2 nm), mesopores (2–50 nm), and macropores (>50 nm) Everett (1972). This classification standard may be more suitable for chemical products (Zhang et al., 2017), but it has poor application for HSR reservoirs. Because the pores in HSR reservoirs are different, specifically their size of chemical products and coal, the pores are generally between a few nanometers and hundreds of nanometers (Lu et al., 2018). The IUPAC classification scheme is too small for HSR reservoirs (Loucks et al., 2012), and we should establish a suitable pore size classification scheme. Previous scholars have used various experimental methods to reveal the pore system of HSR. This included low-temperature nitrogen adsorption/desorption (Wang and Ju 2015), mercury intrusion capillary pressure(MICP) (Clarkson et al., 2013), low-field nuclear magnetic resonance (NMR) (Zeng et al., 2021b), field emission scanning electron microscopy (FE-SEM) (Tian et al., 2013), computed tomography (CT) (Guo et al., 2015). In addition, Photoshop, ImageJ, and SEM combined with fractal theory to obtain pore images can also be used to quantitatively evaluate porosity distribution and pore size classification (Tian et al., 2021). Low-temperature nitrogen adsorption/desorption can only reveal pore spaces <50 nm and cannot describe the pore space of the reservoir on a large scale (Zeng et al., 2021a). FE-SEM and CT directly reflect the size and shape of the pores but cannot describe the distribution of the reservoir pores and the pore throats. MICP is commonly used to characterize pores greater than 50 nm in diameter. Among the above techniques, MICP combined with fractal theory (He and Hua 1988) are worth employing to reveal the relationship between pore throat size and pore throat combination and can effectively reveal the pore structure (Li et al., 2013).

Oil content is a crucial parameter of HSR reservoirs, and its content represents production output (Zou et al., 2014; He et al., 2018). Previous scholars used experimental methods such as rock pyrolysis, solvent extraction, vapor adsorption, and solid-liquid adsorption to document the conventional parameters TOC, S_1, and OSI index (S_1/TOC × 100) (Wang et al., 2020), to indirectly reflect the oil content in the reservoir (Jarvie, 2012; Wang et al., 2021). However, the above methods have shortcoming. These experiments destroy the sample's integrity, affect the calculation of the oil content, and do not directly reveal the oil content of the reservoir (Jiang et al., 2016). Nuclear magnetic resonance (NMR) technology maintains the sample's integrity and has been widely used in reservoir characterization, to detect the porosity, permeability, pore size distribution (Li et al., 2019), and even the wettability (Odusina et al., 2011) of the reservoir. Two-dimensional nuclear magnetic resonance (2D-NMR) was also used to reflect different fluid types (Li et al., 2020). For example, the oil, water, and solid organic matter content can be obtained through 2D-NMR. In addition, although quantitative grain fluorescence on extract (QGF-E) technology has been applied in oil and gas exploration for more than 100 years, it was not widely used in oil exploration until the 1950s (Liu and Eadington 2005). QGF-E is a low-cost technology for the petroleum industry, which is used to detect ancient oil reservoirs and residual oil. In conventional oil reservoirs, QGF-E has been widely used to study oil and gas changes and their migration history. Nevertheless, it is relatively less used in the evaluation of oil-bearing properties of HSR reservoirs. QGF-E technology characterized by low sample requirements, a low cost, reduced time, and high sensitivity (Liu et al., 2019). The enrichment of crude oil is always a major issue of interest to scholars (Song et al., 2021). The enrichment mode of tight oil can be divided into source-reservoir interlayer type (Chang 7 Member of the Ordos Basin) and shale type (Qingshankou Formation in the Songliao Basin). However, there are relatively few studies on the HSR (Jiao et al., 2020). However, there are relatively few studies on the HSR.

Previous research on Jimusar was limited to the eastern slope area. We selected three typical wells in the western sag as the research area, in response to the call for no restricted areas for exploration. In this study, the main lithologies were determined through thin section identification and x-ray diffraction. The pore structural characteristics of the HSR reservoir were studied by MICP and SEM. The oil contents were analyzed by QGF-E and 2D-NMR. The different lithofacies characteristics of the oil content and its controlling factors were systematically evaluated, and an oil enrichment geological model of HSR was summarized. This research provides a geological basis for evaluating and building a reasonable interpretation model of HSR sweet spots.

2 GEOLOGICAL BACKGROUND

The HSR of the Middle Permian Lucaogou Formation was taken as study object, which located in the Jimusar Sag, east of the Junggar Basin (in **Figure 1**) (Xiao et al., 2021). The Jimusar sag is bounded by the Laozhuangwan fault, the Xidi fault, the Santai fault, and the Jimusar fault. The overall area is about 1270 km^2 (Yang et al., 2019), and it can be divided into the eastern slope area and the western sag area. The eastern slope is the main development area of unconventional oil reservoirs, and portions wells have obtained industrial oil flow (Pang et al., 2018). The western region has a low degree of exploration and is in the early stage of exploration but has enormous resource potential.

The Jingjingzigou Formation (P$_2$j), Lucaogou Formation (P$_2$l), and Wutonggou Formation (P$_2$wt) are found in the bottom, middle and top of Jimusar Sag, respectively. During the Lucaogou deposition period, lacustrine delta facies developed in the eastern slope area. And lacustrine sediments were primarily deposited in the western depression area. The thickness of the Lucaogou Formation ranges between 25 and 300 m, with an average thickness of up to 200 m. The burial depth gradually increases from east to the west, and the deepest part of Well JY-1 exceeds 4,800 m, with an average depth of 3,570 m. The deeper burial depths in the western sag will result in different temperature and pressure conditions in the same sag, which will affect key parameters for resource evaluation such as the lithology, physical properties, and oil-bearing properties. The Lucaogou Formation can be divided into two layers (P$_2$l$_1$ and P$_2$l$_2$), which are mainly composed of interbedded dolomite, sandstone, and mudstone. The source rock and reservoir of the Lucaogou Formation are frequently interbedded, and it is a typical HSR oil reservoir of source-reservoir interbeds and source storage adjacent (Huang et al., 2013).

3 MATERIALS AND METHODS

A total of 47 samples were collected from P$_2$l$_1$ in the western depression area of the Lucaogou Formation. Among them, 7 samples were from well JTX-B, 28 samples were from well JTX-A and 12 samples were from well JTX-X. The samples were retrieved following systematic sealed coring to ensure maximum preservation of the original fluid in the HSR. **Figure 2A** shows the location information of the sample. **Figure 2B** shows a schematic diagram of the sample processing. All samples were used to analyze lithology, physical properties, and oil content. Experimental data were obtained from the Jilin Oilfield Exploration and Development Research Institute.

3.1 Mercury Intrusion Capillary Pressure

MICP analysis of all HSR cores was carried out following the SY/T 5346-2005 standard. The analysis of the HSR samples was conducted at a temperature of 25°C, a humidity of 20% and at atmospheric pressure using an Autopore IV 9505 pore analyzer. The contact angle between mercury and the

sample surface is 140°, the surface tension of mercury is 480 dyn/cm, and the pore size range is greater than 3.0 nm.

Previous studies have established many fractal dimension models based on high-pressure mercury injection curves. Although the fractal dimensions calculated by different models may be various, the complexity and heterogeneity of the pore structure in the representative reservoir rocks are similar. Because these models are all derived from a power function that describes the fractal characteristics of porous media (He and Hua 1998). MICP effectively describes the relationship between pore size and pore throat, which is a critical factor controlling reservoir permeability. Pores have self-similarity within a specific scale, and pores at different scales have different fractal dimensions. Therefore, fractal theory can be used to guide the division of different pore types. According to the Laplace-Washburn (1921) equation, the pore size distribution can be obtained from the mercury intake curve:

$$r = \frac{2\sigma \cos\theta}{P_C} \tag{1}$$

Where P_C is the mercury inlet pressure (MPa), r is the aperture (μm), σ is the surface tension (N/m), and θ is the contact angle (°).

The fractal characteristics of pores obtained in MICP analysis can be expressed by the following mathematical equation:

$$S_{Hg} = 1 - \left(\frac{P_C}{P_{C,\,min}}\right)^{D-3} \tag{2}$$

From **Eq. 2** we get:
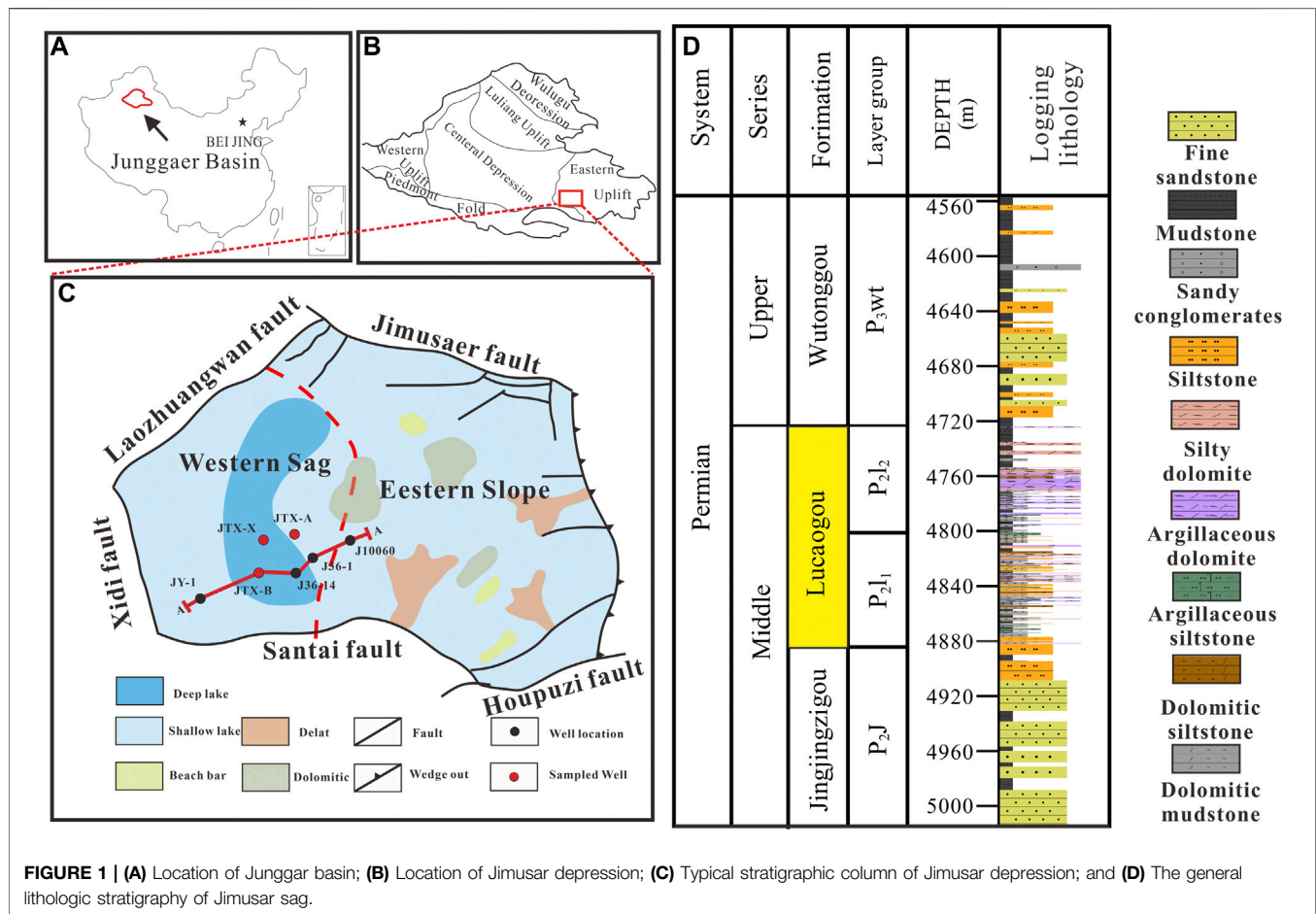
$$\lg(1 - S_{Hg}) = (D-3)\lg p_c - (D-3)\lg p_{cmin} \tag{3}$$

Where P_C is the mercury inlet pressure (MPa), PC, min is the minimum capillary pressure, S_{Hg} is the cumulative mercury inlet percentage of the hole, and D is the fractal size of a dimensionless series.

3.2 Quantitative Grain Fluorescence on Extract

QGF-E analyses of all HSR cores were carried out following the SY/T 7309-2016 standard. The analyses of the HSR samples were conducted at a temperature of 24°C and a humidity of 20% using a Varian Cary-Eclipse particle luminometer under atmospheric pressure. The instrument specifications were: a flashing xenon lamp was used as the light source. The flashing half-peak width was approximately 2 μs. The peak power was equivalent to 75 Kw. The bandwidth was 1.5, 2.5, 10, and 20 nm. The scanning speed reached 24,000 nm/min. The excitation wavelength was 200–900 nm. The emission wavelength was 200–900 nm.

The QGF-E method is an economical and rapid technique used in the oil industry to detect oil content. The QGF-E spectrum represents the fluorescence characteristics of the adsorbed hydrocarbons on the surface of the reservoir particles, which can be used to determine the current oil layer or residual oil layer in exploration and drilling

FIGURE 1 | (A) Location of Junggar basin; **(B)** Location of Jimusar depression; **(C)** Typical stratigraphic column of Jimusar depression; and **(D)** The general lithologic stratigraphy of Jimusar sag.

evaluation. Studies have shown that the QGF-E spectra of the current oil layer or residual oil layer samples have relatively high fluorescence intensities. The fluorescence peak width of heavy oil is approximately 475 nm, and the average value is between 475~600 nm. When the fluorescence spectrum intensity is between 375~475 nm, the QGF-E spectrum intensity of the water layer sample is very low, which is consistent with the fluorescence spectrum of dichloromethane solvent at 320–370 nm. Therefore, the strength of QGF-E can reflect the content of adsorbed hydrocarbons on the surface of reservoir particles, and the content of adsorbed hydrocarbons is positively correlated with oil saturation. The greater the strength of QGF-E is, the higher the oil saturation. The λ_{max} parameter reflects the composition and density of crude oil, while intensity represents oil saturation. When the strength of the QGF-E intensity is higher than 40 PC, there is a confident oil and gas exhibition in conventional sandstone reservoirs (Liu and Eadington 2005).

3.3 Two-Dimensional Nuclear Magnetic Resonance

2D-NMR analysis of all HSR cores was carried out following the SYT-6490-2007 standard. The analysis of the HSR samples was

conducted at a temperature of 24°C, a humidity of 20% and at atmospheric pressure using an MR Cores-XX NMR unconventional core analyzer. The experimental frequency was 23 MHz with a 30 mm diameter probe, and the acquisition dead time was reduced to 15 μs so that the minimum T_2 response of solid organic matter in HSR could be measured.

The T_1-T_2 spectrum is a schematic diagram showing the distribution of different hydrogen atoms in the rock. Previous studies have shown that the T_1-T_2 spectrum can be divided into five signal areas, of which the approximate dividing line is called Zone 1 with T_1 = 10 ms, and is identified as the signal area of solid organic matter. Zone 2 is 0.2 m < T_2 < 1 ms and T_1/T_2 < 100, and zone 3 is T_2 > 1 ms and T_1/T_2 > 10. These latter two zones are considered to be the regions where oil is adsorbed and free oil is present. However, during the test, it was found that these two zones were difficult to distinguish. Zone 4, in the lower-left corner is a compound rich in hydroxyl groups, usually considered a hydroxyl group or a water-bound area, but kerogen may cause area 1 and Zone four to overlap. Finally, the lower right corner of the spectrum is Zone five, which usually signals the presence of free water in the pores or microcracks, but the adsorbed water on the surface of some clay minerals may also increase the signal in this area (Li et al., 2019).
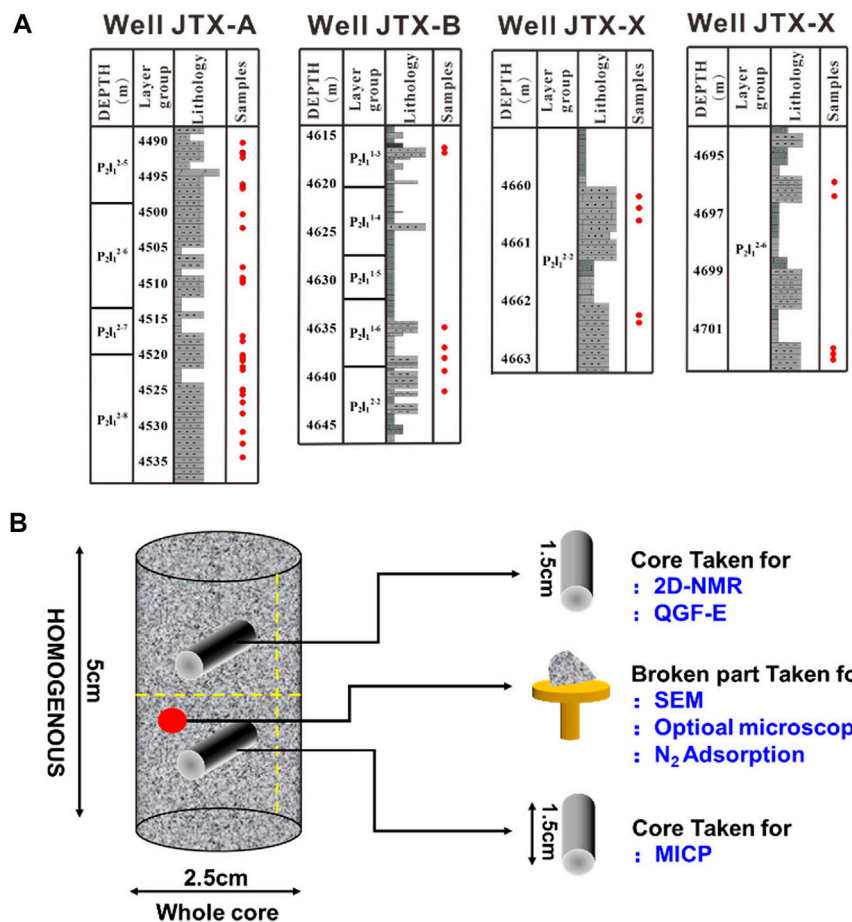
FIGURE 2 | (A) Sample location within each well; **(B)** Schematic diagram of sample processing.

3.4 Other Test Analyses

Low-temperature nitrogen adsorption/desorption analysis of all HSR cores was carried out following the ISO-9277/GB/T19587-2004 standard. The analysis of the HSR samples was conducted at a temperature of 25°C, a humidity of 30~46% and at atmospheric pressure using an American Mike ASAP2460 analyzer. Field emission scanning electron microscopy analysis of all HSR cores was carried out following the GB/T 18295-2001 standard. The analysis of the HSR samples was conducted at a temperature of 26°C, a humidity of 60% and at atmospheric pressure using a FEI Quanta 200F field emission scanning electron microscope. The magnification ranged from × 500 to × 20,000, which corresponds to resolutions of 500 to 12.5 nm.

4 RESULTS

4.1 Lithofacies Types

4.1.1 Mineral Composition and Lithology

The mineral composition of HSR within the Lucaogou is characterized by complexity and heterogeneity (**Figure 3**). Mineral is mainly composed of detrital (feldspar + quartz) and carbonate. P_2l_2

of the sag has a higher clay content than P_2l_1. This may be because P_2l_2 is the cover of the sag. In addition, the pyrite has developed in this area. Since pyrite has conductive properties, it may cause abnormal reservoir resistivity and lead to poor applicability of conventional logging (Xiao et al., 2021). These complex mineral combination characteristics are different from HSR in other basins. This reflect a kind of HSR in the transition between clastic sedimentary rock and chemical sedimentary rock (or the transition between volcaniclastic rock and normal sedimentary rock).

Based on systematic core observations, thin section analysis, and XRD analyses, the lithological characteristics of the western depression area of the Lucaogou Formation in Jimusar are revealed. The results further show that the Lucaogou Formation, which has a shallow lake sedimentary background, can be divided into two parts. The upper part represents a transgression, and the lower part represents the sediment from a regressive system (Qiu et al., 2016). The lithology mainly has the following characteristics in the Lucaogou. It is variable and changes quickly in the vertical direction, and is primarily partitioned in thin interbedded layers. There are various types of minerals, primarily transitional rocks consisting of clastic and chemical rocks. The lithology is divided into more than 20
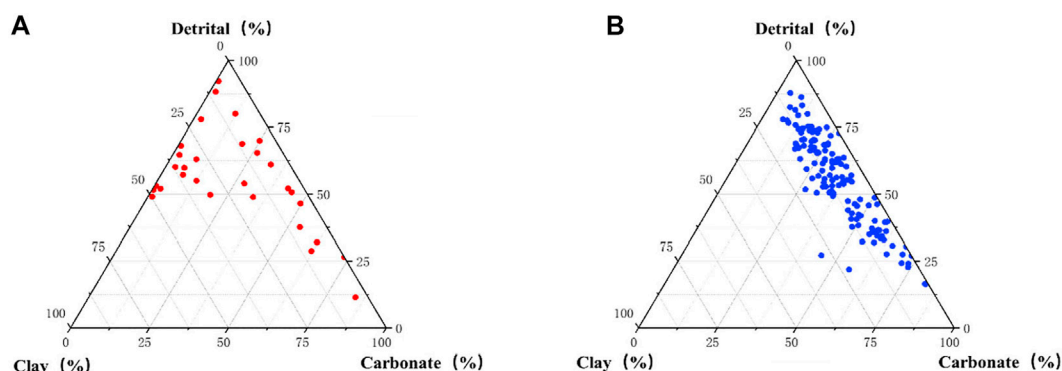
FIGURE 3 | Ternary diagrams of the mineral composition. **(A)** P_2l_2 mineral composition and; **(B)** P_2l_1 mineral composition.
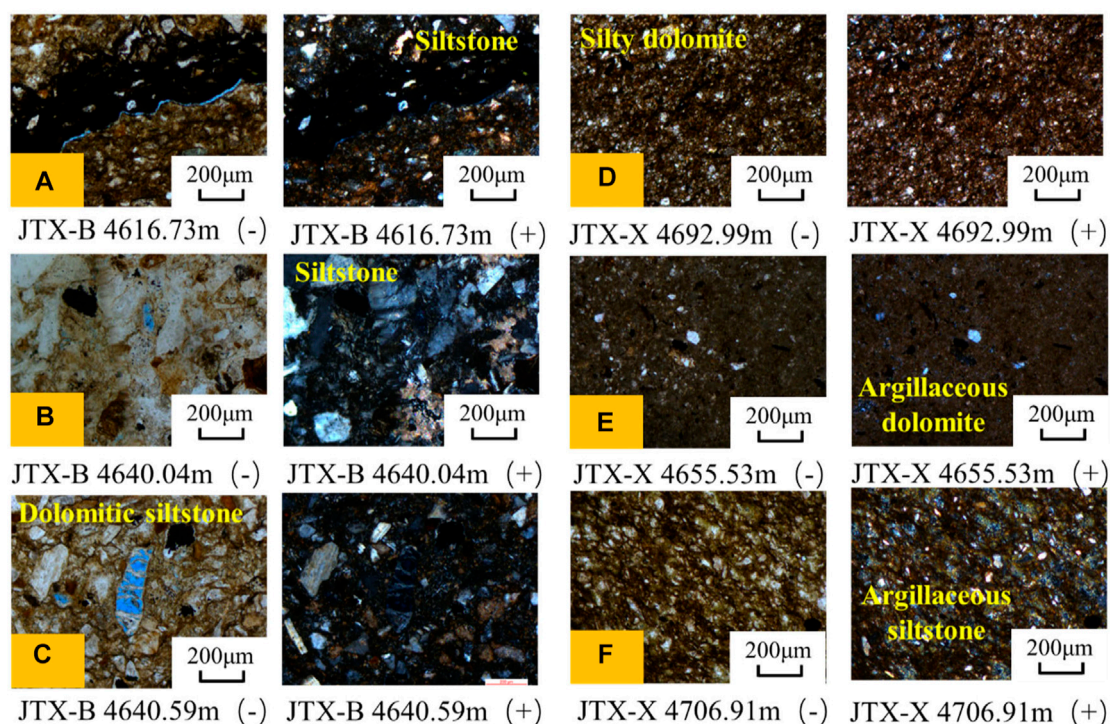
FIGURE 4 | Photomicrographs of reservoir rocks. **(A)** and **(B)** Siltstone; **(C)** Dolomite siltstone; **(D)** Silty dolomite; **(E)** Argillaceous dolomite; and **(F)** Argillaceous siltstone.

categories in the Lucaogou, including the following main lithologies: argillaceous dolomite, silty dolomite, siltstone, dolomitic siltstone, argillaceous siltstone, dolomitic mudstone, and mudstone.
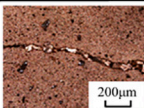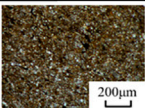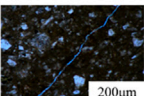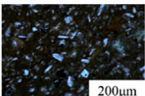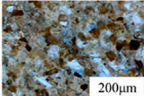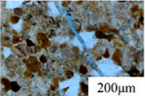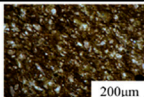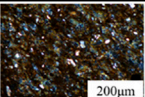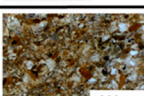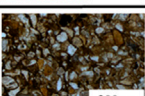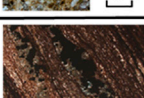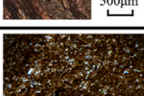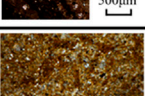
Figure 4 shows that organic matter bands also exist in the siltstone, which may be due to the accumulation of multicomponent mixed sediments. Dolomite siltstone has dissolved pores and shows an uneven suture structure. Silty dolomite exhibits terrigenous clasts and a large amount of organic matter, a small amount of carbon chips, and pyrite, and

the rock is relatively dense. Argillaceous dolomite contains terrigenous clastic, a small amount of asphalt and carbonaceous rocks which are relatively dense, and no pores are observed; argillaceous siltstone is dense with poor physical properties.

4.1.2 Lithofacies
Lithofacies can reflect the accumulation, depositional process, and chemical characteristics (He et al., 2018) of organic matter, and it is a complete manifestation of all essential characteristics of

lithofacies	Sedimentary structure		Observation under the microscope
Massive argillaceous dolomite	Gray-dark and gray, massive, strong compaction		
Massive silty dolomite	Light gray, mixed with dolomite and feldspar, containing a small amount of volcanic ash, belonging to transitional lithofacies		
Massive siltstone	Dark, massive, belonging to sheet sand		
Massive argillaceous siltstone	Gray, massive, belonging to distal sand bar		
Massive dolomitic siltstone	Gray, massive, coarse-grained, belonging to dolomitic sand flat		
Layered mudstone	Dark gray, horizontal laminar layered, belonging to Shallow lake mud		
Massive dolomitic mudstone	Dark gray, massive, belonging to dolomitic mud flat		

FIGURE 5 | Comparison of lithofacies type.

rocks (He et al., 2022). In addition, lithofacies are also the basic unit of HSR reservoirs, which can be used to identify dominant reservoirs. The studies on HSR mainly consist of shale and carbonate rocks. Lithofacies classification of shale is mainly based on the characteristics of mineral composition, structure, biology, and bedding structure (Slatt and Rodriguez 2012). Previous scholars integrated the material composition, sedimentary structure, organic matter characteristics, and other factors such as bioturbation to divide the HSR facies types of the continental lake basin of the Lucaogou Formation in the eastern oblique section of the Jimusar into 26 types (Lin et al., 2021). We found that the HSR reservoirs of the Lucaogou Formation in western Jimusar mainly contain seven lithofacies (**Figure 5**), including massive argillaceous dolomite lithofacies, massive silty dolomite lithofacies, massive siltstone lithofacies, massive argillaceous siltstone lithofacies, massive dolomitic siltstone lithofacies, layered mudstone lithofacies, and massive dolomitic mudstone lithofacies.

Figure 5 shows that massive siltstone lithofacies and massive dolomitic siltstone lithofacies may be the main dominant reservoirs. The cores from these lithofacies are generally gray-black, with thin sections showing grains, microcracks and pores, and the oil-bearing grade are oil trace and oil immersion. Massive
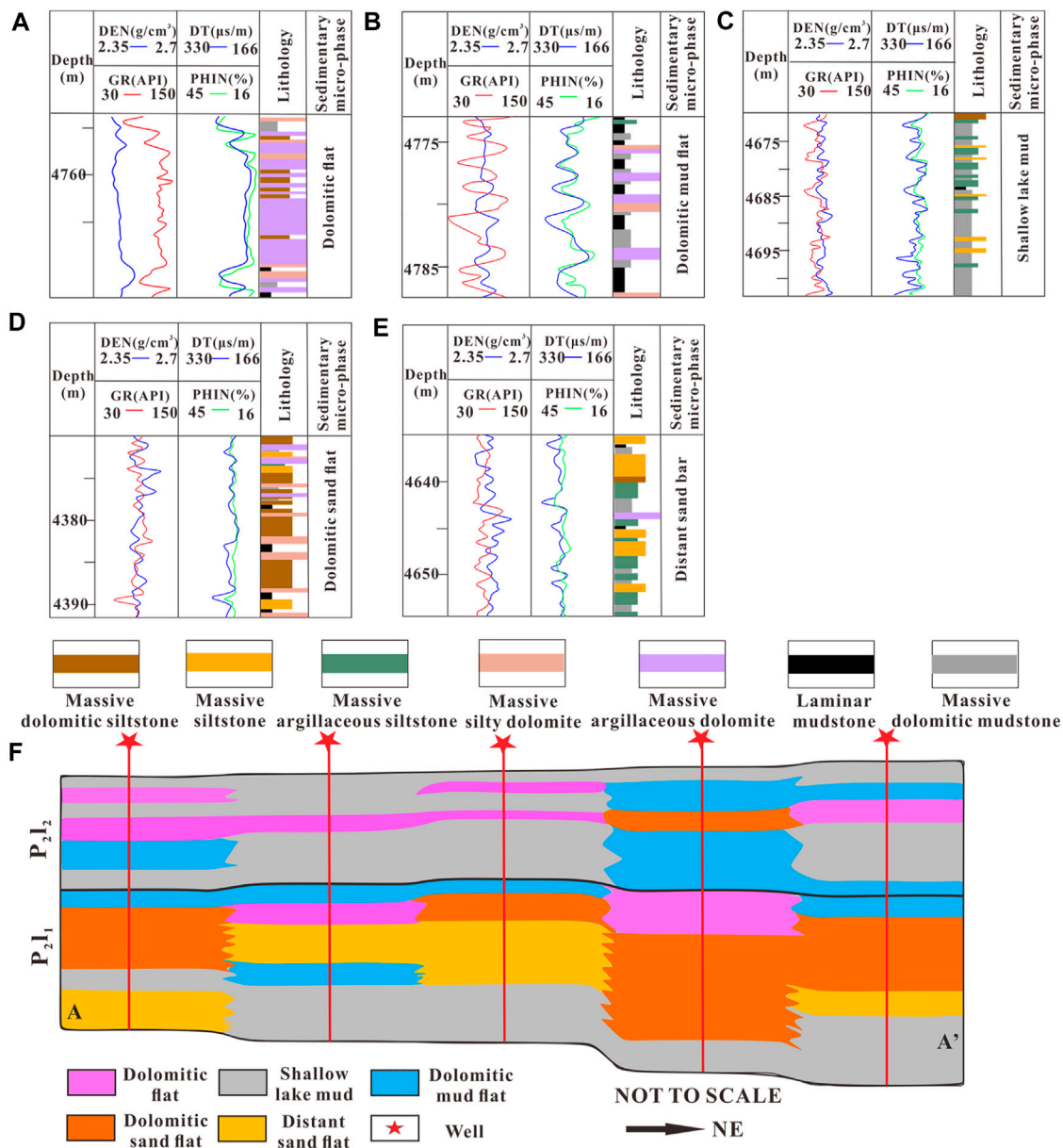
argillaceous siltstone lithofacies are generally gray, with thin sections showing fine-grained features and they belong to distal sand bar microfacies. Massive silty dolomite lithofacies are coarser than the massive argillaceous dolomite lithofacies, and both cores are gray, but the former has cracks. Layered mudstone lithofacies are generally black-gray, with obvious bedding and compact rocks. Massive dolomitic mudstone lithofacies cores are generally black–gray, with undeveloped bedding and dense rocks.

4.1.3 Spatial Distribution of Lithofacies
The HSR reservoir is effectively-identified based on conventional logging data combined with nuclear magnetic logging data and lithology scanning logging data. However, due to frequent interbedded strata, to better reveal the law of lithofacies change of HSR, five types of lithofacies combination of HSR were summarized, according to the lithofacies change characteristics and sedimentary sequence.

Single dolomite lithofacies (**Figure 6A**) refers to a set of strata dominated by dolomite (greater than 50%). The lithofacies is dominated by argillaceous dolomite, with a small amount of silty dolomite and dolomitic siltstone. This lithology type is mainly formed in the coastal dolomitic flat sedimentary environment.

FIGURE 6 | Lithofacies assemblage type of the Lucaogou Formation. (A) Single dolomite lithofacies; (B) Interlayered dolomitic mudstone and dolomite lithofacies; (C) Inter-layered argillaceous siltstone and dolomitic mudstone lithofacies; (D) Dolomitic siltstone and argillaceous sandstone facies; (E) Argillaceous siltstone and siltstone lithofacies; and (F) Northeast-Southwest cross section of the Lucaogou Formation in the Jimusar Sag, Junggar Basin, showing the correlation between the different lithofacies and sedimentary environment.

The hydrodynamic force is weak, and the salinity of the water is high, which is conducive to the precipitation of carbonate minerals. When the hydrodynamic force becomes stronger, it will increase the terrestrial input and develop a dolomite siltstone or silt sandy dolomite interlayer.

Interlayered dolomitic mudstone and dolomite lithofacies is shown in **Figure 6B**. This type of lithofacies is mainly formed in a dolomitic mud flat sedimentary environment. The lithofacies is dominated by dolomitic mudstone interbedded with dolomite, of which mudstone accounts for more than 50%. This type of

assemblage is formed in a relatively deep-water environment, and the salinity of the water is lower, which is not favorable to the formation of dolomite. As the water becomes shallower, if evaporates and the salinity becomes higher, allowing carbonate rocks to locally develop. This type of lithofacies combination makes it difficult to form an effective reservoir.

Interlayered argillaceous siltstone and dolomitic mudstone lithofacies are shown in **Figure 6C**. The lithofacies is dominated by dolomitic mudstone, with thin layers of siltstone and argillaceous siltstone. Dolomite is underdeveloped, and the
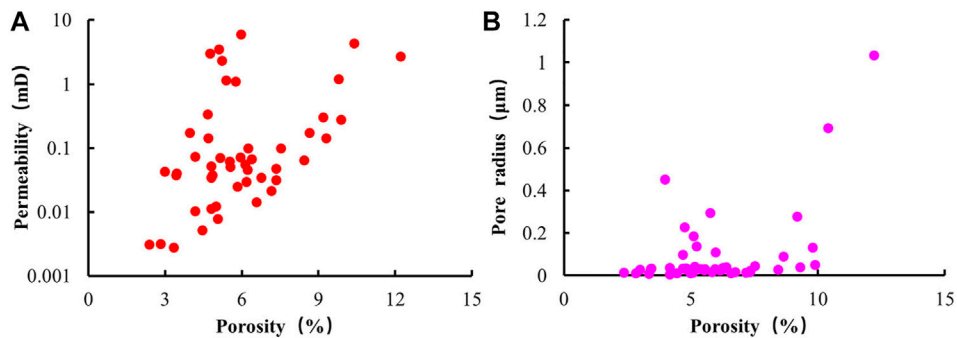
FIGURE 7 | **(A)** The relationship between porosity and permeability; **(B)** The relationship between porosity and pore size.
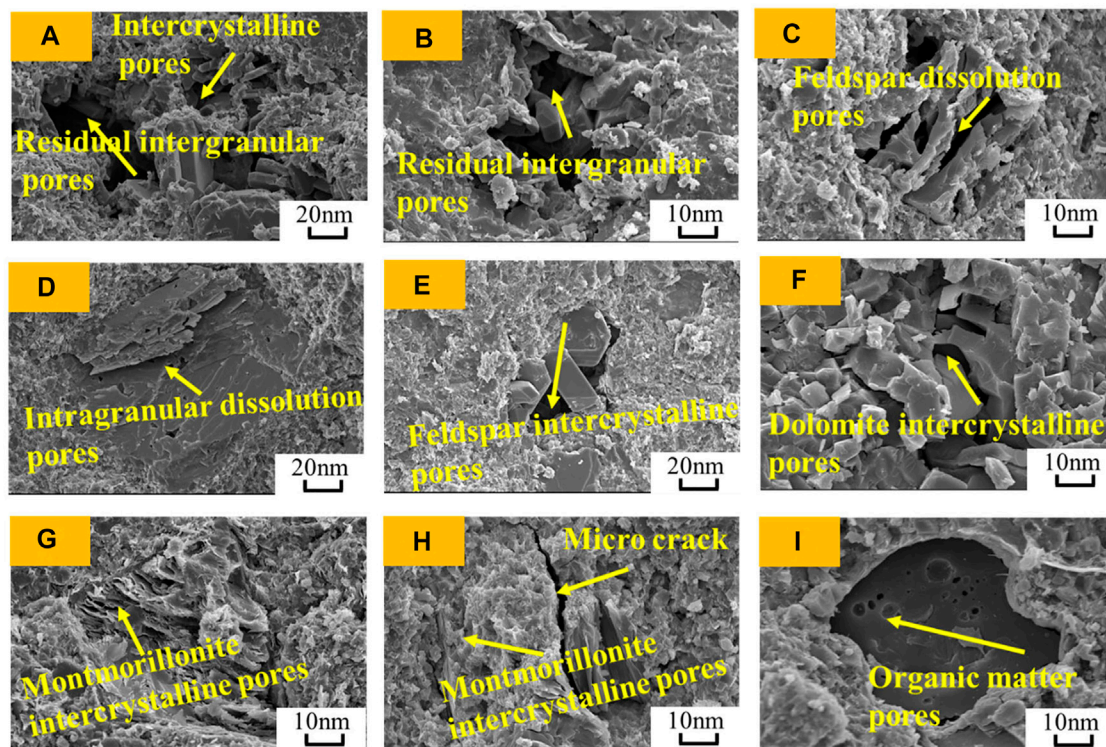
FIGURE 8 | SEM Pore Type Diagram. **(A)** Inter-crystalline pore and residual intergranular pore; **(B)** residual intergranular pore; **(C)** Feldspar dissolution pores; **(D)** Intragranular dissolution pores; **(E)** Feldspar intergranular pore; **(F)** Dolomite inter-crystalline pores; **(G)** Montmorillonite inter-crystalline pores; **(H)** Microcrack and montmorillonite inter-crystalline pores; and **(I)** organic matter pores.

thickness of the mudstone is >50%. This type of lithology is mainly formed in a shallow lake mud sedimentary environment. Similar to the interlayered dolomite mudstone and dolomite lithofacies, it also formed in a deeper water environment, but it was more affected by the source input. Due to the transformation and transportation of lake waves, thin layers of siltstone or argillaceous siltstone can also be formed in a deep-water environment (Kuang et al., 2012). Good reservoirs can be formed in localized areas.

Dolomitic siltstone and argillaceous sandstone lithofacies are shown in **Figure 6D**. Dolomitic siltstone is dominant, and interbedded with silty dolomite and argillaceous siltstone, of which dolomite siltstone accounts for more than 50%. This type of assemblage is mainly formed in the sedimentary environment of the dolomitic sand flat (Zhang et al., 2017). The water has high salinity, the lake wave reformation effect is strong, and the provenance influence is prevalent. Under the dual action of land-source mechanical transportation and chemical
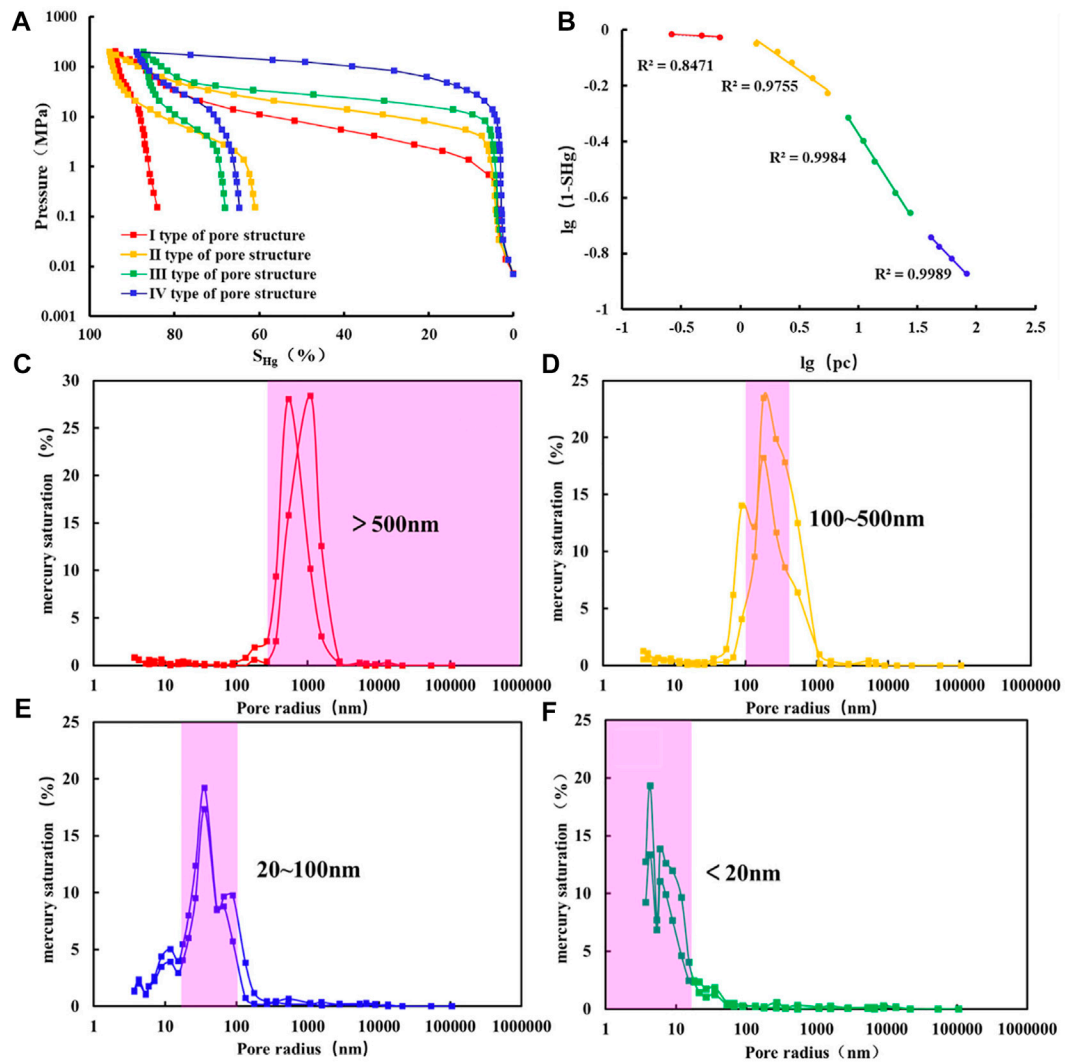
FIGURE 9 | (A) Typical MICP features; (B) Typical MICP fractal features; and (C–F) MICP pore size distribution characteristics.
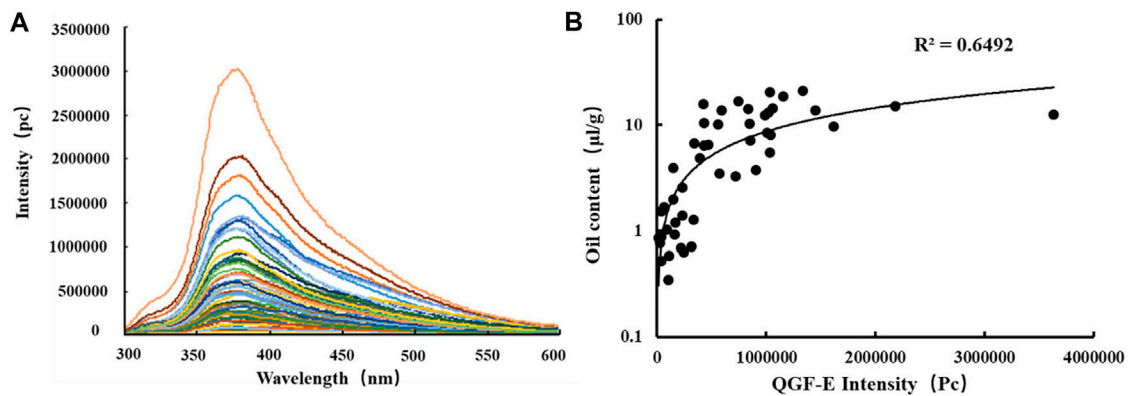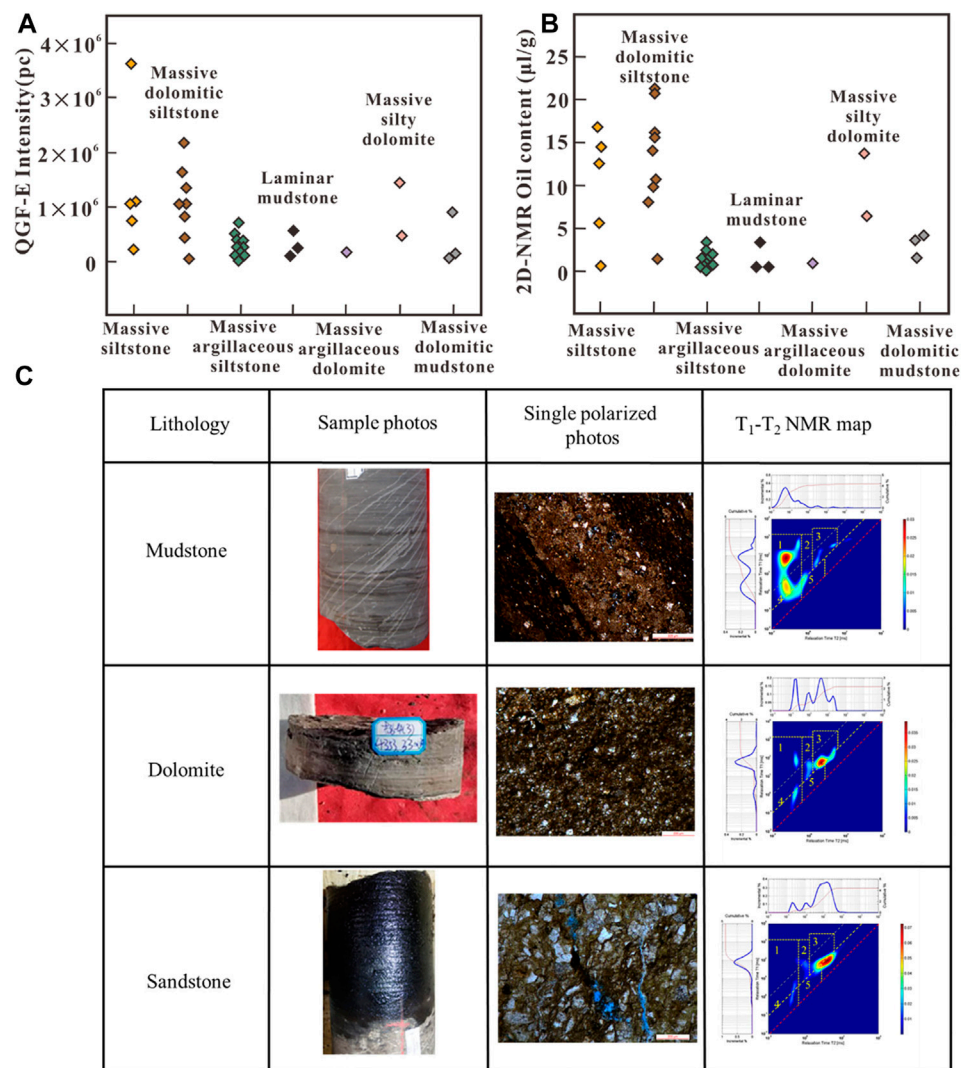

FIGURE 10 | (A) QGF-E analysis; (B) Relationship between oil content and QGF-E intensity.

FIGURE 11 | Oil content analysis of different lithofacies. **(A)** The relationship between lithofacies and QGF-E intensity. **(B)** The relationship between lithofacies and 2D-NMR oil content. **(C)** The relationship between lithofacies and 2D NMR map.

deposition, a large area of clastic-sand flat deposits is formed. This type of combined reservoir is relatively developed and is the main lithofacies involved in oil enrichment.

Argillaceous siltstone and siltstone lithofacies (**Figure 6E**), are mainly composed of siltstone and argillaceous siltstone, with thin layers of argillaceous dolomite and dolomitic siltstone, of which dolomite is <20% and siltstone is >30%. This type of assemblage is formed in the distal sand bar or sheet sand deposits of a delta front, near provenance and with strong wave transformation, which is not conducive to carbonate sedimentation, and the dolomitic content in the rock is low. This type of combined reservoir is also conducive to oil accumulation (Zhang et al., 2019).

Figure 6F shows the lithofacies assemblage cross-section. The result shows that the lithofacies distribution presents the shape of a "sandwich." The lower and upper parts are mainly composed of

interlayered dolomitic mudstone and dolomite lithofacies and interlayered argillaceous siltstone + dolomitic mudstone lithofacies (dolomitic mud flat and shallow lake mud sedimentary environment). The middle is mainly dolomitic siltstone, argillaceous sandstone lithofacies, argillaceous siltstone and siltstone lithofacies (dolomitic sad flat and distal sand bar sedimentary environment). In addition, whole dolomite is mixed with single dolomite lithofacies (dolomitic flat sedimentary environment).

It can be seen from stratigraphic section A to A' in **Figure 6F**, and the position of the stratigraphic section is shown in **Figure 1**. The stratigraphic section shows the depth of the water changing from deep, to shallow, to deep again. The dolomitic mudstone and dolomite interlayer lithofacies developed on the top of P_2l_2 and the bottom of P_2l_1 is
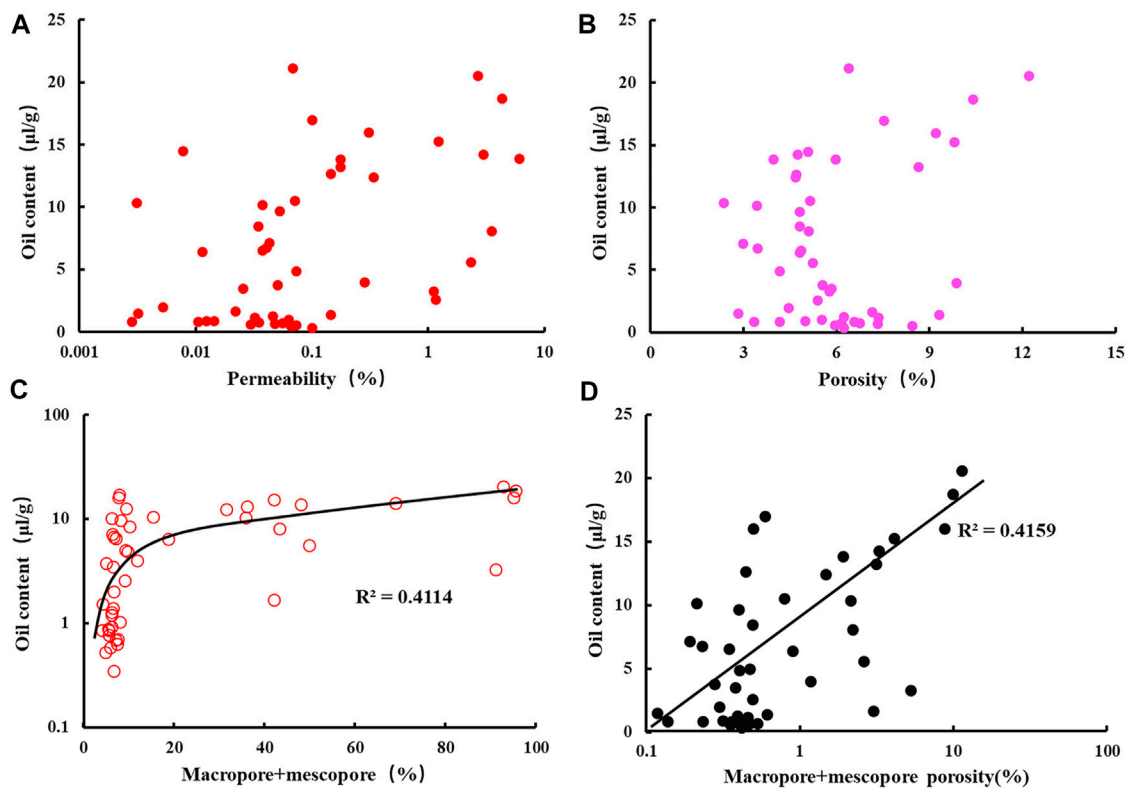
FIGURE 12 | (A) The relationship between permeability and oil content; **(B)** The relationship between porosity and oil content; **(C)** The relationship between macropore + mesopore proportion and oil content; and **(D)** The relationship between macropore + mesopore porosity and oil content.

remains in the sedimentary areas of the shallow lake mud and dolomitic mud flat. It is continuous and thick, and can be used as a roof and floor for capping, thereby effectively preventing the oil generated from the source rock from migrating outwards. The oil generated in the shallow lake mud and dolomitic mud flat sedimentary area can migrate to the dolomitic sand flat and distal sand bar sedimentary areas in the central part, and accumulate to form an oil reservoir close to the source and reservoir. Because of the existence of shallow lake mud and dolomitic mud flat sedimentary areas, siltstone, dolomite, and source rock frequently interbed, and the oil generated from the source rock can also be stored in it, forming a source-reservoir integrated oil reservoir. Among them, the exploration and development prospects of the source-reservoir adjacent oil reservoir may be greater than that of the source-reservoir integrated type.

4.2 Physical Characteristics

Figure 7 shows the basic physical characteristics of the Lucaogou Formation. The results show that the porosity of samples in the western Lucaogou Formation range from 2.36 to 12.21%, and the average porosity is 5.94%. The permeability range is 0.003–6.043 mD, and the average permeability is 0.58 mD. According to the MICP, the pore radius of the core samples range from 0.008 to 1.035 μm, with an average value of 0.098 μm. Overall, the relationship between porosity and permeability is
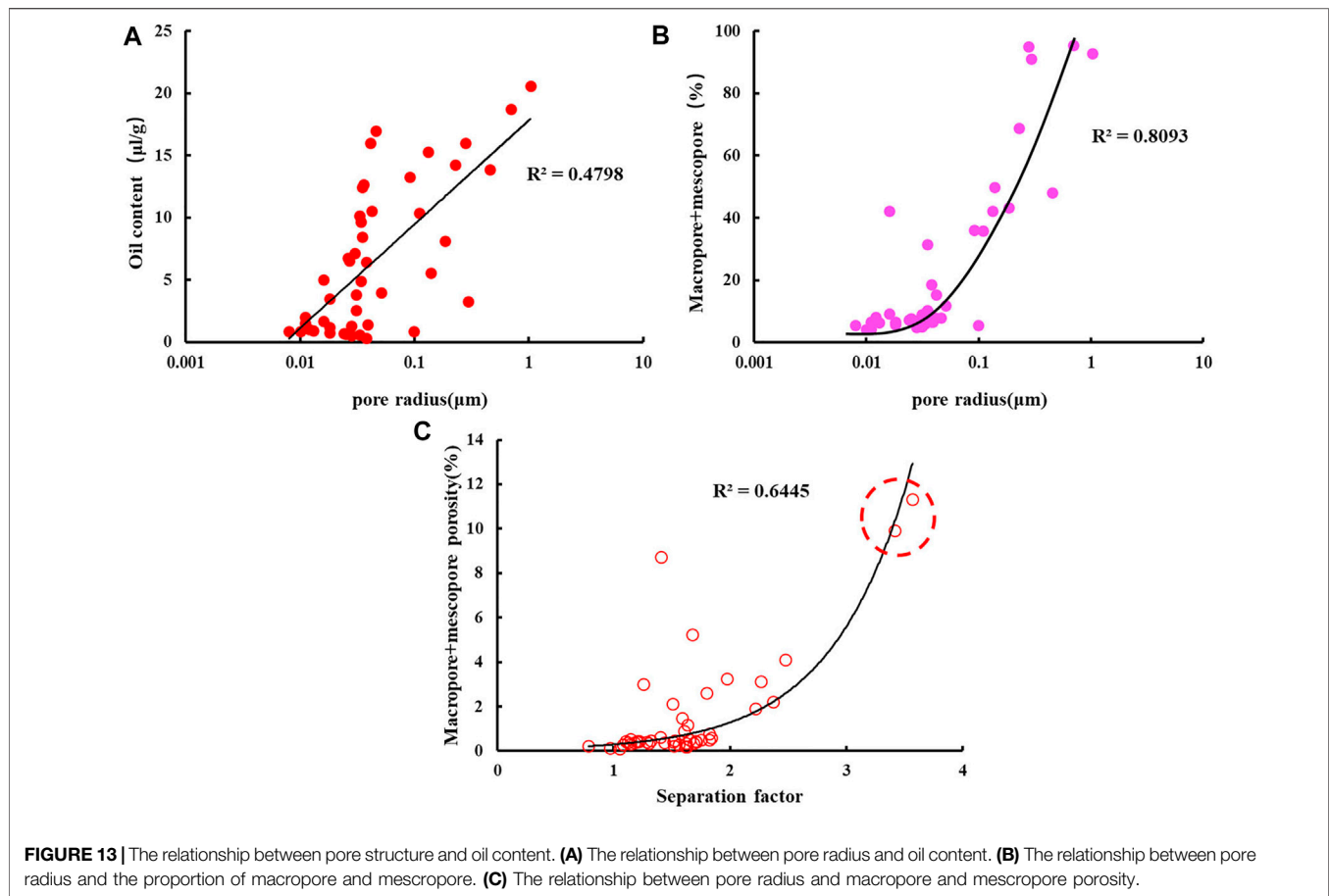
complicated, and there is a poor relationship between porosity and pore radius, mainly due to low porosity and ultralow permeability with typical compact characteristics.

4.2.1 Pore Type

Figure 8 shows a SEM pore type diagram. The results show that HSR develops storage spaces of different scales. According to the genesis of pores, the types of storage spaces are divided into two categories: primary pores and secondary pores. Furthermore, they can be subdivided into five types: residual intergranular pores, intergranular dissolved pores, intragranular dissolved pores, intercrystalline pores, and organic pores. At the same time, there are also local microcracks.

The shape of the residual intergranular pores (**Figures 8A,B**) is mainly elongated, and irregular polygons. The pores remaining mainly after the primary intergranular pores are compacted and cemented, and most of them appear around brittle minerals such as feldspar particles and quartz particles. The pore diameter is usually less than 50 μm, and such pores are mainly developed in the coarse-grained facies.

The shapes of the dissolution pores (**Figures 8C,D**) are mainly long-narrow and jagged, mainly due to pores formed by the dissolution of minerals such as feldspar and dolomite by an acidic liquid. The intergranular dissolution pores have good connectivity, which can significantly improve the physical properties of the reservoir. However, most of the intragranular

FIGURE 13 | The relationship between pore structure and oil content. **(A)** The relationship between pore radius and oil content. **(B)** The relationship between pore radius and the proportion of macropore and mescropore. **(C)** The relationship between pore radius and macropore and mescropore porosity.

dissolved pores have poor connectivity, and whether they improve the reservoir's physical properties is not apparent.

The shapes of the inter-crystalline pores (**Figures 8E–H**) are mainly regular polygons and flakes, mainly formed by the growth of mineral crystals such as dolomite, feldspar, quartz, and clay. Microfractures (**Figure 8H**) are mainly caused by compaction and tectonic stress, which significantly affect the physical properties of the reservoir and are relatively less developed in the area.

Organic pores (**Figure 8I**) are mostly elongated and elliptical, their pore diameters are generally small, and the improvement effect of organic pores on the reservoir's physical properties is not obvious.
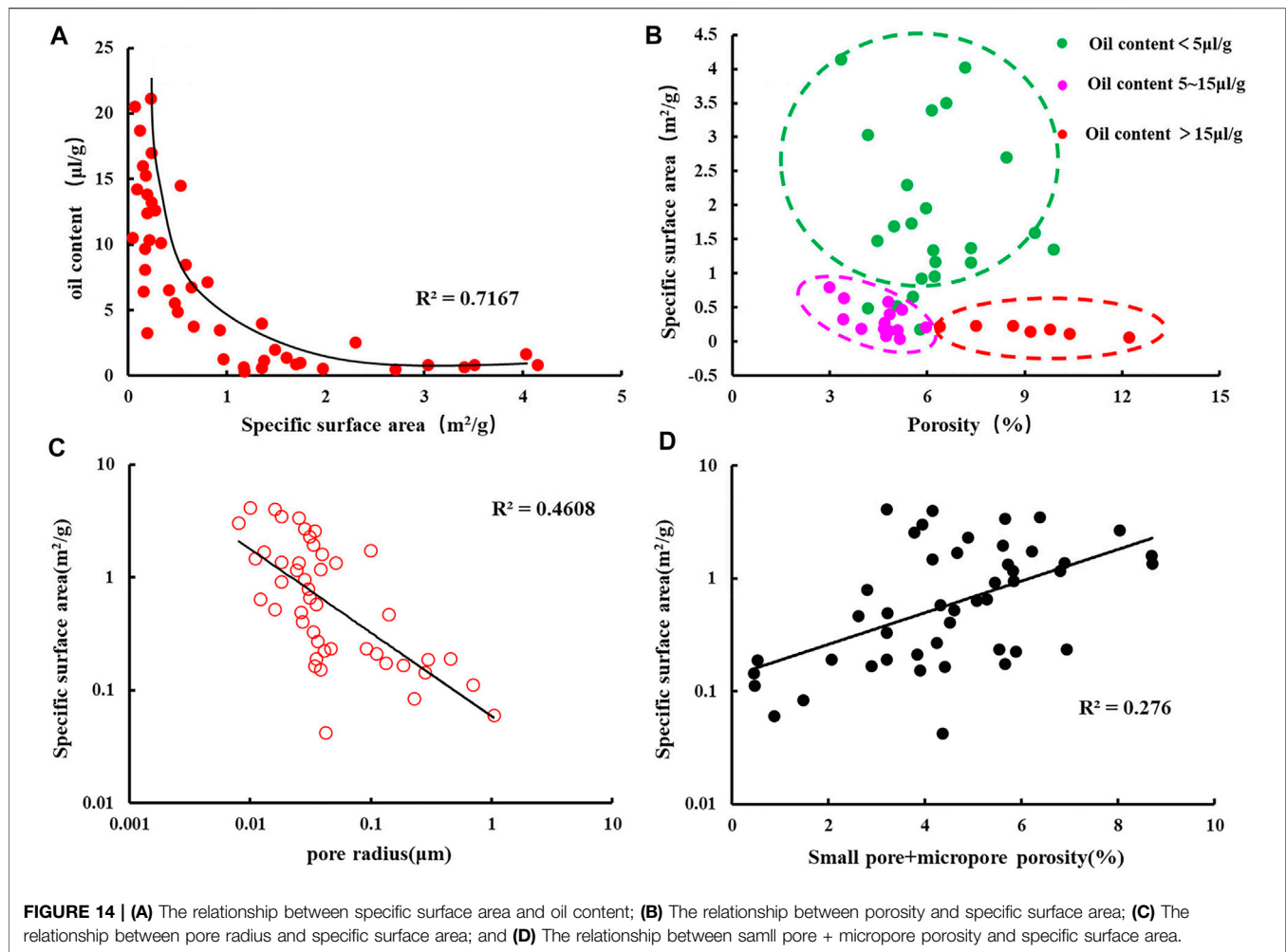
4.2.2 Pore Structure Characteristics
MICP can reveal the pore throat size, connectivity, and sorting information of rocks by recording the process of mercury introduction and mercury withdrawal. The pore throat structure of the HSR reservoir is extremely heterogeneous. The maximum mercury saturation range of the samples is 31.65–97.39%, and the average is 84.98%. The range of the median pore throat radius is 0.006–0.927 μm, and the average is 0.072 μm. The sorting coefficient is between 0.784~3.567, and the average is 1.605.

According to previous studies, pores have self-similarity within a specific scale. (Li et al., 2013). Therefore, fractal theory and cluster analysis can be used to classify pore structure types. Observing the MICP of 47 samples, mercury inflection points generally exist near the three mercury intrusion pressure points of 0.67, 8.25, and 41.33 Mpa (**Figure 9A**). According to the Laplace-Washburn equation, the pore radii corresponding to these three inflection points are 500, 100, and 20 nm. According to fractal theory, these inflection points can be used as the boundaries for pore partitions.

Figure 9B shows that in the lg(1-SHg)-lgpc double logarithmic coordinate system, the mercury intrusion curve of the sample presents a segmented straight line, indicating that the reservoir pore space has multifractal characteristics. The point of intersection of the fractal and the three inflection points of the mercury intrusion curve are consistent with the mercury inlet pressure values. **Figure 9B** also shows that it is reasonable to divide the shale pore space into four intervals using the three inflection points obtained by the MICP injection curve. Macropores (pore radius >500 nm, **Figure 9C**) mainly correspond to pore types such as intergranular pores and intergranular dissolution pores. Mesopores (pore radius 100–500 nm, **Figure 9D**) correspond to intergranular dissolution pores and intragranular dissolution pores, and small pores (pore radius 20–100 nm, **Figure 9E**) mainly correspond to intragranular dissolution pores and inter-crystalline pores.

FIGURE 14 | (A) The relationship between specific surface area and oil content; **(B)** The relationship between porosity and specific surface area; **(C)** The relationship between pore radius and specific surface area; and **(D)** The relationship between samll pore + micropore porosity and specific surface area.

And micropores (pore radius <20 nm, **Figure 9F**) mainly correspond to clay inter-crystalline pores.

4.3 Oil Content

In the QGF-E experiment (**Figure 10A**), after normalizing the sample to 1 g of reservoir particles and 20 ml extraction solution, the fluorescence intensity ranged from at 11,329.2–3,631,111.2 PC, which is significantly higher than the QGF-E intensity of conventional sandstone reservoirs (Downare and Mullins 1995). The result shows a good hydrocarbon-bearing properties. Among them, λmax is between 367–411 nm, showing the characteristics of medium-light oil and a high content of medium components, and the heterogeneity of the oil content is substantial from a longitudinal point of view. 2D-NMR detection also obtained fluid data from the different rock samples. The total fluid volume was 141.81–897.23 μl, with an average of 405.16 μl. The content of hydroxyl group or bound water was 0–14.568 μl/g, with an average value of 3.599 μl/g. The free water content in pores or cracks was 0–3.343 μl/g, with an average value of 0.727 μl/g. The oil content was 0.35–21.162 μl/g, and the concentration was

7.292 μl/g. Among them, the oil content obtained by 2D-NMR has an apparent positive correlation with the strength of QGF-E (**Figure 10B**), which again confirms its excellent oil content.

5 DISCUSSION

5.1 Relationship Lithofacies and Oil Content

Figures 11A,B is the relationship between lithofacies and oil content. The results show that massive siltstone, massive dolomitic siltstone, and massive silty dolomite have higher oil content. Although the massive argillaceous sandstone facies have a relatively coarse grain size, its oil content is relatively low, due to cementation by minerals. Similar to conventional reservoirs, cementation can also damage HSR reservoirs. By observing the thin section, the most of the cementation occurs around the clastic particles, and blocks the intergranular pores. This resulted in the deterioration of the oil content of the massive argillaceous siltstone facies.

The rocks in the sweet spots correspond to massive dolomitic sandstone facies, massive siltstone facies, and massive dolomitic

FIGURE 15 | Oil enrichment geological model of the Lucaogou Formation, Western Jimusar sag.
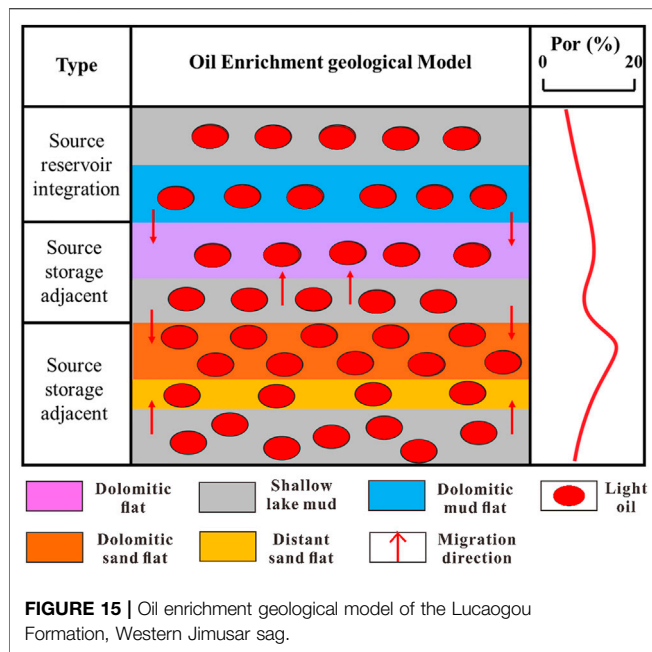
sandstone facies. High-quality source rocks should be layered mudstone facies and massive dolomitic mudstone facies. However, we combined thin sections (**Figure 4A**) and 2D-NMR (**Figure 11C**) to find organic matter in the sandstone facies and dolomite facies, which may be caused by mixed accumulation. Therefore, in addition to mudstone facies, other lithofacies can also have a particular hydrocarbon generation potential. This is one of the most distinct characteristics of HSR.

The mudstone T_1-T_2 map in **Figure 11C** shows a large amount of organic matter and a small amount of oil content in the region 1 and 3, the mudstone facies may be a source-reservoir integrated reservoir. When there is no migration channel around the mudstone facies, the mudstone facies themselves have a small number of pores and can store a certain amount of oil, but the oil content is minimal. The dolomite facies is a transitional facies with moderate physical properties but high oil content in T_1-T_2 map. This may be related to the oil-wetting characteristics of dolomite. Dolomite is oil-wet. Oil is easy to charge when dolomite dominates. Sandstone facies (except for massive argillaceous siltstone) is the best reservoir lithology in this area, with good physical properties and good oil-bearing properties. In addition, it also shows that oil is generated in mudstone facies and migrates a short distance to coarse-grained sandstone facies or to transitional dolomite facies to stay in rich integrated oil reservoirs.

5.2 Influence of Pore Structure on Oil Content

Figures 12A,B is the effect of porosity and permeability on the oil content of the reservoir. The results show that a positive correlation between permeability and oil content is not

apparent. The relationship between porosity and oil content is very complicated and contradictory. Previous studies have shown that porosity is generally positively correlated with oil content (Lu et al., 2012; Li et al., 2015; Hu et al., 2018; Pang et al., 2018). However, other studies have shown that there are two contradictions between large porosity and low oil content and between minor porosity and high oil content (Cao et al., 2017) (**Figure 12B**).

According to the MICP fractal results, the more macropores and mesopores there were, the better the oil content properties of the reservoir. The reason may be related to the difference in wettability of different pore sizes. Previous studies have shown that the Lucaogou Formation HSR reservoir has higher oil saturation. Reservoir wettability is primarily neutral, followed by localized oil-wet (Xu et al., 2019). The surface of the larger pore throats are usually covered by an oil film, which have prominent oil wetting properties. While the relatively small pore throats have no oil film development. This means that macropores are lipophilic and oil-containing, while small pores are hydrophilic and water-containing (Wang et al., 2019; Xu et al., 2019). Therefore, the more macropores and mesopores there are (**Figures 12C,D**), the higher the oil content.

The micropore structure also has an effect on the oil content. Among them, the larger the pore radius is, the higher the oil content (**Figure 13A**). This is because the larger the pore radius is, the weaker the heterogeneity of pores and pore throats, which is more conducive to oil filling (**Figure 13B**). The heterogeneity of the pore structures can be expressed by the sorting coefficient. When the number of medium and large pores increases, the oil content increases linearly (**Figure 13C**). The separation factor is greater than 3 caused by micro-cracks.

5.3 Specific Surface Area Controls The Oil Content

The specific surface area controls the oil content. **Figure 14A** shows that the smaller the specific surface area is, the greater the oil content. **Figure 14B** shows that when the specific surface area is small enough ($A < 1$ m^2/g), the oil content of the sample is positively correlated with the porosity. When the specific surface area of the sample is > 1 m^2/g, the oil content is not related to the porosity. That is, no matter how large the porosity is, the oil content still low.

The specific surface area may affect oil content through pore radius. Pore radius is negatively related to specific surface area (**Figure 14C**). Furthermore, as the specific surface area increases, the number of micropores and small pores increases (**Figure 14D**), and oil filling becomes difficult. Therefore, when the surface area is large, the oil content is low. In this area, the macropores are highly oil-wet and the small pores are highly water-wet. When the proportion of micropores increases, the water-wet of the pore throats will increase, resulting in a decrease in oil content.

We have observed that some samples have large porosity and specific surface area. The proportion of small pores and micropores will increase when the specific surface area

becomes larger. This means that the macroporosity is formed by the accumulation of small pores and micropores. The oil content is not determined only by a single macroscopic physical property, but also by microscopic information such as the abundance of mesopores and macropores, specific surface area comprehensive evaluation.

5.4 An Oil Enrichment Geological Model

In general, the study area has the characteristics of overall oil content. We combined 2D-NMR and QGF-E experimental data to summarize two oil enrichment geological models of the Lucaogou Formation, Western Jimusar sag, Junggar Basin. One of the first, the oil generated in the shallow lake mud and dolomitic mud flat sedimentary areas can be micromigrated to the dolomitic sad flat and distant sand bar sedimentary areas. After accumulation, it is conducive to the formation of "source storage adjacent to the oil reservoirs."

The second of them, when the shallow lake mud and dolomitic mud flat sedimentary areas do not have a migration channel to the dolomitic sad flat and distant sand bar sedimentary areas, the oil generated in the shallow lake mud and dolomitic mud flat sedimentary areas can be accumulated to form a "source reservoir integrated" unconventional oil reservoir (**Figure 15**).

6 CONCLUSION

1) According to the material composition, sedimentary structure, and organic matter characteristics, the HSR in the western depression of the Lucaogou Formation in the Jimusar Sag is divided into seven categories: layered mudstone lithofacies, massive dolomitic mudstone lithofacies, massive argillaceous dolomite lithofacies, massive silty dolomite lithofacies, massive siltstone lithofacies, massive argillaceous siltstone lithofacies and massive dolomitic siltstone lithofacies.

2) Different lithofacies types have clear differences in their reservoir physical properties and oil content. In addition to the lithofacies and pore structure, the oil content is also controlled by the

specific surface area. The oil content of the samples is very low, when the specific surface area exceeds 2 m²/g.

3) Layered mudstone and massive dolomitic mudstone lithofacies have the worst physical properties and oil content properties. However, they do have high organic matter contents and are the main source rocks of the Lucaogou Formation. The massive argillaceous siltstone and massive dolomite lithofacies interbed frequently. Although their physical properties are moderate, oil reservoirs can be formed, due to the adjacent to the source rock. Massive dolomitic siltstone, massive siltstone, and silty dolomite lithofacies have the best physical properties and oil-bearing properties, with the highest proportion of mesopores and macropores. They are the best reservoirs in the Lucaogou Formation.

4) Two types of unconventional oil reservoirs are developed in the western sag of the Lucaogou Formation in Jimusar. Favorable conditions for unconventional oil are formed here, and the resource potential is great.

DATA AVAILABILITY STATEMENT

The original contributions presented in the study are included in the article/Supplementary Material, further inquiries can be directed to the corresponding author.

AUTHOR CONTRIBUTIONS

HX designed the project and wrote the main article. CA and ZD help to draw the figures and to draft the article. DX defined the statement of problem. JY help to discuss the main idea and help to draft the article. GD and PY help to calculate the data and draw the figures. JZ help to revise the figures. All authors reviewed the article.

FUNDING

REFERENCES

Cao, H., Zou, Y.-R., Lei, Y., Xi, D., Wan, X., and Peng, P. a. (2017a). Shale Oil Assessment for the Songliao Basin, Northeastern China, Using Oil Generation-Sorption Method. *Energy Fuels* 31, 4826–4842. doi:10.1021/acs.energyfuels.7b00098

Cao, Z., Liu, G., Xiang, B., Wang, P., Niu, G., Niu, Z., et al. (2017b). Geochemical Characteristics of Crude Oil from a Tight Oil Reservoir in the Lucaogou Formation, Jimusar Sag, Junggar Basin. *Bulletin* 101 (1), 39–72. doi:10.1306/05241614182

Clarkson, C. R., Solano, N., Bustin, R. M., Bustin, A. M. M., Chalmers, G. R. L., He, L., et al. (2013). Pore Structure Characterization of North American Shale Gas Reservoirs Using USANS/SANS, Gas Adsorption, and Mercury Intrusion. *Fuel* 103, 606–616. doi:10.1016/j.fuel.2012.06.119

Downare, T. D., and Mullins, O. C. (1995). Visible and Near-Infrared Fluorescence of Crude Oils. *Appl. Spectrosc.* 49 (6), 754–764. doi:10.1366/0003702953964462

Everett, D. H. (1972). IUPAC Manual of Symbols and Terminology", Appendix 2, Part 1, Colloid and Surface Chemistry. *Pure Appl. Chem.* 31, 578–621. doi:10.1351/pac197231040577

Guo, X., Shen, Y., and He, S. (2015). Quantitative Pore Characterization and the Relationship between Pore Distributions and Organic Matter in Shale Based on Nano-CT Image Analysis: a Case Study for a Lacustrine Shale Reservoir in the Triassic Chang 7 Member, Ordos Basin, China. *J. Nat. Gas Sci. Eng.* 27 (3), 1630–1640. doi:10.1016/j.jngse.2015.10.033

He, C. Z., and Hua, M. Q. (1998). Fractal Geometry Description of Reservoir Pore Structure. *Oil Gas Geology*. 19, 15–23.

He, T., Li, W., Lu, S., Pan, W., Ying, J., Zhu, P., et al. (2022). Mechanism and Geological Significance of Anomalous Negative δ13Ckerogen in the Lower Cambrian, NW Tarim Basin, China. *J. Pet. Sci. Eng.* 208, 109384. doi:10.1016/j.petrol.2021.109384

He, T., Lu, S., Li, W., Tan, Z., and Zhang, X. (2018). Effect of Salinity on Source Rock Formation and its Control on the Oil Content in Shales in the Hetaoyuan Formation from the Biyang Depression, Nanxiang Basin, Central China. *Energy Fuels* 32 (6), 6698–6707. doi:10.1021/acs.energyfuels.8b01075

Hu, T., Pang, X., Jiang, S., Wang, Q., Zheng, X., Ding, X., et al. (2018). Oil Content Evaluation of Lacustrine Organic-Rich Shale with strong Heterogeneity: A Case Study of the Middle Permian Lucaogou Formation in Jimusaer Sag, Junggar Basin, NW China. *Fuel* 221, 196–205. doi:10.1016/j.fuel.2018.02.082

Huang, F. X., Yang, T., and Yan, W. P. (2013). *Geologic Factors of Formation of Tight Oil and its Resource Potential in China*. Pennsylvania: AAPG Annual Convention and Exhibition Pittsburgh.

Jarvie, D. M. (2012). Shale Resource Systems for Oil and Gas: Part 2—Shale-Oil Resource Systems. *AAPG Memoir* 97, 89–119. doi:10.1306/13321447M973489

Jiang, C., Chen, Z., Mort, A., Milovic, M., Robinson, R., Stewart, R., et al. (2016). Hydrocarbon Evaporative Loss from Shale Core Samples as Revealed by Rock-Eval and thermal Desorption-Gas Chromatography Analysis: Its Geochemical and Geological Implications. *Mar. Pet. Geology* 70, 294–303. doi:10.1016/j.marpetgeo.2015.11.021

Jiao, F., Zou, C., and Yang, Z. (2020). Geological Theory and Exploration & Development Practice of Hydrocarbon Accumulation inside continental Source Kitchens. *Pet. Exploration Dev.* 47 (6), 1147–1159. doi:10.3969/j.issn.1672-7703.2018.04.009

Kuang, L., Tang, Y., Lei, D., Chang, Q., Ouyang, M., Hou, L., et al. (2012). Formation Conditions and Exploration Potential of Tight Oil in the Permian saline Lacustrine Dolomitic Rock, Junggar Basin, NW China. *Pet. Exploration Dev.* 39 (6), 700–711. doi:10.1016/S1876-3804(12)60095-0

Li, J., Jiang, C., Wang, M., Lu, S., Chen, Z., Chen, G., et al. (2020). Adsorbed and Free Hydrocarbons in Unconventional Shale Reservoir: A New Insight from NMR T1-T2 Maps. *Mar. Pet. Geology* 116, 104311. doi:10.1016/j.marpetgeo.2020.104311

Li, J., Liu, D., Yao, Y., Cai, Y., and Guo, X. (2013). Physical Characterization of the Pore-Fracture System in Coals, Northeastern China. *Energy Exploration & Exploitation* 31 (2), 267–285. doi:10.1260/0144-5987.31.2.267

Li, J., Lu, S., Chen, G., Wang, M., Tian, S., and Guo, Z. (2019). A New Method for Measuring Shale Porosity with Low-Field Nuclear Magnetic Resonance Considering Non-fluid Signals. *Mar. Pet. Geology.* 102, 535–543. doi:10.1016/j.marpetgeo.2019.01.013

Li, W., Lu, S., Li, J., Wei, Y., Feng, W., Zhang, P., et al. (2021). Geochemical Modeling of Carbon Isotope Fractionation during Methane Transport in Tight Sedimentary Rocks. *Chem. Geology.* 566, 120033. doi:10.1016/j.chemgeo.2020.120033

Li, W., Lu, S., Xue, H., Zhang, P., and Hu, Y. (2015). Oil Content in Argillaceous Dolomite from the Jianghan Basin, China: Application of New Grading Evaluation Criteria to Study Shale Oil Potential. *Fuel* 143 (1), 424–429. doi:10.1016/j.fuel.2014.11.080

Lin, M., Xi, K., Cao, Y., Liu, Q., Zhang, Z., and Li, K. (2021). Petrographic Features and Diagenetic Alteration in the Shale Strata of the Permian Lucaogou Formation, Jimusar Sag, Junggar Basin. *J. Pet. Sci. Eng.* 203, 108684. doi:10.1016/j.petrol.2021.108684

Liu, B., Bai, L., Chi, Y., Jia, R., Fu, X., and Yang, L. (2019). Geochemical Characterization and Quantitative Evaluation of Shale Oil Reservoir by Two-Dimensional Nuclear Magnetic Resonance and Quantitative Grain Fluorescence on Extract: A Case Study from the Qingshankou Formation in Southern Songliao Basin, Northeast China. *Mar. Pet. Geology.* 109, 561–573. doi:10.1016/j.marpetgeo.2019.06.046

Liu, B., Wang, H., Fu, X., Bai, Y., Bai, L., Jia, M., et al. (2019). Lithofacies and Depositional Setting of a Highly Prospective Lacustrine Shale Oil Succession from the Upper Cretaceous Qingshankou Formation in the Gulong Sag, Northern Songliao Basin, Northeast China. *Bulletin* 103 (2), 405–432. doi:10.1306/08031817416

Liu, K., and Eadington, P. (2005). Quantitative Fluorescence Techniques for Detecting Residual Oils and Reconstructing Hydrocarbon Charge History. *Org. Geochem.* 36 (7), 1023–1036. doi:10.1016/j.orggeochem.2005.02.008

Loucks, R. G., Reed, R. M., Ruppel, S. C., and Hammes, U. (2012). Spectrum of Pore Types and Networks in Mudrocks and a Descriptive Classification for Matrix-Related Mudrock Pores. *Bulletin* 96 (6), 1071–1098. doi:10.1306/08171111061

Lu, S., Huang, W., Chen, F., Li, J., Wang, M., Xue, H., et al. (2012). Classification and Evaluation Criteria of Shale Oil and Gas Resources: Discussion and Application. *Pet. exploration Dev.* 39 (2), 268–276. doi:10.1016/s1876-3804(12)60042-1

Lu, S., Li, J., Zhang, P., Xue, H., Wang, G., Zhang, J., et al. (2018). Classification of Microscopic Pore-Throats and the Grading Evaluation on Shale Oil Reservoirs. *Pet. Exploration Dev.* 45 (3), 452–460. doi:10.1016/S1876-3804(18)30050-8

Mount, J. F. (1984). Mixing of Siliciclastic and Carbonate Sediments in Shallow Shelf Environments. *Geol.* 12 (7), 432–435. doi:10.1130/0091-7613(1984)12<432:mosacs>2.0.co;2

Odusina, E., Sondergeld, C., and Rai, C. (2011). An NMR Study on Shale Wettability. in Canadian Unconventional Resources Conference, Calgary, Alberta, Canada, November 2011. doi:10.2118/147371-ms

Pang, H., Pang, X.-q., Dong, L., and Zhao, X. (2018). Factors Impacting on Oil Retention in Lacustrine Shale: Permian Lucaogou Formation in Jimusaer Depression, Junggar Basin. *J. Pet. Sci. Eng.* 163, 79–90. doi:10.1016/j.petrol.2017.12.080

Plint, A. G., MacQuaker, J. H. S., and Varban, B. L. (2012). Bedload Transport of Mud across A Wide, Storm-Influenced Ramp: Cenomanian-Turonian Kaskapau Formation, Western Canada Foreland Basin. *J. Sediment. Res.* 82 (12), 801–822. doi:10.2110/jsr.2012.64

Qiu, Z., Tao, H., Zou, C., Wang, H., Ji, H., and Zhou, S. (2016). Lithofacies and Organic Geochemistry of the Middle Permian Lucaogou Formation in the Jimusar Sag of the Junggar Basin, NW China. *J. Pet. Sci. Eng.* 140, 97–107. doi:10.1016/j.jseaes.2018.08.021

Schieber, J. (1990). Significance of Styles of Epicontinental Shale Sedimentation in the Belt Basin, Mid-proterozoic of Montana. *USA. Sediment. Geol.* 69 (3), 297–312. doi:10.1016/0037-0738(90)90055-X

Slatt, R. M., and Rodriguez, N. D. (2012). Comparative Sequence Stratigraphy and Organic Geochemistry of Gas Shales: Commonality or Coincidence?. *J. Nat. Gas Sci. Eng.* 8, 68–84. doi:10.1016/j.jngse.2012.01.008

Song, Y., Luo, Q., Jiang, Z., Yang, W., and Liu, D. (2021). Enrichment of Tight Oil and its Controlling Factors in central and Western China. *Pet. Exploration Dev.* 48 (2), 492–506. doi:10.1016/S1876-3804(21)60040-X

Tian, H., Pan, L., Xiao, X., Wilkins, R. W. T., Meng, Z., and Huang, B. (2013). A Preliminary Study on the Pore Characterization of Lower Silurian Black Shales in the Chuandong Thrust Fold Belt, Southwestern China Using Low Pressure N2 Adsorption and FE-SEM Methods. *Mar. Pet. Geology.* 48, 8–19. doi:10.1016/j.marpetgeo.2013.07.008

Tian, S., Bowen, L., Liu, B., Zeng, F., Xue, H., Erastova, V., et al. (2021). A Method for Automatic Shale Porosity Quantification Using an Edge-Threshold Automatic Processing (ETAP) Technique. *Fuel* 304, 121319. doi:10.1016/j.fuel.2021.121319

Wang, E., Feng, Y., Liu, G., Chen, S., Wu, Z., and Li, C. (2021). Hydrocarbon Source Potential Evaluation Insight into Source Rocks-A Case Study of the First Member of the Paleogene Shahejie Formation, Nanpu Sag, NE China. *Energ. Rep.* 7, 32–42. doi:10.1016/j.egyr.2020.11.099

Wang, E., Liu, G., Pang, X., Li, C., Zhao, Z., Feng, Y., et al. (2020). An Improved Hydrocarbon Generation Potential Method for Quantifying Hydrocarbon Generation and Expulsion Characteristics with Application Example of Paleogene Shahejie Formation, Nanpu Sag, Bohai Bay Basin. *Mar. Pet. Geology.* 112, 104106. doi:10.1016/j.marpetgeo.2019.104106

Wang, J., and Ju, Y. (2015). Organic Shale Micropore and Mesopore Structure Characterization by Ultra-low Pressure N2 Physisorption: Experimental Procedure and Interpretation Model. *J. Nat. Gas Sci. Eng.* 27 (2), 452–465. doi:10.1016/j.jngse.2015.08.003

Wang, J. G., Zhang, D. W., Yuan, J. Y., Li, X., Huang, C. G., and Shi, Y. J. (2019). Characteristics of Reservoir Genesis and Oil-Gas Accumulation in Lacustrine Carbonate in Yingxi Area of Qaidam Basin. *J. China Univ. Mining Tech.* 48 (1), 110–119. doi:10.13247/j.cnki.jcumt.000873

Xiao, D., Gao, Y., Peng, S., Wang, M., Wang, M., and Lu, S. (2021). Classification and Control Factors of Pore-Throat Systems in Hybrid Sedimentary Rocks of Jimusar Sag, Junggar Basin, NW China. *Pet. Exploration Dev.* 48 (4), 835–849. doi:10.1016/S1876-3804(21)60070-8

Xu, L., Chang, Q. S., Yang, K. C., Tao, Q., Wang, S., Fei, L., et al. (2019). Characteristics and Oil-Bearing Capability of Shale Oil Reservoir in the Permian Lucaogou Formation, Jimusar Sag. *Oil Gas Geology.* 40 (3), 536–540. doi:10.11743/ogg20190309

Yang, Y., Qiu, L., Wan, M., Jia, X., Cao, Y., Lei, D., et al. (2019). Depositional Model for a Salinized Lacustrine basin: The Permian Lucaogou Formation, Jimsar Sag, Junggar Basin, NW China. *J. Asian Earth Sci.* 178, 81–95. doi:10.1016/j.jseaes.2018.08.021

Yang, Z., Hou, L. H., Lin, S. H., Luo, X., Zhang, L. J., Wu, S. T., et al. (2018). Geologic Characteristics and Exploration Potential of Tight Oil and Shale Oil in Lucaogou Formation in Jimsar Sag. *China Pet. Exploration* 23 (4), 76–85. doi:10.3969/j.issn.1672-7703.2018.04.009

Zeng, F., Dong, C. M., Lin, C. Y., Tian, S. S., Wu, Y. Q., Lin, J. L., et al. (2021a). Pore Structure Characteristics of Reservoirs of Xihu Sag in East China Sea Shelf Basin Based on Dual Resolution X-Ray Computed Tomography and Their Influence on Permeability. *Energy*, 122386. doi:10.1016/j.energy.2021.122386

Zeng, F., Dong, C. M., Lin, C. Y., Wu, Y. Q., Tian, S. S., Zhang, X. G., et al. (2021b). Analyzing the Effects of Multi-Scale Pore Systems on Reservoir Properties—A Case Study on Xihu Depression, East China Sea Shelf Basin, China. *J. Pet. Sci. Eng.* 203, 108609. doi:10.1016/j.petrol.2021.108609

Zhang, J., Liu, G., Cao, Z., Tao, S., Felix, M., Kong, Y., et al. (2019). Characteristics and Formation Mechanism of Multi-Source Mixed Sedimentary Rocks in a saline lake, a Case Study of the Permian Lucaogou Formation in the Jimusaer Sag, Northwest China. *Mar. Pet. Geology.* 102, 704–724. doi:10.1016/j.marpetgeo.2019.01.016

Zhang, P., Lu, S., Li, J., Xue, H., Li, W., and Zhang, P. (2017). Characterization of Shale Pore System: a Case Study of Paleogene Xin'gouzui Formation in the Jianghan basin, China. *Mar. Pet. Geology.* 79, 321–334. doi:10.1016/j.marpetgeo.2016.10.014

Zhang, S. M., Cao, Y. C., Zhu, R. K., Xi, K. L., Wang, J., Zhu, N., et al. (2018). Lithofacies Classification of fine-grained Mixed Sedimentary Rocks in the Permain Lucaogou Formation, Jimsar Sag, Junggar Basin. *Earth Sci. Front.* 25 (4), 198–209. doi:10.13745/j.esf.yx.2017-5-2

Zhang, Y. Q., Ma, S. Z., Gao, Y., Li, Y., Zhang, J., Wang, L., et al. (2017). Depositional Facies Analysis on Tight Reservoir of Lucaogou Formation inJimusar Sag. *Acta Sedimentol Sinica* 35 (2), 358–370. doi:10.14027/j.cnki.cjxb.2017.02.013

Zhao, J. H., Jin, Z. J., Jin, Z. K., Wen, X., Geng, Y. K., Yan, C. N., et al. (2016). Lithofacies Types and Sedimentary Environment of Shale in Wufeng-Longmaxi Formation, Sichuan Basin. *Acta Petrolei Sinica* 37 (5), 572–586. doi:10.7623/syxb201605002

Zou, C., Yang, Z., Zhang, G., Hou, L., Zhu, R., Tao, S., et al. (2014). Conventional and Unconventional Petroleum "Orderly Accumulation": Concept and Practical Significance. *Pet. Exploration Dev.* 41 (1), 14–30. doi:10.1016/S1876-3804(14)60002-1

The Control of Diagenesis and Mineral Assemblages on Brittleness of Mudstones

Jiazong Du[1,2], Jingong Cai[2]*, Shengxiang Long[1], Bo Gao[1], Dongjun Feng[1], Zeyang Peng[1] and Xiang Zeng[2]

[1]State Key Laboratory of Shale Oil and Gas Enrichment Mechanisms and Effective Development, SINOPEC, Beijing, China, [2]School of Ocean and Earth Science, Tongji University, Shanghai, China

The variation in mineral composition will affect the rock brittleness, thus the change of mineral assemblages during diagenesis has a potential control on the brittleness of mudstones. In this study, thin section, X-ray diffraction (XRD), and Scanning Electron Microscope (SEM) analyses were used to investigate compositional and microscopic features of mudstones. With the enhancement of diagenesis, three mineral assemblages were divided due to the diagenetic evolution of minerals. Quartz, feldspar, dolomite, chlorite, and illite were regarded as brittle minerals and (quartz + feldspar + dolomite + illite + chlorite)/(detrital mineral + carbonate + clay mineral) was defined as the brittleness evaluation index The mudstone brittleness changed slightly during early diagenesis but increased gradually with enhancement of diagenesis in the late diagenesis stage. Quartz and feldspar were scattered above the clay matrix and the contact of grains was limited, therefore, the contribution of detrital minerals to the brittleness was affected by the properties of clay minerals. The diagenetic transformation of clay minerals resulted in the reduction of ductile components (smectite/I-Sm and kaolinite) and increase of brittle components (illite and chlorite), leading to the enhancement of integral rigidity of the mudstones. Meanwhile, the improved crystallization of carbonate in late diagenesis stage enlarged the carbonate grains which resulted in rigid contact between grains. These results highlighted the influence of diagenesis on mudstone brittleness. Therefore, for evaluation of mudstone brittleness, attention should be paid to the diagenesis process besides mineral composition.

Keywords: mudstone, diagenesis, mineralogical assemblage, brittleness evaluation index, Dongying depression

1 INTRODUCTION

Detrital minerals, carbonates, and clay minerals are the main components of mudstones and the various properties of these components have significant effects on mudstone brittleness. The mudstone brittleness was always considered to be affected by the mineral composition (Jarvie et al., 2007). According to the mechanical properties, minerals in mudstone could be divided into brittle and ductile components. Brittle components consisted of quartz and carbonate (Jin et al., 2015; Rybacki et al., 2016; Ye et al., 2020). The methods of evaluating mudstone brittleness were usually based on the brittle mineral content. Jarvie et al. (2007) defined the quartz content as the main factor controlling the brittleness modulus of a shale, and quartz/(quartz + carbonate + clay minerals) was adopted to quantitatively calculate the brittleness (Jarvie et al., 2007). In addition to quartz, Nelson (1985) considered feldspar and dolomite were also the brittle

Formation		Amount	Depth (m)	Well
Shahejie Formation (Es)	First member (Es1)	9	1,255.00–1,295.00	Y16
	Second member (Es2)	34	1958.00–2,773.61	S142
	Third member (Es3)	26	2,867.80–3,848.11	F8/FS1/ L673/N38/ N872/S142
	Fourth member (Es4)	89	3,397.80–5,647.24	F8/FS1/FS2/ L673/NY1
Kongdian Formation (Ek)		10	4,112.44–4,206.30	W46

components and another evaluation method was proposed. An increase in quartz, feldspar, and dolomite was believed to enhance mudstone brittleness and to promote the development of fractures (Rybacki et al., 2016; Iqbal et al., 2018). Conversely, the increase in the relatively ductile clay minerals would reduce the brittleness of mudstones (Rybacki et al., 2016; Wang, 2016). However, recent studies have shown that the content of brittle minerals was not linearly correlated to mudstone brittleness, and ascribed this phenomenon to the influence of diagenesis (Xiong et al., 2018). Therefore, investigating the effects of mineralogical composition on brittleness during progressive diagenesis may allow a better understanding of mudstone brittleness.

Minerals are not in chemical equilibrium with pore water at the time of deposition. During progressive burial, the increase of temperature and pressure lead to the diagenetic changes of

minerals which allow them to approach equilibrium with the diagenetic environment (Bjørlykke and Jahren, 2012). Detrital minerals (e.g., quartz and feldspar) are chemically stable and barely change during diagenesis. Clay minerals, however, are chemically active and sensitive to the surrounding conditions, in this way, the clay mineral transformations resulted from the changes in the diagenetic environment are widespread. Kaolinite is stable at 70–100°C but will transform into illite at higher temperatures if there is a supply of potassium (Mantovani and Becerro, 2010). Meanwhile, smectite illitization and chloritization are important diagenetic processes of mudstones in most sedimentary basins around the world (Velde and Vasseur, 1992; Pelayo et al., 2016). The smectite and kaolinite can adsorb water in the surface or interlayer space, while illite and chlorite contain minor water molecules. The water content and activity have been proved to control the deformability of clay minerals (Fouché et al., 2004), which means that the higher water activity can result in poor mechanical properties (Wen et al., 2015). Therefore, mineral transformations can result in variations of physicochemical properties, such as the brittleness of the mudstones.

For carbonate in Dongying Depression, dissolution-recrystallization and dolomitization of calcite that are occurred during diagenesis could enlarge the grain size and promote the formation of calcite cement (Zeng et al., 2018). In this way, the cohesiveness between mineral grains is enhanced, resulting in transformation of mechanical properties of mudstones from plasticity to brittleness (Bjørlykke and Høeg, 1997). In addition, the diagenetic conditions (e.g., temperature, pressure, pH, ion types and concentration) are changing constantly during burial diagenesis. Since diagenetic transformation facilitates
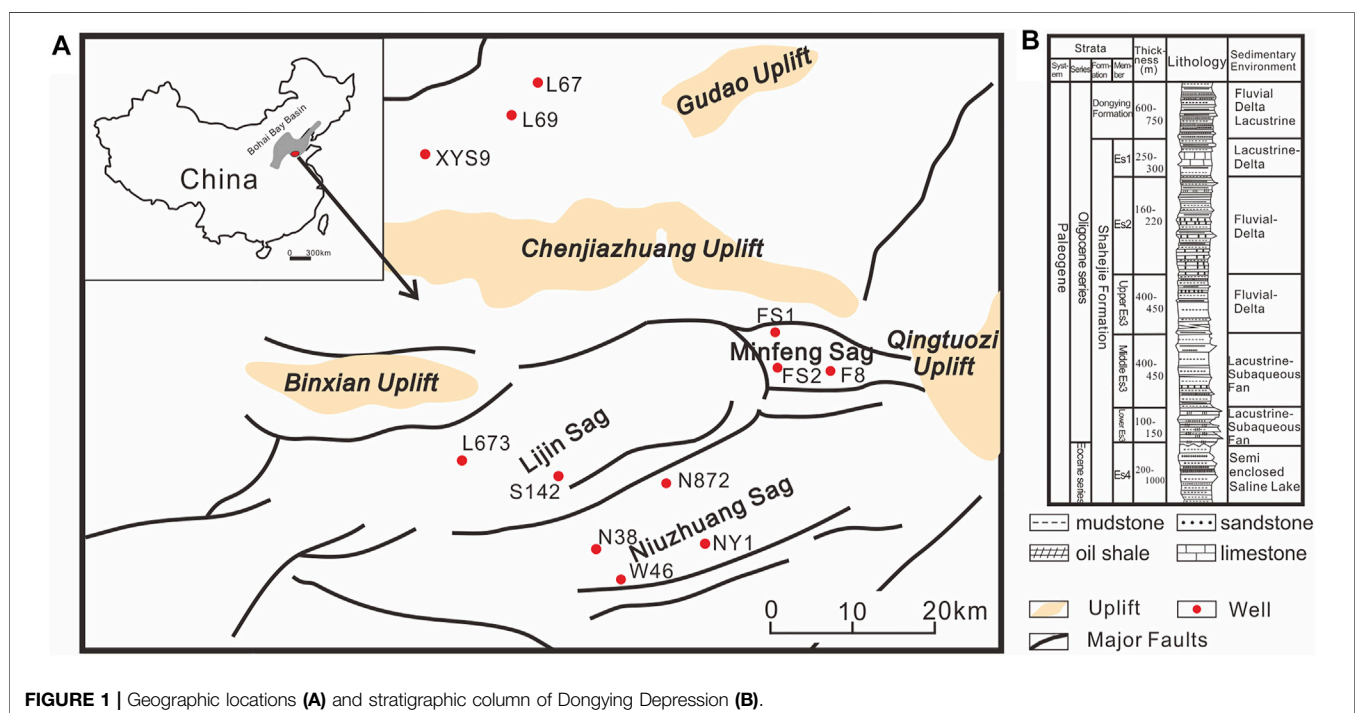
FIGURE 1 | Geographic locations (A) and stratigraphic column of Dongying Depression (B).
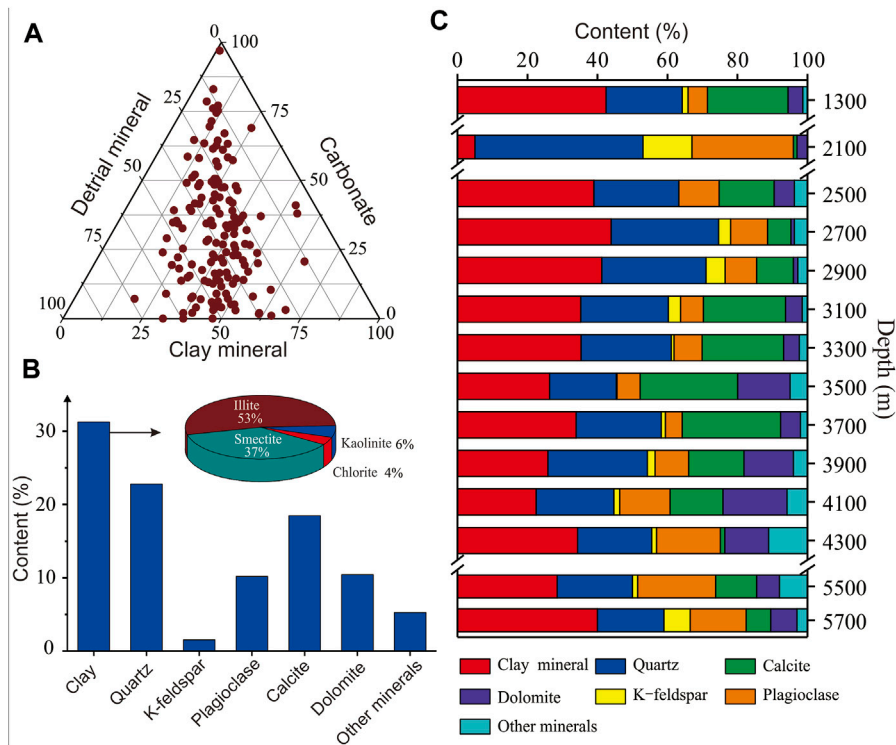
FIGURE 2 | Mineralogical characteristics of mudstones in Dongying Depression. **(A)** Triangular chart of three components in bulk mineralogy; **(B)** Composition of bulk mineralogy and clay minerals; **(C)** Evolution of bulk mineralogy.
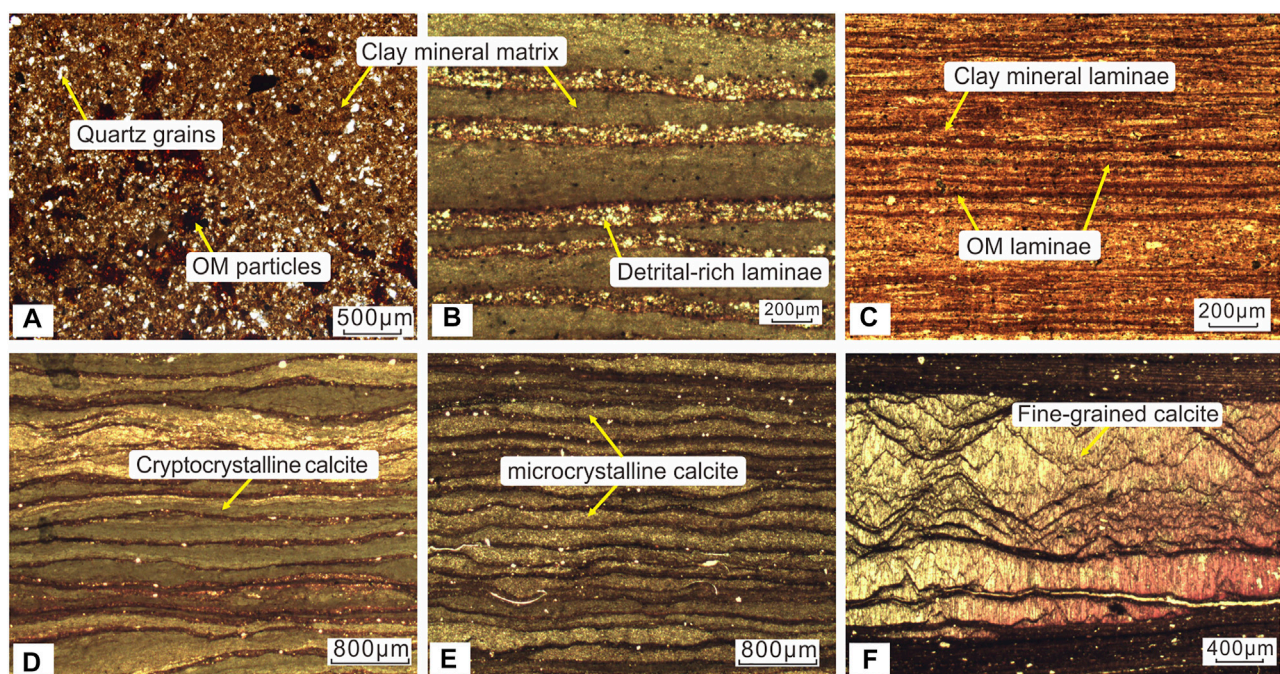
FIGURE 3 | Photomicrographs of various microstructures in samples collected from Dongying Depression. **(A)** massive mudstone. **(B)** laminated mudstone with clay- and detrital-rich laminae. **(C)** laminated mudstone with clay- and OM-rich laminae. **(D)** cryptocrystalline calcite. **(E)** microcrystalline calcite. **(F)** fine-grained calcite.
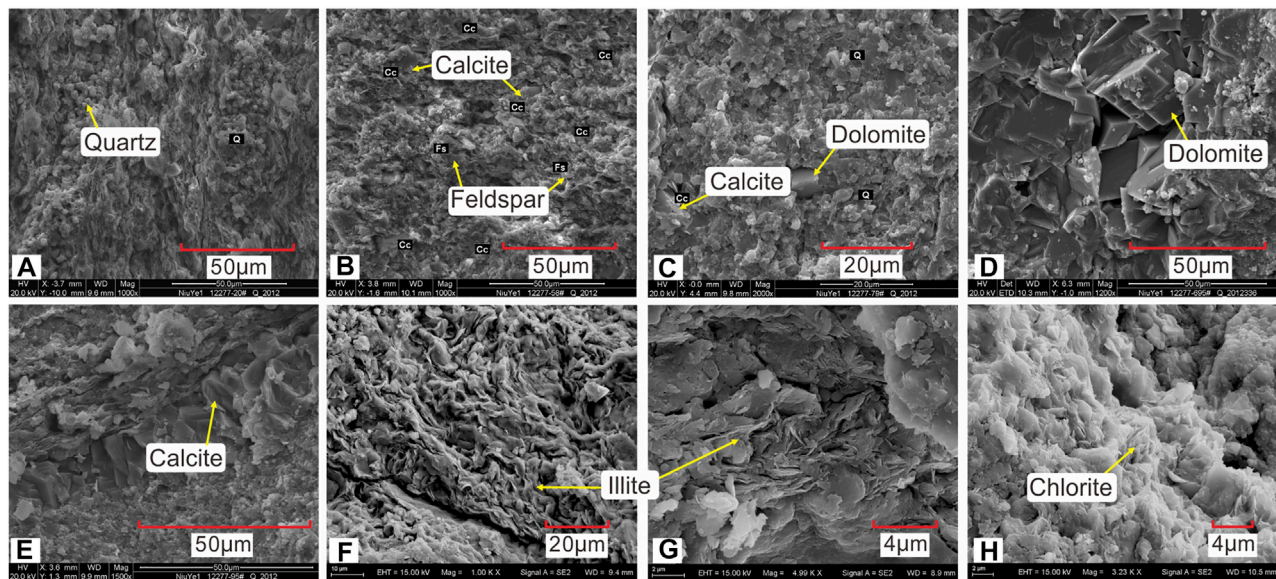
FIGURE 4 | SEM Photographs of mudstone from Dongying Depression. Abbreviations for the minerals are labeled (Q: Quartz; Cc: Calcite; Fs: Feldspar; Ak: Ankerite; I: illite; Ch: Chlorite) **(A)** Quartz crystals fill in the pores (NY1 well, 3,297.03 m). **(B)** Calcite partial dissolves and feldspar exists in the pores (NY1 well, 3,306.62 m). **(C)** Calcite dissolves, authigenous dolomite and small quartz crystals distribute in the pores (NY1 well, 3,312.61 m). **(D)** Dolomite (NY1 well, 3,475.96 m); **(E)** Recrystallized calcite (NY1 well, 3,316.55 m). **(F)** Illite with schistose arrangement (S142 well, 2,677.64 m). **(G)** Illite with schistose arrangement (HK1 well, 3,969.69 m). **(H)** Chlorite is arranged as laminations (HK1 well, 4,019.16 m).

minerals approach equilibrium with diagenetic conditions, specific mineralogical assemblages are formed corresponding to the diagenetic environment (Du et al., 2019). The changes of mineralogical assemblages would inevitably lead to variations in mechanical properties of mudstones. Therefore, investigating the variations of mineralogical assemblages in different diagenetic stages is of great importance for understanding the control of diagenesis on mudstone brittleness.

In this study, mudstones collected from the subsurface of the Dongying Depression (Bohai Bay Basin, NE China) were studied by thin section, X-ray diffraction (XRD) and scanning electron microscopy (SEM) analyses. We investigated the effects of diagenesis on variations in mineralogical assemblages and established a brittleness evaluation index (BEI) with which to monitor changes in brittleness during progressive diagenesis. Correlations between mineralogical components and brittleness were established, and the influence of diagenesis and mineral assemblages on mudstone brittleness were discussed. The study will contribute to the design of mudstone fracture schemes and to the selection of appropriate injection fluids during shale oil or gas development projects.

2 MATERIALS AND METHODS

A total of 168 mudstones from 10 wells (**Table 1**) in the Dongying Depression were collected (**Figure 1**). The samples were

recovered from depths of 1,255.00–5,647.24 m and covered the Shahejie Formation (Es) and Kongdian Formation (Ek) (**Table 1**).

2.1 Thin Section
Samples from well N38 were selected for thin section analysis. The samples were embedded in epoxy resin and sectioned perpendicular to the lamination; the sections were polished using abrasive powder until they reached a thickness of 30 μm. The mineralogical structure and optical properties were then investigated using a ZEISS Axio Imager microscope-photometer under transmitted and reflected white light with magnification of ×50–500.

2.2 X-Ray Diffraction
A Dmax-RA diffractometer was used for XRD analysis which were conducted at 20 mA and 40 kV with CuKα radiation. The bulk mineralogy was analysed using randomly oriented powder samples which were scanned from 3 to 40°2θ. The clay mineral composition of the samples was analysed with oriented slides and multiple treatments: samples were air-dried, glycol-saturated, and heated to 550 °C. The oriented slides were scanned from 3 to 40°2θ at 2°2θ/min with a step width of 0.02°2θ.

2.3 Scanning Electron Microscopy
Samples from wells NY1 and N38 were selected for SEM analysis using a FEI Quanta 200 Scanning Electron Microscope. Prior to SEM analysis, samples were coated with carbon to improve their conductivity, and sample morphology was then analysed at

FIGURE 5 | Variations of mineral contents and mineral assemblages with increasing depth.
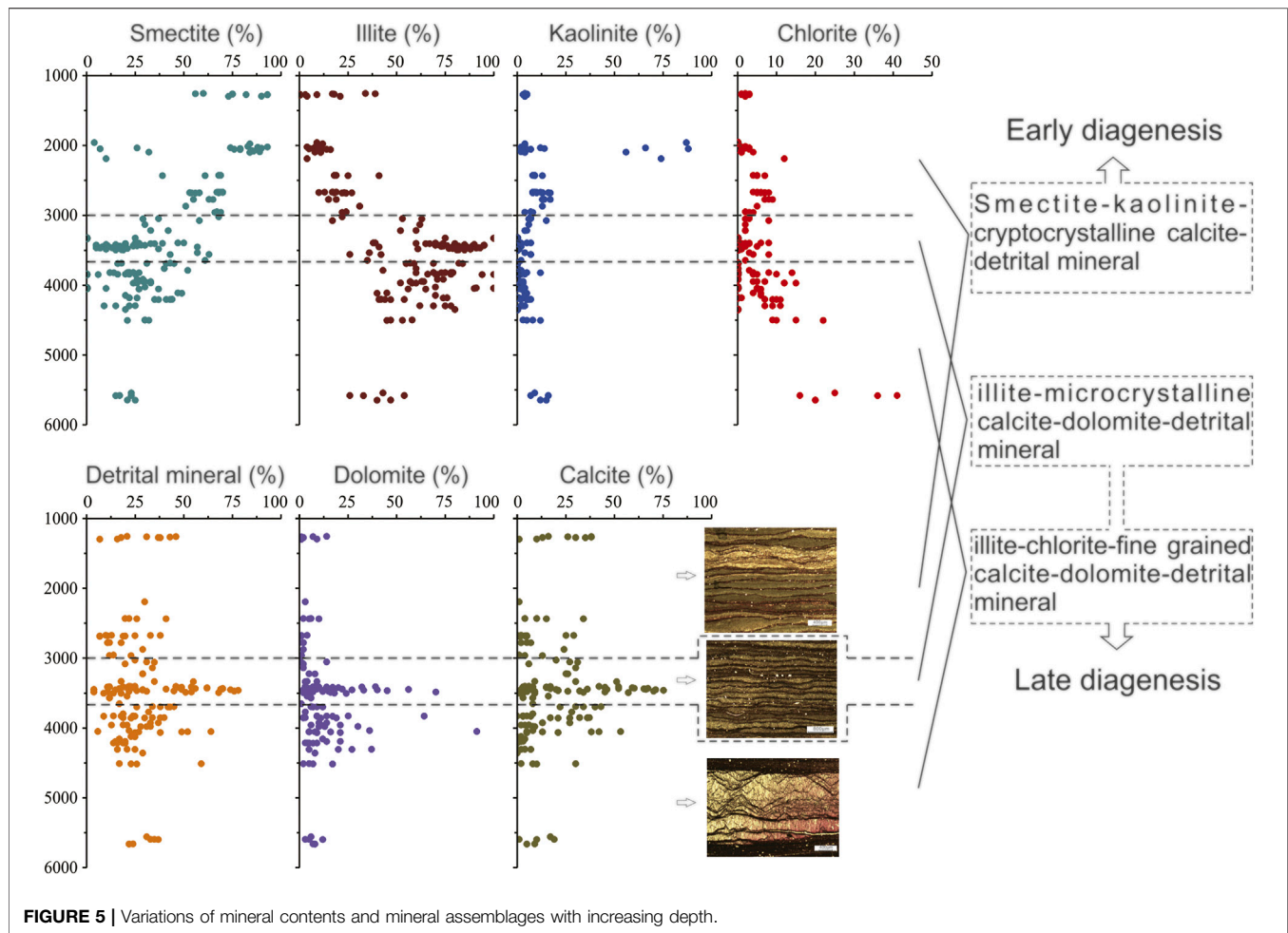
various magnifications to determine the evolution of crystal shape during diagenesis.

3 RESULTS

3.1 Mineral Composition

XRD analysis showed that the mudstones mainly consisted of detrital minerals, clay minerals, and carbonates (**Figure 2A**). Detrital minerals included quartz, K-feldspar, and plagioclase. The quartz content varied little (**Figure 2C**) with maximum and average values of 48 and 23%, respectively. The maximum value of the plagioclase content was 34% with an average of 10%. Only small amount of K-feldspar was present in the samples with an average of 2% (**Figure 2C**). The content of carbonates (calcite and dolomite) varied with depth (**Figure 2C**). The proportion of calcite (average 18%) fell gradually with increasing depth while dolomite (average 10%) increased progressively (**Figure 2C**). Clay minerals had an average content of 31%. Smectite/I-Sm (37%) and illite (53%) were the two main components of the clay minerals, accounting for 90% of the total clay content, while kaolinite and chlorite were present in small proportions (**Figure 2B**).

3.2 Microscopic Characteristics

The depositional fabric of mudstones was either massive or laminated microstructure. Detrital minerals (e.g., quartz and feldspar) were poorly rounded and dispersed within clay matrix (**Figure 3A**). Under SEM, except for some small quartz particles within pore spaces, no well-crystallized quartz and feldspar were observed (**Figure 4A**). In samples with a massive microstructure, clay minerals were present as matrix, on which the organic matter (OM) particles were distributed dispersedly (**Figure 3A**). In laminated mudstone, clay-mineral rich laminae alternated with OM- or detrital-rich laminae (**Figures 3B,C**). Illite showed a schistose morphology (**Figure 4F**) and chlorite typically took the form of rosettes or laminations (**Figure 4H**). As burial depths increased, the crystallinity of illite improved progressively (**Figures 4F,G**).

Two kinds of carbonate were recorded by microscope observations. The first was cryptocrystalline calcite which was distributed as discontinuously banded or lenticular structures. The particles were poorly crystallized and turbid with poor brightness (**Figure 3D**). SEM observations showed that this kind of calcite particles were partially dissolved and coexisted with feldspar particles (**Figure 4B**). The other was sparry carbonate (calcite and dolomite) with large and clear grains

FIGURE 6 | Evolution of BEI in different diagenetic stage.
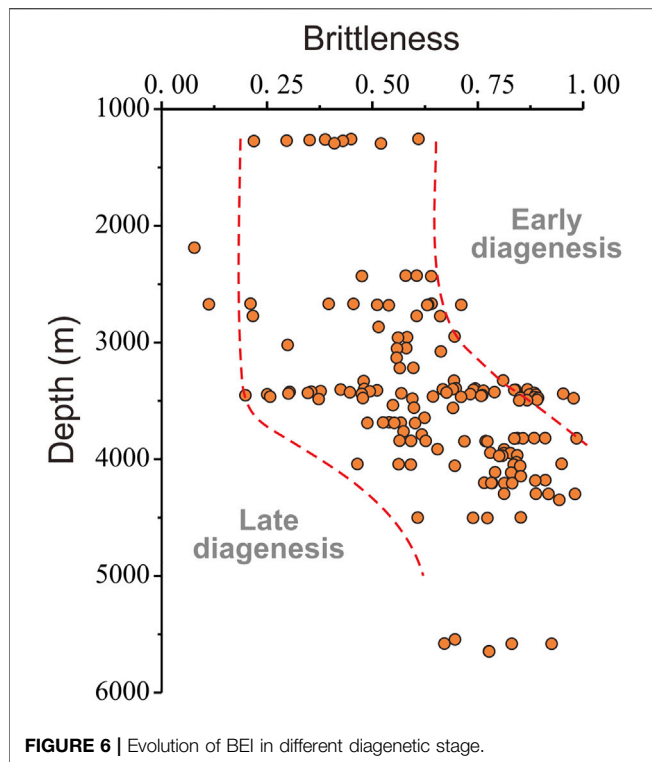
under polarizing microscope (**Figure 3F**), which showed typical crystal morphology and grew among cryptocrystalline calcites. With increasing depth, we could find the enlargement of crystal particles and formation of sparry calcite and dolomite (**Figures**
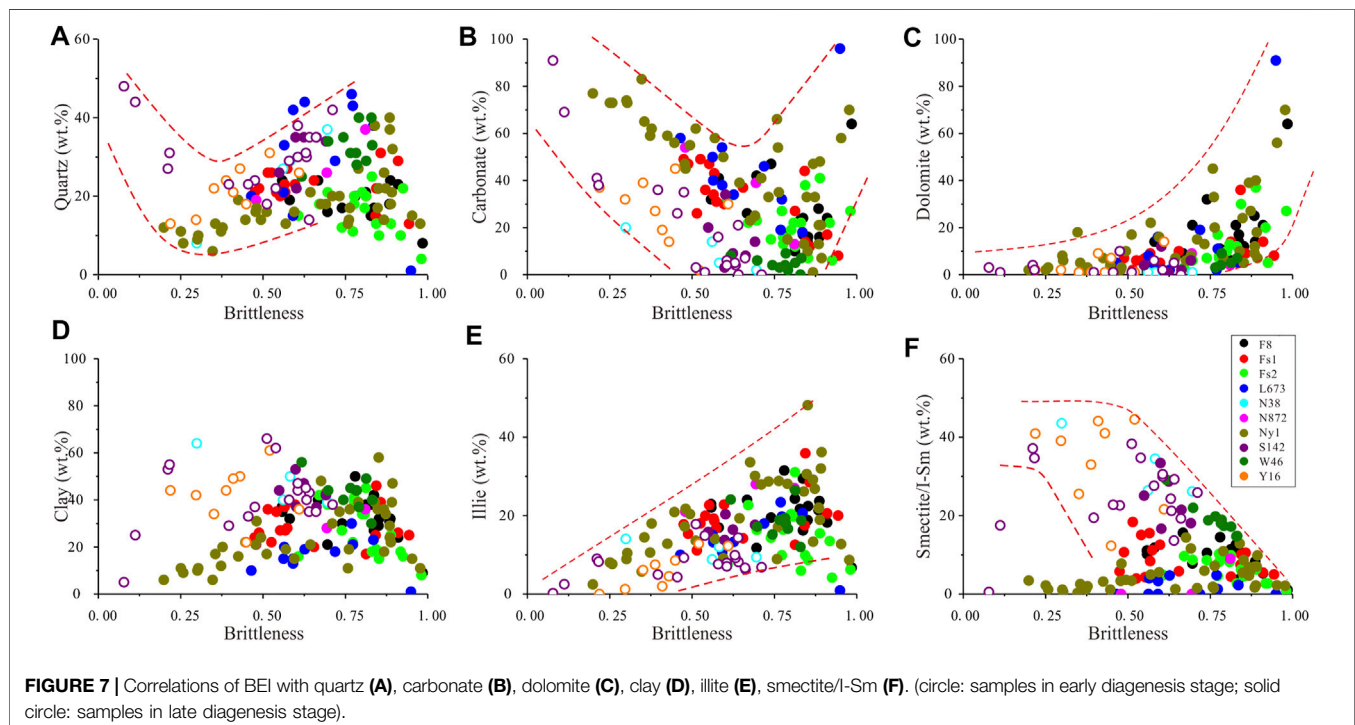
4C–E). Meanwhile, the morphology grew from small crystals into regular and large crystals with enhancement of diagenesis (**Figures 4C–E**).
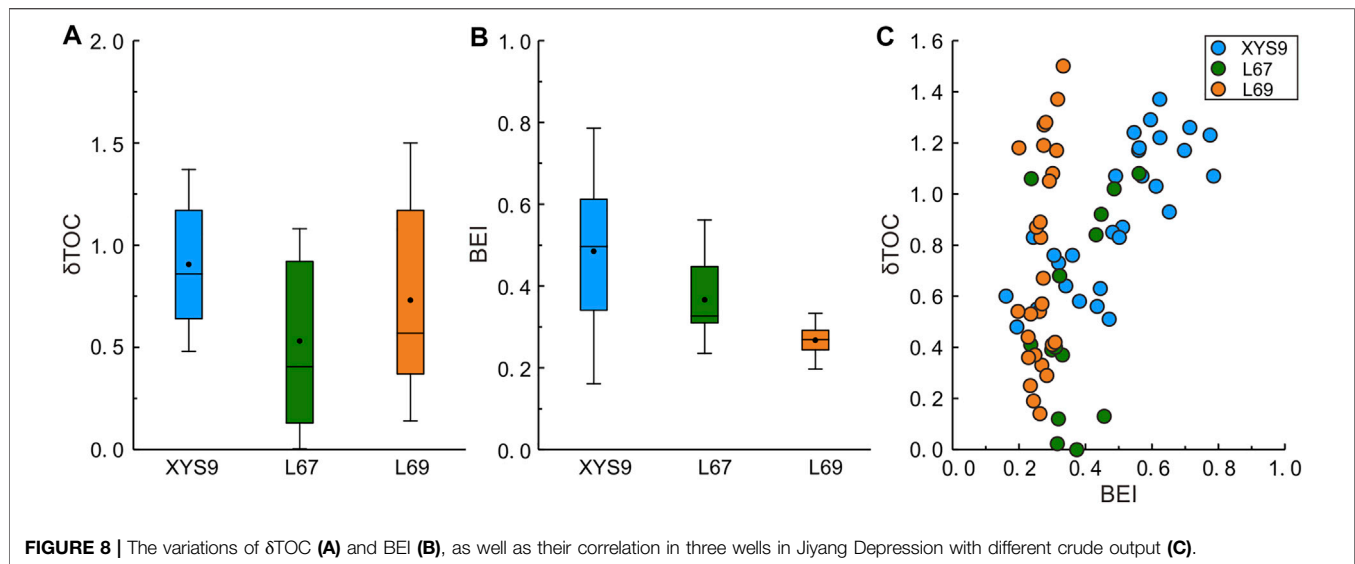
4 DISCUSSION

4.1 Diagenetic Stages and Mineralogical Assemblages

Detrital minerals in the mudstones were composed of quartz and feldspar with large grains. There was no evident relationship between the content of detrital minerals and burial depth (**Figure 2C**). Under SEM, only small quartz particles were observed in pores (**Figure 4**). Previous studies have shown that most of the detrital minerals in mudstones in the Dongying Depression were of terrigenous origin (Zeng et al., 2018). Due to their low chemical activity and relatively stable nature, quartz and feldspar were not significantly affected by the external environment during burial diagenesis.

Cryptocrystalline calcite was in general present at depths above 3,000 m. The mineral grains were micritic under optical microscope and no impurities were found in the calcite lamina (**Figure 3E**). Well-ordered crystals were hard to find by SEM (**Figure 4B**). The formation of this kind of calcite was generally considered to result from changes of the microenvironment lake by sedimentation of plankton during the high salinity period (Bennett et al., 2012). Cryptocrystalline calcite was little changed during diagenesis, but sparry calcite and dolomite began to appear at burial depths greater than 3,000 m and took the form of clean and bright grains. These grains distributed as lenses and veins within laminae that contained abundant

FIGURE 7 | Correlations of BEI with quartz **(A)**, carbonate **(B)**, dolomite **(C)**, clay **(D)**, illite **(E)**, smectite/I-Sm **(F)**. (circle: samples in early diagenesis stage; solid circle: samples in late diagenesis stage).

FIGURE 8 | The variations of δTOC **(A)** and BEI **(B)**, as well as their correlation in three wells in Jiyang Depression with different crude output **(C)**.

carbonate (**Figure 3F**). Moreover, the dissolution of cryptocrystalline calcite was accompanied by the formation of calcite and dolomite crystals (**Figures 4B–E**). Previous studies have confirmed that primary depositional calcite could be partially dissolved by organic acids, and then recrystallized to form sparry calcite (Wang et al., 2005). In the presence of sufficient Fe and Mg, calcite might then be transformed into dolomite (Krajewski and Wozny, 2009).

Due to large adsorption capacity, clay minerals always associate and flocculate with OM, presenting laminated distributions. Therefore, clay minerals in mudstones initially came from the flocculation deposition during the deposition period (Zeng et al., 2018). Clay minerals were chemically active and prone to transformation, such as smectite illitization and chloritization (Velde and Vasseur, 1992; Pelayo et al., 2016). Further analyses of SEM and XRD revealed that the morphology of illite was mainly composed of schistose aggregates and the crystallinity improved gradually with increasing depth. Furthermore, the illite content was negatively correlated with that of smectite/I-Sm. Chlorite presented in the form of rosette aggregates that appeared in large amounts below 3,700 m. These phenomena proved the existence of transformations among different components of clay minerals.

Driven by thermal dynamics and kinetics, the dissolution-precipitation reaction of minerals would take place and form mineral assemblages that equilibrate with certain temperature and pressure (Bjørlykke and Jahren, 2012). In present study, clay minerals and carbonate had experienced an obvious diagenetic process, resulting in significant variation in content and mineral assemblages (**Figure 5**). For diagenetic minerals, the increase of content had a corresponding relationship with the improvement of grain size and crystallinity. Therefore, the variation of mineral assemblages could not only reflect the changes of mineral composition, but also characterized the diagenesis.

According to the evolution of mineral content and microscopic characteristics, three mineral assemblages were recognised:

1) Above 3,000 m, clay minerals mainly consisted of smectite and kaolinite, with a minor amount of illite and chlorite. Although the amount of carbonate was high, the thin section and SEM showed that the carbonate was mainly cryptocrystalline calcite, which had not undergone diagenetic transformation. The content of detrital minerals was high, forming a smectite-kaolinite-cryptocrystalline calcite-detrital mineral assemblage (**Figure 4**).

2) With increasing depth, transformation of smectite into illite led to a reduction of smectite/I-Sm and an increase of illite. Meanwhile, microcrystalline calcite and dolomite were formed through recrystallization and dolomitization of calcite. The diagenesis resulted in an illite-microcrystalline calcite-dolomite-detrital mineral assemblage.

3) Subsequently, a large amount of chlorite appeared due to chloritization of smectite, and clay minerals were dominated by illite and chlorite. The recrystallization of calcite further improved and fine-grained calcite and dolomite appeared. The mineral assemblage turned into illite-chlorite-fine grained calcite-dolomite-detrital mineral.

4.2 Control of Diagenesis on Mudstones Brittleness

4.2.1 The Influence of Mineral Properties on Brittleness

Quartz and feldspar were in general regarded as brittle minerals (Jarvie et al., 2007). Due to the high brittleness, quartz and feldspar were prone to produce cracks under external force, therefore previous researches hold that the higher content of detrital minerals, the better the brittleness of rock (Rybacki et al., 2016). Detrital minerals in mudstones in the Dongying Depression were mainly of terrigenous origin (Zeng et al., 2018). The grains were distributed upon argillaceous matrix and the contact between grains was limited (**Figure 3A**). Therefore, the effects of detrital minerals on brittleness were also controlled by cementation. In addition, Si that released from crystal structures of clay minerals during smectite illitization

would crystallize into quartz which could act as cement to enhance the rock strength (Metwally and Chesnokov, 2012). Meanwhile, carbonate cementation also promoted the formation of solid rock framework. Therefore, the influence of detrital minerals on brittleness in different diagenetic stages required further analysis.

The clay minerals were traditional considered as plastic components mainly because they would expand and deform through hydration during hydraulic fracturing of mudstones or shale. However, the hydration ability of different clay minerals varies greatly. The expandable smectite which has high cation exchange capacity shows strong water adsorption ability and could adsorb water in interlayer and on external surface. Therefore, the smectite is liable to hydrate and deform plastically. Similarly, kaolinite also shows high hydration capacity and becomes plastic after hydration. However, although illite and smectite are both 2:1 phyllosilicate, illite is not expandable due to the high affinity of interlayer potassium to the structural layers. Therefore, illite does not readily hydrate and deform plastically. The same is true for chlorite. The interlayer space of chlorite is filled with a brucite-like sheet, which determines that chlorite is non-expandable and shows weak hydration. Therefore, smectite/I-Sm and kaolinite were considered as ductile components while illite and chlorite were brittle components. Thus, the varying proportions of different clay minerals would affect the mudstone brittleness. In addition, as clay minerals were matrix of mudstones, the properties of clay minerals would affect the contributions of quartz and feldspar to mudstone brittleness. Therefore, in order to evaluate the mudstone brittleness more accurately, the evolution of clay minerals should be taken into account when analysing the effects of clay minerals.

For carbonate, both calcite and dolomite belong to brittle minerals. However, the crystallinity varied considerably during diagenesis. When cryptocrystalline carbonate was dominated, the mineral grains were small and there was no carbonate cementation (**Figure 3D**), contributing little to the brittleness. While when carbonate presented as microcrystalline or fine-grained particles, the rigid contact between mineral grains was enhanced and the formation of carbonate cement enabled brittle minerals (e.g., quartz and feldspar) to form rock framework. Therefore, investigating the control of carbonate on brittleness required attention to the microscopic characteristics besides the composition.

4.2.2 Control of Mineral Assemblage and Diagenesis on Brittleness

The mineralogy and microscopic characteristics revealed that diagenesis altered the content and properties of minerals, forming different mineral assemblages corresponding to diagenetic environment. Therefore, the brittleness of mudstone was definitely affected by diagenesis and mineral assemblages. In order to investigate the control of diagenesis and mineral assemblages on mudstone brittleness, a BEI was established using brittle mineral content. Based on the mineral properties, quartz, feldspar, dolomite, illite, and chlorite were chosen as the brittle components to calculate the BEI. Therefore, a new expression of mudstone brittleness was proposed:

$$BEI = \frac{W_{QFDIC}}{W_{Tot}}$$

Where the W_{QFDIC} is the weight of quartz, feldspar, dolomite, illite, and chlorite, W_{Tot} is the weight of total minerals. The illite and chlorite content has been converted into relative contents in bulk mineralogy (e.g., illite content = clay mineral content×illite proportion in clay). With the enhancement of diagenesis, the variation of brittleness showed two-stage characteristics (**Figure 6**). Brittleness was basically unchanged above 3,000 m, before increasing steadily below 3,000 m. This trend indicated that evolution of brittleness varied in different diagenetic stages, and the brittleness was enhanced significantly in late diagenetic stage.

In order to further determine the effects of diagenesis on brittleness, the different contribution of each mineral to brittleness in different diagenetic stages was compared by analysing the correlation between each mineral component and BEI. The results showed that although quartz was brittle, its contribution to brittleness varied in different stages (**Figure 7A**). In the early diagenesis stage, which was corresponding to smectite-kaolinite-cryptocrystalline calcite-detrital mineral assemblage, the BEI was reduced progressively although quartz content was high. Although the content of detrital minerals was relatively high, they were distributed in the argillaceous matrix and the grains were matrix-supported, resulting in viscous or plastic mechanical properties of rock. Furthermore, the argillaceous matrix was mainly composed of smectite/I-Sm and kaolinite, which were ductile. These two reasons became the main factors limiting the increase of brittleness and led to the negative correlation of quartz content and BEI. In the late diagenetic stages with illite-microcrystalline calcite-dolomite-detrital mineral and illite-chlorite-fine grained calcite-dolomite-detrital mineral assemblages, quartz content and BEI showed a significant positive correlation, indicating that diagenesis enhanced the contribution of quartz to brittleness. In this period, the Si that released from crystal structure of clay minerals during smectite illitization promoted the formation of quartz (Metwally and Chesnokov, 2012; Cai et al., 2018). The neo-formed quartz could act as cement to connect mineral grains, thus enhancing the brittleness of rock framework (Akinbinu, 2015). The correlation of feldspar with BEI was similar to that of quartz with BEI (**Supplementary Figure S1**).

Similar relationship also occurred between carbonate and BEI. Carbonate was negatively correlated with BEI in early diagenesis, followed by a positive correlation between them in late diagenesis (**Figure 7B**). However, different correlations between dolomite and brittleness were observed, in which weak and high positive correlations occurred in early and late diagenesis, respectively (**Figure 7C**). In the case of same mineral composition, the coarser the grains, the better the mudstone brittleness. In early diagenesis, carbonate was mainly composed of cryptocrystalline calcite with poor automorphism and tiny grains, exhibiting obvious plasticity. With the enhancement of diagenesis, cryptocrystalline calcite partially dissolved under the effects of organic acid, and then recrystallized to microcrystalline and fine-grained calcite or

converted into dolomite in case of presence of Fe and Mg (Wang et al., 2005; Krajewski and Wozny, 2009). In this circumstance, crystallization was improved and mineral grains became larger (**Figures 4C–E**). Meanwhile, the carbonate cementation strengthened the cohesiveness between mineral grains, resulting in transformation of mechanical properties from plasticity to brittleness (Luan et al., 2014). Therefore, there was a two-stage correlation between carbonate and BEI. Dolomite appeared in large quantities and the crystallization improved gradually only in the late diagenesis, leading to the overall positive correlation with brittleness.

Previous studies considered that the increase of clay minerals would reduce the brittleness due to the plasticity of clay minerals (Rybacki et al., 2016; Iqbal et al., 2018). This study, however, found that clay minerals have no correlation with BEI in the whole diagenetic period (**Figure 7D**). This indicated that when using mineral components to analyse brittleness, clay minerals cannot be simply regarded as ductile components. Noteworthy was that illite was well positively correlated with BEI (**Figure 7E**). The illite content were low in early diagenesis stage but high in late diagenesis stage (**Figure 7E**), and the same is true of BEI (**Figure 6**). The positive correlation between illite and BEI highlighted the contribution of clay mineral transformation to the increase of mudstone brittleness. The negative correlation between smectite/I-Sm with BEI also confirmed that smectite illitization affected the brittleness of mudstones (**Figure 7F**). During diagenesis, conversions between clay mineral components took place due to variation of diagenetic environment (Li et al., 2016). Mudstones are mainly composed of clay minerals, which serve as the matrix and adhesion agent. The transformation of ductile components (e.g., smectite) into brittle components (e.g., illite) would enhance the integral rigidity of the mudstones. Therefore, the diagenesis of clay minerals should be taken into account when investigate the contribution of clay minerals to brittleness of mudstones.

4.3 Comparison of BEI Between Mudstones With Different Crude Output

Samples from three wells in Jiyang Depression with different crude output were collected to compare the BEI values. XYS9 well is a commercial oil flow well with daily crude output of 38.5 t/d, while L67 and L69 are stripper wells with daily oil production of 2.09 t/d and 0.19 t/d, respectively. Zhu et al. (2019) used the δTOC, which equalled to the difference of TOC between the raw and organic solvent extracted mudstones, to characterize the mobile oil content in mudstones. Here the δTOC of these three wells varied slightly (**Figure 8A**). Therefore, the amount of mobile oil content measured under laboratory conditions was not the main control for the different crude output in these three wells. The brittleness of the mudstones affects the hydraulic fracturing effect, which determined whether oil or gas could be successfully extracted. Therefore, brittleness of the mudstones from these three well was evaluated using the BEI parameter. The BEI varied obviously with the variation trend of $BEI_{XYS9} > BEI_{L67} > BEI_{L69}$ (**Figure 8B**). Further analysis of the relation between δTOC and the BEI showed different

characteristics in these three wells (**Figure 8C**). A positive correlation between δTOC and BEI was found in well XYS9: δTOC was low when the brittleness of mudstones was low (BEI<0.5), while the brittle mudstones (BEI>0.5) corresponded to high δTOC. The match of high brittleness and oil content ensured the successful extraction of oil and the formation of industrial oil flow in XYS9 well. While in L67 and L69 wells, although δTOC also had high values, the low brittleness of the mudstones (BEI<0.5) may result in the poor fracturing effect, which inhibited the oil yield of these two wells. Therefore, the effective matching of oil content and brittleness was the key to determine the crude output in the productions process.

5 CONCLUSION

Three mineral assemblages were recognised in mudstones during diagenesis due to the variations of diagenetic environment, thus two diagenetic stages were divided. Above 3,000 m, the early diagenesis corresponded to smectite-kaolinite-cryptocrystalline calcite-detrital mineral assemblage, while below 3,000 m was the late diagenesis, forming illite-microcrystalline calcite-dolomite-detrital mineral and illite-chlorite-fine grained calcite-dolomite-detrital mineral assemblages. Based on the variations of brittle components (e.g., quartz, feldspar, dolomite, illite, and chlorite), a BEI was established to evaluate the mudstone brittleness. According to BEI, the variation of mudstone brittleness showed two-staged characteristics. The mudstone brittleness changed slightly during early diagenesis but increased gradually with enhancement of diagenesis in the late diagenesis stage.

The contribution of brittle minerals to the mudstone brittleness was controlled by diagenesis to some extent. In early diagenesis, quartz and feldspar were scattered above the clay matrix which were mainly composed of ductile components (e.g., smectite/I-Sm and kaolinite). Meanwhile, carbonates were mainly cryptocrystalline, resulting in a failure to form a tightly compacted rock framework. In late diagenesis, clay minerals transformation was noteworthy. In this process, the replacement of brittle illite and chlorite for ductile components and the formation of quartz cement enhanced the integral rigidity of the mudstones. The recrystallization and dolomitization of cryptocrystalline calcite formed microcrystalline or sparry calcite and dolomite. The enhancement of crystallinity resulted in the rigid contact between carbonate grains.

DATA AVAILABILITY STATEMENT

The original contributions presented in the study are included in the article/**Supplementary Material**, further inquiries can be directed to the corresponding author.

AUTHOR CONTRIBUTIONS

JD: Methodology, Investigation, Writing - Original Draft, Formal analysis. JC: Conceptualization, Funding

acquisition, Supervision, Writing - Original Draft. SL, BG, DF, and ZP: Resources, Investigation. XZ: Methodology, Investigation.

FUNDING

REFERENCES

Akinbinu, V. A. (2015). Increasing Effect of Metamorphism on Rock Properties. *Int. J. Mining Sci. Tech.* 25, 205–211. doi:10.1016/j.ijmst.2015.02.007

Bennett, R. H., Bryant, W. R., and Hulbert, M. H. (2012). *Microstructure of fine-grained Sediments: From Mud to Shale.* New York: Springer.

Bjørlykke, K., and Høeg, K. (1997). Effects on Burial Diagenesis of Stress, Compaction and Fluid Flow in Sedimentary Basins. *Mar. Petrol. Geol.* 14, 267–276. doi:10.1016/S0264-8172(96)00051-7

Bjørlykke, K., and Jahren, J. (2012). Open or Closed Geochemical Systems during Diagenesis in Sedimentary Basins: Constraints on Mass Transfer during Diagenesis and the Prediction of Porosity in sandstone and Carbonate Reservoirs. *Bulletin* 96, 2193–2214. doi:10.1306/04301211139

Cai, J., Du, J., Chen, Z., Lei, T., and Zhu, X. (2018). Hydrothermal Experiments Reveal the Influence of Organic Matter on Smectite Illitization. *Clays Clay Miner.* 66 (1), 28–42. doi:10.1346/CCMN.2017.064083

Du, J., Cai, J., Wang, G., Zeng, X., Bao, Y., and Liu, F. (2019). The Effect of Diagenetic Environment on Hydrocarbon Generation Based on Diagenetic mineral Assemblage in Mudstone. *Pet. Sci. Tech.* 36, 2132–2142. doi:10.1080/10916466.2018.1528274

Fouché, O., Wright, H., Le Cléac'h, J.-M., and Pellenard, P. (2004). Fabric Control on Strain and Rupture of Heterogeneous Shale Samples by Using a Non-conventional Mechanical Test. *Appl. Clay Sci.* 26, 367–387. doi:10.1016/j.clay.2003.12.014

Iqbal, O., Ahmad, M., and Kadir, A. a. (2018). Effective Evaluation of Shale Gas Reservoirs by Means of an Integrated Approach to Petrophysics and Geomechanics for the Optimization of Hydraulic Fracturing: A Case Study of the Permian Roseneath and Murteree Shale Gas Reservoirs, Cooper Basin, Australia. *J. Nat. Gas Sci. Eng.* 58, 34–58. doi:10.1016/j.jngse.2018.07.017

Jarvie, D. M., Hill, R. J., Ruble, T. E., and Pollastro, R. M. (2007). Unconventional Shale-Gas Systems: The Mississippian Barnett Shale of north-central Texas as One Model for Thermogenic Shale-Gas Assessment. *Bulletin* 91, 475–499. doi:10.1306/12190606068

Jin, X., Shah, S. N., Roegiers, J.-C., and Zhang, B. (2015). An Integrated Petrophysics and Geomechanics Approach for Fracability Evaluation in Shale Reservoirs. *J. Nat. Gas Sci. Eng.* 20, 518–526. doi:10.2118/168589-pa

Krajewski, K., and Woźny, E. (2009). Origin of Dolomite–Ankerite Cement in the Bravaisberget Formation (Middle Triassic) in Spitsbergen, Svalbard. *PPRes* 30, 231–248. doi:10.4202/ppres.2009.11

Li, Y., Cai, J., Song, M., Ji, J., and Bao, Y. (2016). Influence of Organic Matter on Smectite Illitization: A Comparison between Red and Dark Mudstones from the Dongying Depression, China. *Am. Mineral.* 101, 134–145. doi:10.2138/am-2016-5263

Luan, X., Di, B., Wei, J., Li, X., Qian, K., Xie, J., et al. (2014). "Laboratory Measurements of Brittleness Anisotropy in Synthetic Shale with Different Cementation," in Proceedings of the 2014 SEG Annual Meeting. Denver: Society of Exploration Geophysicists, 3005–3009.

Mantovani, M., and Becerro, A. I. (2010). Illitization of Kaolinite: The Effect of Pressure on the Reaction Rate. *Clays Clay Miner.* 58, 766–771. doi:10.1346/CCMN.2010.0580604

Metwally, Y. M., and Chesnokov, E. M. (2012). Clay mineral Transformation as a Major Source for Authigenic Quartz in Thermo-Mature Gas Shale. *Appl. Clay Sci.* 55, 138–150. doi:10.1016/j.clay.2011.11.007

Nelson, R. A. (1985). *Geologic Analysis of Naturally Fracture reservoirs:Contributions in Petroleum Geology and Engineering.* Houston: Gulf Publishing Company.

Pelayo, M., García-Romero, E., Labajo, M. A., and Pérez del Villar, L. (2016). Evidence of montmorillonite/Fe-rich smectite transformation in the Morrón de

Mateo bentonite deposit (Spain): Implications for the clayey barrier behaviour. *Appl. Clay Sci.* 131, 59–70. doi:10.1016/j.clay.2015.12.033

Rybacki, E., Meier, T., and Dresen, G. (2016). What Controls the Mechanical Properties of Shale Rocks? - Part II: Brittleness. *J. Pet. Sci. Eng.* 144, 39–58. doi:10.1016/j.petrol.2016.02.022

Velde, B., and Vasseur, G. (1992). Estimation of the Diagenetic Smectite to Illite Transformation in Time-Temperature Space. *Am. Mineral.* 77, 967–976.

Wang, G., Ren, Y., Zhong, J., Ma, Z., and Jiang, Z. (2005). Genetic Analysis on Lamellar Calcite Veins in Paleogene Black Shale of the Jiyang Depression. *Acta Sedimentol. Sin.* 79, 834–838. [in Chinese with English abstract].

Wang, H. (2016). Numerical Investigation of Fracture Spacing and Sequencing Effects on Multiple Hydraulic Fracture Interference and Coalescence in Brittle and Ductile Reservoir Rocks. *Eng. Fracture Mech.* 157, 107–124. doi:10.1016/j.engfracmech.2016.02.025

Wen, H., Chen, M., Jin, Y., Zhang, Y., Ge, W., Du, J., et al. (2015). Water Activity Characteristics of Deep Brittle Shale from Southwest China. *Appl. Clay Sci.* 108, 165–172. doi:10.1016/j.clay.2015.02.015

Xiong, Z., Cao, Y., Wang, G., Yang, Z., Shi, X., Zhang, J., et al. (2018). Controlling Effect of Lacustrine fine-grained Sedimentary Rocks Composition on Fracability. *J. China Univ. Mining Tech.* 47, 538–548. doi:10.13247/j.cnki.jcumt.000827

Ye, Y., Tang, S., and Xi, Z. (2020). Brittleness Evaluation in Shale Gas Reservoirs and its Influence on Fracability. *Energies* 13, 388–409. doi:10.3390/en13020388

Zeng, X., Cai, J., Dong, Z., Bian, L., and Li, Y. (2018). Relationship between Mineral and Organic Matter in Shales: The Case of Shahejie Formation, Dongying Sag, China. *Minerals* 8, 222–242. doi:10.3390/min8060222

Zhu, X., Cai, J., Liu, Q., Li, Z., and Zhang, X. (2019). Thresholds of Petroleum Content and Pore Diameter for Petroleum Mobility in Shale. *Bulletin* 103, 605–617. doi:10.1306/0816181617517009

Advantages of publishing in Frontiers

OPEN ACCESS
Articles are free to read
for greatest visibility
and readership

FAST PUBLICATION
Around 90 days
from submission
to decision

HIGH QUALITY PEER-REVIEW
Rigorous, collaborative,
and constructive
peer-review

TRANSPARENT PEER-REVIEW
Editors and reviewers
acknowledged by name
on published articles

Frontiers
Avenue du Tribunal-Fédéral 34
1005 Lausanne | Switzerland

Visit us: www.frontiersin.org
Contact us: frontiersin.org/about/contact

**REPRODUCIBILITY OF
RESEARCH**
Support open data
and methods to enhance
research reproducibility

DIGITAL PUBLISHING
Articles designed
for optimal readership
across devices

FOLLOW US
@frontiersin

IMPACT METRICS
Advanced article metrics
track visibility across
digital media

EXTENSIVE PROMOTION
Marketing
and promotion
of impactful research

LOOP RESEARCH NETWORK
Our network
increases your
article's readership